JOURNAL OF THE ELECTROCHEMICAL SOCIETY

VOL. 130, NO. 10 OCTOBER 1983

JESOAN 130 (10) 1975-2132, 411C-436C

FUTURE MEETINGS

CINCINNATI, OHIO—MAY 6-11, 1984—HEADQUARTERS AT STOUFFERS CINCINNATI TOWERS

The detailed Call for Papers published in the July-November 1983 issues of **This Journal.** Final program published in the March 1984 issue of **This Journal.**

Planned symposia for the Cincinnati Meeting include the following Divisions, Groups, Subcommittees, and subjects: **Corrosion**—General Session; **Corrosion/High Temperature Materials/Energy Technology**—Fundamental Aspects of High Temperature Corrosion; **Dielectrics and Insulation/Electrodeposition/Electronics**—Electrophoretic Deposition; **Dielectrics and Insulation/Electronics**—Thin Films of Tunneling Dimensions; **Electronics/Dielectrics and Insulation**—Second International Symposium on VLSI Science and Technology: Materials for High Speed/High Density Applications, Joint General Session, Joint Recent News Papers Session; **Energy Technology**—General Session; **High Temperature Materials/Dielectrics and Insulation/Electronics**—Ninth International Conference on Chemical Vapor Deposition; **Industrial Electrolytic**—Advances in the Chlor-Alkali and Chlorate Industry, General Session; **Industrial Electrolytic/Energy Technology**—Electrochemistry in Mineral and Metal Processing; **Luminescence and Display Materials**—General Session; **Organic and Biological Electrochemistry**—Biomass Electrochemistry, Electro-Organic Synthesis, Redox Mechanisms and Interfacial Properties of Molecules of Biological Importance. II, General Session; **Physical Electrochemistry**—Ultramicroelectrodes, General Session; **Physical Electrochemistry/Battery/Industrial Electrolytic**—Separators and Membranes; **Physical Electrochemistry/Corrosion/Battery/Energy Technology/High Temperature Materials**—*In Situ* Nonelectrochemical Techniques for the Study of Electrode Reactions; **New Technology/Electrodeposition/Industrial Electrolytic**—Advances in Pollution Monitoring, Pollution Control, and Metal Abatement in Waste Streams; **Luminescence and Display Materials**—Luminescence in Biological and Biomedical Applications, Phosphor Screening.

NEW ORLEANS, LOUISIANA—OCTOBER 7-12, 1984—HEADQUARTERS AT SHERATON HOTEL

The detailed Call for Papers published in the December 1983-May 1984 issues of **This Journal.** Final program published in the August 1984 issue of **This Journal.**

Planned symposia for the New Orleans Meeting include the following Divisions, Groups, Subcommittee, and subjects: **Battery**—High Temperature Fuel Cells, New Developments in Lead-Acid Batteries, Manganese Dioxide Electrode, General Session; **Battery/Physical Electrochemistry**—Solid Electrolyte Materials and Films: Fundamentals and Applications, Lithium Batteries and Nonaqueous Electrolytes; **Battery/High Temperature Materials**—High Temperature Batteries and Materials; **Corrosion**—Transient Techniques in Corrosion Research, Computerized Collection and Analysis of Corrosion Data, Localized Corrosion, General Session; **Corrosion/New Technology**—Corrosion of Nuclear Waste Containers; **Dielectrics and Insulation/Electronics**—Plasma Processing, Multilevel Metal and Insulator Technology for Devices and Packaging, Glass Applications in Electronics; **Dielectrics and Insulation/Corrosion/Electronics/Energy Technology/High Temperature Materials**—Materials and New Processing Technologies for Photovoltaics; **Electrodeposition**—Alloy Deposition, Electrochemical Coatings for Solar Cells, Analytical Techniques for Investigating Electrodeposition Procedures, Surfaces, and Resulting Materials; **Electrodeposition/New Technology Subcommittee**—Electroless (Autocatalytic) Deposition of Metals; **Electronics**—III-V Semiconductors for High Speed Applications; **Electronics/Dielectrics and Insulation**—Process and Device Modeling, Defect/Contamination Control for VLSI, Measurement and Control of Micrometer and Smaller Dimension Structures, Joint General Session, Joint Recent Newspapers; **Energy Technology**—General Session; **Energy Technology/Corrosion/Dielectrics and Insulation**—Reliability and Failure Analysis of Energy Conversion and Storage Devices; **Energy Technology/Organic and Biological**—Electrochemical Aspects of Biological Energy Conversion Processes; **High Temperature Materials/Physical Electrochemistry**—Electronics and Ionic Grain Boundary Transport; **High Temperature Materials/Dielectrics and Insulation/Electronics**—Electromigration of Metals; **Industrial Electrolytic**—Inorganic Synthesis Other than Chlor-Alkali, General Session; **Luminescence and Display Materials**—Electroluminescent Materials and Devices for Display Applications; **Physical Electrochemistry**—Polymeric and Modified Electrodes, Physical Chemistry of Electrolyte Solutions Especially Concentrated Electrolytes, General Session; **New Technology Subcommittee/Corrosion**—Materials Considerations in Prosthetics and Other Implantable Devices; **New Technology Subcommittee/Battery/Energy Technology/Industrial Electrolytic**—High Rate High Power Electrochemical Systems.

TORONTO, ONTARIO, CANADA—MAY 12-17, 1985—HEADQUARTERS AT THE ROYAL HOTEL YORK

The detailed Call for Papers published in the July-November 1984 issues of **This Journal.** Final program published in the March 1985 issue of **This Journal.**

Planned symposia for the Toronto Meeting include the following Divisions, Groups, Subcommittees, and subjects: **Corrosion**—General Session; **Dielectrics and Insulation/Electronics**—Adhesion, Electronic Processes and Defects in Insulators; **Dielectrics and Insulation/Corrosion**—Anodic Oxidation; **Dielectrics and Insulation/Battery/New Technology Subcommittee**—Conducting Organic Polymers; **Electronics**—On-Line Sensors for Process Monitoring, Advances in Packaging for VLSI; **Electronics/Dielectrics and Insulation**—Third International Symposium on VLSI Science and Technology: Processing, Joint General Session, Joint Recent News Papers Session; **Electronics/New Technology Subcommittee**—Robotics for Use in Manufacture of Electronic Devices; **Energy Technology**—Hydrogen Production Storage and Utilization, General Session; **Energy Technology/Battery**—Requirements of Components and Systems for Energy Conversion and Storage Applications; **High Temperature Materials**—Metal Halide Lamp Science and Technology, Ceramics and Turbines; **High Temperature Materials/Corrosion/Dielectrics and Insulation**—Protective Coatings; **High Temperature Materials/Industrial Electrolytic/Energy Technology**—Electrolytic Production of Hydrogen; **Industrial Electrolytic**—Industrial Electrolytic Processes with Fused Salts, Electrochemical Engineering, Advances in Electrodes; **Luminescence and Display Materials**—Luminescence in Amorphous Materials, General Session, Recent News Papers Session; **Physical Electrochemistry**—Electrochemical Techniques for Thermodynamics and Kinetic Measurement, Includes Irreversible Thermodynamics, Physiochemical Hydrodynamics, General Session; **Physical Electrochemistry/Battery**—Electrocatalytic Systems, Methods of Characterization of Battery Electrodes; **Physical Electrochemistry/Energy Technology**—Photoelectrochemical Systems; **Physical Electrochemistry/Organic and Biological Electrochemistry**—Electroanalytical and Spectroelectrochemical Research; **New Technology Subcommittee**—Application of Information Theory to Electrochemical Experimentation.

DISCUSSION——→COMMENTS

When the **Transactions of The Electrochemical Society** was transformed into the **Journal of The Electrochemical Society** in 1950, one bit of the former was carried over, the Discussion Section. As a transaction of a meeting, the discussion was a large and important part of the publication. True enough, it was not a verbatim record of the discussion at the time of the presentation of the paper. It was, in fact, an edited and spruced up version much as that in the Congressional Record. Also, because many listeners thought of what to say only after leaving the meeting, there was opportunity for contributions written at home at leisure—but of course within a specified time limit.

It was the latter aspect which carried over to **The Journal.** It has been possible to provide written comment on any paper published in **The Journal** by submitting short written pieces by a specified date. Material so provided was collected and published in the June and December issues. Prior to publication, authors of the paper being discussed had opportunity to read the comments and respond in print if they wished.

There has been a continuous stream of these contributions over the years. Most have been critical of method, deduction, or originality. The procedure of collecting and holding them, sometimes until a year had elapsed, reduced their topical nature. Over the years the section seems to have become less than vital and certainly has lost the flavor of the discussions in the **Transactions.**

Considering the desirability of maintaining some means of providing a forum, it has been decided to have a section in each issue of **The Journal** labeled "Comments". In this section, we intend to provide readers a means via short pieces, *i.e.,* a column or less, to applaud or dispute or scoff at the papers published in **The Journal.** Space will be provided for one response to each by the author(s). More general, but **Journal**-pertinent, comments may also be accepted for that space.

The portion of each issue to be used will be limited so it is important to be concise, *i.e.,* make the point and stop. Elaboration interferes with the thought processes so brevity with clarity will be appreciated and applauded. Please no polemics, no feuds, no outcry at long held-in anger at the stupidity of others, or the like.

The editorial group hopes this innovation will prove useful and needed and provide a stimulating diversion from our sometimes stilted, formal but most effective, style of writing papers on new forays into our ignorance about nature and its ways.

Norman Hackerman
Editor

JOURNAL OF THE

JOURNAL OF THE
ELECTROCHEMICAL SOCIETY
(USPS 284-140)
ISSN 0013-4651

The JOURNAL OF THE ELECTROCHEMICAL SOCIETY (USPS 284-140) is published monthly by The Electrochemical Society, Inc. at 215 Canal St., Manchester, N.H. 03108. The address for the Executive Offices, Editorial and Advertising Office, and Circulation Department of The Electrochemical Society, Inc., is 10 South Main St., Pennington, N.J. 08534-2896. Subscription to members as part of membership service; subscription to nonmembers $135.00 plus $15.00 for postage outside U.S. and Canada. Single copies $7.00 to members, $12.00 to nonmembers.

Second Class Postage paid at Pennington, New Jersey and at additional mailing offices.

POSTMASTER: Send address changes to THE ELECTROCHEMICAL SOCIETY, INC., 10 South Main St., Pennington, N.J. 08534-2896.

October 1983

ELECTROCHEMICAL SCIENCE AND TECHNOLOGY

TECHNICAL PAPERS

TECHNICAL NOTES

ELECTROCHEMICAL SOCIETY

Vol. 130 • No. 10

SOLID-STATE SCIENCE AND TECHNOLOGY

TECHNICAL PAPERS

Manuscripts submitted to the JOURNAL should be sent in triplicate to the Editorial Office at 10 South Main Street, Pennington, N.J. 08534-2896. They should conform to the revised "Instructions to Authors" available from Society Headquarters. Manuscripts so submitted, as well as papers presented before a Society technical meeting, become the property of the Society and may not be published elsewhere in whole or in part without written permission of the Society. Address such requests to the Editor.

The Electrochemical Society does not maintain a supply of reprints of papers appearing in its JOURNAL. A photoprint copy of any particular paper may be obtained from University Microfilms, Inc., 300 N. Zeeb St., Ann Arbor, Mich. 48106.

Inquiries regarding positive microfilm copies of issues should be addressed to University Microfilms, Inc., 300 N. Zeeb St., Ann Arbor, Mich. 48106.

Walter J. Johnson, Inc., 355 Chestnut St., Norwood, N.J. 07648, have reprint rights to out-of-print volumes of the JOURNAL, and also have available for sale back volumes and single issues with the exception of the last two calendar years.

The JOURNAL OF THE ELECTROCHEMICAL SOCIETY combines the JOURNAL and TRANSACTIONS OF THE ELECTROCHEMICAL SOCIETY. Statements and opinions given in articles and papers in the JOURNAL OF THE ELECTROCHEMICAL SOCIETY are those of the contributors, and The Electrochemical Society, Inc. assumes no responsibility for them.

Claims for a missing issue should be reported within 60 days of normal delivery date to the Circulation Dept., The Electrochemical Society, Inc., 10 South Main Street, Pennington, N.J. 08534-2896.

Notice of a change in address should be sent to the Circulation Dept., The Electrochemical Society, Inc., 10 South Main Street, Pennington, N.J. 08534-2896. Include the mailing label or the number from the mailing label from your previous issue of the JOURNAL to ensure proper identification.

SOLID-STATE SCIENCE (Cont.)

TECHNICAL NOTES

ACCELERATED BRIEF COMMUNICATIONS

REVIEWS AND NEWS

JOURNAL OF THE ELECTROCHEMICAL SOCIETY

ELECTROCHEMICAL SCIENCE AND TECHNOLOGY

OCTOBER 1983

Thermal Energy Generation of LiAl/FeS Cells

D. M. Chen and H. F. Gibbard*

Gould Incorporated, Gould Research Center, Rolling Meadows, Illinois 60008

ABSTRACT

Two independent methods were employed to determine the rate of thermal energy generation in 200 A-hr lithium-aluminum/iron sulfide cells. The first is an indirect method using thermodynamic calculations based on precise measurements of the cell potential as a function of temperature and state of charge, combined with measurements of the overpotential during discharge. The second is the direct measurement of the cell heat generation using a new high temperature battery calorimeter. The results obtained by these two methods are in excellent agreement. The rate of heat generation is 40-50W per cell during the last 30% of discharge at 100A. Under certain conditions the cell reaction, initially exothermic, becomes endothermic and then exothermic again during discharge. This unusual behavior is caused by the formation of intermediate J-phase ($LiK_6Fe_{24}S_{26}C1$) and X-phase (Li_2FeS_2) compounds during the course of discharge.

High temperature lithium-aluminum/iron sulfide batteries are under development for vehicle propulsion, off-peak energy storage, and satellite power applications. Thermal management is an important aspect of design of these batteries because of their high specific energy of more than 100 W-hr/kg and operating temperature of 400°-500°C. From the viewpoint of thermal management, the most important property of a battery is the variation of temperature with position and time, which is caused primarily by the generation of thermal energy within the cells.

The objective of the present work was to determine the rate of thermal energy generation in LiAl/FeS cells as a function of current and depth of discharge. The ultimate goal of this research is to establish a thermal model to predict the temperature at all points within a battery, given the current and terminal voltage of each cell and known initial and boundary conditions. Values of the rate of thermal energy generation are essential to this thermal modeling.

Two independent methods were used to find the rate of thermal energy generation $\dot{q}$. The first, indirect, method was to measure the cell potential E as a function of temperature, and the total overpotential η, and to compute $\dot{q}$ using the thermodynamic equation (1)

$$\dot{q} = I[-T(\partial E/\partial T)_{P,\xi} + \eta] \qquad [1]$$

where I is current, taken as positive for discharge; P is pressure; and ξ represents the progress of the cell reaction. Several studies of the temperature coefficient of the cell potential have been published (2-4). However, none of these covers the desired range of temperature and state of charge with sufficient precision for our purpose.

The use of Eq. [1] for calculating the rate of thermal energy generation is valid only if the cell is thermodynamically reversible, as defined by Gibbs (5). This has not been shown previously for LiAl/FeS cells. Thus, we have also directly measured the heat flow from isothermal cycling cells, using a high temperature calorimeter (6) specially designed for this purpose. Equation [1] is strictly applicable only for isothermal operation. This condition is closely met for all of the calorimetric results reported here. Thermal modeling and experimental measurements of internal cell temperature have shown maximum internal temperature differences of less than 1°C for cells operated at the currents used in our calorimetric work, *i.e.*, 40A or less.

Experimental

200 A-hr lithium-aluminum/iron sulfide cells.—The cells used in the present study were five-plate, prismatic cells. They contained three lithium-aluminum alloy negative electrodes, two iron sulfide positive electrodes, boron nitride nonwoven separators, and molten LiCl-KCl-LiF (62.7, 28.2, 9.1 mol percent, respectively; melting point, 397°C) electrolyte. Figure 1 shows details of the cell construction. The cells weighed approximately 2.5 kg and had exterior dimensions of 21 × 13.3 × 3.2 cm; their theoretical capacity based on FeS content was 200 A-hr. The amounts of the electrode materials and electrolyte in the cells are given in Table I.

Apparatus.—A cylindrical constant-temperature furnace was built to house the LiAl/FeS cell under test. The furnace core was a 304 stainless steel can (height, 46 cm; diameter, 20 cm) surrounded by

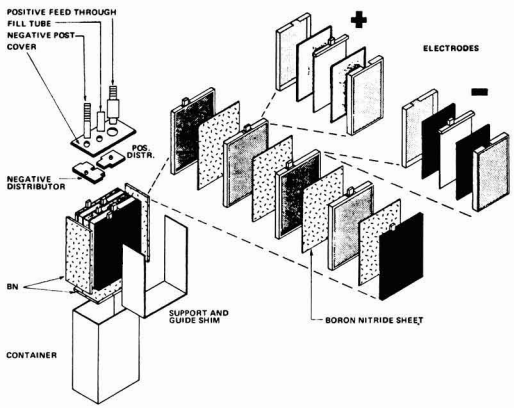

Fig. 1. Five-plate cell construction.

* Electrochemical Society Active Member.
Key words: cell, emf, electrolyte, thermodynamics.

Table I. Masses of components of a 200 A-hr LiAl/FeS cell

Component	Weight, g
Positive electrode	
FeS	185.35
Li_2S	96.74
Fe	129.94
Mo	15.46
C	6.88
LiCl/KCl (eutectic)	134.03
Total positive material	568.40
Negative electrode	
LiAl (18 w/o Li)	237.20
Al	124.80
LiCl/KCl (eutectic)	40.86
Total negative material	402.86
Electrolyte	
LiCl/KCl/LiF (62.7, 28.2, 9.1 mol percent)	536.90

three electrical mica band heaters (Tempco Electric Heater Corporation, Schiller Park, Illinois). This inner container was centered in a cylindrical vessel (height, 112 cm; diameter, 56 cm) filled with thermal insulation material (Fiberfrax Blankets and Fiberfrax Hot Boards, products of Carborundum Company, Niagara Falls, New York). In steady-state operation, this furnace without cell connections, lost to the surroundings the following heats: 195, 182, and 160W at temperatures of 490°, 470°, and 440°C, respectively.

Figure 2 shows schematically the apparatus for the measurement of cell potential. An LiAl/FeS cell was clamped by two constraint plates to eliminate possible shape change of the electrodes and was placed into the furnace. Power cables connected the cell terminals to the battery charge-discharge cycler (Model CDC-50-10, Propel Incorporated, South Plainfield, New Jersey). Two smaller gauge wires were also connected to the cell terminals for potential measurements. Argon gas was passed at a low rate into the furnace to protect the cell terminals from oxidation. The supply of constant power to the heaters through a variable transformer gave a highly stable steady-state temperature, and this method of temperature control was used during measurements of cell potential.

The cell temperature was measured using a calibrated type K thermocouple located at the center of the surface of one of the constraint plates. The cell potential was measured using a Guildline seven-and-one-half-digit multimeter. The precision of the measurements of temperature and cell potential was 0.1°C and 0.01 mV. The criterion of equilibrium was taken as constancy of the cell potential to within 0.01 mV for 1 hr. The time required for attainment of equilibrium after a change of temperature or state of charge was typically 14-18 hr but occasionally reached several days. Changes in state of charge were always carried out at 475°C by 50A constant current charge or discharge. The cell was assumed to be fully charged when its terminal voltage reached 1.55V during charge and completely discharged on reaching 1.00V during discharge. The relatively high current used to change the state of charge has little effect on cell capacity: for discharge at 50A the capacity was 188 A-hr; for 20A discharge it was 194 A-hr; and the theoretical capacity based on the sulfur content of the positive electrode was 200 A-hr. This relatively high current may, however, introduce some uncertainty as to the phases present in the FeS electrode, since no analysis of the electrode was performed. At each depth of discharge, the cell potential was measured from higher temperature to lower temperature and back again.

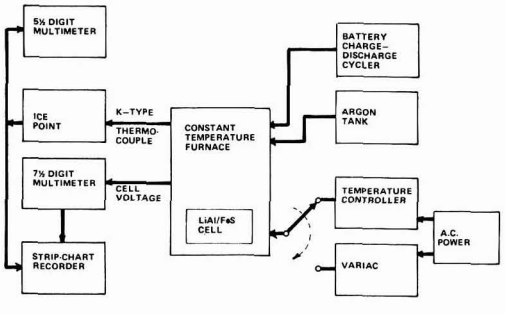

Fig. 2. Block diagram of apparatus used for cell potential measurement.

A high temperature battery calorimeter (Hart Scientific, Provo, Utah) was designed and constructed for measurement of the rate of thermal energy generation of LiAl/FeS cells. The calorimeter was designed with a temperature range of 400°-500°C, a sensitivity of 1 mW, and an upper limit of heat flow of 50W. The details of its construction and principles of operation are presented in Ref. (6).

During early testing of the calorimeter, it was noted that some of the nickel-foil heaters and their power leads oxidized and failed in 15 days of operation. Accordingly, the temperature range of the calorimeter was limited to 410°-435°C. Within these limits the calorimeter functioned as designed. Design changes to remedy its flaws are also presented in Ref. (6).

Results and Discussion

Table II gives the values of the cell potential at various temperatures and depths of discharge. The reproducibility of these results was excellent. For example, at 23% depth of discharge (see Table II), the cell potential was 1.33705V at 476.8°C; after five days at lower temperatures, the cell potential was measured again as 1.33702V at 476.4°C.

The measured cell potentials are plotted in Fig. 3. As can be seen, the temperature derivative of the cell

Table II. Emf of LiAl/FeS cell

Depth of discharge (%)	Temperature (°C)	Emf (V)
0	479.1	1.40476
	464.6	1.40743
	447.2	1.41106
	433.3	1.41398
	417.9	1.41766
12	494.0	1.34681
	471.6	1.34261
	462.4	1.34083
	447.7	1.33796
	416.4	1.33096
	422.8	1.33232
23	476.8	1.33705
	459.9	1.33483
	445.2	1.32276
	415.3	1.33254
	417.5	1.33254
	422.3	1.33190
	428.5	1.33106
	448.3	1.33294
	480.1	1.33773
	488.0	1.33916
	476.4	1.33702
37	474.1	1.33362
	444.0	1.32895
	412.7	1.33267
	418.6	1.33181
	425.4	1.33073
	439.2	1.32872
	483.2	1.33477
	476.0	1.33375
51	485.2	1.32180
	465.6	1.32456
	414.0	1.33284
	430.0	1.33000
	446.3	1.32748
	477.6	1.32270
77	475.3	1.32273
	493.0	1.32011
	439.6	1.32840
	407.5	1.33356
	478.0	1.32204
100	483.2	1.32023
	455.7	1.32649
	428.0	1.33143
	417.0	1.33357
	470.7	1.32292
	474.0	1.32204

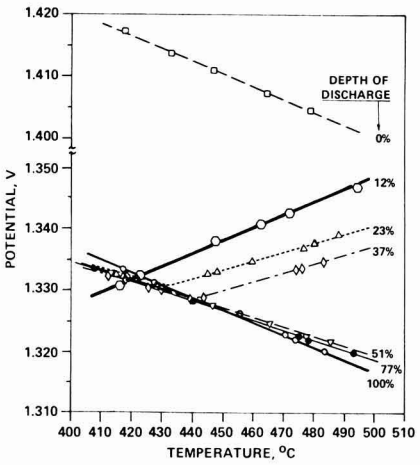

Fig. 3. Cell potential of an LiAl/FeS cell as a function of temperature and depth of discharge.

potential varies strongly with temperature and depth of discharge. For fully charged or discharged cells the temperature coefficient of the emf is negative. However, for partially discharged (23-37% depth of discharge) cells, two linear portions are noted; over the lower portion of the temperature range the temperature coefficient is negative, and at higher temperatures it is positive. The cause of this unusual behavior is believed to be transitions between J-phase ($LiK_6Fe_{24}S_{26}Cl$) and X-phase (Li_2FeS_2) materials identified by workers at Argonne National Laboratories (7, 8). For cells discharged 50% or more, only negative slopes were found over the temperature range of 400°-500°C.

Values of the temperature derivatives at 475° and 420°C, obtained by linear least squares analysis are given in Table III, along with 95% confidence intervals. Figure 4 shows the same results in graphical form.

In addition to the cell potential and its temperature derivative, values of the terminal voltage as a function of current and depth of discharge are required to compute the rate of thermal energy generation. Figure 5 shows the cell voltage during constant-current discharges of 40-100A to a cutoff voltage of 1.00V at 475°C. From these measurements and the cell potentials taken from Fig. 3, the overpotential was calculated, and the rate of thermal energy generation was computed using Eq. [1]. The results are presented in Fig. 6.

The rates of thermal energy generation shown in Fig. 6 are relatively small, even negative (*i.e.*, endothermic), during the first 50% of discharge at 475°C. The reason for this is the positive value of $\partial E/\partial T$ (see Fig. 4), which offsets the polarization heat $I\eta$. Toward the end of discharge, two phenomena contribute to a substantial rise in $\dot{q}$. The thermodynamic contribution

Table III. The emf temperature coefficients of LiAl/FeS cells at various depths of discharge and operating temperatures

Depth of discharge	Temperature coefficient (mV/K)		95% Confidence Interval (± mV/K)	
(%)	475°C	420°C	475°C	420°C
0	−0.210	−0.120	0.023	0.023
12	+0.206	+0.206	0.019	0.019
23	+0.147	−0.126	0.020	0.032
37	+0.150	−0.149	0.016	0.008
51	−0.155	−0.155	0.013	0.013
77	−0.159	−0.159	0.012	0.012
100	−0.202	−0.202	0.007	0.007

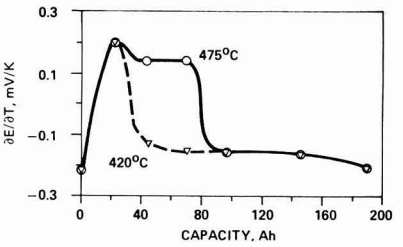

Fig. 4. Temperature derivative of cell potential of a 200 A-hr LiAl/FeS cell.

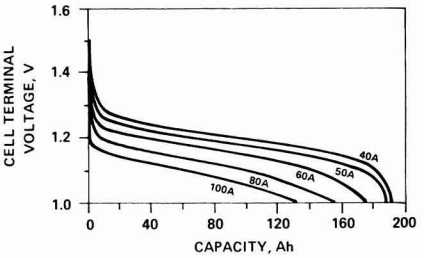

Fig. 5. Discharge curves at various currents at 475°C

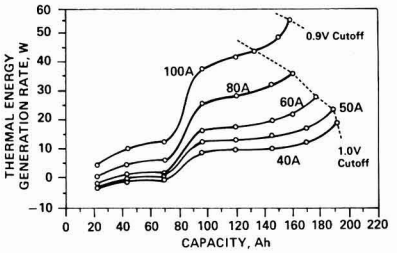

Fig. 6. Thermal energy generation rate of an LiAl/FeS cell during discharge at 475°C.

to $\dot{q}$ changes sign and becomes exothermic, and the cell overvoltage increases rapidly (see Fig. 5). As a result, the rate of thermal energy generation reaches 40 W/cell for a 100A discharge, or 4 kW for a 100-cell battery, such as might be used to power an electric vehicle, for example.

The rates of thermal energy generation measured calorimetrically and computed from Eq. [1] are compared for a 40A discharge at 430°C in Fig. 7. The agreement between the calorimetric (squares, full curve) and the predicted (circles, dotted curve) values of heat flow is seen to be excellent. The polarization heat is also shown; over most of the discharge

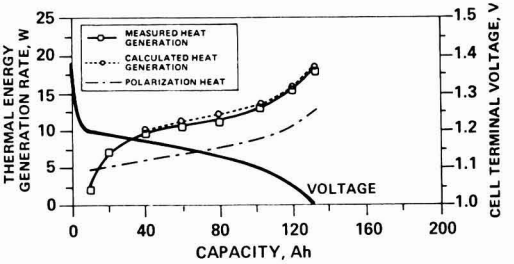

Fig. 7. Thermal energy generation rate and cell terminal voltage of an LiAl/FeS cell at 40A discharge at 430°C.

it lies below and nearly parallel to the curve for the total heat.

Discharge of the cell at a lower rate shows more of the details of the changes in cell thermodynamics. Figure 8 shows the heat flow during a 10A discharge at 435°C. The transition from exothermic to endothermic and back again, which is predicted thermodynamically, is clearly shown by the calorimetric measurements. The agreement between the two methods is not good during the first quarter of the discharge; the calorimetric values are believed more reliable owing to the rapid change of the absolute value of the cell potential with state of charge, which decreased the accuracy of determinations of $\partial E/\partial T$ for high states of charge.

Figures 9 and 10 show the heat flows measured at the lower temperature of 410°C during a 10A discharge. Two points are particularly significant. First, the endothermic effect during discharge was not observed at

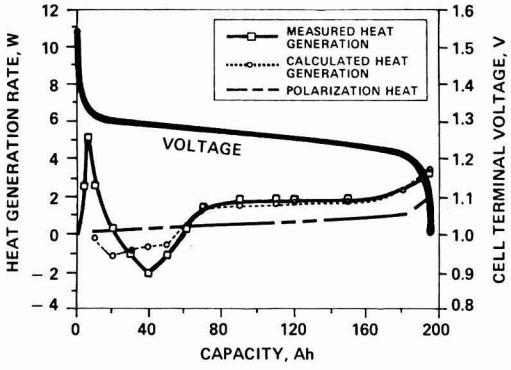

Fig. 8. Thermal energy generation rate and cell terminal voltage of an LiAl/FeS cell during 10A discharge at 435°C.

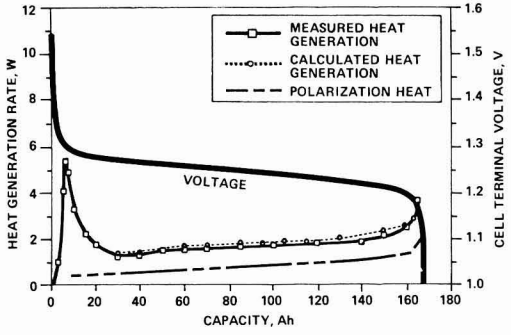

Fig. 9. Thermal energy generation rate and cell terminal voltage of an LiAl/FeS cell during 10A discharge at 410°C.

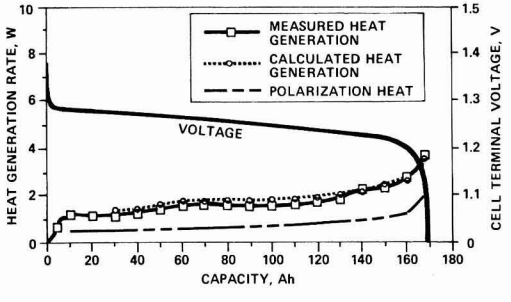

Fig. 10. Thermal energy generation rate and cell terminal voltage of an LiAl/FeS cell during 10A discharge at 410°C.

410°C, in contrast to the case at 435°C (Fig. 8). This result, which is consistent with the emf measurements, indicates that the phase transition of J to X did not occur during discharge at 410°C. Second, at the beginning of discharge, two different heat generation rates were observed (Fig. 9 and 10) because the initial state of the cell was slightly different in each case. For the results in Fig. 9 the cell discharge was begun when the open-circuit voltage was 1.540V. For the results shown in Fig. 10 the cell was allowed to stand at open circuit for several days after a charge to 1.550V; at the beginning of discharge its open-circuit voltage was 1.375V. The exothermic peak during the first 10% of discharge as shown in Fig. 8 and 9 is believed to be associated with the phase transformation of FeS to J (8). Moreover, the absence of this exothermic peak in Fig. 10 indicates that the FeS-to-J transition in a cell charged to 1.55V may take place gradually during open-circuit stand. The cell reaction in the case illustrated by Fig. 10 is believed to be due primarily to the reaction of J to Li_2S.

Figure 11 shows the terminal voltages of an old cell which was overcharged deliberately to 1.98V and subsequently to 1.94V at 420°C at 40A and was then placed on open circuit. The cell voltage dropped during open-circuit stand, underwent a point of inflection in the vicinity of 1.50V, and then leveled off at 1.35V. The transition of FeS to J is thought to be responsible for the inflection.

The entropic contribution to thermal energy generation can be expressed as

$$\dot{q}_S = -IT(\partial E/\partial T)_{P,\xi} = \dot{q} - I\eta \qquad [2]$$

At a particular temperature and state of charge, the temperature derivative is constant. The relationship between $\dot{q}_S$ and I is thus expected to be linear. Figure 12 shows $\dot{q}_S$ for various charge/discharge currents at 50% capacity and a temperature of 420°C. The circles represent the entropic heat, which was obtained by subtracting the polarization heat from the total measured calorimetric heat flow. The solid lines in Fig. 12 indicate the values of $\dot{q}_S$ calculated from the value of $\partial E/\partial T$ derived from emf measurements, -0.155 mV/K. The agreement is excellent for both charge and discharge.

The calorimetric measurements and indirect thermodynamic calculations of thermal energy generation yielded substantially identical results for the types of cells studied in this work. However, battery calorimetry has several advantages over the measurements of cell potentials at open circuit and during current flow.

1. The calorimetric measurement of heat flow is direct and absolute; it requires no assumptions as to the thermodynamic reversibility of the cell.

2. Calorimetry gives precise values for heat flow and does not require differentiation of the results with

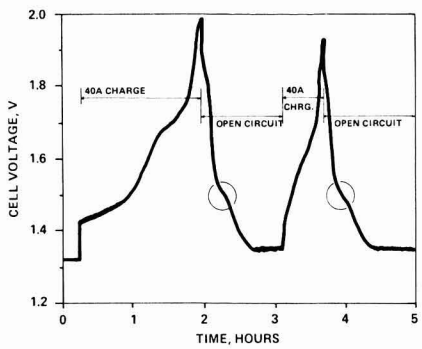

Fig. 11. Cell voltage during overcharge and open circuit

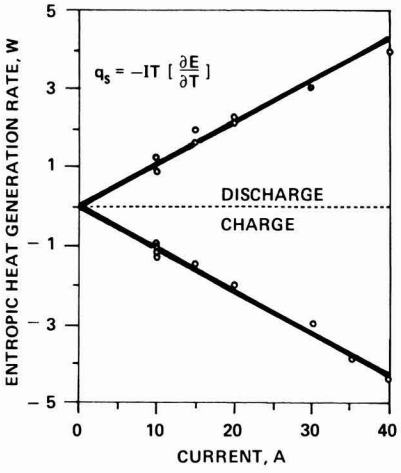

Fig. 12. Entropic heat generation rate as a function of charge/discharge current at 50% capacity at 420°C.

respect to temperature, as does the measurement of emf.

3. Calorimetric measurements are rapid. For the LiAl/FeS cells studied in this work the amount of information collected by calorimetry in one day required more than two weeks to obtain in measurements of cell potentials.

4. The rapidity of calorimetric measurements permits the study of cells in which the state of charge is changing because of a finite rate of self-discharge.

In summary, the precision, speed, and absolute nature of the results of battery calorimetry tend to offset the cost of the instrument, which is higher than that required for precise emf measurements.

Conclusions

The rate of thermal energy generation has been determined for the high temperature lithium-aluminum/iron sulfide cell with boron nitride separator and molten LiCl-KCl-LiF electrolyte by two independent methods. The cell thermal energy generation calculated from a thermodynamic equation is in good agreement with the heat flow measured with an isothermal conduction calorimeter. The results of cell heat generation are valuable for thermal modeling and the temperature control of batteries containing large numbers of cells.

The temperature derivative of the cell potential of the LiAl/FeS cell is a complicated function of temperature and state of charge. The cell reaction for fully charged and fully discharged cells is exothermic; above 430°C, a part of the discharge process is endothermic.

In the calorimetric measurements, cell reactions attributed to the conversions of FeS to J-phase and J- to X-phase during discharge were observed and discussed in this paper. The entropic heat generation of a cell was obtained by subtracting the polarization heat from the total cell heat generation measured by a calorimeter. Although the calculated entropic heat at 50% of capacity is consistent with thermodynamic reversibility, the cell reaction at higher states of charge showed evidence of irreversibility.

Acknowledgments

This work was supported by the U.S. Department of Energy under Contract W-7405-ENG-48 with Lawrence Berkeley Laboratory through subcontract number 4505810. The cooperation of Gould's lithium/iron sulfide group in cell preparation is gratefully acknowledged. One of the authors (D.M.C.) would like to thank J. Phillips and C. C. Chen for many valuable discussions.

Manuscript submitted Jan. 17, 1983; revised manuscript received April 28, 1983.

Gould Incorporated assisted in meeting the publication costs of this article.

REFERENCES

1. H. F. Gibbard, "Thermal Properties of Battery Systems," *This Journal*, **125**, 353 (1978).
2. M. M. Farahat, A. A. Chilenskas, and D. L. Barney, Abstract 86, p. 234, The Electrochemical Society Extended Abstracts, Vol. 80-2, Hollywood, FL, Oct. 5-10, 1980; Argonne National Laboratory Report, ANL-80-49, pp. 58-60 (1980).
3. M. Gauthier, F. Morin, and R. Bellemar, IREQ Report Number 1805C (April 1978).
4. C. Sy, Z. Tomczuk, and M. F. Roche, Argonne National Laboratory Report ANL-77-17, p. 47 (1977).
5. J. W. Gibbs, "Collected Works," Vol. I, pp. 331-349, 406-412, Yale University Press, New Haven (1957).
6. L. D. Hansen, R. M. Hart, D. M. Chen, and H. F. Gibbard, *Rev. Sci. Instrum.*, **53**, 45 (1982).
7. Z. Tomczuk and M. F. Roche, Argonne National Laboratory Report, ANL-79-94, p. 142 (1980).
8. Z. Tomczuk, S. K. Preto, and M. F. Roche, *This Journal*, **128**, 760 (1981).

The Effect of Additives on Current Distribution in Pasted Zinc Electrodes

J. McBreen* and E. Gannon

Brookhaven National Laboratory, Department of Energy and Environment, Upton, New York 11973

ABSTRACT

The effect of additives on current distribution during formation of a pasted zinc electrode was investigated in a two-electrode zinc-nickel oxide cell with a sectioned nickel oxide electrode. The zinc electrodes consisted of zinc oxide, a PTFE binder, and small weight percentage additions of the oxides of high hydrogen overvoltage metals. The square nickel oxide electrode was divided into sixteen square sections, consisting of four center and twelve edge sections. It was assumed that the current to each section was an exact measure of the current to that section of the zinc electrode that was in register with the section. In the case of zinc electrodes with no additive, the average current density at the edge sections was about twice that found at the center sections. Additions of Bi_2O_3, Ga_2O_3, CdO, and HgO had little effect on the current distribution. Additions of Tl_2O_3 and $In(OH)_3$ resulted in very even current distribution over the electrode area. Anomalous effects were found with PbO additions because of leaching of the additive into the electrolyte at the electrode edges.

The principal mode of failure in zinc-silver oxide and zinc-nickel oxide cells with pasted zinc electrodes is shape change. This is a redistribution of the zinc active material that occurs on cycling. When shape change occurs zinc is eroded from the electrode edges and the zinc agglomerates toward the electrode center. Proposed mechanisms for shape change either attribute it to nonuniform current distribution (1) or to separator related electro-osmotic effects which are coupled with electrode reactions to cause nonuniform mass transport (2, 3). Since shape change occurs in cells with microporous separators, which presumably do not give electro-osmotic effects, and is accelerated by membranes which display electro-osmosis, both mechanisms may be operative. Electro-osmosis cannot explain the dramatic effects of substitution of other additives for HgO (4-6), or the incorporation of $Fe(OH)_2$ at the electrode edges (7, 8).

In previous work on the addition of oxides of high hydrogen overvoltage metals to zinc electrodes, it was found that many of these additives were reduced to metal prior to zinc deposition (9). It was also found that some metal oxide additives greatly affect the electrode polarizability and the zinc morphology. It was speculated that the beneficial effects of additives might be due to an improvement in current distribution. The present study was an investigation of current distribution during formation of zinc electrodes with various additives.

Experimental

Cell.—The current distribution cell was very similar in many respects to that described previously (1). The test cell consisted of a standard pasted zinc electrode, a separator system, and a sectioned nickel oxide counterelectrode. A cross section drawing of the cell is shown in Fig. 1. Current distribution was determined by monitoring the current to the various sections of the nickel oxide electrode.

Zinc electrode.—The zinc electrodes consisted of a ZnO/PTFE (polytetrafluoroethylene) mix with the various additives on an expanded silver current collector (Exmet Corporation, 5 Ag12.5-2/0). The method of preparation of the ZnO/PTFE mix (98% ZnO + 2% PTFE) is described elsewhere (9). The ZnO/PTFE mix and the additives were blended in a Waring blender in 120 ml of isopropanol. The suspension was poured over the current collector onto a vacuum table and the liquid drawn off. After that, the electrodes were pressed wet, dried in an oven at 50°C, and given a final dry pressing to the final dimensions (10.52 × 10.52 × 0.073 cm). The vacuum table technique has been described in detail elsewhere (10). Each electrode contained 16.3g of ZnO. Electrodes of the following compositions were evaluated: 98% ZnO + 2% PTFE (control), 89% ZnO + 9.2% Bi_2O_3 + 1.8% PTFE, 96% ZnO + 2% Ga_2O_3 + 2% PTFE, 96% ZnO + 2% CdO + 2% PTFE, 96% ZnO + 2% HgO + 2% PTFE, 96% ZnO + 2% PbO + 2% PTFE, 96% ZnO + 2% Tl_2O_3 + 2% PTFE, 96% ZnO + 2% $In(OH)_3$ + 2% PTFE, 91% ZnO + 2% PbO + 5% Zn + 2% PTFE, 93% ZnO + 5% Zn + 2% PTFE, and 91% ZnO + 5% Zn + 2% HgO + 2% PTFE.

Nickel oxide electrode.—The nickel oxide electrode was prepared by sectioning a nickel plaque into 16 sections (2.54 × 2.54 × 0.13 cm). The sections were then welded on to an array of machined nickel current collectors that were countersunk in an acrylic block (Fig. 1). The spaces between each section and the edges were masked with epoxy. The finished electrode is shown in Fig. 2. The space between each section was 0.12 cm. Except for the coined indentations at the

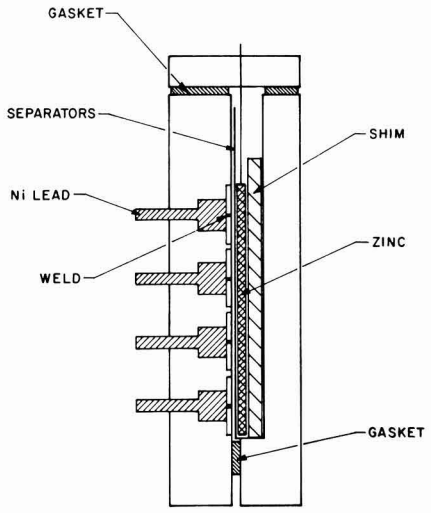

Fig. 1. Schematic of current distribution cell

* Electrochemical Society Active Member.
Key words: battery, cell, electrodeposition.

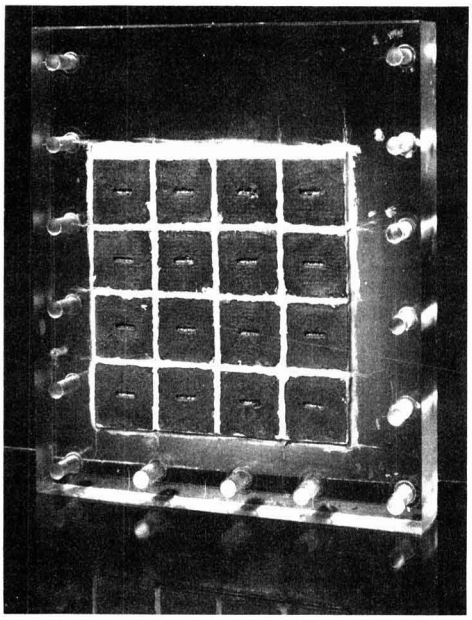

Fig. 2. The sectioned nickel oxide electrode for current distribution measurements.

center welds on each section, the electrode was perfectly flat. The sectioned nickel electrode was impregnated with $Ni(OH)_2$ + 8% $Co(OH)_2$ to a theoretical capacity of 2.87 A-hr using the standard impregnation method (11). The electrode was then given three formation cycles in a 6M KOH + 0.5M LiOH electrolyte.

Cell assembly.—The cell was assembled as follows. A sheet of nonwoven polypropylene (11.0 × 11.0 × 0.013 cm, Pellon Corporation, 2504K4) was placed over the sectioned nickel oxide electrode. The zinc electrode was wrapped in two turns of a microporous separator (Celanese Corporation, Celgard 3501) and then centered over the nonwoven separator, in register with the sectioned nickel oxide electrode. The zinc electrode was placed in such a way that the expanded metal current collector was on the side of the zinc electrode remote from the nickel oxide electrode. The rest of the cell was assembled, as shown in Fig. 1, and bolted together. Provisions were made to ensure an even distribution of thickness in the cell cavity (±0.005 mm). The cell was then wetted down with 20 ml of electrolyte (8.4M KOH + 0.5M LiOH + 0.74M ZnO) and soaked for at least 16 hr prior to the start of the experiment. The cells were operated in the flooded mode with electrolyte extending 2 cm above the top of the zinc electrode.

Experimental procedure.—The cell was first vacuum treated to remove gas bubbles and then connected to the electrical circuitry for measuring the current distribution. This is described in detail elsewhere (1). The cell was charged at 200 mA (1.82 mA/cm²) for 18 hr. The current to the various sections was continuously monitored. After each test the cells were taken apart and the zinc electrodes were visually examined. The nickel oxide electrode was discharged against a nickel sheet electrode, washed three times in hot (60°C) KOH to remove soluble additives, rinsed with distilled water, and allowed to dry overnight at 25°C, prior to the next run.

Results and Discussion

Metal oxide additives and the initial stages of electrode formation.—Depending on the additive, it took up to 20 min for the zinc electrode to reach the zinc deposition potential, during formation. This was true for additions of Tl_2O_3, CdO, HgO, and Bi_2O_3. This was similar to what was observed before (9) and was due to the reduction of the additive oxide to the metal. During this time there were rapid fluctuations in the current distribution. Initially edge sections had a higher current than center sections. However, the current at the edges decreased rapidly as the oxide was consumed and the current to the center sections increased. On reaching the zinc deposition potential, the current distribution reverted to a condition where edge sections had a higher current than center sections. The current distribution became somewhat more even after the first hour of charge and thereafter remained relatively constant. The distribution shown in Fig. 3 is representative of that found for the last 17 hr of charge. In the case of electrodes with no additive and electrodes with additions of Ga_2O_3 and $In(OH)_3$ the zinc deposition potential was reached within seconds. The current to the edge seconds was higher than that to the center sections. The current distribution became more even after about 1 hr and once again the current distribution at the end of charge (Fig. 3) is representative of the current distribution for the last 17 hr of charge. Some of these experiments were repeated several times and the reproducibility was good. The experiments with no additives and with

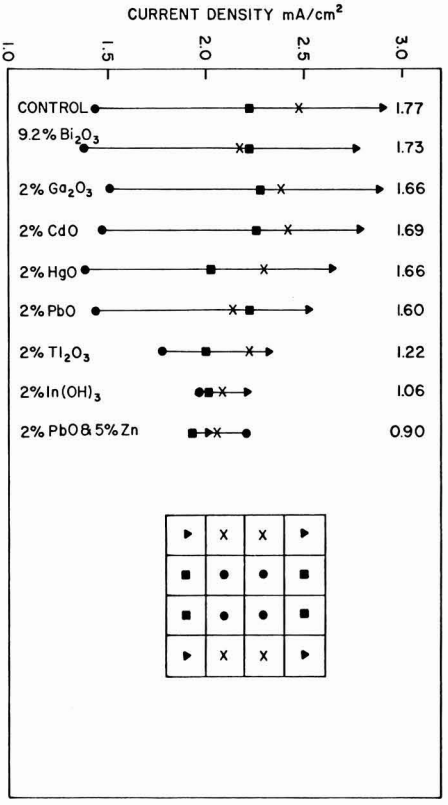

Fig. 3. Current distribution at the end of an 18 hr charge (1.82 mA/cm²) for zinc electrodes with various additives. The currents to the 16 sections are presented as four averages of four sections each. The symbols for the section averages (e.g., ▲ = corner sections and ● = center sections) are indicated in the inset. The numbers to the right of each line are the ratios of the average edge section current density to the average center section current density.

Ga_2O_3 were repeated several times over the course of these experiments to ensure that changes in current distribution from experiment to experiment were not due to some artifact due to aging of the nickel oxide electrode.

The special case of PbO additions.—In the case of the cells with PbO additions, there were rapid fluctuations in the current distribution during the first 10 min of charge. However, the current to the center sections was higher than that to the edge sections. On reaching the zinc deposition potential the current distribution was very uneven with the current density at the electrode edges being as much as eight times higher than that found at the center sections. The current distribution became more even after about 5 hr. The results in Fig. 3 are representative of the current distribution obtained in the last 12 hr of charge. However, the current to the top four sections of the electrode remained abnormally high. The average current to the top four sections was about twice that to the bottom four sections of the electrode. This experiment was repeated several times with similar results. It was observed after the overnight soak that the top edge sections of the zinc electrode (~2 cm wide) were white while the center part of the electrode had the yellowish tinge of PbO. Thus it became evident that the PbO was being leached from the electrode into the electrolyte at electrode edges. The anomalies in the current distribution are attributed to the fact that there was much less additive at the electrode edges. In one test it was found, if the cell was charged for 1 hr and allowed to stand overnight, that on resumption of the charge the current distribution was much more even. This was due to the displacement of soluble lead from the excess electrolyte onto the electrode edge according to

$$HPbO_2^- + OH^- + H_2O + Zn \rightarrow Pb + Zn(OH)_4^=$$

It was then decided to try an electrode formulation consisting of 91% ZnO + 2% PbO + 2% PTFE + 5% Zn (−325 mesh) where the soluble lead would be displaced from the electrolyte by metallic zinc.

Electrode with PbO and Zn additions.—In the case of electrodes with PbO and Zn additions, the zinc deposition potential was immediately established on turning on the charging current. The current distribution was very even throughout charge. A blank run with a 5% Zn addition and one with a 5% Zn + 2% HgO addition gave respective results that were similar to those found for the control and the cell with a 2% HgO addition. The Zn powder displaces the PbO by cementation. The resultant gray Pb could be seen as the electrode was wetted in from the edges, on addition of electrolyte. This result strongly indicates once again that the effect of these additives is related to some substrate effect and is not a codeposition effect (9, 12).

Metal oxide additives and current distribution.—Additives such as Tl_2O_3, PbO, and $In(OH)_2$, which were shown to increase the electrode polarizability (9), result in more even current distribution during electrode formation. However, additives that reduce the polarizability of the electrode do not result in any significant disparity in the measured current distribution over that found for electrodes with no additives. There are at least two possible reasons for this. One, is that the edge sections are large (2.54 × 2.54 cm) and the current is an average over this and does not reflect the true current density at the edge. The other is that the condition here is a current distribution case, wherein both the interelectrode spacing and the polarizability are small. For such a case, it has been shown that even for vanishing polarization the high current density point is very close to the electrode edge (13). Thus there is a limit to the unevenness in current distribution to be expected.

There was qualitative evidence that additives also affect the current distribution within the pores of the zinc electrode. In cells with Ga_2O_3 additives all of the zinc deposit appeared to be in abuttal with the separator. The area around the expanded metal current collector was still white zinc oxide. However, in cells with $In(OH)_3$ and PbO additives most of the zinc deposit was in the vicinity of the current collector. The front of the electrode in abuttal with the separator was largely white zinc oxide. In previous work (9) it was found that additions of Ga_2O_3 yielded electrodes with minimum polarizability and additions of PbO and $In(OH)_3$ gave electrodes with maximum polarizability. The observed distribution of zinc is consistent with this.

Conclusions

1. It has been shown that metal oxide additives can affect the current distribution during formation of pasted zinc battery electrodes.
2. Additives such as Tl_2O_3 and $In(OH)_3$ that increase electrode polarizability improve the current distribution.
3. Leaching effects of soluble additives such as PbO at electrode edges can lead to very uneven current distribution during electrode formation.
4. Results in electrodes with a combination of a PbO/Zn powder additive indicate that the beneficial effect of lead additives is related to a substrate effect and not to a codeposition effect.

Manuscript submitted March 17, 1983; revised manuscript received May 25, 1983.

Brookhaven National Laboratory assisted in meeting the publications costs of this article.

REFERENCES

1. J. McBreen, *This Journal*, **119**, 1620 (1972).
2. K. W. Choi, D. N. Bennion, and J. Newman, *ibid.*, **123**, 1616 (1976).
3. K. W. Choi, D. Hamby, D. N. Bennion, and J. Newman, *ibid.*, **123**, 1628 (1976).
4. A. Himy and O. C. Wagner, U.S. Pat. 4,084,047.
5. O. C. Wagner, A. Almerine, and R. Smith, Proceedings 29th Power Sources Conference, Atlantic City, NJ, June 9-12, 1980. The Electrochemical Society Inc., p. 237 (1981).
6. S-P. Poa, G-M. C. Chiang, and T-C. Lin, *Science Development Monthly (Taiwan)*, **6**, 1013 (1978).
7. J. McBreen, U.S. Pat. 3.876,470.
8. S-P. Poa and C. H. Wu, *J. Appl. Electrochem.*, **8**, 427 (1978).
9. J. McBreen and E. Gannon, *Electrochim. Acta*, **26**, 1439 (1981).
10. J. McBreen, U.S. Pat. 4,000,005.
11. A. Fleischer, *J. (and Trans.) Electrochem Soc.*, **94**, 289 (1948).
12. J. McBreen, M. G. Chu, and G. Adzic, *This Journal*, **128**, 2287 (1981).
13. C. Wagner, *ibid.*, **98**, 116 (1951).

Chloride Accumulation on Indoor Zinc and Aluminum Surfaces

G. B. Munier, L. A. Psota-Kelty, and J. D. Sinclair*

Bell Laboratories, Holmdel, New Jersey 07733

ABSTRACT

The long-term accumulation of chloride and other ions on indoor zinc and aluminum surfaces in 15 U.S. cities has been measured. For most ionic contaminants, the accumulation on zinc and aluminum surfaces is similar, suggesting that particulate deposition is the most likely mode of accumulation. Chloride accumulation on aluminum occurs by particulate deposition, but on zinc surfaces, attack by reactive chlorine containing gases also contributes to accumulation. In New York City and Philadelphia, chloride accumulation is very rapid on all zinc surfaces but not on aluminum surfaces. Volatilization of chloride, probably as HCl or NH_4Cl, seems to contribute to the low chloride concentrations observed on aluminum surfaces in these cities. In Wichita and Houston, deposition of coarse chloride containing particulates produces rapid accumulation of chloride on horizontal zinc and aluminum surfaces while chloride accumulation on vertical surfaces is slow.

As part of a broad study to determine the amounts and effects of major inorganic pollutants in indoor environments (1, 2), the long-term accumulation of chloride on indoor zinc and aluminum surfaces at telephone company switching centers in 15 U.S. cities has been measured (3). In the previous reports (1, 2) on this study, the accumulation of chloride, nitrate, sulfate, sodium, ammonium, potassium, calcium, and magnesium at seven cities was documented. The highly complex nature of the accumulation process and the many indoor, outdoor, and human factors that bear on the accumulation process were discussed, including aerosol size distribution, air flow patterns, temperature and humidity gradients, air filtration systems, air leakage pathways, and concentrations of ammonia, acidic aerosols, and other substances that could interact with surface species to produce volatile products. The sulfate accumulation on zinc and aluminum surfaces was shown to correlate well with sulfate concentrations in the local troposphere but not with SO_2 concentrations, indicating that the primary accumulation process for sulfate is particulate deposition rather than a corrosion reaction with SO_2. Hermance *et al.* (4) have demonstrated that airborne nitrates in the Los Angeles area correlate with nitrate concentrations on surfaces and with the incidence of electrolytic stress corrosion cracking of nickel brass.

For the initial seven cities, the behavior of chloride was highly irregular. In New York City and Council Bluffs (Iowa), chloride accumulation on zinc was rapid, but on aluminum the chloride accumulation was low. In Houston and Cleveland, accumulation on zinc was similar to that on aluminum. It was suggested in the previous reports that preferential volatilization of chloride species from aluminum surfaces might contribute to the lower amounts of chloride at some locations by a process similar to the sulfuric acid aerosol-induced depletion of chloride from sea salt aerosol that has been documented by Hitchcock *et al.* (5). For the sea salt aerosol, the volatile chloride was HCl. In a paper on aerosol chemistry, Weschler and Graedel (6) have discussed evidence that species with saturation vapor pressures $>10^{-7}$ Torr will exist in the vapor phase at remote locations where there are few, if any, local sources, while species with saturation vapor pressures in the 10^{-7}-10^{-8} Torr range will be partitioned between the gas phase and a condensed phase within aerosols. For some indoor surfaces containing chloride, interaction with ammonia or acid ammonium sulfate aerosol could produce NH_4Cl, which has a saturation vapor pressure of 2.4×10^{-5} Torr. Thus, depending on the gas phase concentrations of HCl and NH_3, either HCl or NH_4Cl could volatilize and thereby remove chloride from indoor surfaces.

In this report all the completed field data on chloride and sulfate accumulation are given, as are additional laboratory studies that were intended to further elucidate the cause of the difference in accumulation of chloride on zinc and aluminum.

* Electrochemical Society Active Member.
Key words: corrosion, chloride, aluminum, zinc.

Experimental

The zinc and aluminum surfaces examined in this study were structural surfaces associated with telephone company switching equipment frames. The zinc surfaces were electroplated steel sheets while the aluminum surfaces were 2000 series low copper alloys. These surfaces were not cleaned or disturbed during the accumulation period, which was determined by subtracting the year of manufacture stamped on equipment surfaces from the year in which the equipment was sampled. The sampling was accomplished between October 1978 and October 1982, and most of the equipment was 8-15 yr old. The air exchange rate at these locations was typically in the range of 0.10-0.25 per min. The direction of air flow relative to equipment orientation was variable. The air processing fans were run continuously (except for power outages or servicing). The air filtration systems were equipped to remove most of the large particles (>5 μm aerodynamic diam) from the air intake stream but only about 10% of the fine particles (<2 μm).

Except as noted in previous reports (1, 2), surface extractions were accomplished with moistened pieces (square sections 1.27 cm on a side) of pre-cut Whatman 542 filter paper. The papers were cleaned before placement on a surface by washing them three times with boiling distilled water, and this was followed by oven drying. The volume of water in each paper was determined to be approximately 0.03 ml. The papers were placed on flat surfaces in either a horizontal or a vertical plane and were removed from the surfaces after drying. The sampling interval for each paper was approximately 30 min but was somewhat dependent on the ambient relative humidity. The procedure was carried out three times on each sampled area to insure complete removal of water-soluble contaminants (7). Between 50 and 120 samples were collected from each location. The samples were stored and transported to the laboratory in disposable polystyrene test tubes. In the laboratory, the paper samples were extracted with 10 ml of water, and the extracts were then split for separate cation and anion analysis. All samples were analyzed by ion chromatography. Standard ion exchange pre-columns, separator columns, and suppressor columns were used for the ion analyses. Appropriate blank corrections for the sampling and analytical procedure were made when converting the solution concentrations to surface concentrations. The details and validation of the sampling and analytical procedures are described elsewhere (7).

An adjustment in the total surface concentration of each ion was made to take into account any accumulation that occurred prior to uncrating the equipment at its permanent location. These initial concentrations were estimated by sampling new equipment shortly after uncrating at one location in New York City and

one in New Jersey. A total of 60 samples each on zinc and aluminum surfaces were taken at both locations. The average concentrations of chloride on zinc and aluminum surfaces were 0.04 and 0.24 $\mu g/cm^2$, respectively, while those of sulfate were 0.13 and 0.21 $\mu g/cm^2$.

For surface acidity measurements, at least 60 single paper extracts from a location were jointly extracted in the minimum volume of water necessary to permit measuring the solution pH (on the order of 20 ml). The relative acidities of the surfaces were calculated on an aliquot basis using a water volume of 0.03 ml/paper.

Results and Discussion

Accumulation data.—The accumulation data can be presented either as total surface concentration or as an average annual accumulation based on surface age. Neither method is entirely satisfactory for the purpose of comparing locations or comparing zinc and aluminum surfaces. Clearly, total surface concentrations should not be used to compare surfaces that range from 8 to 15 yr in age. Both total concentration and average annual accumulation are deficient in representing cases in which a species may accumulate to a nearly limiting concentration in the early stages of exposure While it would have been desirable to measure accumulation on a periodic basis and thereby obtain kinetic information, such a study on realistic field surfaces is not practical. In the authors' opinion, the accumulation of chloride and sulfate ions measured in this and the previous work has, except for chloride on aluminum surfaces at some locations, probably occurred at a roughly linear rate. However, presentation of the data as an average annual accumulation in $\mu g/cm^2$ does not imply linearity. Surface passivation could lead to a cessation of accumulation in the case of attack by a corrosive gas. A chemical or physical loss process could also compete equally with accumulation after some exposure interval, halting further apparent accumulation. Both of these possibilities will be considered with regard to the accumulation of chloride on aluminum.

The specific characteristics of the accumulation rate over the exposure period and the units of measure selected for presenting the data will not influence the conclusions of this study. Over short time intervals (hours to weeks), the accumulation rates of particles and gases are likely to vary significantly with outdoor meteorological conditions, indoor RH, loading of the air filters, changes in ambient concentrations, alteration of surface characteristics with time, and numerous other factors. These factors will probably not result in substantial variation in the annual accumulations from year to year.

The average annual accumulations of sulfate on zinc and aluminum surfaces for the cities studied to date are shown in Fig. 1. The data are somewhat scattered, as expected for the highly nonuniform contamination levels typical of field surfaces, but demonstrate a roughly 1:1 correspondence between the accumulation of sulfate on zinc and that on aluminum surfaces. For the limited data presented previously (1, 2) on nitrate, sodium, potassium, calcium, and magnesium, the same type of correspondence was generally evident, though in the case of calcium and magnesium there was a modest preference for zinc surfaces at a few locations.

For the chloride data, as shown in Fig. 2, the accumulation on zinc is roughly similar to that on aluminum in Houston, Wichita, and Orlando. In New York, Philadelphia, Northern New Jersey (Newark and Jersey City), and Council Bluffs, the accumulation on zinc is roughly six to ten times larger than that on aluminum.

These indoor average annual accumulations for chloride and sulfate are about one order of magnitude lower than typical outdoor accumulation rates (8). Indoor and outdoor concentrations of fine particles (<2 μm aerodynamic diam) are usually in the same range, while concentrations of large particles (>2 μm) are usually a factor of 5-10 higher outdoors than indoors (9). In view of the much larger air currents typically present outdoors, an order of magnitude difference in the surface accumulation indoors and outdoors appears reasonable.

The accumulation of chloride, as will be explained, seems to result from three major sources: (a) corrosive gases (primarily HCl); (b) large particulates (primarily crustal materials of aerodynamic diameter >2 μm); and (c) accumulation mode aerosols (primarily of anthropogenic origin with aerodynamic diameters of 0.1-2 μm) (10). In general, the chloride containing gases would be expected to attack horizontal and vertical surfaces with equal efficiency but could attack zinc and aluminum at different rates. The large particulates will accumulate efficiently on horizontal surfaces but usually will not collect on vertical surfaces. The aerodynamic characteristics of the accumulation mode aerosols are expected to produce nearly equal accumulation (assuming all other factors including air flow patterns are identical) on horizontal and vertical surfaces (10). In Table I, the average chloride accumulation on zinc and aluminum surfaces is separated into horizontal and vertical planes. For Houston and Wichita, the accumulation is similarly high on zinc and aluminum horizontal surfaces and considerably lower on the vertical surfaces. Deposition of large particulates is clearly the dominant accumulation process. This result may be related to the dry nature of the crustal materials in these areas. In New York City and Philadelphia, very rapid accumulation takes place on horizontal and vertical zinc surfaces but not on aluminum surfaces. The corrosive gas source most plausibly explains the data, though it is perhaps sur-

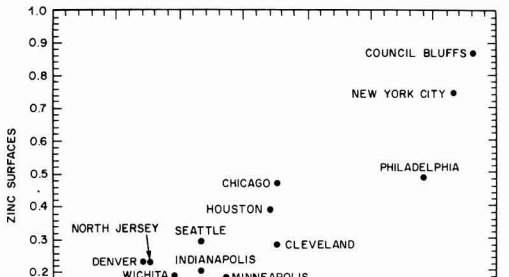

Fig. 1. Average annual sulfate accumulation on zinc and aluminum surfaces ($\mu g/cm^2$).

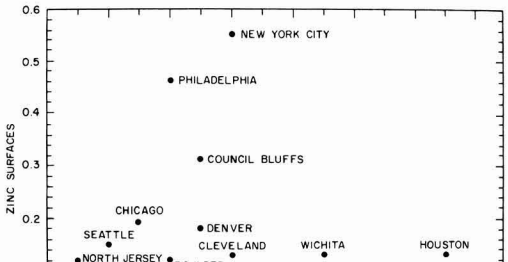

Fig. 2. Average annual chloride accumulation on zinc and aluminum surfaces ($\mu g/cm^2$).

Table I. Chloride average annual accumulation ($\mu g/cm^2$)

City or State		Zinc		Aluminum	
		Horizontal	Vertical	Horizontal	Vertical
Houston	(2)*	0.22	0.03	0.17	0.10
Wichita	(1)	0.23	0.02	0.15	0.03
Council Bluffs	(1)	0.30	0.33	0.03	0.08
Chicago	(2)	0.28	0.09	0.06	0
Seattle	(2)	0.19	0.11	0.04	0
North Jersey	(2)	0.16	0.09	0.01	0
Minneapolis	(2)	0.10	0.09	0	0
Colorado	(3)	0.13	0.13	0.04	0.03
Indianapolis	(2)	0.13	0.03	0.02	0
Cleveland	(2)	0.13	0.13	0.06	0.05
Orlando	(2)	0.09	0.05	0.10	0.01
New York City	(4)	0.49	0.60	0.08	0.05
Philadelphia	(2)	0.56	0.37	0.06	0.01

* Number in parentheses is the number of locations sampled.

prising that the chloride accumulation is a factor of ten greater on zinc than on aluminum. Very little useful data is available on the atmospheric concentrations of corrosive chlorine containing gases in major U.S. cities. Incineration and chemical manufacturing are known to be major sources of HCl that might be expected to produce high concentrations in the Philadelphia and New York City areas. In the majority of cities, combinations of the three chloride sources seem to be responsible for the observed rates.

Accumulation model.—If it is assumed that: (*i*) large particulates accumulate exclusively on horizontal surfaces; (*ii*) small particulates collect at equal rates on horizontal and vertical surfaces; and (*iii*) the accumulation rate on zinc due to corrosive gases at normal ambient concentrations is ten times the rate on aluminum, then

$$Zn_H = G_{Zn} + L + S$$

$$Zn_V = G_{Zn} + S$$

$$Al_H = G_{Al} + L + S$$

$$Al_V = G_{Al} + S$$

where Zn_H, Zn_V, Al_H, and Al_V are the observed rates on zinc and aluminum horizontal and vertical surfaces, G_{Zn} and G_{Al} are the corrosive gas accumulation rates on zinc and aluminum ($G_{Zn} = 10\ G_{Al}$), L is the accumulation rate of large particulates, and S is the accumulation rate of small particulates.

The above system of equations was solved simultaneously using a least squares fit to the observed data. The results are shown in Table II. The negative values in Table II may result, in part, from the approximation $G_{Zn} = 10\ G_{Al}$. All but one of the negative values are for the fine particulate contribution, S. If $G_{Zn}/G_{Al} > 10$, the magnitudes of the negative S values will be reduced. The normal scatter in the data and the limited number of observations also undoubtedly contribute to the negative values. The tabulated values are a quantitative estimate of the qualitative conclusions that have been discussed above.

Explanation of low chloride on aluminum.—Four possible causes for the substantially higher accumulation at some locations of chloride on zinc, under the influence of a corrosive gas, were considered: (*i*) the reaction with aluminum was blocked by the passive oxide film or an unknown environmentally dependent factor; (*ii*) chloride products more readily flake off

Table II. Derived average annual chloride accumulation for the three source categories ($\mu g/cm^2$)

	G_{Zn}	L	S
New York City	0.53	−0.04	0.04
Philadelphia	0.47	0.12	−0.07
Council Bluffs	0.29	0.04	−0.04
Chicago	0.16	0.12	−0.04
Seattle	0.16	0.06	−0.04
North Jersey	0.14	0.04	−0.03
Minneapolis	0.10	0.01	0
Colorado	0.11	0.01	0.02
Indianapolis	0.08	0.06	−0.03
Cleveland	0.09	0.01	0.04
Orlando	0.02	0.06	0.02
Wichita	−0.03	0.16	0.01
Houston	0	0.13	0.07

aluminum surfaces; (*iii*) chloride products were not extractable from aluminum (perhaps due to entrapment in the oxide, the formation of an unknown complex oxychloride, or the existence of an organic film that rendered the surface unwettable); and (*iv*) chloride products on aluminum preferentially volatilize. The oxide film on aluminum is well known to be protective and explanation (*i*) has been assumed to be important. As will be discussed, evidence gathered in this work suggests that explanation (*iv*) is also important at some locations.

Explanation (*ii*) was considered unlikely since the accumulation on vertical surfaces is comparable to that on horizontal surfaces for both zinc and aluminum in the clear-cut cases where a corrosive gas was the major source (New York City and Philadelphia) and in the cases where the corrosive gas and fine particulate sources appear important (Colorado and Cleveland). Gravity effects should produce much lower concentrations on aluminum vertical surfaces if flaking is important. Air currents could influence horizontal and vertical surfaces, though gravity effects would still be expected to yield increased losses from vertical surfaces. Further, gravity and air currents should have roughly the same effect on aluminum surfaces at all locations.

Results pertinent to explanation (*iii*) are shown in Table III. The residues remaining after evaporation of the aqueous extractions of the sampling papers were examined by EDXA. The x-ray intensities are referenced to calcium, which was determined quantitatively in previous work (2) by ion chromatography. Zinc is clearly a significant contributor to the anion-cation balance on zinc surfaces at many locations. The other metal ions observed are present only in trace amounts. On aluminum surfaces, very low contributions to the anion-cation balance were observed for all four metal ions. Thus, very little of the chloride that might have been present on aluminum surfaces in these cities was present as the normally soluble aluminum chloride. If chloride was present, it must have been trapped within the oxide or have formed a considerably less soluble complex salt of unknown composition and structure. EDXA analysis of surfaces removed from normal indoor sites in New York City for subsequent laboratory analysis detected significant amounts of chloride on zinc surfaces but none on aluminum surfaces. While EDXA is not a highly sensitive technique, if chloride in an unextractable form was present on aluminum to the same extent as the extractable chloride on zinc, the chloride should have been detectable by EDXA.

Table III. Relative x-ray intensities of metal ions extracted from surfaces

Metal surface	Ions				
	Calcium	Zinc	Copper	Aluminum	Iron
Zinc	1.0	0.080-0.978	0.017-0.041	0.000-0.073	0.000-0.095
Aluminum	1.0	0.029-0.077	0.020-0.059	0.000-0.008	0.007-0.052

This result demonstrates that chloride is not present, but it does not allow a distinction between passivation effects and volatilization of chloride.

A major fire that occurred at a telephone company switching center in Manhattan in 1975 provided an opportunity to study the volatility of chloride products on aluminum [explanation (*iv*)]. Severe chloride corrosion occurred on both zinc and aluminum surfaces, due to the release of significant amounts of HCl during thermal degradation of wire insulation. These surfaces were sampled by paper extraction during the first 3 months after the fire and then again in 1980. The results are shown in Table IV. The higher chloride concentration on zinc surfaces in 1975 should not be taken as an indication that zinc is more reactive even under the extreme conditions of the fire because: (*i*) normal indoor zinc surfaces of comparable service life in New York City had, on the average, 27 $\mu g/cm^2$ of chloride in 1975 while aluminum surfaces had <2 $\mu g/cm^2$; and (*ii*) the source of the smoke from the fire was closer on the average to the zinc surfaces sampled than to the aluminum surfaces. Five years after the fire, the amount of extractable chloride on aluminum dropped by a factor of five, while that on zinc decreased only slightly. The x-ray spectra in Fig. 3 were taken of heavily corroded aluminum surfaces from the fire location. The spectra show that chloride observed in the pits in 1975 remains present at a high level in 1981. However, in the area adjacent to the pits, appreciable amounts of chloride were detected in 1975 but not in 1981. Presuming that the chloride products did not flake off, it seems very likely from the data in Fig. 3 and Table IV that most of the chloride products from the fire volatilized from the surface between 1975 and 1981 except in the area of the pits. The formation of insoluble complex chlorine containing salts or the trapping of chloride in the surface oxide is not the major cause of the low chloride concentrations that were observed in the extractions of these aluminum surfaces in 1981.

The observations that if indoor HCl concentrations are high enough, aluminum will severely pit and corrode, but when conditions return to normal, that chloride products appear to volatilize, suggest that volatilization may also be significant for normal indoor surfaces.

Volatility of chloride products.—Two cations readily available from sulfate aerosols, hydronium and ammonium, when coupled with chloride yield significantly volatile species. Ammonium is also available from numerous potential indoor sources, including floor and window cleaners, air handling systems, volatile products from construction materials or electronic equipment, and humans. Considering HCl and NH_4Cl, the least volatile is NH_4Cl (as NH_3 and HCl). The Jost cylindrical diffusion model (11) was used to determine if 40 $\mu g/cm^2$ of chloride could be reasonably expected to volatilize in 5 yr from the fire contaminated surfaces, presuming NH_4Cl is the surface specie. In the field environments under study, air convection is clearly important and a diffusion model should substantially underestimate the actual volatilization rate. The model gives $V/t = DqC/l$, where V is the quantity of vapor leaving the top of an assumed evaporation cylinder in time t, D is the diffusivity of the vapor in air, q is the cross-sectional area, C is the equilibrium concentration of the vapor immediately above the solid, and l is

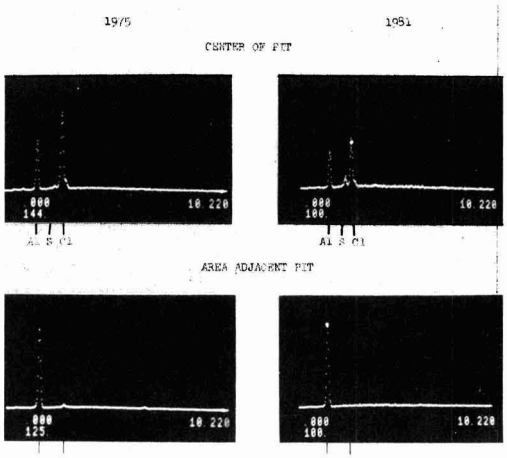

Fig. 3. EDXA analysis of chloride attacked aluminum surfaces from the New York City fire location.

the height of the cylinder above which the pressure of the vapor is assumed to be effectively zero. The model substantially oversimplifies the field situation but is adequate for a crude estimation. A reasonable value for l was determined by gravimetrically monitoring the loss of a sample of ammonium carbonate, which is quite volatile ($C = 1$ Torr). The circular sample pan area was 0.28 cm^2. For $l = 1$ cm, V/t (observed) was 1.2 mg/hr while V/t (calculated) was 0.94 mg/hr. Using $l = 1$ cm, and $C = 2.4 \times 10^{-5}$ Torr, V/t (calculated) for NH_4Cl was 1.4×10^{-5} mg/hr, which yields a maximum possible loss of chloride in 5 yr of 1460 $\mu g/cm^2$. The observed chloride loss is a factor of 36 smaller than the calculated maximum loss, indicating that volatilization of NH_4Cl (as NH_3 and HCl), which could be formed by combination of chloride with deposited ammonia, $(NH_4)_2SO_4$, or $(NH_4)HSO_4$, is plausible. Since HCl is more volatile than NH_4Cl, either could reasonably explain the 40 $\mu g/cm^2$ chloride loss.

The much greater tendency for apparent volatilization of chloride species from aluminum than from zinc surfaces will require further study to be clearly understood. If aluminum surfaces are more acidic than zinc, volatilization of HCl would more readily occur. From Table V, the average relative surface pH's of aluminum surfaces were found to be lower than for zinc surfaces. Complicating the interpretation, though, is the result that the zinc vertical and aluminum horizontal surfaces have similar acidities, yet the average accumulation rate of chloride on zinc is twice that on aluminum. Either the average surface acidity is not the dominant factor or horizontal and vertical surfaces should not be compared because of the coarse particle influence on the former. These acidities, of course, are from macroscopic measurements. There could well be microscopic areas on aluminum surfaces that are con-

Table IV. Average chloride concentrations of fire-contaminated surfaces from New York City ($\mu g/cm^2$)

Surface	1975	1980
Zinc	114	99
Aluminum	49	10

Table V. Acidity and average annual chloride accumulation for all locations

Surface	pH	Chloride ($\mu g/cm^2$)
Zinc		
Horizontal	5.0	0.26
Vertical	4.6	0.20
Aluminum		
Horizontal	4.7	0.09
Vertical	4.0	0.09

siderably more acidic, due to ongoing pitting or the influence of local atmospheric factors.

The authors have made comparisons of the surface pH and surface chloride concentrations reported here with pH and ammonium concentrations in rainfall as reported by the National Atmospheric Deposition Program (12). No meaningful correlations were found. Unfortunately, insufficient data on gaseous ammonia concentrations and the acidity and ammonium concentrations of aerosols in these cities are available for comparisons. As further atmospheric data become available these comparisons should be made.

Concluding remarks.—The previously reported observation that chloride accumulation on indoor zinc surfaces is considerably greater than on aluminum surfaces at some field locations has been supported by further data from additional cities. The contributions of large particulates, fine particulates, and gaseous substances to the accumulated chloride on these surfaces have been estimated by a simple model for the 15 cities studied to date. The lower chloride concentrations on some aluminum surfaces seems to be best explained by a combination of the passive nature of the oxide film and the volatilization of chloride species. Evidence has been offered that aluminum surfaces are slightly more acidic than zinc surfaces, thereby possibly enhancing HCl evolution, and that NH_4Cl, if it can be formed, is sufficiently volatile to remove large amounts of chloride. The specific nature of the volatilization, if it occurs, remains uncertain.

Acknowledgment

The authors are indebted to C. J. Weschler and G. R. Crane for very helpful discussions during the course of this study.

Manuscript submitted Sept. 10, 1982; revised manuscript received June 14, 1983.

Bell Laboratories assisted in meeting publication costs of this article.

REFERENCES

1. G. B. Munier, L. A. Psota, B. T. Reagor, B. Russiello, and J. D. Sinclair, *This Journal*, **2**, 265 (1980).
2. G. B. Munier, L. A. Psota-Kelty, and J. D. Sinclair, "Atmospheric Corrosion," W. H. Ailor, Editor, p. 275, John Wiley and Sons, Inc., New York (1982).
3. G. B. Munier, L. A. Psota-Kelty, and J. D. Sinclair, Paper 22 presented at The Electrochemical Society Meeting, Montreal, Canada, May 9-14, 1982.
4. H. W. Hermance, C. A. Russell, E. J. Bauer, T. F. Egan, and H. V. Wadlow, *Environ. Sci. Technol.*, **5**, 781 (1971).
5. D. R. Hitchcock, L. L. Spiller, and W. E. Wilson, *Atmos. Environ.*, **14**, 165 (1980).
6. C. J. Weschler and T. E. Graedel, *Rev. Geophys. Space Phys.*, To be published.
7. J. D. Sinclair, *Anal. Chem.*, **54**, 1529 (1982).
8. S. E. Lindberg and G. M. Lovett, p. 46, 4th International Conference on Precipitation Scavenging, Dry Deposition, and Resuspension, Santa Monica, CA, Nov. 28-Dec. 3, 1982.
9. C. J. Weschler, S. P. Kelty, and J. E. Lingousky, Submitted to *J. Air Pollut. Control Assoc.*
10. S. K. Friedlander, "Smoke, Dust and Haze—Fundamentals of Aerosol Behavior," John Wiley and Sons, New York (1977).
11. W. Jost, "Diffusion in Solids, Liquids, Gases," p. 9, Academic Press, Inc., New York (1970).
12. J. H. Gibson, Personal communication, Summary listing for Jan. 1, 1980-Dec. 31, 1980.

Electroplating of Cyclic Multilayered Alloy (CMA) Coatings

U. Cohen,*,[1] F. B. Koch,* and R. Sard*,[2]

Bell Laboratories, Murray Hill, New Jersey 07974

ABSTRACT

A new technique has been developed for producing laminated composites of cyclic multilayered alloy (CMA) electrodeposits. The thickness and composition of the individual layers of the CMA deposits are altered precisely and conveniently by cyclic modulation of the cathodic current or potential during electrodeposition. It is thus possible to modify the structure to obtain laminated composite coatings which may have desirable engineering properties. Wear and corrosion resistances, mechanical hardness and strength, as well as certain magnetic, optic, and electronic properties of the plated composite alloys should be, in principle, straightforward to design and fabricate. The CMA technique was demonstrated by plating a wide variety of Ag-Pd CMA structures. Fine structures, with repeat distances as small as 0.05 μm, were obtained. Both square and triangular waveforms were applied to produce sharp or gradual composition variations, respectively. The resulting deposits were found to correspond closely to the intended structures with respect to thickness and composition, when the individual layers were thicker than about 1000Å. The amplitude of the composition modulation diminished rapidly for layer thicknesses below this limit. For the prospective application of Ag-Pd alloys as a contact finish, CMA structures composed of relatively thin Pd-rich layers alternating with thick Ag-rich layers would offer the high corrosion resistance of Pd combined with the low electrical resistance and low cost of Ag. An initial comparison of the CMA deposits with uniform, d-c plated, Ag-Pd alloys did not show any clear difference in contact properties. However, both types of deposit proved satisfactory in the tests which were made.

Lamellar or banded plating structures obtained with direct current have often been observed in both alloy coatings (1-7) and single metals deposited from additive containing baths (7-11). Such structures are largely due to nonequilibrium or dynamic effects and are usually unintentional. In general, they arise due to periodic fluctuations in the electrocrystallization process accompanied by periodic fluctuations of the cathodic polarization (1, 12). Periodic potential fluctuations were also reported in the deposition of banded Cu alloys (13), Fe-Ni (14), Cd-Zn (15), and Nb-Ge (12).

Vacuum evaporation of composition modulated films was introduced by DuMond and Youtz (16). The technique consisted of evaporating alternate layers of the components onto a common substrate. Utilizing a similar technique, Hilliard *et al.* (17, 18) obtained composition-modulated films with short wavelengths for diffusion studies. They used a rotating pinwheel shutter with radial cutouts to facilitate alternate deposition of the two components, which were simultaneously evaporated from separate crucibles. The tech-

* Electrochemical Society Active Member.
[1] Present address: MPI, Santa Clara, California 95051.
[2] Present address: Oxy Metal Industries, Warren, Michigan 48089.
Key words: alloys, laminated composites, contacts, electrodeposition.

nique was further used to obtain composition-modulated films with enhanced elastic modulus (19), magnetization (20-24), and superconductivity (25). Similarly, molecular beam epitaxy (MBE) was used to obtain fine structures of alternating epitaxial layers of GaAs and $Ga_{1-x}Al_xAs$ (26-28). Electroplated structures of alternating layers were described by Blum (29) as early as 1921. They were obtained by plating alternately from separate electrolytes of the two components. Brenner (1) mentioned (without details) the electrodeposition of Cu-Bi alloy with alternating layers of different compositions from a single electrolyte. They were obtained by automatic switching of the current density between two widely separated values. The deposit was cross sectioned and etched to form a small diffraction grating.

In alloy electrodeposition, the current density generally has pronounced effects upon the deposit composition, structure, and properties (1). Usually, an increase of the current density (or the cathode polarization) causes an increase in the relative amount of the less noble metal in the plated alloy. With such alloys, it is possible to control the composition by changes in the plating current. Regularly modulated structures of a plated alloy, made in this way, offer the promise of new types of materials. The wide versatility of this method is due to the following reasons: (*i*) It should be applicable to most alloy systems that can be electroplated. (*ii*) Potential engineering applications for plated alloy films with tailored layer thicknesses and composition modulations should span a wide spectrum. Material properties which might be enhanced by such structures include mechanical strength, wear resistance, corrosion resistance, superconductivity and magnetic properties. (*iii*) For a given plating system the thickness of each individual layer is determined by the time integrated current (charge), and the current efficiency. Its composition is determined by the current amplitude and other plating conditions. (*iv*) Control of the charge can be achieved with a programmable power supply, completely external to the plating cell. (*v*) The concentration profile within each cycle can also be tailored, up to a point, by changing the plating current waveform, *e.g.*, by changing the amplitude and frequency and by utilizing either triangular or square wave signals to obtain gradual or abrupt variations, respectively.

Limitations of the CMA technique include the limited choice of metal pairs capable of alloy plating and the relatively small magnitude of the composition modulation (usually no more than about 20-30%). With very short spacings (~20Å), limitation on the modulation might involve mass transfer effects and epitaxial and pseudoepitaxial phenomena in the solid, in addition to relaxation times of solutes' redistribution in the diffusion layer in the electrolyte. The plated CMA coatings were characterized by Auger emission spectroscopy (AES) with sputter depth profiling and also by scanning electron microscopy (SEM) on etched cross sections. The latter technique relied on the preferential etching rate of the deposit layers. This rate is sensitive to composition and probably also to the microstructure. It increases with the content of Ag in the alloy.

This paper describes experimental results demonstrating the feasibility of electroplating CMA structures of Ag-Pd alloy coatings from a concentrated chloride bath. This alloy was chosen because it is a potential substitute for hard gold plating on electrical contacts (30). CMA structures of the Ag-Pd alloy coatings may exhibit certain desirable properties in such applications. For example, to minimize cost, reduce electrical resistivity, and increase corrosion-resistance, one could conceivably produce a layered structure composed of relatively thick layers of an alloy rich in Ag, alternating with thin layers rich in Pd. To minimize the formation of tarnish films, the outer surface layer would be Pd-rich. A preliminary comparison is made of contact properties of CMA deposits versus those of uniform Ag-Pd alloys plated with direct current. This comparison is based on several tests relevant to contact finishes (*e.g.*, contact resistance stability and contact wear).

Experimental

Plating Procedure

The Ag-Pd plating bath (with total volume of 1300 ml) consisted of:

LiCl	500g
AgCl	12g
$PdCl_2$	3g
HCl	20 ml
H_2O	1000 ml

It was operated at 85° ± 0.5°C with moderate stirring (about 10 cm/sec flow rate). The experimental plating apparatus and the bath preparation are described in detail elsewhere (30). The electroplating cell consisted of a closed vessel fitted with five ground joint openings for thermometer, stirrer, and three electrodes. The counterelectrode was made of a silver sheet with a surface area of about 15 cm^2. An internal reference electrode was made by immersing a Pd wire (0.050 in. diam) in the plating bath. This electrode had a static potential of about −258 mV *vs.* the Ag/AgCl (sat. KCl) reference electrode and was used to follow the cathode polarization, η, in response to the current modulation. The cathodes, or substrates, consisted of strips masked on their edges and back side so that the exposed area was about 2.5-3.0 cm^2. Some substrates consisted of pure silver, while others were CDA 725 copper alloy (89% Cu-9% Ni-2% Sn) protected with a soft gold undercoating (0.2-0.4 μm thick). For more details of the substrate preparation see Ref. (30).

The applied electric signal was produced and controlled by a combination of a potentiostat/galvanostat (PAR 173) and a signal programmer (PAR 175). The time traces of the current, cell voltage, and cathode potential (*vs.* the Pd wire reference) were monitored by a chart recorder and by an X-Y recorder (HP 7004B).

CMA coatings were prepared with two modes of current modulation; square (or stepped), and triangular (or swept) current waves. CMA structures with palladium-rich last layers and with silver-rich last layers were produced by stopping the plating at the appropriate half-cycle in order to study the effect of having the more corrosion resistant Pd-rich layer at the surface.

Microscopic Analysis

Metallographic cross sections were mechanically polished using alumina powder (0.05μ) and etched for 30 sec in a freshly prepared solution of 5g KCN, 5g $(NH_4)_2S_2O_8$, and 200 ml of deionized water. The mounted cross sections were then coated with ~200Å of gold, by sputtering, to improve their electric conduction for SEM examination.

Auger Analysis

The Auger measurements were made with a scanning Auger microprobe (SAM, PHI Model 650) employing a double pass cylindrical mirror analyzer with a concentric 5 kV gun. Composition-depth profiles were obtained with Ar sputtering. Derivative spectra were taken with 5 kV primary energy, $\sim 10 \times 10^{-7}$A beam current, 3V peak to peak modulation, scan rate 3 eV/sec, time constant 0.03 sec, and sputter rate—either ~250 or 60Å/min at 3 kV in 5×10^{-5} Torr of argon.

The primary information was obtained from the principal MNN lines of Pd and Ag (located at 330

and 351 eV, respectively). The relative sensitivity factor for these lines, S_{Ag}/S_{Pd}, was taken as 1.28 based on the determination by Schwartz (31) for a wrought R156 alloy (60% Pd/40% Ag) and the bulk alloy measurement described below. The composition was then determined from the formula $C_{Ag}/C_{Pd} = (I_{Ag}/I_{Pd})/1.28$ where C_{Ag} and C_{Pd} are in atomic percent (a/o) and I_{Ag} and I_{Pd} are peak to peak intensities of the 351 and 330 eV lines, respectively. The increase in Pd surface concentration (relative to the bulk concentration) produced by sputtering, introduced some error into the determination of the bulk concentrations, as described by Schwartz (31). To estimate this effect, a sample of R156 alloy was sputtered for 40 min. After the surface films were removed in the first minute of sputtering, a constant intensity ratio, $I_{Ag}/I_{Pd} = 0.92$, was obtained This ratio, together with a sensitivity ratio of 1.28, indicated a composition of 42% Ag and 58% Pd, in close agreement with the nominal bulk composition of R156. The Pd enhancement effect from sputtering thus was small in this case. The indicated compositions of the electrodeposited alloys were within about 5 a/o of the values obtained by x-ray analysis in the SEM. The error in the Auger measurement of absolute composition is not a serious problem in the present application where the change in the relative amounts of Ag and Pd as a function of depth is of more interest.

Results

Effect of Current Waveform on Structure

In this section, we compare the intended structures, as determined by the current waveform used, with the results obtained by AES and SEM analysis. The effects of substrate roughness and the displacement reaction of Ag from the substrate or the deposit by Pd are also demonstrated.

Square CMA with modulation ≥1000Å.—Figure 1 depicts the time traces of an applied square current wave, and the corresponding cathode polarization (η *vs.* t). These were obtained during a plating experiment designed to produce a structure of alternating thick (1000Å) Ag-rich layers and thin (100Å) Pd-rich layers. Figure 2 shows SEM photographs of an etched cross section of the resulting deposit. A comparison to the 0.1 μm (1000Å) scale marker indicates that the total cycle thickness is very close to the nominal value of 1100Å. This deposit was plated onto a silver strip substrate which had been chemically etched (in NH_4OH/H_2O_2 1:1), and immersed (with no applied current) for 2 min in the Ag-Pd plating bath prior to the CMA plating. It was also left in this bath (with no applied current) for 1 min following the termination of the CMA plating. Pd-rich layers produced by displacement plating can be seen at the boundary between the Ag substrate and the CMA structure, and also on the outer surface. (The etching procedures make the Pd-rich layers appear white in these SEM photographs.) For more details regarding the displacement reactions, see Ref. (30).

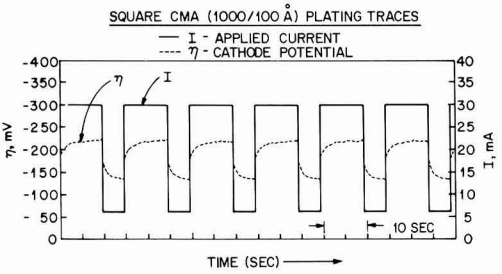

Fig. 1. Time traces of the impressed plating current, *I*, and the cathodic polarization, η (*vs.* Pd-wire reference electrode), for a square waveform designed to produce alternating 1000Å Ag-rich layers and 100Å Pd-rich layers.

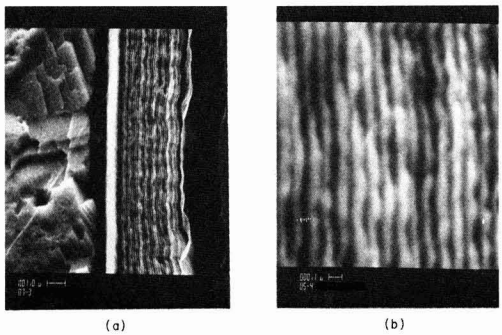

Fig. 2. SEM of an etched cross section of the CMA structure corresponding to Fig. 1. Notice (from left to right) the Ag-substrate, a Pd-enriched displacement layer (white), the 34 cycles of CMA structure, and another Pd-rich displacement layer.

The composition modulation and the Pd surface enhancement of this sample are immediately apparent in the Auger depth profiles shown in Fig. 3. The indicated variation of Pd in the bulk of the sample is between 34 and 37 a/o while corresponding variation in the Ag/Pd ratio is 1.94 to 1.70. The gradual decrease in the amplitude of composition modulation with sputtering time does not represent a real effect in the sample. It results from the gradual loss of depth resolution associated with the analysis technique. This effect is further discussed later. Minor amounts of Cl and S were also detected at about the 1% level. The S was a surface contaminant (presumably a sulfide) which disappears after a sputtering time of less than 1 min. Interestingly, the Cl signal in Fig. 3 shows a moderate peak coinciding with the Pd-rich displacement layer, and very small peaks occur thereafter

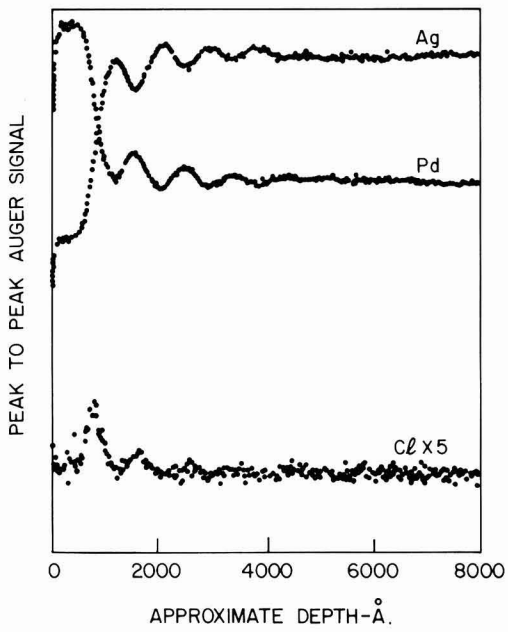

Fig. 3. Auger depth profiles for Ag, Pd, and Cl obtained with the deposit corresponding to Fig. 1 and 2. Notice the Pd-rich outer layer produced by displacement and 3-4 cycles of CMA. Also notice that Cl peaks coincide with Pd peaks.

at depths corresponding to maxima in Pd concentration. When the sputter beam was turned off, the Cl signal increased steadily, indicating this species was migrating to the surface. Presumably, this Cl is incorporated from the plating bath in greater amounts during the intervals of lower current density (*i.e*, Pd-rich layers). The depth profiles in Fig. 3 show quite clearly that the surface layer is enriched in Pd by the displacement reaction. The indicated surface composition is approximately 56% Pd. This surface layer is about 1000Å thick and is variable in thickness from point to point on the sample as can also be seen in Fig. 2.

Results are presented next which illustrate that the Ag-Pd plating tends to smooth small protrusions or irregularities but amplifies large ones. The latter are deleterious since they proceed to develop into nodules, and eventually deteriorate the plating. Figure 5 shows SEM micrographs of an etched cross section of a CMA coating on a very flat and smooth substrate. The Ag substrate was prepared by careful polishing with 0.3 μm alumina. Plating was initiated immediately after immersion, a procedure which avoids the silver displacement reaction with an attendant surface roughening. The applied current waveform and the corresponding time traces of the cathode polarization and cell voltage, obtained during the plating of this sample, are shown in Fig. 4. The designed CMA structure consisted of alternating layers of 1000Å rich in Ag and 200Å rich in Pd. A layer of about 1 μm of soft gold (seen as a white layer) was overplated on this CMA structure in order to facilitate the preparation of the metallographic cross section. Another Ag substrate was roughened by a prolongated etching in NH_4OH/H_2O_2 (1:1) followed by immersion in the plating bath for 2 min with no current applied. Figure 6 shows

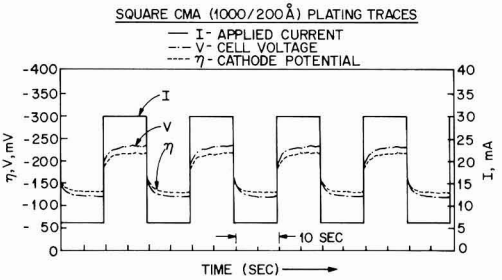

Fig. 4. Time traces of the applied current, the corresponding cathodic polarization, η, and the cell voltage, V, obtained during the plating of a square CMA designed to produce alternating 1000Å Ag-rich layers and 200Å Pd-rich layers.

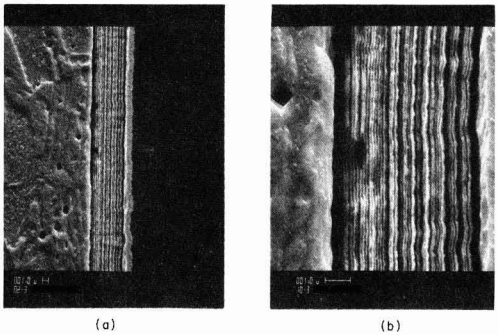

Fig. 5. SEM of an etched cross section of the CMA corresponding to Fig. 4. The outermost layer (white) corresponds to a soft gold (about 1 μm thick) plated over the CMA structure in order to facilitate mechanical polishing of the sample without damage.

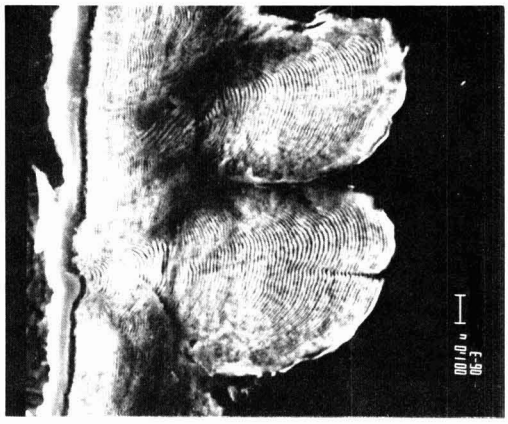

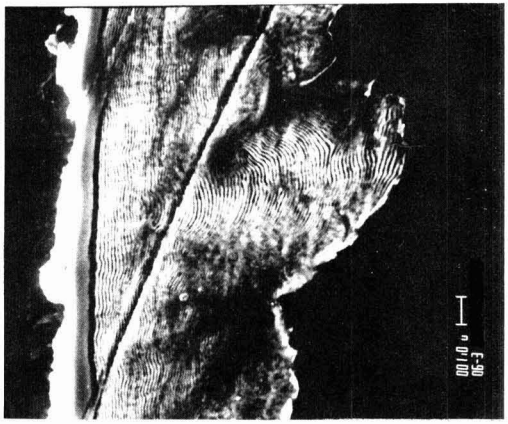

Fig. 6. SEM of an etched cross section demonstrating the effects of substrate roughness (a) and particle inclusions (b) on the stability of the growth interface. CMA structure same as in Fig. 1, 2, and 3.

SEM photographs of the etched cross section of this substrate and the Ag-Pd CMA coating which was plated onto it. The designed CMA structure of this sample was similar to the sample of Fig. 1, 2, and 3 (*i.e.*, alternating layers of 1000Å Ag-rich, and 100Å Pd-rich). Here, however, the substrate roughening produced large protrusions $\geqq$0.5 μm which were subsequently amplified in the CMA deposit. A similar effect was also produced by inclusion of solid particles during the plating (cf. Fig. 6b). Small protrusions originating either in the substrate, or within the CMA deposit due to small fluctuations, are seen to be smoothed out as the deposition proceeds.

Square CMA with modulations of 500-1000Å.— Figure 7 shows the time traces of the applied current and the corresponding cathode polarization and cell voltage during the deposition of a CMA structure designed to produce alternating layers of 500Å Ag-rich, and 250Å Pd-rich. SEM photographs of the etched cross section are shown in Fig. 8. Good agreement between the designed and obtained total cycle thickness may be noted. Also evident is the excellent resolution of the microstructure after etching (better than 500Å).

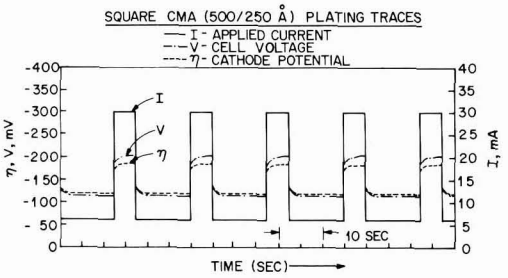

Fig. 7. Time traces obtained during the plating of a square CMA designed to produce alternating 500Å Ag-rich layers and 250Å Pd-rich layers.

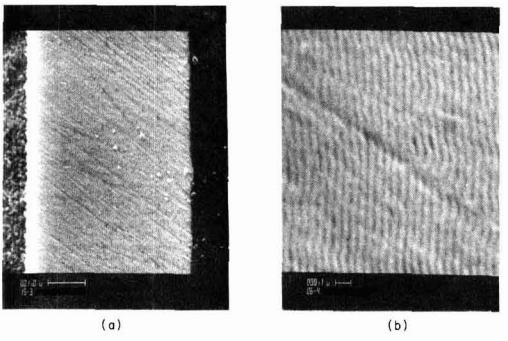

Fig. 8. SEM of an etched cross section corresponding to Fig. 7. Notice the excellent resolution of the etchant. The total deposit thickness is about 6 μm, and there are some 80 cycles, or a total of 160 layers.

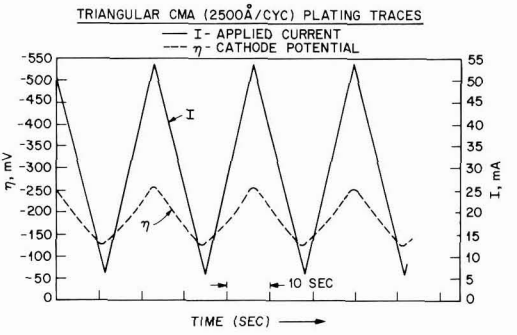

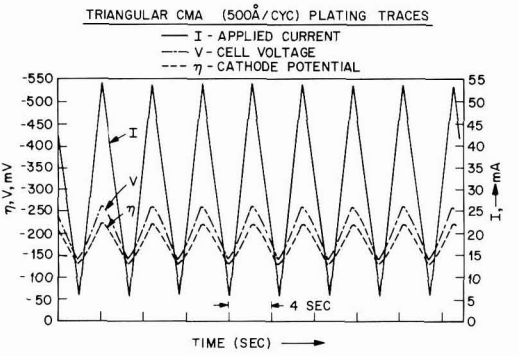

Fig. 9. Time traces obtained during the plating of triangular CMA structures. The current waveforms were designed to produce a structure with cyclic layers 2500Å thick (a) and a structure with cyclic layers 500Å thick (b).

The deep diagonal grooves which run across the coating are probably artifacts caused by minute polishing scratches which were later magnified by the chemical etching procedure. The substrate of this sample consisted of the alloy, CDA 725. It was mechanically polished (with 0.3 μm alumina) and plated with a 0.3 μm thick soft gold undercoating prior to plating of the CMA coating. As discussed elsewhere (30), this procedure avoids vigorous displacement reactions of base metals with the Ag-Pd plating bath. The plating of the CMA structure was started immediately following the immersion of the protected substrate in the Ag-Pd plating bath. Examination of this sample by AES, as well as four other samples with nominal cyclic wavelengths less than 1000Å, failed to show any indication of composition modulation in the sputter profiles. Data scattering was about 2% in the Ag/Pd ratio. Much of the layer delineation seen by SEM for these samples may thus originate from microstructure modulation. The lack of composition resolution by AES depth profiling could also be due to the undulating character of the deposit surface (cf. Fig. 8).

Square CMA with modulation <500Å.—Samples with a designed modulation of less than 500Å show no evidence of modulations by either SEM or AES. Thus, rapid variation of the applied current density does not appear to be reflected in either the deposit microstructure or the composition. This apparent limit on the dynamics of the plating process will be considered in more detail later.

Triangular CMA.—Figures 9a and 9b depict the applied triangular current waveforms, and the time traces η-t and V-t, obtained during the plating of two triangular CMA structures. They were designed to produce structures with cyclic layers of 2500Å and 500Å, respectively. Etched cross sections of similar samples are shown in Fig. 10a and 10b. Whereas it is easy to delineate the CMA structure having cyclic layers of about 2500Å thick (cf. Fig. 10a), a similar delineation is not possible with the deposit designed to produce cyclic layers of 500Å thick (cf. Fig. 10b) nor with several other triangular CMA deposits, designed to have wavelengths shorter than 500Å. The AES depth profiling obtained with a triangular CMA structure having 2500Å wavelength is shown in Fig. 11. In this case, about 3 μm was sputtered away. enough to penetrate through the deposit thickness (nominally 2.75 μm). Approximately 3 or 4 of the 11 layers are resolved and show a triangular variation in the composition. As previously mentioned, the loss of depth resolution, as well as the nonabrupt drop in signal when sputtering had penetrated through the plated alloy, are believed to be artifacts due to sputter-induced microtopographic features. The AES depth profiling was not able to resolve any composition modulation in triangular CMA deposits with designed layer thicknesses of 500Å or shorter, just as with the square CMA structures.

Evaluation of Deposits for Contact Finish Applications

A preliminary evaluation of contact resistance of Ag-Pd CMA and d-c plated alloy coatings was performed. The contact resistance prior to and following exposure to an environment of flowers of sulfur (37) was measured using a four-point probe at 100g force.

One week exposure of both the square CMA and the d-c coatings (50% Ag-50% Pd) to an environment containing flowers of sulfur, 85% relative humidity (RH), and 50°C, had hardly any effect on the contact resistance of either types of deposits. The initial value was about 1.1-1.3 mΩ for all coatings. Figure 12 shows a probability plot of the measured contact resistance values for the wrought R156 alloy, for a uniform (d-c

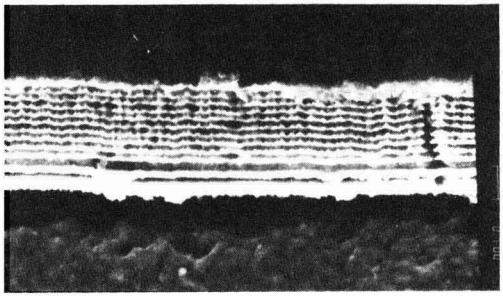

(a)

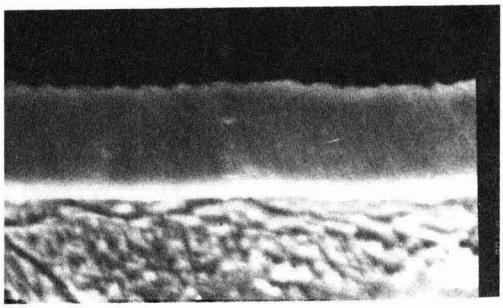

(b)

Fig. 10. SEM of etched cross sections of triangular CMA deposits designed to produce a structure with cyclic layers 2500Å thick (a) and a structure with cyclic layers 500Å thick (b). (See text.)

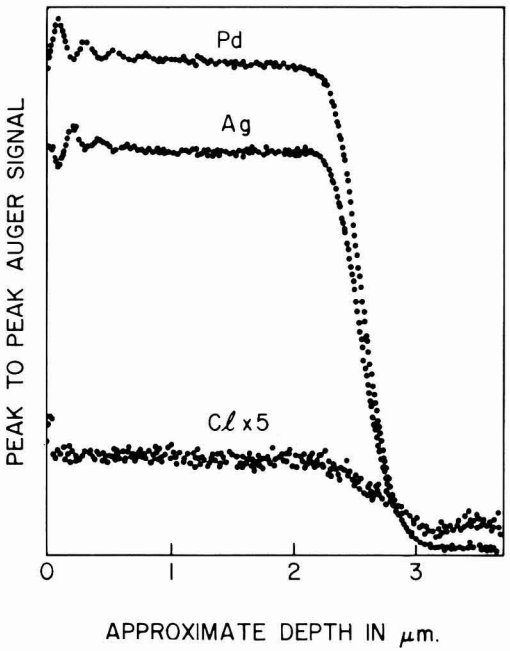

Fig. 11. Auger depth profiles for Ag, Pd, and Cl obtained with samples corresponding to Fig. 9a and 10a. Note the triangular response of the composition to the current.

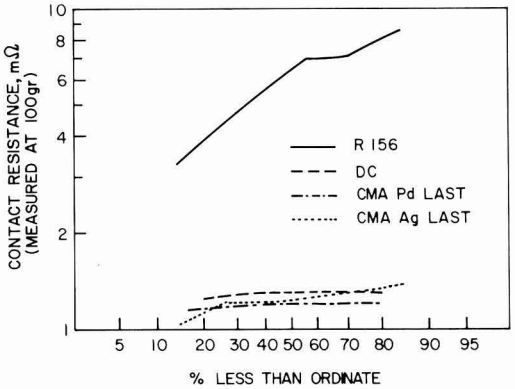

Fig. 12. Contact resistance distribution plot after a flowers of sulfur exposure test. Data were measured with a load of 100 g on a gold probe using the 4 wire method. Samples were exposed to saturated flowers of sulfur for 1 week at 50°C and 85% RH.

plated) deposit, and for two CMA deposits with alternating layers of 1000Å rich in Ag and 200Å rich in Pd. The two CMA deposits differed from each other only in that the plating current was turned off during the plating of an Ag-rich layer (ARL) or during the plating of a Pd-rich layer (PRL). The ARL deposit gave slightly greater scatter than either the PRL or the uniform deposit. However, all three electrodeposits showed substantially less contact resistance increase than did the bulk R156 alloy. This improvement in the contact resistance stability (CRS) of the electrodeposited alloys over the wrought alloy is particularly surprising since the latter contained more Pd than the plated alloys.

The same result was also found in a previous comparison (30) of d-c plated Ag-Pd *vs.* R156 in a flowers of sulfur test. As discussed below, the influence of incorporated Cl and the microstructure will be considered as possible causes for the improved CRS behavior. Wear and friction response of the Ag-Pd CMA coatings was evaluated briefly using the approach described in Ref. (30) and was also found similar to that of d-c Ag-Pd coatings.

CMA and d-c Ag-Pd platings differed in the coating appearance. d-c platings containing less than about 45% Ag had rough surfaces with dark gray matte color. The surface became smoother, and the color lighter, with increased Ag content. Deposits containing more than about 70% Ag exhibited a silver-white color and tended to be powdery. Semi-bright d-c coatings could be obtained only under optimum conditions. CMA deposits, on the other hand, had smoother surfaces and brighter appearance under a wider range of plating conditions. For a given average current density, the brightness increased with the applied wave frequency provided that the high current amplitudes and durations were not excessive (*i.e.*, about 25 mA/cm^2 and 1 min).

Discussion

The analysis of CMA deposits indicates that, within certain limits, the alloy composition and structure do correspond to the applied current waveform. A triangular waveform gives rise to a clearly triangular composition profile (cf. Fig. 11). A square waveform, however, does not appear to cause corresponding sharp composition steps, particularly for short wavelengths. In such cases the composition-depth profiles are rounded, resembling a roughly sinusoidal waveform (cf. Fig. 3). The cathodic polarization also does not change instantaneously with new applied current but approaches a new steady state with a time constant of the order of several seconds. This response time is not

likely to reflect the non-Faradaic effects such as double layer charging, which typically takes place in a millisecond time frame. Rather, this response time probably reflects the ion redistribution in the diffusion layer (concentration polarization) which normally takes place with a time constant of a few seconds (1) such as is observed in Fig. 1. It is thus possible to understand why we observe a clearly defined CMA structure with a cyclic composition only when the wavelength is $\geq$1000Å, corresponding to cycle time >5 sec for the conditions used.

The layers seen in SEM micrographs of CMA deposits where the wavelengths are in the intermediate range (500-1000Å), may reflect a modulation of the microstructure more than of composition (since no modulation is detected by AES profiles of such samples). The general experience in plating both alloys and single metals indicates that microstructure is indeed sensitive to current density variations (1). A study of the microstructure modulations of CMA Ag-Pd deposits by transmission electron microscopy (TEM) of cross sections is planned to confirm this point. A previous study of d-c plated Ag-Pd coatings by TEM and x-ray diffraction (XRD) revealed a homogeneous single phase solid solution with an fcc crystal structure, and very fine grains (100-300Å) (33). Voids of about 20-30Å in size were also noted at the grain boundaries.

It does not seem likely that the loss of AES depth resolution is due to solid-state diffusion. The rates of solid-state interdiffusion of Ag and Pd in the alloy Ag-Pd are extremely low at room temperature. The plating temperature (85°C) is only maintained for short period (about 10 min). Experiments to homogenize adjacent thin layers of Ag and Pd by Tu (34), revealed negligible diffusion after a period of 24 hr at 200°C. Indeed, the diffusion length, computed from the diffusion coefficients of the bulk Ag-Pd alloy, should be only a small fraction of 1Å (during a 24 hr period at 200°C).

Among several possible reasons for the loss of the AES resolution of composition modulations with the depth, we believe that the microtopography of the deposit surface and outer layers is of primary importance. The outer layers of CMA deposits will generally not be perfectly flat. Undulating ripples are clearly seen in Fig. 2, 5, 6, and 8. Before sputtering is begun, the AES analyzing beam excites only the outermost layer surface, regardless of the ripples, so that true surface composition is obtained. However, as depth profiling is set by sputtering, the bottom of the sputtering crater (about 1 mm diameter) advances through the deposit, exposing various depths of a layer, or even more than a single layer, at a time. The topography of the surface will change during the course of the sputtering; it could approach a flat or, more likely, it could develop new microtopography such as the cones often seen on sputtered metals (35). Consequently, the analyzing AES beam (of about 5 μm diameter), focused at the crater's bottom, will generally sample areas at different distances from the original surface at any instant. Such averaging effects add to the rounding of composition profiles of CMA structures obtained with square current waveforms. Esaki and Chang (27) attributed the steady loss of resolution with the sputtering depth to the spatially varying rates on the scale of the area of the focused primary beam.

It is possible to interpret a number of our findings concerning the controlling parameters in the plating process on the basis of a relatively simple model, *i.e.*, that the mass transport of Pd^{+2} ions across the diffusion layer is rate controlling. This is the typical behavior for normal alloy plating where the more noble metal is diffusivity controlled (1). To achieve a maximal effect of modulating the composition, it is necessary to operate under conditions such that modulation of current density produces largest change in the concentration of Pd^{+2} ions at the interface. For the experimental conditions used, increasing the current density modulation, decreasing the total ion concentration of the solution, or decreasing the rate of stirring all should favor larger modulation in the composition of the plated CMA alloy. It is anticipated that CMA Ag-Pd structures with layer thickness $\leq$100Å may be obtained by decreasing the ion concentrations by about an order of magnitude. This, however, may increase erratic fluctuations in composition and morphology of the growth interface.

The smoothness of the deposit is also controlled by the mass transport of the Pd^{+2} ions. We can thus understand that changes in plating parameters which tend to decrease the Pd content in the plated alloy (*e.g.*, increased current density), tend also to destabilize the growth interface of the deposit. In the SEM photographs of etched cross sections (see especially Fig. 6a and 6b), interface protrusions of small dimensions are seen to be gradually smoothed out, whereas protrusions of larger dimensions are seen to be gradually amplified, causing increasing roughness and eventually leading to nodule formation and coating deterioration. Other destabilizing effects due to substrate surface irregularities and particle inclusions during growth can likewise be seen in these figures. The critical size of protrusion which is no longer smoothed is expected to be comparable to the diffusion layer thickness since larger protrusions will penetrate into the diffusion layer, thereby becoming more favored for growth over their surroundings. The faster growth rate on such large protrusions is due to the larger nutrient concentration ahead of the protrusions causing the further amplification of these protrusions. With small protrusions, on the other hand, the diffusion layer can conform to the outlines of the solid surface. The growth of such protrusions is, therefore, not favored over their surroundings. However, the increase of free energy due to the increased interface area of protrusions and the associated surface tension, will tend to smooth out the small protrusions (36, 37).

The SEM photographs of etched cross sections provide insight as to such effects of surface irregularities on rate growth because: (*i*) Each cross-sectional photograph contains a continuous record of the growth interface position and shape. Each contour line (cyclic layer) represents the instantaneous position of the growth interface at a known time (given by the number of lines from the substrate). (*ii*) The growth direction is always normal to the contour lines. (*iii*) The local contour line spacing is proportional to the local rate of growth. *i.e.*, the regions with the largest spacing between lines can be identified as the regions with the fastest growth. In future studies, this information could be more systematically analyzed to provide a new means to study the stability of growth interfaces as well as the macro and microthrowing power of plating baths.

The superior corrosion resistance and contact resistance stability (CRS) of both CMA and d-c plated Ag-Pd alloys (relative to the wrought alloy R-156), as determined in the flowers of sulfur tests, is of practical significance as well as scientific interest. Based on the higher content of Ag in the plated alloy, one would anticipate the opposite behavior. Nevertheless, the plated alloys differ substantially from the wrought alloy in their microstructure and their incorporated trace impurities. As noted previously (30), the grain size of the wrought alloy is of the order of several micrometers, whereas that of the plated alloys is only about 100-300Å. Also, the plated alloy is more homogeneous than its wrought counterpart. The much finer grain size as well as the greater homogeneity of the plated alloy, could reduce the Ag mobility towards the surface, thereby reducing the formation of tarnish films in the sulfiding environment. It is also con-

ceivable that incorporated impurities in the plated alloy may somehow hinder and reduce the mobility of Ag to the surface, thereby improving its tarnish resistance. The presence of incorporated Cl in CMA Ag-Pd coatings, established by AES, may thus contribute to its superior tarnish resistance over that of the wrought alloy.

Summary

With the application of the CMA technique to the plating of Ag-Pd alloys, we have demonstrated the feasibility of preparing new types of laminated composite structures. The technique allows the control of thickness and composition of individual layers within the deposit in a precise and convenient manner. The versatility of the technique has been demonstrated by plating CMA structures by both square and triangular waveforms. The minimum thickness of the individual layers appears to be defined by the response time, of the order of several seconds, required to achieve a new steady state of concentration gradients in the diffusion layer after a change has occurred in the current density. For the conditions of this study, this minimum cycle wavelength was about 500-1000Å. Plating of CMA structures of Ag-Pd alloy with layer thickness below about 100Å is believed to be feasible with lower average current densities and bath concentrations. Detailed studies of etched cross sections of CMA structures provide a new and convenient means to study destabilizing mechanisms of the growth interface and its morphology.

A preliminary comparison between CMA and d-c plated Ag-Pd alloys did not reveal any clear differences in tests relevant to their contact finish properties. Both were found superior to the wrought alloy, R-156, in these tests, although they contained one-third less Pd than the wrought alloy. Indeed the contact finish properties of both types of plated Ag-Pd alloy were found to be generally satisfactory. The only noticeable difference between CMA and d-c plated Ag-Pd alloys was the increasing brightness of CMA deposits with the frequency of the square or triangular waveform.

With the knowledge of the CMA technique gained from the present study, it should be possible to produce other CMA alloys where beneficial effects might be realized from the strongly anisotropic structure. One obvious future application is the preparation of magnetic alloy films for information storage since magnetic properties are sensitive to both film thickness and composition. Other possible areas of application for CMA plating include the preparation of superconducting films, highly protective coatings for use in corrosive environments, and layered structures with optical or improved mechanical properties such as toughness and wear resistance.

Manuscript submitted June 11, 1982; revised manuscript received May 10, 1983. This was Paper 310 presented at the Denver, Colorado, Meeting of the Society, Oct. 11-16, 1981.

Bell Laboratories assisted in meeting publication costs of this article.

APPENDIX A

Design of CMA Structure Parameters

Square Current Wave

The square current wave is characterized by its lower and upper current densities, $i_1 = I_1/A$, and $i_2 = I_2/A$, respectively, and their corresponding periods t_1 and t_2, respectively. Here A is the cathode surface area, and I_1 and I_2 are the applied current steps. The cycle frequency is $f = 1/\tau$, where $\tau = t_1 + t_2$ is the total cycle period. The individual layer thicknesses are calculated from the relationships

$$h_1 = \frac{p_1 I_1 t_1 M_1}{n_1 d_1 A \mathbf{F}} \quad [1]$$

$$h_2 = \frac{p_2 I_2 t_2 M_2}{n_2 d_2 A \mathbf{F}} \quad [2]$$

and

$$\frac{h_1}{h_2} = \frac{p_1 I_1 t_1 M_1 n_2 d_2}{p_2 I_2 t_2 M_2 n_1 d_1} \quad [3]$$

Here p_1 and p_2 are the lower and upper step cathode current efficiencies, respectively, and M_1 and M_2 are the molar weights of the alloy plated at i_1 and i_2, respectively. $\mathbf{F}$ is the Faraday constant (96,500 coulomb/mol). n_1 and n_2 are the numbers of electrons transferred per formula of the alloys plated at i_1 and i_2, respectively, and d_1 and d_2 are the corresponding densities of these alloys. For small magnitude composition modulation, the average parameters can be considered: $P \simeq P_1 \simeq P_2$; $M \simeq M_1 \simeq M_2$; $n \simeq n_1 \simeq n_2$; and $d \simeq d_1 \simeq d_2$.

For this case

$$h_1 = C\frac{I_1 t_1}{A} \quad [1a]$$

$$h_2 = C\frac{I_2 t_2}{A} \quad [2a]$$

and

$$\frac{h_1}{h_2} = \frac{I_1 t_1}{I_2 t_2} \quad [3a]$$

Here $C = pM/nd\mathbf{F}$ is a constant. For Ag-Pd alloys of about 50% Ag-50% Pd, $C \simeq 1.0 \dfrac{\text{cm}^2\ \mu\text{m}}{\text{coulomb}}$ when h_1 and h_2 expressed in μm, I_1 and I_2 in amperes, t_1 and t_2 in sec, and A in cm^2.

Triangular Current Wave

Only average parameters are considered here since the current is continuously swept. The lower and upper limit current densities are $i_1 = I_1/A$ and $i_2 = I_2/A$, respectively. The average current density is $i_{\text{avg}} = \dfrac{i_1 + i_2}{2}$, and the sweep rate is

$$\frac{di}{dt} = \frac{2(i_2 - i_1)}{\tau} \quad [4]$$

where τ is the cycle period. The cyclic layer thickness is calculated from

$$h = Ci_{\text{avg}}\tau = C\frac{I_{\text{avg}}\tau}{A} \quad [5]$$

REFERENCES

1. A. Brenner, "Electrodeposition of Alloys: Principles and Practice," Academic Press, New York (1963).
2. V. Zentner, *Plating*, **52**, 368 (1965).
3. D. W. Endicott and J. R. Knapp, Jr., *ibid.*, **53**, 43 (1960).
4. I. A. Menzies and C. S. Ng, *Trans. Inst. Met. Finish.*, **36**, 48 (1968).
5. J. H. Wiesner and W. B. Distler, *Plating*, **56**, 799 (1969).
6. R. Duva and D. G. Foulke, *ibid.*, **55**, 1056 (1968).
7. E. Raub and K. Muller, "Fundamentals of Metal Deposition," Elsevier, New York (1967).
8. C. A. Snavely, *This Journal*, **97**, 99 (1950).
9. V. A. Lamb, C. E. Johnson, and D. R. Valentine, *ibid.*, **117**, 291C, 341C, 381C (1970).
10. R. Weil and W. N. Jacobus, Jr., *Plating*, **53**, 102 (1966).
11. A. Brenner, V. Zentner, and C. W. Jennings, *ibid.*, **39**, 865, 899, 933 (1952).
12. U. Cohen and W. A. Tiller, To be published.
13. W. R. Meyer and A. Phillips, *Trans. Electrochem. Soc.*, **73**, 377 (1938).
14. K. Aotani, *J. Electrochem. Soc. Jpn.*, **21**, 180 (1953).
15. P. F. Mikhalev, *Compt. Rend. Acad. Sci. URSS*, **24**, 899 (1939).
16. J. DuMond and J. P. Youtz, *J. Appl. Phys.*, **11**, 357 (1940).
17. H. E. Cook and J. E. Hilliard, *ibid.*, **40**, 2191 (1969).
18. E. M. Philofski and J. E. Hilliard, *ibid.*, **40**, 2198 (1969).
19. W. M. C. Yang, T. Tsakalkos, and J. E. Hilliard, *ibid.*, **48**, 876 (1977).

20. B. J. Thaler, J. B. Ketterson, and J. E. Hilliard, *Phys. Rev. Lett.* **41,** 336 (1978).
21. M. B. Brodsky and A. J. Freeman, *ibid.*, **45,** 133 (1980).
22. E. M. Gyorgy, J. F. Dillon, D. B. McWhan, L. W. Rupp, L. R. Testardi, and P. J. Flanders, *ibid.*, **45,** 57 (1980).
23. T. Jarlborg and A. J. Freeman, *ibid.*, **45,** 653 (1980).
24. M. B. Brodsky, *J. Appl. Phys.*, **52,** 1665 (1981).
25. S. T. Ruggiero, T. W. Barbee, and M. R. Beasly, *Phys. Rev. Lett.*, **45,** 1299 (1980).
26. A. Y. Cho, *J. Appl. Phys.*, **41,** 782 (1970).
27. L. Esaki and L. L. Chang, *Thin Solid Films*, **36,** 285 (1976).
28. Z. L. Liau, S. U. Campisano, C. Canali, S. S. Lau, and J. W. Mayer, *This Journal*, **122,** 1696 (1975).
29. W. Blum, *Trans. Am. Electrochem. Soc.*, **40,** 307 (1921).
30. U. Cohen, K. R. Walton, and R. Sard, *This Journal*, To be published.
31. G. P. Schwartz, *Surf. Sci.*, **76,** 113 (1979).
32. A procedure recommended by the B.04 ASTM Committee, designated: "Method of Test for Tarnish Resistance of Electrical Contacts to a Flowers of Sulfur Atmosphere."
33. U. Cohen and S. Nakahara, Unpublished research.
34. K. N. Tu, *J. Appl. Phys.*, **48,** 3400 (1977).
35. G. K. Wehner and D. J. Hajicek, *ibid.*, **42,** 1145 (1971).
36. C. Wagner, *This Journal*, **101,** 225 (1954).
37. A. R. Despic and K. I. Popov, in "Modern Aspects of Electrochemistry," Vol. 7, B. E. Conway and J. O'M. Bockris, Editors, Plenum Press, New York (1972).

Capacitance Characteristics of the Polycrystalline CdS/NaOH and CdS/Cysteine Interfaces

R. Dewitt and A. Kirsch-De Mesmaeker*

Universite Libre de Bruxelles, Faculte des Sciences-CP. 160, Service de Chimie Organique, B-1050 Bruxelles, Belgium

ABSTRACT

Flatband potentials (V_{FB}) of polycrystalline CdS have been determined as a function of pH, in the absence and in the presence of cysteine. From pH 10, the linear dependence of V_{FB} with pH is explained by a hydroxylation of the electrode surface. With cysteine, two V_{FB} negative steps occur at pH's corresponding to the two pK_a's of the reductant, emphasizing the V_{FB} dependence on the degree of ionization of the amino acid.

Several studies (1) have shown that CdS in contact with an aqueous electrolyte solution presents important photoanodic corrosion. Up to now, the most efficient redox electrolytes used to check this are the chalcogenide/polycalcogenide couples (2).

It was interesting to test sulfur containing organic reductants as kinetic inhibitors of CdS photocorrosion (3). According to some choice criteria, cysteine (I) had been chosen as one of these reductants; its behavior at illuminated CdS has been described previously (3). These studies have shown that although cysteine does not behave as an efficient kinetic inhibitor of photocorrosion, the i/V curve characteristics of amorphous CdS are improved under illumination in an aqueous basic solution of cysteine. From x-ray fluorescence and LEEIX measurements (4), it turns out that the photoelectrochemical characteristic improvements can be correlated to hydroxylation of the CdS, strongly enhanced in the presence of cysteine (pH 14).

Nevertheless, a thorough *in situ* study of the CdS-cysteine junction by capacitance measurements could not be carried out because of the nonlinearity of the Mott-Schottky $1/C^2$ *vs.* V plots. This behavior probably stems from the amorphous structure of the studied CdS films, obtained by chemical deposition (5). Consequently, in order to get a deeper insight into the CdS-cysteine interface by capacitance studies, we examined another type of CdS prepared by evaporation and presenting a better crystalline structure. With these samples, we have been able to study more quantitatively the solid-liquid junction, and especially the influence of cysteine and pH on the capacitance characteristics in the dark, which we present in this paper.

* Electrochemical Society Active Member; Research Associate of the National Fund for Scientific Research (Belgium).
Key words: CdS, cysteine, surface modification, flatband potential.

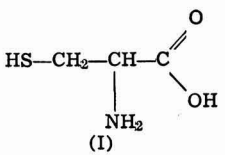

(I)

Experimental

Electrodes.—Polycrystalline n-CdS electrodes prepared by evaporation on brass, were donated by B. Baron (Institute of Energy Conversion, University of Delaware, Newark, Delaware). The microcrystals (hexagonal system) are oriented with the c-axis perpendicular to the support, the thickness of the CdS film is about 25 μm, with an average grain diameter of 1 μm and a resistivity varying between 1 and 3 $\Omega \cdot$ cm from one sample to the other. The donor density ($N_D \simeq 4.5 \pm 0.5\ 10^{18}$ cm^{-3}) was determined by us, from the slope of the Mott-Schottky plot. The N_D value is only indicative because no roughness factor, which can easily reach 2, has been considered. The polycrystalline structure has been checked by SEM (ISI DS 130, no metallization treatment) (Fig. 1) and x-ray diffraction. Figure 1 shows that the surface structure is very different from the nodules of the amorphous CdS (3b) studied before.

Preparation of electrodes.—Each electrode is mounted on a Pyrex support using an insulating glue (Dow Corning RTV 730). Electrical contact is made by a copper wire glued with a conducting silver paint on the back brass surface. Before each measurement, the mounted electrode is etched by HCl 4M (Merck, Titrisol) for 1 min at room temperature in the dark; it is then rinsed five times with tridistilled water and finally the solution is poured into the cell. The measurements are made after a 5 min contact between the solution and the electrode.

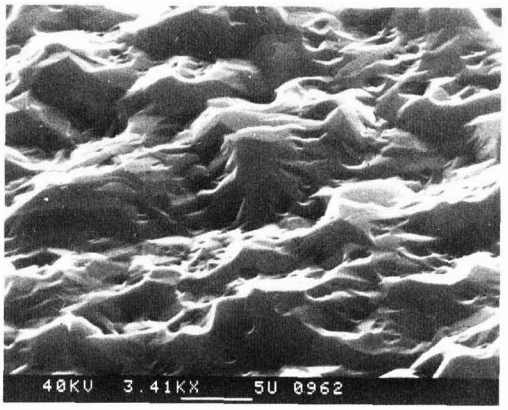

Fig. 1. SEM picture of the CdS film. Beam incidence of 30° with respect to the surface.

Solutions.—All solutions are made with tridistilled water. Traces of ferric ions present in NaOH (P. A. Merck) are removed by coprecipitation with $Mg(OH)_2$ added as $MgSO_4$ to the NaOH stock solution (4M). L-Cysteine ($HSCH_2CH(NH_2)COOH$) (P. A. Aldrich) and $LiNO_3$ (P.A. U.C.B.) are used as such. Na_2SO_4 (P.A. U.C.B.) is recrystallized. The *p*H of each solution is measured with a Philips PR 9403 *p*H meter, equipped with a glass electrode (Philips GA 420, *p*H 0-14). The concentration of cysteine is checked for several experiments by the Ellmann's spectroscopic method (6) (oxidation of cysteine by 3,3′ dithiobis (6 nitrobenzoic) acid giving a free yellow nitro carboxythiolate ion with $\epsilon_{412\,nm} = 13{,}600$). All solutions are deoxygenated by nitrogen bubbling during the solution preparation and before and during the experiments.

Experimental setup.—The impedance measurements are performed by superimposing a sinusoidal signal on a linear potential sweep, applied, via a Tacussel Pit 20-2X Potentiostat, to the CdS working electrode of a one-compartment cell containing also the saturated calomel and counterelectrodes. The resulting cell signal is measured *vs.* the reference signal of the potentiostat, with an Ortec Brookdeal 9503-C Lock-in Amplifier or on a X-t recorder with a signal rectifier.

Results and Discussion

The impedances of the solid-liquid CdS/NaOH and CdS/cysteine junctions are determined in order to point out the cysteine effect on the Schottky barrier. With both junctions, the impedance data fit to a first approximation (within the experimental precision of ± 10%) with a simple equivalent electrical circuit, composed of a resistance R_S in series with a capacitance C with a parallel resistance R_P or "shunt resistance," responsible for the faradaic or leak current.

The actual equivalent electrical circuit is probably a little more complicated in the low frequency region where other electrical elements perturbate by less than 15% the behavior of the simple circuit described above. These other elements of the equivalent circuit are probably responsible for the slight frequency dependence of the slopes of the Mott-Schottky lines ($1/C^2$ *vs.* V), determined in the low frequency region in the absence or in the presence of cysteine (Fig. 2A and B).

Frequency dispersion in Mott-Schottky plots have been often described (8) and it has been shown recently that such a frequency dependence in a low frequency range vanishes with increasing frequency (9). Nevertheless, as shown by Fig. 2A and B, the extrapolated flatband potential (V_{FB}) remains constant within the experimental error (± 10 mV). The fact that only the slope of the function is frequency dependent allows us to evaluate, without appreciable error, the V_{FB} by extrapolation of the straight line.

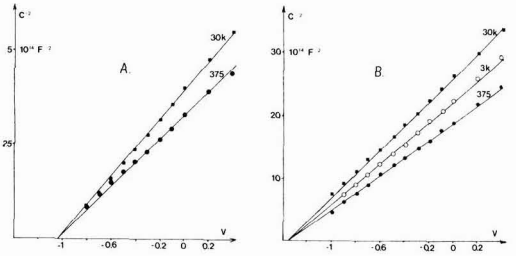

Fig. 2. Mott-Schottky plots for different frequencies. A: CdS/NaOH *p*H 14. B: CdS/cysteine 1M, NaOH *p*H 11.5.

Figure 3 shows the V_{FB} values as a function of *p*H in NaOH alone and with cysteine 1M. All the values are obtained from capacitance measurements made at 375 Hz. We chose this frequency because the $(C\omega)^{-1}$ values are then comprised between 2600Ω ($C \simeq 150$ nF) and 13,000Ω ($C \simeq 30$ nF), which allows to simplify the impedance of the equivalent circuit to the C branch only.

For CdS in NaOH alone, as shown in Fig. 3, the V_{FB} remains constant between *p*H 6 and 10, with a value of approximately −0.910V *vs.* SCE. At *p*H 10, the V_{FB} starts increasing linearly with the *p*H, up to *p*H 13.5 with a slope of 30 mV per *p*H unit. The nature of the electrolyte does not seem to have any major influence on V_{FB} ($LiNO_3$ 0.4M or Na_2SO_4 0.2M). It has to be noticed that, in order to obtain reproducible results, an electrode etching with HCl 4M is required before each measurement. Indeed, if two successive measurements are performed, the first one at a higher *p*H and the second one at a lower *p*H, without chemical etching between both experiments, the V_{FB} value at the lower *p*H is quite irreproducible: the values extend from the actual value obtained after etching, to values close to the ones obtained at the higher *p*H. This behavior, always observed without preliminary etching, most probably stems from an irreversible electrode modification by the highly basic aqueous solution.

Figure 3 also shows that in the presence of cysteine 1M, for all the *p*H values, the CdS V_{FB} is shifted cathodically compared to the V_{FB} obtained in NaOH alone. This negative V_{FB} shift is comparable to the one observed with the S^{2-} ions (2b), with however, in the cysteine case, a more complex relation be-

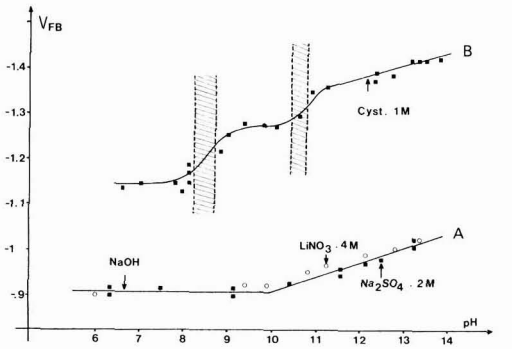

Fig. 3. V_{FB} of nCdS extrapolated from Mott-Schottky plots made at 375 Hz as a function of *p*H. A: NaOH, from *p*H 6 to 13.5; ionic strength is kept constant by adding $LiNO_3$ 0.4M (○) or Na_2SO_4 0.2M (■). B: Cysteine 1M, from *p*H 7 to 14.

tween V_{FB} and the pH. Indeed, as shown in Fig. 3, V_{FB} does not vary linearly with the pH, except for pH higher than 11. Between pH 6 and 11, there are two V_{FB} negative steps as a function of the pH: one around pH 8.5 and the other around pH 10.75. It has not been possible to investigate the pH region lower than 6, because of the cysteine insolubility in acidic medium.

CdS/NaOH junction.—Variation of V_{FB} of CdS in contact with aqueous solutions at different pH has already been investigated by several authors (10); however, the results are somewhat different from one author to the other. Most of the differences could be attributed to different crystallographic faces in contact with the electrolyte which exhibit different V_{FB} dependence with the pH. Recently, this has also been shown in the case of the n-GaAs (10d). Thus we felt that a clarification of the pH effect on our CdS junction was a prerequisite for a study of the effects of cysteine as a function of pH.

In our case, the V_{FB} remains constant from pH 6 to 10 and corresponds to −0.91 V/SCE, in agreement with Watanabe's results; however, from pH 10, contrary to Watanabe's results, the V_{FB} values start shifting negatively by 30 mV/pH up to pH 13.5, similarly to Matsumura's results. This behavior can be explained by taking into account a chemical modification of the CdS induced by the aqueous basic solution under anodic bias. Indeed, it has been shown by x-ray fluorescence and LEEIX measurements (4) that an electrode of amorphous CdS, dipped in an NaOH solution at pH 14, is modified by hydroxyl groups, cadmium oxide, and sulfate-type sulfur. Moreover, under anodic bias with respect to V_{FB}, in the dark and under illumination, the same modification is observed and no sulfur S° from the lattice sulfide oxidation is detected. These experimental observations are in very good agreement with the calculated Pourbaix diagram for CdS (Fig. 4) where the semiconductor between pH 2 and 13.5 corrodes anodically into SO_4^{2-} and Cd^{2+} or different soluble hydroxylated Cd^{2+} or insoluble $Cd(OH)_2$, depending on pH. Such a diagram has already been calculated by Park *et al.* (11) who considered the sulfur S° in the anodic corrosion area. However, the thermodynamic data show that only HSO_4^- and SO_4^{2-} can be considered as the stable thermodynamic sulfur species in the anodic corrosion area of CdS (Fig. 4). Therefore, at $V > -0.5V$ (SCE) where a small oxidation current is observed, the electrode could corrode into SO_4^{2-} and Cd^{2+} ions. The SO_4^{2-} should gradually dissolve into the solution whereas the fate of the Cd^{2+} is critically pH dependent. In neutral or acidic solution, Cd^{2+} is soluble and the electrode merely dissolves without surface chemical modification. On the contrary, in the high pH region (pH 10-13.5), the $Cd(OH)_2$ formed by anodic oxidation would accumulate on the surface and modify the CdS.

Taking into account this chemical modification by corrosion and passivation, the pH effect on the CdS V_{FB} can easily be explained. Indeed, according to the corrosion criteria (*i.e.*, 10^{-6}M for the concentration of soluble species), pH 10 plays a capital role for the CdS/NaOH junction since it represents the boundary between the corrosion ($Cd(OH)^+ + SO_4^{2-}$) and passivation ($Cd(OH)_2 + SO_4^{2-}$) areas. Consequently, for pH < 10, although the electrode is corroding, its superficial chemical composition does not change and is essentially composed of CdS, the V_{FB} of which does not depend on pH. On the contrary, for pH > 10, the electrode surface is passivated by $Cd(OH)_2$, an "active" form of CdO, the V_{FB} of which should be pH dependent as for the oxide semiconductors.

CdS/cysteine junction.—There are two types of cysteine effects on the CdS V_{FB} which are pointed out in Fig. 3. The first one is a negative shift of V_{FB} for

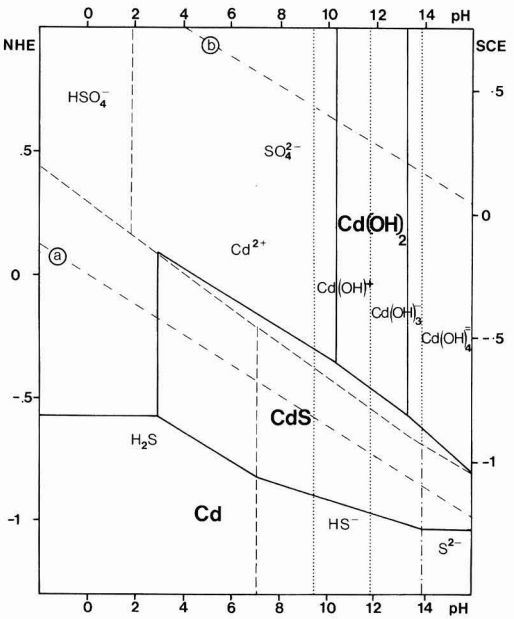

Fig. 4. Pourbaix diagram of CdS. Solid species considered: CdS, Cd, $Cd(OH)_2$, S. Soluble species considered: Cd^{2+}, H_2S, HS^-, HSO_4^-, S^{2-}, SO_4^{2-}, $Cd(OH)^+$, $Cd(OH)_3^-$, $Cd(OH)_4^{2-}$. The thermodynamic data are taken from Ref. (12) and (13). The boundary between two areas involving at least one solid and one soluble species (——) is calculated using the corrosion criterion of 10^{-6}M for the soluble species concentration. (.....) Boundaries between areas involving soluble species of cadmium derivatives; (-----) boundaries between areas involving soluble species of sulfur derivatives. The thermodynamically predominant species are indicated in each area. a and b = redox potentials of water.

all pH values comprised between 7 and 14, compared to the values in NaOH alone. The second is a variation of the amplitude of this shift depending on pH.

Actually, the amino acid (I) has three ionizable acid functions with the following pK_a values (14):

$$R'—COOH \overset{K_a1}{\rightleftharpoons} R'—COO)^{(-)} + H^{(+)} \quad pK_a1 = 1.71$$

$$R'—SH \overset{K_a2}{\rightleftharpoons} R'—S^{(-)} + H^{(+)} \quad pK_a2 = 8.3/8.7$$

$$R'—NH_3^{(+)} \overset{K_a3}{\rightleftharpoons} R'—NH_2 + H^{(+)} \quad pK_a3 = 10.4/10.8$$

These are macroscopic constants. More accurately, the two latter pK_a's can be divided into four microscopic constants:

$$NH_3^{(+)}—R—SH \overset{K_a4}{\rightleftharpoons} NH_3^{(+)}—R—S^{(-)} + H^+ \quad pK_a4 = 8.4/8.7$$

$$NH_3^{(+)}—R—SH \overset{K_a5}{\rightleftharpoons} NH_2—R—SH + H^+ \quad pK_a5 = 8.6/8.9$$

$$NH_3^{(+)}—R—S^{(-)} \overset{K_a6}{\rightleftharpoons} NH_2—R—S^{(-)} + H^+ \quad pK_a6 = 10/10.8$$

$$NH_2—R—SH \overset{K_a7}{\rightleftharpoons} NH_2—R—S^{(-)} + H^+ \quad pK_a7 = 10/10.5$$

where —R— stands for —CH(COO$^{(-)}$)—CH_2—.

If we assume that cysteine adsorbs reversibly on the surface when CdS is dipped in a cysteine solution, we can easily interpret our results. For pH lower than pK_a4 and pK_a5 but $> pK_a1$, cysteine is twice ionized, with a negative charge on the carboxylate group and a positive one on the ammonium group, leading to a resulting charge of zero. In this condition, the V_{FB} cathodic shift, between pH 7 and 8, compared to the value in NaOH alone, could be attributed to a potential drop in the OHP, due to the dipole of the adsorbed "neutral" cysteine. Around pH 8.5, the V_{FB} shifts cathodically because of the acid-base reactions 4 and 5 (first shaded area, Fig. 3), leading to an ion with a total negative charge of 1. Around pH 9.5, the right-member products of equilibria 4 and 5 are the preponderant species in solution. Similarly, at pH 10.75, there is a second V_{FB} step with increasing pH, corresponding to the acid-base reactions 6 and 7 (second shaded area, Fig. 3). These equilibria lead to an ion with a total negative charge of 2. The different V_{FB} shifts would thus depend on the different degree of the cysteine ionization. For pH higher than pK_a6 and pK_a7, V_{FB} shifts linearly with pH with a slope of 30 mV per pH unit. This pH dependence indicates probably a superposition of the cysteine effect and of the NaOH one. If we accept that in this high pH region, as discussed before, the electrode surface in contact with the solution, is covered by $Cd(OH)_2$, the sulfur atoms being dissolved as sulfate ions, the persistence of the cysteine effect in the high pH range (11.5-13.5) on the V_{FB} value (compared to the one in NaOH alone), would indicate that cysteine adsorbs on the Cd atoms (hydroxylated or not).

Conclusions

There are two important results which emerge from this work.

The first one concerns the capacitance results obtained with the CdS/NaOH junction. The pH effect on the V_{FB} indicates that the chemical composition of the surface varies with pH. At pH higher than 10, the linear dependence of the V_{FB} with pH and the examination of the Pourbaix diagram lead to the conclusion that the surface gets hydroxylated at least partially. This conclusion has already been suggested before by Matsumura *et al.* (10c) but has never been clearly discussed.

The second result is that, to our knowledge, it is the first time that a V_{FB} shift, depending on the degree of ionization of the reductant in solution, has been clearly pointed out.

Acknowledgments

We are grateful to Dr. B. Baron from the Institute of Energy Conversion at the University of Delaware for donating the polycrystalline CdS samples and to Dr. L. Devos from the University of Brussels (Zoology Department) for taking the SEM photographs. One of us (R.D.) thanks the "Institut pour l'Encouragement de la Recherche Scientifique dans l'Industrie et l'Agriculture" (IRSIA) for a fellowship.

Manuscript submitted Jan. 10, 1983; revised manuscript received May 24, 1983.

REFERENCES

1. (a) H. Gerischer, *J. Electroanal. Chem.*, **82,** 133 (1977); (b) A. J. Bard and M. S. Wrighton, *This Journal*, **124,** 1706 (1977); (c) H. Gerischer and J. Gobrecht, *Ber. Bunsenges. Phys. Chem.*, **82,** 520 (1978).
2. (a) A. B. Ellis, S. W. Kaiser, and M. S. Wrighton, *J. Am. Chem. Soc.*, **98:22,** 6855 (1976); (b) H. Minoura, T. Oki, and M. Tsuiki, *Chem. Lett.*, 1279 (1976); (c) B. Miller and A. Heller, *Nature*, **262,** 680 (1976); (d) A. B. Ellis, S. W. Kaiser, J. M. Bolts, and M. S. Wrighton, *J. Am. Chem. Soc.*, **99:9,** 2839 (1977).
3. (a) A. Kirsch-De Mesmaeker, A. M. Decoster, and J. Nasielski, *Solar Energy Mater.*, **4,** 203 (1981); (b) A. Kirsch-De Mesmaeker, P. Josseaux, J. Nasielski, and C. Defosse, *ibid.*, **6,** 429 (1982).
4. P. Josseaux, Private communication.
5. N. R. Pavaskar, C. A. Menezes, and A. B. B. Sinha, *This Journal* **124,** 743 (1977).
6. G. L. Ellmann, *Arch. Biochem. Biophys.*, **82,** 70 (1959).
7. (a) V. A. Myamlin and Y. V. Pleskov, "Electrochemistry of Semiconductors," Plenum Press, New York (1967); (b) H. Gerischer, "Physical Chemistry," Vol. IX, p. 463, Academic Press, New York (1970).
8. (a) S. Toshima and I. Uchida, *Electrochim. Acta*, **15,** 1717 (1970);(b) D. M. Tench and E. Yeager, *This Journal*, **120,** 164 (1973); (c) M. J. Madou, F. Cardon, and W. P. Gomes, *ibid.*, **124,** 1623 (1977); (d) E. C. Dutoit, R. L. Van Meirhaeghe, F. Cardon, and W. P. Gomes, *Ber. Bunsenges. Phys. Chem.*, **79,** 1206 (1975).
9. M. Tomkiewicz, *This Journal*, **126,** 2220 (1979).
10. (a) T. Watanabe, A. Fujishima, and K. Honda, *Chem. Lett.*, 897 (1974); (b) D. S. Ginley and M. A. Butler, *This Journal*, **125,** 1968 (1978); (c) M. Matsumura, S. Matsudaira, H. Tsubomura, M. Takata, and H. Yanagida, *Ind. Eng. Chem. Prod. Res. Dev.*, **19,** 415 (1980); (d) K. Rajeshwar and T. Mraz, *J. Phys. Chem.*, **87,** 742 (1983).
11. S. Park and M. E. Barber, *J. Electroanal. Chem.*, **99,** 67 (1979).
12. M. Pourbaix, "Atlas d'équilibres électrochimiques à 25°C," Gauthier-Villars, Paris (1963).
13. (a) W. H. Latimer, "Oxidation Potentials," 2nd ed., Prentice Hall (1952); (b) "Handbook of Materials Science," Vol. 1, CRC Press.
14. (a) P. C. Jocelyn, "Biochemistry of the SH Group," Academic Press, New York (1972); (b) M. Friedman, "The Chemistry and Biochemistry of the Sulfhydryl Group in Amino Acids, Peptides and Proteins," Pergamon Press (1973).

BP-Stabilized n-Si and n-GaAs Photoanodes

D. S. Ginley,* R. J. Baughman, and M. A. Butler*

Sandia National Laboratories, Albuquerque, New Mexico 87185

ABSTRACT

Thin boron phosphide overlayers, employed as transparent conductive windows, have been deposited on n-Si and n-GaAs photoanodes. Significantly enhanced stabilities are observed in ferro-ferricyanide electrolytes. Spectral response and I-V data for aging experiments, as well as a discussion of the energy level diagrams for the heterojunctions, are presented.

The use of heterogeneous photocatalysis for solar energy conversion in photoelectrochemical devices has attracted tremendous attention over the last 7 or so years. Whether employed as discrete semiconductor electrodes or in particulate systems, one of the major requirements in any practical system is that of extended stability. This is especially true in view of the increasing tendency to employ small bandgap non-oxide electrode materials.

Because it is very difficult to find intrinsically stable materials and to develop them to device quality, considerable effort has been expended on electrode modification to improve stability and charge transfer properties. Some of the methods employed or suggested include the use of stabilizing redox couples in the electrolyte (1, 2) or chemically bound on the surface (3) and overcoating of unstable semiconductors with stable electronic (4, 5) or ionic conductors (6).

In this paper, the authors demonstrate that the growth of a degenerate layer of n-type boron phosphide (BP) on either n-Si or n-GaAs can impart great stability to these normally quite unstable photoanodes. This paper reports predominantly on the results on Si substrates, with some results being reported for both substrates. Though the application of semiconductor overlayers had been previously proposed (4), the intent there was to collect photocurrents from both layers and augment open-circuit potentials. Prototypes of these devices suffered greatly from bandedge matching problems, and extremely low quantum efficiencies were the result. The intent here was somewhat different. A number of attempts have been made (7, 8) to use thin metal overlayers as protective films, but light transmission and pinhole problems dominated these devices. The authors desire was to use this concept, but to employ a large bandgap stable degenerate semiconductor upon a smaller bandgap unstable semiconductor. For this to be effective, a number of requirements had to be met. There needed to be an effective heterojunction between the two semiconductors; this implied a high density of interfacial states. The bandgap of the overcoating semiconductor had to be significantly larger than that of the small bandgap material so that reasonable conversion efficiencies could be attained. The overcoating material had to be stable in the required electrolyte environment. All of these requirements could be met using BP layers (bandgap 2.0 eV) on n-Si (bandgap 1.1 eV) and n-GaAs (bandgap 1.4 eV).

Experimental

The substrate materials were single-crystal specimens of n-Si and n-GaAs. The silicon samples were Sb-doped to 0.0005-0.20 Ω/cm and cut perpendicular to the <100> axis. The gallium arsenide samples were Si-doped to 6-7 × 10^{17} and were cut perpendicular to the <100> axis. Before growth, all samples were polished with 1/4 μm diamond paste, acid-etched, and rinsed with spectral grade methanol. The Si contacts were Ti/Pt/Au, and the GaAs contacts were Ge-Au/Ni/Au. All contacts were applied by sputtering and were annealed in vacuum and hydrogen, respectively.

Boron phosphide was deposited by chemical vapor deposition (CVD) from mixtures of B_2H_6, PH_3, and H_2 (9).

The gas nutrient materials used in this work were all Matheson gas products. The hydrogen carrier gas, 99.999% pure, was passed through a Matheson hydrogen purifier Model 8363. The diborane, 99.995% pure, was a 1.10% concentration in UHP hydrogen gas. The phosphine, 99.999% pure, was a 4.48% concentration in hydrogen gas. Both the diborane and phosphine were used directly from the gas cylinder.

Matheson gas flow controllers were used to regulate and control all gas flow. The system included mass flow controller Model 8240, mass flow meter Model 8142, and totalizer Model 8122. Each gas system was calibrated for a specific gas mixture. The exhaust gas was passed through a silicone oil gas trap and was then either burned or vented through a hood.

The growth apparatus is shown schematically in Fig. 1. The outer atmosphere chamber, constructed of fused silica, was 31 cm (length) × 5 cm (diam) and supported the desired growth environment. The chamber

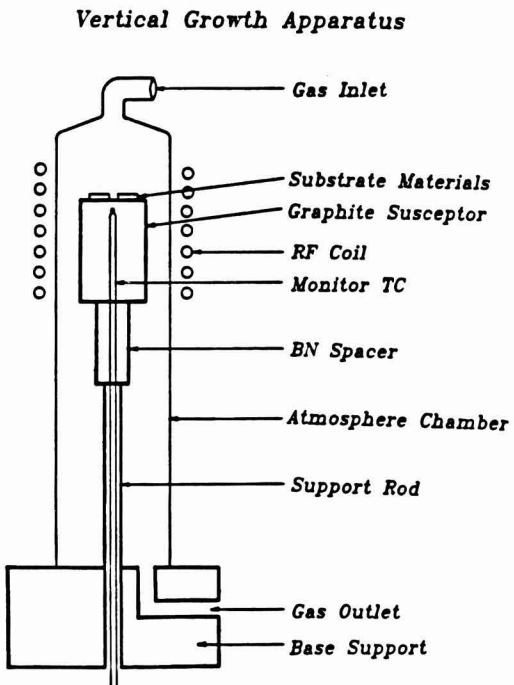

Fig. 1. Schematic of BP vertical growth apparatus

* Electrochemical Society Active Member.

Key words: boron phosphide, corrosion resistant layer, photoelectrochemistry, silicon photoanode, gallium arsenide photoanode.

was friction-fitted into the support base. A gas seal was provided by an "O" ring in the base. This configuration allowed the fused silica growth chamber to disconnect from the base, avoiding rupture in case exhaust tubing became either plugged or restricted during a growth procedure.

All electrochemical measurements were made using a conventional three-electrode electrochemical cell with a saturated calomel reference electrode (SCE), a PAR 173 potentiostat, and a PAR 174 programmer. Illumination was by a 150W Schoeffel medium pressure xenon lamp used with a Schoeffel grating monochrometer where appropriate. Conversion efficiencies were measured using the unfiltered light source attenuated to 80 mW/cm^2.

All electrolytes were prepared from distilled water and analytical purity reagents. The electrolytes employed throughout the bulk of this study were 0.1M potassium ferricyanide and 0.25M potassium ferrocyanide ($pH \cong 7.8$).

All aging experiments were conducted in the above electrolyte in the air. The propensity of the electrolyte to decompose was rectified by periodic electrolyte renewal and by cleaning the cell windows. The BP-coated Si samples were aged at 0.2V *vs.* the ferro-ferricyanide couple (+0.455V [SCE] measured on a Pt metal electrode) to be near the maximum power point of the cell. For the aging experiments, BP-coated GaAs was potentiostated at +0.100V *vs.* SCE and the virgin n-GaAs electrode was potentiostated at +0.260V *vs.* SCE.

Results

Boron phosphide films for this study were grown with P:B atom ratios in the input stream from 1:1 to 24:1. Growth temperature was typically 900°C for both the Si and the GaAs substrates. Total gas flow was held constant at 2500 sccm by correcting with the hydrogen carrier gas flow rate. Normally the layers grown were 2000-5000Å thick, which required growth times from 2 to 4 min for the 1:1 and 24:1 ratios on silicon. BP films are well known to grow epitaxially on silicon (10-12), which was observed in this case. The films, as expected, were grown pinhole-free as viewed in the SEM. The growth on GaAs produced excellent optical quality crystalline films, but grain size and orientation were not determined.

It was determined that sample resistivity (*i.e.*, doping level) was a function of P:B ratio. Figure 2 illustrates a plot of resistivity *vs.* P:B growth ratio for BP on both n- and p-type silicon substrates. It was observed that at P:B ratios below 2:1 the film resistivity, as measured impedance in the PEC, rapidly increased and the films approached an intrinsic value. Even growing at ratios of less than 1:1 would not switch the films from n- to p-type, nor would growing on p-type substrates do so. Above ratios of 2:1, the resistivity rapidly decreased to a low value which was minimum about 12:1. Subsequently, increasing the phosphorous atom percent resulted in a slight increase in conductivity with both the n- and p-substrates. It may be that the additional phosphorous at higher concentrations results in the incorporation of a high density of trap states, reducing majority carrier mobility. To achieve the best results when employing these films as transparent conducting windows, it is desirable to have the conductivity as high as possible but to minimize the number of trap states and defects. This is to assure not only efficient charge transport but to minimize the possibility of decomposition reactions initiating at near surface sites with broken bonds or altered stoichiometry.

The validity of this interpretation seems to be reflected in the dependence of conversion efficiency upon the P:B ratio. Figure 3 illustrates the conversion efficiency *vs.* the P:B ratio for BP on n-Si. This information seems to correlate quite well with that from the previous figure. Where resistance is a minimum, the efficiency is a maximum. As the phosphorous concentration increases past this point, the conversion efficiency decreases. As impedance increases, the efficiency rapidly decreases and reaches zero, where we see the rapid increase in resistivity. The low efficiencies in these cells stem from the nearly linear I-V characteristics between I_{sc} and V_{oc}, producing a very low fill factor. There is also some dark current which gradually decreases with time.

Figure 4 illustrates the I-V curves in ferrocyanide electrolyte for virgin GaAs and BP-coated GaAs electrodes. The overall dark and illuminated I-V curves are quite similar in shape for the virgin and coated electrodes. The leakage current increased somewhat for the coated electrode, although this diminished with time. Fill factors are comparable; the flatband shifted approximately 0.35V to the positive of SCE for the coated electrode.

Aging studies were performed in aqueous ferro-ferricyanide in the air. In retrospect, although the couple was energetically very good, it was particularly inappropriate since it underwent photodecomposition. This required a periodic renewal of the electrolyte and cleaning of the cell windows. The electrode surface was also rinsed in distilled water at these intervals. Much of the erratic nature of the photocurrent with time during aging experiments was a consequence of this electrolyte problem. Figure 5 illustrates a plot of photocurrent *vs.* total interfacial coulombs of a BP-coated Si electrode. The P:B growth ratio of this electrode was 12:1, and the electrode was aged at approximately the maximum power point. Clearly the photocurrent did not decay. In fact, it has a pronounced upward trend indicative of an increasing electrode efficiency. The efficiency increased from roughly 1.97 to 2.75% during the aging experiment, while the dark current dropped somewhat from −1.0 to −0.5 mA at 0.0V (SCE). Open-circuit potentials remained rela-

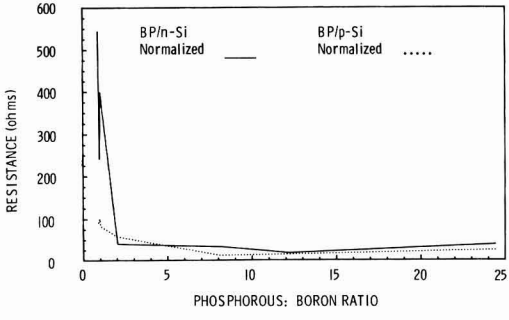

Fig. 2. Plot of sample resistance, as determined by I-V plots in a photoelectrochemical cell *vs.* P:B growth ratio. The solid line is the curve for BP on n-type silicon; the dashed is for BP on p-type silicon.

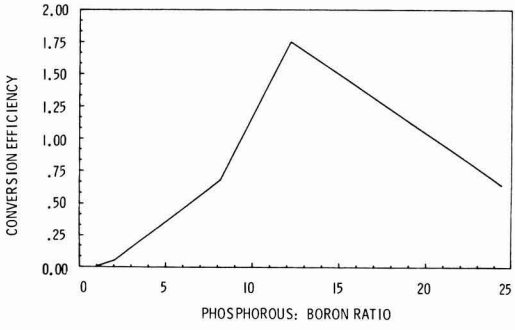

Fig. 3. The plot shows conversion efficiency in percent *vs.* the P:B ratio for a coated p-type silicon substrate in ferro-ferricyanide electrolyte.

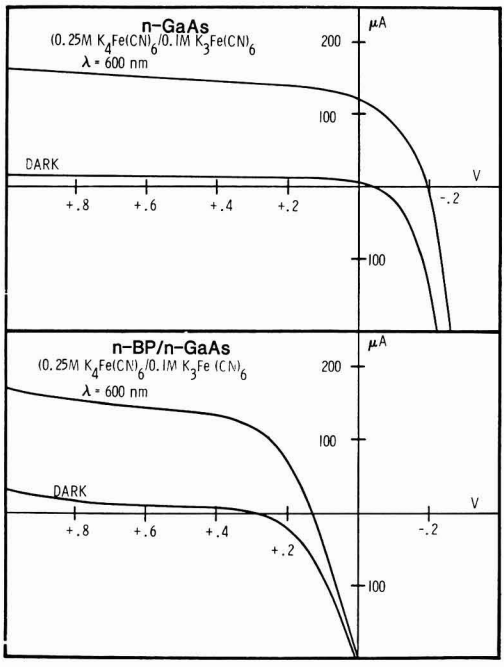

Fig. 4. I-V curves for a virgin n-GaAs photoanode and for a BP-coated n-GaAs photoanode vs. SCE in a ferro-ferricyanide electrolyte.

tively unchanged. The electrode surface showed no change in appearance and showed no pitting or other physical changes under microscopic examination. A virgin n-type silicon electrode was run under comparable conditions in the ferro-ferricyanide electrolyte. Photocurrent decayed to zero after only 0.8C of interfacial current. Figure 6 illustrates the dependence of the spectral response as a function of aging time. The virgin curve looks much as expected with a photocurrent onset near the Si bandedge and a cutoff near the bandedge of the BP. As aging proceeds, there seems to be nonsystematic variations in the longer wavelength portion of the spectrum. These are, however, systematic variations in the short wavelength portion of the spectrum. As aging proceeds, the blue response of the electrode continues to improve.

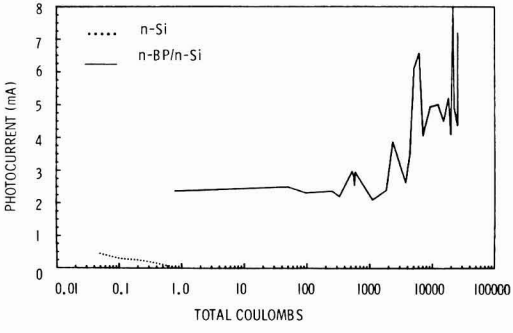

Fig. 5. Plot of extended aging experiment for a virgin n-Si photoanode and a BP-coated n-Si photoanode in a 0.1M $K_3Fe(CN)_6$/0.25M $K_4Fe(CN)_6$ electrolyte. The plot shows photocurrent vs. total interfacial coulombs. The solid line is for the BP-coated electrode; the dashed line is for the uncoated electrode.

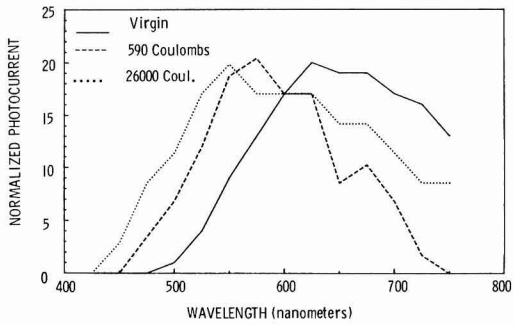

Fig. 6. Spectral response curves as a function of aging for the BP-coated n-silicon electrode shown in Fig. 5. The solid line is before aging; the dashed line is after 590 interfacial coulombs; and the dotted line is after 26,000 interfacial coulombs.

Figure 7 illustrates the aging of a virgin and BP-coated GaAs photoanode in the same ferro-ferricyanide electrolyte. The virgin electrode shows a very rapid decay of photocurrent reaching zero after only 12C. The BP-coated electrode shows an initial rapid decrease of photocurrent followed by a much more gradual decline and by what appears to be a final leveling off. The run was stopped because an orange-green coating began forming on the electrode. Subsequent chemical analysis showed this coating to be composed exclusively of electrolyte decomposition products. When the surface was cleaned, it showed a surface and photoelectrochemical character very similar to that of the preaged electrode.

Discussion and Conclusions

The experiments discussed above illustrate the viability of using a large bandgap semiconductor as a transparent conductive window on smaller bandgap material. In both the n-Si and n-GaAs cases, improved stability was observed while reasonable I-V properties were obtained.

A number of interesting effects were observed relative to the future utility of this method of electrode modification.

Basically, the device inherently resembles a metal overcoated semiconductor electrode. It is, in fact, a solid-state device. This means that the band mismatch between the two semiconductors can play an important role in determining the behavior of the device.

In Fig. 8, the band configurations for BP-overcoated n-Si and n-GaAs are shown. The positions of the bands come from the known bandgaps and the electronegativity model (13). For degenerately doped BP and n-

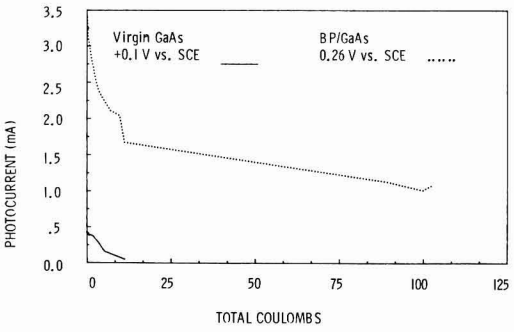

Fig. 7. Plot of extended aging experiment for a virgin n-GaAs photoanode and a BP-coated n-GaAs photoanode in a 0.1M $K_3Fe(CN)_6$/0.25M $K_4Fe(CN)_6$ electrolyte. The plot shows photocurrent vs. total interfacial coulombs. The solid line is for the virgin electrode; the dotted is for the coated electrode.

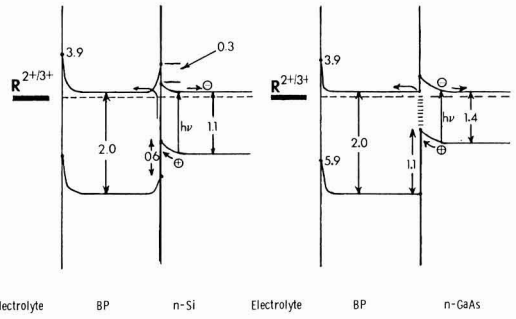

Fig. 8. Expected band structure for BP-coated n-Si and n-GaAs The numbers are band positions and discontinuities in eV.

GaAs, the band positions provide ~0.5V of barrier height at the junction between the two semiconductors. The known position of the ferri-ferrocyanide couple of +0.46V (SCE) suggests that the photocurrent should disappear about 0V (SCE), in reasonable agreement with the data in Fig. 4.

For BP-coated n-Si, the band positions are such that an ohmic contact would be expected between the two, and no photovoltage with the silicon spectral response should be expected. Since both Si and GaAs are quite covalent, Fermi level pinning is expected to occur around 1/3 of the bandgap (14). This is how the band structure is drawn in Fig. 8. Thus, the expected maximum open-circuit voltage is about 0.4V, in reasonable agreement with observations. While Fermi level pinning for GaAs might also be expected, the height of the conduction band discontinuity suggests that pinning would change neither the barrier height nor the maximum open-circuit voltage significantly.

Another important consideration in these systems is the epitaxial growth of protective film on the small gap material. BP grows epitaxially on Si but not on GaAs. It is, however, the GaAs that shows the best junction characteristics, although the Si shows somewhat greater stability. This is to be expected as the higher interface state densities in the GaAs case make it easier for holes to pass through the heterojunction, as shown in Fig. 8. In the Si case, the lack of interface state density impedes the hole transport and provides, in effect, large series resistance for the device. This explains the linear I-V characteristics and poor fill factors that are observed.

The doping of the overcoating semiconductor layer is very important. To achieve the type of device desired—essentially a Schottky barrier device—it is necessary to have sufficient doping for the layer to act essentially as if it were a metal. If doping levels are too low, the device becomes an n/n′ heterojunction device of the type envisaged by Wagner and Nozik (4, 5). In this case, minority carrier transport through the heterojunction is impeded by the band discontinuities. If doping levels are too high, a high density of deep trap states can be introduced, resulting in reduced transmission in the desired portion of the spectrum. While a high density of interface states is desirable to achieve efficient Schottky barrier behavior, a high density of deep trap states, as stated above, can be detrimental to electrode performance. These states can originate with lattice imperfections, impurities, and excess dopant (or a compensated situation). These problems seem to effect the BP-coated silicon electrode to some extent. The gradual increase in efficiency *vs.* time for these electrodes may be due to a reduction of deep trap state density.

In general, the device resembles a Schottky barrier solar cell in series with an electrochemical cell. This situation may occur in quite a few surface-modified systems, and especially must be considered when metals are deposited on semiconductor surfaces. BP has demonstrated an exceptional stability in these devices, with 2000Å layers surviving nearly 30,000C with no detectable deterioration. While this type of device may not be eminently practical, it does provide an excellent test bed for investigating new semiconductors for PEC's and does demonstrate the utility of employing semiconductors as stable transparent conductive windows.

Acknowledgment

This work performed at Sandia National Laboratories supported by the U.S. Department of Energy under Contract DE-AC04-76DP00789.

Manuscript submitted April 6, 1983; revised manuscript received *ca.* June 3, 1983.

Sandia National Laboratories assisted in meeting publication costs of this article.

REFERENCES

1. A. B. Bocarsly, D. C. Bookbinder, R. N. Doiney, N. S. Lewis, and M. S. Wrighton, *J. Am. Chem. Soc.*, **102,** 3683 (1980).
2. A. Heller, H. J. Lewerenz, and B. Miller, *ibid.*, **103,** 200 (1980).
3. J. M. Bolts, A. B. Bocarsly, M. C. Palazotto, E. G. Walton, N. S. Lewis, and M. S. Wrighton, *ibid.*, **101,** 1378 (1979).
4. S. Wagner and J. L. Shay, in "Electrode Materials and Processes for Energy Conversion and Storage," J. D. E. McIntyre and S. Srinivasan, Editors, p. 105, The Electrochemical Society Softbound Proceedings Series, Princeton, NJ (1977).
5. R. Noufi, A. J. Frank, and A. J. Nozik, *J. Am. Chem. Soc.*, **103,** 1849 (1981).
6. R. C. Hughes, D. S. Ginley, and A. K. Hays, *Appl. Phys. Lett.*, **40,** 853 (1982).
7. S. Menezes, A. Heller, and B. Miller, *This Journal*, **127,** 1268 (1980).
8. L. A. Harris and J. A. Hugo, *ibid.*, **128,** 1203 (1981).
9. R. J. Baughman and D. S. Ginley, Submitted to *Solid-State Chem.*
10. T. Takenaka, M. Takigawa, and K. Shohno, *Jpn. J. Appl. Phys.*, **15,** 2235 (1976).
11. K. Shohno, H. Ohtake, and J. Bloem, *J. Cryst. Growth*, **45,** 187 (1978).
12. S. Motojima, S. Yokoe, and K. Sugiyama, *ibid.*, **49,** 1, (1980).
13. M. A. Butler and D. S. Ginley, *This Journal*, **125,** 228 (1978).
14. S. M. Sze, "Physics of Semiconductor Devices," Chap. 5, Wiley, New York (1981).

An Analysis of a Back Fed Porous Electrode for the Br_2/Br^- Redox Reaction

John Van Zee* and Ralph E. White**

Department of Chemical Engineering, Texas A&M University, College Station, Texas 77843

ABSTRACT

An experimental analysis of the Br_2/Br^- redox reaction in a porous back fed ruthenium-coated titanium electrode is described. A mathematical model of the steady-state process is presented. Nonlinear regression of the model against the experimental data gives physically meaningful parameter estimates; these parameters and the model provide a design equation for the porous electrode current as a function of specific surface area, bulk Br_2 concentration, average total overpotential, and the Reynolds number. The design equation shows that the back fed electrode could reduce the loss of Br_2 across the separator and the ohmic loss in a Zn/Br_2 battery.

A flow-by back fed porous electrode, as shown in Fig. 1, is a diffusion electrode. The term "flow-by" emphasizes that the reactant flows outside rather than through the electrode. Consequently, fresh reactant must diffuse to a reaction site within the porous electrode. Typically, the reaction occurs on the side closest to the counterelectrode if the catalyst application and the concentration are uniform. Thus, the back fed electrode may be limited by diffusion if it is too thick. This may be the reason it has been ignored by commercial monopolar Zn/Br_2 battery designers (1, 2).

However, this back fed configuration may provide some advantages for a Zn/Br_2 battery or similar electrochemical system. Specifically, the back fed electrode may reduce the ohmic energy loss and the product (*e.g.*, Br_2) loss across the separator. The ohmic energy loss would be decreased because the solution gap between the electrodes would be reduced to approximately half that of the front fed electrode (compare Fig. 1 and 2). This reduction in electrode gap could decrease the cell's specific resistance by more than 25% in Zn/Br_2 batteries if a relatively nonconducting complexing agent (3) is present in the electrolyte. [This decrease in resistance is approximately 25% because the electrolyte between the electrodes contributes only approximately 50% of the ohmic loss in a Zn/Br_2 battery (1, 4).] The same percentage decrease might be observed in gas generating cells. The loss of product across the separator may be reduced because the porous electrode may act as a separator when the reaction occurs preferentially on the back side (fresh solution side) of the porous electrode (Fig. 1). This reduction of the product loss across the separator would probably decrease the self-discharge rate in a Zn/Br_2 battery.

Even though back fed electrodes are limited by diffusion, the limiting current due to diffusion may be adequate for the specific application. This is evident, for example, in the back fed electrode designs of SPE water electrolyzers (5) where the diffusion limiting current is large because the reactant is in abundance. Even if the reactant is present in low concentration, the process may be limited to some current below the diffusion limited current by slow kinetics or by some other feature of the other electrode. For example, in Zn/Br_2 batteries the Br_2 electrode is not required to operate above 50 mA/cm^2 because of zinc dendrite formation at the zinc electrode (1, 2, 4, 6, 7).

Since the design principles for flow-by back fed porous electrodes are not well known, this paper presents an analysis of this electrode design for the bromine/bromide reaction

$$Br_2 + 2e^- \rightarrow 2Br^- \qquad [1]$$

* Electrochemical Society Student Member.
** Electrochemical Society Active Member.
Key words: battery, current density, mass transport, kinetics.

First, a mechanistic model of the steady-state process is developed. Next, an experimental study of the bromine/bromide redox reaction is presented. Then, least squares regression techniques are used to fit the model to experimental data to obtain physically meaningful parameter estimates. Finally, the regression results and the mechanistic model are used to analyze the physical behavior of a flow-by back fed porous Br_2 electrode.

Previous Work

The previous analyses (8-12) of steady-state mass transfer in porous diffusion electrodes pertinent to the back fed model developed below have been reviewed by Newman and Tiedeman (13).[1] In these previous

[1] The approach of these analyses differs from the approach of single-pore models (see Ref. (14), for example) as described by Tilak *et al.* (15) because it uses a pseudo-homogeneous reaction rate and volume average quantities instead of the single-pore concept.

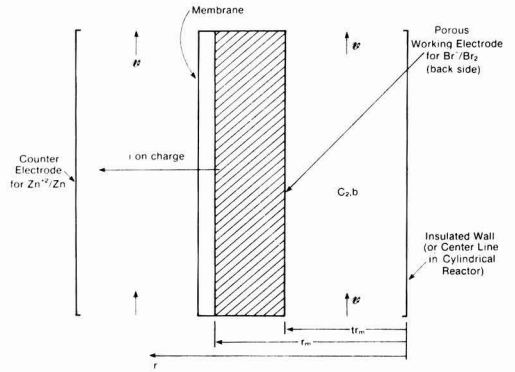

Fig. 1. A schematic of a back fed porous electrode for the bromine/bromide redox reaction in a Zn/Br_2 battery.

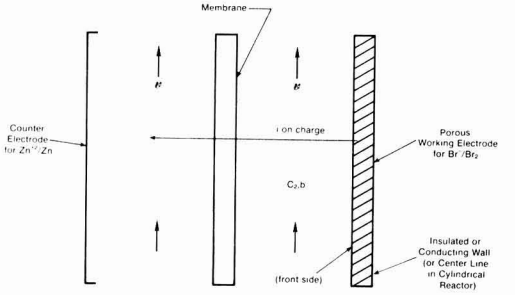

Fig. 2. A schematic of a front fed porous electrode

analyses, the authors have considered redox reactions which have stoichiometric coefficients of +1 and −1 for anodic and cathodic species, respectively, whereas the coefficients used here are +2 and −1 as shown by reaction [1]. These previous models and the model developed here include the assumption of excess supporting electrolyte and, consequently, neglect the effect of ionic migration. The boundary conditions for the concentration in the previous analyses require a known constant concentration of reactant at the edge of the porous region whereas in the model developed below the reactant concentration at the edge of the porous region depends on overpotential, Reynolds number, and the bulk properties of the flowing electrolyte.

The results most closely related to the back fed electrode model presented here are those of Newman and Tiedeman (13) and Austin and Lerner (12) because they neglect the ohmic potential drop in both the matrix and the solution and because they use a complete Butler-Volmer kinetic expression. Newman and Tiedeman (13) give the current/potential relationship in Cartesian coordinates for redox reactions with stoichiometric coefficients of +1 and −1 and a constant concentration at the reservoir-electrode interface. One problem with this fixed concentration boundary condition model is that accurate predictions of the current density from the resulting equations occur only for infinitely large rates of external mass transfer. Austin and Lerner (12) use a stagnant film concept to relax the constant concentration boundary condition and, thereby, include the effect of external mass transport; they show the current potential relationship in Cartesian coordinates in terms of the limiting current. The limiting current density in Ref. (12) could have been but was not given as a function of the external mass transfer coefficient

$$i_L = kc_{i,b}\frac{nF}{s_i} \qquad [2]$$

This mass transfer coefficient k is included in the back fed model developed below. Austin and Lerner (12) discuss the relative importance of the ohmic drop in the solution phase and they show that its neglection may be a reasonable assumption when the reaction occurs over a very short distance as is the case for the model presented here as discussed below.

Model

The model developed here extends similar developments for steady-state mass transfer in porous electrodes (8-13) by including an external mass transfer coefficient and different stoichiometric coefficients for the reactant and product. That is, redox reactions considered in Ref. (8-13) have stoichiometric coefficients of +1 and −1 for the oxidized and reduced species, respectively, whereas the coefficients used here are +2 and −1 as shown by reaction [1].

The model is presented by first stating the assumptions and then developing the equations. The assumptions used in the development of the model are

a. Steady-state is maintained.

b. The porosity and specific catalytic surface area are uniform and they do not change with time.

c. Dilute solution theory (13) applies.

d. Sufficient supporting electrolyte exists so that ionic migration can be neglected (*i.e.*, no potential drop in the solution).

e. Dispersion and convection are not present in the porous section of the electrode.

f. In the porous region, the only important gradients are those in the direction normal to the fluid flow.

g. The separator at the edge opposite the flowing solution is impermeable to the reacting species.

h. The hydrodynamic profile is known in the nonporous region.

i. The potential drop in the matrix is negligible.

j. The concentration of the anodic reactant, Br^-, is large relative to the concentration of the cathodic reactant, Br_2.

k. The kinetic expression follows a Butler-Volmer type expression where the cathodic reaction order is unity and reaction [1] is assumed to be an elementary step.

l. Isothermal conditions exist.

m. The conversion per pass is small.

These assumptions permit the development of a single analytical expression suitable for design over a large range of overpotentials.

The equations of this model can be developed by considering the cylindrical back fed electrode of Fig. 1. (Cylindrical coordinates are used since the experimental data were obtained with a tubular porous electrode.) Bromine is present at a concentration of $c_{2,b}$ in the stream having an axial velocity v. The redox reaction of interest here occurs in the porous electrode which has an outside radius of r_m and an inside radius of tr_m where t is less than one.

The steady-state material balance for the i^{th} species within the porous electrode can be written as (13)

$$-\nabla \cdot N_i + aj_i = 0 \qquad [3]$$

for reaction [1] with subscript i equal to 1 and 2 for Br^- and Br_2, respectively. The volume average production rate aj_i can be written as (16)

$$aj_i = \frac{-s_i a i_{o,b}}{nF}\left\{\prod_i\left(\frac{c_i}{c_{i,b}}\right)^{p_i}\exp\left(\frac{\alpha_a F}{RT}\eta\right) - \prod_i\left(\frac{c_i}{c_{i,b}}\right)^{q_i}\exp\left(\frac{-\alpha_c F}{RT}\eta\right)\right\} \qquad [4]$$

where

$$i_{o,b} = i_o^{\circ}\prod_i\left(\frac{c_{i,b}}{c_i^{\circ}}\right)^{\gamma_i} \qquad [5]$$

$$p_i = \gamma_i + \frac{\alpha_a s_i}{n} \qquad [6]$$

$$q_i = \gamma_i - \frac{\alpha_c s_i}{n} \qquad [7]$$

and

$$\alpha_a + \alpha_c = n \qquad [8]$$

$$\eta = V - \Phi_2 - \Delta U_b \qquad [9]$$

The reaction orders p_i and q_i in Eq. [4] can be related to the stoichiometry for an elementary step (17): (*i*) for anodic reactants, $p_i = s_i$ and $q_i = 0$ and (*ii*) for cathodic reactants, $q_i = -s_i$ and $p_i = 0$. The concentration dependence on the exchange current density of species i, γ_i, is then related simply to the stoichiometric equation. That is, since reaction [1] is assumed to be an elementary step and if it is assumed that $\alpha_a = \alpha_c = 1.0$, for example, then

$$\gamma_1 = 2 - \frac{(1.0)(2)}{2} = 1.0 \qquad [10]$$

and

$$\gamma_2 = 1 + \frac{(1.0)(-1)}{2} = 0.5 \qquad [11]$$

The total overpotential η in Eq. [4] and [9] is the sum of the surface overpotential and the local overpotential from outside the double layer to the bulk solution. This overpotential includes the effect of a reference electrode which differs from the working electrode by the term ΔU_b where

$$\Delta U_b = U^{\theta} - U_{re}{}^{\theta} - \frac{RT}{nF}\sum_i s_i \ln\left(\frac{c_{i,b}}{\rho_o}\right) + \frac{RT}{n_{re}F}\sum_i s_{i,re}\ln\left(\frac{c_{i,re}}{\rho_o}\right) \qquad [12]$$

It is important to note that both $i_{o,b}$ and ΔU_b are based on the same bulk concentration ($c_{2,b}$), and that the potential of the working and reference electrodes must be referenced to the same thermodynamic scale (*e.g.*, H_2 scale).

Neglecting ionic migration according to Assumption d, the specific expression for the flux of Br_2 in the porous electrode is

$$N_2 = -D_e \frac{dc_2}{dr} \quad [13]$$

where

$$D_e = \frac{\epsilon}{\tau} D_2 \quad [14]$$

Substitution of Eq. [4], [13], and [14] into the radial component of the cylindrical form of Eq. [3] yields

$$\frac{d^2c_2}{dr^2} + \frac{1}{r}\frac{dc_2}{dr} - Kc_2 = \frac{-ai_{o,b}}{2FD_e} \exp\left(\frac{\alpha_a F}{RT}\eta\right) \quad [15]$$

where

$$K = \frac{ai_{o,b}}{2FD_e c_{2,b}} \exp\left(\frac{-\alpha_c F}{RT}\eta\right) \quad [16]$$

and the local concentration of Br^- has been assumed to be constant and equal to the bulk concentration of Br^-, according to Assumption j (*i.e.*, $c_1/c_{1,b} = 1.0$).

The following dimensionless variables can be used to simplify Eq. [15]

$$\xi = \frac{r}{r_m}, \quad \theta = \frac{c_2}{c_{2,b}} \quad [17]$$

which when substituted into Eq. [15] yields

$$\frac{d^2\theta}{d\xi^2} + \frac{1}{\xi}\frac{d\theta}{d\xi} - B\theta = -A \quad [18]$$

where

$$B = Kr_m^2 \quad [19]$$

and

$$A = \frac{ai_{o,b}r_m^2}{2FD_e c_{2,b}} \exp\left(\frac{\alpha_a F}{RT}\eta\right) \quad [20]$$

Following Assumptions g, h, and m, the boundary conditions are at

$$r = r_m, \quad \xi = 1 \quad \frac{d\theta}{d\xi} = 0 \quad [21]$$

at

$$r = r_m t, \quad \xi = t \quad \frac{d\theta}{d\xi} = \frac{r_m k}{D_e}(\theta(t) - 1.0) \quad [22]$$

where the gradients are defined to be in the positive direction of ξ. The mass transfer coefficient k in Eq. [22] is an average value over the length of the tubular reactor and is given by (18)

$$k = 1.651 \frac{D_2}{2r_1}\left(N_{Re}N_{Sc}\frac{2r_1}{L}\right)^{1/3} \quad [23]$$

Equation [18] can be solved analytically by assuming a solution of the form

$$\theta(\xi) = \Psi(\xi) + \Gamma \quad [24]$$

where Γ is a constant for a given η and temperature and is given by

$$\Gamma = \exp\left(\frac{2F}{RT}\eta\right) \quad [25]$$

Application of the boundary conditions, Eq. [21] and [22], to the homogeneous part of Eq. [18] gives the solution in terms of modified Bessel functions of the first and second kind (19). The complete solution to Eq. [18] is [see Ref. (20)]

$$\theta(\xi) = G[\theta(t) - 1.0]\left\{\frac{K_1(\sqrt{B})}{I_1(\sqrt{B})} I_o(\sqrt{B}\xi) + K_o(\sqrt{B}\xi)\right\} + \exp\left(\frac{2F}{RT}\eta\right) \quad [26]$$

where the dimensionless surface concentration is

$$\theta(t) = \frac{GK_1(\sqrt{B})I_o(\sqrt{B}t) + GI_1(\sqrt{B})K_o(\sqrt{B}t) - I_1(\sqrt{B})\exp\left(\frac{2F}{RT}\eta\right)}{GK_1(\sqrt{B})I_o(\sqrt{B}t) + GI_1(\sqrt{B})K_o(\sqrt{B}t) - I_1(\sqrt{B})} \quad [27]$$

and

$$G = \frac{r_m k I_1(\sqrt{B})}{D_e\sqrt{B}[K_1(\sqrt{B})I_1(\sqrt{B}t) - I_1(\sqrt{B})K_1(\sqrt{B}t)]} \quad [28]$$

An expression for the current density, consistent with the sign convention that cathodic currents are negative, can be obtained from the dimensional definition of the flux at the inside edge of the porous electrode

$$\frac{i}{2F} = N_2\Big|_{\xi=t} = kc_{2,b}[\theta(t) - 1.0] \quad [29]$$

In addition, the cross-sectional area at the inside edge of the porous electrode can be used to obtain an expression for the total current

$$I = 4\pi t r_m L F k c_{2,b}[\theta(t) - 1.0] \quad [30]$$

Equation [30] can be used to predict the current being passed by a back fed cylindrical porous electrode as a function of the applied potential and the Reynolds number because it includes the dependence of the concentration distribution on the mass transfer coefficient external to the porous electrode. Also, this equation applies to a front fed configuration where the separator and the counterelectrode are located at some radial position less than tr_m (*i.e.*, close to the center line). Thus, the orientation of the coordinate system would be the same as with the back fed electrode and therefore the boundary conditions of Eq. [21] and [22] would still apply. Conceptually, the boundary condition at $\xi = 1$ would be the same because a backing plate would be considered impermeable. In this front fed configuration, the mass transfer coefficient must be adjusted for flow in an annulus (18). (Analogous equations for Cartesian coordinates are shown in the Appendix).

Equation [30] and the model presented here are limited to small conversions per pass because they include the lumped mass transfer coefficient of Eq. [23] (18). However, a small conversion per pass is a reasonable assumption for flow batteries (*e.g.*, Zn/Br_2, Zn/Cl_2, redox) because large concentration changes occur only after many passes. Thus, the model has utility for flow batteries. Also, the model can be utilized to determine kinetic and mass transfer parameters from a reactor built to satisfy Assumption m; the parameters obtained from this differential reactor (laboratory scale) could then be used to design a more complicated pilot plant scale reactor.

A simple form of Eq. [27] for use in Eq. [30] can be obtained for the case where the pseudo-homogeneous rate constant B is large and the electrode is not too thin; that is, for the cases where

$$\sqrt{B} \geq 88 \quad \text{and} \quad t \leq 0.95 \quad [31]$$

Equation [27] becomes

$$(t) = \frac{kr_m + D_e\sqrt{\bar{B}}\exp\left(\frac{2\mathbf{F}}{RT}\eta\right)}{kr_m + D_e\sqrt{\bar{B}}} \quad [32]$$

or

$$\theta(t) = \frac{1 + P\exp\left(\frac{2\mathbf{F}}{RT}\eta\right)}{1 + P} \quad [33]$$

where

$$P = \sqrt{\frac{D_e a i_{o,b}\exp\left(\frac{-\alpha_c\mathbf{F}}{RT}\eta\right)}{k^2 2\mathbf{F}c_{2,b}}} \quad [34]$$

The dimensionless parameter P in Eq. [34] shows the combined effects of internal, external, and charge transfer resistance on the surface concentration.

Experimental Analysis

The experimental analysis of the flow-by back fed cylindrical porous electrode considered the reduction of bromine to bromide according to Eq. [1] and the oxidation of bromide to bromine according to the reverse reaction of Eq. [1]. The experimental data were obtained by potentiostatic determination of the current for a cylindrical flow-by back fed porous Ti-RuO_2 electrode. The dependent variable was the observed steady-state current and the independent variables were applied potential ($V - \Phi_{re}$) and the electrolyte flow which was equivalent to the Reynolds number (N_{Re}) since ν and r_i were assumed to be constant. The experiments were performed at a constant bulk Br_2 concentration ($c_{2,b}$) at different applied potentials and Reynolds numbers. The order of the experiments (*i.e.*, the order for applying different values of the potential) was randomized to remove the effect of any concentration changes with time. This randomization insured that the experimental errors were independent and therefore the data are consistent with the assumptions of the least squares theory discussed below [see also, *e.g.*, Ref. (21)].

Experimental Apparatus

Reactor system.—A schematic of the reactor system is shown in Fig. 3; the negative electrolyte contacted the zinc terminal (*i.e.*, the counterelectrode in this study) and the positive electrolyte contacted the Br_2/Br^- terminal (*i.e.*, the back fed porous working electrode under investigation here). Fisher flowmeters (No. 448-324) with 0.635 cm outside diameter glass floats were used for volumetric flow measurement. Constant speed magnetic induction centrifugal pumps (Eastern No. MD-15T-G01) were used to circulate the electrolytes; peristaltic (*i.e.*, roller) pumps were not used because of reported problems with the surges in pressure caused by the rollers (22). The recycle streams were a necessary result of the constant speed pumps and they formed the reservoir for each electrolyte. Schedule 40, 1.27 cm PVC pipe was used for the system piping and smaller connections were made with Tygon tubing and hose clamps. Some attack of the tubing by Br_2 was noticed over the life of the experiments (~2 months), but no loss of catalytic activity due to organic poisoning of the Br_2 electrode by any dissolved Tygon was observed.

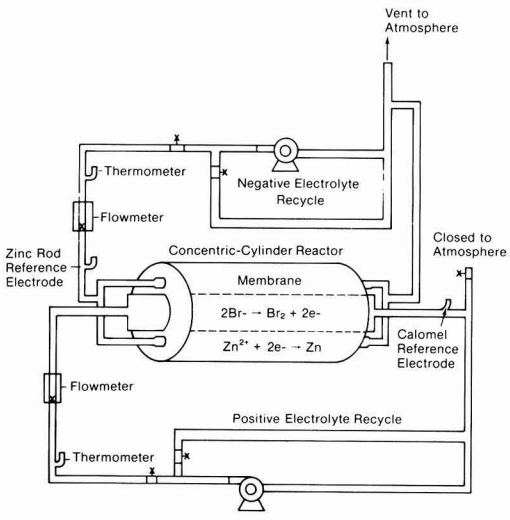

Fig. 3. A schematic of the experimental reactor system shown in the charge mode.

The experimental system was designed as shown in Table I, to be consistent with Assumptions d, i, j, and m used in the development of the theoretical model; the system was also designed in a manner similar to existing Zn/Br_2 batteries (1, 2, 4, 6, 7, 22). The experimental electrolyte was supported wtih excess Na^+ to satisfy Assumption d. Although the specific conductivity κ of the electrolyte was not measured, it was probably about 0.4 Ω^{-1} cm^{-1} (1, 4). Using this κ value, the voltage drop in the solution over the length of a reaction zone on the order of 10^{-2} cm can be calculated by Ohm's law and shown to be on the order of 10 mV (20) at a current density of 50 mA/cm^2 (a small reaction zone is expected for this fast reaction as described below); this voltage drop is consistent with part of Assumption i. The concentration of bromide in Table I is approximately 80 times larger than the limiting reactant, bromine. This concentration ratio is consistent with existing Zn/Br_2 battery design and Assumption j. Table I also shows that the conversion (or production) per pass of bromine is expected to be low for typical currents and Reynolds numbers, as discussed below.

Electrodes.—The zinc terminal (*i.e.*, counterelectrode) consisted of a 2.54 cm OD titanium tube with a wall thickness of 0.125 cm. The negative electrolyte was fed to the inside of the tube through PVC end caps. The end caps fit snugly over the outside of the titanium tube and small leaks were stopped by wrapping Teflon tape around the outside of the tube. The inner electrode hole in the center of the end caps was sealed with an O-ring and the end cap lids. Two equally spaced electrical connections were made between the end caps; no measurable voltage drop existed between the connections or over the length of the counterelectrode. During the anodic or charge mode of the experiment, bromide was oxidized to bromine and zinc was plated at this counterelectrode. Conversely, when cathodic potentials were applied, bromine was reduced to bromide at the porous electrode and zinc was dissolved at the counterelectrode.

Table I. Experimental system design specifications

Negative electrolyte volume	**420 ± 10 cm^3**
Positive electrolyte volume	**580 ± 10 cm^3**
Negative electrolyte composition:	
$ZnBr_2$	**1.05M**
NaBr	**2.08M**
***p*H (lowered from 3.8 with HBr)**	**1-3**
Zyonil	**100 ppm**
Positive electrolyte composition:	
$ZnBr_2$	**1.05M**
NaBr	**2.08M**
Br_2	**0.0510M**
***p*H**	**3.8**
Negative and positive electrolyte density at 22°C	**1.38 g/cm^3**
Electrode length	**12.7 cm**
Counterelectrode plating area	**56.2 cm^2**
Annulus spacing	**0.328 cm**
Positive electrode outside diameter ($2r_m$)	**0.4572 cm**
Positive electrolyte, cathodic reactant conversion per pass for N_{Re} = 100 and 0.25A (assuming 100% faradaic conversion)	**8.0%**

The flow-by back fed electrode (again, the experimental working electrode) consisted of a titanium tube perforated with 400 holes which were drilled with a No. 57 drill (0.10922 cm diam). The titanium tube wall thickness was 0.0889 cm and the outside diameter of the tube was 0.635 cm. The entire tube was coated with RuO_2 by using a standard dimensionally stable anode (DSA) preparation technique. Table II summarizes the electrode fabrication parameters including the calculated (based on geometry) specific surface area and porosity of the perforated tube electrode.

The catalytic surface area is expected to be much greater than the geometric value shown in Table II because the RuO_2 coating was deposited by thermal decomposition and therefore is highly porous. Reported catalytic surface areas for the DSA coating range up to 1000 times larger than the geometric area due to the roughness of the surface (23, 24). Thus, it is this porous coating that corresponds to the classical concept of a homogeneous porous electrode rather than the drilled holes of the titanium tube. Thus, the ratio of porosity and tortuosity for the porous coating would probably be larger than the geometric value for ϵ/τ shown in Table II.

Also shown in Table II is the length of tube before the porous electrode L_{en}. This entrance length can be considered as the length available for the development of the hydrodynamic profile. The required entrance length is a function of the Reynolds number and it can be estimated (25)

$$L_{en} = 0.036\, N_{Re}(2r_i) \qquad [35]$$

At a Reynolds number of 100, the entrance length from Eq. [35] is 1.64 cm. The actual entrance length in the experiment was greater than this because Tygon tubing with an ID approximately equal to r_i was used between the PVC pipe and the perforated tube electrode.

A saturated calomel electrode (SCE) was used as the reference electrode in the experiment and it was positioned downstream of the working electrode as shown in Fig. 3. The actual location (*i.e.*, upstream or downstream) was unimportant because the conversion per pass was small; hence the reference electrode was bathed in a concentration with an essentially constant ratio of Br_2/Br^- throughout an experimental run. This constant concentration was used to calculate the null potential ΔU_b which can be measured at open circuit. A measured value of $\Delta U_b = 0.757 \pm 0.0005$V was observed for all of the experimental data reported here. A calculated value of $\Delta U_b = 0.772$V is predicted according to Eq. [12] with the concentrations of Table I. This discrepancy of 15 mV between the observed and predicted values of ΔU_b may be attributable to the liquid junction potential between the reference electrode and the positive electrolyte which flowed by the SCE; (according to Ref. (26), liquid junction potentials can be on the order of 20 mV).

Table II. Experimental back fed porous electrode fabrication parameters. (Values without superscripts were measured.)

Parameter	Value	Units
ϵ/τ	0.172[1]	none
a	112.4[2]	cm^{-1}
L	12.7	cm
r_m	0.3175	cm
r_i	0.2286	cm
t	0.720	none
ν	0.00903[3]	cm^2/sec
L_{en}	12.7	cm
Electrode area at r_i	18.24	cm^2

[1] Assumed $\tau = 1.0$; ϵ was calculated from geometry of the holes in the perforated tube electrode.
[2] Assumed value based on geometric specific surface area of 15.10 cm^{-1} and a roughness factor of 7.443.
[3] Calculated from assumed value of $\mu = 1.25$ g/cm-sec and a measured value of $\rho = 1.384$ g/cm^3.

Membrane preparation.—The separator used in all experimental runs was a Nafion 315 membrane. The membrane was cut to the required width and then boiled in distilled water for at least 1 hr. The boiling was required to open the pores in the resin of the membrane and distilled water (instead of acid) was used to minimize the diffusion of Br_2 through the Nafion as discussed in Ref. (27). The membrane was allowed to cool to room temperature and then it was wrapped around the outside of the porous electrode. The 0.6 to 0.3 cm seam where the membrane overlapped was glued by using a syringe applicator with an epoxy and hardener (General Electric No. 512 and No. 524). The glue was allowed to dry at room temperature for about 5 days. The electrode/membrane assembly was then tested for leaks with an approximate 30 cm static head of water. The membrane was wrapped tightly around the electrode and hence flow through the electrode (*e.g.*, in one drilled hole and out another) was highly improbable; thus model Assumption e was fulfilled.

Electronics.—Figure 4 shows a schematic of the electrical connections used in the experiment. A Princeton Applied Research potentiostat (PAR 371) was used to control the first independent variable, the applied potential $V - \Phi_{re}$. That is, the potential difference between the porous electrode (*i.e.*, the working electrode) and the SCE were controlled by adjusting the potential applied to the counterelectrode. The applied potential $V - \Phi_{re}$ was not corrected for ohmic drop because the downstream reference electrode was located outside of the potential field which existed between the working electrode and the counterelectrode. Thus, it was assumed that the potential in the solution was the same everywhere in the flow channel and hence $\Phi_{re} = \Phi_2$. Thus, the total overpotential η of Eq. [9] is related to the applied potential $V - \Phi_2 = V - \Phi_{re}$ through the open circuit or null potential ΔU_b (*i.e.*, $\eta = V - \Phi_{re} - \Delta U_b$). Also, the assumption of negligible potential drop within the porous region of the electrode implies that $\Phi_{re} = \Phi_2 = \Phi_{2,o}$. At a given applied potential and

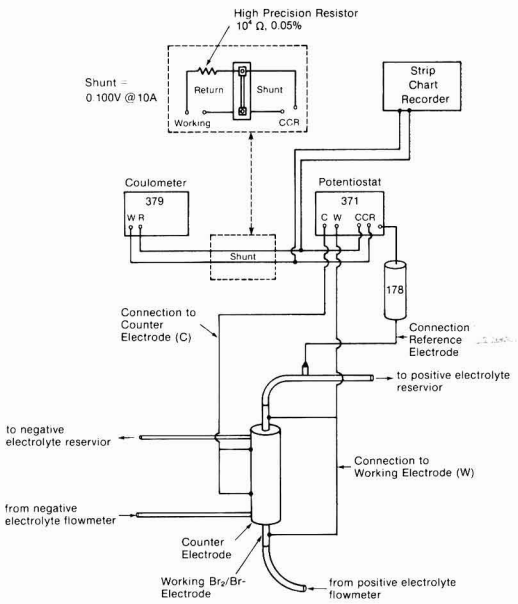

Fig. 4. A schematic of the experimental electronics

Reynolds number, a strip chart recorder (as shown in Fig. 4) was used to verify that steady-state current conditions existed. This current was then read from the analog meter on the PAR 371. The digital coulometer (PAR 379) shown in Fig. 4 was used to record the number of coulombs passed during an experimental run which was then used to calculate the faradaic conversion per pass of the positive electrolyte, as shown in Table I. (The coulometer was connected across a 10,000Ω shunt to reduce the input signal to within the limits of the coulometer.)

Experimental Procedures

Steady-state current measurement.—The procedure for measuring the steady-state current from the back fed electrode began by circulating the electrolyte streams for about an hour until the temperature of each stream was constant followed by an iodometric titration to find the initial Br_2 concentration in the positive electrolyte. Once the bromine concentration was known, the cell was left at open circuit for 30 min and the null potential (*i.e.*, the open-circuit potential between the working electrode and the downstream calomel reference electrode) ΔU_b was recorded every 10 min. Once the null potential was constant, experimental data were obtained; that is, a randomly chosen applied anodic potential difference $V - \Phi_{re}$ was set until a steady-state current was observed on the strip chart recorder. Then, the cell was returned to open circuit and the number of coulombs of charge were recorded. The null potential ΔU_b as measured by the PAR 371 was recorded and the reservoir concentration of the Br_2 above the titrated concentration was calculated by assuming 100% faradaic efficiency. This calculation was used to check the percent conversion.

If the percent conversion was small and if the null voltage was the same after the run as it was for the previous run, the cell was operated according to the above procedure at a randomly chosen cathodic potential difference. If the null potential was different from the value in the prior runs, the cell was charged or discharged at a low rate to adjust the bromine concentration, left at open circuit for 10 min and the null potential checked again. Then, samples were taken to determine the reservoir concentration of Br_2 by titration. If the Br_2 concentration was the same (to within ± 3%) as the previous runs, the cell was operated at a randomly chosen cathodic potential difference according to the above procedure. Then, the above anodic/cathodic sequence was repeated.

Titration of these samples and the measurement of the null potential ΔU_b were used to check the level of the bromine concentration $c_{2,b}$. Thus, the bromine concentration was not controlled during an experimental run but it was measured, and this measurement was used as a basis for including or discarding the results of an experimental data point. However, the titrations involved three 5 ml samples from the reservoir volume which was about 3% of the reservoir volume. Therefore, to minimize additions to the reservoir, samples were taken and titrations were made after four or five experimental runs if the null potential was unchanged. Theoretically, the null potential can be used to predict changes in the bromine concentration to within ± 4% for a 0.5 mV change at the concentrations shown in Table I. Experimentally, an observed change in ΔU_b of 0.5 mV corresponded to a 4% change in the bromine concentration as measured by titration of three samples. Thus, although the bromine concentration was not controlled in the experiment, the experimental error was approximately 4%. To insure that these concentration errors were random, the experimental runs were randomized; hence, any concentration changes with time should not affect the average value of the measured current at a given applied potential and Reynolds number.

Flow control.—The second independent variable, the Reynolds number, was controlled by a needle valve as indicated by a flowmeter. That is, the volumetric flow in the nonporous region of the electrode was adjusted manually so that the Reynolds number remained constant for an experimental data point. The volumetric flow was obtained from a calibration curve which was drawn from manufacturers' data and the experimental kinematic viscosity shown in Table II. The density of the positive electrolyte was measured at 24°C and the viscosity of the electrolyte was obtained from Ref. (1) for this calculation. The approximate error in the experimental Reynolds number was 5%.

Experimental Results

The points in Fig. 5 and 6 show the experimentally determined steady-state current as a function of applied potential and Reynolds number for the perforated tube back fed electrode. The numbers beside each data point correspond to the sequence in which the points were obtained. The data connected by dashed lines indicate the conditions where bubbles were observed in the exit stream. The solid lines in Fig. 5 and 6 are model predictions which are discussed below. The electrode fabrication parameters and electrolyte compositions are shown in Tables I and II. The electrolyte temperature for all data was 28°C. The Br_2 concentration varied by 3% from 0.0510M as shown in the figure but the null potential ΔU_b was essentially constant. The data were reproducible over the 2 month life of the experiment.

The general form of the results in Fig. 5 is similar to the behavior of a rotating disk electrode (RDE) as the rotation speed is increased; that is, the limiting current increases with Reynolds number and thereby shows a region in which external mass transfer controls the rate of reaction. Also, the length of the limiting current plateau decreases as the Reynolds number increases in a manner similar to an RDE system for

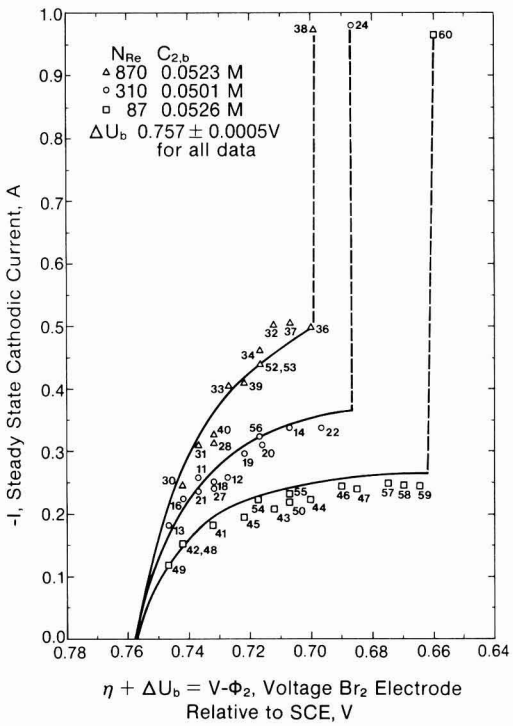

Fig. 5. Experimental cathodic steady-state currents

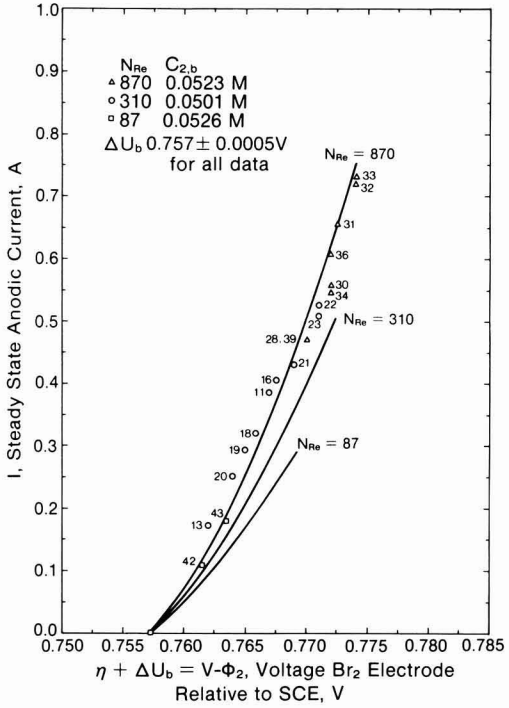

Fig. 6. Experimental anodic steady-state currents

the reduction of Cu^{+2} in acidic electrolyte (28). In Fig. 5, the side reaction characterized by gassing is probably the reduction of hydrogen ion. However, no changes in the pH of the positive electrolyte were noticed, but this could be a result of the small amount of gassing and the large reservoir.

The anodic experimental data in Fig. 6 depend only slightly on the Reynolds number over the range of experimentally applied potentials. This slight dependence is due to the high Br^- concentration in the electrolyte (20).

Least Squares Regression

The model presented above depends on, among other things, the parameters α_c, i_o^o, and D_2. These parameters can be obtained from the literature if available (they are not available for these experimental conditions), determined by independent experiments or determined by applying least squares (LS) regression (21, 29-31) to the model and experimental data. Confidence is gained in the model if the parameter values obtained by LS are physically realistic. If the parameter values are physically realistic, extrapolation beyond the experimental range could be done within the limits of the assumptions. However, even if the parameter values are not physically realistic, LS does provide a set of parameter values suitable for use in the model which could be used for interpolation within the range of the experimental data. It is perhaps this last advantage of LS which is the most important for battery designers. That is, at the LS estimates the model provides the best functional relationship (for the assumed model) between the physical parameters and the experimental data. A better functional relationship may be obtained with a different model but in the absence of another model, the designer should use the LS estimates for interpolation even in preference to literature values.

The LS method consists of minimizing the following nonlinear objective function

$$F(\beta) = \sum_1 \epsilon_1^2 = \sum_1 (I_1 - \hat{I}_1)^2 \qquad [36]$$

where $\hat{I}_1$ = is given by Eq. [30] at the experimental conditions corresponding to the 1^{th} datum. The nonlinearity of Eq. [36] results from the nonlinear model equations, but it does not affect the theory behind LS regression. The computations necessary to minimize this objective function become more complicated with a nonlinear function; however, many computers have subroutine libraries which can perform the necessary calculations [see Ref. (20)]. The nonlinearity does affect the statistical inferences that can be made, and hence, the confidence limits for the parameters are valid only as the number of experimental data points becomes large (29). These confidence limits for the parameters are discussed in Ref. (20) and (32).

Regression Results

Table III presents the results of the application of the LS technique (20). As can be seen in Table III, in the first four cases α_c was set and LS used to determine i_o^o and D_2, and in the last case LS was used to determine α_c, i_o^o, and D_2. The solid lines shown in Fig. 5 and 6 were calculated according to Eq. [30] with the case five parameter values [no noticeable difference in the lines occurs when the case 3 or 4 Table III parameter values are used since the values of Eq. [36] are not significantly different (20)].

Quantitatively, the model predicts all of the experimental data points to within 30% and most of the data to within 10%. The greatest deviations occur at large currents and Reynolds numbers; these deviations could be a result of measurement errors in either the flow rate or bulk Br_2 concentration which are magnified at the large current experimental conditions. This degree of accuracy may be suitable for engineering purposes.

Discussion

Table IV presents a comparison of the LS parameter estimates with literature values. The LS estimate of the diffusion coefficient is the same order of magnitude as the published data which was obtained in a rotating disk experiment (33). The difference in diffusion coefficients may be attributable to the relatively small assumed value of ϵ/τ (0.172). That is, if it is assumed that the value for D_2 given by Osipov *et al.* (33) is correct, then ϵ/τ for the porous electrode

Table III. Least squares estimates

Case[1]	α_c	α_a[2]	$i_o^o \times 10^3$, A/cm²	$D_2 \times 10^5$, cm²/sec	SSE[3]
1	0.50	1.50	190 ± 101	(9.03 ± 2.37)	0.1386
2	0.75	1.25	610 ± 63	(6.99 ± 1.16)	0.1076
3	1.00	1.00	123 ± 41	(5.86 ± 0.73)	0.0965
4	1.50	0.50	58 ± 17	(4.79 ± 0.43)	0.0925
5	1.32 ± 0.52	0.68	79 ± 68	(5.08 ± 1.10)	0.0919

[1] Cases 1-4 are for α_c fixed with i_o^o, and D_2 the LS estimates. Case 5 is for α_c, i_o^o, and D_2 as the LS estimates.
[2] Calculated from Eq. [8] with $n = 2$.
[3] SSE = value of Eq. [36] at LS estimates.

Table IV. Comparison of least squares estimates with literature values for case 5 of Table III

Parameter	Units	Least squares estimate	Literature value/Ref.
D_2	cm²/sec	(5.08 ± 1.10) × 10^{-5}	1.2×10^{-5} (33)
i_o^o	A/cm²	0.079 ± 0.068	0.345 (33)[1]
α_c	none	1.32 ± 0.52	1.2 (32); 1.24-1.57 (35)

[1] i_o^o extrapolated from the reported $i_{o,b}$ values using Eq. [5]-[8] and the LS estimate of $\alpha_c = 1.32$.

studied here would be 0.728. The point is that the product (D_2) (ϵ/τ) (*i.e.*, the effective diffusion coefficient) is the unknown parameter in a porous electrode. The LS estimation procedure gives an estimate of D_2 which when multiplied by the assumed value of ϵ/τ is suitable for design within the range of the data (*i.e.*, for interpolation). The literature value for i_o^o is not directly comparable with the LS estimate in Table IV because the literature value was obtained on a platinum RDE whereas an RuO_2 on Ti electrode was used here. However, the LS estimate for i_o^o is reasonable because platinum should be a better catalyst and therefore result in a larger i_o^o. Another complication in the comparison of i_o^o is that the product of the specific surface area a and the exchange current density appears in the model and the value of a was not measured in this experiment. However, the point is (as with the diffusion coefficient) the LS procedure gives an estimate of i_o^o which can be used in the model with the assumed value of a to interpolate. It should be noted that the LS value of i_o^o gives a relatively large value of $i_{o,b}$ from Eq. [5] which is consistent with the observations of fast Br_2/Br^- kinetics by Zn/Br_2 battery designers (1, 4, 6, 7, 34). The LS estimate of α_c agrees well with the literature values of Ref. (34) and (35). Both i_o^o and α_c have large error bounds due to the small amount of data obtained here for anodic polarizations (see Fig. 6) and for the lack of data on the concentration dependence of γ_i. The model deviations from the experimental anodic data are also a result of the lack of data on the concentration dependence of γ_i.

It is important to note that the model is sensitive to the parameter values throughout the range of the experimental data as demonstrated, for example, by Fig. 7 and 8. Similar predictions can be made for anodic currents (20). It is also important to note that the estimated values of i_o^o and D_2 yield a small ellipse on a contour plot as shown in Fig. 9 with $\alpha_c = 1.0$. Note that the minimum value of the objective appears as a steep narrow ellipse within the vicinity of the LS estimates (case 3, Table III).

With the value of i_o^o obtained by LS and the experimental concentrations, a large value of B results from Eq. [19]. Thus, the model predicts a thin reaction zone as indicated in Fig. 10 by concentration changes only at the edge of the porous region. This implies that only a small fraction of the RuO_2/Ti porous electrode is utilized even at relatively small overpotentials. Figure 10 illustrates an interesting feature of the model presented here. That is, at a given η, $\theta(\xi)$ drops rapidly over a small distance within the porous electrode to a constant value instead of zero as might be expected. The reason for this is the inclusion of the complete Butler-Volmer equation which leads to the Γ term in Eq. [24] (20).

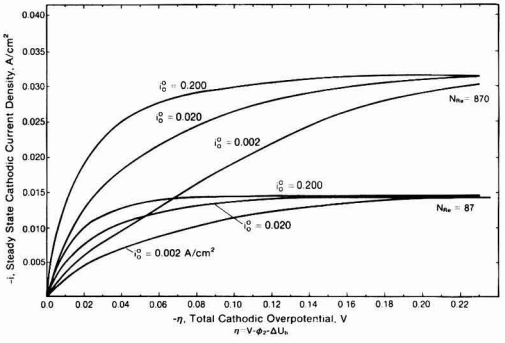

Fig. 7. Model sensitivity to changes in exchange current density for cathodic polarizations at case 5 of Table III values for D_2 and α_c.

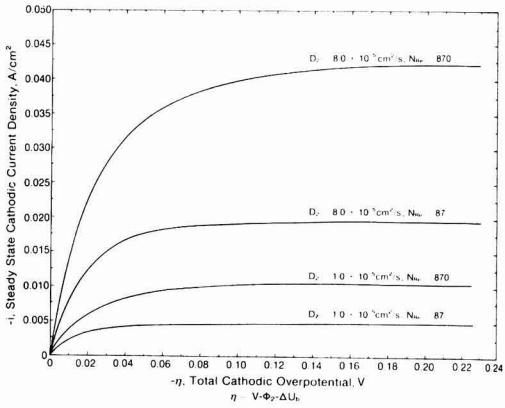

Fig. 8. Model sensitivity to change in the diffusivity for cathodic polarizations at case 5 of Table III values for i_o^o and α_c.

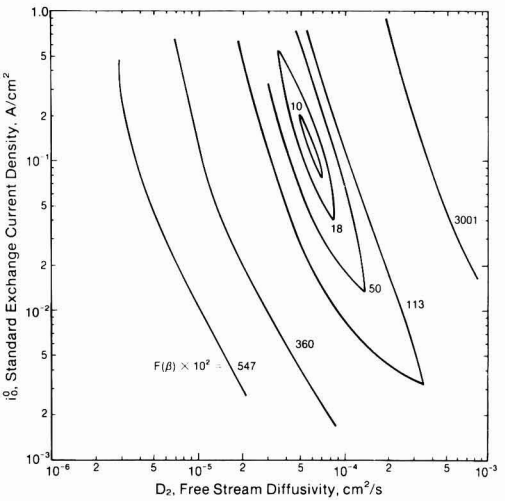

Fig. 9. Contours of the scaled least squares objective function [$F(\beta)$ (as given by Eq. [36]) $\times$ 10^2] for $\alpha_c = 1.0$.

Conclusions

This study of a flow-by back fed porous electrode for the reduction of bromine produced a mechanistic model of the steady-state process. The model consists of a single analytical expression (Eq. [30]) suitable for design purposes. The model is applicable over a large range of overpotentials and includes external mass transfer resistance. Also, the model predicts most of the experimental data presented here to within approximately 10%, and the parameter estimates of α_c, i_o^o, and D_2 obtained here compare favorably with literature values.

Analysis of the flow-by back fed porous electrode for the reduction of bromine revealed that its limiting current is similar to a rotating disk; its limiting current density is characterized by a zero concentration at the surface on the side of the fresh reactant. The reaction zone for the fast reaction studied here is less than 5% of the electrode thickness; hence, the concentration profile is horizontal within the porous electrode and the reaction occurs on the back side of the electrode. This small reaction zone thickness indicates that small ohmic energy losses could be achieved by using thin back fed electrodes. The concentration profile shows that the Br_2 concentration at the separator in a Zn/Br_2 battery could be reduced significantly

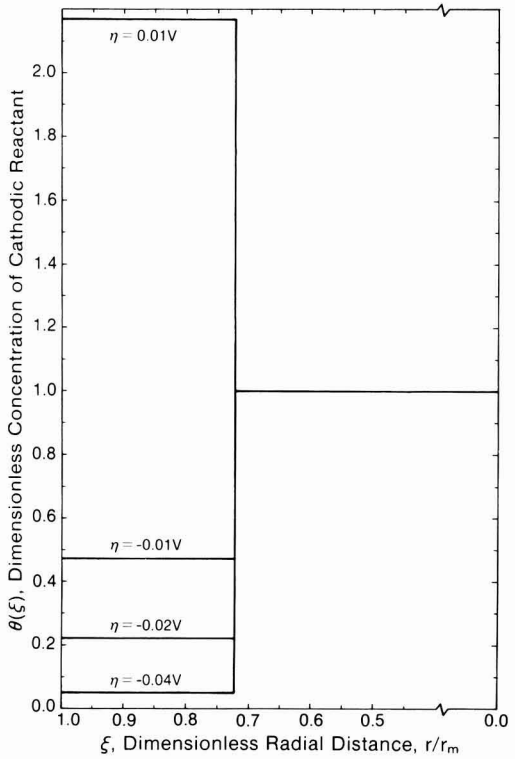

Fig. 10. Concentration profiles in experimental back fed porous electrode for LS parameter estimates of case 5 of Table III.

during discharge which would decrease the loss of Br_2 across the separator. However, on charge, the concentration of Br_2 at the separator would be increased and would cause consequently a greater loss of Br_2.

Acknowledgments

This work was supported by the Center for Energy and Mineral Resources at Texas A&M University. The electrode was coated with catalyst by the Chlor-Alkali Department of the Dow Chemical Company, Texas Division, Freeport, Texas. The experimental Zn/Br_2 reactor was furnished by Gould Incorporated, Rolling Meadows, Illinois. The authors gratefully acknowledge all of this support.

Manuscript submitted Nov. 16, 1982; revised manuscript received *ca.* May 13, 1983.

APPENDIX

The Back Fed Model in Cartesian Coordinates

The governing differential equation for the concentration of a cathodic reactant (*e.g.*, bromine) which corresponds to Eq. [15] in the text is

$$\frac{d^2c_2}{dx^2} - Kc_2 = \frac{-ai_{o,b}}{2FD_e}\exp\left(\frac{\alpha_n F}{RT}\eta\right) \quad [A\text{-}1]$$

where

$$K = \frac{ai_{o,b}}{2FD_e c_{2,b}}\exp\left(\frac{-\alpha_c F}{RT}\eta\right) \quad [A\text{-}2]$$

The following dimensionless variables can be used to simplify Eq. [A-1]

$$\zeta = \frac{x}{x_m}; \quad \theta = \frac{c_2}{c_{2,b}} \quad [A\text{-}3]$$

Then, Eq. [A-1] becomes

$$\frac{d^2\theta}{d\zeta^2} - B\theta = -A \quad [A\text{-}4]$$

where

$$A = \frac{ai_{o,b}x_m^2}{2FD_e c_{2,b}}\exp\left(\frac{\alpha_a F}{RT}\eta\right) \quad [A\text{-}5]$$

and

$$B = K\,x_m^2 \quad [A\text{-}6]$$

The boundary conditions are at

$$x = x_m, \quad \zeta = 1.0, \quad \frac{d\theta}{d\zeta} = 0 \quad [A\text{-}7]$$

at

$$x = 0, \quad \zeta = 0, \quad \frac{d\theta}{d\zeta} = \frac{x_m k}{D_e}(\theta(0) - 1.0) \quad [A\text{-}8]$$

where

$$k = 1.651\frac{D_2}{2r_h}\left(1.5\,N_{Re}\,N_{Sc}\frac{2r_h}{L}\right)^{1/3} \quad [A\text{-}9]$$

and r_h is the hydraulic radius as defined in Ref. (25).

Equation [A-4] can be solved analytically by assuming a solution of the form

$$\theta(\zeta) = \Psi(\zeta) + \Gamma \quad [A\text{-}10]$$

where Γ is a constant at a given η and temperature and is given by

$$\Gamma = \exp\left(\frac{2F}{RT}\eta\right) \quad [A\text{-}11]$$

The general form of $\Psi(\zeta)$ is

$$\Psi(\zeta) = E\sinh(\sqrt{B}\,x) + F\cosh(\sqrt{B}\,x) \quad [A\text{-}12]$$

and application of boundary condition Eq. [A-7] gives

$$F = -E\coth(\sqrt{B}\,x_m) \quad [A\text{-}13]$$

Application of boundary condition Eq. [A-8] gives

$$E = \frac{x_m k}{D_e\sqrt{B}}(\theta(0) - 1.0) \quad [A\text{-}14]$$

Thus, the complete solution for $\theta(\zeta)$ is

$$\theta(\zeta) = E\sinh(\sqrt{B}\,\zeta) - E\coth(\sqrt{B}\,x_m)\cosh(\sqrt{B}\,\zeta) + \exp\left(\frac{2F}{RT}\eta\right) \quad [A\text{-}15]$$

Solving for the unknown surface concentration, $\theta(0)$, in Eq. [A-13] gives

$$\theta(0) = \frac{x_m k\coth(\sqrt{B}\,x_m) + D_e\sqrt{B}\exp\left(\frac{2F}{RT}\eta\right)}{D_e\sqrt{B} + x_m k\coth(\sqrt{B}\,x_m)} \quad [A\text{-}16]$$

Now, consideration of the case where $\sqrt{B} \to 100.0$ gives

$$\theta(0) = \frac{x_m k + D_e\sqrt{B}\exp\left(\frac{2F}{RT}\eta\right)}{x_m k + D_e\sqrt{B}} \quad [A\text{-}17]$$

Finally, an expression for the current density is

$$\frac{i}{2F} = N_2\Big|_{x=0} = kc_{2,b}(\theta(0) - 1.0) \quad [A\text{-}18]$$

where $\theta(0)$ is defined by Eq. [A-16] or [A-17].

LIST OF SYMBOLS

a	specific catalytic surface area of porous electrode, cm^{-1}
c_1, c_2	concentration of i^{th} species, i = 2 for bromine, mol/cm^3
$c_{i,b}$, $c_{2,b}$	bulk concentration of i^{th} species, i = 2 for bromine, mol/cm^3
c_i°	standard reference concentration of i^{th} species $= 10^{-3}$ mol/cm^3
$c_{i,re}$	reference electrode concentration of i^{th} species, mol/cm^3

D_e	effective diffusion coefficient of bromine, cm²/sec
D_2	free stream diffusion coefficient of bromine, cm²/sec
F	faraday's constant, 96,487 C/mol of electrons
$F(\beta)$	least squares objective function, A²
I	total cell current, A
$I_o(\cdot)$	modified Bessel function of the first kind, zero order
$I_1(\cdot)$	modified Bessel function of the first kind, first order
I_l	lth experimentally observed current, A
$\hat{I}_l$	model predictions at experimental conditions corresponding to the lth datum, A
i	steady-state current density, A/cm²
i_L	limiting current density, A/cm²
$i_{o,b}$	exchange current density at bulk concentrations, A/cm²
i_o^*	standard exchange current density at 1*M*, A/cm²
j_l	average production rate per unit area
K	reaction rate function, cm^{-2}
$K_o(\cdot)$	modified Bessel function of the second kind, zero order
$K_1(\cdot)$	modified Bessel function of the second kind, first order
k	mass transfer coefficient, cm/sec
L	electrode length, cm
L_{en}	entrance length, cm (see Eq. [35])
N_i, N_2	flux of ith species, $i = 2$ for bromine, mol/cm²/sec
N_{Re}	Reynolds number
N_{Sc}	Schmidt number
n	number of mols of electrons ($n = 2$ mols of electrons for reaction [1])
p_i, q_i	reaction orders for ith species ($p_{Br^-} = 2$, $q_{Br2} = 1$)
R	gas constant, 8.313 J/mol/K
r	radial coordinate, cm
r_i	inside radius of electrode, cm
r_m	membrane radius, cm
s_i	stoichiometric coefficient of ith species ($s_{Br^-} = 2$, $s_{Br2} = -1$)
T	temperature, K
t	thickness ratio of porous electrode
U^θ	standard open circuit potential of working electrode, V
U_{re}^θ	standard reference electrode potential, V
V	potential of working electrode, V
v	axial velocity behind the back fed electrode, cm/sec

Greek letters

α_a	apparent anodic transfer coefficient
α_c	apparent cathodic transfer coefficient
β	vector of least squares parameters, $= [i_o^* \; D_2 \; \alpha_c]$
γ_i	concentration dependence for exchange current density
ϵ	porosity of electrode
ϵ_l	lth residual of least squares function, A
η	total overpotential, V
$\theta(t)$	dimensionless surface concentration
ν	kinematic viscosity, cm²/sec
ξ	dimensionless radial coordinate
π	3.1416
τ	tortuosity of porous electrode
Φ_{re}	potential in the solution at the reference electrode, V
Φ_2	potential of the solution in flow channel of porous electrode, V
$\Phi_{2,0}$	potential of the solution just outside the double layer, V

REFERENCES

1. R. A. Putt, "Assessment of Technical and Economic Feasibility of Zinc-Bromine Batteries for Utility Load Leveling", Final Report to Electric Power Research Institute, Palo Alto, CA, EM-1059, Research Project 635-1, May 1979.
2. P. Y. Lu, Workshop on Electrodes for Flowing Solution Batteries, summary by L. Nanis for Electric Power Research Institute, Palo Alto, CA, Special Study Project WS-79-192, Section 2, Feb. 1981.
3. D. J. Eustace, *This Journal*, **127**, 528 (1980).
4. F. G. Will, C. D. Iacovangelo, J. S. Jackowski, and F. W. Secor, "Assessment of the Zinc-Bromine Battery for Utility Load Leveling," Final Report to U.S. Dept. of Energy, Division of Energy Storage Systems, Contract No. 2950, EY-76-C-02-2950, March 1978.
5. B. V. Tilak, P. W. T. Lu, J. E. Colman, and S. Srinivasan, in "Comprehensive Treatise of Electrochemistry," Vol. 2, J. O'M. Bockris, B. E. Conway, E. Yeager, and R. E. White, Editors, p. 63, Plenum Press, New York (1981).
6. R. Bellows, D. Estace, P. Grimes, J. Shropshire, and H. Tslen, in 11th International Power Sources Symposium, p. 301, Brighton, England, Sept. 1978.
7. R. Bellows, H. Einstein, P. Grimes, E. Kanter, and K. Newby, in 15th Intersociety Energy Conversion Engineering Conference, Seattle, WA, p. 1465-1470, Aug. 1980.
8. J. S. Newman and C. W. Tobias, *This Journal*, **109**, 1183 (1962).
9. I. G. Gurevich and V. S. Bagotskii, *Electrochim. Acta*, **9**, 1151 (1964).
10. O. S. Ksenzhek, *Zh. Fiz. Khim.*, **36**, 633 (1962).
11. E. A. Grens and C. W. Tobias, *Electrochim. Acta*, **10**, 761 (1965).
12. L. G. Austin and H. Lerner, *ibid.*, **9**, 1469 (1964).
13. J. Newman and W. Tiedeman, *AIChE J.*, **21**, 25 (1975).
14. J. O'M. Bockris and S. Srinivasan, "Fuel Cells: Their Electrochemistry," p. 234, 254, 256, McGraw Hill, New York (1969).
15. B. V. Tilak, R. S. Yeo, and S. Srinivasan, in "Comprehensive Treatise of Electrochemistry," Vol. 3, J. O'M. Bockris, B. E. Conway, E. Yeager and R. E. White, Editors, p. 70, Plenum Press, New York (1981).
16. J. A. Trainham, Ph.D. Dissertation, University of California, Berkeley, CA (1979).
17. J. Newman, "Electrochemical Systems", p. 174, Prentice-Hall, Inc., Englewood Cliffs, NJ (1973).
18. J. Newman, "Electrochemical Systems," Prentice-Hall, Inc., Englewood Cliffs, NJ (1973).
19. H. S. Mickely, T. K. Sherwood, and C. E. Reed, "Applied Mathematics in Chemical Engineering," 2nd ed., p. 197, McGraw-Hill, New York (1957).
20. J. Van Zee, M. S. Thesis, Texas A&M University, College Station, TX (1982).
21. B. Ostle and R. W. Mensing, "Statistics in Research," 3rd ed., pp. 166-178, Iowa State University Press, Ames, Iowa (1975).
22. R. D. Weaver, "Testing and Evaluation Results of Gould Laboratory Prototype Zinc Bromine Cells," Final Report to Electric Power Research Institute, p. 56, Palo Alto, CA, Dec. (1977).
23. P. C. S. Hayfield and W. R. Jacob, in "Modern Chlor-Alkali Technology," M. O. Coulter, Editor, p. 105, Ellis Horwood Ltd., Chichester, West Sussex, England (1980).
24. D. L. Caldwell and M. J. Hazelrigg, in "Modern Chlor-Alkali Technology," M. O. Coulter, Editor, p. 127, Ellis Horwood, Ltd., Chichester, West Sussex, England (1980).
25. R. B. Bird, W. E. Stewart, and E. N. Lightfoot, "Transport Phenomena," p. 47, John Wiley, New York (1960).
26. J. Newman, "Electrochemical Systems," p. 130, Prentice-Hall, Inc., Englewood Cliffs, NJ (1973).
27. F. Will, *This Journal*, **126**, 36 (1979).
28. R. White and J. Newman, *J. Electroanal. Chem.*, **82**, 176 (1977).
29. W. J. Kennedy, Jr. and J. E. Gentle, "Statistical Computing," p. 426, Marcel Decker, Inc., New York (1980).
30. Y. Bard, "Nonlinear Parameter Estimation," Academic Press, New York (1974).
31. R. J. Freund and P. D. Minton, "Regression Methods," Marcel Decker, Inc., New York (1979).
32. A. R. Gallant, *Am. Stat.*, **29**, 73 (1975).
33. O. R. Osipov, M. A. Novitiskii, Yu. M. Povarov, and P. D. Lukovtsev, *Elektrokhimiya*, **8**, 327 (1972).
34. F. Will, in 11th International Power Sources Symposium, p. 9, Brighton, England, Sept. 1978; Personal communication with F. Will, July 2, 1982.
35. I. Rubinstein, *J. Phys. Chem.*, **85**, 1899 (1981).

Photo-oxidation of Organic Compounds at Doped α-Fe_2O_3 Electrodes

J. H. Kennedy* and D. Dünnwald

Chemistry Department, University of California, Santa Barbara, California 93106

ABSTRACT

Photo-oxidation of organic compounds at doped α-Fe_2O_3 electrodes was investigated in aqueous and nonaqueous solutions. Oxalic and formic acids in 0.5M H_2SO_4 showed distinctly different reactivities. Photo-oxidation of alcohols, *e.g.*, methanol and 2-propanol, was investigated in propylene carbonate and compared to their oxidation in water. The oxidation products (formaldehyde, acetone, and oxygen) were analyzed quantitatively; they accounted for 100% of the current. Competition between methanol and 2-propanol, and between these alcohols and water, is also reported.

Although photoelectrochemistry at iron oxide electrodes has been widely investigated in our laboratory (1-7) and in others (8-17), little work has been carried out on the oxidation of organic compounds (16-17). Stability of α-Fe_2O_3 in acid solution has now been demonstrated (7), so that the photo-oxidation of carboxylic acids and alcohols in acidic aqueous solutions could be undertaken. Also, in the present study, the photo-oxidation of alcohols in anhydrous propylene carbonate has been carried out. Competition between alcohols and water was investigated to help establish their relative reactivities.

Experimental

Electrodes were prepared from high purity α-Fe_2O_3 (99.999%, Alfa Products) by doping with 1 atomic percent (a/o) SiO_2. Pellets were pressed, sintered in air at 1365°C for about 20 hr, and then quenched in air to room temperature. The electrodes were about 1 cm^2 area after sintering and 0.1 cm thick. Electrical connection was made on the back with a sputtered gold film followed by silver epoxy to attach a wire lead. The electrode and the wire lead were then sealed in a glass tube with epoxy resin. The resistances of the electrodes measured at 1 kHz with a conductivity bridge were 60-350Ω.

Experiments with the organic acids were carried out in a two-compartment cell separated by a fritted glass disk. The compartment containing the semiconductor electrode was closed and contained a burette for collection of evolved gases. Experiments with alcohols were carried out in a single-compartment cell.

The light source was a 150W Xe lamp with light focused on the electrode by means of a quartz lens. Photocurrent *vs.* potential plots were taken with PAR Model 174 and X-Y recorders. Potentials were measured *vs.* SCE with all photo-oxidation experiments carried out at +1.2V *vs.* SCE. No attempt was made to adjust for the different junction potentials that were created when nonaqueous media were employed.

All chemicals were reagent grade. Propylene carbonate was distilled *in vacuo* and stored over molecular sieves. Tetra-*n*-butylammonium perchlorate, used as supporting electrolyte at a concentration of 0.1M, was dried *in vacuo* at 120° C before use.

CO_2, CO, and O_2 were analyzed by mass spectrometry. Analysis of formaldehyde was made spectrophotometrically using chromotropic acid. Analysis for acetone was made spectrophotometrically using 2,4-dinitrophenylhydrazine.

Results

Several carboxylic acids were investigated in solutions containing 0.5M H_2SO_4 and 0.1M Na_2SO_4. Citric acid and acetic acid, both at 0.5M concentration, showed no influence on the current-potential curves. Essentially all photocurrent resulted in O_2 production (0.8% CO_2 found with acetic acid). On the other hand, formic acid showed a small change and oxalic acid a large change in the I-V curves, as can be seen in Fig. 1. 0.5M oxalic acid shifted the onset of photocurrent 0.4V cathodically, while formic acid caused little shift. The photocurrents were significantly higher than in sulfuric acid alone.

An attempt was made to understand the large cathodic shift in photocurrent onset in oxalic acid by investigating current transients by on-off switching of the light source. In 0.5M H_2SO_4/0.1M Na_2SO_4, the photocurrent onset was +0.65V *vs.* SCE, but the first cathodic photocurrents were not observed until < +0.25V *vs.* SCE. Between +0.3 and +0.6V *vs.* SCE, anodic transients were observed upon illumination and cathodic transients were observed during dark periods. Both transients increased with anodic potential and had about the same magnitude up to +0.6V, thus resulting in no net steady-state photocurrent. It is probable that the flatband potential is near the lower value of +0.25V *vs.* SCE. When the same transient experiment was carried out with 0.5M oxalic acid in 0.5M H_2SO_4/0.1M Na_2SO_4, the photocurrent onset was at +0.225V *vs.* SCE. No cathodic transients were observed above +0.225V *vs.* SCE, and cathodic photocurrents were observed < +0.10V *vs.* SCE. Thus, the flatband potential appeared to be shifted cathodically only 100-150 mV in oxalic solutions, accounting for only a fraction of the 400 mV cathodic shift in photocurrent onset.

Whereas in H_2SO_4 solutions 100% of the photocurrent resulted in O_2 production, increasing amounts of carboxylic acid led to a decrease in O_2 and an increase in CO_2. Small amounts of CO were also detected. As seen in Fig. 2 and 3, formic and oxalic acids showed clearly different reactivities. 0.5M oxalic acid gave 80% CO_2 production while formic acid was much less

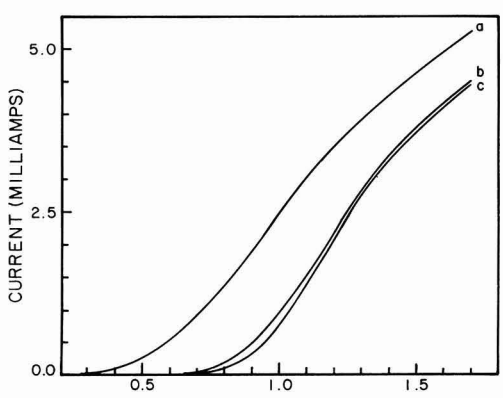

Fig. 1. Photocurrent-potential curves for organic acids in 0.5M H_2SO_4/0.1M Na_2SO_4. (a) 0.5M oxalic acid, (b) 0.5M formic acid, (c) blank.

* Electrochemical Society Active Member.

Key words: α-Fe_2O_3 photoanodes, organic acid photo-oxidation, alcohol photo-oxidation.

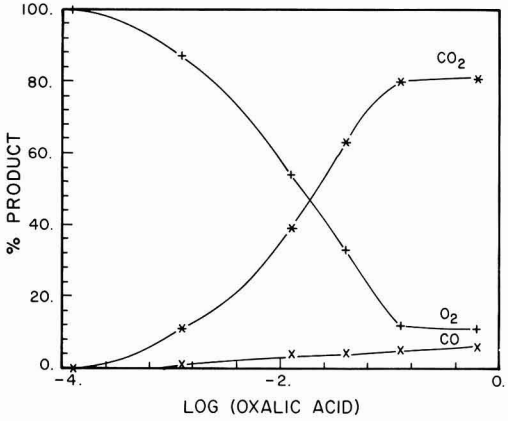

Fig. 2. Photo-oxidation of oxalic acid in 0.5M H_2SO_4/0.1M Na_2SO_4.

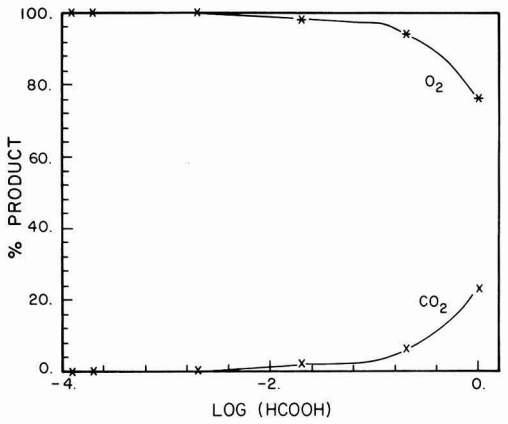

Fig. 3. Photo-oxidation of formic acid in 0.5M H_2SO_4/0.1M Na_2SO_4.

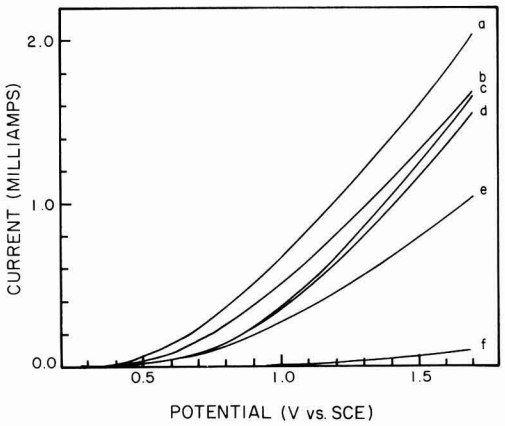

Fig. 4. Photocurrent-potential curves in propylene carbonate containing 0.1M tetra-*n*-butylammonium perchlorate. (a) 2M methanol/2M H_2O, (b) 2M 2-propanol/2M H_2O, (c) 2M methanol, (d) 2M H_2O, (e) 2M 2-propanol, (f) blank.

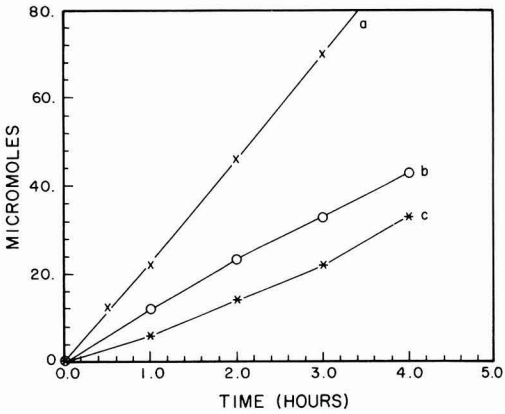

Fig. 5. Photo-oxidation of alcohols. (a) Formaldehyde produced in methanol, (b) formaldehyde produced in 2M methanol in propylene carbonate, (c) acetone produced in 2M 2-propanol in propylene carbonate. All solutions contained 0.1M tetra-*n*-butylammonium perchlorate.

efficient in competing with water for the photogenerated holes.

The photo-oxidation of alcohols was mainly investigated in propylene carbonate (Fig. 4), although the oxidation of pure methanol and aqueous solutions was also carried out. This was possible because the tetra-*n*-butylammonium perchlorate supporting electrolyte was easily soluble in methanol, and a 0.1M solution exhibited a resistance of 350Ω. Pure 2-propanol could not be studied because the electrolyte was only slightly soluble with resistances of about 7 kΩ. The product of photo-oxidation in pure methanol was formaldehyde. It accounted for 100% of the current and increased linearly with time as shown in Fig. 5. However, even in 1:1 methanol:water (0.05M H_2SO_4, 0.1M Na_2SO_4) by volume only 25% of the photocurrent led to formaldehyde. Results from the same experiment with 2-propanol showed that only 2.5% of the photocurrent could be attributed to acetone production.

The following set of experiments was carried out in anhydrous propylene carbonate containing 0.1M tetra-*n*-butylammonium perchlorate, which exhibited resistances of about 400Ω. Except where stated otherwise, the reactant concentration was 2M.

Pure propylene carbonate with 0.1M supporting electrolyte showed only very small photocurrents (Fig. 4). Upon addition of alcohols or water, significant photocurrents were observed and different reactivities for the various reactants could be seen in the I-V curves. Methanol caused the highest increase in anodic photocurrent, followed closely by water, while the effect due to 2-propanol was considerably less. Interestingly, the photocurrent with 1M methanol/1M water mixtures was higher than with 2M methanol or with 2M water, individually.

The photo-oxidation of methanol in propylene carbonate led to formaldehyde as the oxidation product and accounted for 100% of the current. The photocurrent dropped slightly during the experiments, unlike the results observed in pure methanol, thus yielding a nonlinear relationship between illumination time and formaldehyde which was produced (Fig. 5).

The photo-oxidation product of 2-propanol in propylene carbonate was acetone, which also accounted for 100% of the photocurrent. Unlike methanol oxidation, the current increased during the experiments (Fig. 5), leading to smaller differences in photocurrents between the two alcohols than was observed from the initial I-V curves (Fig. 4). However, if the electrode was immersed in the 2-propanol solution for several hours prior to illumination, the photocurrent was stable at the higher value.

Competition between the two alcohols was next studied by photo-oxidation of mixtures containing 2M concentrations of each. Although the analysis for formaldehyde could not be used in the presence of 2-propanol, the amount of acetone could be determined. The amount of formaldehyde was calculated from the coulombs of charge and the yield of acetone. Considerably more methanol was oxidized than 2-propanol, as shown in Fig. 6. Mixtures of methanol and 2-propanol gave less product than additivity would predict. After 4 hr illumination at +1.2V *vs.* SCE, 2M methanol gave 41 μmol of formaldehyde and 2M 2-propanol gave 33 μmol of acetone (Fig. 5). A mixture of 2M methanol/2M 2-propanol gave only 34 μmol of formaldehyde and 16 μmol of acetone under the same conditions (Fig. 6).

Finally, the competition between water and these alcohols was investigated. The presence of 2M H_2O led to a sharp increase in photocurrent (Fig. 4). Surprisingly, the amount of organic product also increased considerably as shown in Fig. 7 and 8. One hundred percent of the additional current resulted in acetone production in 2-propanol/water solution; 80% of the total current resulted in formaldehyde production in methanol/water solutions.

Discussion

In aqueous solutions, it is known that photogenerated holes in α-Fe_2O_3 react rapidly with water or hydroxide ions. Thus, any organic compound that is oxidized in an aqueous medium must compete effectively with water. As can be seen from the results with carboxylic acids, the ability to compete for photogenerated holes varies greatly. Whereas acetic acid is readily oxidized at *n*-TiO_2, this reaction apparently does not proceed at α-Fe_2O_3. Formic acid required high concentrations to show any significant amounts of product, and of the acids studied, only oxalic acid showed high reactivity. Adsorption of the reactants at the α-Fe_2O_3 surface may play a crucial role in determining the reactivity as well as relative rate constants for the competing reactions.

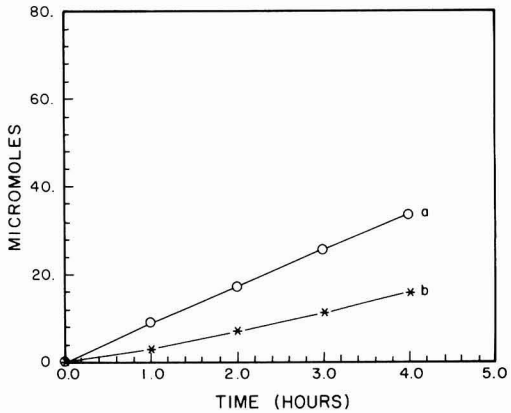

Fig. 6. Competition between 2M methanol and 2M 2-propanol in propylene carbonate. (a) Formaldehyde production, (b) acetone production.

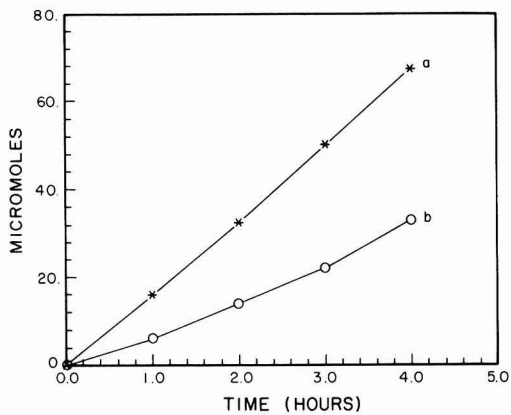

Fig. 7. Effect of water on the photo-oxidation of 2M 2-propanol in propylene carbonate. (a) Acetone production in the presence of 2M H_2O, (b) acetone production in the absence of H_2O.

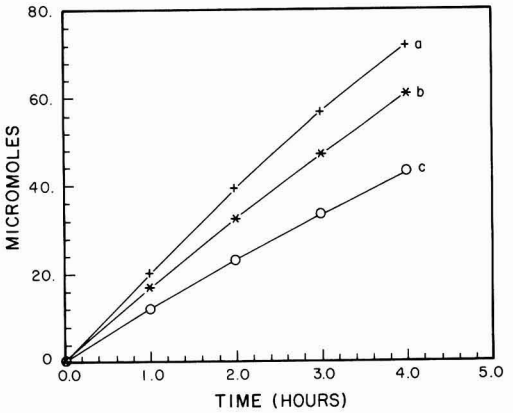

Fig. 8. Effect of water on the photo-oxidation of 2M methanol in propylene carbonate. (a) Calculated amount of formaldehyde if all photocurrent oxidized methanol in the presence of 2M H_2O, (b) amount of formaldehyde produced in the presence of 2M H_2O, (c) amount of formaldehyde produced in the absence of H_2O.

The study of transients showed that the large cathodic shift in photocurrent onset upon addition of oxalic acid was only partially due to a shift in flatband potential. The predominant reason for its high efficiency was the lack of back reaction; *i.e.*, no cathodic transients were observed.

Photo-oxidation of alcohols in aqueous solutions would also require effective competition with water for photogenerated holes. Experiments with 2-propanol in aqueous H_2SO_4 showed almost no organic reaction taking place, but methanol was able to compete reasonably effectively.

However, by working in a nonaqueous solvent, a direct comparison of reactivity could be made. Methanol in propylene carbonate yielded even more photocurrent than water, while 2-propanol was much less reactive. Thermodynamically, each of these substances should be easily oxidized by the photogenerated holes, so the rate of reaction appears to be controlled by the rate of charge transfer compared to surface recombination. It should also be noted that no evidence for current doubling was obtained, which was in contrast to results at TiO_2 electrodes (18) but in agreement with previous reports at iron oxide electrodes (16).

Change in reaction rate with time was also noted for the alcohols. The slight decay in photocurrent observed with methanol solutions may be attributed to a poisoning of the surface by the formaldehyde reaction product. The electrode performance recovered after extensive washing, lending support to this hypothesis. The opposite behavior exhibited by 2-propanol could be accounted for by a slow adsorption process (the slow rate may indicate diffusion into the surface along grain boundaries). This hypothesis is supported by the fact that immersion in 2-propanol solutions for several hours before photo-oxidation produced higher photocurrents.

Direct competition between the two alcohols in propylene carbonate was not additive and, again, may reflect the competition of reactants for active surface sites. The total product formed was not much greater than that from methanol alone, and mixtures of the two alcohols gave less of each product than solutions of the individual alcohols. Methanol was the more effective competitor, with twice as much formaldehyde formed as acetone in a propylene carbonate solution containing 2M methanol and 2M 2-propanol. This is consistent with the photocurrent results shown in Fig. 4. The nonadditivity would be expected if a Langmuir-type adsorption isotherm were involved. With the high concentrations used, it would be expected that most of the active sites would be filled and increases in concentration would result in only small increases in photocurrent as observed. An added complication is the expectation, based on the low photocurrents observed for 2-propanol, that the competition for holes will vary with the species on the surface. Thus, 2-propanol may compete well against methanol for surface sites, but this could lead to more likely surface recombination and lower photocurrents.

The addition of water to propylene carbonate solutions containing alcohol introduced another complication. Two steps in the total oxidation process are observed experimentally. First, the capture of a hole in competition with surface recombination is observed in the form of photocurrent. Second, the final product is observed by chemical analysis. It is quite possible, and indeed the results seem supportive, that one reactant may be effective in capturing a hole to form an active intermediate while another reactant is more effective in its reaction with this intermediate. Thus, the increase in photocurrent observed when water was added to the propylene carbonate solutions containing 2M methanol or 2M 2-propanol indicated the ability of water to capture photogenerated holes. On the other hand, these solutions showed greater production of formaldehyde or acetone when water was added, providing evidence that the alcohols reacted rapidly with the water intermediate, such as the hydroxyl radical. This concept also helps explain the synergistic effect seen in methanol/water mixtures in propylene carbonate in which 1M methanol/1M water gave higher photocurrents than either 2M methanol or 2M water. One reactant, water, was effective in capturing photogenerated holes, while the second reactant was effective in removing the intermediate from the electrode surface to form the final product.

Acknowledgment

This work was supported by the Division of Chemical Sciences, Office of Basic Energy Sciences, U.S. Department of Energy.

Manuscript submitted Jan. 31, 1983; revised manuscript received May 20, 1983.

Chemistry Department, University of California assisted in meeting publication costs of this article.

REFERENCES

1. J. H. Kennedy and K. W. Frese, Jr., *This Journal*, **125,** 709 (1978).
2. J. H. Kennedy and K. W. Frese, Jr., *ibid.*, **125,** 723 (1978).
3. J. H. Kennedy, R. Shinar, and J. D. Ziegler, *ibid.*, **127,** 2307 (1980).
4. J. H. Kennedy, M. Anderman, and R. Shinar, *ibid.*, **128,** 2371 (1981).
5. R. Shinar and J. H. Kennedy, *Sol. Energy Mater.*, **6,** 323 (1982).
6. R. Shinar and J. H. Kennedy, *This Journal*, **130,** 392 (1983).
7. J. H. Kennedy and M. Anderman, *ibid.*, **130,** 848 (1983).
8. K. L. Hardee and A. J. Bard, *ibid.*, **123,** 1024 (1976).
9. K. L. Hardee and A. J. Bard, *ibid.*, **124,** 215 (1977).
10. R. K. Quinn, R. D. Nasby, and R. J. Baughman, *Mater. Res. Bull.*, **11,** 1011 (1976).
11. L. S. R. Yeh and N. Hackerman, *This Journal*, **124,** 833 (1977).
12. H. H. Kung, H. S. Jarrett, A. W. Sleight, and A. Ferretti, *J. Appl. Phys.*, **48,** 2463 (1977).
13. J. S. Curran and W. Gissler, *This Journal*, **126,** 56 (1979).
14. H. Metee, J. W. Otvos, and M. Calvin, *Sol. Energy Mater.*, **4,** 443 (1981).
15. A. F. Sammells and P. G. B. Ang, *This Journal*, **126,** 1831 (1979).
16. S. Miyoshi and A. Kunugi, *Denki Kagaku*, **48,** 476 (1980).
17. R. A. Fredlein and A. J. Bard, *This Journal*, **126,** 1892 (1979).
18. M. Miyake, H. Yoneyawa, and H. Tamura, *Chem. Lett.*, 635 (1976).

The Modulated Flow at a Rotating Disk Electrode

Bernard Tribollet[1] and John Newman*

Department of Chemical Engineering, University of California, Berkeley, California 94720

ABSTRACT

The frequency response analysis for an electrochemical system (current or potential) to a sinusoidal speed modulation at a rotating disk electrode involves, at first, the analysis of the corresponding unsteady laminar flow. This hydrodynamic problem is solved by a numerical integration of the unsteady Navier-Stokes equations, and the four first terms of the instantaneous velocity expansions are given. The study of the unsteady mass transport is the second problem; its solution is a series expansion of $Sc^{-1/3}$, and the two first terms are given. Finally, the expressions of the electrical response of the electrochemical system involves also the element of the electrochemical impedance (the diffusion or convective Warburg impedance, the charge transfer resistance, the electrolyte resistance, and the double-layer capacitance). The results are experimentally confirmed, in potentiostatic and galvanostatic regulations, over a wide frequency range ($10^{-2} < p < 5$) for the reduction of $Fe(CN)_6^{3-}$ to $Fe(CN)_6^{4-}$ in 1M KCl.

The frequency response analysis of an electrochemical system to a sinusoidal speed modulation at a rotating disk electrode is a new experimental method which was originated by Tokuda *et al.* (1) and has been exploited by a few authors (2-4). In these early works, the knowledge of the instantaneous velocity profiles close to the rotating disk was obtained from the work of Sparrow and Gregg (5), which gives a good approximation of this hydrodynamic problem when the modulation frequency is low. The condition of low frequency corresponded to the electrochemical

* Electrochemical Society Active Member.
[1] Present address: Groupe de Recherche No. 4 du CNRS, Physique des Liquides et Electrochimie, Associe´ a l'Universite´ Pierre et Marie Curie, 75230 Paris Cedex 05, France.
Key words: hydrodynamic modulation, mass transport, impedance.

measurements of Tokuda *et al.* (1) and Kanzaki and Bruckenstein (6). However, in a recent work of Deslouis *et al.* (4), higher modulation frequencies could be achieved and the limitation of the theoretical analysis appeared.

An important application of this method is the determination of the diffusion coefficient by means of the Schmidt number. In the unsteady state mass transport problems, the Schmidt number occurs as its cube root and, therefore, good accuracy is needed in order to analyze the experimental data.

In this paper, an analysis is made of the unsteady laminar flow about a rotating disk whose angular velocity is perturbed by a sinusoidal modulation of low amplitude. This problem is solved numerically for a large frequency range, and the results are compared to previous works (5, 7).

For a sinusoidal speed modulation, a numerical solution of the response of the electrical quantity (current or potential) specific to the interface is given for a large frequency range. Excellent agreement between theory and experiment is found for a redox reaction below the limiting current in galvanostatic regulation. In potentiostatic regulation, at the limiting current, we show the influence of the kinetics in the high frequency range.

Theoretical Analysis

Hydrodynamic problem.—The steady flow field created by an infinite disk rotating at a constant angular velocity in a fluid with constant physical properties was first studied by von Karman (8).

For a low amplitude modulation, the equation of continuity and the equation of motion can be numerically solved from the steady-state solution. As a necessary prelude to this solution, we briefly review some of the steady-state solution as given by von Karman (8).

Von Karman's suggestion of a separation-of-variables approach to the solution of the time independent Navier-Stokes equation results in a set of three-coupled nonlinear ordinary differential equations for the components of the fluid velocity vector and an equation for the dynamic pressure in the fluid above the disk as follows

$$2F + H' = 0 \quad [1]$$

$$F^2 - G^2 + HF' - F'' = 0 \quad [2]$$

$$2FG + HG' - G'' = 0 \quad [3]$$

$$P' + HH' - H'' = 0 \quad [4]$$

where the prime designates differentiation with respect to $\zeta = z\sqrt{\bar{\Omega}/\nu}$. The variables are defined as

$$\bar{v}_r = r\bar{\Omega}\,F(\zeta) \quad [5]$$

$$\bar{v}_\theta = r\bar{\Omega}\,G(\zeta) \quad [6]$$

$$\bar{v}_z = \sqrt{\nu\bar{\Omega}}\,H(\zeta) \quad [7]$$

$$\bar{P} = \mu\bar{\Omega}\,P(\zeta) \quad [8]$$

where the overbar designates the steady state. The boundary conditions are

$$F(0) = H(0) = 0 \quad [9]$$

$$G(0) = 1 \quad [10]$$

$$F(\infty) = G(\infty) = 0 \quad [11]$$

For the unsteady situation, the instantaneous value Ω of the angular velocity is defined by

$$\Omega = \bar{\Omega} + \Delta\Omega\,\mathrm{Re}\{e^{j\omega t}\} \quad [12]$$

For a low amplitude modulation ($\Delta\Omega << \bar{\Omega}$), to determine the deviations of the flow from the steady state, we write

$$v_r = r\bar{\Omega}\left[F(\zeta) + \frac{\Delta\Omega}{\bar{\Omega}}\mathrm{Re}\{\tilde{f}(\zeta)e^{j\omega t}\}\right] \quad [13]$$

$$v_\theta = r\bar{\Omega}\left[G(\zeta) + \frac{\Delta\Omega}{\bar{\Omega}}\mathrm{Re}\{\tilde{g}(\zeta)e^{j\omega t}\}\right] \quad [14]$$

$$v_z = \sqrt{\nu\bar{\Omega}}\left[H(\zeta) + \frac{\Delta\Omega}{\bar{\Omega}}\mathrm{Re}\{\tilde{h}(\zeta)e^{j\omega t}\}\right] \quad [15]$$

$$P = \mu\bar{\Omega}\left[P(\zeta) + \frac{\Delta\Omega}{\bar{\Omega}}\mathrm{Re}\{\tilde{p}(\zeta)e^{j\omega t}\}\right] \quad [16]$$

where $\tilde{f}$, $\tilde{g}$, $\tilde{h}$, and $\tilde{p}$ are complex functions.

Each component is expressed as the sum of a known function and the real part of a complex function whose amplitude is presumed to be small. The equation of continuity and the unsteady Navier-Stokes equations are linearized, and the quadratic terms proportional to $(\Delta\Omega/\bar{\Omega})^2$ are neglected. The resulting equations may be written

$$2\tilde{f} + \tilde{h}' = 0 \quad [17]$$

$$j\tilde{f}\mathrm{p} + 2F\tilde{f} - 2G\tilde{g} + H\tilde{f}' + F'\tilde{h} = \tilde{f}'' \quad [18]$$

$$j\tilde{g}\mathrm{p} + 2G\tilde{f} + 2F\tilde{g} + \tilde{h}G' + H\tilde{g}' = \tilde{g}'' \quad [19]$$

$$j\tilde{h}\mathrm{p} + H'\tilde{h} + H\tilde{h}' + \tilde{p}' = \tilde{h}'' \quad [20]$$

where $\mathrm{p} = \omega/\bar{\Omega}$ is the dimensionless frequency of modulation. The boundary conditions are

$$\tilde{f}(0) = \tilde{h}(0) = 0 \quad [21]$$

$$\tilde{g}(0) = 1 \quad [22]$$

$$\tilde{f}(\infty) = \tilde{g}(\infty) = 0 \quad [23]$$

After the velocity profiles are determined, the pressure distribution can be calculated directly from the integrated form of Eq. [20]. Each complex function may be written as the sum of a real function (index 1) and an imaginary function (index 2). The set of three coupled Eq. [17], [18], [19] becomes a set of six coupled linear ordinary differential equations

$$2f_1 + h_1' = 0 \quad [24]$$

$$2f_2 + h_2' = 0 \quad [25]$$

$$-f_2\mathrm{p} + 2Ff_1 - 2Gg_1 + Hf_1' + F'h_1 - f_1'' = 0 \quad [26]$$

$$f_1\mathrm{p} + 2Ff_2 - 2Gg_2 + Hf_2' + F'h_2 - f_2'' = 0 \quad [27]$$

$$-g_2\mathrm{p} + 2Gf_1 + 2Fg_1 + G'h_1 + Hg_1' - g_1'' = 0 \quad [28]$$

$$g_1\mathrm{p} + 2Gf_2 + 2Fg_2 + G'h_2 + Hg_2' - g_2'' = 0 \quad [29]$$

By using Newman's method of solving this kind of problem (9, 10), we derive, for each dimensionless frequency, the solution of the set of six equations.

Cochran (11) has shown that the system of Eq. [1]-[4] can be satisfied by two sets of series expansions for small and large values of ζ. The series solutions for small values of ζ are very useful for the mass transfer problem close to a rotating disk electrode. Therefore, the derivatives at $\zeta = 0$ (given in Table I) are essential in order to determine the first coefficient of the series expansions. The other coefficients are calculated from the first by using the set of Eq. [24]-[29.] In Table II, we recall the steady-state solution, and we give the values of the four first terms of the series for each function.

As the frequency of modulation tends towards zero, we deduce from Eq. [13] that $rf_1(\zeta)$ tends towards the derivative of $\bar{v}_r$ with respect to $\bar{\Omega}$ and from Eq. [27]

Table I. $\tilde{f}'((0,p)$ and $\tilde{g}'(0,p)$ vs. the dimensionless frequency. In polar coordinates, the amplitude is divided by the amplitude for p = 0.

	$\tilde{f}'(0,p)$				$\tilde{g}'(0,p)$			
	In Cartesian coordinates		In polar coordinates		In Cartesian coordinates		In polar coordinates	
p	$f_1'(0,p)$	$f_2'(0,p)$	$A\{\tilde{f}'(p)\}/A\{f'(0)\}$	$-\theta_f$	$g_1'(0,p)$	$g_2'(0,p)$	$A\{\tilde{g}'(p)\}/A\{g'(0)\}$	$\theta_g - 180°$
0.5	0.7513	−0.1077	0.9917	8.2	−0.9235	−0.1857	1.0196	11.4
1	0.6943	−0.2032	0.9452	16.3	−0.9367	−0.3900	1.0982	22.6
1.5	0.6154	−0.2585	0.8721	22.8	−0.9874	−0.5951	1.2478	31.1
2	0.5429	−0.2802	0.7983	27.3	−1.0656	−0.7780	1.4281	36.1
2.5	0.4845	−0.2842	0.7339	30.4	−1.1551	−0.9354	1.6088	39.0
3	0.4389	−0.2802	0.6804	32.6	−1.2465	−1.0719	1.7794	40.7
3.5	0.4029	−0.2731	0.6360	34.1	−1.3360	−1.1925	1.9383	41.8
4	0.3739	−0.2648	0.5987	35.3	−1.4223	−1.3010	2.0864	42.4
4.5	0.3502	−0.2565	0.5672	36.2	−1.5050	−1.4003	2.2251	42.9
5	0.3303	−0.2484	0.5400	36.9	−1.5842	−1.4922	2.3556	43.3
6	0.2988	−0.2337	0.4956	38.0	−1.7330	−1.6591	2.5968	43.8
7	0.2749	−0.2210	0.4609	38.8	−1.8709	−1.8091	2.8169	44.0
8	0.2559	−0.2100	0.4325	39.4	−1.9996	−1.9465	3.0205	44.2
10	0.2275	−0.1921	0.3890	40.2	−2.2355	−2.1940	3.3903	44.5

Table II. Coefficients of the series expansions for the dimensionless components of the fluid velocity. (The values of $f_1'(0,p)$, $f_2'(0,p)$, $g_1'(0,p)$), and $g_2'(0,p)$ are given in Table I.

	F	G	H	f_1	f_2	g_1	g_2	h_1	h_2
ζ^0	0.0	1.0	0.0	0.0	0.0	1.0	0.0	0.0	0.0
ζ^1	0.51023	−0.61592	0.0	$f_1'(0,p)$	$f_2'(0,p)$	$g_1'(0,p)$	$g_2'(0,p)$	0.0	0.0
ζ^2	−0.5	0.0	−0.51023	−1	0.0	0.0	$-p/2$	$-f_1'(0,p)$	$-f_2'(0,p)$
ζ^3	0.205307	0.170077	1/3	$\dfrac{1.23184 - 2g_1' - f_2' \cdot p}{6}$	$\dfrac{-2g_2' + f_1' \cdot p}{6}$	$\dfrac{1.02046 + 2f_1' - g_2' \cdot p}{6}$	$\dfrac{2 \cdot f_2' + g_1' \cdot p}{6}$	2/3	0.0

and [29] that $f_2'(\zeta)$ tends towards zero. Therefore, $\tilde{f}'(0,0) = 3/2\ F'(0) = 0.765345$, and in the same way $\tilde{g}'(0,0) = 3/2\ G'(0) = -0.923883$. These values are used for the calculation of the reduced amplitude of $\tilde{f}'$ and $\tilde{g}'$ in Table I.

The amplitude of $\tilde{g}'(0,p)$ increases with p, and $\tilde{f}'(0,p)$ decreases with p. For mass transfer measurements, that means that the results for an axisymmetric electrode (like a disk or a ring) and a nonaxisymmetric electrode (like a microelectrode off the axis of rotation) may be very different.

Comparison with the results of Sparrow and Gregg (5) and Sharma (7).—Low frequency range.—Sparrow and Gregg (5) solved the unsteady flow problem where the angular rotation speed is a time dependent quantity. Their expressions for the instantaneous components of the fluid velocity were obtained by a series expansion about the value found at a quasi-steady state

$$v_r = r\Omega(F(x) + \beta_1 F_1(x) + \beta_2 F_2(x) + \ldots) \quad [30]$$

$$v_\theta = r\Omega(G(x) + \beta_1 G_1(x) + \beta_2 G_2(x) + \ldots) \quad [31]$$

$$v_z = \sqrt{\Omega\nu}(H(x) + \beta_1 H_1(x) + \beta_2 H_2(x) + \ldots) \quad [32]$$

where $x = z(\Omega/\nu)^{1/2}$ is time dependent, and the expansion parameters depend only on time and are defined by

$$\beta_1 = (d\Omega/dt)/\Omega^2$$

$$\beta_2 = (d^2\Omega/dt^2)/\Omega^3$$

After a numerical integration of the Navier-Stokes equation, Sparrow and Gregg gave the value of the velocity derivatives at $x = 0$

$$H_0''(0) = -1.0205 \qquad G_0'(0) = -0.61592$$

$$H_1''(0) = 0.40967 \qquad G_1'(0) = -0.36922$$

$$H_2''(0) = -0.046224 \qquad G_2'(0) = 0.021185$$

By using these results for a sinusoidal modulation, we can determine the expressions of $\tilde{f}'(0,p)$ and $\tilde{g}'(0,p)$ following our notation

$$\tilde{f}'(0,p) = (0.765345 - 0.023112p^2) - 0.204835pj \quad [33]$$

$$\tilde{g}'(0,p) = (-0.923883 - 0.021185p^2) - 0.36922pj \quad [34]$$

Sharma (7) solved the set of six equations ([24]-[29]) with an important approximation; he expects f_2, g_2, and h_2 to be small relative to f_1, g_1, and h_1, and he neglects $-pf_2$ and $-pg_2$ in Eq. [26] and [28]. Then he finds with our notation

$$\tilde{f}'(0,p) = 0.765345 - 0.20178pj \quad [35]$$

$$\tilde{g}'(0,p) = -0.923883 - 0.52285pj \quad [36]$$

These are exact only for p = 0, and the accuracy of the asymptotic expressions [33] and [34] from Sparrow and Gregg (5) is always better.

High frequency range.—For the high frequencies, Sharma (7) obtained an asymptotic solution; with our notation the expressions of $\tilde{f}'(0,p)$ and $\tilde{g}'(0,p)$ are

$$\tilde{f}'(0,p) = \frac{1}{\sqrt{2p}} - j\left(\frac{1}{\sqrt{2p}} - \frac{0.313}{p}\right) \quad [37]$$

$$\tilde{g}'(0,p) = -\sqrt{\frac{p}{2}} - j\left(\sqrt{\frac{p}{2}} - \frac{3}{2}\frac{0.510}{p}\right) \quad [38]$$

On Fig. 1 and 2, the asymptotic solution of Sparrow and Gregg (5) (Eq. [33], [34]) is compared with our calculation for the low frequency range, and the asymptotic solution of Sharma (7) (Eq. [37], [38]) is compared for the high frequency range. Expression [34] is an approximate solution for $\tilde{g}'$ up to p = 2, and expression [38] is an approximate solution for p higher than 7. Expression [33] gives a good value of

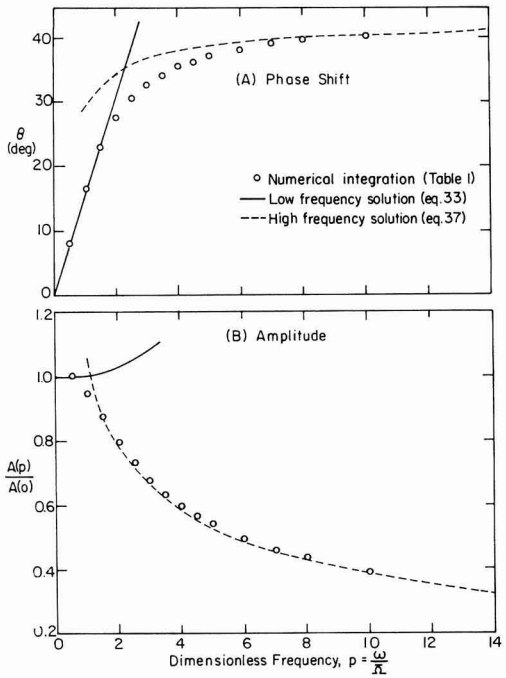

Fig. 1. First coefficient of the series expansion for the unsteady dimensionless component of the radial velocity. Comparison with the results of Sparrow and Gregg (5) and Sharma (7): (A) phase shift of $\tilde{f}'$ (0,p) *vs.* dimensionless frequency, (B) amplitude of $\tilde{f}'$ (0,p) *vs.* dimensionless frequency.

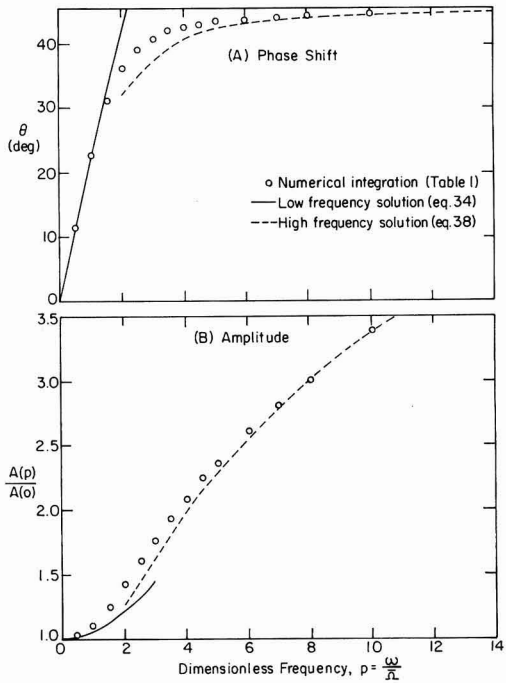

Fig. 2. Second coefficient of the series expansion for the unsteady dimensionless component of the angular velocity. Comparison with the results of Sparrow and Gregg (5) and Sharma (7): (A) phase shift of $\tilde{g}'$ (0,p) *vs.* dimensionless frequency, (B) amplitude of $\tilde{g}'$ (0,p) *vs.* dimensionless frequency.

$\tilde{f}'$ only for $p < 1$, and for $p = 1$ the deviation between the expression [33] and our numerical calculation is, for the amplitude, already 6%. The expression [33] may be used with a good accuracy only for $p \leq 0.5$ and the expression [37] for $p \geq 8$.

Mass transport application.—The concentration in the diffusion layer is governed by the unsteady equation of convective diffusion

$$\frac{\partial c}{\partial t} + v_z \frac{\partial c}{\partial z} = D \frac{\partial^2 c}{\partial z^2} \qquad [39]$$

The development of v_z is obtained from Table II and is limited to the two first terms. In order to obtain an analytic solution, Ref. (3) and (4) limited the development to the first term. On the contrary, Tokuda *et al.* (1), for a numerical integration, used the three first terms of the v_z development. By pitting

$$c = \bar{c} + \mathrm{Re}\{\tilde{c}\, e^{j\omega t}\} \qquad [40]$$

and by using the dimensionless variables and parameters

$$a = 0.51023, \quad K = \frac{\omega}{\bar{\Omega}} \left(\frac{9\nu}{a^2 D}\right)^{1/3}, \quad B = \left(\frac{3}{a^4}\right)^{1/3} \qquad [41]$$

and

$$\xi = \frac{z}{\delta} \text{ with } \delta = \left(\frac{3D}{a\nu}\right)^{1/3} \sqrt{\frac{\nu}{\bar{\Omega}}}$$

(δ is a distance characteristic of the thickness of the steady-state diffusion layer; the equivalent Nernst diffusion layer thickness is $\Gamma(4/3)$ times δ) Eq. [39] becomes

$$\frac{d^2\tilde{c}}{d\xi^2} + \left(3\xi^2 - \frac{B\xi^3}{\mathrm{Sc}^{1/3}} + \dots\right)\frac{d\tilde{c}}{d\xi} - jK\tilde{c}$$

$$= -\frac{\Delta\Omega}{\bar{\Omega}}\left(3\frac{\tilde{f}'(0,p)}{a}\xi^2 - \frac{2B\xi^3}{\mathrm{Sc}^{1/3}} + \dots\right)\frac{d\bar{c}}{d\xi} \qquad [42]$$

where

$$\frac{d\bar{c}}{d\xi} = \left.\frac{d\bar{c}}{d\xi}\right|_0 \exp\left(-\xi^3 + \frac{B\xi^4}{4\mathrm{Sc}^{1/3}} + \dots\right) \qquad [43]$$

and where the steady-state derivative at the surface can be expressed as

$$\left.\frac{d\bar{c}}{d\xi}\right|_0 = \frac{c_\infty - \bar{c}_0}{\int_0^\infty \exp\left(-\xi^3 + \frac{B\xi^4}{4\mathrm{Sc}^{1/3}} + \dots\right) d\xi} \qquad [44]$$

Let $\theta(\xi)$ be a solution of the homogeneous equation satisfying the boundary conditions

$$\theta \to 0 \quad \text{as} \quad \xi \to \infty$$

and

$$\theta = 1 \quad \text{at} \quad \xi = 0$$

In terms of the function θ, the solution of Eq. [42] can be obtained by the technique of reduction in order (12) by setting $\tilde{c} = \lambda(\xi)\theta(\xi)$, where λ satisfies

$$\frac{d^2\lambda}{d\xi^2} + \left(3\xi^2 - \frac{B\xi^3}{\mathrm{Sc}^{1/3}} + \dots + \frac{2\theta'}{\theta}\right)\frac{d\lambda}{d\xi}$$

$$= -\frac{\Delta\Omega}{\bar{\Omega}}\left(3\frac{\tilde{f}'(0,p)}{a}\xi^2 - \frac{2B\xi^3}{\mathrm{Sc}^{1/3}} + \dots\right)\frac{1}{\theta}\frac{d\bar{c}}{d\xi} \qquad [45]$$

Integration gives

$$\tilde{c} = K_2\theta + K_1\theta \int_0^{\xi} \frac{\exp\left(-x^3 + \frac{Bx^4}{4Sc^{1/3}} + \dots\right)}{\theta^2(x)}\,dx - \frac{\Delta\Omega}{\bar{\Omega}}\frac{d\bar{c}}{d\xi}\Bigg|_0 \theta \int_0^{\xi} \frac{\exp\left(-x^3 + \frac{Bx^4}{4Sc^{1/3}} + \dots\right)}{\theta^2(x)} \times \int_0^{x} \left(3\frac{\tilde{f}'(0,p)}{a}x_1^2 - \frac{2Bx_1^3}{Sc^{1/3}} + \dots\right)\theta(x_1)\,dx_1 dx \quad [46]$$

where K_1 and K_2 are two integration constants. K_2 can be identified with $\tilde{c}_0$, the value of the amplitude function at $\xi = 0$. K_1 can be obtained from the boundary condition that $\tilde{c}$ approaches zero as ξ approaches infinity, with the result

$$K_1 = \frac{\Delta\Omega}{\bar{\Omega}}\frac{d\bar{c}}{d\xi}\Bigg|_0 W \quad [47]$$

where

$$W = \int_0^{\infty} \left(3\frac{\tilde{f}'(0,p)}{a}\xi^2 - \frac{2B\xi^3}{Sc^{1/3}} + \dots\right)\theta\,d\xi \quad [48]$$

is a dimensionless quantity whose value is worth tabulating.

The general result of this section is a relationship between the concentration and the concentration derivative, both evaluated at the electrode surface. In terms of the dimensional distance z, this can be expressed as

$$\frac{d\tilde{c}}{dz}\Bigg|_{z=0} = \frac{\tilde{c}_0}{\delta}\theta'(0) + \frac{\Delta\Omega}{\bar{\Omega}}\frac{d\bar{c}}{dz}\Bigg|_{z=0} W \quad [49]$$

where $\theta'(0)$ is, for $\xi = 0$, the derivative of $\theta(\xi)$ relative to ξ.

The boundary condition at $z = 0$ determining the value of $\tilde{c}_0$ involves both the mode of regulation and the electrochemical kinetics at the interface. In order to solve the problem, it is not necessary to study, as in Ref. (3, 4), the particular cases of a constant concentration at the interface [improperly called "potentiostatic" in Ref. (3)], or of a constant concentration gradient at the interface [improperly called "galvanostatic" in Ref. (3)]. This general expression [49] is sufficient for studying the electrochemical application in order to obtain an equivalent expression between the observable electrical quantities: the overall potential and the overall current (see Eq. [64]). Determination and tabulation of the quantities $\theta'(0)$ and W thus provide the basis for a rather general treatment subsequently of the interfacial conditions, even though they might have kinetic and double-layer complications not explicitly contemplated here. This point deserves special emphasis.

The numerical calculation of W requires the calculation of the homogeneous solution θ, which is also the solution to the usual convective Warburg impedance problem, where potential or current is modulated instead of rotation speed.

This problem had been studied by a few authors (13-16); in particular Levart and Schuhmann (13) showed how to write θ as a series expansion in $Sc^{-1/3}$

$$\theta(\xi,Sc,K) = \theta_0(\xi,K) + \frac{\theta_1(\xi,K)}{Sc^{1/3}} + \frac{\theta_2(\xi,K)}{Sc^{2/3}} + \dots \quad [50]$$

We solved numerically the corresponding differential equations for θ_0 and θ_1. Since the reciprocal of $\theta'(0)$ is directly related to the convective Warburg impedance, we have tabulated this quantity in terms of the expansion

$$\frac{-1}{\theta'(0)} = Z_0 + \frac{Z_1}{Sc^{1/3}} + \dots \quad [51]$$

When K tends towards zero, $-1/\theta'(0)$ tends towards $\Gamma(4/3)(1 + 0.2980\ Sc^{-1/3})$ which are the two first terms of the expansion of the mass transfer rate for large Schmidt number given by Newman (17) (see Table III).

The expansion for W is more complicated because θ as expanded depends on $pSc^{1/3}$ while $\tilde{f}(0,p)$ in Eq. [48] depends on p without $Sc^{1/3}$. The expansion for W takes the form

$$W = \tilde{f}'(0,p)(t_1 + jt_2) + \frac{1}{Sc^{1/3}}[\tilde{f}'(0,p)(t_3 + jt_4) + t_5 + jt_6 + \dots] \quad [52]$$

where the t's, given in Table IV as functions of $pSc^{1/3}$, are calculated from the following definitions

$$t_1 = \frac{3}{a}\int_0^{\infty} \xi^2 \mathrm{Re}\{\theta_0\}d\xi \qquad t_2 = \frac{3}{a}\int_0^{\infty} \xi^2 \mathrm{Im}\{\theta_0\}d\xi$$

$$t_3 = \frac{3}{a}\int_0^{\infty} \xi^2 \mathrm{Re}\{\theta_1\}d\xi \qquad t_4 = \frac{3}{a}\int_0^{\infty} \xi^2 \mathrm{Im}\{\theta_1\}d\xi$$

$$t_5 = -2B\int_0^{\infty} \xi^3 \mathrm{Re}\{\theta_0\}d\xi \qquad t_6 = -2B\int_0^{\infty} \xi^3 \mathrm{Im}\{\theta_0\}d\xi \quad [53]$$

Table III. Variation of the diffusion or convective Warburg impedance vs. the reduced frequency $pSc^{1/3}$ [$K = 3.258\ pSc^{1/3}$]

$pSc^{1/3}$	$\mathrm{Re}\left\{\frac{Z_0}{\Gamma(4/3)}\right\}$	$\mathrm{Im}\left\{\frac{Z_0}{\Gamma(4/3)}\right\}$	$\mathrm{Re}\left\{\frac{Z_1}{\Gamma(4/3)}\right\}$	$\mathrm{Im}\left\{\frac{Z_1}{\Gamma(4/3)}\right\}$
0	1	0	+0.2980	0
0.1	+0.9883	−0.0956	+0.2789	−0.0898
0.2	+0.9552	−0.1830	+0.2277	−0.1608
0.3	+0.9062	−0.2560	+0.1594	−0.2026
0.5	+0.7866	−0.3519	+0.0301	−0.2045
0.7	+0.6708	−0.3915	−0.0453	−0.1510
1	+0.5367	−0.3935	−0.0740	−0.0700
1.5	+0.4047	−0.3519	−0.0495	−0.0068
2	+0.3343	−0.3101	−0.0247	+0.0074
3	+0.2627	−0.2536	−0.0060	+0.0060
4	+0.1996	−0.1960	−0.0010	+0.0011
5	+0.1816	−0.1789	−0.0007	+0.0007
7	+0.1677	−0.1656	−0.0005	+0.0004
10	+0.1398	−0.1396	−0.0002	+0.0002
15	+0.1140	−0.1129	−0.0001	+0.0001
20	+0.0988	−0.0977	0.0000	0.0000
30	+0.0807	−0.0796	0.0000	0.0000
40	+0.0701	−0.0688	0.0000	0.0000
50	+0.0628	−0.0614	0.0000	0.0000
70	+0.0533	−0.0517	0.0000	0.0000
100	+0.0449	−0.0431	0.0000	0.0000

Table IV. Coefficients of the W expansion vs. the reduced frequency

$pSc^{1/3}$	t_1	t_2	t_3	t_4	t_5	t_6
0	+0.6533	0	+0.7797	0	−0.5963	0
0.1	+0.6511	−0.0396	+0.7726	−0.0829	−0.5934	+0.0407
0.2	+0.6452	−0.0786	+0.7549	−0.1637	−0.5870	+0.0808
0.3	+0.6356	−0.1166	+0.7263	−0.2402	−0.5767	+0.1197
0.5	+0.6060	−0.1874	+0.6408	−0.3738	−0.5452	+0.1918
0.7	+0.5652	−0.2489	+0.5289	−0.4738	−0.5015	+0.2539
1	+0.4904	−0.3201	+0.3405	−0.5537	−0.4215	+0.3241
1.5	+0.3547	−0.3825	+0.0628	−0.5345	−0.2787	+0.3799
2	+0.2338	−0.3910	−0.1107	−0.4179	−0.1540	+0.3782
3	+0.0725	−0.3328	−0.2063	−0.1762	+0.0029	+0.2992
4	−0.0044	−0.2562	−0.1671	−0.0406	+0.0668	+0.2085
5	−0.0364	−0.1931	−0.1105	+0.0154	+0.0838	+0.1391
6	−0.0472	−0.1466	−0.0667	+0.0320	+0.0812	+0.0918
7	−0.0486	−0.1135	−0.0382	+0.0325	+0.0719	+0.0609
10	−0.0386	−0.0600	−0.0055	+0.0169	+0.0435	+0.0195
15	−0.0234	−0.0290	+0.0008	+0.0044	+0.0199	+0.0043
20	−0.0156	−0.0177	+0.0006	+0.0014	+0.0109	+0.0014
30	−0.0086	−0.0092	+0.0002	+0.0003	+0.0047	+0.0003
40	−0.0056	−0.0058	+0.0001	+0.0001	+0.0026	+0.0001
50	−0.0040	−0.0041	0.0000	0.0000	+0.0016	+0.0001
70	−0.0024	−0.0025	0.0000	0.0000	+0.0008	0.0000
100	−0.0014	−0.0014	0.0000	0.0000	+0.0004	0.0000

$\tilde{f}'(0,p)$ is given in Table I for $p \geq 0.5$ and by Eq. [33] for $p < 0.5$.

Table V and Fig. 3 give values of W for three values of Sc (125, 1000, 8000). The value of the first term, without the term in $Sc^{-1/3}$, is also given to illustrate the importance of the Schmidt-number correction. The importance of the correction depends on the frequency as well as the Schmidt number itself. The values on Fig. 3 could be made to fall more nearly on top of each other if plotted against $pSc^{1/3}$ rather than p itself, although this would also make the graph harder to read.

Values of $-W/\theta'(0)$ are given in Table VI and Fig. 4.

Values of $Z_0\tilde{f}'(0,p)\,(t_1 + jt_2)$ are also given to illustrate the importance of the Schmidt-number correction.

Electrochemical application.—The principal result of the preceding section is Eq. [49] relating the oscillating part of the concentration gradient to the oscillating part of the concentration at the surface ($\tilde{c}_0$) and the modulation of the rotation speed ($\Delta\Omega$). Both $\theta'(0)$ and W depend upon the Schmidt number, and a subscript i should be added to all the relevant quantities to denote that different species i can have different values for the diffusion coefficient D_i. We discuss here the application of this equation to the electrochemical impedance, with simplifications directed toward the system and conditions used for the experimental verification of the effect of the term with W, arising from the modulation of the rotation speed.

A single electrode reaction can be written in symbolic form as

$$\sum_i s_i M_i^{z_i} \rightarrow ne^- \qquad [54]$$

For minor species, in the presence of supporting electrolyte and with neglect of double-layer adsorption of these minor species, the concentration gradient is related to the faradaic current density by

$$D_i \frac{\partial c_i}{\partial z}\bigg|_{z=0} = \frac{s_i}{n\mathbf{F}} i_f \qquad [55]$$

and the faradaic current density is governed by a kinetic expression

$$i_f = f(\eta, c_{i0}) \qquad [56]$$

For a simple redox reaction, we have in mind an expression of the form

$$i = i_0 \left[\frac{c_{P0}}{c_{P\infty}} \exp\left(\frac{\alpha_a \mathbf{F}}{RT}\eta\right) - \frac{c_{R0}}{c_{R\infty}} \exp\left(-\frac{\alpha_c \mathbf{F}}{RT}\eta\right)\right] \qquad [57]$$

where η is the total overpotential (sum of concentration overpotential and surface overpotential) and i_0 is the exchange current density at the bulk composition ($c_{P\infty}$ and $c_{R\infty}$). This expression contains the essential features of the concentration overpotential, which may be the only relevant part for an inherently fast reaction. The double-layer capacity is taken to be in parallel across the interface and the diffusion layer in such a manner that the total current density is given by

$$i = i_f + C\frac{d\eta}{dt} \qquad [58]$$

and the electrode potential V measured with respect to a reference electrode placed in the bulk of the solution includes the ohmic potential drop according to

$$V = R_e i + \eta \qquad [59]$$

where R_e is the solution resistance. [Actually, the effect of the nonuniform ohmic potential drop to a disk electrode should be taken into account. but the calculations are then quite complicated (18, 19, 20).]

For impedance calculations, all these expressions can be linearized and the transient parts treated as small departures from the steady-state parts. If a sinusoidal perturbation of very small amplitude is applied to the system, all variables involved will oscillate with the same frequency prescribed by the external perturbation, and each variable can be written as

$$x = \bar{x} + \mathrm{Re}\{\tilde{x}e^{j\omega t}\} \qquad [60]$$

Table V. Variation of W vs. the reduced frequency from Eq. [52]

$pSc^{1/3}$	Sc = 125				Sc = 1000				Sc = 8000			
0	W 0.50179		$\tilde{f}'(0,p)\,(t_1+jt_2)$ 0.50000		W 0.50090		$\tilde{f}'(0,p)\,(t_1+jt_2)$ 0.50000		W 0.50045		$\tilde{f}'(0,p)\,(t_1+jt_2)$ 0.50000	
	A/A(0)	θ	A/A(0)	θ	A/A(0)	θ	A/A(0)	θ	A/A(0)	θ	A/A(0)	θ
0.1	0.9980	4.4	0.9985	3.8	0.9982	3.9	0.9985	3.6	0.9983	3.7	0.9985	3.6
0.2	0.9933	8.8	0.9949	7.6	0.9940	7.8	0.9949	7.3	0.9945	7.4	0.9949	7.1
0.3	0.9857	13.1	0.9892	11.3	0.9873	11.7	0.9891	10.9	0.9885	11.0	0.9891	10.6
0.5	0.9621	21.6	0.9710	18.7	0.9661	19.3	0.9710	18.0	0.9683	18.2	0.9709	17.6
0.7	0.9292	29.9	0.9454	25.9	0.9365	26.7	0.9453	24.8	0.9409	25.2	0.9453	24.3
1	0.8672	41.5	0.8966	36.2	0.8808	37.1	0.8964	34.7	0.8883	35.1	0.8964	33.9
1.5	0.7487	58.8	0.7989	51.8	0.7714	52.6	0.7986	49.4	0.7849	49.8	0.7985	48.3
2	0.6328	73.3	0.6980	65.3	0.6624	65.6	0.6975	62.2	0.6800	62.3	0.6974	60.7
3	0.4465	95.5	0.5224	86.9	0.4810	85.7	0.5216	82.3	0.5018	81.5	0.5214	80.0
4	0.3220	111.35	0.3937	103.3	0.3542	100.0	0.3926	98.0	0.3741	95.2	0.3923	94.1
5	0.2220	124.3	0.2843	117	0.2671	111.4	0.3012	108.4	0.2854	105.3	0.3009	104.5
7	0.1257	139.1	0.1674	134.6	0.1654	124.9	0.1895	123.9	0.1790	118.7	0.1891	118.6
10	0.0651	151.3	0.0872	150.1	0.0922	138.6	0.1032	139.1	0.1030	130.7	0.1094	130.4
15	0.0298	160.7	0.0388	161.5	0.0461	148.8	0.0497	151.7	0.0530	140.4	0.0572	140.4
20	0.0169	165.3	0.0216	166.7	0.0265	157.5	0.0288	158.7	0.0330	146.8	0.0341	147.7
30	0.0076	170.1	0.0095	171.3	0.0121	164.8	0.0131	165.6	0.0163	155.3	0.0168	155.8
40	0.0043	172.2	0.0053	173.5	0.0069	168.2	0.0074	169.3	0.0096	160.5	0.0099	161.3
50	0.0033	174.5	0.0034	174.6	0.0045	170.5	0.0047	171.2	0.0063	164.0	0.0065	164.1
70					0.0024	172.9	0.0025	173.2	0.0033	168.1	0.0034	167.6
100					0.0014	174.7	0.0015	175.0	0.0016	172.0	0.0016	172.1

Table VI. Variation of $-W/\theta'(0)$ vs. the reduced frequency; W is obtained from Eq. [52] and $-1/\theta'(0)$ is obtained from Eq. [51]

	Sc = 125				Sc = 1000				Sc = 8000			
	$-\frac{W}{\theta'(0)}$		$\tilde{Z}_0 f'(0,p)(t_1+jt_2)$		$-\frac{W}{\theta'(0)}$		$\tilde{Z}_0 f'(0,p)(t_1+jt_2)$		$-\frac{W}{\theta'(0)}$		$\tilde{Z}_0 f'(0,p)(t_1+jt_2)$	
$pSc^{1/3}$	A/A(0)	θ	A/A(0)	θ	A/A(0)	θ	A/A(0)	θ	A/A(0)	θ	A/A(0)	θ
0.1	0.9896	10.5	0.9844	9.3	0.9904	9.7	0.9844	9.1	0.9908	9.4	0.9844	9.1
0.2	0.9690	20.8	0.9676	18.4	0.9682	19.2	0.9676	18.1	0.9684	18.7	0.9676	17.9
0.3	0.9163	30.6	0.9315	27.1	0.9234	28.4	0.9314	26.7	0.9275	27.2	0.9891	26.4
0.5	0.8043	48.0	0.8367	42.8	0.8195	44.6	0.8367	42.1	0.8277	42.9	0.8367	41.7
0.7	0.6887	62.5	0.7343	56.2	0.7161	58.1	0.7342	55.1	0.7219	56.0	0.7342	54.6
1	0.5419	79.6	0.5967	72.4	0.5677	74.3	0.5966	70.9	0.5817	71.8	0.5966	70.1
1.5	0.3740	100.7	0.4285	97.2	0.3990	94.0	0.4283	90.4	0.4111	91.3	0.4283	89.3
2	0.2693	116.5	0.3183	108.1	0.2916	108.6	0.3181	105.0	0.3046	105.2	0.3180	103.5
3	0.1530	139.5	0.1907	130.9	0.1701	129.7	0.1904	126.3	0.1803	125.5	0.1904	124.0
4	0.08485	155.9	0.1101	147.8	0.09609	144.5	0.1098	142.5	0.1031	139.7	0.1097	138.6
5	0.05332	168.9	0.07247	161.6	0.06608	156.0	0.07678	153.0	0.07164	149.9	0.07670	149.1
7	0.02792	183.8	0.03946	179.2	0.03783	169.6	0.04467	168.5	0.04155	163.4	0.04457	163.2
10	0.01213	196.3	0.01723	195.0	0.01767	183.6	0.02039	184.0	0.02004	175.7	0.02162	175.3
15	0.00451	205.7	0.00622	206.2	0.00718	193.8	0.00797	196.4	0.0837	185.4	0.00917	185.1
20	0.00221	210.3	0.00300	211.4	0.00357	202.5	0.00400	203.4	0.00452	191.8	0.00474	192.4
30	0.00081	215.1	0.00108	215.9	0.00133	209.8	0.00149	210.2	0.00182	200.3	0.00191	200.4
40	0.00040	217.2	0.00052	218.0	0.00066	213.2	0.00073	213.8	0.00093	205.5	0.00097	205.8
50	0.00027	219.5	0.00030	218.6	0.00038	215.5	0.00041	215.0	0.00055	209.0	0.00057	208.1
70					0.00017	217.9	0.00019	217.3	0.00024	213.1	0.00025	211.7
100					0.00007	219.3	0.00009	218.8	0.00010	216.0	0.00010	215.9

Eq. [56] then becomes

$$\tilde{i}_f = \left(\frac{\partial f}{\partial \eta}\right)_{c_{i0}} \tilde{\eta} + \sum_i \left(\frac{\partial f}{\partial c_{i0}}\right)_{\substack{\eta, c_{j0} \\ j \neq i}} \tilde{c}_{i0} \qquad [61]$$

The usual charge-transfer resistance R_t can be identified as the reciprocal of $(\partial f/\partial \eta)_{c_{i0}}$, although this may be directly measurable at the prevailing steady-state surface concentration. By substitution of Eq. [49] and [55], we obtain

$$\tilde{\eta} = R_t \tilde{i}_f - \sum_i R_t \left(\frac{\partial f}{\partial c_{i0}}\right)_{\eta, c_{j0}} \left[\frac{\delta_i}{\theta_i'(0)} \frac{s_i}{n\mathbf{F}D_i} \tilde{i}_f - \frac{\Delta\Omega}{\bar{\Omega}} \frac{W_i \delta_i}{\theta_i'(0)} \frac{s_i \bar{i}}{n\mathbf{F}D_i}\right] = R_t \tilde{i}_f + Z_D \tilde{i}_f + \frac{\Delta\Omega}{\bar{\Omega}} \frac{\bar{i} R_t}{n\mathbf{F}} \sum_i \left(\frac{\partial f}{\partial c_{i0}}\right)_{\substack{\eta, c_{j0} \\ j \neq i}} \frac{W_i \delta_i}{\theta_i'(0)} \frac{s_i}{D_i} \qquad [62]$$

where

$$Z_D = -R_t \sum_i \left(\frac{\partial f}{\partial c_{i0}}\right)_{\substack{\eta, c_{j0} \\ j \neq 1}} \frac{\delta_i s_i}{n\mathbf{F}D_i \theta_i'(0)} \qquad [63]$$

can be termed the diffusion or convective Warburg impedance.

Inclusion of the ohmic potential drop and double-layer capacity according to Eq. [58] and [59] causes Eq. [2] to become

$$\tilde{V} = Z\tilde{i} + \frac{\Delta\Omega}{\bar{\Omega}} \frac{1}{1 + j\omega C(R_t + Z_D)} \frac{\bar{i} R_t}{n\mathbf{F}} \times \sum_i \left(\frac{\partial f}{\partial c_{i0}}\right)_{\substack{\eta, c_{j0} \\ j \neq i}} \frac{W_i \delta_i}{\theta_i'(0)} \frac{s_i}{D_i} \qquad [64]$$

where

$$Z = R_e + \frac{R_t + Z_D}{1 + j\omega C(R_t + Z_D)} \qquad [65]$$

is the electrochemical impedance $(\tilde{V}/\tilde{i})_{\Delta\Omega=0}$. Under the conditions of the experiments, ω is low enough for ωCR_t and ωCZ_D to be neglected compared to unity.

Furthermore, the formulation based on Eq. [56] obscures the simple relationships which prevail if the kinetics are inherently fast and the overpotential reduces to the concentration overpotential

$$\eta = \eta_c = \frac{RT}{n\mathbf{F}} \sum_i s_i \ln\left(\frac{c_{i\infty}}{c_{i0}}\right) \qquad [66]$$

or

$$\tilde{\eta} = \tilde{\eta}_c = -\frac{RT}{n\mathbf{F}} \sum_i s_i \frac{\tilde{c}_{i0}}{\bar{c}_{i0}} \qquad [67]$$

Equation [64] would then be replaced by

$$\tilde{V} = Z\tilde{i} + \frac{\Delta\Omega}{\bar{\Omega}} \frac{1}{1 + j\omega CZ_D} \frac{\tilde{i} RT}{n\mathbf{F}} \sum_i \frac{W_i \delta_i}{\theta_i'(0)} \frac{s_i^2}{n\mathbf{F}D_i \bar{c}_{i0}} \qquad [68]$$

where

$$Z = R_e + \frac{Z_D}{1 + j\omega CZ_D}$$

and

$$Z_D = \frac{RT}{n\mathbf{F}} \sum_i \frac{s_i}{\bar{c}_{i0}} \left(-\frac{\delta_i}{\theta_i'(0)} \frac{s_i}{n\mathbf{F}D_i}\right) \qquad [69]$$

Galvanostatic mode, $\tilde{i} = 0$: Eq. [64] yields

$$\frac{\tilde{V}}{\Delta\Omega} = \frac{\bar{i} R_t / n\mathbf{F}\bar{\Omega}}{1 + j\omega C(R_t + Z_D)} \sum_i \left(\frac{\partial f}{\partial c_{i0}}\right)_{\substack{\eta, c_{j0} \\ j \neq i}} \frac{W_i \delta_i s_i}{\theta_i'(0) D_i} \qquad [70]$$

If the diffusion coefficients are equal for reactants and products, W_i becomes a constant in the sum, and this simplifies to

$$\frac{\tilde{V}}{\Delta\Omega} = \frac{-\bar{i} Z_D / \bar{\Omega}}{1 + j\omega C(R_t + Z_D)} W \qquad [71]$$

Equations [68] and [69] yield to Eq. [71] with $R_t = 0$.

For the relatively low values of ω dealt with here, the approximate form would be

$$\frac{\tilde{V}}{\Delta\Omega} = -\frac{\bar{i}}{\bar{\Omega}} Z_D W \qquad [72]$$

If we normalize $(\tilde{V}/\Delta\Omega)$ by dividing by its value for $\omega = 0$, we obtain a function of only two parameters p and $Sc^{1/3}$. For this reason, values of $-W/\theta'(0)$ were given in Table VI and Fig. 4.

In the potentiostatic mode, $\tilde{V} = 0$, and Eq. [64] defines the value of the ratio $\tilde{i}/\Delta\Omega$. Where, again, the diffusion coefficients of reacting species are equal, this yields

$$\frac{\tilde{i}}{\Delta\Omega} = \frac{\bar{i}}{\bar{\Omega}} \frac{1}{1 + j\omega C(R_t + Z_D)} \frac{Z_D}{Z} W \qquad [73]$$

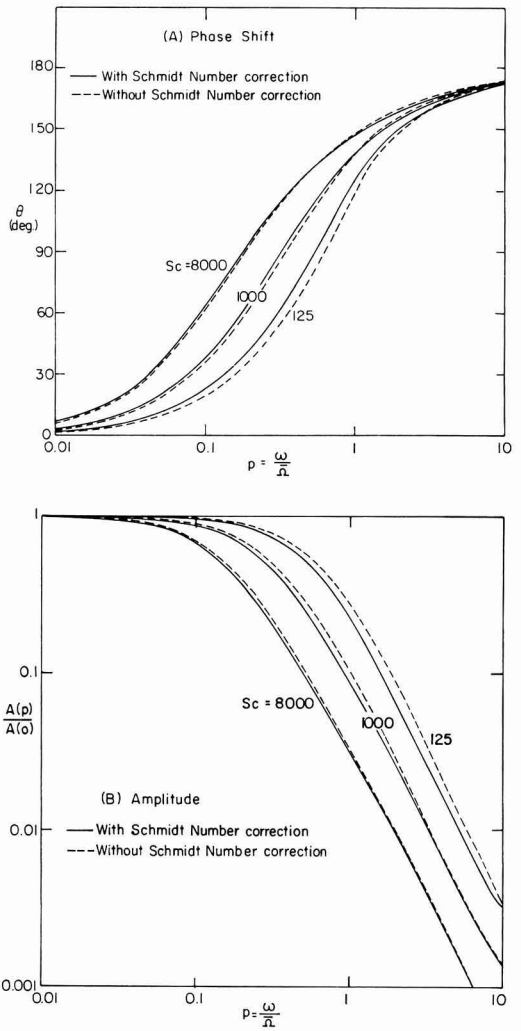

Fig. 3. (A) Phase shift of W vs. dimensionless frequency, (B) normalized amplitude of W vs. dimensionless frequency. In conditions of Eq. [75] or [79], the normalized quantities $(\tilde{i}/\Delta\Omega)$ and W are identical.

In the presence of an excess of supporting electrolyte and for the frequency used in this experiment, the electrolyte resistance (R_e) may be neglected compared to the sum of the charge-transfer resistance (R_t) and the convective-Warburg impedance (Z_D). Then Eq. [73] becomes

$$\frac{\tilde{i}}{\Delta\Omega} = \frac{\bar{i}}{\bar{\Omega}} \frac{Z_D}{R_t + Z_D} W \qquad [74]$$

With the assumption of a small electrolyte resistance Eq. [68] and [69] yield to

$$\frac{\tilde{i}}{\Delta\Omega} = \frac{\bar{i}}{\bar{\Omega}} W \qquad [75]$$

As an aside, we may note from Eq. [64] that if Z denotes the electrochemical impedance $(\tilde{V}/\tilde{i})_{\Delta\Omega=0}$, then it follows that

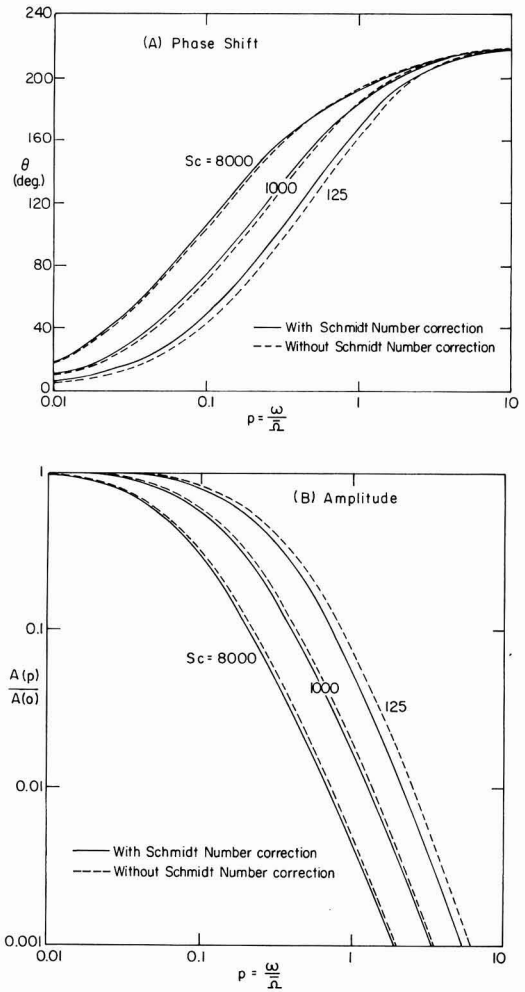

Fig. 4. (A) Phase shift of $-W/\theta'$ (0) vs. dimensionless frequency, (B) normalized amplitude of $-W/\theta'$ (0) vs. dimensionless frequency. In conditions of Eq. [72], the normalized quantities $(\tilde{V}/\Delta\Omega)$ are identical.

$$\left(\frac{\tilde{i}}{\Delta\Omega}\right)_{V=0}^{\sim} = -\left(\frac{\tilde{V}}{\Delta\Omega}\right)_{i=0}^{\sim} \frac{1}{Z} \qquad [76]$$

which is similar to the relation (21)

$$\left(\frac{\partial i}{\partial \Omega}\right)_V = -\left(\frac{\partial V}{\partial \Omega}\right)_i \left(\frac{\partial i}{\partial V}\right)_\Omega \qquad [77]$$

Assuming that we understand the electrochemical impedance Z of the system, the test under hydrodynamic modulation, whether it be potentiostatic or galvanostatic or otherwise, essentially tests for the applicability of the theory developed for W.

We can pick out the value of W for the oxidized or reduced species separately, without the assumption that $D_R = D_P$, by choosing our steady state under conditions where one term or the other in Eq. [57] is negligible. If we are on the cathodic limiting current plateau, we can regard our fixed potential conditions to mean that $c_R = 0$ or that both $\bar{c}_R$ and $\tilde{c}_R$ are zero. The clearest route to the hydrodynamic impedance is then Eq. [45] applied to species R. With Eq. [55], [58],

and [59], we have

$$\frac{\tilde{i}}{\Delta\Omega} = \frac{\bar{i}_{lim}/\bar{\Omega}}{1 + j\omega CR_e} W_R \qquad [78]$$

Again, we can test the theory for W_R. Equation [78] can also be obtained from Eq. [73] by recognizing that Z_D becomes infinite under limiting current conditions. For the values of ω used here, Eq. [78] simplifies further to

$$\frac{\tilde{i}}{\Delta\Omega} = \frac{\bar{i}_{lim}}{\bar{\Omega}} W_R \qquad [79]$$

This relation is similar to Eq. [75] obtained with the assumption that the kinetics are inherently fast and that $R_e << Z_D$.

Experimental

The aim of these experimental measurements is to obtain a comparison with theory on a large frequency range for galvanostatic and potentiostatic regulation. For this reason, we use a well-known electrochemical reaction: the reduction step of a rapid redox system (potassium ferricyanide-ferrocyanide (0.005M) with 1M KCl as supporting electrolyte). The temperature was fixed at 25°C, and the Schmidt number was 1200.

The electrical scheme of the experimental device had been given in Ref. (2) and (4). However, for the present study, a new electrooptical tachometer has been used in order to obtain good regulation of the instantaneous angular velocity even for a low mean velocity (as low as 60 rpm). The measurements are performed thanks to a two-channel transfer function analyzer (DFTA). The remaining parasitic noises are diminished by supplying the potentiostat by Ni-Cd batteries and by using a battery and a large resistance as a galvanostat.

In Fig. 5a and 5b, we give the experimental results obtained at 120 rpm (2 Hz) with a platinum rotating disk electrode (diam = 5 mm) for galvanostatic regulation at $\bar{i} = \frac{1}{2}\, i_{lim}$ ($i_{lim} = 170\ \mu A$). The theoretical curve is obtained from expression [72] with the Schmidt number correction; and for the amplitude, the experimental curve is normalized by the experimental value of $\tilde{V}/\Delta\Omega$ when p tends towards zero. The agreement between the theory and experiment is good for both the phase shift and the amplitude over the whole frequency range.

In Fig. 6a and 6b, we give the experimental results obtained at 120 rpm with the same rotating disk electrode but for potentiostatic regulation at the limiting current ($V = -100$ mV *vs.* saturated calomel reference electrode). The theoretical curve is obtained from expression [79] (with the assumption that $\tilde{c} = 0$ at the interface and $\omega CR_e << 1$).

For $p < 1$, the agreement between theory and experiment is good. For higher frequencies, the deviation increases with p. This deviation may be due to the assumption of $\tilde{c} = 0$ at the interface, which is equivalent to $(R_t + R_e) << Z_D$. Z_D decreases with the frequency, and for p higher than 1, the assumption may not be valid; therefore, it is necessary to use the general expression [73].

From Eq. [57] we have

$$\bar{i} = -\bar{i}_0 \left[\frac{\bar{c}_{R0}}{c_{R\infty}} \exp\left(-\frac{\alpha_c \mathbf{F}}{RT} \bar{\eta} \right) \right] \qquad [80]$$

and

$$R_t = \frac{RT}{\alpha_c \mathbf{F}} \cdot \frac{1}{\bar{i}} \qquad [81]$$

With $\alpha_c = 0.5$, $\bar{i} = 850\ \mu A/cm^2$, $R = 8.314$ J/mol · K, $T = 298$ K, and $\mathbf{F} = 96487$ C/equiv., we obtain 60

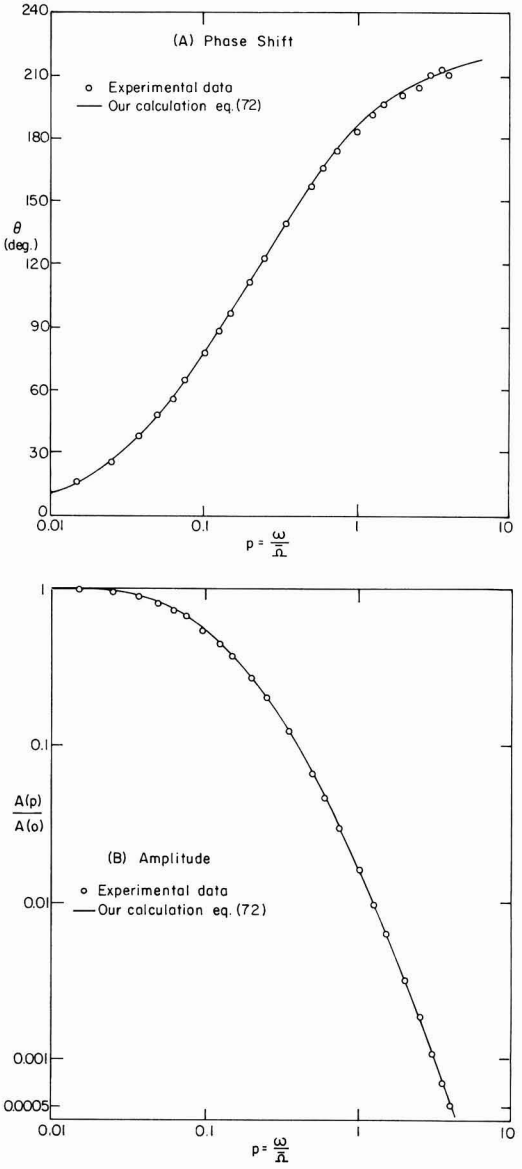

Fig. 5. Comparison between the theoretical curve from Eq. [72] and the experimental data in galvanostatic mode. The data were obtained with the $Fe(CN)_6^{3-}/Fe(CN)_6^{4-}$ system at $i = 1/2\ i_{lim}$. Supporting electrolyte |KCl| = 1M, Sc = 1200. $\bar{\Omega}$ = 120 rpm: (A) phase shift vs. dimensionless frequency, (B) normalized amplitude vs. dimensionless frequency.

$\Omega \cdot cm^2$. And from Eq. [53] with $D_R = 0.765 \cdot 10^{-5}$ cm^2/sec and $\nu = 0.0094$ cm^2/sec, $Z_D(\omega = 0) = \frac{2 \cdot 10^{-4}}{\bar{c}_{R0}}\ \Omega \cdot cm^2$.

The measurements correspond to the beginning of the plateau; then we may assume $\bar{c}_{R0} = 0.01\ c_{R\infty}$ and $Z_D(\omega = 0) = 4\ k\Omega \cdot cm^2$. With these values, R_e is negligible compared to R_t and Z_D, and we may use Eq. [74]. The values of Z_D may be obtained from Table V, and we may calculate the ratio $Z_D/(R_t + Z_D)$. The results are given in Table VII, and the corre-

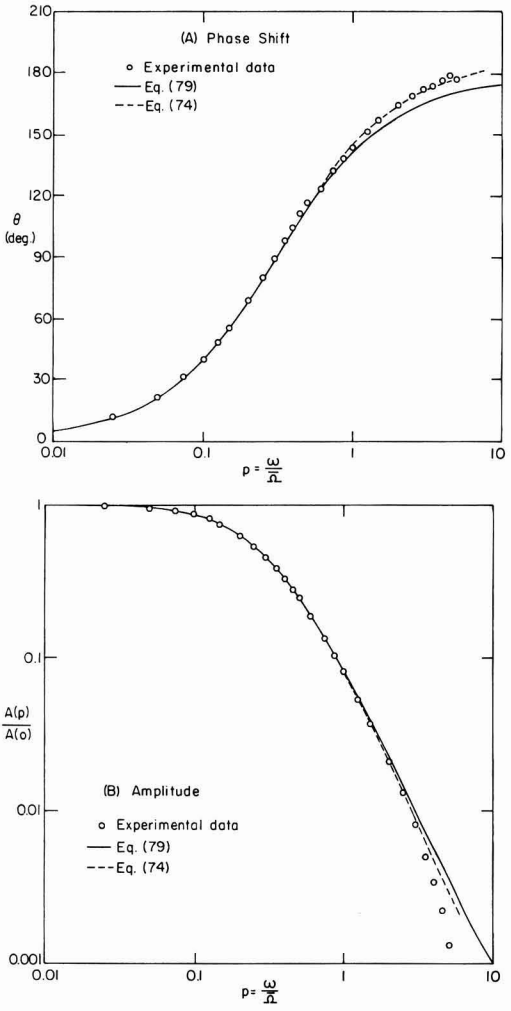

Fig. 6. Comparison between the theoretical curve and the experimental data in potentiostatic mode at the limiting current, the solid lines correspond to Eq. [79] and the dashed lines to Eq. [74]: (A) phase shift vs. dimensionless frequency, (B) normalized amplitude vs. dimensionless frequency.

sponding corrections are given in dashed lines on Fig. 6a and 6b.

With this correction, the agreement between the theory and experiment is good over the whole frequency range for the phase shift and until $p = 3$ for the amplitude. The deviation for the higher frequencies may be due to the weakness of the signal compared to the residual noise of the electronic device, in particular the potentiostat. This problem is less important in galvanostatic regulation because the galvanostat made with a battery may be considered without noise.

From the comparison of our experimental measurements to the theoretical curve, we have shown on the diffusion plateau the effect of the charge-transfer resistance for higher frequencies. This effect may be more important for intermediate kinetics because R_t is higher and Z_D is smaller. Then below the limiting current, with the assumption $D_R = D_P$ and $\omega C(R_t + Z_D) << 1$, the analysis of the normalized data is easier in galvanostatic regulation (their values depend

Table VII. Variations of $\frac{Z_D}{R_t + Z_D}$

p	1	1.5	2	3	4	5
A	0.95	0.93	0.925	0.91	0.90	0.89
θ	3	3.5	4	5	5.5	6

only on the dimensionless frequency $p(p = \omega/\bar{\Omega})$ and the cubic root of the Schmidt number). However in potentiostatic regulation at limiting current, this nonstationary method may give some original information because the electrochemical impedance cannot be used in this low frequency range.

An application of this method is the determination of the diffusion coefficient for the electroactive species. These electrohydrodynamical impedances, in galvanostatic or potentiostatic mode, may be written as a series expansion of $Sc^{-1/3}$; in order to obtain sufficient accuracy, it is necessary to use the two first terms of this series. A best accuracy is obtained if the data analysis is done on a large frequency range. Then, for example, comparison of Fig. 6 with Fig. 3 or of Fig. 5 with Fig. 4 would permit the determination of Sc, with a minor difficulty being associated with the inclusion of the Schmidt number correction. Since we are working with a well-known mass transfer system, it has not been necessary for us to try to infer here the value of the Schmidt number from the experimental results. Tables I-V give results of integration of the unsteady Navier-Stokes equations to cover all frequencies which can be achieved experimentally.

Acknowledgment

This work was supported by the National Science Foundation through an Exchange Visitor Program with Centre National de la Recherche Scientifique No. G050252.

Manuscript submitted July 8, 1982; revised manuscript received Oct. 5, 1982.

LIST OF SYMBOLS

a	constant = 0.51023
B	constant = $(3/a^4)^{1/3}$
c	concentration of the electroactive species, mol/cm³
C	double layer capacity, farad/cm²
D	diffusion coefficient, cm²/sec
f	dimensionless unsteady component of the radial velocity (see Eq. [13])
F	dimensionless steady component of the radial velocity
$\mathbf{F}$	Faraday's constant, 96,487 C/equiv.
g	dimensionless unsteady component of the angular velocity
G	dimensionless steady component of the velocity in θ-direction
h	dimensionless unsteady component of the axial velocity
H	dimensionless steady component of the axial velocity
i	current density, A/cm²
i_o	exchange current density at the bulk composition, A/cm²
i_f	Faradaic current density, A/cm²
i_{lim}	limiting current density, A/cm²
j	$=\sqrt{-1}$
K	dimensionless frequency = 3.2576 p $Sc^{1/3}$
K_1, K_2	integration constants (see Eq. [46])
n	number of electrons involved in electrode reaction
p	dimensionless unsteady component of the dynamic pressure
p	dimensionless frequency = $\omega/\bar{\Omega}$
P	dynamic pressure, dyne/cm²
P	dimensionless steady component of the dynamic pressure
r	radial distance in cylindrical coordinates
R	universal gas constant, 8.3143 J/mol-K
R_e	electrolyte resistance, Ω · cm²
R_t	charge transfer resistance, Ω · cm²

s_i	stoichiometric coefficient of species i in electrode reactions
Sc	Schmidt number
t	time, sec
t_i	parameters of the W expansion ($j = 1$ to 6) (see Table IV)
T	absolute temperature, K
v_r	radial component of the fluid velocity, cm/sec
v_θ	angular component of the fluid velocity, cm/sec
v_z	axial component of the fluid velocity, cm/sec
V	electrode potential measured with respect to a reference electrode placed in the bulk of the solution, V
W	function defined in Eq. [48] (see Table V, Fig. 3)
z	axial distance in cylindrical coordinates, cm
z_i	charge number of species i
Z	electrochemical impedance, $\Omega \cdot cm^2$
Z_D	diffusion or convective Warburg impedance, $\Omega \cdot cm^2$
Z_o, Z_1	coefficients of the series expansion of $-1/\theta'(o)$ in $Sc^{-1/3}$, (see Eq. [45], Table III)
α_a, α_c	transfer coefficients
β_1, β_2	expansion parameters (see Eq. [30]-[32])
$\Gamma(4/3)$	$= 0.89298$, the gamma function of 4/3
δ	distance characteristic of the thickness of diffusion layer, see Eq. [34], cm
ζ	dimensionless axial distance from disk ($=z\sqrt{\Omega/\nu}$)
η	total overpotential, V
θ	solution of the unsteady homogeneous equation of convective diffusion
θ	angle in cylindrical coordinates, radian
θ_j	coefficients of the series expansion of θ in $Sc^{-1/3}$, ($j = 0, 1, 2 \ldots$)
μ	viscosity, g/cm-sec
ν	kinematic viscosity, cm^2/sec
ξ	dimensionless axial distance from disk ($=z/\delta$)
ω	modulation frequency, radian/sec
$\Delta\Omega$	amplitude modulation of the rotation speed, radian/sec
Ω	disk rotation speed, radian/sec
χ	dimensionless axial distance from disk ($= z\sqrt{\Omega/\nu}$)

Subscripts

o	at electrode surface
∞	in bulk solution
i	relative to species i
P	produced species
R	reacting species

Superscripts

overbar	steady state
~	unsteady component

REFERENCES

1. K. Tokuda, S. Bruckenstein, and B. Miller, *This Journal*, **122**, 1316 (1975).
2. C. Deslouis, I. Epelboin, C. Gabrielli, and B. Tribollet, *J. Electroanal. Chem.*, **82**, 251 (1977).
3. W. J. Albery, A. R. Hillman, and S. Bruckenstein, *ibid.*, **100**, 687 (1979).
4. C. Deslouis, C. Gabrielli, Ph. Sainte-Rose Fanchine, and B. Tribollet, *This Journal*, **129**, 107 (1982).
5. E. M. Sparrow and J. L. Gregg, *J. Aerospace Sci.*, **27**, 252 (1960).
6. Y. Kanzaki and S. Bruckenstein, *This Journal*, **126**, 437 (1979).
7. V. P. Sharma, *Acta Mechanica*, **32**, 19 (1979).
8. Th. Von Karmán and Z. Angew, *Math. Mech.*, **1**, 233 (1921).
9. J. Newman, "Electrochemical Systems," Prentice Hall, Inc., Englewood Cliffs, NJ (1973).
10. J. Newman, *Ind. Eng. Chem.*, **7**, 514 (1968).
11. W. G. Cochran, *Proc. Cambridge Phil. Soc.*, **30**, 365 (1934).
12. F. B. Hildebrand, "Advanced Calculus for Applications," p. 29, Prentice Hall, Inc., Englewood Cliffs, NJ (1948).
13. E. Levart and D. Schuhmann, *J. Electroanal. Chem.*, **28**, 45 (1970).
14. C. Deslouis, Thése de Doctorat d'Etat, Paris, No. A.O. 11014 (1975).
15. D. A. Scherson and J. Newman, *This Journal*, **127**, 110 (1980).
16. R. V. Homsy and J. Newman, *ibid.*, **121**, 521 (1974).
17. J. Newman, *J. Phys. Chem.*, **70**, 1327 (1966).
18. J. Newman, *This Journal*, **113**, 1235 (1966).
19. J. Newman, *ibid.*, **117**, 198 (1970).
20. P. Appel, Ph.D. Dissertation, University of California, Berkeley (1976).
21. C. Deslouis, I. Epelboin, C. Gabrielli, Ph. Sainte-Rose Fanchine, and B. Tribollet, *J. Electroanal. Chem.*, **107**, 193 (1980).

The Kinetic Parameters of the $Fe(CN)_6^{3-/4-}$ Redox System

New Results with the Ring Electrode in Turbulent Pipe Flow

T. Iwasita and W. Schmickler*

Institut für Physikalische Chemie, Universität Düsseldorf, Düsseldorf, Germany

J. Herrmann and U. Vogel

Institut für Physikalische Chemie, Universität Bonn, Bonn, Germany

ABSTRACT

A theoretical analysis of a ring electrode in turbulent pipe flow is given in order to estimate the limits of resolution of a given experimental setup. Special attention is paid to error analysis, which is necessary for the correct evaluation of the data. To demonstrate the potentialities of this method for kinetic studies, the apparent exchange current density of the ferro-ferricyanide system was measured. The values obtained are higher than those reported in the literature.

The study of electrode kinetics has been improved with the development of the methods to measure the reaction rates with increasing accuracy. Stationary and nonstationary methods are employed in a more or less successful way in order to eliminate the diffusional contribution to the electrode process in systems having standard rate constants, k_o, smaller than about 10^{-3} cm/sec. Above this limit the selection of the appropriate technique becomes more and more difficult. With the rotating disk electrode (RDE) rate

* Electrochemical Society Active Member.

Key words: mass transport, kinetics.

constants in the order of 10^{-2} cm/sec have been measured. Some transient techniques have extended this limit by less than one order of magnitude. A rapid analysis of the data for the system $Fe(CN)_6^{3-/4-}$ given in Table I shows that the values of k_o obtained by different methods under the same conditions (electrode metal and supporting electrolyte), vary by a factor greater than two. The differences come probably from the fact that the limit of the methods employed has been exceeded. Factors such as uncompensated *IR* drop or electrode pretreatment can also be reasons for the differences observed, and they contribute to enlarge the errors to a higher extent, thus making the situation even more unfavorable.

Very seldom can one find in the literature a correct limit for the use of an experimental method. The maximum measurable rate constant is normally overestimated on the basis of theoretical calculations without real experimental proof. These idealized limits do not take into account the increasing technical problems one has to confront in a real experiment as the reaction rate becomes larger.

From the transient techniques, the one offering the most attractive possibilities is probably the coulostatic pulse method. Its main advantage is the absence of ohmic drop effects. If the voltage recording system has very fast recovery properties, the η-t curve can be measured at very short times (0.5 μsec after cessation of the pulse), before the diffusional process becomes important (6). Theoretically, rate constants as large as 0.4 cm/sec can be evaluated by means of a simple log η-t relationship, or with cumbersome mathematical treatment 1-5 cm/sec could eventually be measured (6). These limits have still not been experimentally demonstrated.

Recently, a ring electrode in turbulent pipe flow (RTP) has allowed the determination of the rate constant of the redox couple $Fe(bipy)_3^{3+/2+}$, $k_o = 0.9$ cm/sec, with data from stationary current-potential curves (7, 8). In order to achieve high enough stationary flow rates in a 1 cm diam pipe, the experimental arrangements required a relatively large amount of solution (about 5 liters). In our laboratory, the experimental setup was improved in order to reduce the required volume to about 300 ml (9) and to allow a satisfactory reduction of the ohmic resistance. As a test of the new device, the often investigated system $Fe(CN)_6^{3-/4-}$ was measured on platinum and gold electrodes. The results obtained at the ring in turbulent pipe flow are compared with those of RDE experiments and with those of some nonstationary methods. The rotating disk electrode so far has been considered to be sufficient to measure the rate constant of the redox couple $Fe(CN)_6^{3-/4-}$ (3, 10).

The Theoretically Expected Limitations of RTP Measurements

The method of evaluation of the kinetic parameters from the experimental stationary current-potential curve.—In the following discussion we refer to the reaction rate in terms of the standard exchange current density j_{oo} which is defined as follows (11)

$$j_{oo} = n\mathbf{F}k_o c^* \qquad [1]$$

where c^* is a standard concentration $= 10^{-3}$ mol/cm^3 and $\mathbf{F}$ = the Faraday constant, *ca.* 10^5 As/equivalent. A rate constant $k_o = 1$ cm/sec is equivalent to a standard exchange current density of about 100 A/cm^2. The exchange current density at concentrations c_{ox} and c_{red} is related to the standard rate constant according to

$$j_o = j_{oo}\left[\frac{c_{ox}}{c^*}\right]^{\alpha}\left[\frac{c_{red}}{c^*}\right]^{(1-\alpha)} \qquad [2]$$

with c_{ox}, c_{red} = bulk concentrations in mol/cm^3.

The experimental stationary current-potential curves corrected for ohmic drop result from the contribution of mass and charge transfer. A reaction having an infinite rate of charge transfer (k_o or $j_{oo} \to \infty$) can be described in terms of a reversible current, I_{rev}

$$I_{rev} = \frac{I_{lim}^a\,[1 - \exp(-n\mathbf{F}\eta/RT)]}{1 + \dfrac{I_{lim}^a}{I_{lim}^c}\exp(-n\mathbf{F}\eta/RT)} \qquad [3]$$

Equation [3] can be easily obtained for stationary conditions, when the mass transport is proportional to the concentration gradient (I_{lim}^a, I_{lim}^c = anodic and cathodic limiting currents). The reversible current is determined only by the parameters affecting the mass transfer (via I_{lim}^a and I_{lim}^c) and by the overpotential.

For a reaction having a finite rate of charge transfer ($0 < k_o < \infty$) the observed current I, will be smaller than I_{rev} under the same experimental conditions. The evaluation method (8, 12) uses the relationship of both currents introducing a dimensionless parameter u defined as follows

$$u = \frac{2}{3}\frac{I_{rev}}{I_k} \qquad [4]$$

where I_k is the current associated with a reaction controlled by charge transfer alone

$$I_k = I_o \exp(\alpha n\mathbf{F}\eta/RT)\,[1 - \exp(-n\mathbf{F}\eta/RT)]$$

It can be easily seen that

$$u = \frac{2I_{lim}^a/A}{3j_o \exp(\alpha n\mathbf{F}\eta/RT)\left[1 + \dfrac{I_{lim}^a}{I_{lim}^c}\exp(-n\mathbf{F}\eta/RT)\right]} \qquad [5]$$

with A = electrode area. The current ratio I/I_{rev} is related to the parameter u

$$I/I_{rev} = 1 - 2u + 2u^2 \ln(1 + 1/u) \qquad [6]$$

Equation [6] contains the experimental current I and the reversible current I_{rev} which can be calculated from the measured limiting currents according to Eq. [3]. Once the value of u is known for several given overpotentials, the exchange current density j_o and the transfer coefficient α can be evaluated from Eq. [5]. A computer fitting procedure can give reliable statistical mean values of the kinetic parameters.

At high overpotentials Eq. [5] can be written

$$-\ln u = -\ln\frac{2}{3}\frac{I_{lim}^a}{Aj_o} + \frac{\alpha n\mathbf{F}\eta}{RT}, \quad \text{for } \eta >> \frac{RT}{\mathbf{F}}$$

and [7]

$$-\ln u = -\ln\frac{2}{3}\frac{I_{lim}^c}{Aj_o} + \frac{(1-\alpha)n\mathbf{F}\eta}{RT}, \quad \text{for } \eta << -\frac{RT}{\mathbf{F}}$$

These linear ln u *vs.* η relationships can be used as an alternative for the calculation.

The evaluation procedure described above makes use of the experimental limiting currents. For systems having poorly defined limiting currents it is possible to obtain I_k by extrapolating the current I to infinitely fast mass transport; details are given elsewhere (13).

Simulated current-potential curves for the RTP and RDE methods.—A better understanding of the potentialities of the methods can be achieved by simulating with a computer the expected current-potential curves for different values of j_{oo} at given mass transfer conditions determined by the experimental setup.

The theoretical current-potential curves for the RTP were calculated by means of Eq. [3]-[6] and the following expression for the limiting current (8, 9)

$$I_{\lim}{}^{a} = 0.276 A n \mathbf{F} D_{red}{}^{2/3} \nu^{1/3} \mathrm{Re}^{7/12} L^{-1/3} d^{-2/3} c_{red} \quad [8]$$

where D = diffusion coefficient, ν = kinematic viscosity, Re = Reynolds number, L = electrode length, d = pipe diameter, and A = electrode area.

The computer generated curves are shown in Fig 1. The values of the parameters employed are indicated in the figure.[1]

In the case of the RDE the curves I_{rev} and I *vs.* η were simulated with the help of Eq. [3] and the equation for the kinetic and diffusion-controlled current as follows (3, 15)

$$\frac{1}{I} = \frac{1}{A j_o \exp(\alpha n \mathbf{F}\eta/RT)\,[1 - \exp(-n\mathbf{F}\eta/RT)]} + \frac{1 + \dfrac{I_{\lim}{}^{a}}{I_{\lim}{}^{c}} \exp(-n\mathbf{F}\eta/RT)}{I_{\lim}{}^{a}\,[1 - \exp(-n\mathbf{F}\eta/RT)]} \quad [9]$$

where the limiting current is given by (15)

$$I_{\lim}{}^{a} = 0.620 A n \mathbf{F} D_{red}{}^{2/3} \nu^{-1/6} c_{red} \omega^{1/2} \quad [10]$$

The respective I_{rev} and I curves are shown in Fig. 2. The selected parameters are also indicated.

In the limit of $j_o \to \infty$, Eq. [9] and [3] are identical. For intermediate kinetics ($0 < j_o < \infty$), a dimensionless parameter u can be defined for the RDE as follows

$$u = \frac{I_{\lim}{}^{a}/A}{j_o \exp(\alpha n \mathbf{F}\eta/RT)\left[1 + \dfrac{I_{\lim}{}^{a}}{I_{\lim}{}^{c}} \exp(-n\mathbf{F}\eta/RT\right]} \quad [11]$$

and the observed current I is given by

$$I/I_{rev} = (1 + u)^{-1} \quad [12]$$

The average flow velocity used to simulate the curves in Fig. 1 (v = 13.77 m/sec, Re number = 30,000) can be easily attained with our experimental arrangement. On the other hand, the rotation speed used to simulate the curves at the RDE (Fig. 2) is almost the practical limit of this technique. Therefore, a comparison of Fig. 1 and 2 clearly shows the superiority of the RTP method. The resolution of the curves for different values of the exchange current

[1] The diffusion coefficients and kinematic viscosity correspond to a solution of $Fe(CN)_6^{3-/4-}$ in 0.5M K_2SO_4 at 20°C.

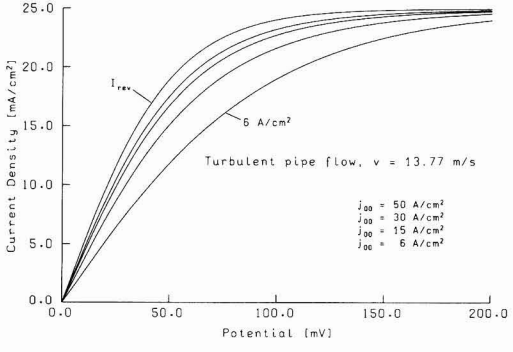

Fig. 1. Computer simulated current-potential curves for the ring electrode in turbulent pipe flow. Electrode length = 0.01 cm; pipe diameter = 0.22 cm, T = 20°C, $c_{ox} = c_{red}$ = 2.5 · 10⁻³M, D_{ox} = 6.22 · 10⁻⁶ cm²/sec, D_{red} = 5.93 · 10⁻⁶ cm²/sec, kinematic viscosity = 1.01 · 10⁻² cm²/sec, α = 0.5. The average flow velocity v corresponds to an Re number of 30,000.

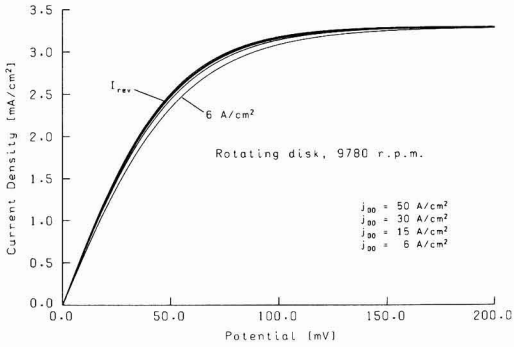

Fig. 2. Computer simulated current-potential curves for the rotating disk electrode. T = 20°C, $c_{ox} = c_{red}$ = 2.5 · 10⁻³M, D_{ox} = 6.22 · 10⁻⁶ cm²/sec, D_{red} = 5.93 · 10⁻⁶ cm²/sec, kinematic viscosity = 1.01 · 10⁻² cm²/sec, α = 0.5.

density attained with the RTP cannot be reached by the RDE even at a high speed of rotation (10,000 rpm).

From the plots of Fig. 2 we can conclude that the maximum value for the standard exchange current density to be measured with the RDE is about 10A cm⁻². This limit can be reached only under optimum experimental conditions. The curves also show that the extrapolated exchange current density is very sensitive to small errors in the current and/or overpotential. This effect is even more pronounced at lower speeds of rotation. Therefore, it is convenient to perform the evaluation of j_o and α from experimental data taken at the highest possible speed of rotation and by means of a fitting procedure through Eq. [9] or [11]. The accurate control of the *IR* drop is also of great importance. Equations [5] and [11] represent important steps in the calculation of the experimental data of the RTP and RDE methods, respectively. The statistical fitting of these relationships gives reliable results that can be conveniently presented in the form of a ln u-η plot. Such curves were simulated for the RTP with selected mass and charge transfer conditions as shown in Fig. 3.

Increasing the convective mass transfer produces a displacement of the curves to higher u values. The linear relationship at high overpotentials predicted by Eq. [7] can also be observed.

Estimation of error in the RTP method.—The errors in the RTP method, as in any experimental technique, can be systematic or random. In the first group we include the instrumental errors, the uncontrolled *IR*

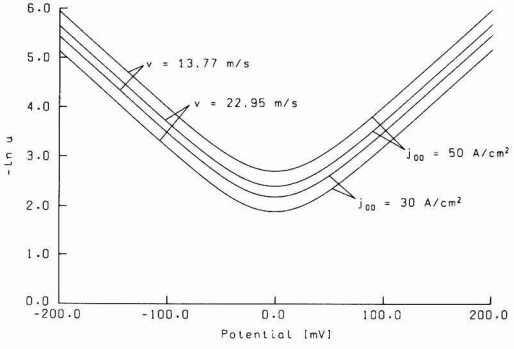

Fig. 3. Computer simulated semilogarithmic plot of the potential dependence of the parameter u for a ring electrode under the same conditions as in Fig. 1.

drop, the errors produced by impurities in the solution, and the failure in the temperature control. In the RTP method in particular, an unsatisfactory mounting of the ring electrode can produce large systematic errors. On the other hand, a test of the state of the ring electrode can be easily done by taking a cyclic voltammogram in 0.5M H_2SO_4 and by checking that the relationship I_{lim}-$Re^{7/12}$ (Eq. [8]) is obeyed. The cyclic voltammogram allows a control of the electrode surface and the I-$Re^{7/12}$ plot proves the fulfillment of the hydrodynamic conditions for the validity of the evaluation procedure.

In the course of one experiment an increase of several degrees in temperature can be observed if the solution is not properly cooled. Therefore, the temperature has to be measured and kept constant, and the temperature control device must be placed very close to the electrode.

The main random error is obviously given by the precision of the instrumental device used to record the current-potential curve. In the case of very fast reactions the ratio I/I_{rev} can be very close to unity giving very low values of the parameter u (see Eq. [6]). Therefore, the propagation of the uncertainty in the I/I_{rev} ratio on the parameter u is of great interest. The current depends on the applied potential. Therefore, the error in the current may come from its own inherent uncertainty and from the random fluctuations of the potential. The reversible current can be determined with high accuracy, especially if there exists a well-defined limiting current region. This is the case for the $Fe(CN)_6^{3-/4-}$ redox system on noble metal electrodes which we have used as a test system. We, therefore, assume that the error ΔI_{rev} is negligible. The propagation of the undetermined error (14) ΔI for the evaluation of the parameter u is given by the relationship

$$\Delta \ln u \simeq \frac{\Delta I}{I_{rev} u} [-2 + 4u \ln (1 + 1/u) - 2/(1 + 1/u)]^{-1} \quad [13]$$

which is obtained from Eq. [6] by differentiation.

Equation [13] shows that the error $\Delta \ln u$ will vary during one experiment due to its complex dependence on u, ΔI, and I_{rev}. For a given error ΔI, Eq. [13] implies smaller $\Delta \ln u$ errors for increasing I_{rev} and u values. At a given overpotential these two parameters can be increased by accelerating the rate of convective mass transport. On the other hand, ΔI can be diminished by improving the sensitivity of the recording system. The random error in the current depends on the particular experimental arrangement used. We have used Eq. [13] to calculate the errors in our experimental u values. They are reported together with our results.

Experimental

Apparatus.—The electrolysis cell used (Fig. 4) consists of a single compartment with a capacity of about 400 cm^3. The counterelectrode and the thermometer are placed directly through standard joints. The solution can be deaerated by bubbling nitrogen or argon through a frit. The temperature is controlled by means of a double spiral inside the cell connected to a cryostat. The hydrodynamic conditions at the working electrode are determined by the pipe which consists of a glass tube of about 18 cm length with an inside diameter of 0.22 cm. It is placed in the cell through a standard joint.

Two metal rings at about 3 cm from the end of the pipe are used as reference and working electrodes (Fig. 5). The pump, a Verder 114-ty-316 Micropump capable of producing a maximal pressure of 5 bar, allows the controlled circulation of the solution with an adjustable velocity. The maximum average velocity is 16 m/sec at 20°C and the maximum Reynolds number is near 35,000.

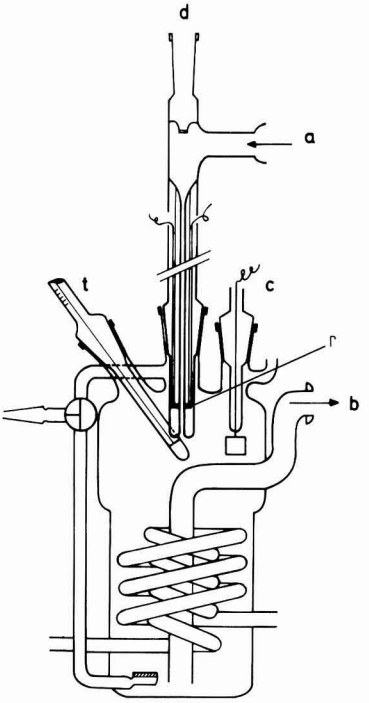

Fig. 4. Electrolysis cell with pipe assembly. The direction of the flow is indicated by the arrows a and b, r = ring electrodes (see details in Fig. 5), c = counterelectrode, d = compartment for an extra reference electrode, t = thermometer.

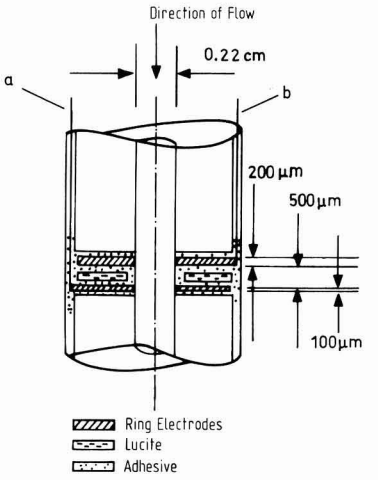

Fig. 5. Diagram showing the double ring electrode assembly. The first ring in the direction of the flow is the reference electrode, the second is the working electrode. a and b are the external contacts.

The potentiostatic current-potential curves were obtained by applying a slow (6 mV/sec) potential sweep through a potentiostat Stonehart BC 1200. The curves were plotted on a X-Y-Recorder Hewlett Packard 7004 B.

The double ring electrode and the control of the ohmic drop.—Pt and Au were employed as metals for the double ring electrode (Fig. 5). Special care was taken in the construction of this unit. Two metal sheets

(0.2 and 0.1 mm thick) separated by a thin Lucite or plastic ring were stuck together between two capillary tubes of 2.2 mm inner diameter. Glycidether-Epikure 113 from Shell was used as adhesive. The metals were then drilled to 1.6 mm diam. By grinding capillary tubes of 2.2 mm inner diameter. Glycidether-sults. After polishing with Al_2O_3 (13 to 1μ mesh) with the help of a Lucite rod and finally with a PTFE coated spindle, a smooth surface is obtained.

The first (0.2 mm thick) ring was used as a reference electrode and the second (0.1 mm thick) as a working electrode. The ohmic resistance between both rings was 2.6Ω in KF and 3.5Ω in K_2SO_4).[2] All overpotentials were corrected for these values. In our case, however, the correction amounts to about 3.5% for the exchange current density.

As an alternative procedure a parallel series of measurements was performed with a calomel reference electrode. This can be of interest if the flow system is constructed with only one ring or if the two rings are to be used as working electrodes as in some kinetic studies (9). In this case the reference electrode was placed in a separate compartment 2 cm before the entrance of the pipe (see Fig. 4). The high ohmic resistance can produce a considerable potential drop between the working and reference electrodes, although our measurements show that the current in this part of the circuit is only about 8-10% of the total current.

A five-electrode arrangement in order to eliminate the ohmic drop in continuous flow systems (16) was used here (Fig. 6). Two extra electrodes, a calomel electrode R_2 and a Pt (or Au) wire W_2 were included in the circuit. R_2 is connected to the input of a second potentiostat P_2. The output is connected to the first reference electrode R_1 and to the counterelectrode C. This arrangement makes the potential drops W_2-R_2 and W_2-R_1 equal so that the return loop current vanishes.

Solutions.—The solutions were prepared with water purified by a double deionization procedure followed by filtration through a Milli-Q unit from Millipore. Potassium ferri- and ferrocyanide were Merck reagent grade. The supporting electrolytes were potassium sulfate Merck reagent grade and potassium fluoride Merck Suprapur.

Pretreatment of the electrodes.—The current-potential curves of the $Fe(CN)_6^{3-/4-}$ redox couple are highly sensitive to small traces of impurities that can be adsorbed at the electrode, producing a partial blocking of the surface. Therefore, special care has to be taken for the cleaning procedure of the pump, the cell, the electrodes, and all materials in contact with the solution. Before taking a curve the electrode was activated by cycling the potential at about 1 V/sec, between the onset of H_2 evolution and shortly before the beginning of O_2 evolution. After a pause of 10 sec at the cathodic end, the curves were recorded at a sweep rate of 6 mV/sec.

A set of current-potential curves at a platinum electrode in K_2SO_4 as supporting electrolyte is shown in Fig. 7. A good test for the experimental arrangement, in particular for the quality of the electrode, is the linear dependence of the limiting current on $Re^{7/12}$, which is shown in Fig. 8.

The roughness factor of the electrodes, measured by the potentiodynamic sweep technique (17-19) was between 2 and 3.5 for Pt and between 2.5 and 6 for Au. Repeated experiments showed that the current per geometric area of the electrode is independent of the roughness factor, so all our results are referred to the geometric area. Apparently it is the geometric area of the ring which determines the rate of mass transport to the electrode and hence the current. Only when the surface roughness is so considerable that it disturbs the flow in the boundary layer, does it affect the experiments (7, 8). The electrode preparation described above assured smooth surfaces and an undisturbed flow of the solution.

[2] Measured via a potentiostatic square wave function and the *IR* drop correction bridge of the Stonehart potentiostat.

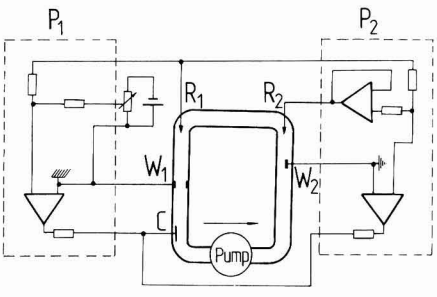

Fig. 6. Diagram of the five-electrode circuit for ohmic drop control. P_1, P_2 = potentiostats, W_1 = working electrode, C = counterelectrode, R_1 = reference electrode, R_1 and R_2 are identical, W_1 and W_2 are of the same metal.

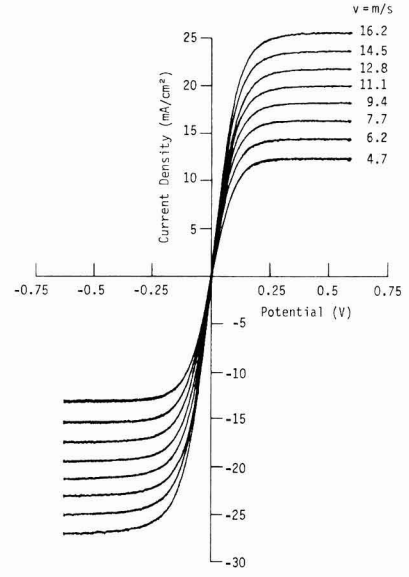

Fig. 7. Experimental current-potential curves for $Fe(CN)_6^{3-/4-}$ redox system at a Pt ring electrode in turbulent pipe flow. The experiments were made with a calomel reference electrode and the five-electrode arrangement shown in Fig. 6. T = 20°C, c_{ox} = 2.5 · 10^{-3}M, c_{red} = 2.5 · 10^{-3}M, 0.5M K_2SO_4.

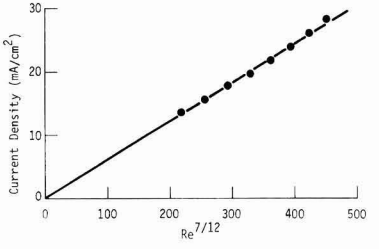

Fig. 8. Plot according to Eq. [8] of the I_{lim}-$Re^{7/12}$ dependence for the anodic branch of the curves shown in Fig. 7.

Table I. Values of the apparent standard rate constant for the system $Fe(CN)_6^{3-/4-}$ obtained by different methods as reported in the literature

Metal	Supporting electrolyte	Concentration* (mol/liter)	Technique	T (°C)	k_o (cm/sec)	Reference
Pt	1M KCl	10^{-2}	Current pulse	25	0.24	(1)
Pt	1M KCl	$\sim 5 \cdot 10^{-4}$	Faradaic impedance	20	0.09	(2)
Pt	0.5M K_2SO_4	10^{-2}	RDE	25	0.067	(3)†
Pt	0.5M K_2SO_4	$\sim 5 \cdot 10^{-4}$	Faradaic impedance	20	0.13	(2)
Au	0.1-10M KF	$5 \cdot 10^{-3}$	Coulostatic pulse	—	0.01 to 0.3	(4)‡
Au	1M KF	$3 \cdot 10^{-2}$-$2 \cdot 10^{-3}$	Potential step	—	0.037	(5)

* Bulk concentration of each component of the redox couple.
† Value calculated from the standard exchange current density, given in the reference, in A cm^{-2}.
‡ The values of k_o are dependent on the concentration of the supporting electrolyte.

Evaluation of the measurements.—The evaluation of the kinetic parameters, j_{oo} and α was performed according to the procedure already described. A computer program was used to calculate the parameter u and to fit the u-η values by a least squares method (20) in Eq. [5]. According to the dependence of the error $\Delta \ln u$ on the u and I_{rev} value (Eq. [13]), smaller statistical weights were given to the values at both extremes (high and low overpotentials) of the curve.

Results and Discussion

A semilogarithmic ln u-η plot of the experimental results for a gold electrode in KF as supporting electrolyte is shown in Fig. 9. The continuous curve corresponds to the fitted values. The error $\Delta \ln u$ was calculated with help of Eq. [13]. The random error ΔI was assumed to be given by the precision of the readings of the current-potential data on the millimeter paper of the X-Y recorder. To a first approximation $\Delta I = \pm \Delta r$ cm · scale factor, with Δr between 0.05 and 0.2. In Table II are included some values of u, I_{rev}, and ΔI used in Eq. [13] to calculate $\Delta \ln u$ for the curve shown in Fig. 9. The errors, represented by vertical traces on the experimental points, are larger at high and low overpotentials. Accordingly, smaller statistical weights were given to these points in the fitting procedure. The standard error for j_{oo} given in Fig. 9 is a measure for the deviation of the experimental values from the fitted curve for a single experiment. The reproducibility of the method can be better described by the standard deviation (14) of a set of different experiments.

In Table III the values of the standard exchange current density and transfer coefficient at Pt and Au electrodes are given for the two supporting electrolytes employed. The standard deviation reported in Table III indicates quite a good reproducibility of the data and a high precision of the method.

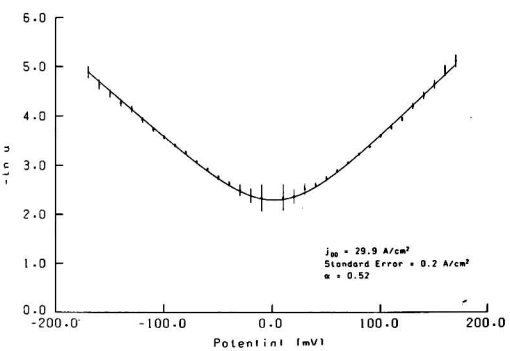

Fig. 9. Experimental ln u-η plots for $Fe(CN)_6^{3-/4-}$ at an Au ring electrode in turbulent pipe flow. $T = 20°C$, $c_{ox} = 2.2 \cdot 10^{-3}$M, $c_{red} = 2.5 \cdot 10^{-3}$M, 1M KF. The continuous line represents the fitted curve. The vertical traces represent the error, according to Eq. [13].

Table II. Parameters I_{rev}, u, and the estimated random error ΔI used in Eq. [10] to calculate the propagated error $\Delta \ln u$

mV	ΔI (μA)	I_{rev} (μA)	u (10^2)	$\Delta \ln u$
−170	± 0.23	134.69	0.759	0.120
−140	± 0.23	133.99	1.412	0.068
−110	± 0.23	131.77	2.412	0.044
−80	± 0.23	124.70	3.834	0.029
−50	± 0.45	103.83	6.390	0.049
−20	± 0.91	53.01	9.237	0.150
+20	± 0.91	56.28	9.352	0.150
+50	± 0.45	117.22	6.497	0.043
+80	± 0.23	144.58	3.997	0.026
+110	± 0.23	154.18	2.335	0.038
+140	± 0.23	157.25	1.221	0.066
+170	± 0.23	158.20	0.605	0.127

Table III. Values of the apparent standard rate constant, apparent standard exchange current density, and transfer coefficient measured with the ring electrode in turbulent pipe flow at 20°C. The standard deviation for a number N of experiments is also given.

Metal	Supporting electrolyte	k_o (cm sec^{-1})	j_{oo} (A cm^{-2})	α	N
Pt	1M KF	0.42	40 ± 6	0.48 ± 0.04	9
Pt	0.5M K_2SO_4	0.35	34 ± 4	0.51 ± 0.03	14
Au	1M KF	0.38	37 ± 4	0.47 ± 0.01	8
Au	0.5M K_2SO_4	0.27	26 ± 2	0.49 ± 0.03	11

In order to compare our results with those of the literature (Table I), we report in Table III the k_o values too. It is evident that with the RTP method we have obtained the highest values for the rate constant of the $Fe(CN)_6^{3-/4-}$ system reported up to the present.

In view of our previous theoretical analysis of the features of this technique in comparison to the RDE, it is obvious that such high reaction rates cannot be measured by the latter method, and the results reported in the literature reflect the enormous effect that small errors can produce when the RDE is used beyond the limits of its possibilities. In the case of the transient techniques for us, the question of the limit of validity remains open, and a revision of the results that have led to a mechanistic interpretation of the ferri-ferrocyanide reaction (4, 5, 21-23) seems to be necessary.

Acknowledgments

The authors are indebted to Professors W. Vielstich and J. W. Schultze for helpful discussions. Financial support by the Deutsche Forschungsgemeinschaft is gratefully acknowledged. This paper is dedicated to Professor W. Vielstich on the occasion of his 60th birthday.

Manuscript submitted Nov. 15, 1982; revised manuscript received May 25, 1983.

Universität Bonn assisted in meeting the publication costs of this article.

LIST OF SYMBOLS

A	electrode area
c^*	standard concentration in 10^{-3} mol/cm^3

c_{ox}, c_{red} bulk concentrations in mol/cm³
D diffusion coefficient
d ring electrode diameter
I experimental current
I_{lim}^a, I_{lim}^c anodic and cathodic limiting currents
I_k current for pure kinetic control
I_{rev} current for pure mass transfer control
j_o exchange current density
j_{oo} apparent standard exchange current density
k_o apparent standard rate constant
L electrode length
Re Reynolds number
u dimensionless parameter relating I to I_{rev}
ν kinematic viscosity
ω angular rotation speed

REFERENCES

1. P. H. Daum and C. G. Enke, *Anal. Chem.*, **41**, 653 (1969).
2. J. E. B. Randles and K. W. Somerton, *Trans. Faraday Soc.*, **48**, 937 (1952).
3. D. Jahn and W. Vielstich, *This Journal*, **109**, 849 (1962); W. Vielstich, Private communication.
4. L. M. Peter, W. Dürr, P. Bindra, and H. Gerischer, *J. Electroanal. Chem.*, **71**, 31 (1976).
5. V. Marecek, Z. Samec, and J. Weber, *ibid.*, **94**, 169 (1978).
6. H. P. van Leeuwen, *Electrochim. Acta*, **23**, 207 (1978).
7. Ch. Bernstein, A. Heindrichs, and W. Vielstich, *J. Electroanal. Chem.*, **87**, 81 (1978).
8. Ch. Bernstein and W. Vielstich, in "Electrode Processes," p. 350, The Electrochemical Society Softbound Proceedings Series, Princeton, NJ (1980).
9. J. Herrmann, Dissertation, Bonn (1983).
10. D. H. Angel and T. Dickinson, *J. Electroanal. Chem.*, **35**, 55 (1972).
11. W. Vielstich and W. Schmickler, "Elektrochemie II," Steinkopff Verlag, Darmstadt (1976).
12. L. N. Klatt and W. J. Blaedel, *Anal. Chem.*, **39**, 1065 (1967).
13. T. Iwasita, W. Schmickler, and J. W. Schultze, in "The Chemistry and Physics of Electrocatalysis," The Electrochemical Society Softbound Proceedings Series, Pennington, NJ (1983).
14. E. Hulzsch, Ausgleichs-Rechnung, Akademische Verlagsgesellschaft, Leipzig (1966).
15. Yu. U. Pleskov and V. Yu. Filinovskii, "The Rotating Disk Electrode," Consultants Bureau, New York (1976).
16. B. A. Coles, N. A. Hampson, A. T. Chadwick, and W. J. Albery, *J. Electroanal. Chem.*, **71**, 125 (1976).
17. R. Woods, in "Electroanalytical Chemistry," Vol. 9, A. J. Bard, Editor, Marcel Decker, New York (1976).
18. D. Dickertmann, J. W. Schultze, and K. J. Vetter, *J. Electroanal. Chem.*, **55**, 429 (1974).
19. A. A. Michri, A. G. Pschenichnikov, and R. Kh. Burshtein, *Elektrokhimiya*, **8**, 364 (1972).
20. D. W. Marquardt, *J. Soc. Industr. Appl. Math.*, **11**, 431 (1963).
21. R. Sohr and L. Müller, *Electrochim. Acta*, **20**, 451 (1975).
22. L. Müller and S. Dietzsch, *J. Electroanal. Chem.*, **121**, 255 (1981).
23. R. R. Dogonadze, J. Ulstrup, and Yu. Kharkats, *ibid.*, **39**, 47 (1972).

Standard Potentials of Li, Na, and K Electrodes and Transfer Free Energies of LiCl, NaCl, and KCl in Selected Ethanol-Water and Methanol-Water Solvents

J. Mazzarese and O. Popovych

Department of Chemistry, Brooklyn College of the City University of New York, Brooklyn, New York 11210

ABSTRACT

Standard potentials of the cell M(Hg)(l)|M^+, Cl^-|AgCl(s); Ag(s) (where M = Li, Na, and K) were determined at 25°C in a number of ethanol-water and methanol-water solvents, and the corresponding standard potentials of the M^+/M electrodes were calculated with the aid of literature data. The Li and Na cells were studied over the entire range of ethanol-water solvents at about 10 weight percent (w/o) intervals of solvent composition, but only in a limited number of methanol-water media. The K cell was studied only in ~ 30, 50, 70, 90, and 100 w/o methanol. For each of the solvent-electrolyte combinations, a function describing the mean ionic activity coefficients of MCl was obtained. Changes in the standard free energy of MCl upon transfer from water to each of the nonaqueous media were calculated from the E°'s. Variation of the transfer free energies with solvent composition was interpreted in terms of individual ionic contributions.

The long-term objective of research in this laboratory has been to study ion-solvent interactions in nonaqueous media, with particular emphasis on the determination of the transfer free energies of electrolytes and ions. The transfer free energy, $\Delta G^{\circ}_t(i)$, and the transfer activity coefficient (medium effect), $_m\gamma_i$, are commonly defined as follows

$$\Delta G^{\circ}_t(i) \equiv {}_sG^{\circ}_i - {}_wG^{\circ}_i = RT \ln {}_m\gamma_i \qquad [1]$$

where ${}_sG^{\circ}_i$ and ${}_wG^{\circ}_i$ are the (partial molal) standard free energies of the solute i in the nonaqueous solvent and in water, respectively. Transfer activity coefficients provide a quantitative correlation between equilibrium constants, rate constants, ion activity scales, and emf series in different solvents. The subject of correlating the energic properties of solutes in different solvents, including the methods of evaluating transfer activity coefficients, has been reviewed (1-3).

A common method of determining ΔG°_t values utilizes the standard potentials, E°, of electrodes reversible to the ions of interest. Recalling that for any electrode process, $\Delta G^{\circ} = -n\mathbf{F}\Delta E^{\circ}$, one can obtain, for example, the sum $[\Delta G^{\circ}_t(M^+) + \Delta G^{\circ}_t(Cl^-)]$ from the E°'s of cell I in water and given nonaqueous solvent

$$M(Hg)\,(l)\,|M^+, Cl^-|AgCl(s)\,;\,Ag(s) \qquad [I]$$

In the present study, the E°'s of cell I were determined in methanol-water and ethanol-water media using dropping amalgam electrodes, where M = Li, Na, and K. These measurements were carried out at intervals of about 10 w/o of each alcohol for those electrolyte-solvent combinations where literature data were either

Key words: electrode potentials, transfer free energies, lithium, sodium, potassium, methanol, ethanol, water.

unavailable or conflicting. The primary objective was to determine the transfer free energies of LiCl, NaCl, and KCl from water to each of the alcohol-water media. Furthermore, from emf measurements of cell I with amalgams of accurately known composition, the standard potentials of the M^+/M electrodes and an expression for the activity coefficients of MCl in each of the solvents were derived.

Analogous work using cell I with K(Hg) electrodes was already reported from this laboratory for the entire range of ethanol-water solvents (4). Here the studies using the K(Hg) electrode were extended to methanol-water mixtures containing about 30, 50, 70, 90, and 100 w/o methanol. Measurements of cell I with Na(Hg) and Li(Hg) electrodes were carried out over the entire range of ethanol-water solvents. In the methanol-water system, the Li(Hg) electrode was studied in water and in 30, 50, 70, 90, and 100 w/o methanol, while the Na(Hg) electrode was investigated only in 70 and 100 w/o methanol. For the methanol-water mixtures omitted from this study, the values of $\Delta G°_t$ of KCl, NaCl, or LiCl were already reported in the literature (5, 6). Values of $\Delta G°_t$ for KCl over the entire methanol-water range were determined previously in this laboratory by two different methods not involving amalgam electrodes (7); they were partially duplicated here because of a history of discrepancies among the literature values.

Experimental

Materials.—Anhydrous methanol was prepared by refluxing 4 liters of Fisher spectroanalyzed or Baker Photrex reagent absolute methanol over 21g of Al powder and 5g of $HgCl_2$ for 24 hr and then distilling through a 22 cm vigreux column, collecting the middle 3 liters. The purified methanol had a density of 0.7865 g/ml at 25°C, in agreement with the literature values of 0.78654 (8) and 0.7866 g/ml (9). The water was deionized with a specific conductance of (2-4) $\times 10^{-7}$ mho cm^{-1}. Methanol-water mixtures were prepared as previously described (10). Also the purification of ethanol, the preparation of ethanol-water mixtures, and that of the alkali-halide solutions were carried out as before (4). LiCl, NaCl, KCl, LiOH, NaOH, and KOH were all Fisher-certified ACS reagent grade and were dried before use.

Electrodes and measurements.—Amalgam electrodes were prepared by electrolysis of the corresponding 1m hydroxides employing a procedure described previously (4). The Li(Hg) contained 0.001-0.003 w/o Li; the Na(Hg), 0.01-0.02 w/o Na; and the K(Hg), 0.02-0.04 w/o K. The Ag-AgCl electrodes were of the thermal electrolytic type prepared by a procedure described by Bates (11). The voltages were measured with an Electro Scientific Instruments Model 330 potentiometer to ±0.1 mV. The apparatus and the measuring procedure were the same as described previously in great detail (4).

Results and Discussion

Standard electrode potentials and activity coefficients.—The potential E_I of cell I at 25°C is given by

$$E_I = E°_I + 0.05916 \log a_{M(Hg)} - 0.05916 \log a_{MCl} \quad [2]$$

where $E°_I = E°_{AgCl} - E°_{M(Hg)}$, referred to $E°_H = 0$ in the given solvent, $a_{M(Hg)}$ is the activity of the alkali metal in the amalgam, and a_{MCl} is the activity of the alkali-metal halide in solution. In order to evaluate $E°_I$ and the activity coefficients of MCl, it is convenient to define the quantity $E°'$

$$E°' = E°_I + 0.05916 \log a_{M(Hg)} \quad [3]$$

and to express the electrolyte activity in terms of its molality, m_{MCl}, the mean molal activity coefficient, $\gamma_\pm$, and the degree of dissociation, α. Upon rearrangement, Eq. [2] becomes

$$E_I + 0.1183 \log (\alpha m_{MCl}) = E°' - 0.1183 \log \gamma_\pm \quad [4a]$$

For purposes of extrapolation, it is now common practice (4, 7, 12) to express $\log \gamma_\pm$ as a polynominal in $I^{1/2}$, where I is the ionic strength. Then, $E°'$ is obtained as the intercept from a plot of the left-hand side of Eq. [4a] *vs.* $I^{1/2}$. In the present study, these plots were straight lines, indicating that the data could be adequately represented by Eq. [4b]

$$E_I + 0.1183 \log (\alpha m_{MCl}) = E°' + 0.1183\, A I^{1/2} \quad [4b]$$

Consequently, for each electrolyte-solvent combination, the constant A obtained from the slope of Eq. [4b] can be used to calculate the activity coefficients of MCl in the concentration range employed here by using the relationship $-\log \gamma_\pm = A I^{1/2}$. Values of $E°_I$ were calculated from those of $E°'$ and the literature data on amalgam activities with the aid of Eq. [3]. Complete ionic dissociation could be assumed for all of these solutions, except those of LiCl in 50-100% ethanol and of NaCl in 100% ethanol, which exhibited slight ion pairing. For these systems, the values of α required in Eq. [4b] were calculated from the literature values of the ion pair association constants (13-15). The ranges of the α's involved are indicated in the footnotes of Tables I and II. The calculations were carried out on an IBM 370-145 computer.

A fundamental quantity in electrochemistry is the standard potential of an alkali-metal electrode, $E°_M$. It is the standard potential of the cell

$$Pt; H_2(g) | H^+ || M^+ | M(s) \quad [II]$$

which cannot be determined directly in solvents that react with alkali metals, but is evaluated by combining the $E°$'s of cells I, III, and IV

$$M(Hg)\ (1) | M^+ \text{ (inert solvent)} | M(s) \quad [III]$$

$$Pt; H_2(g) | H^+, Cl^- \text{ (given solvent)} | AgCl(s); Ag(s) \quad [IV]$$

It is obvious that

$$E°_M = E°_{III} + E°_{IV} - E°_I \quad [5]$$

From the standard potentials $E°_I$ determined in this study, the authors calculated the values of $E°_{Li}$, $E°_{Na}$, and $E°_K$ in each of the solvents with the aid of Eq. [5] by using the relevant literature data for $E°_{III}$ and $E°_{IV}$.

Table I summarizes the results derived from the emf of Li(Hg)—Ag-AgCl cell in solutions of LiCl. Each $E°_I$ was calculated via Eq. [3] from an experimentally determined $E°'$ using literature values (16) for the activity coefficients of Li in its amalgams and $E°_{III} = -0.8480$V, which was determined for the Li cell containing propylene carbonate as the inert solvent (17). Throughout this study, values of $E°_{IV}$ were interpolated for the exact solvent compositions from large-scale graphs of literature data for ethanol-water (18-24) and methanol-water (20, 25-29) solvents.

Table II summarizes the results derived from the emf of the Na(Hg)—Ag-AgCl cells in solutions of NaCl. Since the activities of Na in its amalgams as reported by Bent and Swift (30) are referred to sodium metal (rather than to an infinitely dilute amalgam) as the standard state, the experimentally determined $E°'$ values were converted directly to the tabulated quantity $(E°_{III} - E°_I)$, rather than to $E°_I$.

Table III lists the results derived from the emf of K(Hg)—Ag-AgCl cells in solutions of KCl. The amalgam actvities required to convert $E°'$ to $E°_I$ were interpolated from the data of Armbruster and Crenshaw (31). For the potassium cell, $E°_{III} = -0.9521$V, as reported from this laboratory previously (4), based on the data of Lewis and Keyes (32).

The results in Tables I-III were subjected to a complete error analysis from which the following absolute precisions of the $E°$'s of the alkali-metal electrodes were calculated by the method of propagation of errors. Most of the $E°_M$ values are precise to 0.001V. A pre-

Table I. Results derived from the emf of cell Li(Hg)(I) | Li^+, Cl^- | AgCl(s); Ag(s)*

Solvent	Eq. [4b] A	Eq. [4b] $E^{\circ\prime}$	E°_{I}	E°_{IV}	Eq. [5] E°_{Li}	Eq. [1] ΔG°_t(LiCl) kcal/mol	Eq. [1] ($\log m\gamma_{Li} + \log m\gamma_{Cl}$) (molal scale)
Water	0.475	2.2192	2.4126	0.22234	−3.0383	0	0
	0.533	2.2184	2.4139	0.22234	−3.0386	0	0
	0.487	2.2314	2.4135	0.22234	−3.0392	0	0
	0.467	2.2319	2.4135	0.22234	−3.0392	0	0
w/o Ethanol							
10.0	0.968	2.1900	2.3920	0.2146	−3.025	0.493	0.362
20.1	1.060	2.1765	2.3737	0.2074	−3.014	0.915	0.671
30.4	1.066	2.1708	2.3536	0.2001	−3.002	1.379	1.011
40.3	1.107	2.1350	2.3364	0.1934	−2.991	1.775	1.302
49.9	1.010	2.1297	2.3197	0.1848	−2.983	2.160	1.584
60.3	0.927	2.0845	2.2992	0.172	−2.975	2.633	1.930
70.3	1.491	2.0762	2.2680	0.155	−2.961	3.35	2.46
80.4	1.144	2.0454	2.231	0.127	−2.952	4.20	3.08
90.4	1.798	1.9752	2.181	0.088	−2.942	5.35	3.92
100.0	3.338	1.9102	2.087	−0.081	−3.016 [−3.042(33)]	7.53	5.52
w/o Methanol							
30.0	0.585	2.1748	2.3747	0.2031	−3.020	0.892	0.654
50.3	0.652	2.1301	2.3429	0.1904	−3.001	1.625	1.192
69.3	0.678	2.1081	2.3148	0.1684	−2.994	2.273	1.667
90.0	1.486	2.0713	2.2716	0.1135	−3.006	3.269	2.397
100.0	1.522	2.0581	2.2368	−0.0101	−3.095 [−3.653(34), −3.045(35), −3.0845(36)]	4.07	2.985

* All E° values are in volts. $E^\circ_{III}(Li) = -0.8480V$ (17). The concentration range of LiCl was generally 0.02-0.05 or 0.06m. In the ethanol-water system, the α range was 0.88-0.92 in 100% ethanol, 0.90-0.93 in 90.4%, 0.92-0.94 in 80.4%, 0.94-0.95 in 70.3%, 0.94-0.96 in 60.3%, 0.96-0.97 in 49.9%.

Table II. Results derived from the emf of cell Na(Hg)(I) | Na^+, Cl^- | AgCl(s); Ag(s)*

Solvent	Eq. [4b] A	Eq. [4b] $E^{\circ\prime}$	($E^\circ_{III} - E^\circ_{I}$)	E°_{IV}	Eq. [5] E°_{Na}	Eq. [1] ΔG°_t(NaCl) kcal/mol	Eq. [1] ($\log m\gamma_{Na} + \log m\gamma_{Cl}$) (molal scale)
w/o Ethanol							
10.0	0.494	1.9927	−2.9157	0.2145	−2.701	0.457	0.335
20.4	0.443	1.9627	−2.8953	0.2072	−2.688	0.927	0.680
30.8	0.535	1.9398	−2.8715	0.1998	−2.672	1.476	1.082
40.6	0.647	1.9202	−2.8491	0.1932	−2.656	1.992	1.460
50.5	0.795	1.8935	−2.8232	0.1842	−2.639	2.589	1.898
60.6	0.833	1.8706	−2.7972	0.171	−2.626	3.189	2.338
69.9	0.939	1.8394	−2.7640	0.157	−2.607	3.954	2.899
80.0	0.946	1.7896	−2.7249	0.128	−2.597	4.856	3.560
90.5	2.14	1.7118	−2.644	0.087	−2.557	6.73	4.93
100.0	2.83	1.6299	−2.562	−0.081	−2.643 [−2.657(33), −2.646(37)]	8.62	6.32
w/o Methanol							
69.8	0.804	1.8678	−2.7953	0.1686	−2.627	3.232	2.370
100.0	1.390	1.7908	−2.7157	−0.0101	−2.726 [−2.7152(34), −2.7132(34), −2.728(38)]	5.068	3.715

* All E° values are in volts. The concentration range of NaCl was generally 0.02-0.05 or 0.06m, except in 100% ethanol where it was 4×10^{-3}—1×10^{-2}m. In ethanol, the α range was 0.97-0.98.

Table III. Results derived from the emf of cell K(Hg)(I) | K^+, Cl^- | AgCl(s); Ag(s)*

Solvent w/o Methanol	m range of KCl	Eq. [4b] A	Eq. [4b] $E^{\circ\prime}$	E°_{I}	E°_{IV}	Eq. [5] E°_{K}	Eq. [1] ΔG°_t(KCl) kcal/mol	Eq. [1] ($\log m\gamma_{K} + \log m\gamma_{Cl}$) (molal scale)
28.9	0.01-0.06	0.582	1.9761	2.1399	0.2037	−2.888	1.229	0.901
49.7	0.01-0.1	0.547	1.9335	2.0994	0.1908	−2.861	2.163	1.586
70.1	0.02-0.07	0.867	1.8779	2.0490	0.1682	−2.833	3.325	2.438
90.6	0.02-0.05	1.080	1.8413	1.9933	0.1096	−2.836	4.609	3.379
100.0	0.018-0.044	1.271	1.8012	1.966	−0.0101	−2.928 [−2.9116(34), −2.9362(36), −2.933(39)]	5.238	3.840

* All E° values are in volts. $E^\circ_{III}(K) = -0.9521V$ (4).

cision of 0.002V was found for E°_{Li} in 80.4, 90.4, and 100.0% ethanol and in 100.0% methanol, as well as for E°_{Na} in 90.5 and 100.0% ethanol. In another test of the precision and also of the accuracy of our results, the E°_{Li} in water was determined four times using different amalgam concentrations. The four results (shown in Table I) gave an average $E^\circ_{Li} = -3.0388 \pm 0.0004V$. Modern literature values of E°_{Li} in water are −3.0401 (33) and −3.0431V (17). Literature values of the E°'s of the alkali metals in the anhydrous alcohols are included in the tables for comparison with these results.

Transfer free energies.—The changes which the standard free energies of the alkali-metal chlorides experience upon transfer of the electrolytes from water to the alcohol-water mixtures, $\Delta G°_t$, and the corresponding transfer activity coefficients, log $_m\gamma$, are compiled in the last two columns of Tables I-III. The quantity (log $_m\gamma_M$ + log $_m\gamma_{Cl}$) was calculated from the corresponding $E°$'s of cell I in water, $_wE°_I$, and the nonaqueous solvent, $_sE°_I$, at 25°C using the equation

$$\log {}_m\gamma_M + \log {}_m\gamma_{Cl} = \frac{{}_wE°_I - {}_sE°_I}{0.05916} \qquad [6]$$

$\Delta G°_t$ and log $_m\gamma$ are related via Eq. [1].

As pointed out in the introduction, most of the present work in methanol-water media was complementary in nature, *i.e.*, designed to fill the gaps in the existing data on $\Delta G°_t$ of alkali-metal halides. Intentional duplication of literature data was carried out only for KCl in the methanol-water system, where serious discrepancies have existed among some of the reported values. In order to compare our results with those from other sources, minor graphical interpolation to integral solvent composition was usually necessary. The existing data on the $\Delta G°_t$ of KCl from water to methanol-water solvents are compared in Table IV. While agreement among different laboratories and techniques is good in the middle range of methanol-water composition, it is less than satisfactory at both extremes of the solvent scale. Based on the method of propagation of errors, the precision of the $\Delta G°_t$ values should be no worse than 0.01 kcal/mol for most systems and of the order of 0.02 kcal/mol for some media of high alcohol content. The complementary data on $\Delta G°_t$ of LiCl and NaCl obtained in methanol-water media fit well on the curves (not shown here) of existing literature data (5, 6) as a function of solvent composition. The values of $\Delta G°_t$ for LiCl, NaCl, and KCl in the alcohol-water media experience a monotonous increase with increasing alcohol content in the mixed solvent.

Additional insight into the ion-solvent interactions that determine the variation of $\Delta G°_t$(MCl) as a function of solvent composition can be gained by apportioning the corresponding transfer activity coefficients into their individual ionic contributions. Here, this can be done only for the ethanol-water system, for which transfer activity coefficients of the chloride ion, log $_m\gamma_{Cl}$, have been estimated (40) by the well-known tetraphenylborate assumption. In this assumption, log $_m\gamma$ of the tetraphenylborate anion is set equal to that of the tetraphenylarsonium or the tetraphenylphosphonium cation and the log $_m\gamma$ values for all other ions are calculated on that basis (2, 3). Table V shows the quantities (log $_m\gamma_{Li}$ + log $_m\gamma_{Cl}$) and (log $_m\gamma_{Na}$ + log $_m\gamma_{Cl}$) determined in this study (interpolated to integral solvent composition), the literature values of log $_m\gamma_{Cl}$) determined in this study (interpolated to obtained by difference. The variation of the ionic transfer activity coefficients in ethanol-water media is depicted in Fig. 1. A positive log $_m\gamma$ means that the ion exists in a lower energy state in water (more favorable solvation) than in the nonaqueous medium and vice versa. The behavior of the log $_m\gamma$ of ions as a function of ethanol-water composition depicted in Fig. 1 can be analyzed in terms of a superimposition of two types of major ion-solvent interactions. These are (*i*) the nonspecific long-range interactions and (*ii*) specific chemical interactions in the primary solvation shell. Long-range electrostatic interactions, the magnitude of which has been traditionally estimated from the Born charging equation, make a positive contribution to log $_m\gamma$ of all ions transferred from water to solvents of lower dielectric constant, as can be seen from Eq. [7]

$$\log {}_m\gamma(\text{Born}) = \frac{121.6}{r}\left[\frac{1}{{}_sD} - 0.0128\right] \qquad [7]$$

where r is the ionic radius in angstroms and $_sD$ is the dielectric constant of the nonaqueous solvent. Because this contribution increases as the dielectric constant of the medium decreases, all curves in Fig. 1 would exhibit a continuous rise if Born charging were the major governing energy term. Among the ions represented in Fig. 1, only Na^+ follows very roughly the type of function predicted by the Born equation, since it is an ion which is relatively free of specific solvent interactions in contrast to Li^+ and Cl^- ions for which there is evidence of significant contributions from

Table IV. Standard free energies of transfer for potassium chloride from water to methanol-water solvents, $\Delta G_t°$ (kcal/mol, molal scale) in 25°C

w/o Methanol	This study	Ref. (5)	Ref. (6)[1]	Ref. (7) From solubility[2]	Ref. (7) From emf	Ref. (34)
10		0.407	0.413	0.250	0.281	
20		0.837	0.844	0.690	0.554	
30	1.277			1.22	1.22	
40		1.723	1.739	1.65	1.65	
50	2.179			2.15	2.15	
60		2.732	2.75	2.74	2.74	
70	3.320			3.26	3.26	
80		3.974	3.97	3.98	3.93	
90	4.574			4.65	4.65	
99		5.160		5.25	5.75	
100	5.238			5.31	5.90	5.056

[1] Calculated in Ref. (5) from data in Ref. (6). [2] Calculated from the solubility of KCl in water and the methanol-water solvents. [3] Calculated from the emf of a cell composed of a K-glass electrode and a calomel electrode.

Table V. Transfer activity coefficients of LiCl, NaCl, and of the individual ions in ethanol-water solvents

w/o Ethanol	(log $_m\gamma_{Li}$ + log $_m\gamma_{Cl}$)	(log $_m\gamma_{Na}$ + log $_m\gamma_{Cl}$)	log $_m\gamma_{Cl}$(40)	log $_m\gamma_{Li}$	log $_m\gamma_{Na}$
10.0	0.362	0.330	0.05	0.31	0.28
20.0	0.668	0.666	0.19	0.48	0.48
30.0	0.999	1.050	0.43	0.57	0.62
40.0	1.294	1.436	0.79	0.50	0.65
50.0	1.587	1.876	1.24	0.35	0.64
60.0	1.920	2.313	1.59	0.33	0.72
70.0	2.44	2.906	1.98	0.46	0.93
80.0	3.06	3.560	2.24	0.82	1.32
90.0	3.89	4.87	2.67	1.22	2.20
100.0	5.52	6.32	3.45	2.07	2.87

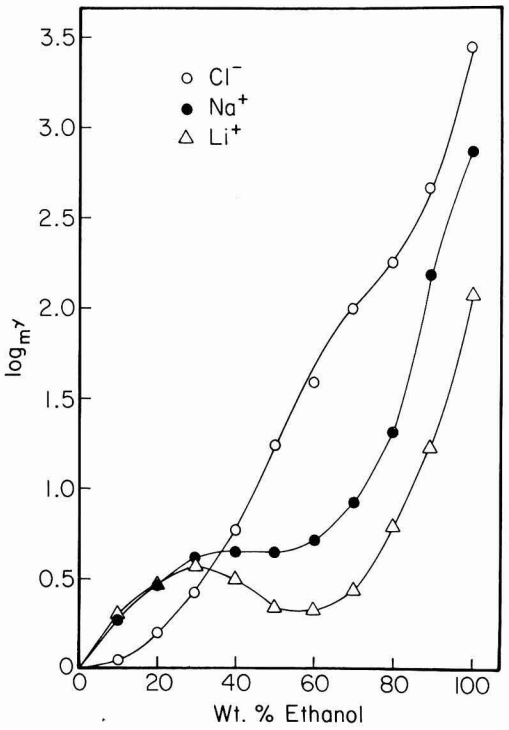

Fig. 1. Transfer activity coefficients of ions in ethanol-water solvents.

short-range ion-solvent interactions. The data for log $_{m}\gamma_{K}$, though available from our previous study (40), were not included in Fig. 1 because they would almost overlap the log $_{m}\gamma_{Na}$ curve. Hydration of the Cl^- ion is known to be reinforced through hydrogen bonding to water molecules. Since the relative H-bonding ability of water is superior to that of ethanol and its mixtures, the transfer of Cl^- from water to these media is energetically disfavored, leading to even more positive values of log $_{m}\gamma_{Cl}$ than would be expected on the grounds of lower dielectric constants alone. More interesting, however, is the behavior of log $_{m}\gamma_{Li}$, which first rises at low ethanol contents, then drops to a minimum in the middle range of solvent composition and finally rises again steeply in the ethanol-rich region. It is noteworthy that the above pattern parallels the behavior of the transfer activity coefficient of the hydrogen ion, log $_{m}\gamma_{H}$, in ethanol-water media, which was already reported from this laboratory (40). The appearance of the minimum in log $_{m}\gamma_{H}$ roughly in the middle range of ethanol-water composition was interpreted (3, 40) in terms of changes in the solvent structure that produce an ethanol-water mixture of maximum basicity. This corresponds to a minimum in log $_{m}\gamma_{H}$, which has the value of −0.86 at 70 w/o ethanol (40). While in the case of the Li^+ ion, the minimum occurs at a positive value of log $_{m}\gamma_{Li}$ (0.33), meaning that water is still the preferred solvator for Li^+ (and that $H^+$is a stronger acid than Li^+), the extent to which log $_{m}\gamma_{Li}$ is lowered relative to "normal" behavior, such as approximated by Na^+, indicates that specific acid-base-type interactions between Li^+ and ethanol-water solvents do make a significant contribution. The Li^+-solvent interaction involved here is of the type usually referred to as lone pair donation from the oxygens of the solvent molecules and it increases with the donor ability (basicity) of the solvent. It is not surprising that this specific interaction is greatest for the smallest cation, Li^+ (r = 0.60Å), which has the highest charge density, and significantly less pronounced for the larger cations, Na^+ (r = 0.95Å) and K^+ (r = 1.33Å) (K^+—not shown here) with log $_{m}\gamma_{Na}$ and log $_{m}\gamma_{K}$ exhibiting plateaus rather than minima in the middle range of ethanol-water composition.

The interesting maximum in the log $_{m}\gamma_{Li}$ at low ethanol content also mirrors its counterpart in log $_{m}\gamma_{H}$ (40). This maximum is believed to occur in a region where water structure has been reinforced by the presence of small amount of ethanol. The transfer of a strongly interacting ion like Li^+ from water to a solvent that is even more structured is enthalpically disfavored (3), leading to a positive contribution to log $_{m}\gamma_{Li}$.

This qualitative interpretation of ionic solvation is obviously far from complete. Significant contributions to transfer free energies can be expected to originate also from ion-dipole, ion-quadrupole, dispersion, and nonelectrostatic interactions, to name just the major components of solvation energy. Unfortunately, present knowledge of the structure of nonaqueous (including mixed) solvents and of the parameters that govern ionic solvation in them is too limited to attempt a more ambitious interpretation.

Acknowledgment

This research was supported in part by Grant 13681 from the PSC-CUNY Research Award Program of the City University of New York.

Manuscript submitted Feb. 28, 1983; revised manuscript received May 19, 1983.

REFERENCES

1. O. Popovych, *Crit. Rev. Anal. Chem.*, **1**, 73 (1970).
2. O. Popovych, in "Treatise on Analytical Chemistry," Part I, Vol. I, 2nd ed., I. M. Kolthoff and P. J. Elving, Editors, Chapter 12, Wiley-Interscience, New York (1978).
3. O. Popovych and R. P. T. Tomkins, "Nonaqueous Solution Chemistry," Chapter 5, John Wiley and Sons, New York (1981).
4. A. J. Dill, L. M. Itzkowitz, and O. Popovych, *J. Phys. Chem.*, **72**, 4580 (1968).
5. D. Feakins and P. J. Voice, *J. Chem. Soc.*, 1390 (1972).
6. G. Akerlof, *J. Am. Chem. Soc.*, **52**, 2353 (1930).
7. L. Malahias and O. Popovych, *J. Chem. Eng. Data*, **27**, 105 (1982).
8. V. A. Griffith, *J. Chem. Soc.*, 860 (1954).
9. R. G. Bates and R. A. Robinson, in "Chemical Properties of Ionic Solutions," B. E. Conway and R. G. Barradas, Editors, Chapter 12, John Wiley and Sons, New York (1966).
10. P. J. LaBrocca, R. Phillips, S. S. Goldberg, and O. Popovych, *J. Chem. Eng. Data*, **24**, 215 (1979).
11. R. G. Bates, "Determination of pH," p. 281, John Wiley and Sons, New York (1964).
12. D. Sen, D. A. Johnson, and R. N. Roy, *J. Phys. Chem.*, **71**, 1523 (1967).
13. A. J. Dill and O. Popovych, *J. Chem. Eng. Data*, **14**, 156 (1969).
14. R. L. Kay, *J. Am. Chem. Soc.*, **82**, 2099 (1960).
15. H. O. Spivey and T. Shedlovsky, *J. Phys. Chem.*, **71**, 2165 (1967).
16. P. Longhi, S. Rondini, S. Ardizzone, and T. Mussini, *Ann. Chim.*, **67**, 177 (1977).
17. S. Rondini, P. Longhi, and T. Mussini, *ibid.*, **67**, 305 (1977).
18. A. Patterson and W. A. Felsing, *J. Am. Chem. Soc.*, **64**, 1478 (1942).
19. H. S. Harned and D. S. Allen, *J. Phys. Chem.*, **58**, 191 (1954).
20. I. T. Oiwa, *ibid.*, **60**, 754 (1956).
21. G. Scatchard, *J. Am. Chem. Soc.*, **48**, 2026 (1926).
22. H. S. Harned and M. E. Fleyscher, *ibid.*, **47**, 82 (1929).
23. K. Schwabe and M. Kunz, *Z. Elektrochem.*, **64**, 1188 (1960).
24. H. Taniguchi and G. J. Janz, *J. Phys. Chem.*, **61**, 688 (1957).

25. H. S. Harned and H. C. Thomas, *J. Am. Chem. Soc.*, **57**, 1666 (1935).
26. R. G. Bates, M. Paabo, and R. A. Robinson, *Anal. Chem.*, **37**, 462 (1965).
27. R. G. Bates and D. Rosenthal, *J. Phys. Chem.*, **67**, 1088 (1963).
28. R. A. Robinson and R. H. Stokes, "Electrolyte Solutions," p. 470, Buttersworth, London (1959).
29. B. E. Conway, "Electrochemical Data," Elsevier, Amsterdam (1952).
30. H. E. Bent and E. Swift, Jr., *J. Am. Chem. Soc.*, **58**, 2216 (1936).
31. M. H. Armbruster and J. L. Crenshaw, *ibid.*, **56**, 2525 (1934).
32. G. N. Lewis and F. G. Keyes, *ibid.*, **34**, 119 (1912).
33. A. McFarlane and H. Harley, *Phil. Mag.*, **13**, 425 (1932).
34. M. Solomon, "Physical Chemistry of Organic Solvent Systems," A. K. Covington and T. Dickinson, Editor, Ch. 2, Part 2, Plenum Press, London (1973).
35. H. Hartley and A. McFarlane, *Phil. Mag.*, **10**, 611 (1935).
36. A. M. Shkodin and L. Ya. Shapovalova, *Izv. Vyssh. Ucheb. Zaved. Khim. Tekhnol.*, **9**, 563 (1966).
37. N. A. Izmaylov and E. F. Ivanova, *Zh. Fiz. Khim.*, **29**, 1614 (1955).
38. P. S. Buckley and H. Hartley, *Phil Mag.*, **8**, 320 (1929).
39. K. Bräuer and H. Strehlow, *Z. Phys. Chem., N.F.*, **17**, 346 (1958).
40. O. Popovych, A. Gibofsky, and D. H. Berne, *Anal. Chem.*, **44**, 811 (1972).

Effect of Carbon on the Reactivity of Lithium with SO_2 and $SOCl_2$ Battery Electrolytes

Stanley D. James,* Patricia H. Smith,* and William P. Kilroy*

Electrochemistry Branch, Naval Surface Weapons Center, Silver Spring, Maryland 20910

ABSTRACT

The normal inertness of lithium to $SOCl_2$ and SO_2 battery electrolytes changes dramatically if the Li has first been ground with carbon black. Spontaneous ignition on mixing then becomes common, especially with $SOCl_2$ electrolyte. We examined the effect of the nature and proportion of carbon in Li-C grinds on their reactivity. We concluded that the carbon's external surface area acting via local electrochemical cells is crucial to its catalytic activity.

Recent investigations in our laboratory indicate that carbon black, which is the cathode substrate for most primary lithium cells, may act as a powerful catalyst for the reaction of lithium with thinoyl chloride or sulfur dioxide. It is known that lithium is relatively inert to the $SOCl_2$ or SO_2 battery electrolytes. This is due to the formation of a protective film which prevents continuing reaction while allowing discharge to proceed via mobile Li ions. However, the presence of carbon results in an increased activation of the reaction between lithium and the battery oxidant (1, 2). This effect may generate potentially hazardous situations with lithium batteries. In an attempt to study the behavior of various carbon blacks, a qualitative and quantitative (calorimetric) investigation of the reactivity of thionyl chloride or sulfur dioxide electrolytes with intimate mixtures of carbon and lithium was undertaken.

Experimental

Qualitative studies were performed in a Dry Room ($< 0.5\%$ relative humidity) by measuring the relative reactivity of lithium-carbon mixtures with $SOCl_2$ or SO_2 electrolyte. The mixture reactivity was assessed using the following qualitative scale: (A) no reaction, (B) electrolyte boiled, (C) sparks observed, or (D) spontaneous ignition.

Weighed amounts (7 mg) of lithium (99.9% Foote Mineral) and carbon (outgassed at 120°C for two days) were vigorously ground in a Pyrex ignition tube (Corning No. 9860-10) using the flame-polished end of a Pyrex rod. The uniform black, compacted mass thus produced was broken up with a stainless steel spatula and the process was repeated once or twice more till the mixture appeared homogeneous. The grinding procedure took about 10 min at which time the reactivity was recorded after adding 70 μl of electrolyte. A 1.6M $LiAlCl_4$-$SOCl_2$ electrolyte was prepared by adding Polaroquality $LiAlCl_4$ to $SOCl_2$ (J. T. Baker) that had been refluxed under argon for 20 hr with lithium followed by distillation under argon. The SO_2 electrolyte was 72.8, 18.2, and 8.9 weight percent (w/o) in SO_2, CH_3CN, and $LiAsF_6$, respectively. It was prepared by Honeywell Power Sources Incorporated, Horsham, Pennsylvania and is referred to as "reserve electrolyte."

A quantitative investigation of the carbon-catalyzed Li-$SOCl_2$ electrolyte reaction was accomplished by measuring the heat liberated when Li-C mixtures were added to 1.5M $LiAlCl_4$-$SOCl_2$ electrolyte (obtained from Lithium Corporation of America) in a calorimeter under an inert argon atmosphere. Samples were prepared by grinding carbon (outgassed at 100°C) and lithium (1:1 weight ratio) with a glass mortar and pestle in a helium glove box. The compacted mass which was produced was broken up with a stainless steel spatula and the process repeated for approximately 15 min until the Li-C particles were no larger than 2-3 mm in diameter. Between 30-60 mg of this mixture were accurately weighed into a glass ladle and set inside the head of the calorimeter (Fig. 1). The body of the calorimeter contained 25 $\pm$ 1 ml of electrolyte and a Teflon-coated stirring bar. After the calorimeter was assembled, the entire apparatus was insulated with a ½ in. layer of Fiberfrax then wrapped with several layers of Al foil. When the calorimeter had reached thermal equilibrium, the ladle was lowered into the stirred $SOCl_2$-$LiAlCl_4$ solution and the temperature change recorded. Calibration of the system was accomplished at the end of each run by determining the quantity of electrical work ($i \times V \times t$) required to yield a comparable increase in temperature. During this process a d-c current, i, of 2.5A, was passed through the heating coil during a known time interval, t, while the potential, V, across the heating coil was recorded. The heat capacity of the system was found to be constant from run to run.

* Electrochemical Society Active Member.
Key words: battery, carbon, catalysis, cathode.

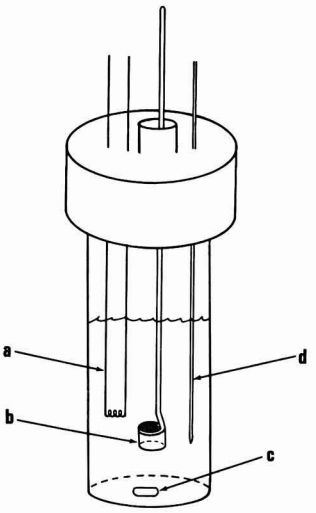

Fig. 1. Schematic diagram of Teflon calorimeter, (a) heater, chromel A; (b) Pyrex sample ladle with stainless steel mesh lid; (c) Teflon-coated stirrer; (d) Chromel-Alumel thermocouple.

Results and Discussion

A recent differential scanning calorimeter (DSC) study revealed that carbon black catalyzes reactions of Li with battery oxidant (1). The mixtures were highly reactive with an unpredictable initiation temperature, indicating that carbon greatly enhances the reactivity of Li with $SOCl_2$ or SO_2 battery electrolytes. The results of the present study reaffirm these observations.

Qualitative study.—Table I summarizes the effect of carbon content on the average reactivity of ground Li-C mixtures with SO_2 reserve electrolyte and $SOCl_2$ electrolyte. Each entry averages the results of 3 to 5 tests. It was observed that traces of carbon are insufficient to activate the lithium-oxidant reaction. Only when the carbon content of Li-C mixes rose above approximately 12 and 40 w/o, respectively, for the $SOCl_2$ and SO_2 electrolytes, was perceptible energy liberated. Of the two electrolytes, the $SOCl_2$ electrolyte was substantially more reactive; spontaneous ignition routinely occurred above about 25 w/o carbon. Spontaneous ignition occasionally occurred with SO_2 electrolyte above 60% carbon but this is not apparent in Table I which depicts only average reactivities. For both electrolytes, decreasing carbon content led to a fall in spontaneous flammability.

Several other variables were qualitatively examined. Investigations on the degree of mixing Li and C revealed that mixtures activated by some grinding or by hammering the Li and C together were substantially more reactive to $SOCl_2$ or SO_2 electrolyte than mixtures of Li and C that were merely "pressed." Pressed mixtures containing 50-91% carbon only warmed the $SOCl_2$ electrolyte (class B). This contrasts with the far greater reactivity of ground mixtures where typical reactivities were found to belong to class D. Ground mixtures were also found to be far more reactive than pressed mixtures to SO_2 reserve electrolyte.

Table I. Reactivity of Li-C ground mixtures with 1.6M $LiAlCl_4$-$SOCl_2$

Li/C ratio	w/o C	SO_2 reactivity	$SOCl_2$ reactivity
0.1	91	Class C	Class D
0.5	67	Class C	Class D
1.0	50	Class B	Class D
1.5	40	Class B	Class D
2.0	33	Class A	Class D
2.5	29	Class A	Class D
3.0	25	—	Class D
4.0	20	—	Class C
5.0	17	—	Class B
7.0	12	—	Class B
8.0	11	—	Class A
9.0	10	—	Class A

Class A; no reaction; class B; electrolyte boiled; class C; sparks observed; class D; spontaneous ignition.

Further studies were performed to determine what effect the SO_2 concentration and the nature of the conducting salt might have on the reactivity of 1:1 (by weight) Li-C mixtures with SO_2. Eight tests conducted on each of LiBr and $LiAsF_6$-sulfur dioxide battery electrolyte, revealed no divergence from a class B reactivity. As the SO_2 concentration in the electrolyte decreased from 14M SO_2, the observed reactivity similarly decreased to the point where very dilute SO_2 solutions were no more reactive than AN or AN-$LiAsF_6$ solutions totally free of SO_2.

We compared the reactivities of ground 1:1 Li-C mixtures with (*i*) various distillate fractions of $SOCl_2$ and (*ii*) 1.6M $LiAlCl_4$-$SOCl_2$ (Polaroquality salt) *vs.* 1.6M $AlCl_3$ in $SOCl_2$ saturated with LiCl. No noticeable difference in reactivity was observed in either case, with the exception that the LiCl-saturated solutions were more reactive (class D) than the $LiAlCl_4$ solutions (class A) with Li-C mixtures containing 12 w/o carbon.

The effect of omitting salt from the electrolyte was studied. Pressed Li-C mixtures (50% carbon) consistently (6 tests out of 6) caused $LiAlCl_4$-$SOCl_2$ to boil (class B), whereas they were totally (4 tests out of 4) unreactive to salt-free $SOCl_2$. Ground mixtures were equally reactive (class D) whether salt was present or absent. As the carbon content of the ground Li-C mixtures decreased, the reactivity to salt-free $SOCl_2$ decreased until at 13% carbon, the mixtures appeared totally inert.

Quantitative study.—The reactivity of 1:1 (by weight) ground mixtures of lithium and carbon with $SOCl_2$ electrolyte was quantitatively measured under an inert helium atmosphere. Table II summarizes the calorimetric data together with various physical and chemical parameters of the carbons investigated. As the particle size decreases or the BET surface area of the carbon blacks increases (Fig. 2), the reactivity of the Li-C mixtures with $SOCl_2$ electrolyte increases. This is not entirely unexpected as an increase of activity with carbon black surface area has been observed in other reactions (3). However, surface area or particle size is critical, as indicated by the apparent nonreactivity of the Sterling FT carbon black (15 m^2/g) which contrasts with the sudden rise in reactivity with a relatively small increase in surface area. Conflicting trends in Table II show that degree of crystallinity is not a controlling factor though it may have secondary importance. The similar unreactivity of Sterling and Superior Graphite 9039 correlates with their similar surface area rather than with their very different crystallinity. On the other hand, the amorphous Monarch 1300 was significantly more reactive than the crystalline Superior Graphite 9042 though their areas were very close. Thus crystallinity seems to confer some degree of inertness. It should be noted that the lithium/carbon black ground mixtures were solid black masses whereas a similar mixture of lithium with the Superior Graphite 9039 yielded a golden metallic material, similar in appearance to LiC_6 and showed no evidence of dispersed carbon particles.

Shawinigan carbon black containing Teflon was ground with lithium and its average reactivity with $SOCl_2$ electrolyte was compared to the average reactivity without Teflon. The presence of Teflon enhanced the exothermicity by approximately 56%. The heats of reaction listed in Table II are much smaller than

Table II. Effect of carbon type on the reactivity of Li-C ground mixtures (50 w/w %) with 1.5M $LiAlCl_4$-$SOCl_2$

Carbon (manufacturer)	Type	Particle size (mμ)	Carbon purity (%)	B.E.T. surface area (m^2/g)	Reactivity (calories/g mixture)	2σ (number of runs)
Sterling FT (Cabot)	Carbon black	180[a]	99.5[a]	15[a]	0	0 ($n = 4$)
Shawinigan (Gulf Oil)	Carbon black	42[b]	99.5[b]	60[b]	3550	616 ($n = 4$)
Elftex 12 (Cabot)	Carbon black	37[c]	99.0[c]	47[d]/43[c]	3984	875 ($n = 3$)
Vulcan 6 (Cabot)	Carbon black	22[a]	99.0[a]	119[a]	4311	166 ($n = 3$)
Monarch 700 (Cabot)	Carbon black	18[c]	98.5[c]	200[c]	5190	714 ($n = 4$)
Monarch 1300 (Cabot)	Carbon black	13[c]	90.5[c]	560[c]	7456	880 ($n = 4$)
9039 (Superior Graphite)	Synthetic graphite	5000[e]	—	16[d]	0	— ($n = 2$)
9042 (Superior Graphite)	Synthetic graphite	<500[e]	—	574[d]	4975	— ($n = 2$)
80% Shawinigan, 20% Teflon (Honeywell)	—	—	—	—	5528	— ($n = 2$)

[a] Cabot pigment brochure.
[b] Data supplied by Gulf Oil Chemical Company.
[c] Cabot Technical report S-36.
[d] Analysis performed by Micromeritics (Norcross, Georgia).
[e] Data supplied by Superior Graphite.

the calculated value for the generally accepted battery reaction ($4Li + 2SOCl_2 = 4LiCl + SO_2 + S$), $\Delta H = -364$ kcal/mol of Li or -26 kcal/g of 1:1 Li-C mixture. Thus the greatest heat listed in Table II, 7.456 kcal/g corresponds to about 29% reaction of the Li.

Mechanism of carbon catalysis.—We explored four possible mechanisms for the catalytic behavior of carbon: (*i*) local electrochemical cell, (*ii*) increased lithium surface area, (*iii*) formation of an active compound during the grind, and (*iv*) surface functional groups on the carbon.

In the first mechanism, each carbon particle in contact with lithium is viewed as a small cathode which is short-circuited to the lithium anode. When an electrolyte solution containing $SOCl_2$ or SO_2 is added, this short-circuited cell discharges at a high rate generating sufficient heat to cause, in the extreme case, ignition. This agrees with data (4) showing that the corrosion of a variety of metals in $LiAlCl_4$-$SOCl_2$ electrolyte is greatly accelerated if the metal is electrically contacted to carbon. By analogy with the behavior of large scale cells, one would expect that eliminating the supporting electrolyte salt from the electrolyte solution would significantly increase the solution resistance, reduce the rate at which the short-circuited cells could discharge, and, thus, reduce the heat that would be generated. This was found to be the case with pressed 1 to 1 Li-C mixtures. In six out of six tests, pressed Li-C caused $LiAlCl_4$-$SOCl_2$ solutions to boil, whereas, the Li-C mixture was totally unreactive in four tests in salt-free $SOCl_2$. In contrast, however, ground 1 to 1 Li-C mixtures were highly reactive toward salt-free $SOCl_2$. We suggest that these results can, nonetheless, be understood in terms of a shorted cell mechanism. Grinding the mixtures creates an extensive Li-C interface effectively lowering the path length for electrolyte conduction in shorted cells to the range of the diffusion layer thickness. Thus in this case, the absence of supporting electrolyte salt is relatively unimportant, as significant currents can be maintained through diffusion of the ions produced by the anode and cathode reactions. With pressed mixtures, on the other hand, the combination of high path length and low conductance in salt-free $SOCl_2$ apparently depresses the shorted cell currents to negligible levels.

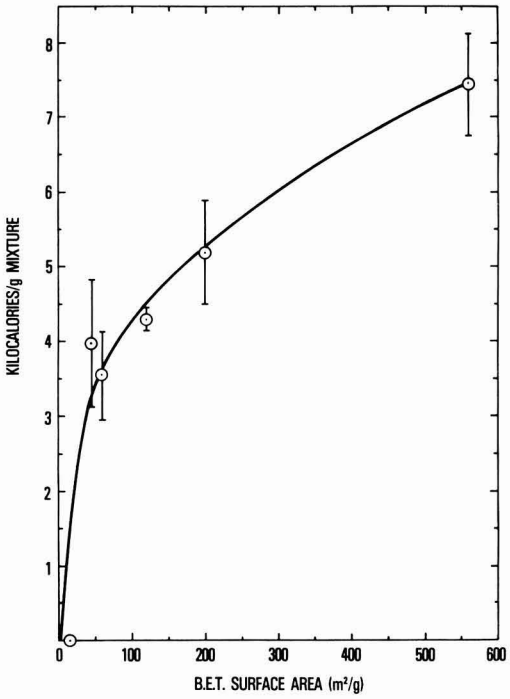

Fig. 2. Reactivity vs. surface area for ground mixtures of Li and C (1:1 by weight) with 1.5M $LiAlCl_4$-$SOCl_2$.

Another explanation of carbon catalysis may be increased Li surface area. In this case finely divided carbon is just a vehicle for producing a very extensive Li-$SOCl_2$ interface. When the carbon becomes coated with Li the reaction interface is raised by many orders of magnitude. Thus when electrolyte is added, in spite of Li passivation, enough heat is generated for ignition to occur. This theory was tested by grinding lithium with powdered Al_2O_3 (surface area, 200 m^2/g). If carbon were simply a vehicle for dispersion of Li, then the alumina should also give rise to increased activation. However, a calorimetric study indicated that a ground mixture of Li and alumina (1:1 weight ratio) was quite inert to $LiAlCl_4$-$SOCl_2$.

A third plausible explanation involves the formation of an active compound when grinding the lithium and carbon together. This active compound would then be responsible for the catalytic effect. X-ray analysis

of ground Li-carbon black mixtures indicated formation of an Li-C compound other than acetylide (5). The 2θ values differed by approximately 1° from a stage 5 lithium-graphite compound. Perhaps this difference is due to the fact that relatively amorphous carbon black was used in place of graphite. We ruled out the participation of other active compounds such as Li_2C_2, Li_3N, Li_2O, Li_2O_2 by testing their reactivity to battery electrolyte, both alone and after grinding with lithium. All were inert. The intercalation compound, LiC_6, was also found to be inert to $SOCl_2$-$LiAlCl_4$. It remains possible however that some unidentified amorphous, Li-C compound, formed during the grinding, played a part in the enhanced reactivity.

Finally we considered the possibility that surface functional groups on the carbon particles are responsible for the catalysis. Carbon black is known to contain superficial H and O which may control its absorptive, catalytic, and electrical behavior (6). Recent studies of Shawinigan carbon black have revealed a substantial ESR signal (7). Energetic surface groups might react with $SOCl_2$ forming labile species (8) which could accelerate its reactivity. To check this hypothesis we heat-treated a sample of Shawinigan black so as to drive off its O and H content. The carbon was fired in an He atmosphere at 950°C for 5 hr. This should remove all of its O and most of its H (9). The carbon was then cooled under He, ground in He with Li (50% mixture) and transported in sealed containers for immediate testing in an Ar glove-bag. Qualitative reactivity testing with five samples of these ground mixtures showed a high, consistent reactivity identical with that of untreated carbon. Thus it is unlikely that superficial O or H are involved in carbon black's catalysis of the Li-$SOCl_2$ reaction.

Conclusions

1. Carbon black promotes reactivity of lithium with Li/SO_2 or Li/$SOCl_2$ battery electrolytes. Lithium-carbon mixtures that are ground together (as may occur in severely warped or sheared batteries) can spontaneously ignite with SO_2 or $SOCl_2$ battery electrolytes. This reactivity occurs both in dry air and also in inert gas atmosphere thus excluding air contamination as a factor in this type of hazard.

2. The order of reactivity of the various battery electrolytes to ground Li-C mixes was $SOCl_2$-$LiAlCl_4$ >> SO_2-AN-$LiAsF_6$ ~ SO_2-AN-LiBr. Decreasing the concentration of SO_2 in the SO_2 battery electrolyte lowers its reactivity.

3. Traces of carbon are insufficient to activate the Li-oxidant reaction. Perceptible energy is liberated only when the C content (in Li-C mixes) exceeds 12 and 40 w/o, respectively, for the $SOCl_2$ and SO_2 electrolytes. Lowering the carbon content of Li-C mixes gives rise to decreasing flammability with battery electrolyte.

4. A variety of carbons was examined. The external surface area of the particles was judged to be the most important factor in the ability of carbon to promote reactivity.

5. No evidence was uncovered for any mechanism of carbon's catalytic activity on the Li-oxidant reactions other than that of shorted electrochemical cells. Grinding of Li with C black generated some Li-C compound but this could neither be identified nor specifically linked with enhanced reactivity.

Acknowledgments

The authors thank the Independent Research Program of the Naval Surface Weapons Center and the Naval Sea Systems Command, Electrochemistry Technology Block Program for financial support of this work.

We also thank Dr. JoAnne Milliken for the x-ray studies, Dr. Victor R. Deitz of the Naval Research Laboratory, Washington, D.C., and Mr. Larry Newman of Cabot Corporation for providing samples of carbon.

Manuscript submitted Dec. 21, 1982; revised manuscript received April 27, 1983.

The Naval Surface Weapons Center assisted in meeting publication costs of this article.

REFERENCES

1. S. Dallek, S. D. James, and W. P. Kilroy, *This Journal*, **128**, 508 (1981).
2. W. P. Kilroy and S. D. James, *ibid.*, **128**, 934 (1981).
3. R. Yoshida, A. Arkawa, K. Kaiko, and O. Ogawa, *Netsv. Sokutei*, **81**, 2 (1981).
4. A. N. Dey, Final Report ERADCOM DELET TR 74-0109-E, July 1978.
5. W. P. Kilroy, S. D. James, and J. Milliken, NSWC TR 81-127, Sept. 1981.
6. R. N. Smith, *Quart. Rev.*, **13**, 287 (1959).
7. R. Ake, D. M. Oglesby, and W. P. Kilroy, Paper 298 presented at The Electrochemical Society Meeting, Detroit, MI, Oct. 17-21, 1982.
8. R. W. Murray, *Accounts of Chem. Res.*, **13**, 135 (1980).
9. W. R. Smith, "Encyclopedia of Chemical Technology," Kirk-Othmer, 2nd ed., Vol. 4, p. 253, Interscience, New York (1964).

Technical Notes

Solution Growth and Electrodeposited $CuInSe_2$ Thin Films

R. N. Bhattacharya*

Department of Structural Chemistry, The Weizmann Institute of Science, 76100 Rehovot, Israel
and
Thin Film Solid State Technology Cell, Department of Physics, I. I. T., Delhi, India

The solution growth deposition of Bi_2Se_3 (1), Bi_2S_3 (2), Sb_2Se_3 (3), α-PbO_2 and Tl_2O_3 (4), and $Cu_{1.8}S$ and TlSe (5) thin films have been reported previously. The growth and photoelectrochemical solar cell based on electrodeposited $CdSe_{1-x}Te_x$ thin films have also been reported (6-8). The deposition of $CuInSe_2$ thin films by solution growth and also by the electroplating method is presented here. The primary interest in such semiconductor films has been directed toward the application for photovoltaic cells.

Present address: Department of Chemistry, The University of Texas at Arlington, Arlington, Texas 76019.

Solution Growth Method

Thin $CuInSe_2$ films with a thickness in the range of 200-300Å are produced by the solution growth method on glass and SnO_2:F coated conducting glass substrates at room temperature. The conducting base SnO_2:F is

Table I. X-ray diffraction and TEM data for $CuInSe_2$ thin films: calculated and experimental values

Calculated				Observed d	
d	2θ (deg)	hkl	Relative intensity	TEM	X-ray
5.2	17.05	101	4	—	—
3.34	26.69	112	100	3.33	3.33
3.22	27.71	103	3	—	—
2.52	35.63	211	4	—	—
2.155	41.92	105,213	2	—	—
2.04	44.42	220,204	70	2.03	2.02
1.743	50.50	116,312	40	1.75	1.79
1.445	64.49	400,008	11	1.44	1.44
1.327	71.04	332,316	16	1.32	1.32

obtained by spray pyrolysis on glass substrates. The film thicknesses are measured using a Taylor Hobson Talystep instrument.

The deposition of $CuInSe_2$ films is based on the slow reaction between a solution of triethanolamine complexed with both In^{3+} and Cu^{1+}, and sodium selenosulfate solution. The sodium selenosulfate solution is prepared by refluxing 5g selenium powder with 12g of sodium sulfite in 200 ml water for about 10 hr. The deposition mixture contains 12.5 ml 0.05M In^{3+} solution, 10 ml 0.05M Cu^{1+} solution, 20 ml 0.3M sodium selenosulfate solution, ~0.03% (volume) triethanolamine, and ~0.04% (volume) ammonia solution.

The films are analyzed by transmission electron diffraction (TEM) and x-ray diffraction methods. Postdeposition treatments are used for the films deposited on glass substrates. This included annealing in argon gas, which results primarily in the recrystallization of the films. The films deposited on SnO_2:F coated glass substrates are polycrystalline with a grain size of about 0.08 μm. The calculated and experimental values of x-ray diffraction and TEM data are given in Table I.

The bandgap is obtained from transmission measurements made using Unicam SP 700 A Spectrophotometer. The transmission T as a function of photon energy $h\nu$ is measured from four different samples deposited on glass substrates with different film thickness d (d_1:800Å; d_2:1000Å; d_3:2000Å; d_4:3000Å). The optical energy gap is found to be 1.08 eV (Fig. 1). The bandgap is determined from the variation of α^2 as a function of energy $h\nu$ (α: absorption coefficient).

Electroplating Method

The electrodeposited $CuInSe_2$ thin films are prepared under potentiostatic conditions on conducting glasses (SnO_2:F coated). For the electroplating, the plating solution is prepared from 0.018M $InCl_3$, 0.018M CuCl, 0.025M selenium dioxide solution, 0.006% (volume) triethanolamine, and 0.007% (volume) ammonia solution. The pH of the deposition mixture is adjusted at ~1 by adding dilute HCl. The deposition is carried out under constant stirring and at room temperature. The voltage is maintained at ~700 mV *vs.* SCE. The plating current is ~15 mA/cm².

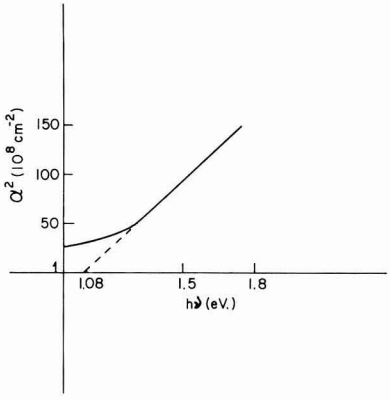

Fig. 1. Variation of α^2 as a function of energy $h\nu$ for solution growth $CuInSe_2$ thin films deposited on glass substrates.

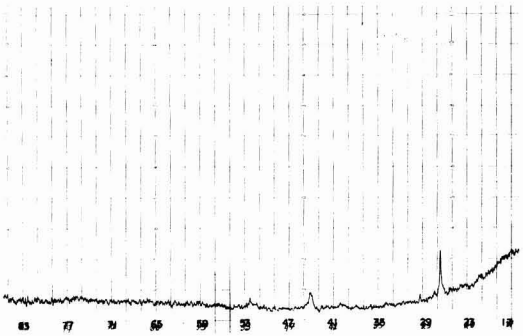

Fig. 2a. X-ray pattern of the as-deposited electroplated $CuInSe_2$ thin films (scale: 4 × 10^2 CPS).

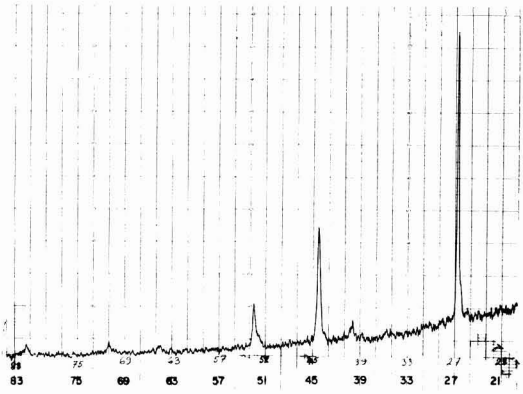

Fig. 2b. X-ray pattern of the electrodeposited and annealed $CuInSe_2$ thin films (scale: 4 × 10^2 CPS).

The x-ray analysis of the films is shown in Fig. 2a and b. Figure 2a represents the as-deposited electroplated films. Figure 2b shows the x-ray diffraction pattern for the single-phase $CuInSe_2$ films when the electroplated films are annealed in argon gas at ~600°C for 1 hr.

Recently the films have also been deposited (both solution growth and electroplated) on titanium substrates. The photoelectrochemical solar cell studies of the $CuInSe_2$ thin films are in progress.

Acknowledgment

The author wishes to express his thanks to Professor K. L. Chopra of Thin Film Solid State Technology Cell, Department of Physics, I.I.T. Delhi, India and also to Dr. David Cahen and Dr. Gary Hodes of The Weizmann Institute of Science, Israel) for their gracious hospitality during the experiments.

Manuscript submitted March 4, 1983; revised manuscript received May 25, 1983.

REFERENCES

1. P. Pramanik, R. N. Bhattacharya, and A. Mondal, *This Journal*, **127**, 1857 (1980).
2. P. Pramanik and R. N. Bhattacharya, *ibid.*, **127**, 2087 (1980).
3. R. N. Bhattacharya and P. Pramanik, *J. Solid State Chem.*, **44**, 425 (1982).
4. R. N. Bhattacharya and P. Pramanik, *Bull. Mater.*

Sci., **2**, 287 (1980).
5. R. N. Bhattacharya and P. Pramanik, *ibid.*, **3**, 403 (1981).
6. G. Hodes, J. Manassen, S. Neagu, D. Cahen, and Y. Mirovsky, *Thin Solid Films*, **90**, 433 (1982).
7. Y. Mirovsky, R. Tenne, G. Hodes, and D. Cahen, *ibid.*, **91**, 349 (1982).
8. R. N. Bhattacharya, S. P. S. Arya, D. K. Pandya, and K. L. Chopra, Solar Energy India Symposium, December 1982.

Stability of Conducting Polythiophene and Derivatives

G. Tourillon* and F. Garnier

Laboratoire de Photochimie Solaire, CNRS., 94320 - Thiais, France

Many organic conducting polymers such as polyacetylene, PA (1); polyparaphenylene, PPP (2); polyparaphenylenesulfide, PPS (2); and polypyrrole, PP (3) have been proposed in the literature. These polymers show reversibility of the doping-undoping process, making them of interest in energy storage. One of the key problems, however, is the poor stability of most of these polymers. Polyacetylene, PA, must be prepared and stored under a rigorously O_2 free atmosphere and at a low temperature (4). Polypyrrole, PP, although stable in its conducting state, is also sensitive to O_2 in its semiconducting undoped state (5). As a matter of fact, a progressive redoping by O_2 occurs due to the value of the polymer oxidation potential ($E_{ox} \simeq -0.3$) which lies in the same range as that for the reduction of O_2.

PPP and PPS show a higher oxidation stability mainly in the undoped state ($E_{ox} \simeq +1.6$V), and their sensitivity to O_2 is less pronounced, but information on the doped state is scarce. The authors recently reported the electrochemical generation of thin films of new organic conducting polymers, polythiophene, polyfuran, and derivatives (6) which also appear as interesting candidates for organic electrodes for energy storage or display.

In this paper, the stability characteristics of these new polymers is presented under various experimental conditions (O_2, H_2O, H^+, OH^-, temperature).

Experimental

The polymers have been generated, as previously described (6), either as thin films grafted on a Pt electrode or as thick deposits which are then scratched off, rinsed, and dried. The analyzed polymers were polythiophene, PT; poly-3-methylthiophene, PMeT; poly-3,4 dimethylthiophene, $P(Me)_2T$; and polypyrrole, PP doped with $CF_3SO_3^-$ from $N(Bu)_4\ CF_3SO_3$ salt.

They were characterized by infrared, ESR, elemental microanalysis, and d-c conductivity initially, just after their synthesis, and after 8 months storage in air at room temperature.

The stability in electrolytic medium [CH_3CN, $N(Bu)_4\ PF_6$] has also been determined after 20 cycles between oxidized and reduced state, using XPS (AEI, Mg kα anticathode 1253.6 eV).

Results and Discussion

The doped PMeT properties (Table I) show that the storage in air affects neither the $CF_3SO_3^-$ doping level nor the conductivity. These results are confirmed by the infrared analysis: this conducting polymer is characterized by a large broad band in the near infrared (4000-1600 cm^{-1}) due to free carriers and by absorption patterns (1600-600 cm^{-1}) associated with the dopant $CF_3SO_3^-$ (Fig. 1). After 8 months storage time in air, a very similar absorption spectrum is obtained which bears out the long term stability.

The undoped PMeT behaves in the same way. After 8 months storage in ambient air, neither oxygen nor H_2O could be detected, in contrast to polypyrrole which has been shown to be very sensitive to oxygen. Furthermore, PMeT can be doped again after 8 months by electrochemical oxidation to the same level as before, about 25-30%.

Table I. Physicochemical and electrical properties of a $SO_3CF_3^-$ doped PMeT just after synthesis and after being kept 8 months in air.

Physicochemical properties	Just after synthesis	Kept 8 months in air
Microanalysis (anion doping level per monomer unit)	25%	24.5%
Conductivity $\sigma(\Omega^{-1}cm^{-1})$	12	10

PT and $P(Me)_2T$ show the same interesting stability characteristics, compared to the experimental precautions which must be taken with other types of organic conducting polymers.

These materials have great thermal stability; 200°-250°C in air and 700°-800°C in inert atmosphere or vacuum. They are stable in concentrated acidic medium but are slowly attacked in basic solution.

The stability under electrochemical treatment was also studied. PP and PMeT were polarized between their oxidized and reduced neutral states during 20 cycles in CH_3CN-$N(Bu)_4PF_6$ medium. Their I-V and XPS characteristics were recorded before and after this polarization (Fig. 2 and 3).

With PP, the oxidation and reduction peaks are not well defined and XPS spectra are greatly modified: the peak due to P is no longer detected, the intensity of the F peak decreases, but the O peak increases. Similar results were recently obtained by Salaneck *et al.* (7) and Street *et al.* (8).

These results show that the dopant PF_6^- is replaced by O_2 during the electrochemical treatment. The authors do not agree with the results of Street *et al.* (8) who proposed that a complex is formed between the oxygen and the nitrogen atom of the cycle: only one nitrogen chemical type was always detected. The same result was also observed with the carbon element. So oxygen must have the same doping property as I_2 or AsF_5.

In contrast, PMeT exhibits good electrochemical stability as shown by the same I-V curve and XPS spectra before and after polarization. Two parameters

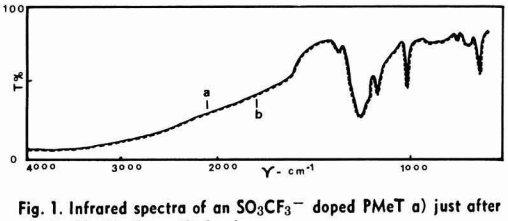

Fig. 1. Infrared spectra of an $SO_3CF_3^-$ doped PMeT a) just after synthesis; b) after 8 months in air.

* Electrochemical Society Active Member.
Key words: organic conducting polymer, thin films, stability.

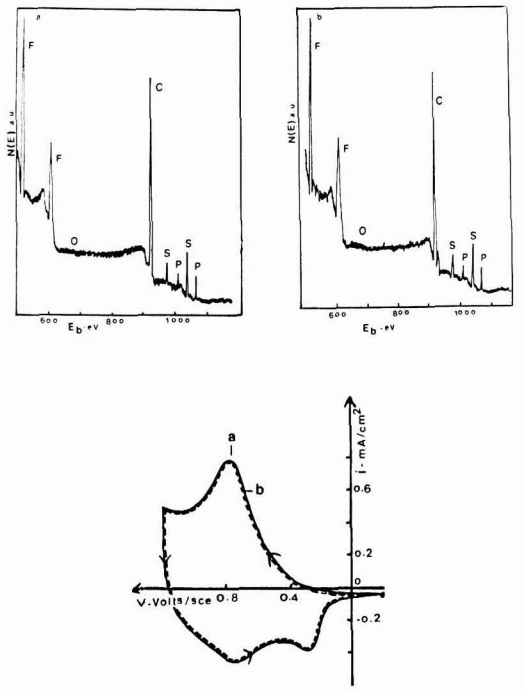

Fig. 2. I-V curves and XPS spectra of thin PMet grafted on Pt sweep rate, 50 mV/sec; electrolytic medium, CH_3CN-$N(Bu)_4PF_6$ 10^{-1} M/liter; XPS spectra, AEI with Mg anticathode; kinetic energy, 1253.6 eV. a) XPS spectrum just after polymerization; b) XPS spectrum after 20 cycles between oxidized and reduced states.

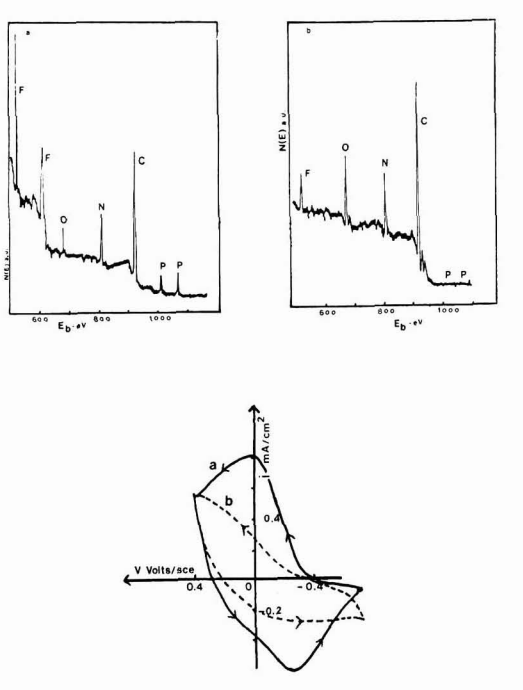

Fig. 3. Same as Fig. 2 but for polypyrrole instead of PMeT

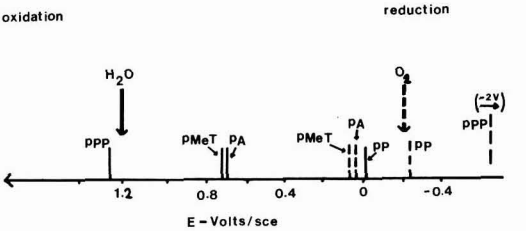

Fig. 4. Oxidation and reduction potentials of several polymers compared with O_2 reduction potential and H_2O oxidation potential. (PP, polypyrrole; PA, polyacetylene; PPP, polyparaphenylene; PMeT, poly-3 methyl thiophene). Solid line, oxidation; dashed line, reduction.

appear to be important for obtaining stable polymers; their oxidation-reduction potentials and their chemical reactivity. In Fig. 4, the authors have reported the oxidation and reduction potential ranges of several polymers together with the O_2 reduction potential and the H_2O oxidation potential. The scheme clearly shows why PP, for example, is not stable in its undoped (reduced) neutral state: it lies close to the O_2 reduction potential and will be slowly oxidized by O_2 to a conducting state which is the electrochemical stable form.

In the same manner, PPP, with a very high oxidation potential (+1.6V), higher than the oxidation potential of water, should be not stable to H_2O in its doped state but should be stable in its neutral form. With this scheme, PMeT and PA should be stable in both states due to the fact that their oxidation-reduction potentials lie between those for O_2 reduction and H_2O values. This is verified in the case of PMeT but not with PA. In this last case with PA, the other important parameter is the chemical reactivity of the material. It is composed of linear chains with an alternation of single and double bonds. Chemical reaction of O_2 with a double bond can easily occur and leads either to oxygen bridging between chains or to a break down of the chains. There is no more π electron delocalization and the electrical properties are greatly affected. In contrast, PMeT is more stable to O_2, as the authors have seen. This stability must be related to the bridging of the polymer double bonds by the sulfur hetero atom.

In conclusion, electrochemically generated PT and derivatives show good stability to O_2 and moisture in both doped and neutral states. Compared to other polymers such as PA or PP, where drastic conditions must be employed to avoid exposure to air and moisture, these new polymers appear to be very attractive.

Their stabilities argue for exploitation of the very promising electrochromic properties that the authors have recently observed (9). It must also be pointed out that these polymers can be obtained either in thin-grafted films or as thick deposits with a very high reproducibility.

Manuscript submitted March 17, 1983; revised manuscript received June 22, 1983.

REFERENCES

1. H. Shirakawa, E. J. Louis, A. G. Mac Diarmid, C. K. Chiang, and A. J. Heeger, *J. Chem. Soc. Chem. Commun.*, 578 (1977).
2. R. H. Baughman, J. L. Bredas, and R. R. Chance, "Polymer Science and Technology," Vol. 15, R. B. Seymour, Editor, p. 137, New York (1982).
3. A. F. Diaz and K. K. Kanazawa, in "Extended Linear Chain Compounds," Vol. 3, G. S. Miller, Editor, p. 417, Plenum Press, New York (1982).
4. H. Naarman, in "Polymeres Electro-Actifs," Font-Romeu, France (1982).
5. A. F. Diaz, J. Crowley, J. Baryon, G. P. Gardini, and J. B. Torrance, *J. Electroanal. Chem.*, **121**, 355 (1981).
6. G. Tourillon and F. Garnier, *ibid.*, **135**, 173 (1982).

7. W. R. Salaneck, R. Erlandsson, J. Prejzci, I. Lundström, C. B. Duke, and W. K. Ford, Organic Polymers, p. 120, American Chemical Society Meeting, Las Vegas, NV (1982).
8. P. Pfluger, M. Krounbi, G. B. Street, and G. Weiser, *J. Phys. Chem.*, In press.
9. F. Garnier, G. Tourillon, M. Gazard, and J. C. Dubois, *J. Electroanal. Chem.*, **198**, 299 (1983).

An Analytical Solution of the Nonsteady Convective Diffusion Equation for Rotating Electrodes

C. Deslouis, C. Gabrielli, and B. Tribollet

Groupe de Recherche No. 4 du CNRS, Physique des Liquides et Electrochimie, associé à l'Université Pierre et Marie Curie, 75230 Paris Cedex 05, France

In electrochemistry, the study of mass transport is often carried out by means of rotating electrodes. The development of nonsteady-state techniques such as electrochemical (1, 2) or electrohydrodynamical (3, 4) impedances leads to derivations in which increasingly more complex forms of the convective diffusion equation are involved.

So far, this equation has only been analytically solved in a few cases. However, an analytical solution can be interesting, especially for performing a fitting procedure on experimental data. Therefore, in this paper an approximate analytical solution of the convective diffusion equation is given in the vicinity of a rotating electrode. This derivation is applicable both to steady-state and nonsteady-state (impedances) conditions, as will be demonstrated by some examples.

The convective diffusion equation is generally written as

$$\frac{\partial c}{\partial t} = D\,\nabla^2 c - \vec{V}\,\vec{\text{grad}}\,c \qquad [1]$$

where c is the concentration of the diffusing species, D the diffusion coefficient, and $\vec{V}$ the fluid velocity, the normal component of which is proportional to the square of the distance to the electrode. For a sinusoidal modulation of small amplitude, the concentration is

$$c = c_o + \delta c \exp j\omega t \quad (j = \sqrt{-1})$$

where c_o is the steady-state concentration, and ω the angular frequency.

By using a concentration $U_o + \delta U \exp j\omega t$, a normal coordinate η, and a frequency K put into a dimensionless form according to the geometry, the nonsteady part of Eq. [1] can be generally written as

$$\frac{d^2\delta U}{d\eta^2} + a\eta^2\frac{d\delta U}{d\eta} - (b\eta + j\mathrm{K})\,\delta U = f(\eta, j\mathrm{K}) \qquad [2]$$

with boundary condition

$$\delta U \to 0 \quad \text{when} \quad \eta \to \infty$$

By means of the variable change

$$x = (b + a)^{1/3}\eta \qquad [3]$$

$$s = (b + a)^{-2/3}\mathrm{K}j \qquad [4]$$

and the function change

$$\phi(x, s) = \delta U\,(x, s)\exp\left(+\frac{a}{a+b}\frac{x^3}{6}\right) \qquad [5]$$

Eq. [2] leads to

$$\frac{d^2\phi}{dx^2} - \left(x + \frac{a}{a+b}\frac{x^4}{4} + s\right)\phi = g(x, s) \qquad [6]$$

where

$$g(x, s) = (b + a)^{-2/3} f(x, s)\exp\left(\frac{a}{a+b}\frac{x^3}{6}\right)$$

By the above procedure, $0 \leq x \leq 1$, so $x > x^4$, and we must consider the following cases: at mean and high frequencies $|s + x| >> x^4$ and the term $\frac{a}{a+b}\frac{x^4}{4}\phi(x, s)$ can be neglected. At low frequencies, we can substitute for the term $\frac{a}{a+b}\frac{x^4}{4}\phi(x, s)$ the first term of its Taylor expansion in s (*i.e.*, $\frac{a}{a+b}\frac{x^4}{4}\phi(x, 0)$) with

$$\phi(x, 0) = U_o\,(x)\exp\left(\frac{a}{a+b}\frac{x^3}{6}\right)$$

In Eq. [5], indeed, $\delta U(x, 0)$ may be replaced by the stationary solution $U_o(x)$.

Hence, Eq. [6] becomes

$$\frac{d^2\phi}{dx^2} - (x + s)\,\phi = g(x, s) + \frac{a}{a+b}\frac{x^4}{4}U_o(x)\exp\left(\frac{a}{a+b}\frac{x^3}{6}\right) \qquad [7]$$

The homogeneous equation derived from [7] is an Airy's equation whose solution is an Airy function $Ai(x + s)$ of the first kind according to the boundary condition.

The solution of full Eq. [7] may then be put as

$$\phi = Ai\{x + s\} \cdot q(x, s) \qquad [8]$$

and one finds

$$Ai\{x + s\} \cdot q'' + 2Ai'\{x + s\} \cdot q' = g(x + s) + \frac{a}{a+b}\frac{x^4}{4}U_o(x)\exp\left(\frac{a}{a+b}\frac{x^3}{6}\right) \qquad [9]$$

If

$$q' = Ai^{-2}\{x + s\} \cdot Y(x, s) \qquad [10]$$

then

$$Y'(x, s) = Ai\{x + s\} \cdot g(x, s) + \frac{a}{a+b}\frac{x^4}{4}U_o(x)\exp\left(\frac{a}{a+b}\frac{x^3}{6}\right) \qquad [11]$$

Hence

$$\delta U(x, s) = \exp\left(-\frac{a}{a+b}\frac{x^3}{6}\right)Ai\{x + s\} \left\{\int_0^x (Ai\{\xi + s\})^{-2}\left[\int_0^\xi Ai\{\xi' + s\} \cdot g(\xi', s)\,d\xi' + K_1(s) + \int_0^\xi Ai\{\xi' + s\} \cdot \frac{a}{a+b}\frac{\xi'^4}{4}U_o(\xi')\exp\left(\frac{a}{a+b}\frac{\xi'^3}{6}\right)d\xi' + K_o(s)\right]d\xi + K_2(s)\right\} \qquad [12]$$

$K_2(s)$ is obtained by using the boundary condition at the electrode surface ($x = 0$) which depends on the analyzed problem. The boundary condition at infinity ($x \to \infty$) leads to

$$K_1(s) = -\int_0^\infty Ai\{\xi' + s\}\, g(\xi', s)\, d\xi' \qquad [13]$$

and for low frequencies

$$K_o(s) = -\int_0^\infty Ai\{\xi' + s\}\, \frac{a}{a+b}\, \frac{\xi'^4}{4}\, U_o(\xi') \exp\left(\frac{a}{a+b}\, \frac{\xi'^3}{6}\right) d\xi' \qquad [14]$$

If $Ai\{\xi' + s\}$ is expanded as a Taylor series

$$Ai\{\xi' + s\} = Ai\{\xi'\} + sAi'\{\xi'\} + \ldots + \frac{s^n}{n!} Ai^n\{\xi'\} + \ldots \qquad [15]$$

$K_o(s)$ can be calculated as

$$K_o(s) = I_o + sI_1 + \ldots + \frac{s^n}{n!} I_n + \ldots \qquad [16]$$

where

$$I_n = -\frac{s^n}{n!} \int_0^\infty Ai^n\{\xi'\}\, \frac{a}{a+b}\, \frac{\xi'}{4}\, U_o(\xi') \exp \frac{a}{a+b}\, \frac{\xi'^3}{6}\, d\xi' \qquad [17]$$

The corrective term $K_o(s)$ can be determined when the stationary solution $U_o(x)$ is known. For mean and high frequencies $K_o(s) = 0$.

Diffusion impedance for a rotating disk electrode—A numerical solution of this problem has been given by Levart and Schuhmann (5). In that case, the relevant values of the parameters in Eq. [2] are, for large value of Sc, $a = 1$, $b = 0$, $f(\eta, jK) = 0$, and $\eta = (0.51023\ \mathrm{Sc})^{1/3} \sqrt{\Omega/\nu}\ z$. For a single electron transfer process the current may be written as

$$I = n\mathbf{F}\, A\, k\, c_o(0) \exp(\alpha V) \qquad [18]$$

A is the electrode area, $\mathbf{F}$ the Faraday number, k the reaction rate, and α the Tafel slope.

The diffusion impedance Z_D is then defined as

$$Z_D(s) = \frac{1}{\alpha c_o} \frac{\delta c}{\delta I}\bigg|_o = -\frac{1}{n\mathbf{F}\, D\, A\, \alpha c_o} \cdot \frac{\delta c|_o}{\dfrac{\partial(\delta c)}{\partial z}\bigg|_o} \qquad [19]$$

where

$$Z_D(s) = \frac{1}{n\mathbf{F}\, D\, A\, \alpha c_o} \cdot \frac{\delta U|_o}{\dfrac{\partial \delta U}{\partial x}\bigg|_o \cdot \dfrac{\partial x}{\partial z}} \qquad [20]$$

The exact solution of the stationary problem with the boundary conditions

$$U_o(x) \to 0 \quad \text{when} \quad x = \infty$$

$$U_o(0) = 1 \quad \text{when} \quad x = 0$$

is

$$U_o(x) = 1 - \frac{\displaystyle\int_0^x \exp\left(-\frac{t^3}{3}\right) dt}{\displaystyle\int_0^\infty \exp\left(-\frac{t^3}{3}\right) dt} \qquad [21]$$

After Eq. [12], the nonstationary solution is

$$\delta U(x, s) = \exp\left(-\frac{x^3}{6}\right) Ai\{x + s\} \left\{ \int_0^x (Ai\{\xi + s\})^{-2} \left[\int_0^\xi Ai\{\xi' + s\}\, \frac{\xi'^4}{4}\, U_o(\xi') \exp\left(\frac{\xi'^3}{6}\right) d\xi' + K_o(s) \right] d\xi + K_2(s) \right\} \qquad [22]$$

where

$$K_o(s) = -\int_0^\infty Ai\{\xi' + s\}\, \frac{\xi'^4}{4}\, U_o(\xi') \exp\left(\frac{\xi'^3}{6}\right) d\xi' \qquad [23]$$

$$K_2(s) = \frac{1}{Ai(s)} \qquad (U(0, s) = 1) \qquad [24]$$

Hence

$$Z_D(s) = -\frac{1}{n\mathbf{F}\, D\, A\, \alpha c_o\, a^{1/3}}\, \frac{Ai\{s\}}{Ai'\{s\}} \left(\frac{1}{1 + \dfrac{K_o(s)}{Ai'(s)}} \right) \qquad [25]$$

From Ref. (10)

$$Ai'(s) = -0.25882\ (1 + s^3/3) + 0.35502\ s^2/2$$

and from Filinovskii *et al.* (6)

$$\frac{Ai(s)}{Ai'(s)} = -\frac{\sqrt{1.877 + s}}{1 + s} \qquad [26]$$

After computation of I_o, I_1, I_2, I_3, by Eq. [17] one can get for $|s| < 1$ the expression of Z_D

$$Z_D = -\frac{1.2514}{n\mathbf{F}\, D\, A\, \alpha c_o} \cdot \frac{\sqrt{1.877 + s}}{1 + s}\ (0.93844 + 0.07591\, s - 0.07392\, s^2 + 0.06769\, s^3) \qquad [27]$$

When $|s| > 1$, $K_o(s) = 0$ and the Eq. [27] is simplified

$$Z_D = -\frac{1.2514}{n\mathbf{F}\, D\, A\, \alpha c_o}\, \frac{\sqrt{1.877 + s}}{1 + s} \qquad [27a]$$

whence the asymptotic expression of Warburg

$$Z_D \propto -s^{-1/2}$$

For comparison, the values of the real (X_o) and imaginary (Y_o) parts of the diffusion impedance calculated by Levart and Schuhmann (5) are given in Table I along with the values calculated from Eq. [27] and [27a]. Agreement is good over the whole frequency range.

Electrohydrodynamical impedance for a rotating disk electrode.—The electrohydrodynamical impedance is the transfer function between the sine wave modulation of the rotating speed and the response of the electrochemical interface.

The convective diffusion equation is Eq. [2] where $a = 1$, $b = 0$, and $f(\eta, jK) = \eta^2 \exp(-\eta^3/3)$. The analytical solution is given in Ref. (8).

Diffusion impedance on a hemispherical rotating electrode.—Recently this problem has been analyzed by Chin (9). The author has showed that the adimensional concentration M can be expanded in a spherical coordinate system as a function of the angular coordinate θ

$$M = [M_1(z) + \theta^2 M_3(z) + \ldots]\, e^{jKSc^{1/3}/\tau} \qquad [28]$$

The notations used are those of Ref. (9), where τ is the adimensional time and $\tau = \Omega t$ (Ω is the angular rotation speed). The convective diffusion equation is then equivalent to the system

Table I. Real and imaginary components of the diffusion impedance on a rotating disk electrode

	Numerical From (5)		Analytical From Eq. [25]	
1.566 K	X_o	$-Y_o$	X_o	$-Y_o$
0.01	1.6109	0.010	1.611	0.010
0.02	1.6107	0.0199	1.611	0.021
0.05	1.6090	0.0498	1.609	0.052
0.07	1.6071	0.0696	1.607	0.073
0.1	1.6033	0.0992	1.600	0.104
0.2	1.5806	0.1944	1.574	0.204
0.5	1.4431	0.4314	1.426	0.445
0.7	1.3205	0.5353	1.302	0.553
1	1.1362	0.6183	1.125	0.663
2	0.7304	0.5999	0.7098	0.5962
5	0.4097	0.3961	0.4082	0.3939
7	0.3419	0.3344	0.3406	0.3332
10	0.2840	0.2797	0.2828	0.2789
20	0.1998	0.1978	0.1987	0.1974
50	0.1263	0.1250	0.1253	0.1250
70	0.1068	0.1058	0.1059	0.1057
100	0.0896	0.0884	0.0886	0.0884
200	0.0635	0.0626	0.0626	0.0626
500	0.0404	0.0396	0.0396	0.0396
1000	0.0287	0.0280	0.028	0.028

From (5) ($Sc \to \infty$).
From Eq. [25] with LF correction.

$$\frac{d^2M_1}{dz^2} + 0.51023\, z^2 Sc \frac{dM_1}{dz} - jKSc^{2/3}\, M_1 = 0 \quad [29]$$

$$\frac{d^2M_3}{dz^2} + 0.51023\, z^2 Sc \frac{dM_3}{dz} - (1.02046\, zSc + jKSc^{2/3})M_3 = 0.52762\, z^2 Sc \frac{dM_1}{dz} \quad [30]$$

with the boundary condition in $z = 0$: $dM_1/dz = -1$ and $dM_3/dz = 0$.

These equations have been numerically solved in (9). However, by using the previous derivation an approximate analytical solution can be obtained. Equation [29] is equivalent to Eq. [2] where $a = 0.51023$ Sc, $b = 0$, and $f(\eta, K) = 0$. This problem is similar, as mentioned by Chin, to that of the diffusion impedance on a rotating disk electrode. However, the boundary condition in $z = 0$ ($dM_1/dz = -1$) is different from that given previously.

The solution of Eq. [29] for K = 0 is then

$$M_1^\circ(z)\, Sc^{1/3} = 1.611 - Sc^{1/3} \int_0^z \exp\left(-\frac{0.51023\, Sc}{3}\xi^3\right) d\xi \quad [31]$$

and

$$\frac{dM_1^\circ}{dz} = -\exp\left(-\frac{0.51023\, Sc}{3} z^3\right)$$

Equation [30] is equivalent to Eq. [2] where $a = 0.51023$ Sc, $b = 1.02046$ Sc, and $f(z, Kj) = 0.52762\, z^2\, Sc\, dM_1/dz$.

For K = 0, an approximate analytical solution of the Eq. [30] is

$$M_3^\circ(z)\, Sc^{1/3} = 0.20682\, Sc^{1/3}\, z \exp\left(-\frac{a}{3}z^3\right) + 0.69337\, Ai\{(3a)^{1/3}z\} \exp\left(-\frac{az^3}{6}\right) \quad [32]$$

By the way described in the first part of this paper, an analytical solution of Eq. [30] can then be calculated. In the low frequency range by using a Taylor expansion, we obtain

$$M_{30}Sc^{1/3} = (0.246 - 1.19\, K^2) - j\, 0.53\, K \quad [33]$$

For $|s| > 1$, then for $K > 0.6$ $K_o(s) = 0$ and the analytical expression of $M_{30}Sc^{1/3}$ can be used

Table II. Values of $M_{30}\, Sc^{1/3}$

	Analytical from Eq. [33]		Numerical Ref. (9)	
K	Real part	Imaginary part	Real part	Imaginary part
0.01	0.246	−0.0053	0.24324	−0.00542
0.015	0.2457	−0.00795	0.24309	−0.00760
0.02	0.2455	−0.0106	0.24297	−0.01013
0.03	0.2449	−0.0159	0.24258	−0.01519
0.04	0.2441	−0.0212	0.24207	−0.02021
0.06	0.2417	−0.0318	0.24066	−0.03022
0.08	0.2384	−0.0424	0.23868	−0.04004
0.1	0.2341	−0.053	0.23617	−0.04967
	Analytical from Eq. [35]		Numerical Ref. (9)	
8	0.00206	0.000015	0.00216	0.00011
10	0.00132	0.000007	0.00136	0.00001
20	0.00033	0.0000006	0.00033	~0
30	0.000147	0.0000002	0.00015	~0
40	0.000083	0.0000001	0.00008	~0
60	0.000037	~0	0.00004	~0
80	0.000021	~0	0.00002	~0
100	0.000013	~0	0.000013	~0
150	0.0000059	~0	0.000006	~0

$$M_{30}Sc^{1/3} = -1.294 \int_0^\infty \frac{x^2 Ai\{x+s\}\, Ai' \left\{ \frac{x}{3^{1/3}} + 3^{2/3} s \right\} dx}{Ai'\{s\}\, Ai'\{3^{2/3}s\}} \quad [34]$$

For large value of K, an equivalent of $M_{30}Sc^{1/3}$ can be obtained by substituting the Airy's function by their expansions (10).

$$M_{30}Sc^{1/3} = -\frac{0.132}{K^2} - j\frac{0.0223}{K^{7/2}} \quad [35]$$

The agreement is very good with the numerical solution given in (9) for $K \geq 10$ (see Table II).

In conclusion, analytical solutions of the convective diffusion equation have been derived for fluid flows of the same type as the rotating disk system. These solutions corresponding to the general Eq. [12] are complementary to a numerical solution of a problem. They clearly establish the asymptotic behavior and they can be used for a fitting of the parameter to the experimental results. [Sc, for instance, and electrical elements of the equivalent circuit in impedance measurements (2)].

Three applications have been presented in this note; however, this derivation can be applied to the impedance problem for a ring electrode, a cone electrode or a Couette flow. More generally, this type of derivation could be extended to any axisymmetrical problem.

Manuscript submitted April 17, 1981; revised manuscript received June 17, 1982.

Groupe de Recherche No. 4 du CNRS assisted in meeting the publication costs of this article.

REFERENCES

1. C. Deslouis, I. Epelboin, M. Keddam, and J. C. Lestrade, *Electroanal. Chem. Interfacial Electrochem.*, **28**, 57 (1970).
2. C. Deslouis and B. Tribollet, *Electrochim. Acta*, **23**, 935 (1978).
3. K. Tokuda, S. Bruckenstein, and B. Miller, *This Journal*, **122**, 1316 (1975).
4. C. Deslouis, I. Epelboin, C. Gabrielli, and B. Tribollet, *J. Electroanal. Chem.*, **82**, 251 (1977).
5. E. Levart and D. Schumann, *ibid.*, **28**, 45 (1970).
6. V. Y. Filinovskii and V. A. Kir'Yanov, *Dokl. Akad. Nauk. S.S.R.*, **156**, 1412 (1964).
7. W. J. Albery, A. R. Hillman, and S. Bruckenstein, *J. Electroanal. Chem.*, **100**, 687 (1979).
8. C. Deslouis, C. Gabrielli, Ph. Sainte-Rose Fanchine, and B. Tribollet, *This Journal*, **129**, 107 (1982).
9. D-T. Chin, *ibid.*, **127**, 2162 (1980).
10. M. Abramovitz and I. A. Stegun, "Handbook of Mathematical Functions," N.B.S., Washington, DC (1964).

JOURNAL OF THE ELECTROCHEMICAL SOCIETY

SOLID-STATE SCIENCE AND TECHNOLOGY

OCTOBER 1983

Evaluation of Crystalline Quality by Ultraviolet Reflectivity Measurement (UVRM)

T. Itoh* and H. Takai

School of Science and Engineering, Waseda University, Tokyo 160, Japan

ABSTRACT

The damage distribution in ion-implanted silicon and the crystalline quality of epitaxial films are evaluated by detecting the reflectivity change in a sample at 275 nm with reference to the reflectivity at 330 nm, and experimental results are compared with the Rutherford backscattering spectra. The damage distribution induced by P^+ implantation is clearly distinguished from that by Si^+ implantation in both P^+- and Si^+-implanted samples. The recrystallization process of the Si^+-implanted region is identified by UVRM. The distribution profile of crystalline imperfection in a silicon epitaxial film on a porous silicon layer is evaluated by UVRM, and is in good agreement with the depth profile of dechanneled fraction obtained by RBS measurement.

Since ion implantation became an indispensable technique to fabricate silicon devices, many workers have attempted to investigate the damage distribution and the recrystallization process in ion-implanted regions. Successive results can be obtained by Rutherford backscattering (RBS) measurements and transmission electron microscope (TEM) observations, but it is difficult to obtain accurate depth profiles of the damage distributions and the recrystallization in the region of interest.

The optical reflectivity measurement coupled with stripping of surface layers by anodic oxidation is one of the most practical techniques for obtaining the depth profile of crystalline imperfection in silicon (1-3). The crystalline damage induced by the ion implantation causes variations of the optical parameters of silicon. The optical reflectivity of the crystalline silicon show sharp peaks at the wavelengths of 275 nm and 340 nm, which correspond to the threshold energies for the direct interband transition at x and Γ points, respectively. On the other hand, the reflectivity at 330 nm changes only 1-3% for the state from the single-crystal to amorphous. Evaluation of the crystalline imperfection by UVRM presented in this paper is based on detecting variations of the optical reflectivity in samples.

The authors have developed an apparatus for measuring UV reflectivity, and have investigated the damage distribution profiles in ion-implanted silicon wafers by measuring the relative reflectivity at 275 nm with reference to the reflectivity at 330 nm. In addition, the authors have applied UVRM to evaluate the crystalline quality of silicon epitaxial film grown on a porous silicon layer. Profiles of the crystalline imperfection obtained by UVRM are compared with results obtained by RBS.

Experimental

Figure 1 shows the apparatus developed in order to measure variations of UV reflectivity on a sample surface. The system consists of a monochromatic light source, reflectors, and a detector. The incident light transmits through the half mirror and the polarizer and is reflected on the sample surface. The intensity of reflected light is detected by the photomultiplier. The intensity of incident light is monitored by a solar cell. The system is set in a box filled with dry N_2 gas to reduce the absorption of UV light by oxygen in air. In this optical system, the reflected light intensity I is given by the following relation

$$I = T_{HM} \times T_P^2 \times R_{HM} \times R_S^2 \times R_R \times I_i$$

where T_{HM} and T_P correspond to the transmissivity of the half mirror and the polarizer, and R_{HM}, R_R, and R_S to the reflectivity of the half mirror, the reflector, and the sample surface, respectively. The crystalline imperfection in surface region of a sample is defined as the following equation

$$\text{Imperfection} = \frac{I_c(\lambda_1)/I_c(\lambda_2) - I_s(\lambda_1)/I_s(\lambda_2)}{I_c(\lambda_1)/I_c(\lambda_2) - I_a(\lambda_1)/I_a(\lambda_2)}$$

where $I(\lambda_1)$ and $I(\lambda_2)$ correspond to the reflected light intensities at 275 and 330 nm, respectively, and c and a denote the control samples for the crystalline and amorphous, respectively, and s to the sample under test. Values of the crystalline imperfection given by this method have a correlation to the density of defects and the degree of damage in a sample. Optical

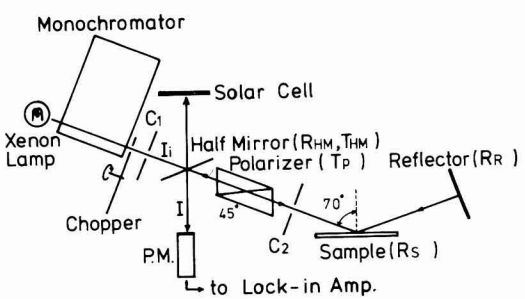

Fig. 1. Schematic diagram of the apparatus for UVRM. C_1, C_2: collimator, P.M.: photomultiplier.

* Electrochemical Society Active Member.

parameters depending on the system are eliminated by calculating the difference of the reflected light intensities between the measured sample and the control samples. The experimental errors due to the surface contaminations can be minimized by calculating the ratio of the reflected light intensities at λ_1 and λ_2. A depth profile of the crystalline imperfection, i.e., crystalline damage and quality in a sample, is obtained by successive reflectivity measurements followed by the anodic oxidization and stripping of surface layer. In the anodic oxidation process, a mixture of N-methylacetamide (NMA) and potassium nitride (KNO_3) is used as the electrolyte in order to form constant oxide thickness in silicon wafers with various impurity concentrations and defect densities. The depth of stripping by each anodic oxidization process was defined as an averaged value calculated from total etched depth and numbers of anodic oxidization.

To investigate distribution profiles of damage induced by ion implantation, P^+ and Si^+ were implanted into (100) oriented silicon wafers at room temperature. Thermal treatments at various temperatures were performed in dry N_2 gas for 10 min. Crystalline quality of silicon epitaxial film was also evaluated by UVRM. A silicon film with a thickness of 200 nm was grown on a porous silicon layer by means of the plasma dissociation of pure silane (4). A porous silicon layer of 2 μm was formed in a p-type silicon wafer with a resistivity of 0.003 Ω-cm by the anodization in 50% HF solution. The anodic current density was controlled at 5 mA/cm^2. Damage distribution profiles and the recrystallization process in ion-implanted regions, and the crystalline quality of epitaxial film were also evaluated by RBS with 400 keV $^3He^+$.

Results and Discussion

Figure 2 shows an aligned and a random RBS spectra from a P^+- and Si^+-implanted sample. Silicon ions of 5×10^{14}/cm^2 were implanted with the energy of 140 keV before P^+ implantation of 5×10^{14}/cm^2 at 100 keV. These spectra show only that the amorphous state is formed by the ion implantations except for the surface region. On the other hand, the depth profile of the crystalline imperfection in the same sample obtained by UVRM indicates, as shown in Fig. 3, that

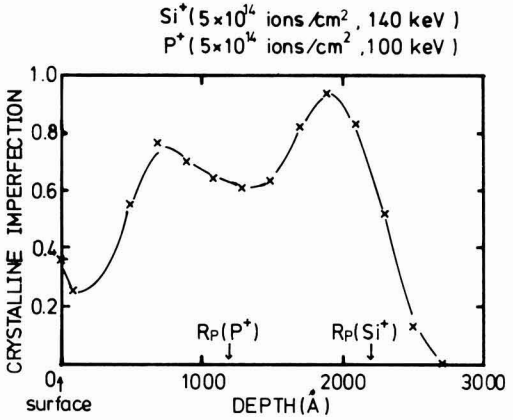

Fig. 3. Depth profile of the crystalline imperfection in P^+- and Si^+-implanted sample.

the amorphous state is not formed in the ion-implanted region. Two peaks of the crystalline imperfection are clearly detected by UVRM at the depth of 80 and 200 nm. These peaks seem to correspond to distributions of damage induced by P^+ and Si^+ implantation, respectively. It is revealed that UVRM has high resolution upon the degree of damage compared with RBS measurement.

Figure 4 shows RBS spectra of Si^+-implanted silicon. Silicon ions of 1×10^{15}/cm^2 were implanted with the energy of 110 keV. The aligned spectra after the ion implantation seem to indicate that the amorphous region is formed in the implanted region except for the surface layer of 40 nm. After the annealing at 500°C, the aligned spectrum of the implanted region shows that the recrystallization proceeds from the surface region in addition to the recrystallization from the substrate. The aligned yield from the implanted region decreases with increasing the annealing temperature, however, the depth profile of residual dam-

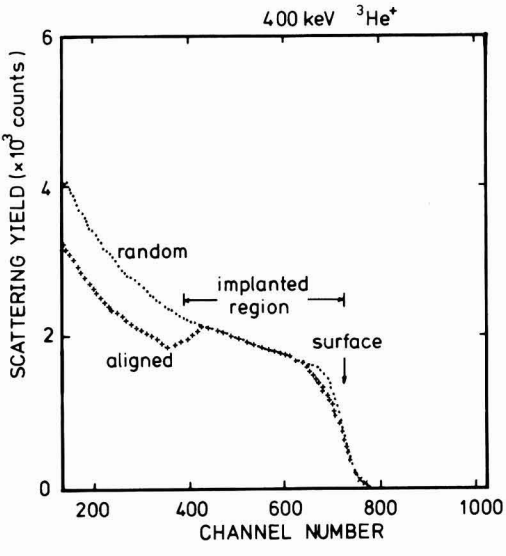

Fig. 2. Backscattering spectra of P^+- and Si^+-implanted silicon. Silicon ions of 5×10^{14}/cm^2 are implanted with the energy of 140 keV before P^+ implantation of 5×10^{14}/cm^2 at 100 keV.

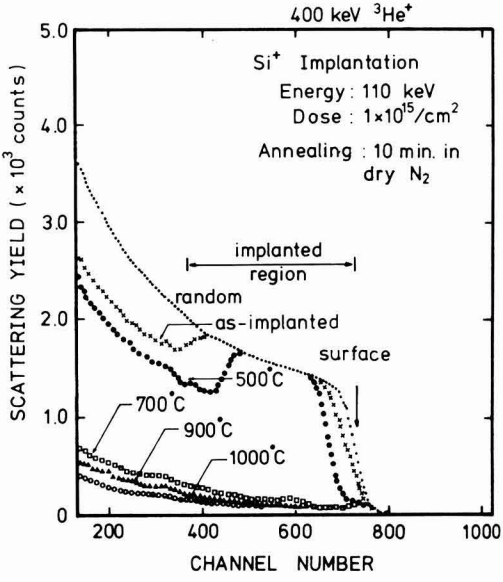

Fig. 4. RBS spectra of Si^+-implanted silicon. Silicon ions of 1×10^{15}/cm^2 were implanted with the energy of 110 keV, and annealed at 500°, 700°, 900°, and 1000°C for 10 min.

age after the annealing above 700°C cannot be determined in these spectra.

Depth profiles of the crystalline imperfection in the same samples obtained by UVRM are shown in Fig. 5. It is evident that the amorphous state is not formed by Si^+ implantation with a dose of $1 \times 10^{15}/cm^2$, and that the degree of damage in the surface region of 40 nm is less than that in the region between 40 and 240 nm. It is considered that the amorphous state was not formed in the implanted region because of increase of the substrate temperature during the ion implantation. As observed in RBS spectra, it is evident from UVRM spectra that the recrystallization proceeds from the substrate toward the surface, and that the recrystallization also takes place from the surface by the annealing at 500°C. It is clear that the damage induced by the ion implantation remains in the region between 80 and 180 nm. In the case of the annealing at higher temperature, the residual damage can be detected by UVRM. The implanted region is recrystallized mainly from the substrate toward the surface by the annealing above 700°C. After the annealing at 1000°C, the damage still remains in the surface region of 100 nm, and it is considered that the surface region is not recrystallized completely because the crystalline quality of this region, that acts as a seed for the recrystallization from the surface, is poor compared with the substrate. The annealing for a longer time is required for the complete recrystallization of the implanted region.

The depth profile of both the crystalline imperfection obtained by UVRM and the dechanneled fraction by RBS in the epitaxial film on a porous silicon layer are shown in Fig. 6. Dechanneled fractions were calculated from the ratio between the aligned yield and the random yield at the same depth, and have a correlation to the defect density. A large value of the dechanneled fraction near the interface indicates existence of a transition region from the porous structure to a uniform epitaxial film, where micropores are pinching off quickly according to the film growth. A tendency of increase of the crystalline imperfection given by UVRM is in good agreement with the distribution profile of the dechanneled fraction obtained by RBS measurement. It is revealed that UVRM is also available in the evaluation of the crystalline quality of silicon epitaxial films.

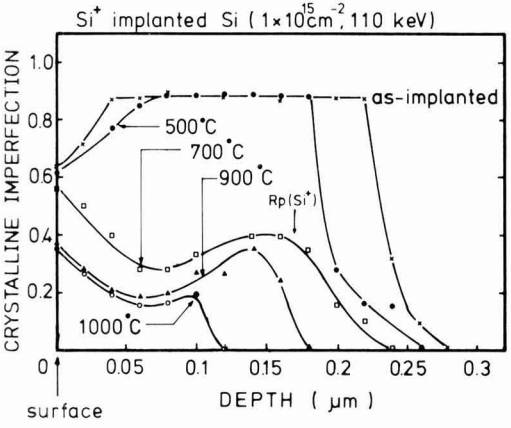

Fig. 5. UVRM spectra of Si^+-implanted silicon

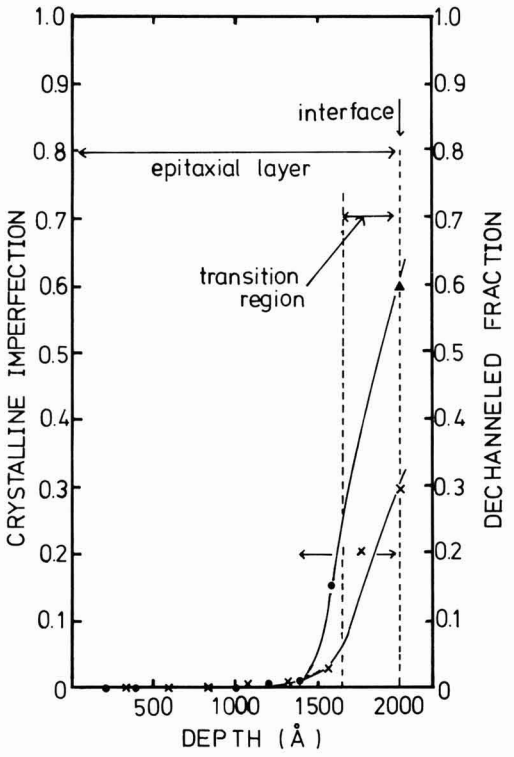

Fig. 6. Comparison between the crystalline imperfection given by UVRM and the dechanneled fraction by RBS measurement. Silicon film of 0.2 μm was grown on a porous silicon layer of 2 μm. ▲ shows the crystalline imperfection of original surface of the porous silicon layer measured before the epitaxy.

Conclusion

Ultraviolet reflectivity measurement is an excellent technique for the evaluation of the crystalline qualities of epitaxial films and damage in ion-implanted regions. Though the dependence of the optical reflectivity on the lattice damage is not well identified, it is considered that the aligned yield obtained by RBS measurement depends on the density of atoms displaced from the crystalline sites, and that the reflectivity change at 275 nm is caused by the increase and broadening of state density near the conduction band bottom to the lower energy side by the lattice damage. Accordingly, the degree of crystalline imperfection given by UVRM does not always agree with the experimental results obtained by RBS measurement, but detailed distribution profiles of the crystalline imperfection in silicon can be obtained by UVRM with successive stripping of the surface layer.

Manuscript submitted Oct. 22, 1982; revised manuscript received May 31, 1983.

REFERENCES

1. M. Miyao, T. Miyazaki, and T. Tokuyama, *Jpn. J. Appl. Phys.*, **17**, 955 (1978).
2. J. E. Fredrickson, C. N. Waddell, G. Spitzer, and G. K. Hubler, *Appl. Phys. Lett.*, **40**, 172 (1982).
3. E. A. Irene and D. W. Dong, *This Journal*, **126**, 1347 (1982).
4. T. Itoh and H. Takai, *Jpn. J. Appl. Phys.*, **22**, (1983).

The Mechanism of Orientation in Si Graphoepitaxy by Laser or Strip Heater Recrystallization

Henry I. Smith and C. V. Thompson[1]

Department of Electrical Engineering and Computer Science, Massachusetts Institute of Technology, Cambridge, Massachusetts 02139

M. W. Geis

Lincoln Laboratory, Massachusetts Institute of Technology, Lexington, Massachusetts 02173

R. A. Lemons,[2] **and M. A. Bosch**

Bell Laboratories, Holmdel, New Jersey 07733

ABSTRACT

An explanation is presented for the (100) texture and <100> orientation observed in Si graphoepitaxy by laser and strip heater recrystallization. With radiational heating, solid crystalline ribbons and islands, having a predominance of (100) texture, can coexist with molten Si. Crystallites with (100) texture and <100> parallel to the axis of a surface-relief grating are preferentially retained in partially molten regions, and these crystallites seed subsequent solidification, yielding the overall orientation.

In earlier papers (1-4), experiments on a type of graphoepitaxy in which amorphous or polycrystalline Si films were deposited over surface relief gratings in SiO_2 and then recrystallized[3] using a scanning laser beam or a strip heater oven were described. The resulting films were composed of large grains with (100) texture and a preferred orientation of <100> crystallographic axes along the grating axis. In this paper, we present an explanation for this texture and orientation [see also Ref. (4)].

The initial silicon graphoepitaxy research (1, 2) utilized a CW Ar-ion laser to recrystallize amorphous or polycrystalline silicon deposited over surface relief gratings of 3.8 μm spatial period in fused silica. A (100) texture and orientation of a <100> direction relative to the grating axis were observed only if recrystallization was carried out in an oxygen containing ambient (generally air was used). The oxygen caused an SiO_2 layer or cap, ~100 nm thick, to form over the Si. The (100) texture and <100> orientation showed angular spreads of $\sim\pm2°$ and $\sim\pm10°$, respectively (1-3). The orientation effect was reduced if the grating profile was degraded. Over a narrow range of laser power the silicon appeared to be partially molten and only under these conditions was orientation observed. (The partially molten condition was apparent in an image formed with the laser beam reflected off the sample.) If the silicon was fully melted, or if the recrystallization was carried out in an inert gas, or nitrogen, no orientation or texture was observed.

When these results were initially reported, there was considerable skepticism that a silicon film, heated by laser radiation, could exist in a partially molten configuration. However, recent work by Bösch and Lemons (5-7) and Biegelson and Hawkins (8, 9) has shown that one can indeed achieve a stable configuration of solid silicon crystallites in a pool of molten silicon, provided that the silicon is heated radiatively. This liquid-solid coexistence is stable only when the Si is contacted on both sides by an oxide. (The oxide on the top side can form in an O_2 containing ambient such as air, or be deposited.) The silicon crystallites are generally a few micrometers wide and have characteristic elongated shapes. They have been variously referred to as "filaments," "lamellae," or "worms" (5-9). However, since the solid extends through the thickness of the film, which is usually 5-10 times smaller than the width of the crystallites, we will refer to elongated crystallites as solid ribbons and to isolated segments of roughly equal length and width as solid islands. The width of the ribbons is remarkably constant, as is their spacing, if ribbons are densely packed.

Figure 1 illustrates the pattern of ribbons and islands in a film heated in air with an Ar-ion laser. As discussed below, it is believed that the <100> graphoepitaxial orientation effect is a product of the interaction of such ribbon and island crystallites with the surface relief grating.

The configuration of solid crystallites separated by molten Si is stable in that the fraction of material that is solid and the fraction that is liquid remain constant with time, for constant laser power input. Under Ar ion laser irradiation, the individual ribbons change shape with time and appear to move about. In some cases, small crystallite islands appear to break off from ribbons and move independently through the melt. Such motion is only apparent; the solid material itself is fixed relative to the substrate and cap. As material solidifies on one edge of a crystallite an equal amount tends to melt from the opposite edge, giving the appearance of motion. Careful observation has shown that ribbons and islands do not nucleate spontaneously in the melt. They are either unmelted remnants of the polycrystalline material, or they are the product of growth from unmelted crystallites.

Hawkins and Biegelson (8, 9) have presented a theoretical model to explain the dynamic stability of the partially molten configuration. This model takes into account the large increase in reflectivity of Si when it melts (a semiconductor-to-metal transition). The power density required to maintain a pool of fully molten Si, P_2, is higher than the power density required to heat solid Si up to the threshold of melting, P_1. At any power density intermediate between P_1 and P_2, the fraction of the film that is in the solid phase is intermediate between one and zero. If silicon is melted nonradiatively, such as by thermal conduction (9) or an electrical discharge (10), no ribbons or islands form.

[1] IBM Postdoctoral Fellow. Currently, Department of Materials Science and Engineering, Massachusetts Institute of Technology.

[2] Present address: Los Alamos National Laboratory, Los Alamos, New Mexico 87545.

Key words: recrystallization, graphoepitaxy, silicon, semiconductor.

[3] We use the term "recrystallization" to encompass both the traditional meaning (solid-state processes involving grain nucleation and/or growth) and melting followed by solidification, in accord with recent usage.

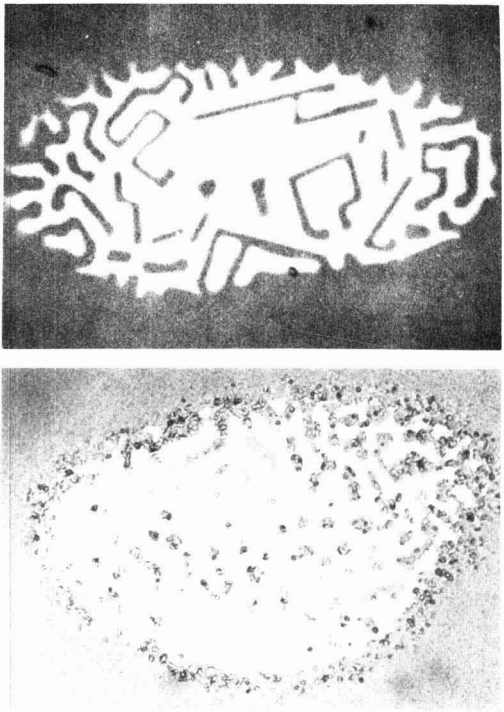

Fig. 1. Ar^+ laser irradiated area of a $\sim 1/2$ μm thick poly-Si film on fused silica. (a, top) Optical micrograph made from the back side in reflected light. Solid Si appears dark, molten Si appears bright. (b, bottom) Optical micrograph made in reflected light from the front side [a different sample than in (a)]. A thin SiO_2 encapsulation layer is formed in the air ambient. The granular appearance on the perimeter of the partially molten region probably indicates solid-state recrystallization or grain growth. Some islands in the partially molten region also have a granular appearance suggesting they have remained unmelted.

For an elliptical laser spot, such as shown in Fig. 1, ribbons extend inward from a perimeter of polycrystalline silicon. The material on the perimeter has a rough, granular appearance, as shown in Fig. 1b. This suggests that rapid solid-state recrystallization or grain growth (11) occurs in this material, which is close to the melting temperature. If so, the grain size appears to be of the order of micrometers, which is much larger than the size of polycrystalline grains away from the high temperature region ($\lesssim 0.1$ μm). If the laser power is increased, the perimeter expands and the central region can become fully molten. As the laser power is decreased, the solid ribbons grow inward, leading eventually to complete solidification.

The solid ribbons and islands tend to be parallel-sided and take on shapes with angular features close to 90°, suggesting (100) texture (see Fig. 1). As described elsewhere (10) and below, x-ray measurements, taken after solidification of the partially melted "transition region," confirm a predominance of (100) texture. The development of (100) texture among solid ribbons and islands may be explainable by thermodynamic arguments. It is speculated that the interfacial energy between Si crystallites and the SiO_2 of the cap and substrate is lowest for crystallites with (100) texture. Although there is no direct proof that this interface is the least energetic, it is well known that it has the lowest densities of fixed oxide charge and interface electronic states (12). Also, oxidation-enhanced diffusion and the rate of growth of stacking faults are maximum for (100) Si-SiO_2 (13). We do not believe a direct calculation of the interfacial energy would be meaningful in the absence of an experimentally verified model for the Si-SiO_2 interface.

Given that Si crystallites with (100) planes parallel to the cap and substrate oxides have the lowest surface-energy contributions to their total energy, grains with (100) texture should dominate in solid-state recrystallization or grain growth immediately prior to melting. Also, (100) textured crystallites, isolated by partial melting, will have a slightly higher melting temperature ($\sim 10^{-2}$ K if one assumes a surface-energy difference of 0.01 J/m^2 for (100) Si-SiO_2, as shown in the Appendix). Since the temperature of the entire partially molten region is stabilized by the mechanism described by Hawkins *et al.* (9), even this small difference in melting temperature might lead to preferential retention of (100)-textured crystals. Regardless of whether solid-state grain enlargement or melting-temperature differential is responsible for preferential retention of (100)-textured crystallites, if a surface relief structure of square-wave cross section is present, unmelted crystallites having (100) texture and <100> directions perpendicular to (and therefore also parallel with) the grating axis should be preferentially retained (14, 15).

Recently, we studied laser recrystallization over surface relief gratings (3.8 μm period, 0.1 μm depth, square-wave cross section) in SiO_2 using an Ar-ion laser and an apparatus that permitted optical microscopy during laser irradiation (5-7). As the laser power was increased and total melting approached, the last crystallites to melt were located along the grating corners, and these tended to have oriented, square shapes (Fig. 2), suggesting <100> orientation along the grating axis. Also, ribbons tended to be parallel to the surface relief grating. When molten Si came in contact with the relief grating in SiO_2, the profile was very rapidly rounded due to plastic flow at the high temperature (1412°C). Grating profile was preserved only underneath those crystallites which had not been melted (Fig. 2). We believe such unmelted crystallites seed solidification. Since the resolidified material is oriented with <100> predominantly along the grating axis, the seeds from which it originated must also have been oriented. Thus, orientation can take place only if the seeds are located on a grating whose profile has not been degraded by plastic flow. This speculation is fully consistent with earlier observations that total melting eliminated orientation (1-4).

In the initial experiments using a stationary strip heater oven (3), larger grains were obtained than in the case of the laser and somewhat narrower angular spreads in the texture ($\sim \pm 0.5°$) and azimuthal orientation ($\sim \pm 5°$). The Si films were intentionally capped with ~ 2 μm of SiO_2, rather than a natural oxide. Recently, we investigated the mechanism of orientation for the case of strip heater Si graphoepitaxy, using substrates of thermal SiO_2 over silicon wafers. Gratings of 3.8 μm period were etched into the SiO_2 over a central 1 cm^2 region prior to deposition of 0.5 μm of Si and a cap of 2 μm SiO_2, 30 nm Si_3N_4. Using a stationary strip heater, samples were preheated to 1100°-1300°C on the lower strip and then radiation from the upper strip melted an elliptically shaped molten zone, which grew radially at 10-100 mm/sec. When the power to the upper strip was turned off, the molten zone solidified rapidly. If this resolidification took place after the elliptically shaped molten zone had grown beyond the area of the grating, (100) texture was observed, but no orientation relative to the grating. (This is consistent with the observation discussed above that total melting destroys the grating and eliminates orientation.)

After resolidification, three distinct zones are clearly discernable: zone 1, a central region that had been fully melted and resolidified, composed of large

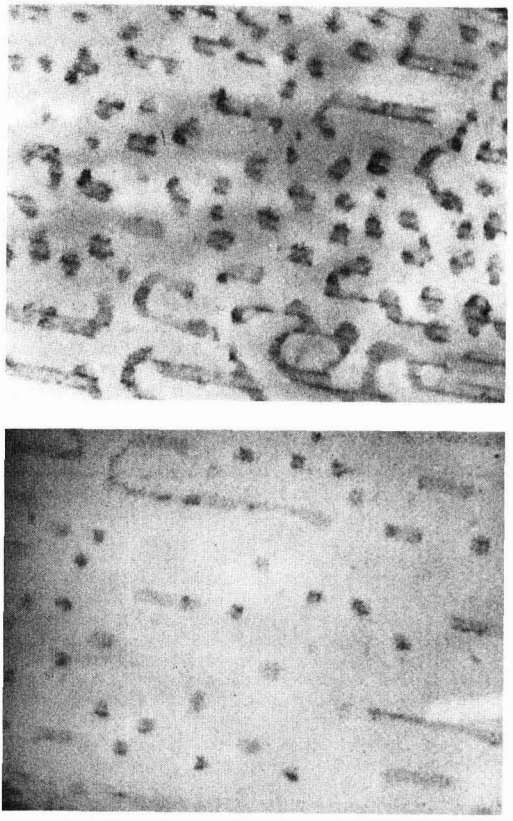

Fig. 2. Ar^+ laser irradiated area of a ~1/2 μm thick poly-Si film on a fused silica substrate in which a 3.8 μm-period surface relief grating has been etched to a depth of 0.1 μm. Photographs have been taken from a TV monitor. Corners of grating appear as dark lines at the edge of crystallites. (a, top) Note that grating profile is retained only underneath unmelted crystallites. (b, bottom) Same area after further melting.

($\gtrsim$1 mm) crystalline grains; zone 2, a narrow, annular transition region at the border of zone 1, composed of crystalline grains a few μm in diameter; and zone 3, beyond the transition region, composed of fine grain (<0.1 μm) polycrystalline silicon which had not melted or seen any significant grain growth. We believe the transition region corresponds to the condition of partial melting described above. X-ray diffraction analysis shows that there is a strong predominance of (100) texture in the transition zone, even for SiO_2 encapsulants <250 nm thick, as shown in Fig. 4 of Ref. (10). We were unable to determine if there was <100> orientation with respect to the grating within the transition region (zone 2) either during or after recrystallization. Efforts to prepare samples of transition regions for TEM analysis were invariably unsuccessful. Because of this difficulty, a "grid-of-etch-pits" technique (16) was developed to analyze grain orientation in zone 1, immediately adjacent to the transition region, zone 2. The orientation of grains in zone 1 was assumed to reflect the orientation of the smaller grains within the transition region from which they had grown. [Grains within the transition region are too small (~2 μm) to analyze by the grid-of-etch-pits technique.] Figure 3 is a histogram of the azimuthal orientation of those crystalline grains that have (100) texture and are located immediately adjacent to the transition region. Clearly, there is a preference for orientation of <100> parallel to the grating axis.

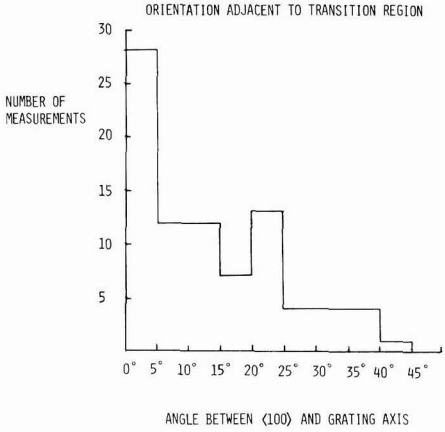

Fig. 3. Histogram of measurements of the angle between the grating axis and the <100> directions of etch pits immediately adjacent to the transition region. The etch pits were located on a square grid of 50 μm period. Measurements were taken only when the pit shape indicated (100) texture.

Histograms of grain orientation along the edges of transition regions that are not over gratings show no preferential azimuthal orientation. From these results, we conclude that orientation with respect to the surface relief grating takes place in the transition region and that crystallites in the transition region act as oriented seeds during solidification of zone 1. This is the same mechanism as is operative in laser recrystallization, discussed above: orientation takes place only in a region of partially molten silicon; (100) texture is predominant among crystallites in this partially molten region; if a surface relief grating is present, the (100)-textured crystallites have a predominant <100> orientation along the grating axis, and seed subsequent solidification. During solidification of the melt in zone 1, the grating has no further influence on orientation. The grating profile is destroyed by contact with molten Si. Moreover, even if its profile were preserved, a surface relief grating would not be expected to alter the orientation during solidification. No orientation relative to a surface relief grating was observed with a movable strip heater. In this case, orientation is along the direction of zone motion, due to directional solidification and occlusion (10, 17).

A surface relief grating does, however, change the characteristics of zone melting in one interesting way. On smooth SiO_2 surfaces, dendritic growth competes with (100)-textured growth at zone scanning speeds in excess of ~1 mm/sec (10, 17). Over surface relief gratings, the onset of dendritic growth occurred at ~3 mm/sec. We believe the surface relief structure greatly decreases the distance between interior corners of the faceted solid-liquid interface, which would support a higher rate of solidification (18). This speculation is supported by the observation that subboundaries are frequently entrained by, and run parallel to, the grating lines.

In addition to the grains having (100) texture, there are grains in the transition region, and adjacent to it, that have other textures but no specific orientation relative to the grating. These can also act as seeds during solidification of zone 1. However, as discussed in Ref. (10, 17), their growth is occluded by the growth of (100)-textured grains. The occlusion phenomenon may explain why larger grains and better texture were obtained with the stationary strip heater than with the laser (3). The analysis of orientation by x-ray pole plotting was done only in the solidified zone 1, so that grains whose texture deviated from (100) were eliminated by the occlusion effect.

The *in situ* observations of the morphology and dynamics of ribbons and islands in laser recrystallization (Fig. 1 and 2) lead us to speculate that high quality orientation (*i.e.*, much smaller angular spread in texture and orientation) with respect to artificial surface relief gratings might be realizable by laser recrystallization if one could avoid degradation of the grating profile, for example, by use of substrates with higher softening temperature. Furthermore, by oscillating the input power density, the solid ribbons and islands might be induced to settle into their lowest free-energy highly oriented configuration. However, the general view is that graphoepitaxy, especially of Si and other semiconductors, will have a far greater impact if it can be accomplished by means of low temperature processes that do not involve melting (19).

Acknowledgments

This work was sponsored by the Defense Advanced Research Projects Agency. The authors are grateful to J. M. Carter and C. L. Doherty for technical assistance, and D. A. Antoniadis, D. K. Biegelsen, J. D. Plummer, F. Spaepen, W. Tiller, and many others for helpful discussions.

Manuscript submitted Jan. 14, 1983; revised manuscript received May 25, 1983.

Massachusetts Institute of Technology assisted in meeting the publication costs of this article.

APPENDIX

The Dependence of Melting Temperature on Crystallographic Texture

Consider two crystals of Si with equal cross-sectional area A and thickness t surrounded by liquid Si. We assume one of the crystals has (100) texture, that the surface energy for the interface between the crystal and an amorphous SiO_2 layer is γ_{100}, and that the other crystal has (111) texture with surface energy γ_{111}. The interfaces between the crystals and the melt also have equal area, A', and will be assigned the surface energy γ_{ls}. For the sake of simplicity, it will be assumed that γ_{ls} is isotropic. For a bulk free energy ΔG_v and atomic volume $\bar{V}$, the chemical potential for the (100) crystal is

$$\mu_{100} = (-2\gamma_{100}A - \gamma_{ls}A' + At\,\Delta G_v)/(At/\bar{V})$$

similarly

$$\mu_{111} = (-2\gamma_{111}A - \gamma_{ls}A' + At\,\Delta G_v)/(At/\bar{V})$$

The difference in chemical potential is therefore

$$\Delta\mu = \mu_{100} - \mu_{111} = \frac{2\Delta\gamma\bar{V}}{t}$$

where $\Delta\gamma = \gamma_{111} - \gamma_{100}$. Assuming a small difference in the heat capacities of the liquid and solid (20)

$$\Delta\mu = \Delta S_f\,\Delta T_m$$

where ΔS_f is the entropy of fusion per atom and ΔT_m is the difference in melting temperature [$(\Delta T_m = T_m(100) - T_m(111)]$. Thus

$$\Delta T_m = \frac{2\Delta\gamma\bar{V}}{t\Delta S_f}$$

If we assume that the average surface energy is about 0.1 Jm^{-2} and that the difference in the surface energy between (100) and (111) is about 10% (*i.e.*, $\Delta\gamma \cong 0.01$ Jm^{-2}) then for a 0.5 μm thick film, the difference in melting temperature should be 0.016°C. This effect is enhanced by larger surface-energy anisotropy and smaller film thicknesses.

REFERENCES

1. M. W. Geis, D. C. Flanders, and H. I. Smith, *Appl. Phys. Lett.*, **35**, 71 (1979).
2. M. W. Geis, D. C. Flanders, H. I. Smith, and D. A. Antoniadis, *J. Vac. Sci. Technol.*, **16**, 1640 (1979).
3. M. W. Geis, D. A. Antoniadis, D. J. Silversmith, R. W. Mountain, and H. I. Smith, *Appl. Phys. Lett.*, **37**, 454 (1980).
4. H. I. Smith and M. W. Geis, Abstract 155, p. 249, The Electrochemical Society Extended Abstracts, Vol. 82-1, Montreal, Que., Canada, May 9-14, 1982.
5. M. A. Bosch and R. A. Lemons, *Phys. Rev. Lett.*, **47**, 1151 (1981).
6. R. A. Lemons and M. A. Bosch, *Appl. Phys. Lett.*, **39**, 343 (1981).
7. R. A. Lemons and M. A. Bosch, *ibid.*, **40**, 703 (1982).
8. D. K. Biegelsen, N. M. Johnson, and M. D. Moyer, Abstract 142, p. 229, The Electrochemical Society Extended Abstracts, Vol. 82-1, Montreal, Que., Canada, May 9-14, 1982.
9. H. G. Hawkins and D. K. Biegelsen, *Appl. Phys. Lett.*, **42**, 358 (1983).
10. M. W. Geis, H. I. Smith, B-Y Tsaur, J. C. C. Fan, D. J. Silversmith, and R. W. Mountain, *This Journal*, **129**, 2812 (1982).
11. Y. Wada and S. Nishimatsu, *ibid.*, 125, 1499 (1978).
12. S. M. Sze, "Physics of Semiconductor Devices," 2nd ed., John Wiley & Sons, New York (1981).
13. S. M. Hu, *J. Appl. Phys.*, **45**, 1567 (1974).
14. D. C. Flanders, Ph.D. dissertation (M.I.T., 1978); reprinted as Lincoln Laboratory Technical Report 533 (1978).
15. H. I. Smith and D. C. Flanders, *Appl. Phys. Lett.*, **32**, 349 (1978).
16. K. A. Bezjian, H. I. Smith, J. M. Carter, and M. W. Geis, *This Journal*, **129**, 1848 (1982).
17. M. W. Geis, H. I. Smith, B-Y Tsaur, J. C. C. Fan, E. W. Maby, and D. A. Antoniadis, *Appl. Phys. Lett.*, **40**, 158 (1982).
18. M. W. Geis, H. I. Smith, D. J. Silversmith, R. W. Mountain, and C. V. Thompson, *This Journal*, **130**, 1178 (1983).
19. H. I. Smith, M. W. Geis, C. V. Thompson, and H. A. Atwater, To be published in *J. Crystal Growth*.
20. C. V. Thompson and F. Spaepen, *Acta. Metall.*, **27**, 1855 (1979).

Oxidation of Sputtered Niobium Nitride Films

P. K. Gallagher, W. R. Sinclair,* D. D. Bacon, and G. W. Kammlott

Bell Laboratories, Murray Hill, New Jersey 07974

ABSTRACT

Isothermal (440°-540°C) weight change measurements were made in 0.1% O_2 in Ar on films of cubic niobium nitride deposited on fused silica or sapphire substrates. The data were fit to various rate laws using a fraction-reacted from 0.2 to 0.9. The best fitting rate equation over these ranges of temperature and fraction-reacted was the Avrami equation, but several others fit nearly as well. The Arrhenius parameters derived from these data had an activation energy of 44.3 kcal mol^{-1} and a log pre-exponential term of 9.26 sec^{-1}. The value of the activation energy was virtually independent of the choice of the best fitting rate law. This apparent activation energy agrees well with that reported for the diffusion of oxygen in Nb_2O_5. It is suggested that the mechanism is analogous to the oxidation of niobium metal and the rate controlling step is diffusion of oxygen through a thin continuous layer of initial product. Studies of the oxidation showed no significant dependence of reaction rate on P_{O2}. The average weight gain was 25.0±0.9 (weight percent) w/o which leads to a film stoichiometry of $NbN_{0.96\pm0.06}$ based upon a stoichiometric Nb_2O_5 product. X-ray diffraction above 450°C studies indicated that the product films were the low temperature polymorph of Nb_2O_5. Below 450°C, the entire product films were amorphous or microcrystalline. In spite of the large lattice expansion associated with this oxidation, scanning electron microscopy revealed that the product films were adherent and continuous without large (>0.1 μm) cracks or pores. Matching the thermal expansion of the substrate and film does not seem important since similar results were obtained with both substrates.

Superconducting niobium nitride films are of interest as materials for Josephson junction devices (1, 2). These films have been prepared by d-c reactive magnetron sputtering of niobium in nitrogen-argon mixtures (3). The preparation of a thin continuous insulating surface layer on these films is an essential part of such devices. These surface layers are prepared by controlled oxidation of the film.

Earlier studies (4) on polycrystalline δ-$NbN_{0.9}$ prepared from bulk powder arrived at the following conclusions: (*i*) there is an enormous expansion accompanying the oxidation of δ-$NbN_{0.9}$. (*ii*) The oxidation best followed a pseudo first-order rate law. (*iii*) Both isothermal and dynamic studies gave an apparent activation energy of 50 kcal mol^{-1}. (*iv*) The product of the oxidation was Nb_2O_5 without the formation of intermediate oxynitrides or lower valent oxides of niobium.

It is the purpose of this study to determine if these conclusions are valid also for the oxidation of thin films, and if there are any significant effects induced by changing the substrate or partial pressure of oxygen.

Experimental Procedures and Results

Film preparation.—Niobium nitride films were prepared by d-c reactive magnetron sputtering in a 15% N_2-85% Ar ambient as has been recently described (3). This procedure leads to films having a T_c = 14.2 K and an average grain size of 5 nm. Sputtering was upwards from a Research Sputter Gun (5) onto substrates (1 × 2 × 0.1 cm). Substrates were either cleaned fused silica or cleaned single-crystal sapphire. After deposition of about 1 μm of film, the process was stopped, the system opened to air, and the substrates turned over for a similar deposition on the other side.

Weight change.—A Theta TG system was used to follow the isothermal weight change. An Omega Model 165 temperature controller replaced the controller packaged as part of the apparatus in order to achieve better isothermal operation. The output from a thermocouple in close proximity to the suspended sample and the output from the balance were fed to a Fluke Model 2500 data acquisition, control, and processor system. A premixed atmosphere of 0.093% O_2 in Ar or pure O_2 was flowed through the fused quartz hang down tube (1 in. diam) at 100 ml min^{-1}.

The data were least squares-fitted to those calculated for a variety of models for solid-state reactions or decompositions (6). A relatively wide range of fraction reaction (α) was used in this procedure, *i.e.*, $0.2 \leq \alpha \leq 0.9$. Of the 16 equations tested, three fit reasonably well. These were the Avrami equation (Eq. [1]), the Prout-Tompkins equation (Eq. [2]), and the simple linear equation (Eq. [3]), in which k represents the rate constant in sec^{-1}

$$[-\ln(1-\alpha)]^{1/3} = k_1 t \quad [1]$$

$$\ln[\alpha/(1-\alpha)] = k_2 t \quad [2]$$

$$\alpha = k_3 t \quad [3]$$

Table I presents the rate constants derived for these three equations. A plot of the data according to the Arrhenius equation (Eq. [4]

$$\log k = \log A - E/2.303RT \quad [4]$$

is shown in Fig. 1 for the Avrami and the Prout-Tompkins equations. The linear equations gave rate constants very similar to those of the Avrami equation. The lines in Fig. 1 represent the least squares fit to this equation for the data determined in 0.093% O_2 in Ar. Values of the apparent activation energy E and the log of the pre-exponential term A are given in Table I for each equation.

From the weights of the samples before and after oxidation, it is possible to make inferences with regard to the stoichiometry of the initial material, assuming that the final product is stoichiometric Nb_2O_5 and that the initial sample contained no signifi-

Table I. Rate data for the oxidation of cubic niobium nitride films in 0.1% O_2 in Ar or in pure O_2 (see Eq. [1], [2], and [3] in the text)

Temperature (K)	Substrate	k_1 (sec^{-1})	k_2 (sec^{-1})	k_3 (sec^{-1})
708.6	Sapphire	4.65×10^{-5}	2.27×10^{-4}	4.79×10^{-5}
708.6*	Sapphire	6.15×10^{-5}	3.00×10^{-4}	6.49×10^{-5}
708.8	Fused quartz	3.65×10^{-5}	1.78×10^{-4}	3.79×10^{-5}
723.9	Fused quartz	7.63×10^{-5}	3.74×10^{-4}	7.92×10^{-5}
729.7	Fused quartz	8.79×10^{-5}	4.30×10^{-4}	9.14×10^{-5}
733.9	Sapphire	1.43×10^{-4}	7.00×10^{-4}	1.53×10^{-4}
747.4	Fused Quartz	1.94×10^{-4}	9.54×10^{-4}	2.02×10^{-4}
754.8	Sapphire	2.10×10^{-4}	1.02×10^{-3}	2.23×10^{-4}
772.1	Sapphire	4.28×10^{-4}	2.08×10^{-3}	4.60×10^{-4}
769.0	Fused quartz	5.00×10^{-4}	2.45×10^{-3}	5.27×10^{-4}
773.0	Sapphire	4.94×10^{-4}	2.39×10^{-3}	5.34×10^{-4}
783.0*	Sapphire	6.16×10^{-4}	3.00×10^{-3}	6.41×10^{-4}
817.7	Fused quartz	3.15×10^{-3}	1.54×10^{-2}	3.28×10^{-3}
	E (kcal mol^{-1})	44.3	44.3	44.6
	$\log A$ (sec^{-1})	9.26	9.94	9.36

* Run in pure O_2. Not used for the calculation of Arrhenius parameters.

* Electrochemical Society Active Member.

Key words: kinetics, mechanisms, niobium oxide.

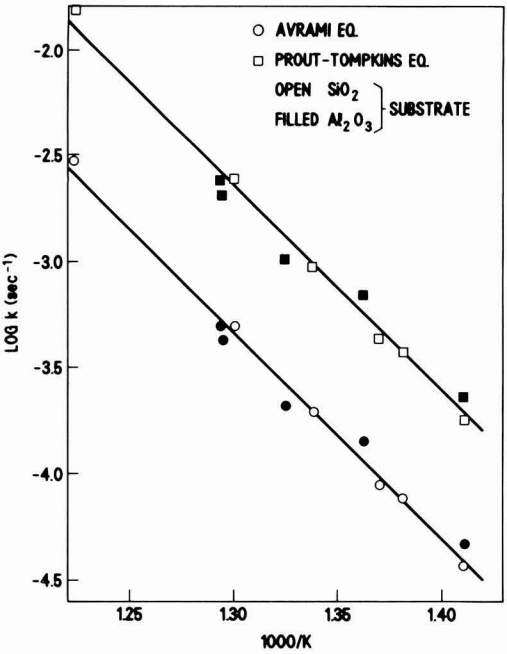

Fig. 1. Arrhenius plots for the oxidation of sputtered films of cubic niobium nitride.

cant impurities. The average weight gain of the samples oxidized to completion was 25.0 ± 0.9 w/o. This leads to a calculated initial stoichiometry of $NbN_{0.96\pm0.06}$. The nitride content is somewhat higher than $NbN_{0.9}$ observed in the previous study of the polycrystalline target material (4). This calculation neglects the contribution of carbon which is a known impurity.

Structure.—X-ray diffraction studies were made of the starting film and product films prepared at various temperatures in both 0.1% O_2 in Ar and pure O_2. The starting material was the cubic form generally referred to as δ-$NbN_{0.9}$. At the lowest temperature used for oxidation, 709 K, the product films were amorphous or microcrystalline. At higher temperatures, the same product was observed as for the oxidation of bulk polycrystalline powder (4), *i.e.*, the low temperature polymorph of Nb_2O_5.

Figure 2 presents SEM micrographs of films before and after oxidation. The product films are insulating and a covering layer of carbon has been deposited to reduce charging.

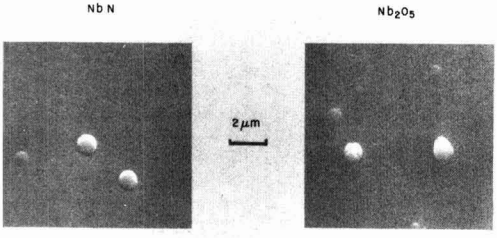

Fig. 2. Scanning electron micrographs of sputtered films of cubic niobium nitride before and after oxidation.

The change in film thickness for both amorphous and crystalline products was determined by the step height for as-deposited nitride on sapphire and after complete oxidation at 440° and 500°C. Results are presented in Table II.

Discussion

Overall weight gain and x-ray diffraction of the initial and final films indicate that the reaction under investigation is the oxidation of cubic substoichiometric niobium nitride, δ-$NbN_{0.95}$, to Nb_2O_5. In spite of the very large change in volume known to accompany this oxidation (4), see Table III, the SEM results in Fig. 2 do not indicate any blistering, cracking, or peeling of the films at this magnification. It would appear that any cracks or pores formed are less than about 0.1 μm. This is true whether the substrate is fused quartz or sapphire. Oxidation of the metal, on the other hand, requires an even greater volume change, see Table III, and the initial oxide film is protective but at greater thicknesses, blisters and cracks develop which are initially a few tenths of μm in size (7).

From the data in Table III, one would expect the product oxide film to be considerably thicker by a factor of about 2.3, depending upon its porosity, than the starting nitride film. The data in Table II indicate an increase by a factor of three in the thickness after oxidation. This does not appear to be greatly affected by the crystallinity of the product. The greater expansion would imply significant microcracks or microporosity. These pores or cracks do not arise from differences in thermal expansion of the substrate and film as substantiated by the lack of any observed difference between films deposited on fused quartz or on sapphire.

No single rate law provided consistently the best fitting oxidation rate equation. The best were those of Eq. [1], [2], and [3], and mechanistic inferences cannot be made solely from the data fitting. Substantiating evidence, generally microscopic, is necessary to confirm a particular reaction path (8). For comparison, a change from the parabolic to the linear rate law is observed for the oxidation of niobium metal once the protective nature of the oxide film has broken down by blister and crack formation. The parabolic rate is attributed to the rate being determined by diffusion of the reactant through an ever growing product layer. The linear law implies free access of the reactant and an essentially constant reaction cross section.

Examination of Fig. 1 and the Arrhenius parameters given in Table I suggests that any "reasonably" fitting rate equation will yield nearly the same value of apparent activation energy. The value of 44 kcal mol^{-1} is in good agreement with previous work on oxidation of nitride powders (4, 9) and of polycrystalline plates (9), 45-50 kcal mol.

Marker measurements for the oxidation of niobium have shown that oxide formation occurs at the metal/oxide interface (7). This is consistent with the fact that

Table II. Thickness measurements before and after oxidation

Nitride thickness (μm)	Temperature of oxidation (°C)	Oxide thickness (μm)
0.33	440	1.00
0.32	500	0.97

Table III. Molar volume of selected compounds of niobium

Compound	Molar volume (cm^3/Nb)
Nb (bcc)	10.9
$NbN_{0.9}$ (cubic)	12.8
NbN (hexagonal)	12.25
Nb_2O_5 (monoclinic)	29.15

Nb_2O_3 is an n-type semiconductor having an oxygen deficient stoichiometry. Chen and Jackson (10) have measured the oxygen diffusion constant in nearly stoichiometric Nb_2O_5 over the temperature range from 850° to 1200°C and obtained an activation energy of 49.4 ± 3.3 kcal mol. Comparison of the oxidation of the nitride herein with that of the metal (7) suggests a similar mechanism. During the very early stages or at low temperatures (<400°C), the amorphous product layer (oxide or oxynitride) is impervious and severely inhibits further growth. At higher temperatures, however, either rapid grain boundary diffusion becomes effective or microcracks or micropores are formed and the rate tends toward linearity. These pores or cracks need not be large to allow for sufficient diffusion of oxygen (11).

One would expect that the diffusion of oxygen through the continuous, amorphous, product film would be rate controlling in the low temperature regime provided that the out-diffusion of nitrogen occurs more readily. At higher temperatures where the rate law becomes more linear, one might expect the solid-state diffusion of oxygen to no longer be the rate determining step. However, the regime of constant rate does not preclude the diffusion of oxygen from being determining but merely requires the length of the path, presumably the impervious film thickness, to remain constant. Since the oxygen diffuses inward to the product/metal interface, it is suggested that the product formed at this point is the continuous, probably amorphous, phase. As the thickness increases beyond a certain value, the exterior surface becomes microporous or cracked, allowing for relatively free access of oxygen to the bulk oxide/amorphous product film interface. This transformation may be associated with strains, crystallization, or further oxidation of initial amorphous phase. The good agreement between the observed apparent activation energy for the oxidation of cubic niobium nitride during all stages of the reaction and that of the reported activation energy for the diffusion of oxygen in Nb_2O_5 (10) strongly suggests that this mechanism applies.

In the high temperature regime where linear rate behavior is approached, the values of k_3 given in Table I can be converted directly to a rate of interface motion if the motion is assumed inward and perpendicular to the surface. The film thickness for the kinetic samples was approximately 1 μm. Hence $d\alpha/dt$ of 2×10^{-4} sec^{-1} corresponds to about 2 A/sec. Despite the great caution which should be exercised in extrapolating from the data in Table I to the low temperature regime, there is excellent agreement with recent Auger spectroscopic results obtained near room temperature (12).

Manuscript submitted Jan. 9, 1983; revised manuscript received June 24, 1983.

Bell Laboratories assisted in meeting the publication costs of this article.

REFERENCES

1. F. Shinoki, S. Takada, S. Kosaka, and H. Hayakawa, *Jpn. J. Appl. Phys.*, **19**, Suppl. **19-1**, 591 (1980).
2. R. B. Van Dover, D. D. Bacon, and W. R. Sinclair, *Appl. Phys. Lett.*, **41**, 764 (1982).
3. D. D. Bacon, A. T. English, S. Nakahara, F. G. Peters, H. Schreiber, W. R. Sinclair, and R. B. van Dover, *J. Appl. Phys.*, To be published.
4. P. K. Gallagher and W. R. Sinclair, *Isr. J. Chem.*, **22**, 222 (1982).
5. A trademark of Sputtered Films Inc., Santa Barbara, CA.
6. D. W. Johnson, Jr., and P. K. Gallagher, *J. Phys. Chem.*, **75**, 1179 (1971).
7. J. V. Cathcart, J. J. Campbell, and G. P. Smith, *This Journal*, **105**, 443 (1958).
8. P. K. Gallagher, E. M. Gyorgy, and H. E. Bair, *J. Chem. Phys.*, **71**, 830 (1979).
9. P. Lefort, J. Desmaison, and M. Billy, *Mater. Res. Bull.*, **14**, 479 (1979).
10. W. K. Chen and R. A. Jackson, *J. Chem. Phys.*, **47**, 1144 (1967).
11. E. A. Irene, *This Journal*, **129**, 413 (1982).
12. R. P. Frankenthal, D. J. Siconolfi, W. R. Sinclair, and D. D. Bacon, *ibid.*, **130**, 2056 (1983).

Thermal Oxidation of Niobium Nitride Films at Temperatures from 20°-400°C

I. The Surface Reaction

R. P. Frankenthal,* D. J. Siconolfi,* W. R. Sinclair,* and D. D. Bacon

Bell Laboratories, Murray Hill, New Jersey 07974

ABSTRACT

The air oxidation of cubic δ-NbN has been studied by Auger electron spectroscopy at temperatures from ambient to 400°C. At temperatures of 180°C or less, only the first one or two monolayers are oxidized, the reaction product being an oxynitride of niobium. Above 200°C, oxidation is not limited and obeys a linear rate law. At these higher temperatures, the reaction product initially is an oxynitride but, as the reaction proceeds, eventually becomes Nb_2O_5. The reaction proceeds by the diffusion of oxygen through the reaction product to the NbN interface. Grain boundary diffusion of oxygen into the NbN is rapid and competes with the oxidation reaction.

In some recent studies, superconducting niobium nitride has been used as the base electrode in Josephson tunnel junction devices (1-4). Several oxides, including niobium oxide, have been proposed as the barrier layer on NbN to provide tunnel diodes, and it has been shown that the air oxidation of niobium nitride at temperatures from ambient to 90°C produces suitable junctions (4). There have, however, only been a few studies of the oxidation of niobium nitride, all at temperatures above 400°C (5-7). At these temperatures, bulk oxidation is rapid, and the thin films required for a good junction cannot be formed reliably. Therefore, we have undertaken a study of the oxidation of niobium nitride thin films in air over the temperature range from 20° to 400°C.

* Electrochemical Society Active Member.
Key words: Auger electron spectroscopy, Josephson junction, oxynitride, superconductor.

Experimental

Films of cubic NbN, commonly referred to as δ-$NbN_{0.9}$, 150-550 nm in thickness, were deposited on

silicon substrates by d-c reactive magnetron sputtering of niobium in a 15% N_2-85% Ar gas mixture (4). The films have an average grain size of 5 nm and a superconducting transition temperature of 14 K. The thickness of the films was calculated from the weight gain during deposition, assuming a density of 8.4 g/cm^3 for NbN. Films of Nb_2O_5, 15-28 nm in thickness, were deposited on silicon substrates by d-c reactive magnetron sputtering of niobium in an O_2 ambient. The thickness of these films was also calculated from the weight gain, assuming a density of 4.47 g/cm^3 for Nb_2O_5.

The NbN films were oxidized in air at temperatures from ambient to 400°C for times ranging from 0.5 to 64 hr.

The oxidized films were analyzed by Auger electron spectroscopy. All spectra were obtained in the derivative mode with a Physical Electronics Industries thin film analyzer (TFA) system. Operating conditions were 5 kV electron gun voltage, 10 μA beam current, and 2 eV modulation amplitude. The spectral data were digitized with a TransEra 752 A/D converter that interfaced a Tektronix 4052 microcomputer to the TFA. Depth profiles through the films were obtained by argon ion sputter etching and measuring the intensities (peak-to-peak heights) of the Nb 167 eV, O 510 eV, and N 380 eV peaks. The argon pressure was 7 mPa (5×10^{-5} Torr). The ion beam voltage and emission current were 2 kV and 30 mA, respectively. The sputter rates, determined from the time to sputter through the films and their known thicknesses, were 5.7 $\pm$ 0.3 nm/min for the NbN films and 11 $\pm$ 1 nm/min for the Nb_2O_5 films.

Results and Discussion

Electron stimulated effects.—Initially, both the oxygen and nitrogen peaks rapidly decrease in intensity due to electron-stimulated desorption of adsorbed oxygen and nitrogen. The O peak continues to decay, but more slowly, for an additional 10-20 min before it attains its steady-state intensity. The behavior of the N peak is a function of the reaction product thickness. For very thin films about 1 monolayer in thickness (see below), *i.e.*, those formed below 100°C, the N peak also continues to decay slowly until it reaches a steady state at about the same time that the O peak does. For reaction products of intermediate or several monolayers in thicknesses, the N peak, after the initial rapid decrease, reaches a minimum and then slowly increases until it reaches a steady state. For films formed at 400°C, the N peak rapidly reaches its steady-state value with the initial desorption. It is concluded that after adsorbed oxygen and nitrogen are desorbed, some electron-stimulated decomposition of the reaction product occurs. This accounts for the slow decrease in the O intensity after the initial rapid decrease. It also explains, for the films of intermediate thickness, the increase in the N intensity after the minimum. As the film is decomposed, *i.e.*, thinned by the electron beam, the signal from the NbN substrate becomes stronger. This is not observed for the films formed at 400°C because the quantity decomposed is most likely only a fraction of a monolayer and is too little to have a measurable effect when the reaction product is reasonably thick. The continuing decrease in the N peak intensity during electron-stimulated decomposition of the films formed below 100°C indicates that the reaction product contains some N and is probably a niobium oxynitride. Additional data confirming this is given below.

Ion sputter profiles.—Nitrogen depth profiles are shown in Fig. 1 for three reaction product films of different thickness. Each profile is the intensity, I_N, of the N peak normalized against the intensity, $I_{Nb'}$, of the Nb peak from the bulk NbN film. Normalization removes the effect of any instrumental variations from one experiment to the next.

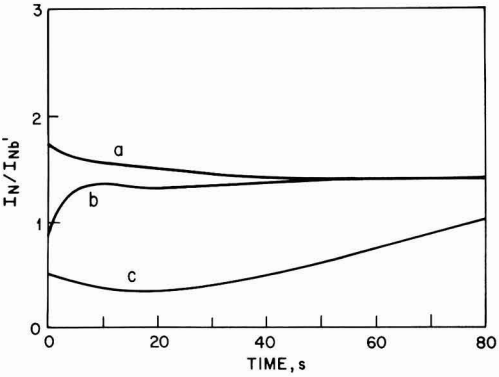

Fig. 1. Nitrogen depth profiles for oxidation at (a) 20°C for 24 hr, (b) 270°C for 16 hr, and (c) 400°C for 2 hr.

During sputter etching of the thinnest films, *i.e.*, those formed at temperatures below 100°C, the N peak decreases slowly in intensity until it reaches the steady state, corresponding to bulk NbN (Fig. 1, curve a). For films of intermediate thickness formed at 180°C, or at 270°C for oxidation times less than 20 hr, the N peak first increases in intensity, goes through a small maximum, and then decreases to the steady state (Fig. 1, curve b). For the films formed at 400°C, the N peak intensity first exhibits a small decline that is followed by a continuous increase as the reaction product is etched (Fig. 1, curve c). For the products of intermediate thickness, the initial increase in the N intensity is due to the thinning of the film with sputtering. The decrease after the maximum may be caused by some preferential sputtering of N from NbN. For the thin film, the initial decrease in the N intensity indicates that there is N associated with the outer layer of the surface. This means either that the oxidation product is discontinuous, that is, NbN is exposed at holes in the film, or that it contains both O and N. Since it is known that these films are good junctions and that they are made reproducibly (4), the film cannot be be discontinuous. Thus, it is thought that the thin reaction product is not a pure oxide but, more likely, an oxynitride. Additional confirmation for this is an observed change in shape of the N peak as the oxidation product is etched and the NbN film is exposed (Fig.2), indicating that the N-spectral peak comes from a species other than NbN.

The oxygen depth profiles are shown in Fig. 3-5 as a function of temperature and time of oxidation. Since the reaction products formed at temperatures of 180°C and below are probably oxynitrides of niobium, the sputter rate most likely lies between those for NbN and Nb_2O_5. At 20°C, the product is limited to a thickness of less than 0.5 nm, that is, to the first molecular layer (Fig. 3).[1] It does not grow thicker with further exposure to air. As noted above, the film formed at this temperature is probably an oxynitride. At 95°C, the limiting thickness is also only a monolayer of an oxynitride (Fig. 3). The initial O intensity at this temperature is greater than that observed at 20°C, which implies that the composition of the oxynitride is not fixed but is a function of the oxidation conditions. At 180°C, the steady state appears to have been reached after oxidizing for 64 hr. At this temperature, the product is 1-1.5 nm in thickness and extends into the second or, perhaps, third molecular layer (Fig. 3). The shape of

[1] For $NbN_{0.9}$, a_o is 0.439 nm and the unit cell contains 4 molecules of NbN (8).

Fig. 2. N KLL Auger electron peaks from (a) specimen oxidized at 95°C and (b) NbN.

the N peak indicates that this film is also an oxynitride.

At 270°C, a limiting thickness for the reaction product is not observed (Fig. 4, 6). Instead the oxidation reaction appears to follow a linear rate law. The same phenomenon is observed at 400°C (Fig. 5, 7) and is consistent with the results of Gallagher *et al.* (7) who studied the oxidation of similar NbN films at temperatures above 435°C. Since, as is shown below, the reaction product at these temperatures contains Nb_2O_5, the thicknesses in Fig. 6 and 7 were calculated assuming the sputter rate for Nb_2O_5. Although at temperatures below 435°C, the oxidation reaction could not be followed by techniques that measure changes in bulk properties (5-7), Auger electron spectroscopy in conjunction with depth profiling can do so easily.

At 270°C, the presence of an oxynitride in the oxidation product is indicated by the shape of the N peak. However, it is not possible to determine whether the oxynitride is present throughout the product or only at the NbN interface. At 400°C, N is detected at low levels throughout the oxidation product (Fig. 1), the concentration at the surface being slightly higher than in the bulk of the product.

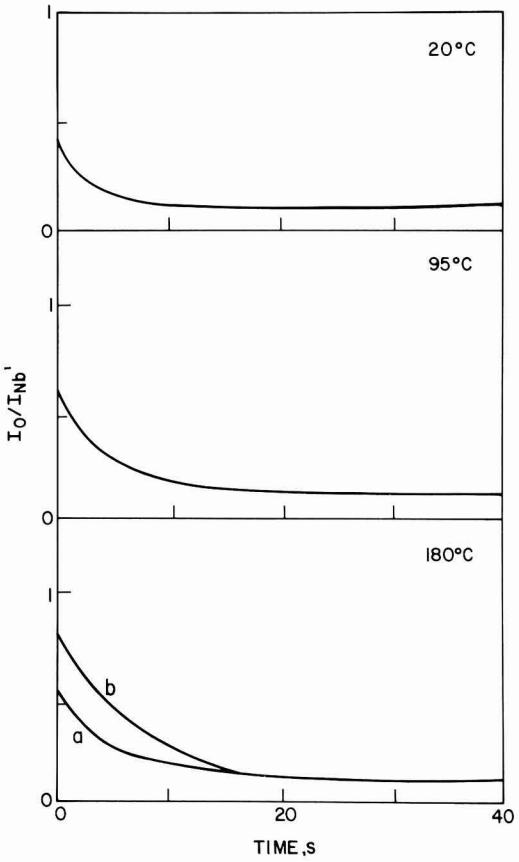

Fig. 3. Oxygen deptn profiles for oxidation at 20°C for 24 hr, 95°C for 64 hr, and 180°C for (a) 0.5 hr and (b) 64 hr.

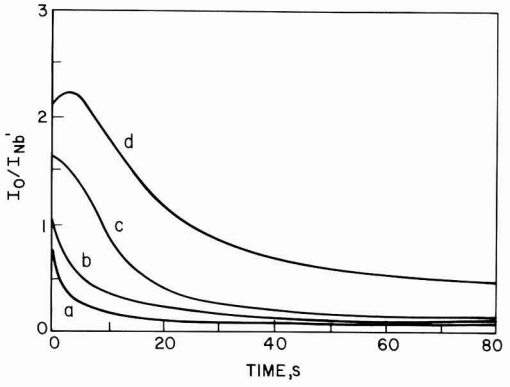

Fig. 4. Oxygen depth profiles for oxidation at 270°C for (a) 0.5 hr, (b) 16 hr, (c) 30 hr, and (d) 64 hr.

The N peak at this temperature is too small to analyze its shape. However, as the NbN substrate is approached during sputter etching, the peak corresponding to the oxynitride is observed.

To understand better the composition of the oxidation product, the shape of the MNN Nb peaks from each oxidized specimen was compared wih the shape of the peaks from the NbN substrate and from Nb_2O_5 (Fig. 9). For temperatures from 20° to 180°C and

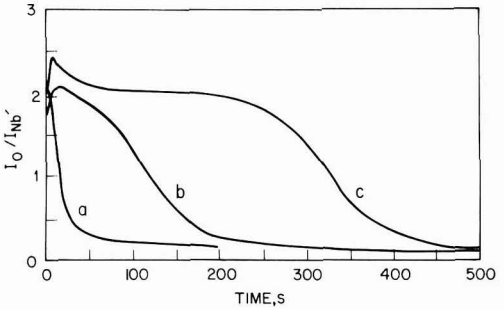

Fig. 5. Oxygen depth profiles for oxidation at 400°C for (a) 0.5 hr, (b) 2 hr, and (c) 4 hr.

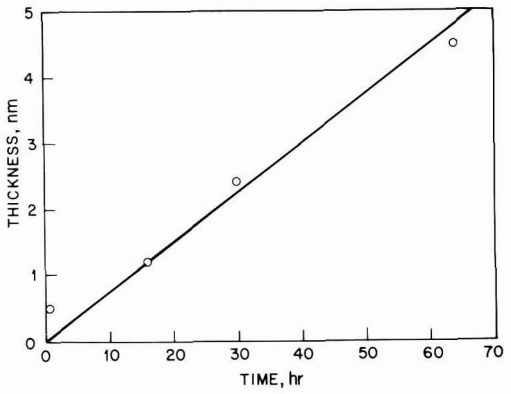

Fig. 6. Reaction product thickness vs. oxidation time at 270°C, showing apparent linear rate law.

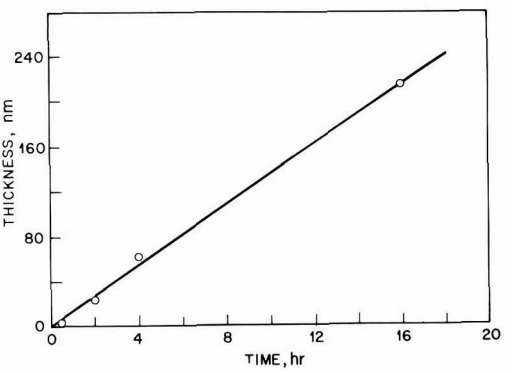

Fig. 7. Reaction product thickness vs. oxidation time at 400°C, showing apparent linear rate law.

for films less than 2 nm in thickness at the higher temperatures, Nb_2O_5 was not detected. At 270° and 400°C for reaction product films thicker than about 2 nm, the product appears to be Nb_2O_5, except at the surface, where the N concentration is greater than in the bulk (Fig. 1). There the Nb-peak shape is more like that of the oxynitrides. This suggests that, after initial formation of an oxynitride, the reaction proceeds by the inward diffusion of oxygen to the NbN interface where it reacts. In all cases, as the oxidation product is etched down to the NbN substrate, the shape of the Nb peak slowly changes to that for NbN.

The data in Ref. (7) obeyed a linear rate law

$$\alpha = kt \qquad [1]$$

in which k is the rate constant, t is the time, and α is the fraction of film reacted, *i.e.*, l/l^o in which l is the depth of NbN film of original thickness l^o that has been oxidized. Plots of the rate constant against reciprocal temperature yielded an apparent activation energy of 44.6 kcal/mol and a pre-exponential term of 2.3×10^9 sec^{-1}. Since the extent of oxidation in the present study is independent of NbN film thickness, a new rate constant k' is defined

$$k' = l^o k \qquad [2]$$

so that

$$l = k't \qquad [3]$$

To determine whether the rate constants obtained in the present study at 270° and 400°C are consistent with those reported at higher temperatures (7), k' was calculated from the data in Fig. 6 and 7 by multiplying the slopes of the linear plots by the ratio of the molar density of Nb_2O_5 (3.36×10^{-2} mol/cm^3) to that of NbN (7.86×10^{-2} mol/cm^3). These rate constants, as well as those calculated from the data in Table II of Ref. (7), are plotted against the reciprocal temperature in Fig. 8. The solid line is calculated from the activation energy and pre-exponential term in Ref. (7). The agreement between the two sets of measurements is excellent, especially when it is realized that one set was done thermogravimetrically (7), a bulk measurement, and the other was done by Auger electron spectroscopy, a surface sensitive technique. At lower temperatures, the apparent activation energy is expected to change as the mechanism shifts from one that gives a linear rate law to one that produces a limiting film thickness.

As seen in Fig. 3-5, O is found in the bulk NbN film and extends through it to the silicon substrate. It is believed that this results from the diffusion of

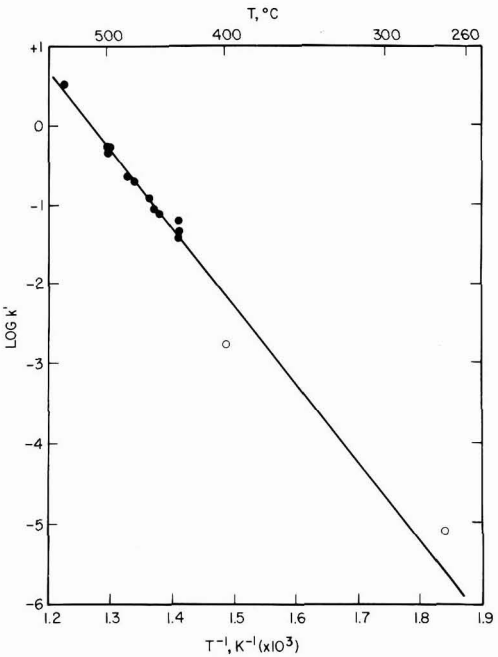

Fig. 8. Linear rate constant vs. reciprocal temperature. ●—High temperature data from Gallagher *et al.* (7); ○—This study. Solid line from Ref. (7).

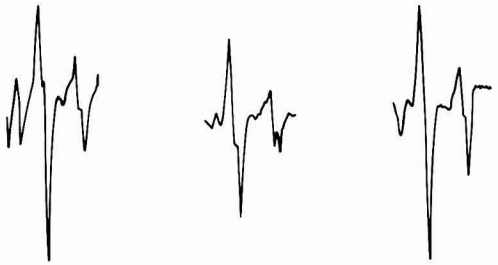

Fig. 9. Nb MNN Auger electron peaks from (a) Nb_2O_5, (b) specimen oxidized at 95°C, and (c) NbN.

oxygen down grain boundaries at a rate that must be more rapid than the rate of oxidation, at least after the first molecular layer has been oxidized. This is being studied further.

Conclusions

Based on the present data, it is concluded that at temperatures below about 200°C, surface oxidation of NbN is limited to one to two molecular layers, and the reaction product is most likely a niobium oxynitride. At higher temperatures, oxidation is not limited and follows a linear rate law. Initially, the reaction product is an oxynitride, but as the reaction proceeds, Nb_2O_5 is formed. Since the oxynitride is maintained at the surface, the reaction probably proceeds by the inward diffusion of oxygen to the product/NbN interface. Oxygen not only reacts at that interface but also diffuses through the entire NbN film, presumably along grain boundaries. It appears, therefore, that grain boundary diffusion is rapid compared to the oxidation rate, at least after the first monolayer has reacted.

Acknowledgment

The authors thank P. C. Milner for valuable discussions.

Manuscript submitted March 23, 1983; revised manuscript received May 18, 1983. This was Paper 309 presented at the Washington, DC, Meeting of the Society, Oct. 9-14, 1983.

Bell Laboratories assisted in meeting the publication costs of this article.

REFERENCES

1. F. Shinoki, S. Takada, S. Kosaka, and H. Hayakawa, *Jpn. J. Appl. Phys.*, **19,** 591 (1980).
2. S. Kosaka, F. Shinoki, S. Takada, and H. Hayakawa, *IEEE Trans. Magn.*, **mag-17,** 314 (1981).
3. A. Snoji, F. Shinoki, S. Kosaka, and H. Hayakawa, *Jpn. J. Appl. Phys.*, **20,** L587 (1981).
4. R. B. van Dover, D. D. Bacon, and W. R. Sinclair, *Appl. Phys. Lett.*, **41,** 764 (1982).
5. P. Lefort, J. Desmaison, and M. Billy, *Mater. Res. Bull.*, **14,** 479 (1979).
6. P. K. Gallagher and W. R. Sinclair, *Isr. J. Chem.*, **22,** 222 (1982).
7. P. K. Gallagher, W. R. Sinclair, D. D. Bacon, and G. W. Kammlott, *This Journal*, **130,** 2054 (1983).
8. "Gmelins Handbuch der Anorganischen Chemie," 8th ed., Nb[B1], p. 113 (1970).

The Influence of Back End Processing on the Fixed Charges Density in the Si-SiO_2 Interface

R. M. Levin*,[1]

Bell Laboratories, Murray Hill, New Jersey 07974

ABSTRACT

Variations in the density of fixed surface charges (Q_f/q) at the Si-SiO_2 interface during back end processing steps are reported. After the deposition of phosphosilicate glass (P-glass) films (LPCVD at 630°C, from TEOS, phosphine, and oxygen), Q_f/q measured on aluminum gate capacitors is in the range of $5\text{-}30\times10^{10}$ cm^{-2}. Densification of the P-glass by means of heat-treatment affects Q_f/q in a similar fashion to previously reported post thermal oxidation treatments. The effectiveness of the densification ambient in reducing Q_f/q can be ranked in the order: steam > oxygen > argon > steam + argon. After polycrystalline silicon/aluminum metallization, which involves polysilicon deposition followed by heat-treatment (doping) and aluminum deposition, Q_f/q depends very strongly on the premetallization treatment. When this metallization is applied over undensified glass, Q_f/q can be higher than 1×10^{12} cm^{-2}. It increases with increasing the doping time, the doping temperature, the glass thickness, or the phosphine to oxygen flow rate ratio during the P-glass deposition. Polysilicon/aluminum metallization applied over densified glass yields much lower Q_f/q, with the final Q_f/q value depending strongly on the densification conditions. For example, densification in steam or oxygen at 950°C for 10 min yields Q_f/q of less than 5×10^{10} cm^{-2} after the silicon/aluminum metallization. The results can be explained on a basis of oxygen deficiency in as deposited P-glass films and rearrangement of the Si-SiO_2 interface in the presence of a polysilicon cap film over the glass.

The quality of the Si-SiO_2 interface has been a subject for extensive studies during the last two decades, due to its importance in the MOS (metal-oxide-semiconductor) technology (1). In particular, charges and states in the vicinity of the Si-SiO_2 interface play a significant role in determining the electrical properties of MOSFET's. Although there is a difference of opinion concerning the origin of the surface charges and surface states, it is generally agreed that the main contribution comes from the astoichiometric nature of the interface and from bonds and structure defects in the interface (2). Most of the published works deal with the dependence of the density of the surface charges and surface states on the oxidation process and the post oxidation heat-treatments. Very little is reported on the influence of back end processing steps (after poly gate definition in a standard IC process) on the interface (3-5). In the present work, we concentrate on the influence of P-glass (phosphorus-doped SiO_2) deposition and densification, and polycrystalline sili-

* Electrochemical Society Active Member.
[1] Present address: National Semiconductor Israel Ltd., Herzliya-B, 46103, Israel.
Key words: dielectric, capacitor, glass, anneal, CVD, integrated circuits.

con/aluminum metallization process on the fixed surface charge density (Q_f).

P-glass is widely used in the integrated circuits technology to passivate the devices. The P-glass, which is applied by means of chemical vapor deposition (CVD), usually suffers from nonconformal step coverage (6-8). High temperature heat-treatment (~1050°C) is used to flow the glass in order to smooth its surface (6, 7). This treatment is intolerable in VLSI technology where very shallow p-n junctions in the source and drain are desired. Recently, it has been demonstrated that by using a P-glass deposition process in which tetraethyl orthosilicate (TEOS), phosphine, and oxygen are the reactive gases (to be referred to as P-TEOS glass), an excellent step coverage of the P-glass can be achieved, making the high temperature glass flow unnecessary (8, 9, 10). A moderate temperature (800°-950°C) heat-treatment is still necessary to densify the P-glass in order to increase its resistance to water absorption (11, 12).

A major problem of VLSI circuits, aluminum spiking through shallow p-n junctions into the Si substrate, has led to the use of polysilicon/aluminum structure for metallization (13-15). In this process, a polysilicon layer is deposited at 600°-700°C, and doped at 900°-1100°C before the aluminum metallization.

To study the influence of the three processes, P-TEOS deposition, P-TEOS densification, and polysilicon/aluminum metallization on Q_f, we carried out high frequency capacitance-voltage measurements on silicon/thermal oxide/P-TEOS/aluminum and on silicon/thermal oxide/P-TEOS/polysilicon/aluminum capacitors. We have found considerable variations of Q_f which are induced by the above treatments. The value of Q_f is affected not only by the final heat-treatment given to the sample before the aluminum evaporation, but also by previous treatments as well. The results can be explained qualitatively on the basis of oxygen deficiency in the P-TEOS glass.

Experimental Procedure

Wafers of 0.7-1.0 Ω-cm p-type single-crystal (100) silicon were thermally oxidized at 1000°C to a thickness of 1000Å, and annealed in argon for 15 min at the same temperature. P-TEOS glass was deposited at 630°C in a low pressure CVD reactor (9). The phosphorus oxide concentration in the films was determined from infrared absorption spectra as described by Levin and Adams (9). Unless otherwise noted, the phosphorus oxide concentration is 6 ± 1 mol percent (m/o), and the glass thickness is 5000 ± 500Å. The deposition samples were heat-treated at 700°-950°C in argon, oxygen, or steam ambients (densification). Polysilicon, when it was used, was then deposited by LPCVD at 625°C using SiH_4. It was phosphorus-doped at 950°C from a PBr_3 source, then dip-etched in 50:1 HF for 10 min to remove the P-glass grown on top of the polysilicon. Some samples were annealed in argon after the polysilicon deposition and the polysilicon was stripped using CF_4/O_2 plasma etching. We will refer to the heat-treatment after the polysilicon deposition (PBr_3 or argon ambient) as "polysilicon treatment." Silicon nitride was deposited on a few samples (instead of polysilicon) by LPCVD at 750°C, from SiH_2Cl_2-NH_3. The nitride was etched in hot phosphoric acid after argon annealing.

Typically, capacitors were prepared and measured at three points of the processing; after the P-TEOS deposition ("as-deposited" samples), after the densification treatment ("densified" samples), and after the polysilicon treatment. The samples were annealed in hydrogen at 450°C for 30 min. Aluminum was evaporated on all samples with only the doped polysilicon samples having polysilicon/aluminum gates, and dots of 40 mil diam were photolithographically defined and etched (aluminum in wet chemicals, polysilicon in CF_4/O_2 plasma). Every dot is surrounded by a ring electrode which is used to control the surface potential near the edge of the capacitor in order to prevent the formation of an inversion layer at the silicon surface beyond the field plate. In the presence of such an inversion layer, the capacitance-voltage characteristic is distorted (16), making it impossible to extract the dopant concentration in the silicon from the characteristic. The back surface layers were then removed and aluminum was evaporated to form the back side contact. Some small variations in the sample preparation will be mentioned later.

High frequency (1 MHz) capacitance-voltage measurements were made with a Boonton 72AD capacitance meter connected to a minicomputer-controlled measurement system. The minicomputer determined capacitance values in accumulation and inversion, computed a value for flatband capacitance, and then found the flatband voltage. This procedure was repeated for 36 devices on a wafer, so that statistics could be obtained for fixed charges, oxide thickness, etc. (The work function values used to calculate Q_f were: Al-3.35 eV; N^+-doped poly-3.25 eV; intrinsic Si-3.8 eV.) The distribution in Q_f on a wafer is typically less than ±10%.

Experimental Results

As-deposited glass.—The number of fixed surface charges measured on samples having the 1000Å thermal oxide only, is always in the low 10^{10} cm^{-2} range. After the P-TEOS deposition, the shift in the flatband voltage corresponds to surface charges density of 5-30 × 10^{10} charges/cm^2. There is no clear correlation between the surface charge density and the deposition conditions or the phosphorus oxide concentration (up to 8 m/o). A large distribution in the surface charge density after the P-glass deposition was reported previously by Drobek and Adda (17), who used P-TEOS films deposited at atmospheric pressure as well as silox glass films deposited at reduced pressure.

Densified glass.—To improve their properties, the P-glass films are usually densified by means of heat-treatment (11, 12). At 950°C, the glass is densified during the first 10 min with very small additional effects at longer heat-treatments. Table I presents the dependence of Q_f/q (where q is the electronic charge) on the densification time and the densification ambient. The densification was carried out at a temperature of 950°C in argon, oxygen, and steam. After densification treatment of 10 min, Q_f/q is highest for steam ambient (~3 × 10^{11} cm^{-2}) and lowest for argon ambient (~1.6 × 10^{11} cm^{-2}). Longer dry heat-treatment yields lower Q_f. Further reduction in Q_f/q can be achieved by a two step densification treatment in which densification in steam ambient is followed by a densification in argon (0.5 × 10^{11} cm^{-2}). This is in agreement with the results of Drobek and Adda (17).

To confirm that the charges are located at the Si-SiO_2 interface, we etched off small thicknesses of the glass and measured the shift in the flatband voltage as a function of the glass thickness. (To thin the P-glass, the field plate was stripped, some P-glass was etched, aluminum was evaporated on the sample, and dots were redefined.) We found that the shift is linearly

Table I. Number of charges per cm^2 (Q_f/q) in the Si-SiO_2 interface, after various densification treatments at 950°C (aluminum metallization).

Ambient	Densification time (min)	Q_f/q (10^{10} cm^{-2})
Argon	10	10-17
Argon	60	10
Oxygen	10	23
Oxygen	60	16
Steam	10	28
Steam	60	29
Steam + argon	10+10	9
Steam + argon	10+30	6
Steam + oxygen	10+10	17
Steam + oxygen	10+30	16

dependent on the glass thickness (*i.e.*, the calculated Q_f/q is independent of the glass thickness within 5%) for a thickness range of 0-5000Å. The same flatband shift was measured even after etching 500Å of the underneath thermally grown SiO_2. These results indicate that the charges are indeed located at the Si-SiO_2 interface. Similar measurements and results were obtained on some of the samples reported below.

Polysilicon treatment of undensified glass.—Deposition and phosphorus doping of polysilicon over undensified glass has been found to degrade the quality of the Si-SiO_2 interface. Figure 1 shows that Q_f/q increases from 1×10^{11} cm^{-2}, measured for undoped samples (poly-deposited and immediately stripped before the aluminum metallization), to 1.4×10^{12} cm^{-2} after 60 min doping at 950°C. Q_f/q increases sharply at the first few minutes of the doping and then tends to saturate. Stripping the doped polysilicon layer prior to the aluminum metallization as well as replacing the PBr_3 doping treatment by argon annealing of the samples (and then stripping the polysilicon before the aluminum metallization) do not change these results. The use of an Si_3N_4 film instead of polysilicon has no effect on the results. Doping temperatures lower than 950°C yield lower Q_f/q (Fig. 2). Doping at 700°C for 60 min does not affect the interface. Figure 3 indicates that Q_f/q is linearly dependent on the P-TEOS glass thickness in the polysilicon treatment. Extrapolation of the results to zero glass thickness yields Q_f/q of 1×10^{11} cm^{-2}, which is a typical result measured on as-deposited or argon densified samples. In contrast, Q_f/q is independent of the thickness of the thermally grown SiO_2 (in the range of 0.1-1.0μ).

The dependence of Q_f/q on the glass deposition conditions is summarized in Fig. 4 and 5. In Fig. 4, the phosphorus oxide concentration was changed by changing the phosphine flow rate, while keeping the oxygen flow rate constant. Q_f/q increases slowly with increasing phosphorus oxide concentration up to 5.5 m/o, from which it starts to increase much faster. Figure 5 shows that the important parameter is not the phosphorus oxide concentration but the phosphine to oxygen flow rate ratio during the deposition. Samples containing 3.9 and 7.0 m/o P_2O_5 have almost the same Q_f/q when the phosphine to oxygen flow rate ratio used in the deposition is the same, while samples with similar P_2O_5 concentration (4.6 and 4.7 m/o) show a large difference in Q_f/q (1.0×10^{11} and 1.6×10^{12} cm^{-2}, respectively) when the flow rate ratio is different. It is shown in Fig. 5 that Q_f/q increases with increasing the phosphine to oxygen flow rate ratio.

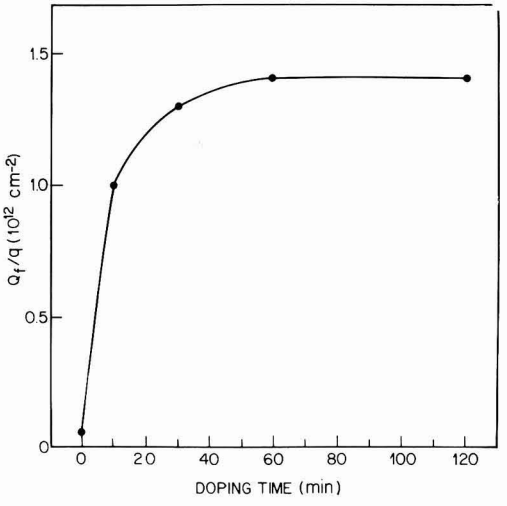

Fig. 1. Q_f/q after polysilicon treatment performed on undensified glass as a function of the polysilicon doping time. The doping temperature is 950°C.

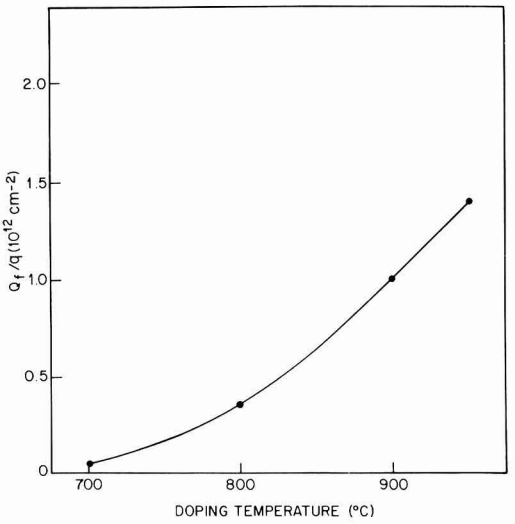

Fig. 2. Q_f/q after polysilicon treatment performed on undensified glass as a function of the doping temperature. The doping time is 60 min.

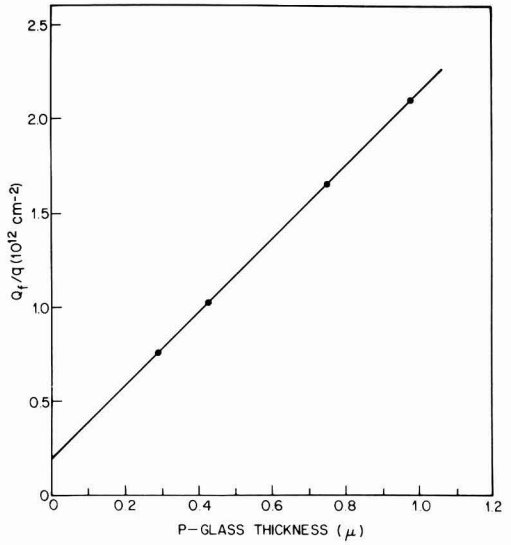

Fig. 3. Q_f/q after polysilicon treatment (950°C, 60 min) performed on an undensified glass as a function of the P-glass thickness.

It should be mentioned here that quality of the Si-SiO_2 interface can be recovered by further heat-treatments. For example, steam annealing of the samples after stripping the polysilicon layer reduces Q_f/q to the low 10^{11} cm^{-2} range.

Polysilicon treatment of densified glass.—Polysilicon treatment carried out on samples having densified P-TEOS glass yielded lower Q_f/q compared to samples having undensified glass. The dependence of Q_f/q on the densification time and the densification ambient is presented in Fig. 6. Polysilicon treatment carried out on glass which was densified in stream or oxygen ambients at 950°C for more than 10 min yielded low Q_f/q

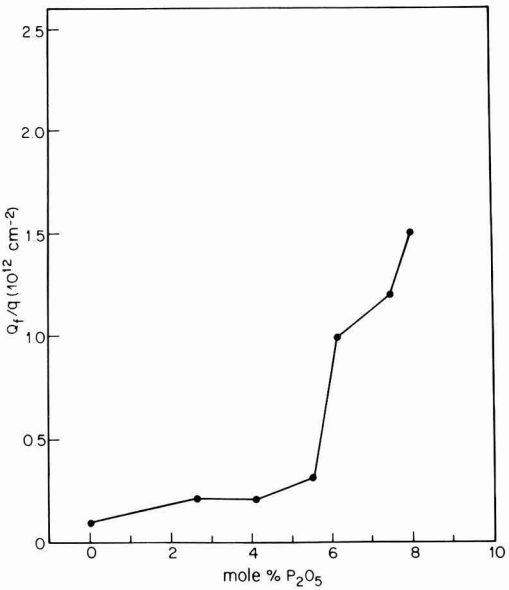

Fig. 4. Q_f/q after polysilicon treatment (950°C, 60 min) performed on an undensified glass as a function of the phosphorus oxide concentration in the glass. The phosphorus oxide concentration is varied by varying the phosphine flow rate, keeping the oxygen flow rate constant (95 cm^3/min).

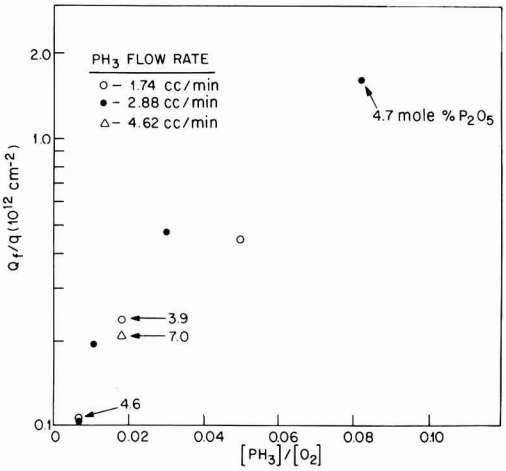

Fig. 5. Q_f/q after polysilicon treatment (950°C, 60 min) performed on an undensified glass as a function of the phosphine to oxygen flow rate ratio in the P-glass deposition.

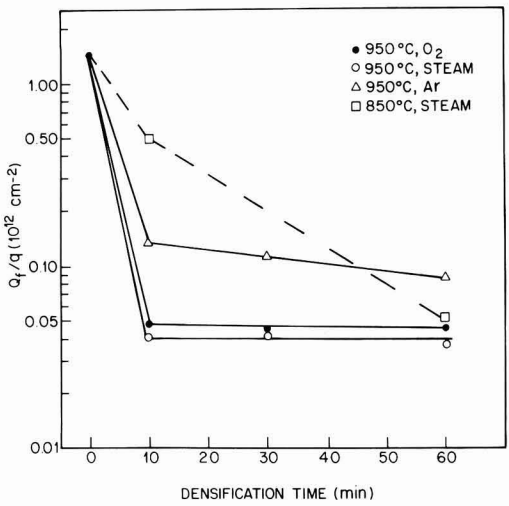

Fig. 6. Q_f/q after a polysilicon treatment (950°C, 60 min) as a function of the P-glass densification time, with densification ambient and densification temperature as parameters.

(3-6 × 10^{10} cm^{-2}). This number is independent of the densification time (if it is longer than 10 min), and the original Q_f/q measured on the as-deposited glass. The influence of densification done in argon is more gradual and depends on the densification time. The dependence of Q_f/q after the poly treatment on the densification temperature is also presented in Fig. 6. It is shown that while steam densification carried out for short time at 850°C is less effective (from the point of view of Q_f/q after the polysilicon treatment) than that carried out at 950°C, they are equivalent after densification of 60 min. After 60 min, the 850°C steam densification is more effective than the 950°C argon densification.

Discussion

Before discussing the experimental results it should be mentioned that two parameters which may affect Q_f have not been monitored in this work; the presence of water molecules in the deposition and subsequent annealing ambients, and the possible presence of carbon monoxide in the glass deposition ambient. It is well known that Q_f is affected by the presence of water species in silicon dioxide (18), and therefore, it depends on the concentration of water molecules in the ambient during heat-treatments. Carbon monoxide may be one of the products in the decomposition of TEOS (8). It was proposed by Fowkes and Hess (19) that CO may remove oxygen atoms from the oxide, and as a result affect Q_f.

It is usually stated in the literature that the surface charge density in the Si-SiO_2 interface is mainly determined by the last oxidation or annealing condition (20). This also has been found to be true up to a certain degree when P-TEOS glass/SiO_2/Si structure is used without the polysilicon treatment (see Table I). Also, the dependence of Q_f on the densifying ambient, Q_f (steam) > Q_f (oxygen) > Q_f (argon) is similar to that reported in the literature (20). However, after the polysilicon treatment, Q_f depends strongly on former heat-treatments (Fig. 6).

One possible explanation for the dependence of Q_f on former heat-treatments given to the sample is that during the heat-treatment, which is a part of the polysilicon treatment, undensified glass starts to be densified. Since the glass is covered with a polysilicon film, large stresses may be introduced into the Si-SiO_2 interface, and the interface quality degrades. However, this model fails to explain the gradual effect of a prior argon densification on the Q_f/q measured after the polysilicon treatment (Fig. 6). It was reported previously (11, 12) that at 950°C the P-glass densification takes place during the first few minutes of the treatment, when oxidizing ambients as well as inert ambients are used. Also, this model does not explain the strong dependency found between the P-glass deposition conditions and Q_f/q (Fig. 4 and 5).

The increase in Q_f/q with increasing the phosphine to oxygen flow ratio in the deposition (Fig. 5), as well as the effectiveness of the densification done in oxidizing ambients in reducing the Q_f/q after the polysilicon treatment (Fig. 6), indicate that the source of the phenomenon is oxygen deficiency in the P-TEOS glass films. The deposition process of the P-TEOS glass is

described by

$$SiO_4C_8H_{20} \rightarrow SiO_2 + 4C_2H_4 + 2H_2O$$

$$2PH_3 + 4\,O_2 \rightarrow P_2O_5 + 3H_2O$$

It has been reported that if oxygen is not introduced into the system during the deposition, unoxidized phosphorus ions exist in the deposited glass (9). Thus, it is possible that even in the presence of oxygen the oxidation of phosphorus is not completed when the phosphine to oxygen ratio is too high. When the undensified glass is capped with the polysilicon layer and heat-treated, oxygen is reduced from the Si-SiO_2 interface to complete the oxidation of the phosphorus ions and the density of the fixed surface charges increases.

The experimental results presented in this paper can be explained qualitatively on the basis of oxygen deficiency in the P-glass and oxygen reduction from the interface. It is expected that the process of oxygen reduction from the interface will be slower at lower temperatures, which explains the results of Fig. 2. The linear dependence found between Q_f/q and the P-glass thickness (Fig. 3) also becomes clear, because the number of the initially unsatisfied phosphorus-oxygen bonds in the glass depends linearly on the glass thickness (assuming the glass structure is uniform). The more oxygen introduced into the deposition system the less unsatisfied phosphorus-oxygen bonds there will be in the glass, which explains the results of Fig. 4 and 5. The influence of the densification treatment is also explained. The phosphorus oxidation is completed by oxygen ions which are supplied from the ambient in the course of the densification treatment of the uncapped glass. The supply of oxygen from the ambient is slower at lower densification temperatures, and at lower partial pressure of oxidizing species (which is the case of argon treatment). As a result, the influence of the densification treatment done in steam at 850°C or in argon at 950°C on Q_f/q after the polysilicon treatment is more gradual than that of densification treatment done at 950°C in oxidizing ambients.

To further verify the proposed model of oxygen deficiency in the P-glass, oxygen ions were implanted into undensified P-glass (120 keV, 1×10^{14} cm^{-2}), and polysilicon treatment was given to the samples. Indeed, we measured Q_f/q of 1.2×10^{11} cm^{-2} for the implanted samples, as compared to 7×10^{11} cm^{-2} measured for the control unimplanted samples.

Conclusion

The influence of some back end process steps on the density of the fixed surface charges in the Si-SiO_2 interface has been studied. The results can be summarized as follows:

1. Q_f/q varies in the range 5-30 $\times$ 10^{10} cm^{-2} after the P-TEOS glass deposition (aluminum metallization).

2. Densification of the P-glass by means of heat-treatment affects the Si-SiO_2 interface. Q_f/q is a function of the densification ambient and can be ranked as Q_f (steam) $>$ Q_f (oxygen) $=$ Q_f (steam + oxygen) $>$ Q_f (argon) $>$ Q_f (steam + argon). Q_f/q decreases with increasing densification time in dry ambients (aluminum metallization).

3. Q_f/q increases sharply after polysilicon treatment when it is performed on undensified P-TEOS glass films. It increases with increasing doping time (and tends to saturate), doping temperature, glass thickness (linearly), and phosphine to oxygen flow rate ratio during the glass deposition. It is independent of the initial thermal oxide thickness.

4. By densification of the glass in oxidizing ambients prior to the polysilicon treatment, one can achieve low Q_f/q ($<5 \times 10^{10}$ cm^{-2}) after the polysilicon treatment. The effect is very fast for a densification treatment done at 950°C, but more gradual for densification done at lower temperatures.

5. An argon densification ambient (prior to the polysilicon treatment) is not as effective as oxidizing ambients in reducing Q_f/q after the polysilicon treatment.

6. Oxygen implantation into the P-glass prior to the polysilicon treatment is also effective in lowering Q_f/q after the treatment.

7. The experimental results of this work can be explained qualitatively on the basis of oxygen deficiency in the as-deposited P-TEOS glass film, and rearrangement in the Si-SiO_2 interface for capped P-TEOS glass/SiO_2/Si structure.

Acknowledgments

The author wishes to thank W. T. Lynch for his continuing interest and support, and for the suggestion to do the oxygen implantation experiment. Thanks are also expressed to L. P. Adda, J. Drobek, H. J. Levinstein, S. P. Murarka, E. H. Nicollian, and F. Vratny for valuable discussions, E. I. Povilonis for his assistance in the preparation of the samples, and P. Heimann, J. G. Barnes, and T. E. Smith for their help in the electrical measurements.

Manuscript submitted Feb. 14, 1983; revised manuscript received June 6, 1983.

National Semiconductor Corporation assisted in meeting publication costs of this article.

REFERENCES

1. For reviews of the subject see: (a) R. P. Donovan, "Integrated Silicon Devices Technology, Vol. VII, Oxidation," Technical Report No. ASD-TDR-63-316, RTI, June (1965); (b) A. Goetzberger, E. Klausman, and M. J. Schultz, *Crit. Rev. Solid State Sci.*, **6**, 1 (1976); (c) E. N. Nicollian and J. R. Brews, "MOS Physics and Technology," John Wiley & Sons, New York (1982).
2. B. E. Deal, in "Semiconducting Silicon 1977," H. Huff and E. Sirtl, Editors, p. 276, The Electrochemical Society Softbound Proceedings Series, Princeton, NJ (1977).
3. E. H. Snow and B. E. Deal, *This Journal*, **113**, 263 (1966).
4. J. M. Eldridge, R. B. Laibowitz, and P. Balk, *J. Appl. Phys.*, **40**, 1922 (1969).
5. J. M. Eldridge and D. R. Kerr, *This Journal*, **118**, 986 (1971).
6. W. Kern, *R.C.A. Rev.*, **34**, 655 (1973).
7. W. E. Armstrong and B. L. Tolliver, *This Journal*, **121**, 307 (1974).
8. K. Sugawara, Y. Yoshimi, and H. Sakai, in "5th International Conference on Chemical Vapor Deposition," J. M. Blocher, Jr., H. R. Hinterman, and L. H. Hall, Editors, p. 407, The Electrochemical Society Softbound Proceedings Series, Princeton, NJ (1975).
9. R. M. Levin and A. C. Adams, *This Journal*, To be published.
10. J. Drobek and M. K. Becker, Private communication.
11. W. Kern, *R.C.A. Rev.*, **37**, 55 (1976).
12. R. M. Levin, *This Journal*, To be published.
13. R. C. Henderson and G. Nash, Annual Report prepared for Naval Electronic Systems Command under contract N00173-76-C-0144, October (1977).
14. R. K. Wallace, A. J. Learn, and K. W. Schuette, *IEEE ISSCC Tech. Dig.*, 148 (1980).
15. T. Tsujide, N. Yasuoka, T. Tara, K. Tokushinge, N. Hirakawa, S. Matsue, and O. Kurakawi, *IEEE ISSCC Tech. Dig.*, 20 (1981).
16. E. H. Nicollian and A. Goetzberger, *IEEE Trans. Electron Devices*, **ed-12**, 108 (1965).
17. J. Drobek and L. P. Adda, Private communication.
18. E. H. Nicollian and J. R. Brews, "MOS Physics and Technology," John Wiley & Sons, New York (1982).
19. F. M. Fowkes and D. W. Hess, *Appl. Phys. Lett.*, **22**, 377 (1973).
20. B. E. Deal, M. Sklar, A. S. Grove, and E. H. Snow, *This Journal*, **114**, 266 (1967).

Comparative Study of Phosphorescence and Photostimulated Luminescence in Zinc Silicate Phosphors and Their Description by a Tunneling Model

P. Thioulouse, I. F. Chang,* and E. A. Giess

IBM Thomas J. Watson Research Center, Yorktown Heights, New York 10598

ABSTRACT

A tunneling pair recombination model has been proposed to describe the themostimulated luminescence in an earlier paper (1). Under the same concept but assuming two tunneling levels for the electron trap, a description of phosphorescence decay (PP via one tunneling level) and photostimulated luminescence (PSL via a second tunneling level) is presented. Experimental results on PP and PSL for manganese-doped silicates with and without arsenic codoping are reported. A novel method of comparing PP and PSL in the temperature and time domain leads to the determination of energy values of the tunneling states.

In an earlier paper (1) (referred to as I), we studied the thermally stimulated luminescence (TSL) of zinc silicate phosphors and applied a tunneling pair recombination model for its description. We also derived a general expression and a simplified analytical expression for TSL as a function of temperature and correlated them with experimental data obtained from manganese-doped zinc silicate single crystals with or without arsenic codoping. To obtain trap activation energies, one generally applies the so-called Hoogenstraaten method, which analyzes the shift of the TSL peaks with changes in the temperature scanning rate $\beta(T = T_o + \beta T)$. T_m being the temperature of the maximum of a TSL peak, Hoogenstraaten (7) calculated that the slope of the curve $\ln(\beta/T_m^2)$ *vs.* $1/T_m$ would give the activation energy E. In Paper I, we showed that the Hoogenstraaten method, once established assuming that electrons were thermally released into the conduction band, was still valid in the tunneling model, providing that E is defined as the energy of the trap tunneling level above trap ground state. In this paper, using the same tunneling interpretation, we develop a parallel analysis of phosphorescence decay (PP) and photostimulated luminescence (PSL) peak intensity with a two tunneling state model and describe a novel method for quantitatively determining the trap energy levels. The photostimulation effect, described elsewhere (2-4), was introduced in phosphor studies as a means of investigating deep traps. In the two-tunneling state model, we assume that the photostimulation excites the trapped electron to a higher tunneling state whereas the thermostimulation excites to a lower tunneling state as schematically shown in Fig. 1. We present the model first, then report supporting experimental results of PP and PSL measurements carried out on the same zinc silicate samples as the ones used in Ref. (1) and using the experimental setup as illustrated in Fig. 1. The numerical values for the trap energies are then derived.

Identity of Traps Involved in PP, TSL, and PSL

Connecting a coulomb meter to the output of a photomultiplier tube, we measured the total quantity of photons (with Q_{TSL1} a proportionality constant) released during a thermoglow experiment after exposing the Zn_2SiO_4:Mn sample to UV light ($\lambda = 254$ nm) for 2 min at a temperature T_{UV}. We then measured the quantity of photostimulated light Q_{PSL} released during 2 min by 633 nm photostimulation on the same sample at the same temperature T_{UV} after the same UV excitation conditions. Finally, we measured the quantity of light Q_{TSL2} released by thermoluminescence, *i.e.*, by warming the sample up at the same rate as for TSL_1, after red light was removed. For various temperatures of T_{UV} (−190°, −150°, and −100°C, selected because of high photostimulation efficiency), we obtained an invariant relation: $Q_{TSL1} = Q_{TSL2} + Q_{PSL}$. Measurements on a sample codoped with arsenic yielded the same equality. This means that the traps emptied by the photostimulation effect are the very same ones involved in thermal stimulation. Consequently, one may conclude that thermally originated phosphorescence and photostimulated luminescence involve the same distribution of traps. This very important statement emphasizes the interest of comparative measurements of PP and PSL discussed below.

Single Tunneling Level Model

Phosphorescence.—Let us recall the details of the tunneling model presented in I. Long-lived PP is accounted for by the tunneling of trapped electrons towards ionized manganese centers and their radiative recombination with captured holes. The state of the phosphor after UV excitation is characterized by a concentration (5, 6) of ionized pairs: that is pairs with an activator having captured a hole and a trap having captured an electron. This concentration p is a function of the separation R between donor and activator; $p(R,t)dR$ is the number of closest donor-activator ionized pairs which have a separation between R and $R + dR$, $p(R,t)$ may include a "nearest neighbor factor" for large impurity densities. It decays radiatively at a rate

$$\frac{dp(R,t)}{dt} = -p(R,t)W_1(R) \qquad [1]$$

where

$$W_1(R) = A_1 e^{-2R/a} f \qquad [2]$$

The parameter f is the fraction of ionized pairs whose trapping center is in a tunneling state. After UV light removal at $t = 0$, the phosphorescence intensity is given by

$$L(t) = -\frac{dp}{dt}(t) = -\int_0^\infty \frac{dp}{dt}(R,t)dR = \int_0^\infty p(R,t)W_1(R)dR \qquad [3]$$

which is a function of time. At steady temperature and with no photostimulation or excitation, and noting that $\exp -E/kT << 1$, we obtain: $f \cong \exp(-E/kT)$. Therefore, the PP intensity is

$$L_1(t,T) = A_1 e^{-E/kT} \int_0^\infty p(R,t)e^{-2R/a}dR \qquad [4]$$

* Electrochemical Society Active Member.

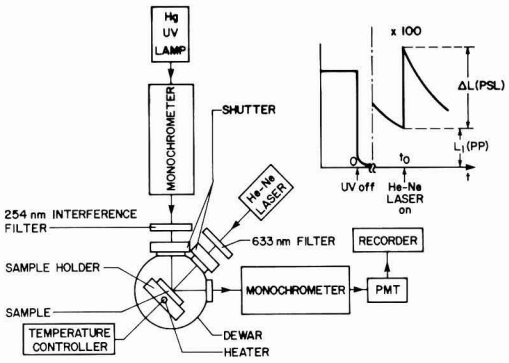

Fig. 1. Apparatus for investigation of PP and PSL

PSL peak intensity.—Let us assume as a first step that, in both thermal PP and optical PSL effects, the trapped electrons are excited to the same tunneling level located at energy E above the ground state of the trap. If, at time t_0 after UV removal, we expose the sample to visible photostimulating light, the overall luminescence is instantaneously raised to a new value L_2

$$L_2(T,I) = A_1 f(T,I) \int_0^\infty p(R,t_0) e^{-2R/a}\, dR \qquad [5]$$

where $p(R)$ is the pair concentration after a t_0 second PP decay and where $f(T,I)$ is the new value under an incident photostimulating light of intensity I. The expression for $f(T,I)$ has been found in Ref. (1) by considering that the trapped electrons are in equilibrium between the ground state and the tunneling state

$$f(T,I) \cong (\exp(-E/kT) + \alpha_1 I/C_1)/(1 + \alpha_1 I/C_1) \qquad [6]$$

In all practical cases, we have $\alpha_1 I/C_1 << 1$. Then, $f(T,I) \cong \exp(-E/kT) + \alpha_1 I/C_1$.

Taking the ratio of PSL intensity, $\Delta L(T,I) = L_2(T,I) - L_1(t,T)$ over PP intensity $L_1(t_0,T)$ at time t_0, we find

$$r = r(T,I) = \frac{f(T,I)}{f(T,0)} - 1 = (\alpha_1 I/C_1) \exp(E/kT) \qquad [7]$$

This ratio is independent of the time t_0 elapsed between UV removal and PSL excitation and can be rewritten as

$$\ln r = \frac{E}{kT} + \ln\left(\frac{\alpha_1 I}{C_1}\right) \qquad [8]$$

Therefore, measuring the ratio r at different temperatures T and plotting $\ln r$ *vs.* $1/kT$ would give a straight line with a slope E, the activation energy of the tunneling level.

The particular interest of this method arises because the ratio r of instantaneous PSL luminescence over PP intensity at the same time cancels the contribution of the pair distribution [the integral in (4) and (5)]; the analytical expression for r does not require any assumption concerning this distribution.

However, using a 633 nm He-Ne laser as PSL excitation source, we experimentally found that, at any temperature, the ratio r was dependent on the time elapsed between UV removal and the red PSL excitation, thereby invalidating our single tunneling level model for the 633 nm PSL effect. This discrepancy can be explained by the significant difference between the He-Ne laser optical energy 1.96 eV and the trap activation energy 0.7 eV as determined by the Hoogenstraaten method (7) (see the section on Experimental Results below). However, this simple single tunneling level should be valid for the PSL effect using an infrared source with optical energy close to the activation energy E. Such experiments are yet to be carried out with a tunable infrared laser.

Two Tunneling Level Model

We shall assume in this section that, although thermal activation and optical stimulation involve the same trap distribution, the PSL activated electrons are excited to a shallower and less localized tunneling state. Let us call E' the energy of the shallower tunneling level above the ground state of the trap and W_2 the corresponding tunneling rate. Let ϵ be the ground state energy of the trap measured with respect to the conduction band. Figure 2 shows the energy band diagram of this model.

PP expression.—PP is occurring from tunneling of electrons from the same trapping state (State 1 in Fig. 2) as in the single tunneling level model. Equations [1]-[4] are still valid. Here we derive a more explicit expression of $L_1(t,T)$ needed for further calculations. Starting from expression [3] for luminescence, the following calculation is very similar to Delbecq's (5) and our analysis in section II.E of I. The PP intensity is

$$L_1(t,T) = \int_0^\infty W_1(R) p(R,t)\, dR = \int_0^\infty p_0(R) W_1(R) e^{-W_1(R)t} dR \qquad [9]$$

with

$$p(R,t) = p_0(R) e^{-W_1(R)t}$$

where $p_0(R)$ is the ionized pair concentration when UV light is just removed.

The function $g(R) = W_1(R) e^{-W_1(R)t}$ reaches its maximum at $R = R_c$, *i.e.*

$$W_1(R_c)\, t = 1$$

or

$$R_c(t) = \frac{a}{2} \ln(A_1 e^{-E/kT} t) \qquad [10]$$

We shall keep the same assumption, the relation [13] in section II.E. of I, that is: $A_1 \exp(E/kT) >> 1\ \text{sec}^{-1}$. Then, for t larger than 1 sec, $R_c(T)$ is much larger than a. In the same manner as in section II.E, one can demonstrate that $g(R)$ is much smaller than $g(R_c)$ outside a "narrow" region of width a around R_c. Assuming that $p_0(R)$ is varying slowly with R compared to $g(R)$, we can take the concentration function out of the integral and obtain

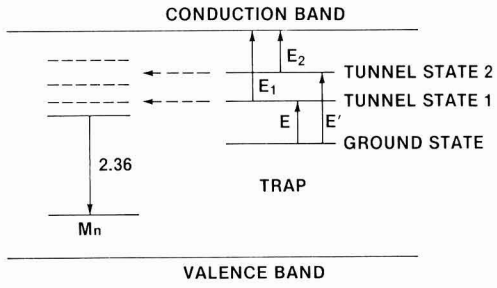

Fig. 2. Energy band diagram for manganese activated zinc silicate (with or without arsenic codoping) in the two tunneling level interpretation of phosphorescence and photostimulated luminescence. Thermally activated electrons are transferred from traps to excited Mn centers through the low energy tunneling state 1 while optically excited electrons are proceeding through the higher and thereby less localized tunneling level 2.

$$L_1(t,T) = p_0(R_c)\int_0^\infty W_1(R)e^{-W_1(R)t}dR \quad [11]$$

Employing an intermediate integration variable $v = e^{-W_1(R)t}$, and using again $A_1 \exp^{-E/kT} >> 1$ sec^{-1} and $t > 1$ sec, we get

$$L_1(t,T) = \frac{a}{2t}\,p_0(R_c) \quad [12]$$

where $R_c(t)$ is given by [10].

This expression is similar to that obtained by Delbecq (5), except that we keep a nonexplicit term for the pair concentration $p_0(R)$.

PSL peak intensity.—Let t_0 be the time elapsed after UV removal when we apply PSL light and ΔL be the PSL peak intensity at that time. At time t_0, the pair concentration is the one after a PP decay of t_0 sec, that is $p(R,t_0) = p_0(R)e^{-W_1(R)t_0}$. The PSL peak is due to photoexcited electrons tunneling to manganese centers from the shallower tunneling level at a rate $W_2(R)$ and can be expressed as

$$\Delta L(T,I) = \int_0^\infty P(R,t_0)\,W_2(R,I)\,dR$$

$$= \int_0^\infty p_0(R)e^{-W_1(R)t_0}\,W_2(R,I)\,dR \quad [13]$$

The rate $W_2(R,I)$ is given by

$$W_2(R,I) = A_2e^{-2R/b}f_2(T,I)$$

where b is the radius of wave function for the shallower trap tunneling level overlapping with the manganese ($b > a$) and where f_2 is the fraction of trapped electrons excited to this shallower level. This level, located high above the ground state, is likely to be only populated by photoexcited electrons; therefore

$$e^{-E'/kT} << \frac{\alpha_2 I}{c_2} << 1 \text{ and } f_2(T,I) \cong \frac{\alpha_2 I/C_2}{1+\alpha_2 I/C_2} \cong \frac{\alpha_2 I}{C_2}$$

where C_2 and α_2 are the capture cross section and photoexcitation efficiency associated with the shallower tunneling level. Similar to $g(R)$, the function $h(R) = W_2(R,I)e^{-W_1(R)t_0}$ reaches its maximum at R_d

$$R_d = \frac{a}{2}\left[\ln\left(t_0A_1e^{-E/kT}\right) + \ln\left(\frac{b}{a}\right)\right] \quad [14]$$

Assuming the relation in [13] in I as above, and noting that b/a is experimentally found to be of the order of 2, we find that R_d is almost equal to R_c and much bigger than the "width" $a + b/2$ of the function h. Following the same reasoning as in the previous section, we have

$$\Delta L(T,I) \cong A_2\frac{\alpha_2 I}{C_2}\,p_0(R_d)\int_0^\infty e^{-2R/b}\,e^{-W_1(R)t_0}dR$$

We define a new integration variable: $w = W_1(R)t_0$. Then: $dw = -\frac{2}{a}\,w\,dR$ and the integral becomes

$$G = \int_0^\infty e^{-2R/b}\,e^{-W_1(R)t_0}dR =$$

$$-\frac{a}{2}\left(A_1e^{-E/kT}t_0\right)^{-b/a}\int_{W_1(0)t_0}^0 w^{(a/b)-1}\,e^{-w}dw \quad [15]$$

where the lower integral limit is much greater than unity. Therefore, we have

$$G \cong \frac{a}{2}\left(A_1e^{-E/kT}t_0\right)\Gamma\left(\frac{a}{b}\right)$$

and

$$\Delta L(T,I)$$

$$\cong A_1^{-\frac{a}{b}}\,\frac{a}{2}A_2\Gamma\left(\frac{a}{b}\right)\frac{\alpha_2 I}{C_2}\,p_0(R_d)\,t_0^{-\frac{a}{b}}\,e^{+\frac{a}{b}\frac{E}{kT}} \quad [16]$$

Expression for the ratio $\Delta L/L_1$.—Comparing [10] and [14], we have

$$(R_d - R_c)/R_c$$

$$= \left(\ln\frac{b}{a}\right) \Big/ \ln\left(t_0A_1\exp\left(-E/kT\right)\right) << 1$$

Thus we can assume $p_0(R_d) \cong p_0(R_c)$ and derive the expression for the ratio $r(t_0,T,I) = \Delta L(T,I)/L_1(t_0,T)$ to be

$$r(t_1,T,I) = Kt_0^{\left(1-\frac{a}{b}\right)}\,e^{\frac{a}{b}\frac{E}{kT}} \quad [17]$$

where $K = A_1^{-(a/b)}A_2\Gamma(a/b)\,\alpha_2 I/C_2$. One notes that, in our tunneling level model, r becomes time-dependent (comparing [17] and [7]). This time dependence is a simple power law as opposed to the case of PP (L_1) and PSL (ΔL) whose individual behavior with time is complicated by factors of $p_0(R_c(t))$ and $p_0(R_d(t))$ with unknown t-dependence.

Experimental application.—Based on the theory above, one can devise the following experimental methods to verify its validity:

Experiment 1—Keeping a steady temperature, measuring the ratio $r(t_0)$ of the PSL peak ΔL over PP intensity L_1 at a time t_0 after UV excitation removal and repeating this experiment at the same UV excitation conditions but for various values of t_0 should give us the time-dependence of r. A plot of $\log r(t_0)$ *vs.* $\log t_0$ should yield a straight line with a slope of $1 - a/b$, thereby determining the value of a/b.

Experiment 2—Repeating the same experiment for a fixed amount of time t_0, but at various temperatures, should give us the temperature dependence of r. A plot of $\ln r(t_0)$ *vs.* $1/kT$ should give a straight line with a slope of $(a/b)E$. Knowing a/b from experiment 1 we can then determine E.

We shall defer the discussion of experimental results to a later section.

A simple quantum analysis.—Let E_1 (and E_2) be the energy depth of the deeper (and shallower) tunneling level with respect to the conduction band. The constants a and b in the tunneling rate expressions are in fact the Bohr radii of the two electron excited levels in the trapping centers. Quantum theory yields that a and b are respectively proportional to $E_1^{-1/2}$ and $E_2^{-1/2}$. Therefore, we have

$$E_1/E_2 = b^2/a^2 \quad [18]$$

From [18] and $\epsilon = E + E_1 = E_2 + E'$ (see Fig. 2), we obtain

$$E_1 = (E' - E)/(1 - a^2/b^2)$$

and

$$E_2 = (E' - E)/(b^2/a^2 - 1) \quad [19]$$

Knowing the values of E and a/b from the experimental method described above and determining the energy E' of the optical excitation separately, one could then obtain the numerical values for E_1, E_2, and ϵ and get a complete and quantitative energy level relationship for the trapping centers.

Experimental Results

The experimental methods described above have been shown to be self-sufficient and to give straight forward values for E and a/b from measurements of the time and temperature dependence of the ratio $\Delta L/L_1$. However, in order to verify their accuracy, we apply the Hoogenstraaten method (validated in the tunneling process scheme in I) to get a fairly accurate value of E from TSL measurements. We then determine a/b from Experiment 1, the time dependence of r, and from Experiment 2, the temperature dependence of r, a second value of a/b which can be compared with

each other to check the validity of our two tunneling level model.

Two manganese-doped zinc silicate single crystals (8) were studied: the first one is codoped with arsenic (2228B, Mn: 0.067 w/o, As: 0.0011 w/o), the second one is arsenic-free (2159°C, Mn: 0.6 w/o). The experimental results are discussed below.

Mn-As codoped sample.—(*i*) Our thermoglow measurements show a well-defined peak at 260 K for various heating rates and the Hoogenstraaten method yields an activation energy E of 0.69 eV as shown in Fig. 3.

(*ii*) We irradiated the sample with a 254 nm Hg line for 3 min and exposed it to a 633 nm He-Ne laser beam 3 min after UV removal ($t_0 = 180$ sec). At time t_0, we measured the PP intensity L_1 (just before red light illumination) and the PSL peak intensity ΔL and calculated the ratio r. The same experiment was repeated every ten degrees from −80° to −10°C. Figure 4 gives an Arrhenius plot of L_1 (PP) and ΔL (PSL) showing their temperature dependence. An Arrhenius plot of r gave a straight line over more than two orders of magnitude as shown in Fig. 5. The slope determines that $(a/b)E = 0.46$ eV. One may point out that the experiment is limited on the high temperature side by the weakness of the PSL signal compared to PP fluctuations. The deviation of the experimental curve from the straight line on the low-temperature side can be explained in the following way: at low temperature, ln $(t_0 A_1 \exp(-E/kT))$ can no longer be assumed to be much greater than ln b/a (or unity), R_d can no longer be considered equal to R_c and thus $p_0(R)$ may not be considered as a constant in the integral of the luminescence expression.

(*iii*) Combining the value of $(a/b)E$ found in (*ii*) with the value of E determined by the thermoglow measurements in (*i*), we obtain $a/b = 0.667$.

(*iv*) We selected the temperature −40°C in the straight part of the curve and repeated the same experiment for various times t_0. Log-log plots of PP intensity and PSL peak intensity as a function of time show two different nonlinear curves (Fig. 6). However, the ratio $r = \Delta L/L_1$ displays a power law dependence on time t_0 as $t^{0.28}$ yielding a value of 0.72 for a/b. This is in good agreement with the value (0.667) obtained from the temperature dependence measurements thus confirming the analysis in a previous section.

(*v*) The energy E' of the higher tunneling level of the traps is limited by the He-Ne laser energy which is 1.96 eV, i.e., $E' \leq 1.96$ eV.

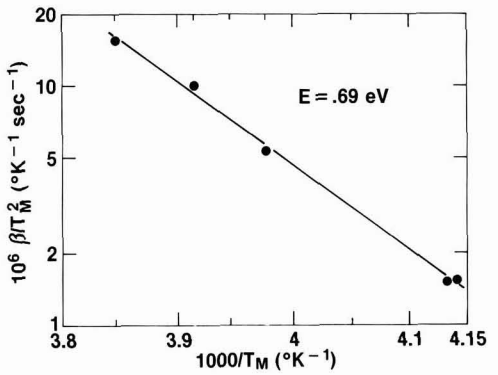

Fig. 3. A Hoogenstraaten plot for the 260 K thermoglow peak of the Zn_2SiO_4:Mn,As sample. We measured the temperature T_M of the TSL peak for various heating rates β. For all thermoglow runs, the sample was irradiated with UV light of 254 nm for 2 min at −190°C. The slope yields the activation energy: $E = 0.69$ eV.

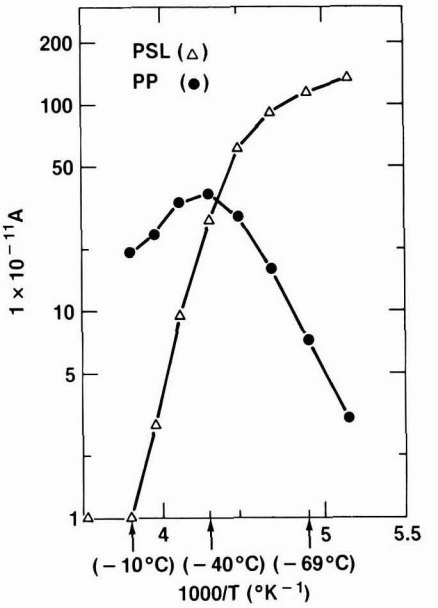

Fig. 4. Temperature dependence of the phosphorescence intensity (PP) measured 3 min after UV exposure was stopped and of the photostimulation luminescence peak intensity (PSL) induced by 633 nm He-Ne light exposure at the same time. The phosphor is Zn_2SiO_4:Mn, As. Conditions of UV exposure are 254 nm light for 3 min.

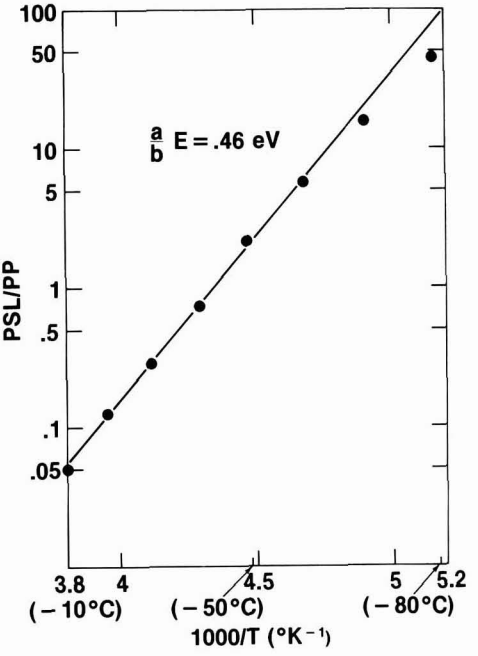

Fig. 5. Temperature dependence of the ratio $r = \Delta L/L_1$ for the Zn_2SiO_4:Mn,As sample. We used the values of ΔL (PSL) and L_1 (PP) plotted in Fig. 3. The slope yields (a/b) $E = 0.46$ eV.

From expression [19], $E = 0.69$ eV and $a/b = 0.667$, we obtain

$$E_1 \leq 2.28 \text{ eV}$$
$$E_2 \leq 1.02 \text{ eV}$$

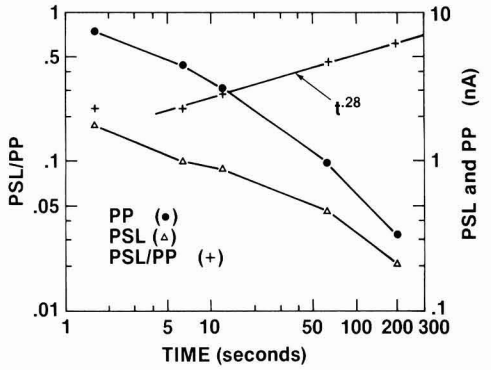

Fig. 6. Dependence of phosphorescence L_1(PP), photostimulated luminescence ΔL(PSL) and ratio $r = \Delta L/L_1$ on time elapsed after UV light is removed (temperature is at −40°C, excitation is 254 nm light for 3 min). The ratio shows a power dependence on time: $t^{0.28}$ which yields $a/b = 0.72$.

This yields a ground state energy for the trap that is equal to or less than 2.97 eV below the conduction band. The precise value of the ground state energy can be determined if one can use a high power tunable light source to determine E' precisely.

Mn doped sample.—(*i*) For this sample, thermoglow measurements show one strong peak, noted 1, at 229 K and another well separated one, noted 2, at 361 K. We did not study the first two TSL peaks (located at 140 and 179 K) because it is difficult to isolate them from the main peak. Again using the Hoogenstraaten method, we obtain an activation energy 0.68 eV for the first peak and 0.96 eV for the second one shown in Fig. 7 and Fig. 8, respectively.

(*ii*) The same experiments as for the Mn-As codoped sample were carried out. Arrhenius plots of PP intensity and PSL peak intensity (Fig. 9) at ($t_0 = 180$ sec after UV removal) show curves similar to those for Mn-As codoped samples (Fig. 7) for the low temperature region though shifted towards lower temperatures. The high temperature TSL peak introduces an additional peak in these curves. Applying the same

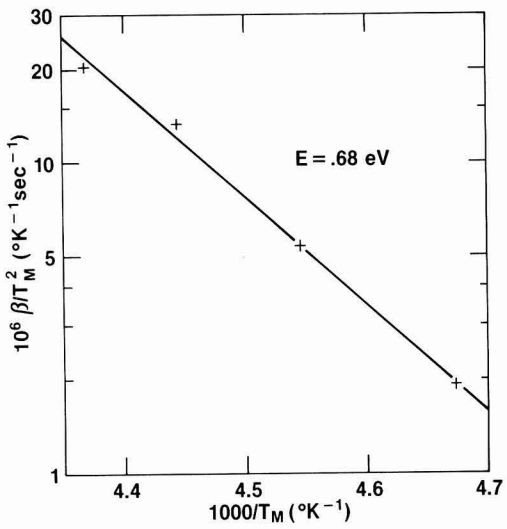

Fig. 7. A Hoogenstraaten plot for the 229 K thermoglow peak of the Zn_2SiO_4:Mn,As sample. We excited the sample with 254 nm UV light for 2 min at −190°C. The slope yields: $E = 0.68$ eV.

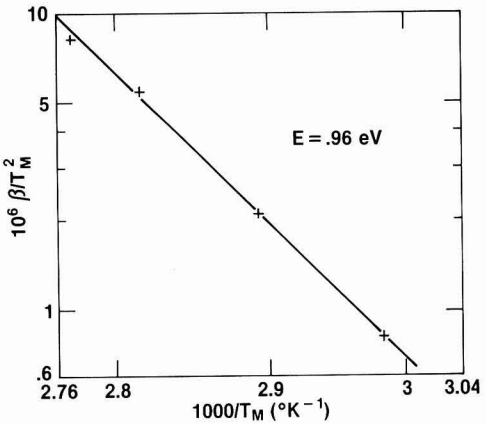

Fig. 8. A Hoogenstraaten plot for the 361 K thermoglow peak of the Zn_2SiO_4:Mn sample (we used the same TSL experiments as in Fig. 7). The activation energy found is: $E = 0.96$ eV.

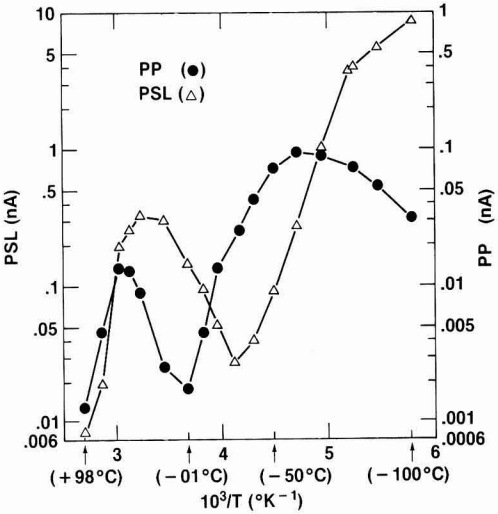

Fig. 9. Temperature dependence of L_1(PP) and ΔL(PSL) for the Zn_2SiO_4:Mn sample. The measurements were carried out in exactly the same conditions as for the sample codoped with arsenic (Fig. 4-6).

method as for the Mn-As codoped sample, the plot of $\ln r$ *vs.* $1/T$ yields a straight line over almost two orders of magnitude in the peak 1 temperature region (Fig. 10) and over one and a half orders of magnitude in the peak 2 region (Fig. 11). In Fig. 10 (peak 1), the data were limited on the low temperature side by interaction with the first two TSL peaks, on the high temperature side by involvement of the higher temperature peak in the PSL effect.

(*iii*) Analysis of peak 1. Plot of the temperature-dependence of r gives: $(a/b)E = 0.45$ eV (Fig. 10). Substituting the value of E (0.68 eV) found in the thermoglow measurements yields: $a/b = 0.662$. A plot of the time dependence of r at $T = -61$°C shows a power law behavior: $r \cong t^{0.23}$ which yields $a/b = 0.77$ (Fig. 12) which again is in good agreement with the first value calculated from the temperature dependence of r.

Similar to section above on an Mn-As codoped sample, taking the red laser energy (1.96 eV) as the

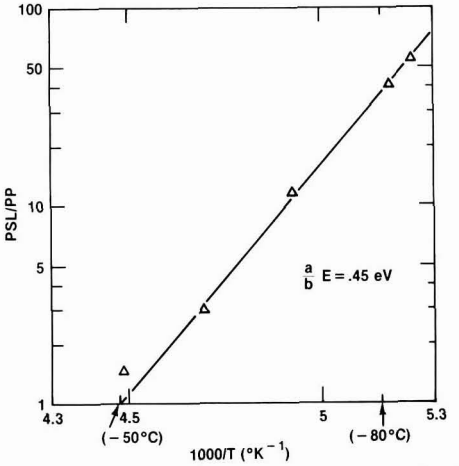

Fig. 10. Temperature dependence of ratio $\Delta L/L_1$ for the Zn_2SiO_4:Mn sample in the TSL peak 1 region. Values were computed from experimental results shown in Fig. 8. The slope determines: $(a/b)E = 0.45$ eV.

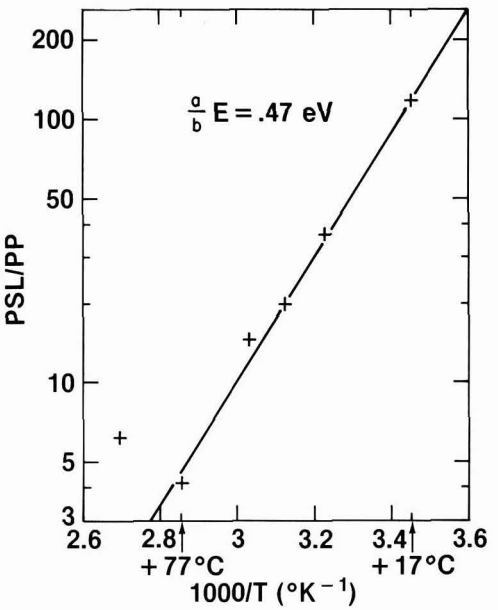

Fig. 11. Temperature dependence of ratio $\Delta L/L_1$ for the Zn_2SiO_4:Mn sample in the TSL peak 2 region. We used the data plotted in Fig. 8. The slope of this curve yields: $(a/b)E = 0.47$ eV.

maximum value for E', $E = 0.68$ eV, and $a/b = 0.662$, we obtain: $E_1 \leq 2.28$, $E_2 \leq 1$ eV, and $\epsilon \leq 2.96$ eV. One notes that these energy values are close to those determined for the Mn-As codoped sample. Moreover, for both samples, there is a similar temperature dependence of τ as shown in Fig. 13. These similarities suggest that the traps responsible for PP and PSL observed (peak 1) in the Mn doped sample may be of the same nature as those in the Mn-As codoped sample. Differences in apparent PP and PSL magnitudes and their temperature dependence (compare Fig. 4 and Fig. 9) observed from one sample to the other may be due to very different pair distributions.

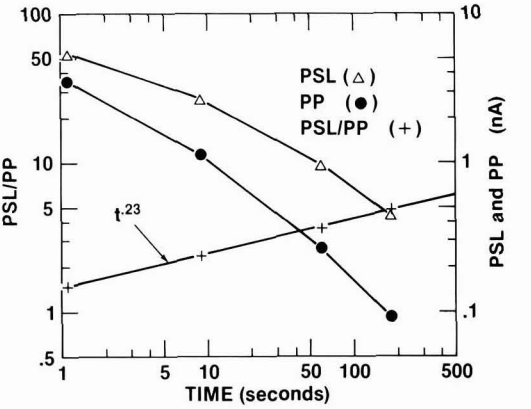

Fig. 12. Time dependence of L_1(PP), ΔL(PSL), and $r = \Delta L/L_1$ for the Zn_2SiO_4:Mn sample. Experimental conditions were similar to the ones of the Fig. 10 measurements. The temperature was at −61°C. The ratio r has a $t^{0.23}$ dependence, which yields: $a/b = 0.77$.

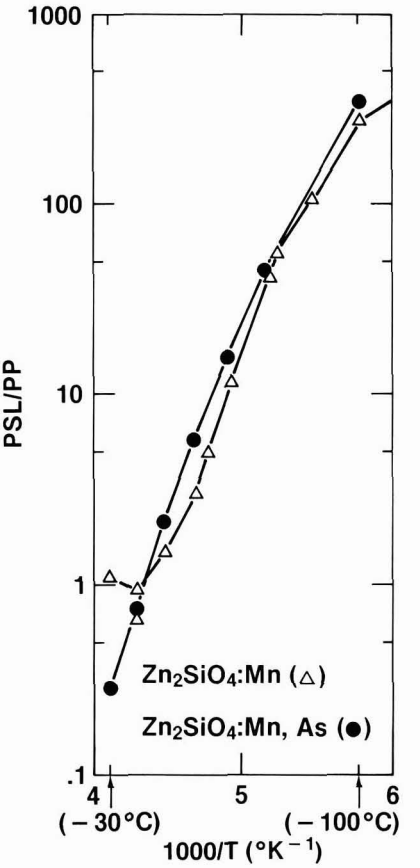

Fig. 13. Temperature dependence of the ratio $r = \Delta L/L_1$ for samples both with and without arsenic codoping. Both curves follow the same pattern over more than two orders of magnitude.

(*iv*) Analysis of peak 2. A plot of the temperature dependence of τ for the peak 2 region yields $(a/b)E = 0.47$ eV (Fig. 11). Taking the Hoogenstraaten value of E as 0.96 eV, we obtain that $a/b = 0.49$. However, as

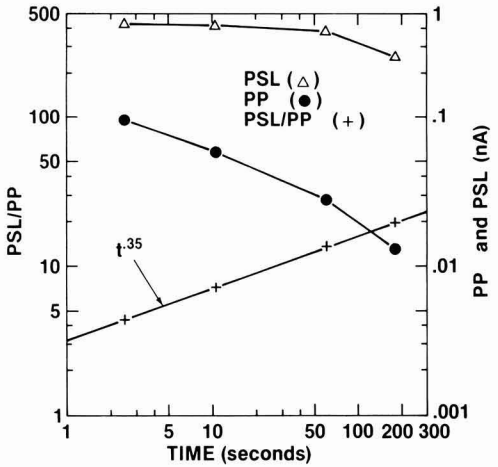

Fig. 14. Time dependence of L_1(PP), ΔL(PSL), and $r = \Delta L/L_1$ for Zn_2SiO_4: Mn sample. Experimental conditions were the same as in Fig. 6 and 12; the temperature was at +47°C. The ratio r displays a power dependence, $t^{0.35}$, leading to $a/b = 0.65$.

shown in Fig. 14, the time dependence measurement at $T = +47$°C (Fig. 14) yields: $a/b \cong 0.65$. Thus, there is a large discrepancy between the two values ($\cong$ 30%). Furthermore, as one recalls the peculiar behavior of the TSL peak 2 to the variation of excitation conditions (see Fig. 4 and 5 of paper I), one may suggest that the charge transfer from the peak 2 set of trapping centers to luminescent centers is not limited to a tunneling process and may involve the conduction band.

Summary

Using a pair recombination model with two tunneling levels, we carried out a comparative study of PP and PSL in Mn-doped zinc silicate phosphors (with or without As) for 254 nm UV excitation and 633 nm photostimulation. Using a single tunneling level model, one predicts that the ratio r of $\Delta L(\text{PSL})/L_1(\text{PP})$ is independent of time and follows an exp $-E/kT$ temperature dependence (the activation energy E may be obtained from a Hoogenstraaten plot). However this is inconsistent with experimental data which showed a power law behavior for r *vs.* time and an exp $-\alpha E/kT$ dependence of r upon temperature with $\alpha < 1$. We presented a two tunneling level model which could account for both of these experimental t- and T-dependencies of r. Moreover, in this interpretation we could predict, in good agreement with experiment, that t- and T-dependences of r were related to each other by a common parameter a/b, that is: $r(t) = Kt(1 - a/b)$ whereas $r(T) = K' \exp - a/b\ E/kT$. Furthermore, this model yielded, through experimental determination of a/b, a complete energy level diagram of the traps responsible for PP and PSL. We determined numerical values for the depths of trap ground state and tunneling levels which are as follows. For Mn and As codoped sample, $E = 0.69$ eV, $a/b = 0.66$ by temperature dependence data and $a/b = 0.72$ by time dependence data; thus $E_1 = 2.3$ eV, $E_2 = 1.0$ eV, and $E = 3.0$ eV. For Mn-doped sample, $E = 0.68$ eV, $a/b = 0.67$ and 0.77 corresponding to the two methods. The traps present in samples both with and without arsenic are found to be of the same type but with different distribution (we exclude the high temperature set of traps of the sample without As). These results may suggest that arsenic codoping may induce a change in the trap spatial distribution rather than in the nature of the traps themselves. In the limit that the photostimulation energy is the same as the thermostimulation energy, the two tunneling level model should be reduced to a single tunneling level model which can account for the PP and PSL behavior. This should be observable if one uses a tunable light source in the infrared of sufficient intensity.

Acknowledgment

We would like to thank Ms. Sandy Macuirzynski and Ms. Evelyn Margulis for typing this manuscript. One of us (PT) would like to thank the CNET and IBM T. J. Watson Research Center for supporting this work and his one-year stay in the Phosphor Research Group at the IBM Yorktown Heights Research Center.

Manuscript submitted June 25, 1982; revised manuscript received March 15, 1983.

IBM T. J. Watson Research Center assisted in meeting the publication costs of this article.

REFERENCES

1. P. Thioulouse, E. A. Giess, and I. F. Chang, *J. Appl. Phys.*, **53**, 9015 (1982). Also see I. F. Chang and P. Thioulouse, *ibid.*, **53**, 5873 (1982).
2. I. F. Chang and G. A. Sai-Halasz, *This Journal*, **127**, 2458 (1980).
3. I. F. Chang, G. A. Sai-Halasz, and M. W. Shafer, *J. Lumin.*, **21**, 323 (1980).
4. I. F. Chang, P. Thioulouse, E. E. Mendez, E. A. Giess, D. B. Dove, and T. Takamori, Int. Lumin. Conf. Proceeding, Berlin, July 1981; *J. Lumin.*, **24/25**, 313 (1981).
5. C. J. Delbecq, Y. Toyozawa, and P. H. Yuster, *Phys. Rev.*, **B9**, 4497 (1974).
6. P. Avouris and T. N. Morgan, *J. Chem. Phys.*, **74**, 4347 (1981).
7. W. Hoogenstraaten, *Philips Res. Rep.*, **13**, 515 (1958).
8. E. A. Giess, C. F. Guerci, J. D. Kuptsis, I. F. Chang, and D. J. Robbins, *J. Cryst. Growth*, **60**, 219 (1982).

Aspects of GaAs Selective Area Growth by Molecular Beam Epitaxy with Patterning by SiO_2 Masking

A-z. Li

Shanghai Institute of Metallurgy, Shanghai, China

H. Cheng and A. G. Milnes*

Carnegie-Mellon, Institute, Pittsburgh, Pennsylvania 15213

ABSTRACT

The selective epitaxy of GaAs through windows in SiO_2 deposited on semi-insulating GaAs substrates has been studied. Etching of the (100) substrates for planar inlaid deposition may incur problems of irregular nonflat-bottomed profiles to the troughs, and problems of voids after deposition because of the SiO_2 undercutting. It is shown that flat-bottomed holes may be obtained by use of an etch of composition $1H_2SO_4$:$2.5H_2O_2$:$50H_2O$ and that this has a suitable etch rate. The problem of voids because of SiO_2 undercutting may be solved by an extra step that removes the overhangs. Many orientations of patterns were studied on the substrates to confirm the effectiveness of the recommended procedures.

Selective epitaxy is likely to become an increasingly important technology for the fabrication of monolithic gallium arsenide integrated circuits since it opens up the possibility that structures may be made that differ from those currently achieved in GaAs by ion implantation or diffusion processes.

Typically, the selective epitaxy process uses deposited SiO_2 or thermal oxide Ga_2O_3 patterned to form windows on semi-insulating (100) GaAs through which the growth takes place. The GaAs under these windows may be etched to form troughs into which epitaxial GaAs is inlaid or the GaAs may be epitaxially grown on the original substrate surface to form low profile mesa structures. The epitaxy technologies that have been considered are liquid phase epitaxy LPE (1-4), vapor phase epitaxy VPE (5-10), and molecular beam epitaxy MBE (11-20). In MBE, the growth is by impinging thermal energy beams of atoms or molecular species such as As_4 or As_2 onto the heated substrate. The result is that deposition occurs both on the exposed GaAs in the window area where the growth is epitaxial and on the insulator region SiO_2 or Ga_2O_3 where the deposit is fine grain polycrystalline GaAs that is effectively semi-insulating. If the polycrystalline GaAs is very high in resistance, it may be left in place or, if it is unwanted or lower in resistance because of doping during the growth, it may be removed after deposition.

A special feature of the MBE process is that it is a direct line of flight process and therefore in the etch-and-fill technology, epitaxy of monocrystalline GaAs takes place from the bottom of the etched trough and there is virtually no overgrowth problem at the edges of the trough. This is in contrast to LPE and VPE techniques where growth proceeds from the walls inward as well as from the bottom upward. This leads to low quality monocrystalline growth at the perimeter of the trough, facet formation, and a tendency for overgrowth of the edges with rough large grain polycrystalline GaAs. This distorts the size and shape of the effective window and the effect is orientation dependent. Hence LPE and VPE are not good processes unless overgrowth is deliberately being sought, as when burying the metal grid of a permeable base transistor or in the cleaved film process for solar cells.

However, in MBE selective epitaxy by etch-and-fill, there is need to prevent an insulator profile that arises from undercutting and results in the presence of edge voids in the refilling stage. Furthermore, for planar filling, the etched hole must be flat-bottomed. This paper discusses etching and masking procedures that accomplish these ends.

Specimen Preparation

The (100) substrates of GaAs used in the experiments were either Cr-doped or LEC semi-insulating material or conducting substrates with Si or Te doping. A normal organic solvent and acid cleaning procedure was applied and the clean polished surfaces were then coated with SiO_2 by chemical vapor deposition from SiH_4 and oxygen or by sputtering. SiO_2 thicknesses ranging from 3000 to 1000Å were used. Standard photolithographic techniques were applied and the SiO_2 in the photoresist window areas was removed by etching with buffered HF solution.[1]

After a further organic solvent treatment, the substrates on which mesas were to be grown were given an oxide removing etch of 10% HCl and rinsed in deionizing water. The substrates for the etch-and-fill experiments were etched to depths of several microns through the SiO_2 windows with a solution of $1H_2SO_4$: $2.5H_2O_2$: $50H_2O$ at room temperature (these etch proportions are discussed in the section that follows) and rinsed in DI water.

Selective Etching Studies

The surface preparation for the procedure shown in Fig. 1(a) has the aim of merely cleaning the original substrate surface of residual SiO_2, photoresist, and native oxide prior to growth and for this 10% HCl is the acid etch used. For the etch-and-fill technology of Fig. 1(b), the flatness of the bottom of the etched hole is of importance and we have studied this for a number of etch solutions.

The H_2SO_4-H_2O_2-H_2O system is the one most commonly used as a surface polishing etchant for GaAs and this is the one we have concentrated on. The proportions of this etch were found to have a considerable influence on the profile of the etched hole. Shaw (21) has reported that when using the mixture $5H_2SO_4$:$1H_2O_2$:$1H_2O$ for selective etching the bottom of the holes were very nonplanar with the greatest etching occurring near the mask edges. The etching process is considered to be as follows

$$GaAs + 4H_2O_2 = GaAsO_4 + 4H_2O$$

$$2GaAsO_4 + 3H_2SO_4 = Ga_2(SO_4)_3 + 2H_3AsO_4$$

* Electrochemical Society Active Member.

Key words: etching, orientation, semi-insulating GaAs, polycrystalline GaAs.

[1] Supplied by the Transene Company Incorporated, Rowley, Massachusetts, and consisting of a fluoride, bifluoride, and hydrofluoride acid buffer solution. U.S. Pat. 2,732,326.

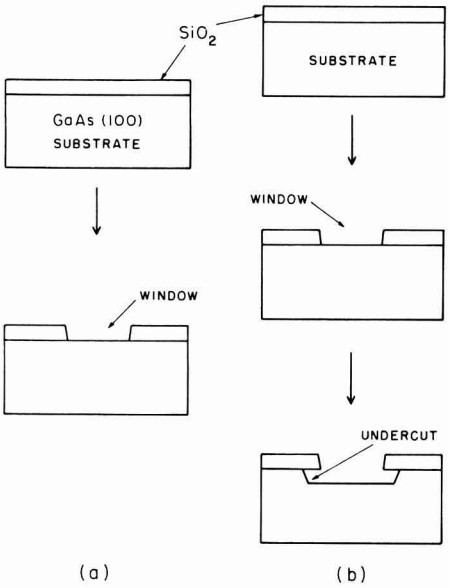

Fig. 1. Structure of specimens for selective epitaxy. (a) For growth on original substrate surface. (b) With etching of the GaAs showing the undercut effect.

These are oxidation and dissolution processes where H_2O_2 is the oxidizer and H_2SO_4 causes the dissolution. The process may be limited either by diffusion rates or chemical reaction rates. Shaw attributes the enhanced etching rates near the mask edge to the surface diffusion of adsorbed moleculars along the protective mask which effectively results in a greater flux of etchant at the mask edge. Improved results were obtained when Shaw used 0.7M H_2O_2-1M NaOH as the etchant. Other etches also have been studied (24-29).

Representative etching profiles in our work as determined by a Sloan Dektak surface profiler are shown in Fig. 2. We see preferential etching at the mask edge of a 25 μm wide window for etches of composition 6:1:1 and 3:1:1. However, for the composition $1H_2SO_4$: $2.5H_2O_2$:$50H_2O$ very flat-bottomed results are obtained, Fig. 2(c). The advantages of low H_2SO_4 solutions have been observed by Iida and Ito (22).

The etched depths *vs.* time for the various solutions are shown in Fig. 3 for (100) GaAs at 30°C. The rate for the preferred $1H_2SO_4$:$2.5H_2O_2$:$50H_2O$ solution is seen to be a convenient 0.38 μm/min and is independent of whether the GaAs is n^+ doped or semi-insulating. The other compositions are rather fast etching and exhibit deeper edges as shown by the bars and the rates are increased by ultrasonic stirring to quite unsuitable values.

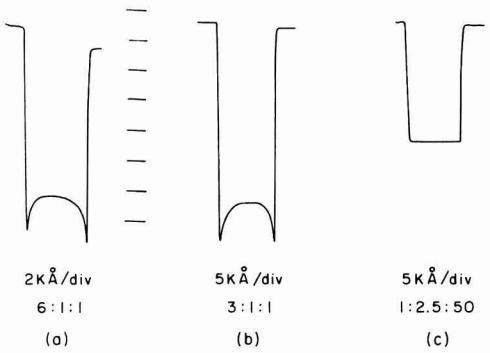

Fig. 2. The flatness of hole bottom after etching GaAs in various composition ratios of the H_2SO_4:H_2O_2:H_2O solutions. (a) 6:1:1, (b) 3:1:1, and (c) 1:2.5:50.

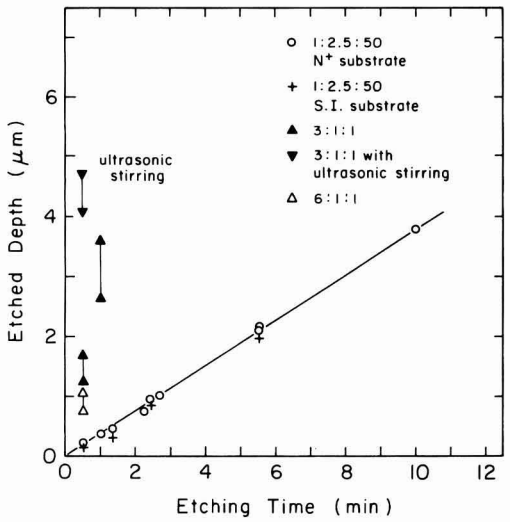

Fig. 3. Etching depth *vs.* etching time in various composition ratios of H_2SO_4:H_2O_2:H_2O and various substrates (n^+ GaAs and SI GaAs) at 30°C. (Error bar lines represent edge effect.)

The effect of temperature was explored as part of our calibration of the 1:2.5:50 etch and is shown in Fig. 4. Since this etch seemed to be a reproducible and very well-behaved one, we used it in our subsequent studies in conjunction with a mask capable of creating many orientations of rectangular windows in the SiO_2 layer.

Selective MBE Growth

The MBE system used was a Perkin Elmer Model 400 and the procedure followed that described else-

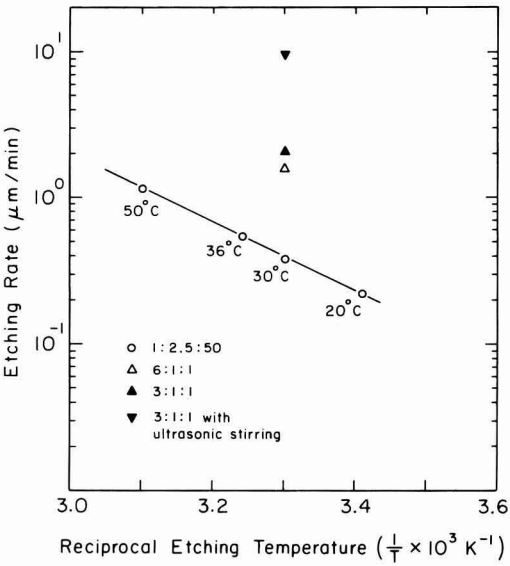

Fig. 4. Etching rate *vs.* reciprocal absolute temperature in various composition ratios of the H_2SO_4:H_2O_2:H_2O solutions.

where (23). The substrates after loading were preheated to about 610°C in the analysis chamber for 5 min to heat clean the surface and then were transferred to the growth chamber. The substrate temperature was 570°C during growth and the arsenic As_4 pressure from an arsenic effusion cell was 4.5×10^{-6} Torr. The Ga oven temperature was 1030°C and the As_4 to Ga flux ratio therefore about 5:1 with a growth rate of about 0.8 μm/hr. Ge was used as the n-type dopant and Be as the p-type dopant in some of the growths.

In one set of growths, no etching of the GaAs substrate was made except a light HCl etch to clean the original surface after the window was opened in the SiO_2 by buffered HF solution, Fig. 1(a). The GaAs ($\sim 10^{16}/cm^3$) deposited in the window was single crystal and that deposited on the SiO_2 was fine-grain polycrystalline material of high resistivity. The window edges showed no signs of faceted over-growth of large grain material unlike the effects seen with LPE and VPE. A scanning electron microscope photograph showing no distortion or overgrowth of the windows of all orientations is shown in Fig. 5.

In the second set of experiments, the GaAs in the window regions was etched with the flat-bottom etch $1H_2SO_4:2.5H_2O_2:50H_2O$ to a depth of typically 2 μm. This procedure, however, results in undercutting of the SiO_2 mask as suggested by the sketch in Fig. 1(b). The result after MBE growth is that voids are left under the overhanging SiO_2 as seen in the scanning electron microscope photograph of Fig. 6. The epitaxial GaAs layer in the window region is seen to be similar in thickness to the GaAs deposition on the SiO_2.

The GaAs undercut action and the effect of the SiO_2 overhang in creating crevasse-like perimeters between the grown epilayer in the window and the surrounding polycrystalline GaAs has been reported previously by Cho and co-workers (11-14, 16). In some applications, this is a desirable effect. For instance, Tsang and Cho point out this could be of value in the fabrication of integrated optics components such as channel optical waveguides.

In other applications such as the incorporation of refilled GaAs regions in semi-insulating substrates for monolithic circuit fabrication, the crevasses are undesirable and a complete fill is required so that metallization may cross as a planar structure. The overhang problem may be solved in principle by making the SiO_2 layer thicker than the overhang.

Removal of the overhanging SiO_2 is then possible by etching in HF (diluted to 20:1) as shown in Fig. 7(a), although this at the same time thins the complete SiO_2 layer. Since the SiO_2 overhang may be several micrometers long (depending on the depth of the etching in the GaAs window area), this procedure usually requires an excessive thickness of SiO_2 to be grown.

A better solution to the problem, we believe, is to leave the SiO_2 protected with photoresist while etching away the SiO_2 overhang from the underside as suggested by the sequence of Fig. 7(b).

We have demonstrated the practicality of this procedure using both Shipley AZ positive photoresist and Kodak negative photoresist and lateral etching with the Transene buffer HF solution. The SiO_2 etching *vs.* time for this solution at room temperature, without stirring or ultrasonic vibration, is shown in Fig. 8 and the rate is observed to be convenient.

After etching away the SiO_2 overhang to the perimeter of the GaAs trough as seen in Fig. 9, the photoresist is still in place and must be removed by solvents before the MBE growth is made. The results after MBE growth show no voids between the trough sides

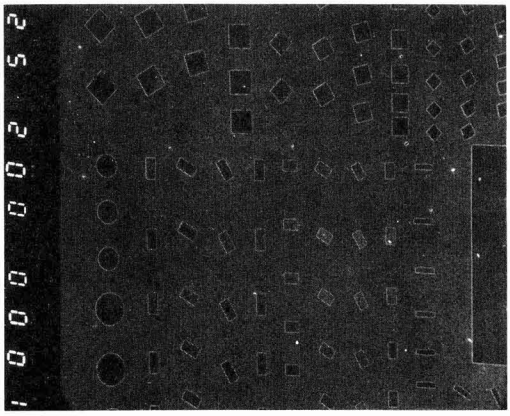

Fig. 5. An SEM photograph that shows the various window orientations in which GaAs has been grown on the original (100) substrate and the absence of any edge growth distorting the window shape.

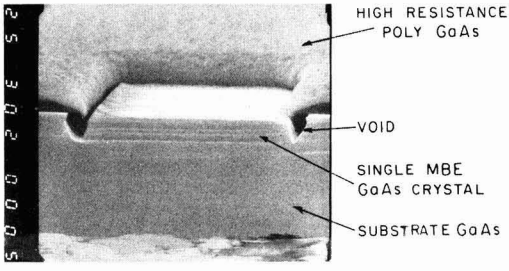

Fig. 6. An SEM photograph of an etch-and-fill growth showing the SiO_2 overhang and the resultant voids between the single crystal GaAs in the window area and the fine grain high resistance GaAs on the SiO_2.

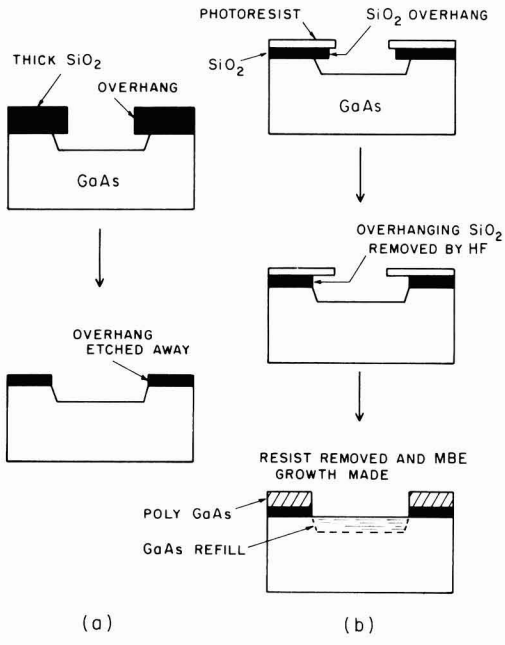

Fig. 7. Procedures for removal of SiO_2 overhang. (a) With thick SiO_2 and HF etching. (b) With thin SiO_2 protected by photoresist.

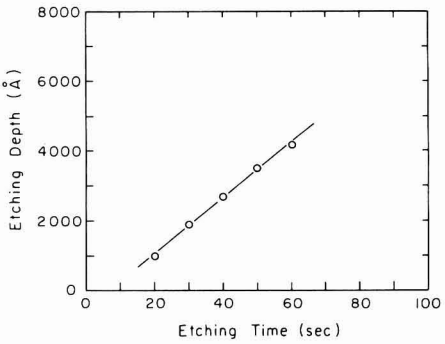

Fig. 8. Etching of SiO_2 vs. time in buffered HF solution

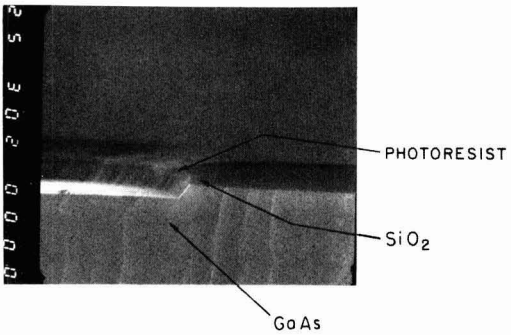

Fig. 9. GaAs trough with SiO_2 overhang etched back to the edge and the photoresist still overhanging.

and the epigrown single crystal GaAs, see Fig. 10. Also there is no sign of facet growth between the GaAs in the window and the polycrystalline GaAs on top of the SiO_2. Depending on the doping of the GaAs in the window, the polycrystalline GaAs may be high enough in resistance to leave in place in some circuit applications. In other applications, it may have to be removed.

Conclusions

The selective etching and selective deposition of GaAs has been studied on (100) substrates.

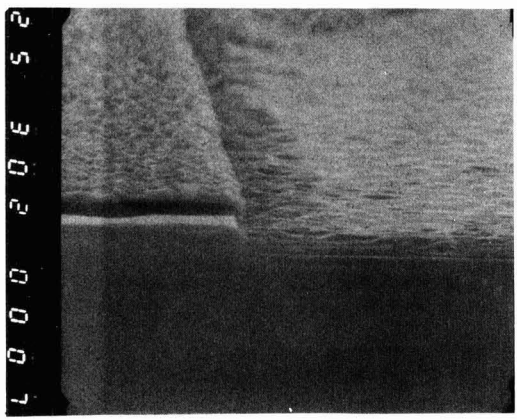

Fig. 10. The specimen of Fig. 9 after MBE growth, showing no voids at the edge between the refill GaAs and the substrate. The masking SiO_2 and the polycrystalline high resistivity GaAs deposited on it are still in place.

An etching solution with $1H_2SO_4:2.5H_2O_2:50H_2O$ composition was found that gives flat-bottomed holes, constant and suitable etching rates, and can be withstood by the photoresist.

Different shape and size patterns were used for selective MBE growth studies. Selective MBE growth does not cause overgrowth and edge distortion effects that are problems in selective LPE and VPE growth.

Etching undercutting effects can cause crevices to occur at the window edge. If these are not desired, they can be eliminated by removal of the SiO_2 overhang with buffered HF solution and the etching rates for this are given.

Acknowledgments

This work was supported in part by NSF Grant ECS 8013773. We wish to thank Shanghai Institute of Metallurgy, Chinese Academy of Sciences for supplying the mask which was used for selective orientation studies.

Manuscript submitted Dec. 4, 1982; revised manuscript received *ca.* April 15, 1983.

Carnegie-Mellon University assisted in meeting the publication costs of this article.

REFERENCES

1. M. M. Piskorski and G. D. Stareev, *Solid-State Electron.*, **18**, 859 (1975).
2. O. Ishihara, M. Otsubo, and S. Mitsui, *Jpn. J. Appl. Phys.*, **16**, 2109 (1977).
3. X. F. Yang, L. Huang, and H. C. Gatos, *This Journal*, **129**, 194 (1982).
4. A. Z. Li, J. H. Qin, and C. C. Li, Symposium on the National Conference on Microwave, Photoelectronic Devices and Compound Semiconductors, Nanjing, China (1979).
5. F. W. Tausch, Jr., and A. G. Lapierre, III, *This Journal*, **112**, 707 (1965).
6. D. W. Shaw, *ibid.*, **113**, 904 (1966).
7. Y. Ishibashi and M. Yamaguchi, *Jpn. J. Appl. Phys.*, **9**, 1007 (1970).
8. Y. Ishibashi and M. Yamaguchi, *ibid.*, **10**, 525 (1971).
9. S. Iida and K. Ito, *J. Cryst. Growth.*, **13-14**, 336 (1972).
10. F. Z. Lu and Y. C. Ding, Symposium on the National Conference on Microwave, Photoelectronic Devices and Compound Semiconductors, Nanjing, China (1979).
11. A. Y. Cho, *J. Appl. Phys.*, **46**, 783 (1975).
12. W. C. Ballamy and A. Y. Cho, *IEEE Trans. Electron Devices*, **ed-23**, 481 (1976).
13. A. Y. Cho, J. V. Dilorenzo, and G. E. Mahoney, *ibid.*, **ed-24**, 1186 (1977).
14. W. T. Tsang and A. Y. Cho, *Appl. Phys. Lett.*, **30** (6), 293 (1977).
15. W. T. Tsang and M. Ilegems, *ibid.*, **31** (4), 301 (1977).
16. W. T. Tsang and A. Y. Cho, *ibid.*, **32** (8), 491 (1978).
17. S. Hiyamizu, K. Nanbu, T. Fujii, T. Sakurai, H. Hashimoto, and O. Ryuzan, *This Journal*, **127**, 1562 (1980).
18. G. M. Metze, H. M. Levy, D. W. Woodard, C. E. C. Wood, and L. F. Eastman, *Appl. Phys. Lett.*, **37** (7), 628 (1980).
19. T. Yao, T. Minato, and S. Maekawa, *J. Appl. Phys.*, **53**, 4236 (1982).
20. P. N. Favennec, L. Henry, A. Regreny, and M. Salvi, *Electron. Lett.*, **18**, 933 (1982).
21. D. W. Shaw, *This Journal*, **113**, 958 (1966).
22. S. Iida and K. Ito, *ibid.*, **118**, 768 (1971).
23. A. Z. Li, S. H. Xin, and A. G. Milnes, *J. Electron. Mater.*, **12**, 71 (1983).
24. Y. Tarui, Y. Komiya, and Y. Harada, *This Journal*, **118**, 768 (1971).
25. J. J. Gannon and C. J. Nuese, *ibid.*, **121**, 1215 (1971).
26. J. Angilello, R. M. Potemski, and G. R. Woolhouse, *J. Appl. Phys.*, **46**, 2315 (1975).
27. W-T. Tsang and S. Wang, *Appl. Phys. Lett.*, **28**, 44 (1976).
28. Y. Mori and N. Watanabe, *This Journal*, **125**, 1510 (1978).
29. D. W. Shaw, *J. Cryst. Growth*, **47**, 509 (1979).

The Relation Between the Correction Factor and the Local Slope in Spreading Resistance

John Albers

Semiconductor Devices and Circuits Division, National Bureau of Standards, Washington, DC 20234

ABSTRACT

Dickey had proposed a technique, known as the local slope method, for the calculation of the correction factor which is used to obtain resistivity profiles from spreading resistance data. The technique is founded upon two asymptotic models for the conduction process involved in the spreading resistance measurement for the cases of (*i*) a conducting layer over an insulating substrate, and (*ii*) a high resistivity layer over a low resistivity or conducting substrate. The results of these two extreme cases are bridged by means of an assumed functional relation between the correction factor and the local slope of the spreading resistance data. This paper examines the two asymptotic models as well as the assumed functional relation between the correction factor and the local slope. It is shown that the asymptotic models adequately describe the behavior of the correction factor for a thin uniform layer over insulating or conducting boundaries. In addition, the single-valued relation between the correction factor and the local slope, which is assumed by the local slope method, is shown not to be an adequate representation of the multiple-valued relation between these two quantities found from multilayer data. For the cases considered, this distinction leads to an error in the resistivities as interpreted by the local slope method by as much as 60%. Nonetheless, the local slope results qualitatively follow the multilayer results thus making the technique a usable one for the calculation of approximate correction factors. A comparison of the two correction factor *vs.* local slope relations provides a basis for the behavior of the interpreted resistivities when they are compared with the input resistivities.

Spreading resistance measurements on bevel-sectioned materials of nonuniform resistivity provide a technique for the determination of the resistivity profiles of these materials. The relation between the spreading resistance, $R(x)$, and the resistivity, $\rho(x)$, is given by the equation

$$R(x) = \frac{\rho(x)}{2a} C(x) \qquad [1]$$

where x is the depth, a is the electrical probe radius, and $C(x)$ is the correction factor which depends upon the details of the underlying resistivity structure and the electrical probe radius. Central to the effective use of this technique is the calculation of the correction factor which provides for the extraction of the resistivity from the spreading resistance. In the calculation of the correction factor, Schumann and Gardner (1, 2) have presented a technique based upon the multilayer solution of the Laplace equation. The focal point of the multilayer Laplace equation analysis is that the correction factor may be expressed as

$$C(x) = 8 \int_0^\infty A(x,\lambda) \left\{ \frac{J_1(\lambda a)}{\lambda a} - \frac{J_0(\lambda S)}{2} \right\} I_\nu(\lambda a)\, a d\lambda \qquad [2]$$

where S is the separation between the probes, $J_0(\lambda a)$ and $J_1(\lambda S)$ are the Bessel functions of zero and first order, respectively, $A(x,\lambda)$ is the kernel of the integral and is related to the resistivity structure, $I_\nu(\lambda a)$ is the Hankel transform of the generalized probe-current density (3), and λ is the integration variable. In the analysis presented here, the origin of the coordinate system is at the substrate so that the variable x increases away from the substrate. The implementation of this technique has been greatly simplified by the recursion relation for the kernel of the correction factor integral as developed by Choo *et al.* (4). The first successful use of this method has been presented by D'Avanzo *et al.* (5, 6) who make use of the recursion relation in conjunction with a partial integral scheme for the kernel of the correction factor integral. More recently, Berkowitz and Lux (7) have greatly simplified the implementation by making use of a 22-point integration scheme.

An alternative technique for the calculation of the correction factor, known as the local slope method, has been presented by Dickey (8, 9). The focal point of this method is the investigation of the behavior of the correction factor for thin layers over insulating or conducting boundaries. By making use of parallel or series conduction models, Dickey has proposed that the correction factor may be related to the local slope of the spreading resistance data, $M(x)$, defined as

$$M(x) = \frac{d \ln R(x)}{dx} \qquad [3]$$

where the derivative is evaluated in the direction of the substrate. This analysis is based upon the asymptotic models for the cases where $M(x) \to +\infty$ and $M(x) \to -\infty$. The behavior of the correction factor as a function of the local slope between these limiting cases is provided for by an assumed single-valued relation between the correction factor and the local slope. This relation is required by construction to yield the parallel and series conduction limits as $M(x)$ becomes large and positive or large and negative. It should be noted that the philosophy of the local slope method is to bypass the integral inversion required by Eq. [2] and focus upon the spreading resistance data directly. In other words, in order to use Eq. [1] and [2], the resistivity is varied until the calculated spreading resistance agrees with the measured spreading resistance to within a given accuracy. The local slope method, on the other hand, employs the value of $M(x)$ to extract $C(x)$ by means of an assumed simple algebraic relation.

Previously, a comparison of the results of the technique of D'Avanzo *et al.* and the local slope technique for correcting model spreading resistance data has been presented (10). There it was found that the technique of D'Avanzo *et al.* gave back the resistivities used in the original model data calculation. The local slope method gave rise to resistivities which qualitatively followed the original resistivities. This agreement was particularly impressive in that the model data was constructed to take the local slope between negative and positive values. The question which naturally arose was whether the local slope equation could be derived from the more general multilayer Laplace equation. In particular, the possibility of the local slope equation being the first-order form of a more general equation relating the correction factor to the local slope was considered.

The purpose of this paper is to address this question and to show that the more general multilayer Laplace

equation does not admit to a single-valued relation between the correction factor and the local slope. In general, the multilayer equation gives rise to a multiple-valued relation between the correction factor and the local slope, which implies that the local slope is not a good variable in which to express the correction factor. Nonetheless, the local slope relation does fall in the region of the curve given by the multilayer equation. This behavior provides a basis for the understanding of why, for example, the resistivities interpreted by local slope are sometimes larger than and sometimes smaller than the original resistivities.

The Local Slope Method

The first of the asymptotic models used in the local slope derivation is that of the parallel conduction model. This is assumed to correctly describe the conduction mechanism in a thin nonuniform layer over an insulating substrate. In this model, the conduction is assumed to take place in parallel through the sublayers between the probes (akin to the model used in sheet resistance measurements). In both this model and the series conduction model, the conductivity (or resistivity) is assumed to be constant over the thickness, $\Delta x = t$, of the sublayer. The conductivity at the position x in the structure (measured from the insulating boundary) is then related to the differences between the inverses of the spreading resistances (or spreading conductances) at the positions x and $x - t$ according to

$$\sigma(x) = \frac{\ln (S/a)}{\pi t} \left\{ \frac{1}{R(x)} - \frac{1}{R(x-t)} \right\} \quad [4]$$

where $R(x)$ and $R(x - t)$ are the spreading resistances at the positions x and $x - t$, respectively. The corresponding relation between the correction factor and the local slope of the spreading resistance is

$$C(x) = K_1 M(x) \quad [5]$$

where the local slope of the spreading resistance, $M(x)$, is given by Eq. [3] and

$$K_1 = \frac{2a \ln (S/a)}{\pi} \quad [6]$$

The second asymptotic model, known as the series conduction model, is assumed to hold for the conduction mechanism in a thin nonuniform layer of high resistivity over a conducting substrate. In this model, the conduction through the high resistivity material is viewed as taking place through a cylinder of radius a until the conducting substrate is encountered where the current is shorted to the second cylinder under the second probe. For this case, the model would predict that the resistivity at the position x is related to the differences between the spreading resistances at the positions x and $x - t$ according to the relation

$$\rho(x) = \frac{\pi a^2}{2t} \{R(x) - R(x-t)\} \quad [7]$$

The corresponding relation between the correction factor and the local slope of the spreading resistance is

$$C(x) = -\frac{K_2}{M(x)} \quad [8]$$

where

$$K_2 = \frac{4}{\pi a} \quad [9]$$

and $M(x)$, the local slope, is defined by Eq. [3].

For most cases of physical interest, the resistivity structure will lie somewhere in between those used in the parallel and series conduction models. For the intermediate cases, the local slope method assumes that it is possible to express the correction factor as a single-valued function of the local slope. In particular, this single-valued function is required to reduce to Eq. [5] as $M(x) \to +\infty$ and to Eq. [8] as $M(x) \to -\infty$. The general form of the function which is proposed to satisfy these requirements is given by

$$C(x) = \frac{K_1 M(x)}{2} + \left\{ \left\{ \frac{K_1 M(x)}{2} \right\}^2 + \kappa \right\}^{1/2} \quad [10]$$

The three commonly used forms of the function, κ, include: (*i*) $\kappa = K_1 K_2$, (*ii*) $\kappa = 1$, and (*iii*) $\kappa = K_3$, where

$$K_3 = 1 + \{K_1 K_2 - 1\} \frac{2}{\pi} \tan^{-1} \left\{ \log \frac{R(x)}{R(x-a)} \right\} \quad [11]$$

where $R(x)$ is the spreading resistance of the point being considered and $R(x - a)$ is the spreading resistance one probe radius deeper into the structure. It should be obvious that the above forms of κ in the relation between the correction factor and the local slope are arbitrary, subject only to the limiting conditions where $M(x) \to +\infty$, $M(x) \to -\infty$, and $M(x) \to 0$. In particular, the first form, *i.e.*, $\kappa = K_1 K_2$, gives rise to the correct asymptotic results in the limits as $M(x) \to +\infty$, $M(x) \to -\infty$ but does not give rise to a correction factor of unity when the local slope is zero. The second form, *i.e.*, $\kappa = 1$, does not yield the asymptotic model results exactly but does reproduce a correction factor of unity for a zero value of the local slope. The third form, *i.e.*, $\kappa = K_3$, is an attempt to remedy both of these situations. However, as has been shown previously (10), this particular form has a difficulty of yielding very large resistivities (very small correction factors) in the regions where the local slope is large and negative. As indicated previously, the purpose of the present paper is to investigate the validity of Eq. [5], [8], and [10] in terms of the spreading resistance calculated from the multilayer Laplace equation.

Calculations

Test of asymptotic models.—The first set of calculations to be discussed addresses the validity of the two asymptotic models embodied in Eq. [4] and [7]. In particular, if these are adequate descriptions of the conduction processes in these two extreme cases, then their validity should be easily checked in the cases of uniform layers over insulating or conducting boundaries. For the case of a uniform layer over an insulating boundary, it is straightforward to show from Eq. [1] that Eq. [4] reduces to the form

$$\frac{2a \ln (S/a)}{\pi t} \left\{ \frac{1}{C(x)} - \frac{1}{C(x-t)} \right\} = U_{\text{ins}}(x) = 1 \quad [12]$$

Also, for the case of a uniform layer over a conducting boundary, Eq. [7] reduces to the form

$$\frac{\pi a}{4t} \{C(x) - C(x-t)\} = U_{\text{con}}(x) = 1 \quad [13]$$

In order to test Eq. [12] and [13], model spreading resistance data were generated for the cases of a uniform layer over an insulating boundary and a conducting boundary, respectively. In all cases, a probe radius of $a = 2$ μm was used. For these two situations, the kernel of the spreading resistance correction factor integral (as given by Eq. [2]) is of the form $A(\lambda x) = \coth(\lambda x)$ and $A(\lambda x) = \tanh(\lambda x)$, respectively (7). In addition to using each of these two forms of the kernel, the correction factor calculations made use of several forms of the probe-current density (3). The results of these calculations are presented in Fig. 1-4.

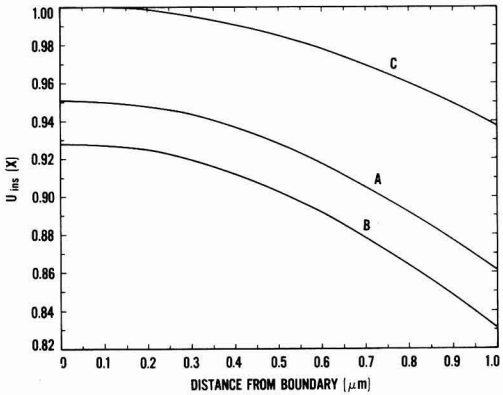

Fig. 1. Behavior of the left-hand side of Eq. [12] for the case of a uniform layer over an insulating boundary. The curves corresponding to the three current densities are as follows: Schumann and Gardner (A); Choo uniform (B); and ring delta function (C). The specific value of the probe spacing is $S = 50$ μm.

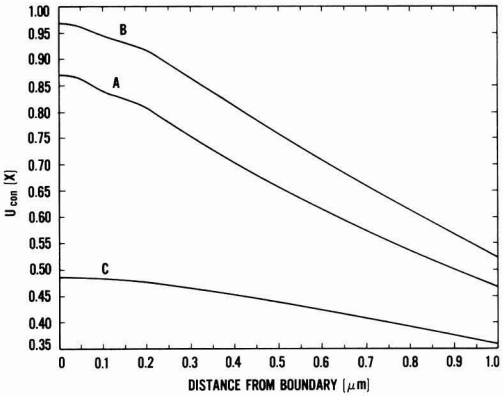

Fig. 3. Behavior of the left-hand side of Eq. [13] for the case of a uniform layer over a conducting boundary. The curves corresponding to the three current densities are as follows: Schumann and Gardner (A); Choo uniform (B); and ring delta function (C). The value of the probe separation used is $S = 50$ μm.

In Fig. 1, the left-hand side of Eq. [12] is plotted as a function of the distance from the insulating boundary for the three current densities and for a value of the probe separation, $S = 50$ μm. In particular, the three probe-current densities which were used were the Schumann and Gardner, the Choo uniform, and the ring delta function forms. These current densities and their extent of current constriction are discussed in detail elsewhere (3). These three forms of the current density gave rise to the curves denoted by A, B, and C, respectively. It is clear that the ring delta function results yield a value of unity for this situation. In Fig. 2, the ring delta function current density results are presented for several values of the probe separation. For small distances from the boundary, all values of S yield identical results. For large distances from the insulating boundary, the agreement improves with increased values of S as might be expected from the similarity of the model with the sheet resistance model. For the case of a conducting boundary, the plots presented in Fig. 3 represent the left-hand side of Eq. [13] for the three forms of the probe current density for a value of $S = 50$ μm. The Choo uniform current density clearly yields the best results. In addition, the behavior of the uniform current density results for several values of S is presented in Fig. 4. It is clear that the results are independent of S as would be expected from the nature of the conduction mechanism.

From this analysis, it can be concluded that the asymptotic models contain the correct conduction mechanisms for thin uniform layers. In addition, the two asymptotic models are in agreement with the forms of the probe current densities which would be assumed to describe the current flow pattern at the probe-material interface. The insulating boundary causes current constriction and allows current flow only at the perimeter of the probe while the conducting boundary allows current flow to be approximately uniform over the entire area of the probe-material interface.

Correction factor-local slope relation for nonuniform layers.—While the above analysis indicates that the two asymptotic models provide a good description of the conduction process for the appropriate boundary

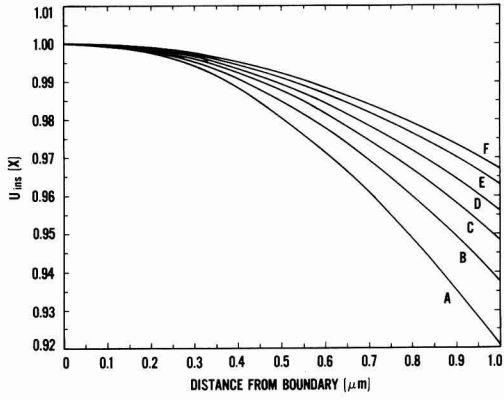

Fig. 2. This figure depicts the behavior of the left-hand side of Eq. [12] for the ring delta function current density for several values of the probe separation. The specific values of the probe separation are as follows: 25 μm (A); 50 μm (B); 100 μm (C); 200 μm (D); 500 μm (E); and 1000 μm (F).

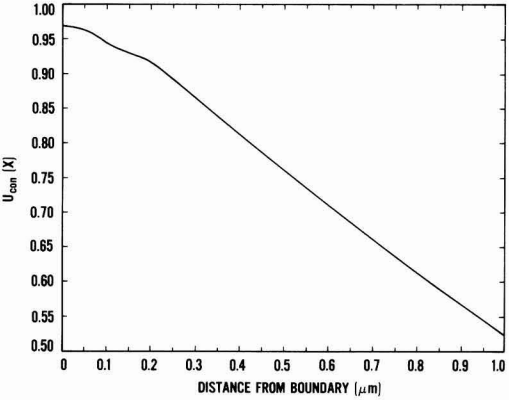

Fig. 4. This figure depicts the behavior of the results of Eq. [13] for a uniform layer over a conducting boundary for the Choo uniform current density. The curves for the values of the probe spacing used (25, 50, 100, 200, 500, and 1000 μm) all lie on top of each other. This indicates that the correction factor and, hence, the spreading resistance, is independent of the probe spacing. This is contained in the fact that the dominant contribution is the series conduction through the top layer.

conditions, the most important question focuses on the validity of the assumed single-valued relation between the correction factor and the local slope. In order to test the validity of this relation, model spreading resistance data were used. In particular, resistivity profiles typical of implant structures were employed in this investigation. The correction factor and the spreading resistance were calculated according to the Laplace multilayer equations (10) as given by Eq. [2] and [1], respectively. The local slope was then obtained from Eq. [3] and was used in Eq. [10] to obtain the corresponding local slope results. Typical resistivity results obtained for $\kappa = K_1K_2$ are contained in Fig. 5. In addition, typical results of the correction factors as a function of depth are presented in Fig. 6. It is clear from Fig. 5 that the resistivity profile obtained by the local slope method semiquantitatively agrees with the resistivity used in the multilayer method. However, there does appear to be an inconsistency in the way in which the resistivity is obtained. This is borne out by the corresponding correction factor plots presented in Fig. 6. In particular, from Fig. 5 it can be seen that there is a region up to about 0.3 μm where the local slope results are larger than the input resistivities and a region past 0.3 μm where the local slope results are smaller than the input resistivities. The reason for this nonsystematic difference can be explained by comparing the correction factor *vs.* local slope results obtained from the local slope method and from the multilayer calculations. A comparison of this type is presented in Fig. 7. The local slope results, denoted by B, are seen to be single-valued, *i.e.*, for a given value of the local slope there is only one value of the correction factor. On the other hand, the multilayer results, denoted by A, show a multiple-valued behavior, *i.e.*, for a given value of the local slope there is no unique value of the correction factor. Indeed, the feature of the multilayer curve which is most striking is that the correction factor depends upon the location along the profile. It is clear that up to about 0.3 μm, the local slope correction factor is smaller than the multilayer value, thus making the local slope resistivity larger than the input values. Beyond 0.3 μm, the local slope correction factor is larger than the multilayer value thus making the local slope resistivity smaller than the input values. In fact, the local slope curve lies in the same region of the correction factor-local slope plane as the multilayer curve. It is this fact which makes the

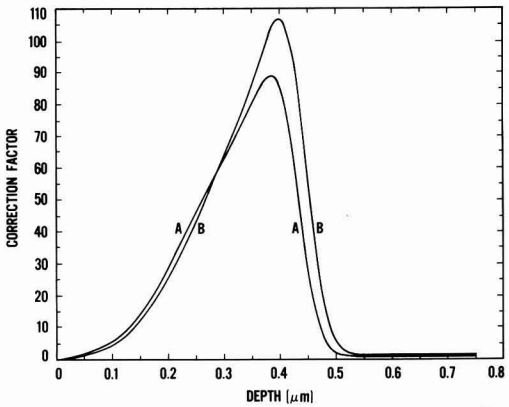

Fig. 6. This figure contains the correction factor as a function of depth as obtained from the multilayer equations (curve A) and from the K_1K_2 form of the local slope equation (curve B). The multilayer results are obtained from the input resistivities used in the multilayer equations while the local slope results are obtained from the local slope analysis of the calculated spreading resistance data. Note that the plot is not logarithmic along the y-axis. The correction factors in the region near the origin are less than unity, being on the order of 0.1.

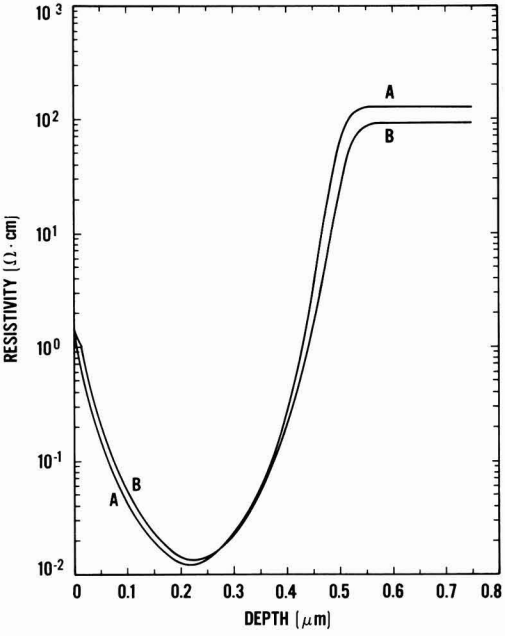

Fig. 5. This figure contains the original resistivity used to generate the model spreading resistance data (denoted by curve A) and the resistivity obtained by using the K_1K_2 form of the local slope equation on the calculated spreading resistance data. This interpreted resistivity profile is denoted by the curve B.

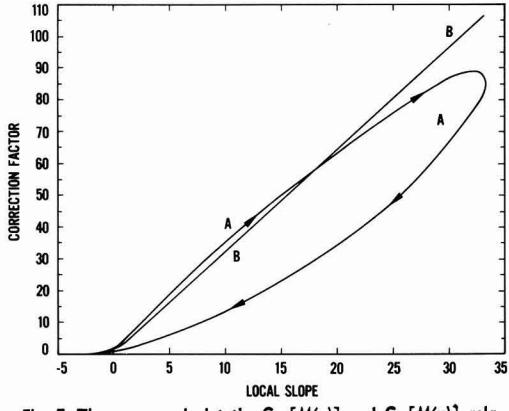

Fig. 7. These curves depict the $C_{ex}[M(x)]$ and $C_{ls}[M(x)]$ relations obtained from the multilayer and the K_1K_2 form of the local slope equation on the model spreading resistance data. The multilayer equations yield the $C(x)$ *vs.* $M(x)$ curve denoted by A while the local slope method gives rise to the $C(x)$ *vs.* $M(x)$ curve denoted by B. The arrow on the A curve indicates the path taken during the calculation from the top surface to the substrate. The path taken by the local slope method proceeds up the B curve to the maximum value and then changes direction and goes back down the B curve. The region before the crossing of the two curves is that where $C_{ex}(x) > C_{ls}(x)$ [or $\rho_{ex}(x) < \rho_{ls}(x)$]. The two correction factors are equal at the crossing point [which corresponds to the depth point at $x = 0.3$ μm of Fig. (5)]. Beyond the crossing point, $C_{ex}(x) < C_{ls}(x)$ [or $\rho_{ex}(x) > \rho_{ls}(x)$]. Similar results are obtained for the $\kappa = K3$ form and the $\kappa = 1$ form of the local slope equation.

local slope results qualitatively correct when compared with the multilayer results. It is important to emphasize that while the above results are obtained for the $\kappa = K_1K_2$ form of the local slope equation, similar results were obtained for the other two forms of κ. In particular, the $\kappa = 1$ form gave the correct substrate resistivity value and reproduced the $\kappa = K_1K_2$ form for the implant region of the structure. On the other hand, the $\kappa = K_3$ form gave rise to larger resistivities in the surface region of the implant and followed the $\kappa = K_1K_2$ form from the peak to the substrate where it went over to the correct substrate resistivity value. In all cases, the plot of the correction factor *vs.* local slope from each of these forms were very similar and did not reproduce the multiple-valued multilayer Laplace equation results. It might be argued that the square root form of the local slope equation is really double-valued. However, there is no *a priori* reason to choose one sign of the square root over another. One possible *ad hoc* way of dealing with this is to let the sign of the derivative of the local slope determine which sign to choose. This has been attempted with the present data. It was found that choosing the sign one way led to the usual local slope results while the other choice led to negative values of the correction factor, which is clearly unphysical.

Similar results were found for a number of structures. It is clear that the expansion of the correction factor in terms of the local slope is only of limited value. While the construction of a function of the form of Eq. [10] subject to the agreement with the asymptotic results as $M(x) \rightarrow +\infty$ and $M(x) \rightarrow -\infty$ appears to be a potentially useful one, there is implicit in it an assumption of single-valued behavior. However, the above analysis demonstrates that the correct relation is multiple valued. This means that the local slope is not the only variable at play in the determination of the correction factor. An alternative way of viewing this may be obtained from the expression between the spreading resistance and the correction factor as given in Eq. [1]. By taking the derivative of this equation with respect to x, it is possible to show that

$$M(x) = \frac{d \ln \rho(x)}{dx} + \frac{d \ln C(x)}{dx} \qquad [14]$$

For the case of a uniform layer, the first term on the right-hand side is zero. In this case, the resulting equation can be evaluated as

$$C(x) = C(0) \exp\left\{ \int_0^x M(x')\,dx' \right\} \qquad [15]$$

For this situation, the correction factor depends only upon the local slope. However, for a nonuniform resistivity case, Eq. [14] may be simply rearranged to yield

$$\frac{d \ln C(x)}{dx} = M(x) - \frac{d \ln \rho(x)}{dx} \qquad [16]$$

In this form, the equation states that the correction factor depends upon not only the local slope but also on the local variation of the resistivity. It is this additional term which gives rise to the multiple-valued behavior of the multilayer results when compared with the local slope prediction. Implicit in the use of the local slope method is the assumption that the correction factor may be obtained simply from the measured local slope. It is clear from Eq. [16] that the variation of the resistivity is neglected. In point of fact, it is not just $C(x)$ which is responsible for the specific form of $M(x)$, but it is really the product $\rho(x)C(x)$ which is mirrored in $M(x)$. This fact hinders the derivation of the local slope equations from the multilayer equations and causes the kind of behavior found in Fig. 7.

Conclusions

The asymptotic models used in the local slope method, as well as the local slope method itself, have been critically investigated. It has been shown that the asymptotic models give a good representation of the correction factor when compared with the predictions of the multilayer theory supplemented with either insulating or conducting boundary conditions. In addition, the assumption that the correction factor may be written as a single-valued function of the local slope has been addressed from the point of view of model spreading resistance data. The model data, which were calculated from the multilayer theory, show a multiple-valued relation between the correction factor and the local slope. This precludes the derivation of the local slope equations from the more general Laplace equation multilayer technique. In addition, the basic assumption implicit in the local slope method has been shown to be that the variation of the resistivity may be neglected and that the correction factor depends only upon the local slope. This assumption has been shown to be incorrect. It is the variation of the resistivity which leads to the multiple-valued relation between the correction factor and the local slope, which is obtained from the Laplace equation technique. This distinction accounts for the nonsystematic difference between the multilayer and local slope calculations exemplified in Fig. 5.

In conclusion, it is important to note that while the local slope method may not be obtained from the multilayer equations, the technique does offer qualitative and semiquantitative results which are useful in profile analysis.

Acknowledgment

This research was conducted as part of the National Bureau of Standards Semiconductor Technology Program.

Manuscript submitted Feb. 17, 1983; revised manuscript received June 9, 1983.

The National Bureau of Standards assisted in meeting publication costs of this article.

REFERENCES

1. P. A. Schumann and E. E. Gardner, *This Journal*, **116**, 87 (1969).
2. E. E. Gardner and P. A. Schumann, *Solid-State Electron.*, **12**, 371 (1969).
3. H. L. Berkowitz and R. A. Lux, *This Journal*, **126**, 1479 (1979).
4. S. C. Choo, M. S. Leong, and K. L. Kuan, *Solid-State Electron.*, **19**, 561 (1976).
5. D. C. D'Avanzo, R. D. Rung, and R. W. Dutton, Technical Report 5013-2, Stanford Electronics Laboratory, Stanford University, Stanford (1977).
6. D. C. D'Avanzo, R. D. Rung, A. Gat, and R. W. Dutton, *This Journal*, **125**, 1170 (1978).
7. H. L. Berkowitz and R. A. Lux, *ibid.*, **128**, 1137 (1981).
8. D. H. Dickey, in "Semiconductor Measurement Technology: Spreading Resistance Symposium," pp. 45-50, NBS Special Publication 400-10 (1974).
9. D. H. Dickey and J. R. Ehrstein, in "Semiconductor Measurement Technology: Spreading Resistance Analysis for Silicon Layers with Nonuniform Resistivity," pp. 15-18, NBS Special Publication 400-48 (1979).
10. J. Albers, *Solid-State Electron.*, **23**, 1197 (1980).

Growth of Single-Crystalline Epitaxial Group II Fluoride Films on InP(001) by Molecular-Beam Epitaxy

C. W. Tu, T. T. Sheng, M. H. Read, A. R. Schlier, J. G. Johnson,[1] W. D. Johnston, Jr., and W. A. Bonner

Bell Laboratories, Murray Hill, New Jersey 07974

ABSTRACT

Twin-free, single-crystalline, lattice-mismatched as well as lattice-matched, epitaxial dielectric films of group II cubic fluorides (SrF_2, CaF_2, and $Ba_xSr_{1-x}F_2$) have been grown on InP(001) substrates by molecular-beam epitaxy. The InP(001) surface was cleaned in vacuum by heating under phosphorus overpressure until a well-ordered and stoichiometric surface was obtained. The film growth of MF_2, where M is Ba, Sr, Ca, or Ba_xSr_{1-x}, was followed by reflection high energy electron diffraction (RHEED). The diffraction patterns indicate a parallel epitaxial relationship: $MF_2(001)\|InP(001)$ and $MF_2[110]\|InP[110]$. At low growth temperature (~250°C) and low growth rate we could obtain twin-free single-crystalline CaF_2 films. Transmission electron microscopy show the absence of any grains. At higher growth temperature (~350°C) we could obtain twin-free single-crystalline SrF_2, CaF_2, and $Ba_xSr_{1-x}F_2$ films. The latter can be lattice-matched to InP(001) at room temperature.

InP(001) has become very important in recent years because it is the substrate material for long-wavelength optical communication and high speed devices. If a dielectric film on a semiconductor substrate, such as InP(001), can be single crystalline and lattice matched to the substrate, the interface trap densities may be lowered (1). Thus, the film may be suitable for passivation and metal-insulator-semiconductor structures. Recently Harrison *et al.* showed that a CaF_2 film, E-beam evaporated on Si(111), could be a candidate as an electron resist and optical storage medium (2). Furthermore, Cho has grown epitaxial GaP on CaF_2(111) substrate by molecular-beam epitaxy (MBE) (3). Thus, there exist possibilities for epitaxial III-V semiconductor-insulator-semiconductor structures, which may be a basis for three-dimensional integration, waveguiding and device isolation in integrated optics, and other novel devices. In fact, recently we have grown the first epitaxial InP/fluoride/InP(001) double heterostructures by MBE (4). The results will be presented elsewhere.

Group II cubic fluorides are interesting for III-V compound semiconductors because they have similar crystal structure to InP and related compounds. The cubic fluorite structure consists of three interpenetrating face-centered cubic (fcc) lattices (5), whereas the zinc-blende structure of the substrate consists of two fcc lattices. Furthermore, the lattice constants of the fluorides bracket that of InP, the lattice mismatch ranging from −6.9 to +5.6% (5). Farrow *et al.* first showed epitaxial growth of BaF_2 on the (001) face of CdTe and InP at a substrate temperature of $\gtrsim$ 200°C (6). For room temperature deposition the films were polycrystalline. By modulated beam mass spectroscopy they showed that the fluoride films grow by simple nondissociative molecular sublimation and condensation (6, 7). They found film resistivities in the range of 10^{12}-10^{13} Ω/cm at room temperature. Then, Ishiwara and Asano grew epitaxial CaF_2 on Si(001) and (111) surfaces and Si/CaF_2/Si(111) at a substrate temperature of ~600°C by vacuum evaporation (8). Concurrent with the present work, Phillips *et al.* deposited epitaxial BaF_2 on Ge(111) and InP(001) also by vacuum evaporation (9). The last two groups confirmed the stoichiometry of the films by Rutherford backscattering. More recently, Sullivan *et al.* reported results on BaF_2, CaF_2, and $Ba_xCa_{1-x}F_2$ grown on InP(001) (10).

In this paper we report on the epitaxial growth of the group II cubic fluoride films, *i.e.*, CaF_2, SrF_2, BaF_2, and $Ba_xSr_{1-x}F_2$, on InP(001) by MBE. All except BaF_2 are single crystalline without twinning. We characterize the films by reflection high energy electron diffraction (RHEED), transmission electron microscopy (TEM), x-ray texture pattern, ellipsometry, and Nomarski interference-contrast microscopy.

[1] Summer employee from Cornell University, Ithaca, New York.

Key words: dielectrics, RHEED, TEM, sublimation.

Experimental Setup

The MBE system.—The MBE system, shown in Fig. 1, consists of a loadlock and an 18 in. diam Varian RHEED chamber. The loadlock has a magnetically coupled transfer rod and is pumped by an 8 liters/sec ion pump. The main chamber is pumped by a 500 liter/sec ion pump, and the wall of the chamber can be cooled by chilled water. Two Knudsen cells, surrounded by a liquid-nitrogen (LN_2) shroud, contain pieces of single-crystalline fluorides, and the third cell, also surrounded by an LN_2 shroud, contains undoped polycrystalline InP for the phosphorus source. The base pressure of the chamber could be in the mid 10^{-11} Torr (10^{-9} Pa) range, but normally between runs the base pressure was in the low 10^{-10} Torr (10^{-8} Pa) range. During film growth the pressure was ~ 2-5 × 10^{-9} Torr (~3-7 × 10^{-7} Pa). The MBE chamber contains a cylindrical mirror analyzer (CMA) with an integral electron gun for Auger analysis, a residual gas analyzer (RGA) for monitoring background gas composition and phosphorus overpressure during substrate cleaning, a 5 keV RHEED gun, a phosphorus screen, and a thin-film quartz monitor for thickness monitoring. The film thickness and refractive index were measured with an ellipsometer.

Substrate cleaning.—S-doped (10^{18} cm^{-3}) n-type InP(001) substrates were used. Many authors have shown that the surface prior to epitaxial growth is a critical factor in the quality of the grown film (11). Therefore, we shall describe our cleaning procedure in detail. The substrate was polished in Br-methanol. The final polish was done with 1% Br-methanol, rinsed with methanol, and spun dry. The quality of the polish was checked by the amount of scattering of a laser beam from the substrate. With proper polishing the Auger signals for C and O could be small [Fig. 2(a)], but the RHEED pattern was diffuse, indicating an amorphous oxide film on the surface. To produce an atomically clean surface on InP, Farrow *et al.* cleaned their surface by low energy (500 eV) Ar ion bombardment and annealing at 250°C to produce a (1 × 1) RHEED pattern (6). As in the case of GaAs (001), the (1 × 1) pattern can mean an In-rich surface (14) or the presence of carbon on the surface (11). From our own experience with ion bombardment (12) and annealing (13) of InP(001), the resulting surface, although clean, is never stoichiometric. The

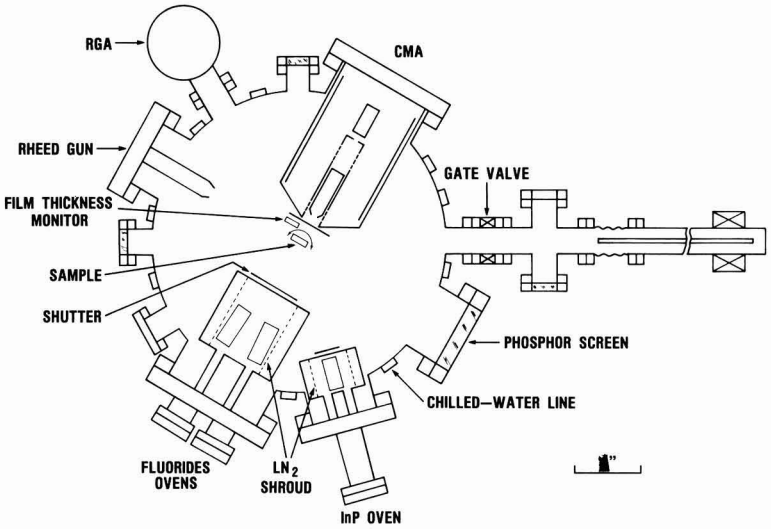

Fig. 1. A schematic diagram of the MBE system. After the initial study of cleaning procedures the CMA was removed from the chamber.

ratio of P/In as determined by x-ray photoelectron spectroscopy is about 0.9 after prolonged annealing at 300°C (13).

Our approach to cleaning the substrate is similar to that of Cheng *et al.*, who, before depositing an $In_xGa_{1-x}As$ film on InP, cleaned the InP substrate by heating it under As overpressure (15). We heated the substrate to $\lesssim$ 500°C under a P_2 beam (16) exposure from a Knudsen cell containing polycrystalline InP pieces. The total pressure as read by an ion gauge was $\gtrsim 3 \times 10^{-6}$ Torr (4×10^{-4} Pa) during exposure. The gas composition was monitored by RGA, which showed almost all phosphorus. In the beginning of the experiment the surface was monitored by Auger electron spectroscopy (AES) and electron energy-loss spectroscopy (ELS). The AES spectrum in Fig. 2(b), which is identical to that of vacuum-cleaved InP(110), shows that the surface was atomically clean and stoichiometric after being heated in phosphorus overpressure. To check further the presence of metallic In, which cannot be revealed by AES easily (12), an ELS spectrum was taken (Fig. 3). The ELS spectrum shows only the bulk and surface plasmon of InP, but not of In. Because the surface is stabilized by the phosphorus beam, the [110] and [$\bar{1}$10] azimuth show ½- and ¼-order diffraction streaks from surface reconstruction (15) as shown in Fig. 4(a) and Fig. 8(a).

Results and Discussion

Low growth temperature (~250°C).—Once the surface was cleaned, the substrate temperature was lowered to ~250°C. Figure 4 shows RHEED patterns for different stages of BaF_2 film growth. Figure 4(a) shows the ½-order surface reconstruction along the [110] azimuth. Figure 4(b) shows the BaF_2 film at 15Å. The RHEED pattern shows some streaks but mostly spots. The streaks indicate that the growth mechanism may be two-dimensional layer growth as suggested by Farrow *et al.* (6), but the electron beam charged and roughened the surface to produce a spot pattern. The area where the electron beam impinged on the sample is clearly visible. Figure 4(c) shows single-crystal-like sharp spot patterns of a film of 950Å. The (1 × 1) pattern along the [110] azimuth indicates the parallel epitaxial relationship, $BaF_2(001)||$

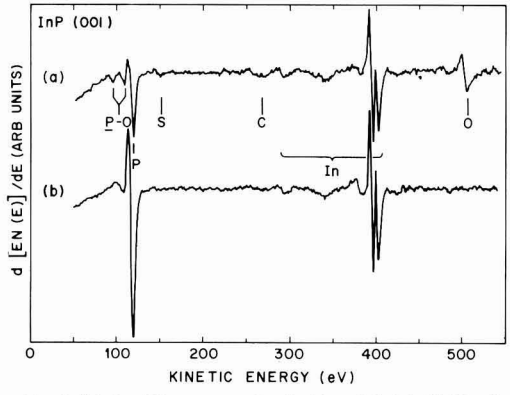

Fig. 2. (a) An AES spectrum of a freshly polished InP(001) substrate. (b) An AES spectrum of the substrate after being heated in phosphorus overpressure. The spectrum is identical to that obtained on a vacuum-cleaved InP(110) surface. The incident 3 keV electrons were normal to the surface. The peak-to-peak modulation voltage was 1.6V.

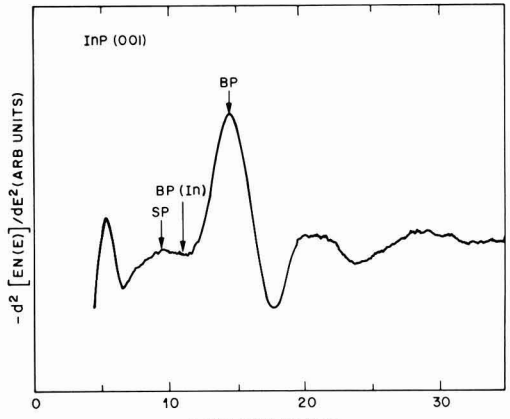

Fig. 3. An ELS spectrum of a clean InP(001) substrate. BP and SP denote bulk plasmon and surface plasmon of InP, respectively. BP(In) denotes the bulk plasmon of In. The incident 500 eV electrons were normal to the surface. The peak-to-peak modulation voltage was 1.6V.

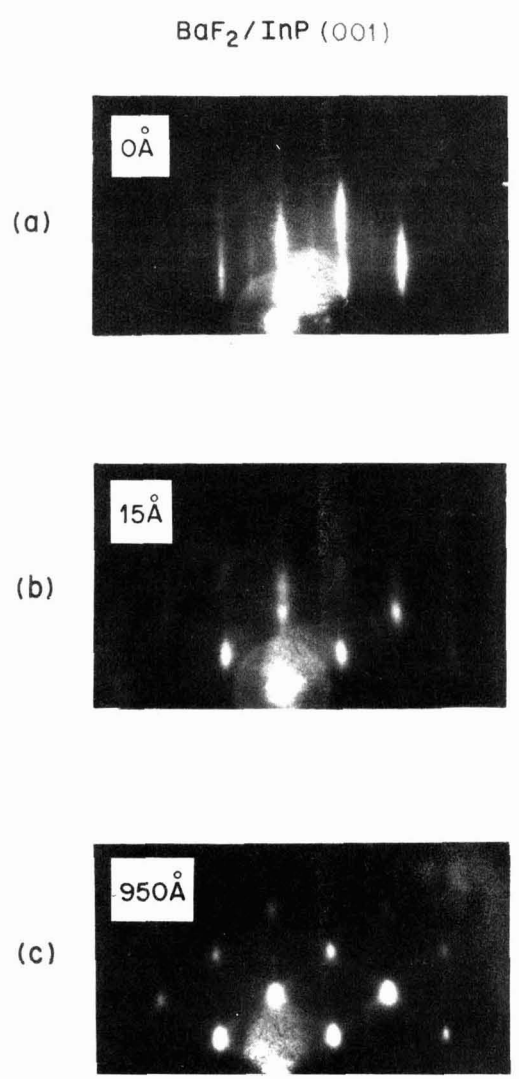

Fig. 4. RHEED patterns (5 keV) of epitaxial growth of BaF_2 on InP(001) at substrate temperature of ~250°C. (a) The initial clean surface showing the [110] azimuth-1/2 order surface reconstruction. (b) After growth of 15Å. (c) After growth of 950Å.

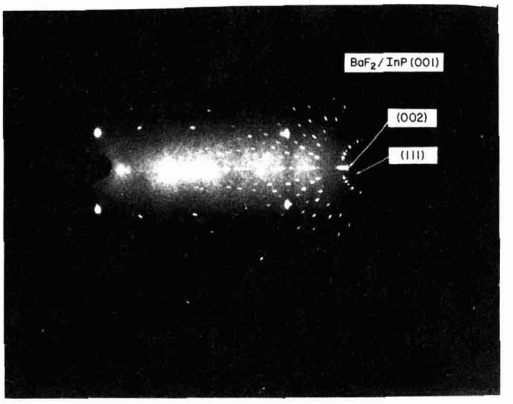

Fig. 5. An x-ray texture pattern of BaF_2 film on InP(001). Most of the spots are from the substrate. The (111) polycrystalline ring and the (002) spot from the film are indicated.

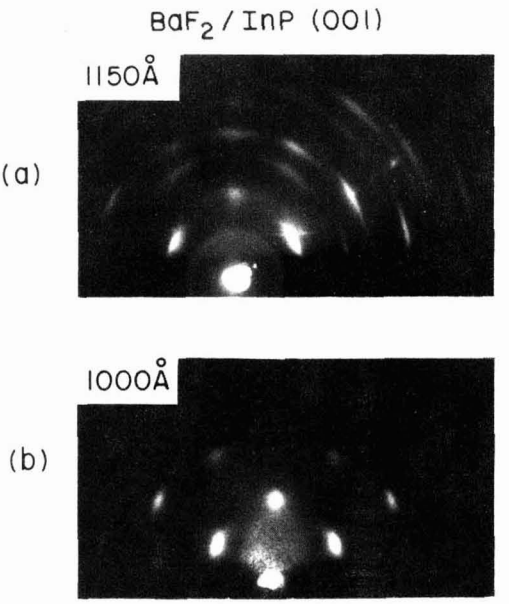

Fig. 6. RHEED patterns (5 keV) of BaF_2 films on InP(001) at (a) high growth rate (8600 Å/hr) and (b) lower than optimal growth rate (535 Å/hr).

InP(001), and BaF_2[110]||InP[110] (16). The diffraction lines connecting the spots suggest microfaceting on the {111} planes as a result of electron bombardment. Although there are no polycrystalline rings in the RHEED pattern, the film is actually a highly oriented polycrystalline film because the x-ray texture pattern (Fig. 5), taken with a Read camera (18), shows a (111) polycrystalline ring. Most of the spots are from the substrate. The strongest spot from the film is (002), confirming the parallel epitaxial relationship.

The quality of epitaxy is found to depend on the growth rate. There seems to be an optimum range in growth rate for a sharp spot pattern. Figure 6 shows the BaF_2 RHEED patterns for (a) high growth rate (8600 Å/hr) and (b) low growth rate (535 Å/hr). For the case of high growth rate the film is clearly polycrystalline with preferred (001) orientation. For the case of low growth rate the film shows a spot pattern, but the spots have a slight curvature, indicating imperfect epitaxy. The optimal growth rate of BaF_2 is ~1000 Å/hr.

Figure 7 shows RHEED patterns of SrF_2 and CaF_2 films on InP (001). Figure 7(a) shows 430Å of SrF_2 at an optimal growth rate of 430 Å/hr. Figure 7(b) shows 535Å of CaF_2 at an optimal growth rate of ~230 Å/hr. Higher growth rate results in similar patterns to Fig. 6(a).

TEM micrographs and associated transmission electron diffraction (TED) patterns show that the BaF_2 and the SrF_2 films consist of many small (~1500Å), highly oriented crystallites. However, the CaF_2 film is single crystalline as indicated by the absence of any grain boundaries. TEM results are discussed in the next section.

Nomarski interference-contrast microscopy of the films shows that they are transparent and have no visible defects, except where the electron beam impinged.

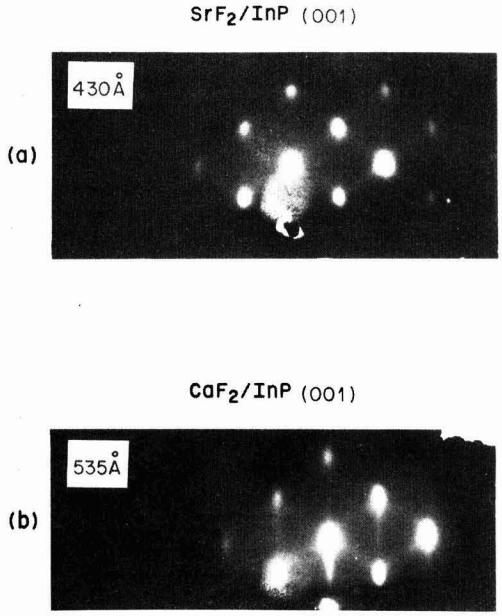

Fig. 7. RHEED pattern (5 keV) of epitaxial SrF_2 and CaF_2 on InP(001) at substrate temperature of ~250°C. (a) After growth of 430Å SrF_2 film. (b) After growth of 535Å CaF_2 film.

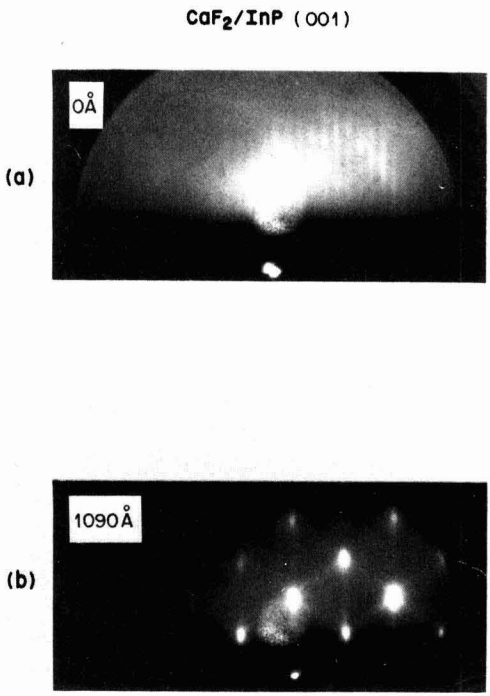

Fig. 8. RHEED pattern (5 keV) of epitaxial CaF_2 on InP(001) at substrate temperature of ~350°C. The initial surface shows the $[1\bar{1}0]$ azimuth-1/4 order surface reconstruction. (b) After growth of 1090Å.

High growth temperature (~350°C).—When the substrate temperature was raised to ~350°C, close to the congruent evaporation point of InP, ~365°C, (19), the growth rate could be much higher to achieve sharp spot patterns in RHEED. Figure 8 shows a CaF_2 film grown at 600 Å/hr. Figure 8(a) shows the ¼-order surface reconstruction along the $[1\bar{1}0]$ direction. Figure 8(b) shows the RHEED pattern of the film with no polycrystalline rings. The BaF_2 and SrF_2 films also showed good spot RHEED patterns.

TEM analysis shows that BaF_2 films grown at higher substrate temperature are still polycrystalline and are oriented strongly along the [001] direction. However, SrF_2 films improve in quality as shown in Fig. 9. Although the TED pattern in Fig. 9(a) shows polycrystalline rings along with the spot pattern, the films are single crystalline with the inclusion of ~2000Å wide grains, as shown by the bright-field and dark-field TEM micrographs [Fig. 9(b) and (c), respectively]. Figure 10(a) shows the TED pattern of a CaF_2 film. No polycrystalline rings are present. The film appears to be single crystalline with no defects as shown in Fig. 10(b). Figure 10(b) also shows that the film broke off along <110> directions during thinning for TEM analysis.

With Nomarski interference-contrast microscopy we find that 1000Å thick CaF_2 films, but neither BaF_2 nor SrF_2 films, show crazing along the <110> directions, which was also observed by Sullivan *et al.* (10). They attributed crazing to increased lattice mismatch at room temperature compared to the growth temperature. However, thicker BaF_2 and SrF_2 films (~4000Å) also exhibit crazing as shown in Fig. 11. Since the orientation of the film is (001), the <110> directions are consistent with crazing occurring on the {111} cleavage planes of the cubic fluorides. The cause of crazing is most likely a combination of strains from large lattice mismatch ($\Delta a/a$) and from a large difference in the thermal expansion coefficients ($\Delta\alpha$). The thermal expansion coefficients of the fluorides are larger than that of InP (~20×10^{-6} *vs.* 6×10^{-6} K^{-1}). As $\Delta a/a$ becomes smaller, $\Delta\alpha$ becomes more important and crazing starts to appear at thicker film thickness. For the same film thickness, SrF_2 ($\Delta a/a = -1.2\%$) exhibits the least crazing among the three fluorides. When a mixture of fluorides ($Ba_xSr_{1-x}F_2$) was grown to achieve lattice matching to the substrate, the crazing did not appear for ~4000Å thick films, but appeared for $\gtrsim 1\mu$ thick films.

Lattice matching to InP(001).—A mixture of the fluorides, $Ba_xSr_{1-x}F_2$, was grown on InP(001) at ~350°C by adjusting the temperature of the two ovens containing BaF_2 and SrF_2. Films lattice matched to the substrate could be obtained. The lattice parameter was measured by double-crystal x-ray diffractometry. The films are also single crystalline without twinning. The TEM micrographs are similar to those of Fig. 10, but show fewer inclusions. As mentioned earlier the ~4000Å film lattice matched to the substrate shows no crazing under Nomarski interference-contrast microscope. Further studies of the lattice matched single-crystalline dielectric films are reported elsewhere (20).

Summary

We have grown epitaxial dielectric films of the group-II cubic fluorides, CaF_2, SrF_2, BaF_2, and $Ba_xSr_{1-x}F_2$, on InP(001) at relatively low substrate temperatures (~250° and ~350°C). As expected, the higher the growth temperature is, the better the epitaxy. At ~250°C, the CaF_2 film is single crystalline as shown by the absence of grains in the TEM micrograph. However, the SrF_2 and BaF_2 films consist of many highly oriented crystallites even though they show good spot RHEED patterns. At ~350°C, CaF_2, SrF_2, and $Ba_xSr_{1-x}F_2$ films are single crystalline, but BaF_2 films are not. These results show that the amount of misfit is not an important factor for epitaxy, similar to other film-substrate systems (19). The substrate

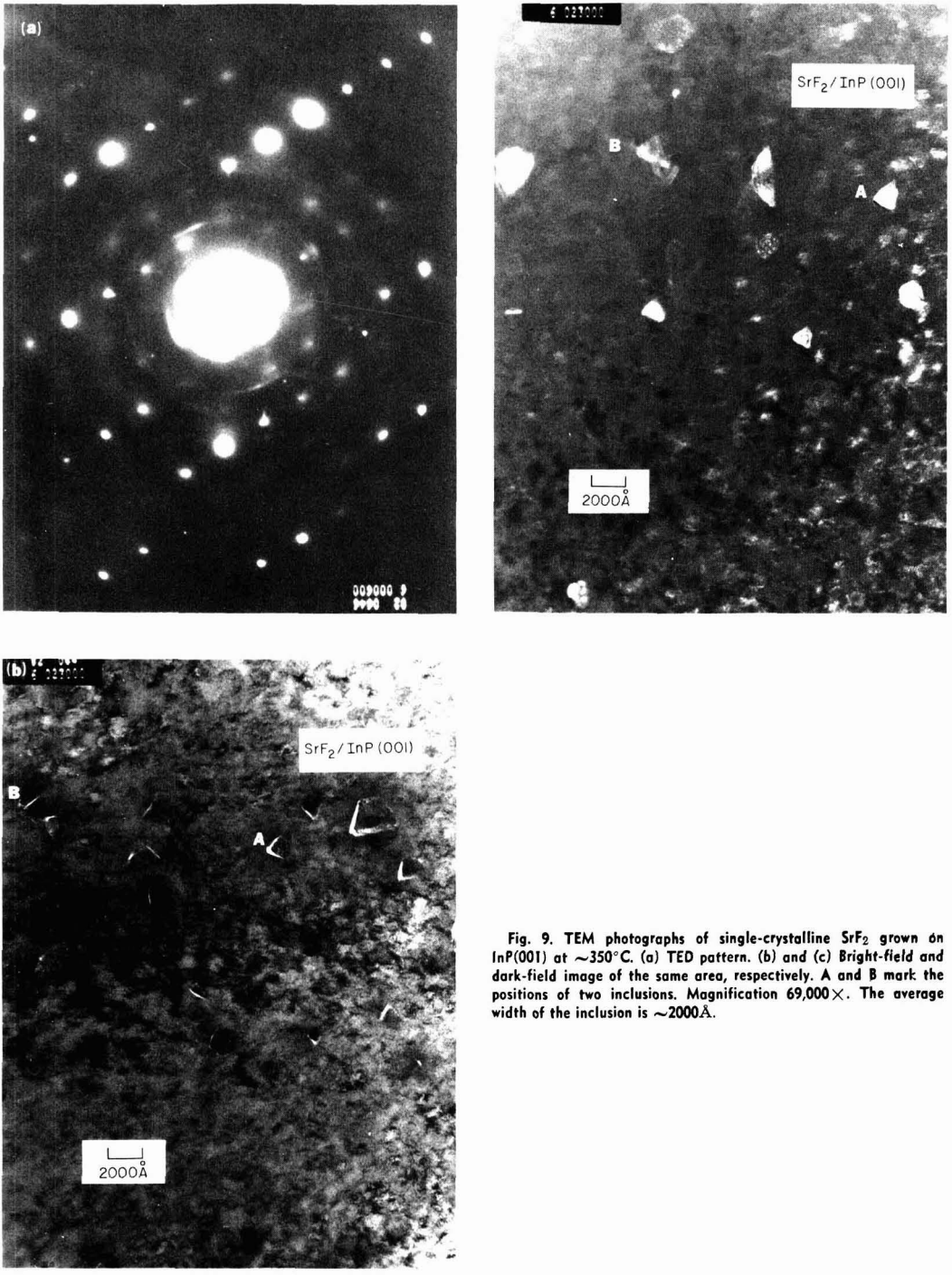

Fig. 9. TEM photographs of single-crystalline SrF_2 grown on InP(001) at ~350°C. (a) TED pattern. (b) and (c) Bright-field and dark-field image of the same area, respectively. A and B mark the positions of two inclusions. Magnification 69,000×. The average width of the inclusion is ~2000Å.

temperature and the growth rate are the crucial parameters (20) to achieve single crystallinity.

Acknowledgment

We wish to thank R. B. Marcus for his encouragement and support; T. Y. Chang, A. Y. Cho, J. C. M. Hwang, R. A. Stall, and W.-T. Tsang for helpful discussions on various aspects of MBE; S. N. G. Chu and C. M. Jodlauk for doing energy-dispersive x-ray analysis on some samples; A. T. Macrander for the measurement of lattice parameters; K. E. Strege and D. L. Mitcham for providing invaluable hints on substrate polishing; H. J. Guggenheim and G. J. Zydzik for providing the fluoride crystals; and R. H. Burton and C. L. Hollien for the use of their ellipsometer.

Manuscript submitted March 11, 1983; revised manuscript received June 6, 1983. This was Paper 337 pre-

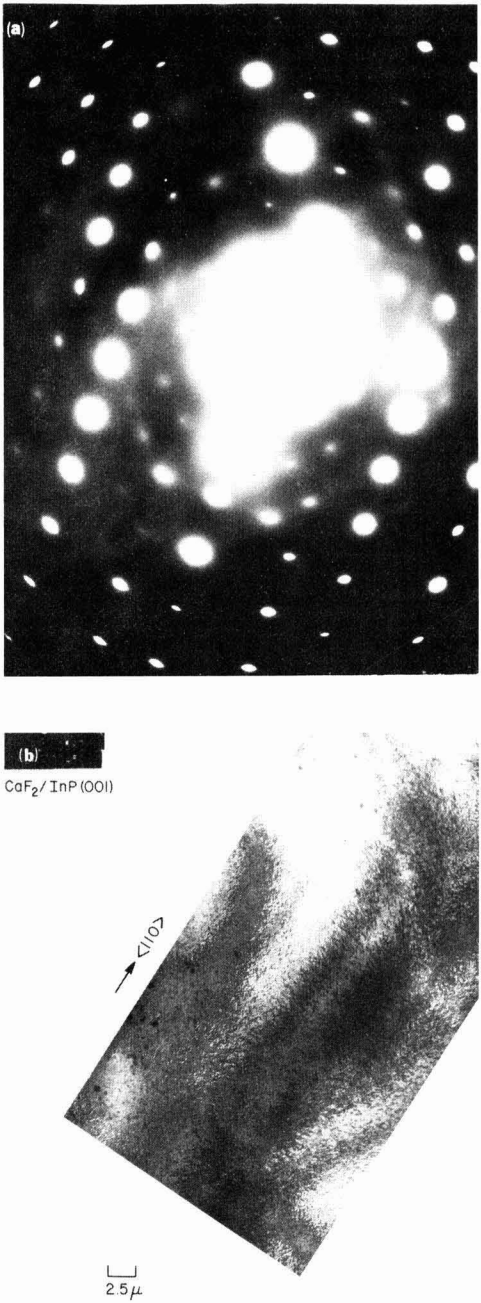

Fig. 10. TEM photographs of single-crystalline CaF_2 grown on InP(001) at ~350°C. (a) TED pattern. (b) Bright-field image. Magnification 4350×. Note the absence of any grains.

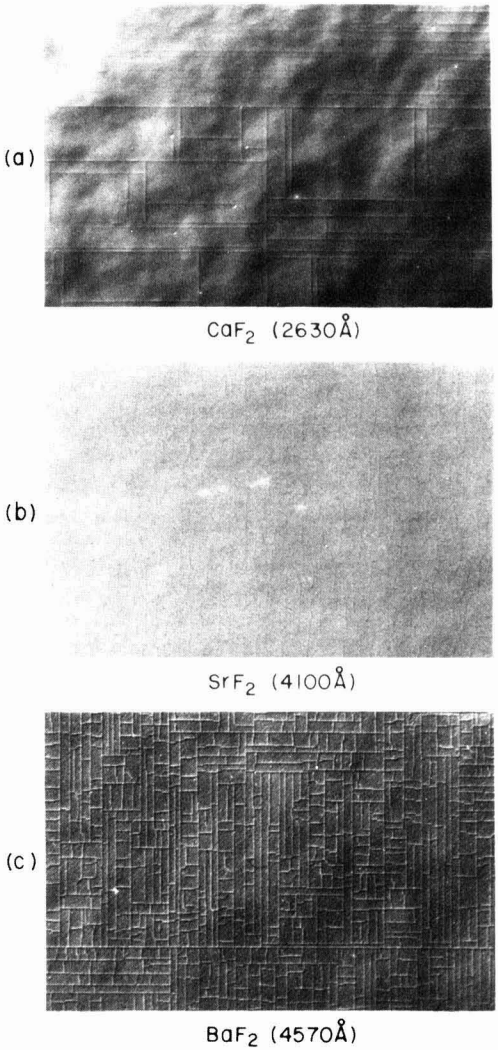

Fig. 11. A Nomarski interference-contrast micrograph of (a) 2650Å CaF_2, (b) 4100Å SrF_2, and (c) 4500Å BaF_2. The crazing is along <110> directions. Magnification 400×.

sented at the San Francisco, CA, Meeting of the Society, May 8-13, 1983.

Bell Laboratories assisted in meeting the publication costs of this article.

REFERENCES

1. J. Singh and A. Madhukar, *J. Vac. Sci. Technol.*, **19,** 437 (1981).
2. T. R. Harrison, P. M. Mankiewich, and A. H. Dayem, *Appl. Phys. Lett.*, **41,** 1102 (1982).
3. A. Y. Cho, *J. Appl. Phys.*, **41,** 782 (1970).
4. C. W. Tu, S. R. Forrest, and W. D. Johnston, Jr., *Appl. Phys. Lett.*, **43,** 569 (1983).
5. W. Hayes, in "Crystals with the Fluorite Structure," W. Hayes, Editor, Oxford University Press, Oxford (1974).
6. R. F. C. Farrow, P. W. Sullivan, G. M. Williams, G. R. Jones, and D. C. Cameron, *J. Vac. Sci. Technol.*, **19,** 415 (1981).
7. P. W. Sullivan, T. I. Cox, R. F. C. Farrow, G. R. Jones, D. B. Gasson, and C. S. Smith, *ibid.*, **20,** 731 (1982).
8. H. Ishiwara and T. Asano, *Appl. Phys. Lett.*, **40,** 66 (1982).
9. J. M. Phillips, L. C. Feldman, J. M. Gibson, and M. L. McDonald, *J. Vac. Sci. Technol.*, **81,** 246 (1983).
10. P. W. Sullivan, R. F. C. Farrow, and G. R. Jones, *J. Cryst. Growth*, **60,** 403 (1982).
11. *E.g.*, C.-A. Chang, *J. Vac. Sci. Technol.*, **21,** 663 (1982).
12. C. W. Tu and A. R. Schlier, *Appl. Surf. Sci.*, **11/12,** 335 (1982).
13. C. W. Tu, Unpublished.
14. A. Y. Cho, *J. Appl. Phys.*, **47,** 2841 (1976).

15. K. Y. Cheng, A. Y. Cho, W, R. Wagner, and W. A. Bonner, *ibid.*, **52**, 1015 (1981).
16. R. F. C. Farrow, *J. Phys. D*, **7**, 2436 (1976).
17. K. W. Andrews, D. J. Dyson, and S. R. Keown, "Interpretation of Electron Diffraction Patterns," p. 152, Plenum Press, New York (1971).
18. M. H. Read, 27th Annual Pittsburgh Diffraction Conference, Pittsburgh, PA, November 1964.
19. R. F. C. Farrow, *J. Phys. D*, **7**, L121 (1974).
20. C. W. Tu, T. T. Sheng, A. T. Macrander, J. M. Phillips, and H. J. Guggenheim, *J. Vac. Sci. Technol.*, To be published.
21. A. K. Green, J. Dancy, and E. Bauer, *J. Vac. Sci. Technol.*, **7**, 159 (1970).
22. J. H. Kahn, in "Handbook of Thin Film Technology," L. I. Maissel and R. Glang, Editors, McGraw-Hill, New York (1970).

Cerium-Activated Halophosphate Phosphors

I. Strontium Fluoroapatites

R. G. Pappalardo,* J. Walsh, and R. B. Hunt, Jr.

GTE Laboratories Incorporated, Precision Materials Technology Center, Waltham, Massachusetts 02254

ABSTRACT

In the search for alternative yellow emitting phosphors for the current commercial high brightness phosphor blends of the Lite-White type, the authors have prepared and characterized by a variety of techniques an Sr-analog of calcium fluoroapatite:Sb;Mn, with Ce replacing Sb as the sensitizer of the Mn emission. Materials with the desired emission characteristics are obtained from starting formulations containing a strong fluoride excess over the standard formulations for alkali-earth apatites. Phosphors have been obtained with emission parameters closely approaching those of Yellow Halo (YH), and only 10% lower in brightness. Lamp tests on these phosphors revealed that the efficiency of the Ce-Mn coactivated materials, as presently formulated, degrades as a result of the lamp-making process. Preliminary observations related to the mechanism of phosphor degradation are reported. Possible commercial application in lamps of the wide class of Ce-activated apatites crucially depends on identifying, and later eliminating, the degradation of phosphor efficiency during lamp fabrication.

The recent development of Lite-White blends for low pressure fluorescent lamps has signaled a marked departure from established tenets of the lighting industry. The low pressure fluorescent lamp was originally conceived as a desirable replacement for incandescent lamps, and until recently its phosphors were generally engineered so as to mimic as closely as possible the spectral-energy distribution from black-body radiators and from the sun.

In the early 1970's, Philips (1, 2) pioneered with the tricolor lamp, a novel scheme for the generation of white fields in fluorescent lamps, by the use of a combination of phosphors emitting in the spectral range of miximum sensitivity of the human eye receptors. The new lamps, incorporating both the new phosphor blends and modifications in the discharge parameters, aim at providing greater efficacies [up to 90-100 lumens per watt (lpw)] and also high color rendering. The drawback in this approach is the high cost of the rare earth phosphors required.

In 1977, GE introduced a scheme aimed at increasing the efficacy (lpw) in low pressure fluorescent lamps, at some loss in color rendering (3). The approach, embodied in the Watt-Miser II lamps and then in the Lite-White lamps, hinges on producing a high efficacy white field by a combination of narrow-band emitters in the blue, at 448 nm, and in the yellow, at 575 nm (4).

Both in the Philips and in the GE scheme, the fluorescent lamp is no longer constrained to replicate the spectral-emission distribution from incandescent sources, but its unique potentialities are now freely exercised. In terms of phosphor development this means a new set of performance objectives expected of phosphors. Materials that in the past were not competitive with the standard Sb-Mn coactivated fluoro-chloroapatites, may become superior in performance under the new set of specifications. Therefore, a renewed careful study of the spectral properties of phosphors is now required to identify those systems that can realize most efficiently the scheme of u.v.-to-visible conversion embodied in the Lite-White approach. The present report addresses the first stage of such a search, namely, the possible replacement of the yellow emitting component of the Lite-White blend.

Yellow Emitting Component for the Lite-White Blend

The requirements for a yellow emitting phosphor for the Lite-White-type blend (3, 4) are as follows: (*i*) emission peak at $\simeq$575 nm; (*ii*) narrow emission band; and (*iii*) high ($\simeq$70%) quantum efficiency. These requirements are presently well satisfied by the so-called Yellow Halo (YH) phosphor of approximate composition $Ca_5(PO_4)_3F$:Sb;Mn As for materials capable of satisfying the three aforementioned requirements, it should be pointed out that among nonlanthanide emitters, only Mn tends to exhibit relatively narrow emission bands. Also, given the nature of the Mn emitting level, as defined by a Tanabe-Sugano diagram (5), in order to have emission in the yellow, it is necessary to incorporate Mn in a site of high crystal field and relatively low distortion from cubic symmetry. In addition, Mn has to be coordinated to ionic ligands that do not promote the delocalization of the 3d-electronic cloud of Mn^{2+}.

In practice, this translates into the requirement for a fluoride matrix or a fluoride containing matrix that is also compatible with operation inside a lamp: a fluoroapatite matrix is still the best candidate to meet the aforementioned requisites. At present, the avenues open for alternatives to YH are therefore restricted to: (*a*) modifications of the basic fluoroapatite matrix; and (*b*) replacement of Sb^{3+} with a different sensitizer. Along this general direction, the authors discuss in what follows the results of the synthesis and characterization of Ce-Mn-coactivated fluoroapatite (FAP) phosphors, and specifically of SrFAP: Ce;Mn.

Synthesis of Strontium Fluoroapatites

Early attempts to prepare Sr apatites coactivated with Ce and Mn, with halide content approaching

* Electrochemical Society Active Member.

that of $Sr_5(PO_4)_3(F,Cl)$, gave materials with low brightness and deep orange emission. Yellow emitting, bright phosphors were obtained when the halide content greatly exceeded one formula unit, as for instance using the following starting formulation

$$Sr_{4.30}Ce_{0.295}Mn_{0.147}(PO_4)_{3.0}F_{1.72} \quad [1]$$

In pioneer work by Henderson and Ranby (6, 7), the fluoride excess was even greater, the phosphor materials of optimum brightness being formulated, for the purpose of comparison with [1], as

$$Sr_{4.50}Ce_{0.196}Mn_{0.245}(PO_4)_{3.0}F_{5.1} \quad [2]$$

In our preparations, the reaction components were weighed and blended in a Spex Mixer-Mill Model 8000. The blend was then loaded in shallow alumina boats ($\simeq$2.5 × 1.5 × ⅝ in.) provided with loose quartz covers, and lots of four-to-six boats were introduced into the hot zone of a quartz tube inserted in a tubular furnace. The atmosphere in the reaction zone was purged of oxygen by a preliminary pump-down, and then continually swept at 10 liter/min flow of nitrogen gas, or nitrogen gas containing 5% hydrogen. After the firing treatment at the desired temperature, the quartz tube containing the boats was allowed to cool to $\simeq$450°C, still under constant gas flow. The quartz tube was then removed and the samples extracted. The materials from this first firing were then ground, sieved (generally through a 100 mesh screen), and then refired. The second firing was carried out in inert or mildly reducing atmosphere and increased the emission efficiency of the phosphors by a few percent.

An increase in Mn content over 0.15 formula units produced marked sintering after the first firing at temperatures ranging from 950° to 1050°C. The use of a nitrogen hydrogen mixture (5% hydrogen) as firing atmosphere reduced the tendency to sintering and eliminated the pale green body color frequently observed in the nitrogen-fired phosphors. The second firing was carried out in nitrogen atmosphere at temperatures ranging from 850° to 1025°C. In some cases, a third firing of the phosphor at 850°C in "wet" forming gas (95% nitrogen/5% hydrogen) was investigated, but it resulted in a slight discoloration of the phosphor powder and in a 7% brightness loss. This approach was therefore abandoned.

The highest brightness was observed in a material formulated as

$$Sr_{4.25}Ce_{0.295}Mn_{0.245}(PO_4)_{3.0}F_{1.92} \quad [3]$$

using the reagents and firing conditions listed in Table I.

A gradient in emission brightness was observed in the doubly fired material from this run, the measured peak intensity of Mn ranging from 86.1 to 89.8% of the corresponding quantity for our internal standard (YH, GTE Sylvania Type 4381, Lot PPP 9780).

Phosphor Characterization

Phase identification.—The x-ray diffraction patterns of the powders were measured by means of a Philips vertical diffractometer, using copper radiation of 1.5405A. The source was run at 35 kV and 16 mA. The diffraction patterns were measured at a scan rate of 1°/min, using a solid-state scintillator counter and a graphite monochromator. X-ray diffraction measurements on the materials obtained from a variety of runs showed a dominant phase with hexagonal apatite lattice, isostructural with, and somewhat expanded relatively to, $Sr_2Pr_8(SiO_4)_6O_2$, the latter (8, 9) with lattice parameters: a = 9.612Å and c = 7.143Å.

A comparison of the diffraction data pertinent to $Sr_2Pr_8(SiO_4)_6O_2$ and the SrFAP:Ce;Mn material formulated according to [3] is given in Table II. Inspection of the table reveals the close agreement in the relative intensity of the diffraction lines for the two systems and the slight expansion ($\simeq$1%) of the SrFAP:Ce;Mn lattice. Four additional weak lines (with intensity of 1-2%) in the diffraction pattern suggested the presence of a minor phase ($\simeq$1%) of $CePO_4$.

Similar measurements were also performed on singly activated (Ce) and triply activated (Ce;Mn:Dy) materials briefly discussed in the text and prepared according to the data of Tables III and IV. Again the predominant phase was a hexagonal apatite, with a possible minor phase of $CePO_4$, estimated from the diffraction data as amounting to $\simeq$2% for

Table I. Reagents and phosphor formulation for optimum brightness

Starting formulation: $Sr_{4.25}Ce_{0.295}Mn_{0.245}(PO_4)_{3.0}F_{1.92}$; fired 1 hr at 950°C in 95% nitrogen/5% hydrogen; refired 1 hr in nitrogen at 1025°C

Reagents	Grams	Mol units
$SrHPO_4$ (GTE Sylvania)	8.4	3.0
$SrCO_3$ (GTE Sylvania)	1.65	0.733
$MnCO_3$ (GTE Sylvania)	0.43	0.245
CeF_3 (K&K Labs)	0.887	0.295
SrF_2 (Varacloid Chemical Company)	0.99	0.516

Table II. X-ray diffraction data for $Sr_2Pr_8(SiO_4)_6O_2$

[ASTM Ref 29-1310] (columns labeled R); and for Sr fluoroapatite:Ce;Mn (columns labeled S)

d, A		I(0)/I(1)		hkl
R	S	R	S	R
4.81		3		110
4.17	4.181	16	9.8	200
3.99		14		111
3.58	3.602	10	18.7	002
3.28	3.308	25	19.5	102
3.15	3.161	20	29.7	210
2.873	2.893	100	100	211, 112
2.774	2.788	20	29.9	300
2.711	2.729	3	4.6	202
2.310	2.320	5	7.1	310
2.278	2.206	3	4.9	221
2.191	2.150	4	6.5	302
2.135		10		113
2.081	2.091	4	2.4	400
2.067		2		203
1.994	2.007	18	18.9	222
1.939	1.950	10	13.2	312
1.910		5		320
1.900	1.913	25	22.1	213
1.845	1.855	12	6.4	321
1.817	1.825	16	16.2	410
1.798	1.808	18	11.4	402
1.786		8		004
1.641		3		204
1.573		3		420
1.553	1.567	5	6.7	214
1.509	1.516	6	7.0	502
1.502	1.500	5	4.7	304
1.490		5		323
1.462	1.471	6	7.2	332
1.369		1		115
1.355		2		404
1.304	1.313	2	3.6	324
1.301		5		215
1.273	1.283	8	5.1	414
1.270		3		305
1.249	1.257	8	6.3	522
	1.189		3.5	
	1.136		3.5	

Table III. Reagents and starting formulation for singly activated SrFAP

Starting formulation $Sr_{1.30}Ce_{0.295}Mg_{0.146}(PO_4)_{3.0}F_{1.72}$; fired in 10 liter/min nitrogen at 1000°C for 1 hr; refired 1 hr in the same atmosphere at 900°C

Reagents	Grams	Mol units
$SrHPO_4$ (GTE Sylvania)	5.6	3.0
$SrCO_3$ (GTE Sylvania)	1.32	0.879
$MgCO_3$	0.126	0.146
CeF_3 (K&K Labs)	0.59	0.295
SrF_2 (Varacloid Chemical Company)	0.533	0.417

Table IV. Reagents and starting formulation for triply activated SrFAP

Starting formulation $Sr_{4.25}Ce_{0.295}Dy_{0.04}Mn_{0.140}(PO_4)_{3.0}F_{1.76}$; fired in 10 liter/min nitrogen at 1000°C for 1 hr; refired 1 hr in the same atmosphere at 900°C

Reagents	Grams	Mol units
$SrHPO_4$ (GTE Sylvania)	5.6	3.0
$SrCO_3$ (GTE Sylvania)	1.32	0.879
$MnCO_3$	0.172	0.146
CeF_3 (K&K Labs)	0.59	0.295
DyF_3	0.09	0.04
SrF_2 (Varacloid Chemical Company)	0.44	0.344

the triply activated material and ≃1% for the two remaining materials.

Infrared properties.—The infrared absorbance spectra of the phosphor powders (2% by weight in KBr disks) were measured with a Nicolet Fourier-Transform Infrared Spectrometer MX1, Model 3600E, and were displayed on a Zeta digital plotter.

The infrared absorbance spectrum for samples of formulation [3] is given in Fig. 1, in the spectral region (420-2400 cm^{-1}) of main interest for the detection of nonapatitic orthophosphate and pyrophosphate phases. The spectrum of SrFAP:Ce;Mn is contrasted to the corresponding spectrum of the Ca-FAP:Sb;Mn material (YH) used as internal standard and known to be a bona fide apatite, containing approximately 1.4% of Ca-pyrophosphate (β-phase). The spectrum of SrFAP:Ce;Mn reproduces faithfully the main features of the spectrum of CaFAP:Sb;Mn and does not show the weak line at ≃690 cm^{-1}, commonly associated with pyrophosphate phases.

Chemical analysis.—Materials formulated as

$$Sr_{4.25}Ce_{0.295}Mn_{0.245}(PO_4)_{3.0}F_{1.92} \quad [3]$$

gave on analysis the results listed in Table V. From the chemical analysis (Table V) of the products obtained from the firing of samples of starting formulation [3], one can derive, on the assumption of three P atoms per molecule in the final product, the following phosphor composition

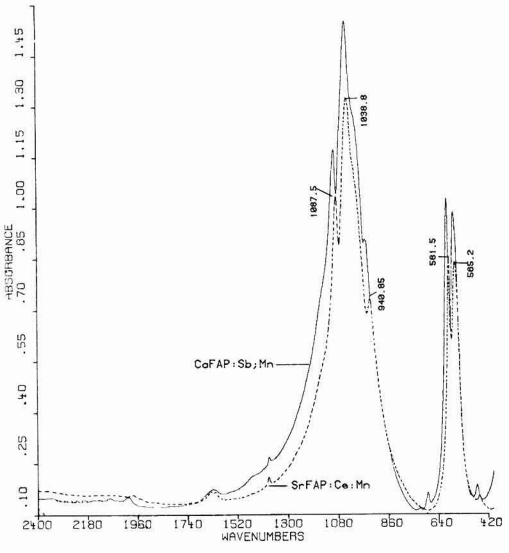

Fig. 1. Infrared absorbance of CaFAP:Sb;Mn (solid line) and of SrFAP:Ce;Mn (dashed line) in the spectral region of the main absorptions.

Table V. Results of chemical analyses on phosphors

Starting formulation: $Sr_{4.25}Ce_{0.295}Mn_{0.245}(PO_4)_{3.0}F_{1.92}$

Element	Weight percent found	Method	Error bar* (%)	Formula units†
Sr	49.5	Atom. absor.	±3	4.20
Ce	6.2	Neutron act.	±5	0.33
Mn	1.94	Atom. absor.	±5	0.26
P	12.5	Neutron act.	±3	3.0
F	2.88	Electrochem	±7	1.16

* For the quantities listed in Column 2.
† Assuming P = 3.

$$Sr_{4.20}Ce_{0.33}Mn_{0.26}(PO_x)_{3.0}F_{1.16} \quad [4]$$

namely, the fluoride content is markedly reduced in the final product, but still exceeds by ≃15% the fluoride content for a stoichiometry alkaline-earth halophosphate. Similar analytical results on the fluoride content were reported by Henderson and Ranby (6).

The total formal charge of the cations is derived from [4] as being 9.91 (assuming that all of the Ce is present as the trivalent species). The total anion charge adds up to 10.16, if one assumes that $x = 4$ in Eq. [4]. Until the chemical analyses can provide a reliable determination of both the relative content in the Ce^{3+} and Ce^{4+} species, and of the oxygen content, further discussion of the finer details of the phosphor composition and related charge compensation is of necessity in the nature of speculation.

Optical Spectroscopy of the FAP Phosphors

Experimental setup.—Spectroscopic measurements were performed both under steady-state excitation (and detection) of the phosphors and under conditions of pulse excitation of the materials. For the steady-state measurements, a modified commercial spectrophotometer, Perkin-Elmer fluorescence spectrophotometer Model MPF 44-A was utilized. The measurements on the decay kinetics of the phosphors were carried out using a nitrogen-laser-pumped dye laser Model DL12 from Molectron, and time-resolved sampling techniques in detection. The dye laser emission could be frequency-doubled, so as to have available excitation pulses of 10 nsec duration in the short u.v., at 254 nm.

Both the measurements with the spectrophotometer and with the dye laser were transferred in real time to the central computer of the GTE Labs by means of IBM Device Couplers, Model 7406. Digital pulses from TTL signal generators and pulse conditioners provided suitable master clocking for the acquisition and transfer of the measured data. An extensive software development in APL language supported various phases of data acquisition and processing. The final results were plotted on a Tektronix 4662 digital plotter.

Emission spectra.—The response of the phosphor under excitation at 254 nm are the main concern at this stage. Figure 2 contrasts, under identical excitation and detection conditions, the emission spectrum of YH and of sample RL24 of starting formulation

$$Sr_{4.25}Ce_{0.295}Mn_{0.245}(PO_4)_{3.0}F_{1.92} \quad [3]$$

The emission from YH consists of a residual Sb^{3+} emission in the blue, with peak at ≃500 nm, and of the yellow emission from Mn^{2+}, with peak at ≃575 nm. The SrFAP:Ce;Mn emission in turn comprises a Ce^{3+} emission band in the long u.v., with peak at ≃345 nm, and the Mn^{2+} emission in the yellow. The peak intensity of the Ce emission is roughly 25% that of the Mn emission in the same material. In turn the peak intensity of the Mn emission in the SrFAP sample is ≃90% the corresponding peak intensity in

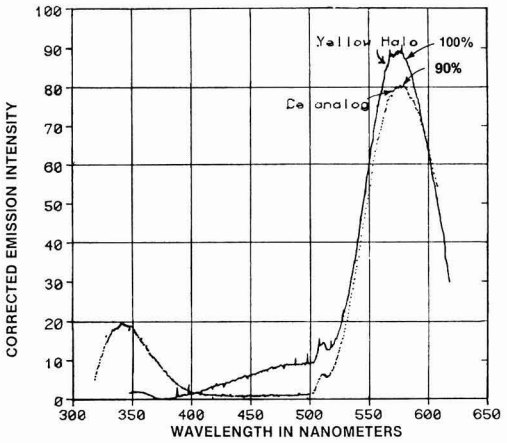

Fig. 2. Comparison of the corrected emission spectra of YH and SrFAP:Ce;Mn (sample RL24). Excitation at 254 nm. The narrow structure at 508 nm is due to scattered exciting radiation detected in second order.

YH. The emission spectra are truncated at ≃615 nm, the limiting wavelength of the corrected emission spectra directly obtainable from the MPF-44A fluorimeter.

Figure 3 shows a detailed view of the Mn emission in YH and in a somewhat less bright sample from the same SrFAP run. The emission peak is now ≃85% that of YH, and is slightly shifted to longer wavelengths, by comparison with YH. An opposite wavelength shift is found in samples with reduced Mn content, as for example in Fig. 4 for sample D7, with starting formation

$$Sr_{4.30}Ce_{0.295}Mn_{0.147}(PO_4)_{3.0}F_{1.72} \quad [5]$$

These shifts in the spectral location of the emission peak are associated with the Mn^{2+} concentration, the higher Mn content shifting the emission to longer wavelengths.

Excitation spectra.—The excitation spectra obtained on monitoring the emission at 575 nm are contrasted in Fig. 5 for the case of YH and SrFAP:Ce;Mn. In YH the absorption in the u.v. is provided by Sb^{3+} and rises rather rapidly from ≃300 nm toward shorter

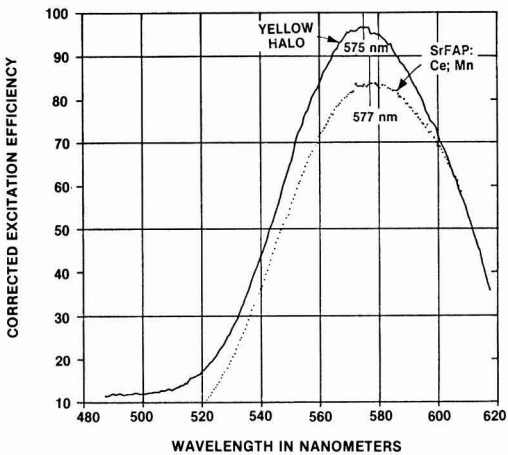

Fig. 3. Detail of the Mn emission in YH and SrFAP:Ce showing the respective peak location of the Mn emission. Excitation at 254 nm.

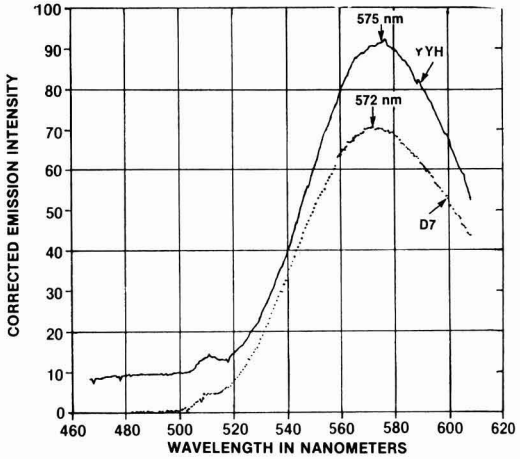

Fig. 4. Same as Fig. 3, but for an SrFAP:Ce;Mn sample with lower Mn content. The emission peak is shifted to shorter wavelengths when the Mn content is reduced.

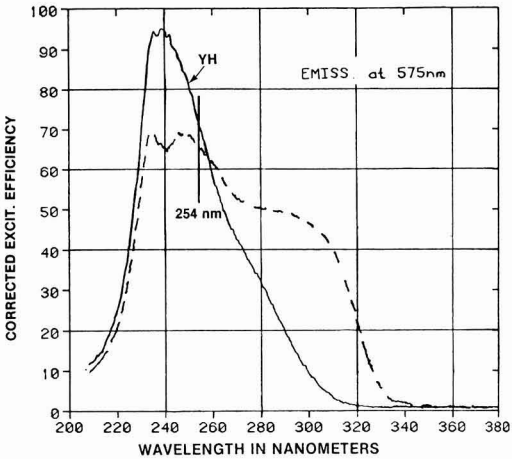

Fig. 5. Comparison of the corrected excitation efficiency (arbitrary, but same normalization) for emission monitored at 575 nm in YH and SrFAP:Ce;Mn. Note the broader excitation region for the latter.

wavelengths, peaking at 240 nm. By comparison with YH, the Ce-activated Sr fluoroapatite exhibits a broader, stronger excitation efficiency in the long u.v. and a less intense excitation efficiency at wavelengths shorter than 254 nm. The Ce^{3+} excitation peaks are located at ≃300, ≃248, and 234 nm. Excitation efficiency values at wavelengths shorter than ≃230 nm are not reliable, because of the drastic intensity drop in the exciting radiation.

Some interesting differences are noticeable in measuring the excitation spectra for Ce emission and for Mn emission in the same sample. This is exemplified in Fig. 6, again for a sample of starting formulation [3]. The excitation spectrum for Ce^{3+} emission shows a more structured level distribution and some maxima in the excitation spectra of Ce correspond to minima in the analogous excitation for Mn emission, as if the two processes were in part mutually exclusive. These differences in the two excitation spectra suggest that transfer from Ce to Mn occurs for Ce-Mn associates, the proximity of the Ce-Mn centers being indicated by the broadening of the Ce levels.

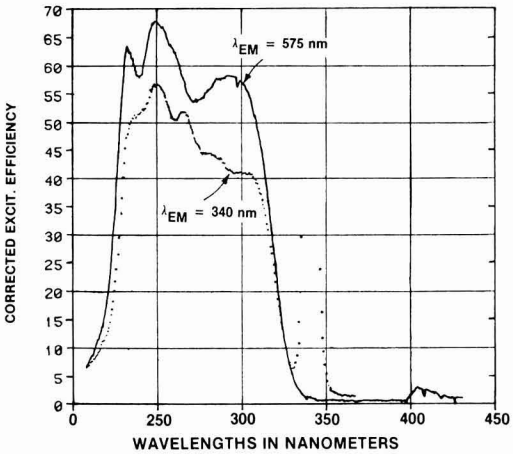

Fig. 6. Comparison of the corrected excitation efficiency in the same SrFAP:Ce;Mn material, while monitoring the emission near the peak of the Ce band in the u.v., and that of the Mn band at 575 nm. There are definite structural differences in the two excitation bands.

It can also be concluded from Fig. 6 that the absorption by Ce^{3+} at 254 nm, followed by sensitization of the Mn emission, is roughly 30 times more effective than direct absorption by Mn^{2+}, as occurring at $\simeq$405 nm, followed by Mn emission.

A detailed view of the excitation spectra in the long u.v. and in the visible, arising from direct absorption by Mn^{2+}, is given in Fig. 7 for YH (sample RL63) and for SrFAP, sample RL68 of starting formulation [3]. The tail of the Ce excitation band in the latter partially masks the weak excitation regions of Mn^{2+} centered at 350 nm. The overall shape of the excitation spectra on the long-wavelength side of 350 nm is remarkably similar in both phosphors. The characteristic narrow peak at $\simeq$405 nm is followed by a broader, symmetric band centered at 485 nm. The 405 nm excitation peak is actually stronger in SrFAP than in YH, suggesting a greater content

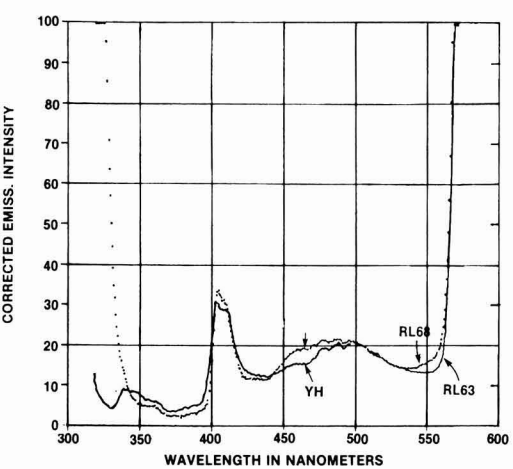

Fig. 7. Corrected excitation efficiency for YH and SrFAP:Ce;Mn (sample RL68; see text) in the spectral region of direct absorption by Mn^{2+}, while monitoring the emission at 575 nm. The marked similarity in the two excitation curves strongly suggests a similar site coordination around Mn^{2+} in both lattices, in spite of the strong fluoride excess in SrFAP.

of Mn^{2+} incorporated in the apatitic structure of the former. On the whole, the spectral measurements confirm the conclusion of the x-ray diffraction data, in the sense that despite the halide excess, the Mn^{2+} coordination in SrFAP markedly resembles that in YH.

Reflection spectra and remission spectra.—The excitation spectra detailed in the previous section map out the spectral regions that contribute to emission, after absorption of the exciting radiation, but do not provide a direct measure of the exciting radiation actually absorbed by the phosphor. Since the authors are dealing with powders, instead of measuring absorption spectra, as would be the case with transparent materials, they are restricted to measuring a complementary quantity, namely, the reflectance of the powder.

Reflectance measurements were carried out with the Perkin-Elmer spectrofluorimeter used to determine the emission and excitation properties of the phosphors. The two monochromators of the MPF-44A were set at the same wavelength, and scanned in tandem. Raw reflectance data were converted to an absolute scale by running the corresponding reflectance spectrum of a material of known properties, namely, the Eastman Kodak reflectance standard 6091. From the reflectance spectra of thick layers of powders one can derive the remission function

$$k/s = (1 - R)^2/2R \qquad [6]$$

namely, the ratio of the absorption coefficient k to the scattering coefficient s. For particles of similar morphology, and in spectral regions of intense absorption, it is justified to use the remission function as a comparative measure of the absorption of the materials considered. By deriving the remission function from the absolute reflectance data, one obtains curves that should approximate the absorption coefficient spectrum of the bulk material. An example of such remittance functions is given in Fig. 8, where we compare YH with SrFAP:Ce;Mn, sample RL68. The Ce^{3+} absorption dominates at $\simeq$300 nm and decreases at shorter wavelengths. The Sb^{3+} absorption in YH is fairly minimal at 300 nm and rises rapidly at shorter wavelengths, peaking at 240 and at $\simeq$222 nm. The curves for the two phosphors actually cross in the vicinity of 250 nm.

The excitation spectrum for Mn^{2+} emission from YH reproduces rather well the shape of the corre-

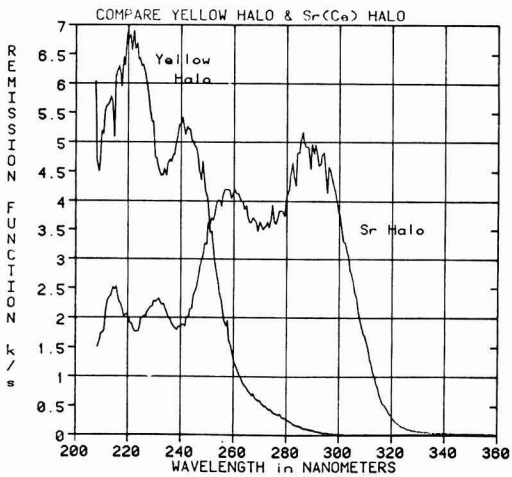

Fig. 8. Plot of the remission function k/s, namely, the ratio of the absorption coefficient to the scattering coefficient, for SrFAP: Ce;Mn (sample RL 68) and YH.

sponding remission function, up to ≃235 nm (Fig. 5 and 8). On the contrary, a comparison of the excitation spectra (with ordinates suitably scaled) and the remission spectra for sample RL68 shows that the Mn emission is more efficiently excited in the short u.v. around 250 nm than at the stronger absorption peak located at ≃290 nm (Fig. 9).

Spectral measurements at liquid-nitrogen temperatures.—A partial characterization of the spectral properties of SrFAP:Ce;Mn was performed on a sample of starting formulation [3] and with peak Mn emission at the 84% value of the YH standard. Figure 10 shows a comparison of the emission spectra at room temperature and at 77 K, for excitation at 254 nm. The Ce emission at low temperatures is split into two components located at 330 and 348 nm: this effect is due most likely to radiative transitions from a single emitting level to two J-manifolds (10) of the ^2F ground term of Ce^{3+}. Both Ce and Mn emissions increase in intensity at low temperatures, the former by almost a factor of two. The Mn emission also shifts to longer wavelengths on cooling. This can be explained on the basis of Tanabe and Sugano's diagram (5), as arising from a thermally induced increase in crystal field around Mn^{2+}. This type of long wavelength shift in the Mn^{2+} emission is also observed in YH.

Figure 11 shows the excitation spectrum at 77 K, obtained while monitoring the Mn emission at its peak. At least four excitation peaks, at 234, 250, 260, and 290 nm, are in evidence at low temperatures. Unfortunately, the corresponding excitation spectrum at room tempearture for the very same sample is not available. As an indication of the changes taking place in the shape of the excitation spectrum on cooling the phosphor, the low temperature excitation spectrum was contrasted with the room temperature excitation spectrum of Fig. 9. Cooling enhances the excitation intensity of the long wavelength portion of the excitation band, from ≃260 to ≃320 nm.

Excitation spectra at 77 K were measured in the region of direct absorption by Mn^{2+}, while monitoring the emission at 585 nm (Fig. 12). The curve of Fig. 12 should be compared with the corresponding

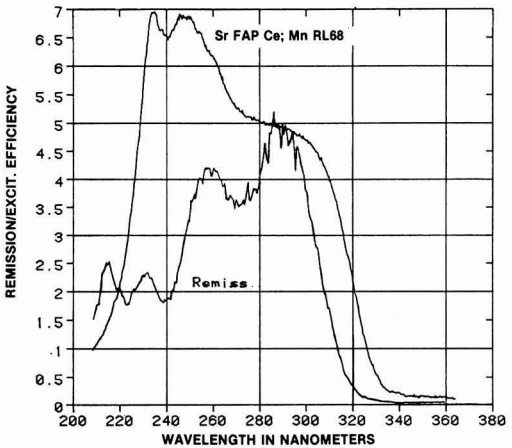

Fig. 9. Comparison of the remission function for SrFAP:Ce;Mn (sample RL68) and the excitation spectrum for Mn emission at 575 nm in the same sample. For convenience in plotting, the excitation-spectrum ordinates have been scaled down by a factor of 10.

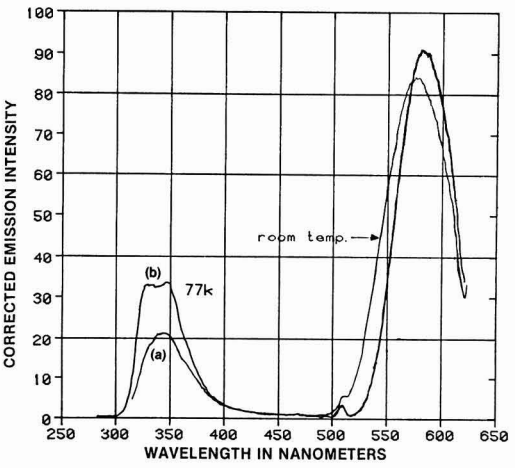

Fig. 10. Effect of temperature decrease on the emission from SrFAP:Ce;Mn. Excitation at 254 nm. (a) Room temperature, (b) at 77 K. Same excitation and detection conditions.

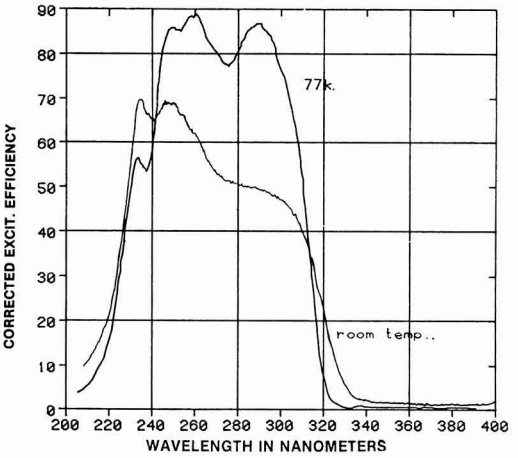

Fig. 11. Effect of the temperature decrease on the excitation spectrum for Mn emission at 575 nm in SrFAP:Ce;Mn.

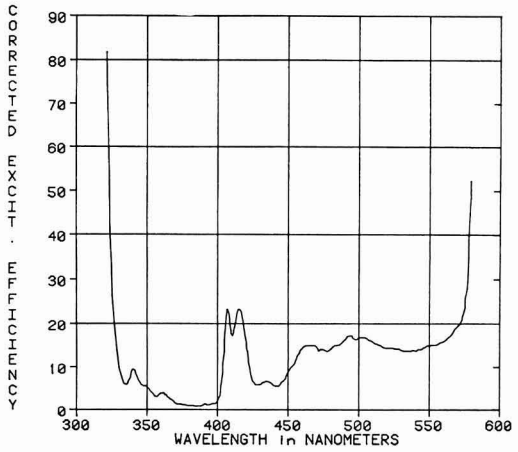

Fig. 12. Low temperature (77 K) excitation spectra for SrFAP: Ce;Mn, while monitoring the emission at 585 nm. This spectrum should be contrasted with that of Fig. 7.

curves of Fig. 7. The tail of the Ce^{3+} band is decreased in intensity at 77 K, so the Mn^{2+} group at $\simeq$350 nm becomes quite evident at low temperatures. The sharp peak at $\simeq$410 nm has now a definite doublet structure, with peaks at 406 and 415 nm. An additional weaker peak appears at 434 nm. The broader excitation region at longer wavelengths is now resolved into two components with peaks at 465 and 500 nm. Similar excitation spectra for YH have been reported by Wachtel and Ryan (11).

Emission-decay kinetics.—A useful property of phosphor activators, which is accessible to measurement and relevant to phosphor efficiency and to the sensitization process, is the decay rate of the corresponding radiative process and how it is affected by the concentration of activators and killer impurities.

The emission lifetimes for the active ions in question, Ce^{3+} and Mn^{2+}, differ by six orders of magnitude, the Ce^{3+} emission being generally of the order of 10^{-8} sec., and that of Mn^{2+} of the order of 0.01 sec. The kinetics of the emission decay from SrFAP were followed after dye laser pulsed excitation at 254 nm. In the singly activated materials (see Table III) of starting formulation

$$Sr_{4.30}Ce_{0.295}Mg_{0.146}(PO_4)_{3.0}F_{1.72} \qquad [7]$$

the emission decay of Ce^{3+} for excitation at 254 nm was fairly exponential in nature, with a decay constant of $\simeq$28 nsec. The Ce decay was much faster in the presence of Mn^{2+}, because of the additional decay channel involving transfer of excitation energy from Ce^{3+} to Mn^{2+}. This is evident from an inspection of Fig. 13, where the Ce decay in the doubly activated material is almost twice as fast.

Since the decay process being measured in the case of the Ce^{3+} emission takes place during a time comparable to the excitation process, the observed emission pulse is a convolution of the exciting pulse and of the corresponding emission pulse. In order to extract the decay kinetic from the observed emission pulse, we successively convolute the excitation pulse (as measured by our detection system) with singly exponential decay processes, until a good match is obtained between synthesized and observed emission pulses. The result of one such convolution is shown in Fig. 14 for a sample doubly activated with Ce and Mn. The measured emission pulse is consistent with a decay constant for Ce of 11 nsec.

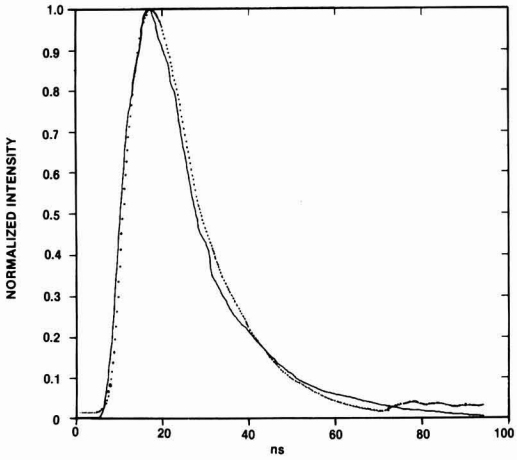

Fig. 14. Result of the convolution procedure used to extract emission decay constants from measured Ce-emission pulses. Sample of SrFAP:Ce;Mn at room temperature. The synthesized pulse (dotted curve) is the convolution of the system response function with an exponential decay of 11 nsec time constant.

The measured decay pulses of the Ce emission were not greatly affected by a decrease in sample temperature, down to $\simeq$100 K. A further decrease in sample temperature from 100 to 80 K caused the normalized emission pulse to broaden and the decay appeared to have a slower, later component (Fig. 15 and 16). Further measurements are required for a possible correlation of this abrupt change in decay characteristics with a thermally activated energy-transfer and/or sensitization process.

At room temperature the decay of the Mn emission for excitation at 254 nm is exponential (Fig. 17), with a decay constant of 14.8 msec. This value is quite close to the value measured for the Mn^{2+} emission in YH, where we find at room temperature a decay constant of 15 msec.

Singly activated strontium FAP.—Before discussing the lamp evaluation and air firing of the doubly activated SrFAP, some of the spectral properties of the

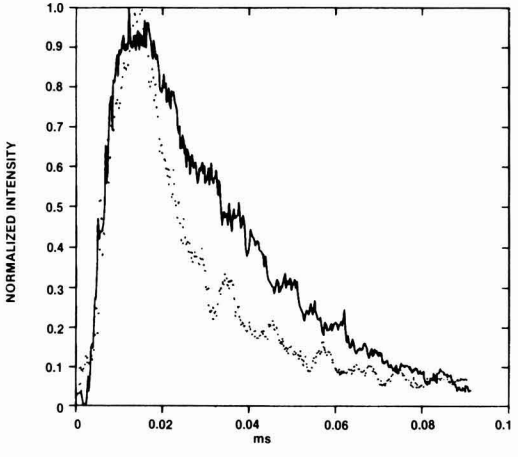

Fig. 13. Ce^{3+} emission pulse at 350 nm, following dye-laser excitation at 254 nm. Samples at room temperature. Solid line: emission from SrFAP:Ce;Mg. Dotted line: emission from SrFAP:Ce;Mn. The oscillations in the decay curves are due to rf pickup from the nitrogen-laser discharge.

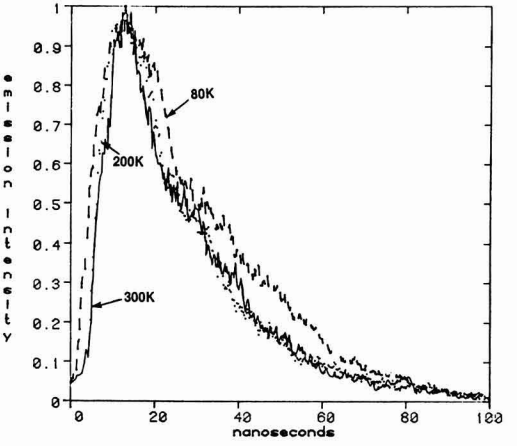

Fig. 15. Effect of decreasing temperature on the decay kinetics of Ce^{3+} emission from SrFAP:Ce;Mn. An appreciable lengthening of the decay is found at 80 K. Dye-laser excitation at 254 nm.

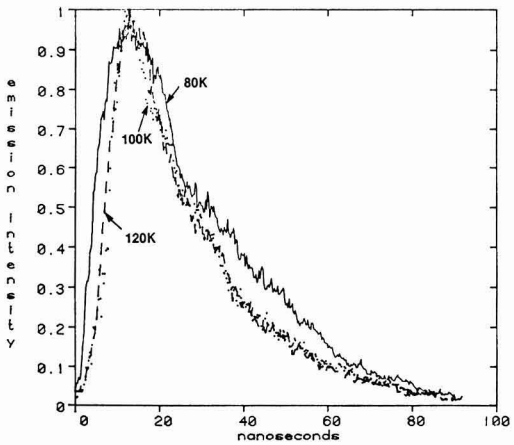

Fig. 16. Same as previous figure, but for a narrower temperature range, from 120 to 80 K. The change in the shape of the emission pulse occurs rather abruptly in going from 100 to 80 K.

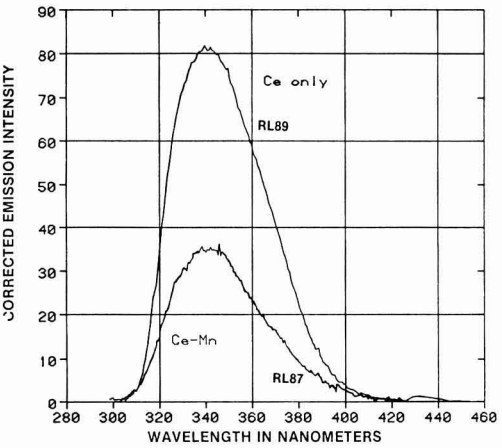

Fig. 18. Emission due to Ce^{3+} in two SrFAP:Ce phosphors, one containing both Ce and Mn, and the other with Mg replacing Mn. The Ce emission in the former is reduced by almost a factor of three, because of efficient energy transfer to the Mn^{2+} centers. The shape of the Ce^{3+} emission band is very similar in both cases.

Ce-activated SrFAP of starting formulation (7) are mentioned, since they are relevant to the lamp performance of the doubly activated phosphors. The emission from the singly activated phosphor consists of the already familiar Ce^{3+} band, with peak at $\simeq$340 nm and half-width at half-maximum of $\simeq$50 nm (Fig. 18). The Ce emission is reduced by more than half in the doubly activated sample, as seen in Fig. 18. The corresponding excitation spectra for emission at 348 nm are shown in Fig. 19. The replacement of Mg by Mn in the singly activated material produces a marked broadening of the excitation band of Ce^{3+}. This is again evidence for Ce-Mn associates in the doubly activated material.

Triple activation of SrFAP.—One of the advantages in using Ce^{3+} instead of Sb^{3+} as sensitizer in the apatite structure is the ability of Ce^{3+} to sensitize not only the emission of Mn^{2+}, but also that of trivalent rare earth ions. Sensitization of Tb^{3+} emission by Ce^{3+} in fluoroapatites has been reported by Ranby and Hobbs (12). To demonstrate the possibility of Ce-RE^{3+} sensitization even in the presence of Mn^{2+}, some preparations of SrFAP activated with Ce, Mn, and one of the rare earths were carried out

The results obtained when the rare earth ion was Dy^{3+} are given in Fig. 20. The emission consists of the now familiar Ce emission in the long u.v., of the yellow emission from Mn^{2+} and, in addition, of two line groups located at 470 and 570 nm and contributed by Dy^{3+}. In principle this combination of blue and of composite yellow emission from a single phosphor could provide the overall white field that in the Lite-White scheme is obtained using a blend of two phosphors.

A combination of Ce, Mn, and rare earth emission was also observed on activation with Tb^{3+}.

Lamp Evaluation of Doubly Activated SrFAP

Standard 40W low pressure fluorescent lamps were coated with SrFAP:Ce;Mn phosphors of starting formulation [3]. As internal standards, lamps were also fabricated with YH. The original plaque brightness of the SrFAP:Ce;Mn was approximately 85% that of

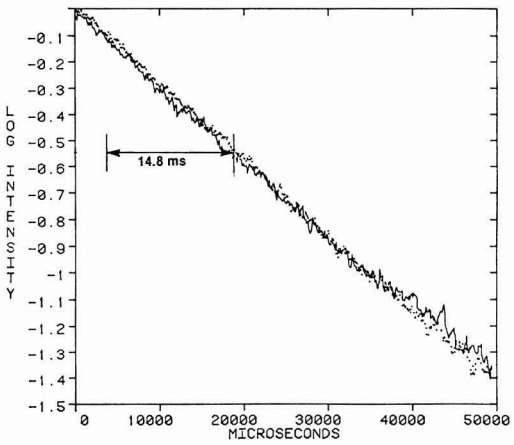

Fig. 17. Semilog plot of the emission decay at 580 nm from SrFAP:Ce;Mn as a result of dye-laser excitation at 254 nm. A decay constant of $\simeq$14.8 msec can be extracted from the straight semilog plot.

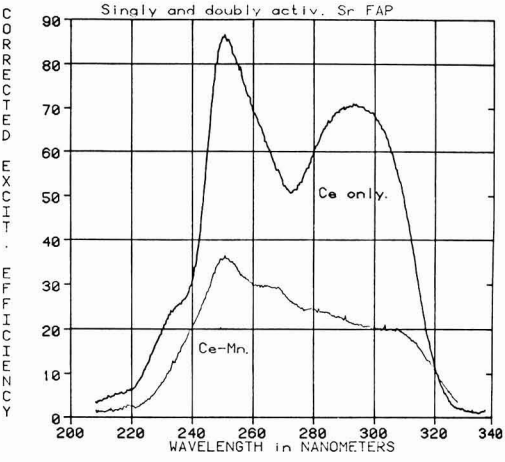

Fig. 19. Same two samples as in previous figure, but now the excitation efficiency for Ce emission at 348 nm is being monitored. The replacement of Mg with Mn markedly broadens the Ce level distribution.

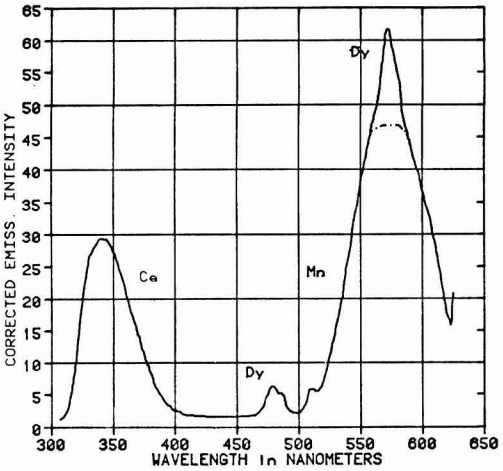

Fig. 20. Emission spectrum of a triply activated SrFAP:Ce;Mn:Dy phosphor for excitation at 254 nm. In addition to emitting in the u.v., Ce sensitizes both the Mn^{2+} emission and that of Dy^{3+}, with line groups at 470 and 570 nm.

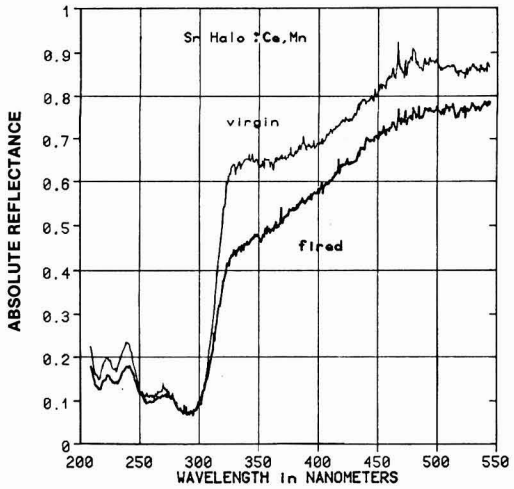

Fig. 21. Effect of air firing on the reflectivity of the SrFAP:Ce;Mn phosphors. The absorbance of the material is fairly unchanged at 254 nm, but increases from ~310 nm to longer wavelengths.

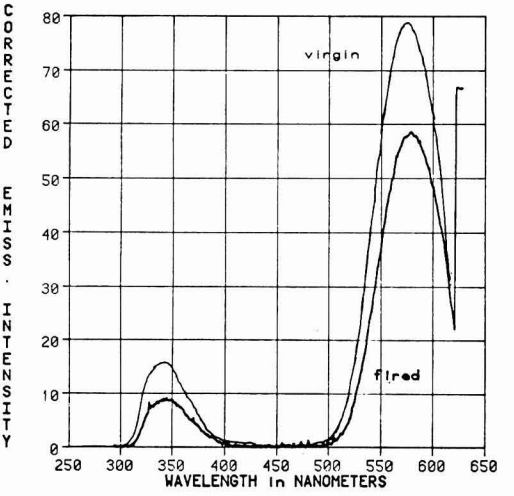

Fig. 22. Effect of air firing on the emission properties of SrFAP:Ce;Mn. Excitation at 254 nm. The emission loss is relatively higher for the u.v. emission band.

YH. At zero hour the corresponding lamp output was already down to ~73% that of the lamp coated with YH, an indication of serious baking and short-term brightness losses. At 100 hr the output maintenance was poor, 85.4%, compared to the 97.6% maintenance for YH. It appears therefore that the phosphor, as presently formulated, although exhibiting suitable plaque brightness, is not stable to the lamp-making process.

The remainder of the present report is devoted to a preliminary inquiry into the causes of such a phosphor deterioration, namely, to determining whether the effect is associated with the matrix itself or with the oxidation of Ce^{3+} and/or of Mn^{2+}.

Effect of Air Firing on Brightness

In order to roughly simulate the conditions seen by the phosphor during baking, small amounts of the phosphor of starting formulation [3], *i.e.*, about 1g batches, were fired in air for 15 min at 640°C. This firing treatment caused a change in the body color from pale green to light tan. This effect can also be followed in the reflectance data of Fig. 21. The absorbance of the powder around 254 nm, in the region of absorption by Ce^{3+}, is barely affected by the firing treatment, while a broad continuous absorption sets in from 325 nm down into the visible region. Both in the spectral region of Ce emission and of Mn emission, the fired material is definitely more absorbing than the virgin phosphor. Therefore, it is not surprising that the increased absorbance is accompanied by serious losses in emission intensity. In effect, the emission band of Ce is decreased at the peak by almost 50%, while the Mn emission is reduced by 25% (Fig. 22). The excitation spectra for emission at 580 nm are plotted in Fig. 23 for the virgin and for the fired phosphors: the loss in excitation efficiency is highest at the shortest wavelengths (~50% at the 235 nm excitation peak), while it is only 20% at the broad excitation peak at 290 nm.

These results on the doubly activated SrFAP should now be contrasted with the behavior of the singly activated analog of starting formulation [7]. On firing the latter, the original pale green body color of the powder veered to white. In addition, the reflectance spectra of Fig. 24 show no change in the strength of the u.v. absorption peaks of Ce^{3+}, namely, no evidence of oxidation of Ce^{3+} is seen, while there is a partial bleaching of the absorption responsible for the original green body color. As a result of the air firing, we actually register an increase in Ce^{3+} emission (Fig. 25). The preliminary conclusion is that during the air firing, and the lamp making processes, the sensitive component is not Ce^{3+} but probably Mn^{2+}, or possibly the Ce-Mn associates.

Conclusion

The first stage in the search for suitable alternatives for the yellow emitting component for the Lite-White blend has demonstrated the potentialities of Ce-Mn-coactivated fluoroapatite phosphors in providing plaque brightness approaching that of YH.

The lamp tests also revealed that the Ce-Mn Sr fluoroapatite phosphors, as presently formulated, are apparently damaged in the baking and in the lamp making process. The question of lamp compatibility is therefore central to further development and synthesis optimization of the Ce-Mn fluoroapatite phosphors. Since Ce is a more versatile sensitizer than Sb,

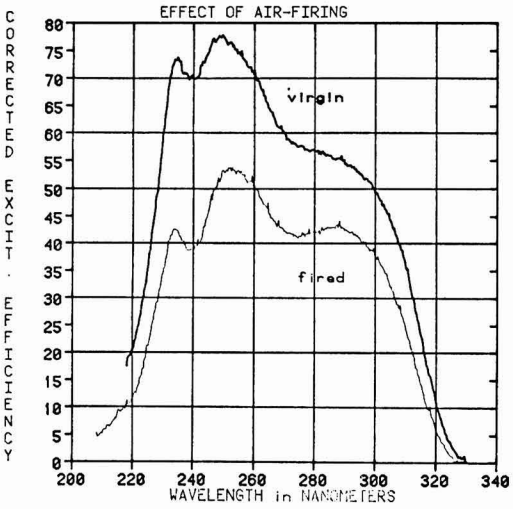

Fig. 23. Changes in the excitation spectrum for emission at 580 nm from SrFAP:Ce;Mn as a result of air firing. The efficiency loss increases toward shorter wavelengths.

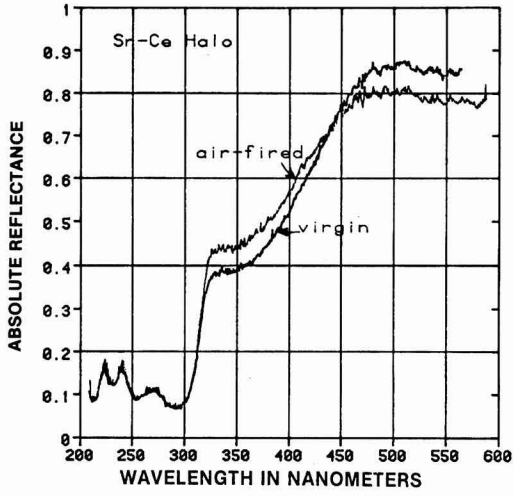

Fig. 24. Changes in the reflectance of singly activated SrFAP:Ce after air firing. No appreciable change in Ce^{3+} absorbance at 254 nm is noticeable. The absorption band centered around 350 nm, and responsible for the pale green body color, is actually decreased as a result of the air firing.

if the lamp processing losses were brought under control, a wide versatile new class of halophosphate phosphors would become available.

Acknowledgments

The writers wish to express their appreciation and thanks for the help and cooperation provided by the following GTE personnel: C. Chenot and A. Kasenga of the Towanda PMG for the preparation of those phosphor samples that were later submitted for lamp testing and for many valuable discussions on phosphor properties; J. T. Smith and J. McColl of the GTE Labs for a critical reading of the manuscript; C. Persiani and F. Durkin of the GTE Labs, and the staff of the Analytical Group of the Towanda PMG for the chemical analyses; M. Downey and G. Hamill for the x-ray powder-diffraction work; C. Miller and K. Ostreicher for the scanning electron microscopy of the samples; and P. Martakos for the infrared spectral measurements.

Manuscript submitted Feb. 8, 1982; revised manuscript received June 13, 1983. This was Paper 176 presented at the Minneapolis, Minnesota, Meeting of the Society, May 10-15, 1981.

GTE Laboratories Incorporated assisted in meeting the publication costs of this article.

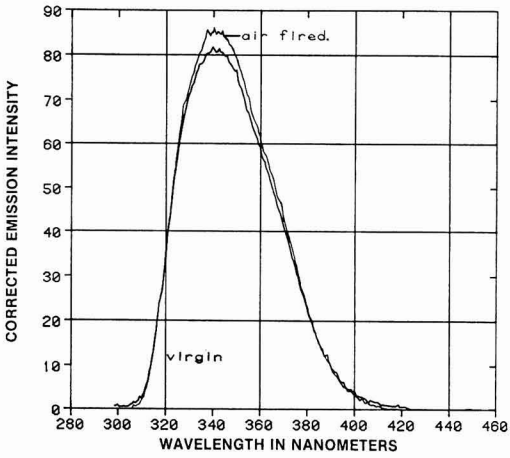

Fig. 25. Emission spectrum of the singly activated SrFAP:Ce of the previous figure, before and after air firing. The air-fired material has a stronger Ce emission, ≃6% higher at the peak.

REFERENCES

1. J. M. P. J. Verstegen, D. Radielovic, and L. E. Vrenken, *This Journal*, **121**, 427 (1974).
2. L. E. Vrenken, *Lighting Res. Technol.*, 8211 (1976).
3. W. W. Piper, J. S. Prener, and C. G. R. Gillooly, U.S. Pat. 4,075,532 (1978).
4. H. F. Ivey, *J. Opt. Soc. Am.*, **53**, 1185 (1963).
5. Y. Tanabe and S. Sugano, *J. Phys. Soc. Jpn.*, **9**, 753 (1954).
6. S. T. Henderson and P. W. Ranby, *This Journal*, **104**, 612 (1957).
7. P. W. Ranby, Br. Pat. 792,598 (1958).
8. ASTM Powder Diffraction File 29-1310.
9. C. Smith and G. McCarthy, Pennsylvania State University (1977).
10. M. A. Elyashevich, "Spectra of Rare-Earths," p. 392, State Publishing House, Moscow (1953).
11. A. Wachtel and F. A. Ryan, *This Journal*, **120**, 693 (1973).
12. P. W. Ranby and D. Y. Hobbs, Ger. Pat. 25 35 446 (1976).

Delineation of p-n Junction in Thin InGaAsP Layers Using Chemical Etching

J. A. Lourenco

Bell Laboratories, Murray Hill, New Jersey 07974

ABSTRACT

A method for the delineation of the p-n junction inside the active layers of InGaAsP/InP double heterostructures is presented. A chemical etch used with illumination on a grooved sample can accurately delineate the diffusion front of the p-dopant in quaternary layers. Using a conventional optical microscope, the technique can be used for active layers as thin as 0.1 μm. Good correlation with scanning electron microscope techniques (EBIC) is observed. The technique presented here can easily be used as a routine step during wafer characterization.

In InGaAsP/InP double heterostructures (DH) grown by liquid phase epitaxy (LPE), the p-n junction position in the nominally undoped InGaAsP active layer is formed by diffusion of the acceptor, commonly Zn, from the p-type InP confining layer. However, the Zn flux into the quaternary layer is dependent on its concentration in the confining layer and the diffusion depth can be altered by varying the time that the wafer remains at high temperature after the InGaAsP active layer has been grown. In addition, the position of the p-n junction has been found to depend on the doping level of the active layer (1, 2), and lattice mismatch, which influences the bulk properties of the epi, can also affect the Zn diffusion length (3). Consequently, the position of p-n junction can shift from run to run, and its misplacement has been a problem, particularly in very thin layers (1, 4).

An accurate way of determining the p-n junction in a double heterostructure is with the electron beam-induced current (EBIC) (5) mode of a scanning electron microscope. The EBIC method, however, is too complex to be used routinely. A simple and quick alternate method is therefore desirable. Often, chemical staining of a cleaved edge is the method of choice and it works well with thick layers (greater than 2.0 μm). It has been successfully applied to thick InGaAsP layers, although the exact procedure and the type of stain were not mentioned (2). However, when the active layer thickness is less than ~2.0 μm, the resolution of an optical microscope is limiting. Also, if the p-n junction is very close to one of the interfaces of the active layer, the junction and this interface become indistinguishable, even in a thick layer, and no information can be obtained.

In this paper, a technique is presented which can accurately reveal the position of the p-n junction inside InGaAsP layers as thin as 0.1 μm. A chemical etch is used with illumination. Coupled with the arcuic trigonometric method of calculating layer depth (6), it provides a quick and easy way of routinely determining the position of the diffusion front inside the active layer.

Experimental

A small sample (~1.5 × 3.0 mm) is cut from an LPE double heterostructure, mounted on a thin glass cover plate, and grooved using a sectioner from Philtec Instrument Company. The detailed procedure for mounting and grooving the sample has been described by McDonald and Goetzberger (7). The groove depth must be carefully controlled: it must be deep enough to completely cut through the active layer but should not go much deeper than the bottom of the layer in order to maximize the groove width-to-depth ratio. The sample is then cleaned and stained under illumination from a microscope lamp with a 15W tungsten filament bulb placed directly over the groove. The stain solution consists of 100 ml of H_2O, 8g KOH, and 0.5g $K_3Fe(CN)_6$ (8). Although the time required for staining depends strongly on dopant concentration, in most samples 5-10 sec was enough to delineate the p-n junction. Usually the surface on the p-side of the quaternary active layer becomes very rough, probably because it is more strongly attacked by the chemical etch than the n-side. After staining, the thickness of the active layer can be calculated and the exact position of the junction can be determined (6, 7). Figure 1 shows a grooved sample which has been stained for delineation of the active layer boundaries and the p-n junction position.

To evaluate the validity of this technique, several samples were analyzed using both the groove-and-stain method and the EBIC method. Figure 2 shows two scanning electron micrographs of cleaved edges of InGaAsP/InP DH light emitting diodes (LED's). The EBIC signals place the p-n junction (a) at the top of the active layer, very close to the p-InP, and (b) deep inside the active layer, closer to the n-InP. Figure 3 shows the two samples from Fig. 2, this time using the groove-and-stain technique to delineate the quaternary layer interfaces and the p-n junction. Again, the p-n junction appears (a) at the top of the active layer, and (b) closer to the bottom of the layer.

A few samples were stained without using illumination. A loss of sharpness at the p-n junction was observed and a much longer staining time was required.

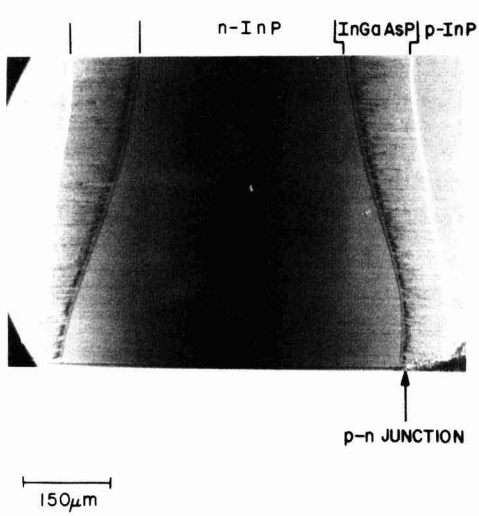

Fig. 1. Interference contrast micrograph of a grooved sample which has been stained for layer delineation and for determination of the p-n junction position.

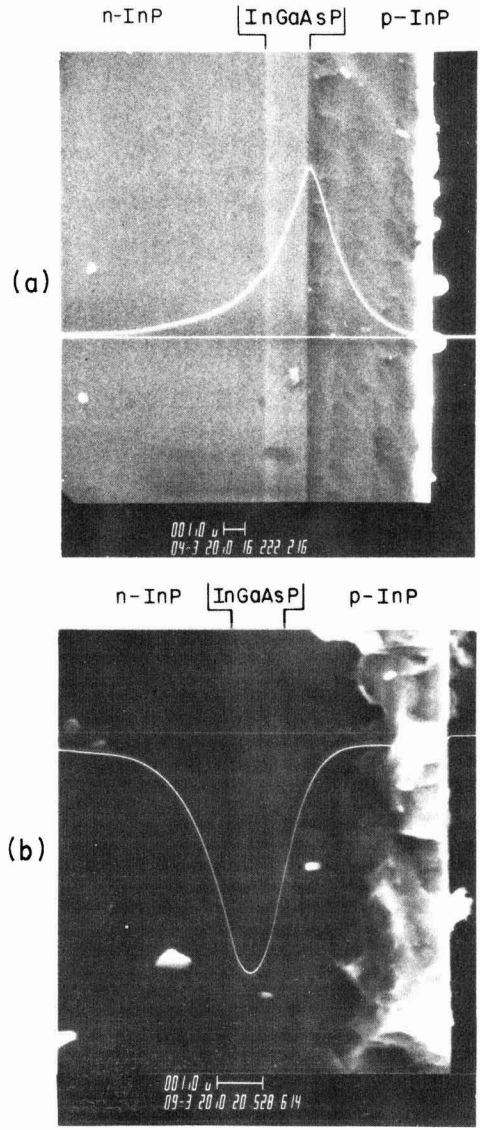

Fig. 2. Scanning electron micrograph of a cleaved edge of a InGaAsP/InP DH LED. The EBIC signal shows the p-n junction (a) at the top of the active layer, next to the InP confining layer; (b) deep inside the active layer, closer to the InP buffer layer.

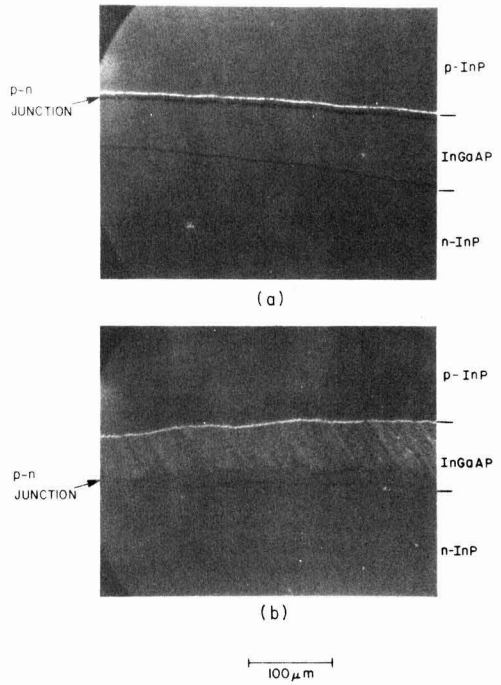

Fig. 3. Interference contrast micrograph of the same samples from Fig. 2 with the p-n junction delineated using the groove and stain method: (a) junction present at top of the active layer; (b) junction deep inside the layer.

This resulted in partial removal of the active layer with consequent loss of accuracy. Several stain compositions of the same components were tried, but the composition described above seemed to give the best results. In particular, compositions where the concentration of $K_3Fe(CN)_6$ is increased, like the ones usually used for quaternary layer removal (9), were too strong for staining purposes: although they delineate the p-n junction they also etch away the active layer very quickly, starting towards the center of the groove where the layer is thinnest. They are, therefore, not practical because accuracy is lost, and p-n junctions very close to the bottom of the active region cannot be detected. Delineation of the junction right at the bottom of the layer, as illustrated in Fig. 1, would be impossible if any appreciable layer removal had taken place. Other known InGaAsP etchants were tried, such as the AB etch (10), but these were also too fast at attacking the quaternary layer.

Most of this experimental work was done on wafers in which the active layer was nominally undoped n-InGaAsP. The p-n junction was formed by Zn diffusion from the Zn-doped InP confining layer. This technique was also successfully tried on a wafer where Cd was used as the p-dopant.

Discussion

A 100 ml solution of 8.0g potassium hydroxide and 0.5g potassium ferricyanide is strong enough to delineate th p-n junction inside a quaternary layer, but weak enough to do so without appreciable removal of InGaAsP.

Excellent correlation is observed between the EBIC and the groove-and-stain methods. However, the EBIC technique consists of a scanning electron micrograph with a superimposed EBIC signal, and the two are not always easy to align. In the groove-and-stain technique, the active layer boundaries and the p-n junction are delineated in only one step, and they are usually very sharp. Therefore, the groove-and-stain method is possibly more accurate. In this technique, illumination is necessary if sharpness of delineation and quickness are to be attained.

The major advantage of this technique is the accurate delineation of the p-n junction inside very thin layers, which is hard to do even with EBIC. Because a very shallow layer can be transformed by grooving into a width easily resolved by optical microscopes, and because the etch described above stains much faster than it etches away InGaAsP, the p-n junction can be determined in layers as thin as ≈ 0.1 μm. (See, for example, Fig. 4.) Also, junction displacement from metallurgical boundary of $\lesssim 0.1$ μm can be resolved, as illustrated in Fig. 3a. In addition, this is a quick

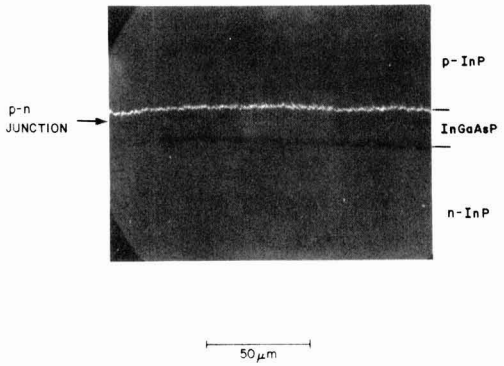

Fig. 4. Interference contrast micrograph of grooved and stained sample showing the p-n junction position inside an InGaAsP layer 0.16 μm thick.

and simple technique which can easily be used as a routine step in wafer characterization.

Acknowledgments

The author would like to thank H. Temkin and F. Ermanis for the EBIC results, A. K. Chin for useful comments, B. H. Chin for helpful guidance, and R. H. Saul for his support.

Manuscript submitted Feb. 4, 1983; revised manuscript received *ca.* May 27, 1983.

Bell Laboratories assisted in meeting publication costs of this article.

REFERENCES

1. N. Tamari, *Appl. Phys. Lett.*, **40,** 108 (1982).
2. P. D. Wright, Y. G. Chai, and G. A. Antypas, *IEEE Trans. Electron Devices*, **ed-26,** 1220 (1979).
3. M. M. Tashima, L. W. Cook, N. Tabatabaie, and G. E. Stillman, *Appl. Phys. Lett.*, **38,** 1009 (1981).
4. J. J. Coleman and F. R. Nash, *Electron Lett.*, **14,** 558 (1978).
5. L. J. Balk, E. Kubalek, and E. Menzel, *IEEE Trans. Electron Devices*, **ed-22,** 707 (1975).
6. C. L. Aley and R. S. Turner, *Semicond. Intern.*, **3,** 135 (May 1980).
7. B. McDonald and A. Goetzberger, *This Journal*, **109,** 141 (1962).
8. J. J. Hsieh, J. A. Rossi, and J. P. Donnelly, *Appl. Phys. Lett.*, **28,** 709 (1976).
9. K. L. Conway, A. G. Dentai, and J. C. Campbell, *J. Appl. Phys.*, **53,** 1836 (1982).
10. M. S. Abrahams and C. J. Buiocchi, *ibid.*, **36,** 2855 (1965).

Dependence of the Characteristics of ZnSe MBE Grown on GaAs and GaP on Thermal Treatment in a Vacuum

T. Niina, K. Yoneda, and T. Toda

Sanyo Electric Company, Limited, Research Center, 1-18-13, Hashiridani, Hirakata, Osaka, 573, Japan

ABSTRACT

The dependence of the surface morphologies, electrical and optical properties of MBE grown ZnSe layers on the surface cleanliness of both GaAs and GaP substrates after being treated by a thermal treatment procedure in a vacuum prior to growth was studied by using RHEED and AES and by measuring the Hall effect and photoluminescence. The major contaminants on the surface of both GaAs and GaP after chemical treatment are carbon and oxygen. Carbon absorbed on the surface of both GaAs and GaP can be easily decomposed by thermal treatment above 420°C. On the other hand, there is quite a difference between GaAs and GaP concerning the removal behavior of the residual oxide layers. The thermal treatment temperatures required to completely remove these oxide layers are 560°C for GaAs and 620°C for GaP. The characteristics of the MBE grown ZnSe layers depend mainly on the surface cleanliness of the substrate after the thermal removal of the residual oxide layers. In order to achieve a high quality grown layer, it is recommended that the thermal treatment be in the comparatively wide region between 560° and 630°C for the growth of ZnSe on GaAs and in the extremely narrow region between 620° and 630°C for the growth of ZnSe on GaP.

Cleaning the surface of the substrate prior to growth is an essential procedure in the preparation of a high quality epitaxial film using molecular beam epitaxy (MBE). In the case of GaAs, which has been widely used as a substrate for the MBE growth of III-V compound semiconductors, the major contaminants are oxygen and carbon. Oxygen contaminates the surface during and after chemical treatment, forming unavoidable thin oxide layers which consist of arsenic and gallium oxides (1). Arsenic and gallium oxides can be removed by thermal treatment in a vacuum, with temperatures above 370° and 570°C, respectively (2). On the other hand, carbon is easily absorbed from an ambient and a cleaning solvent (3). Ordinary carbon contaminants can be effectively decomposed by thermal treatment in a vacuum above 350°C. However, when the substrate has been exposed to an ionized beam, carbon cannot be removed by thermal treatment unless temperatures above 600°C are used (4). The presence of such residual carbon contaminants across the interface of the grown layers results in the generation of defects and affects the surface morphologies of the grown layers (5).

Key words: molecular beam epitaxy, zinc selenide, reflection high energy electron diffraction, Auger electron spectroscopy, photoluminescence, Van der Pauw method.

Recently, MBE has been extensively applied in the growth of II-VI compound semiconductor films. In particular, for the growth of ZnSe, the possibility of achieving a precisely controlled, highly conductive layer for use in blue light emitting diodes has been demonstrated (6, 7). So far GaAs has been commonly used as the substrate for the MBE growth of ZnSe because of its closed lattice match. GaP can also be used in spite of its large lattice misfit of ~ 4% (8). As in the growth of III-V compounds, the preparation of a smooth, clean, and undamaged substrate surface is also an important requirement for achieving a high quality layer in the case of ZnSe MBE growth.

In this paper, we investigated thermal treatment procedures required not only to decompose carbon contaminants but also to remove residual oxide layers

on the surface of both GaAs and GaP, and the relation between the surface cleanliness of the substrate and the characteristics of ZnSe layers grown on both GaAs and GaP. These investigations were performed by using reflection high energy electron diffraction (RHEED), Auger electron spectroscopy (AES), Hall effect measurement, and photoluminescence measurement.

Experimental Procedures

The substrates used in the present study were Cr-O doped semi-insulating GaAs (100) with a resistivity of greater than 3×10^7 Ω-cm, and also Zn-doped p-type GaP (100) with a resistivity of ~0.2 Ω-cm and a carrier concentration of $5 \sim 10 \times 10^{17}$ cm^{-3}.

After mechanical and chemical polishing, they were degreased with trichloroethylene by boiling, acetone, ethanol, and deionized water. Then, in the case of GaAs, the substrates were etched with a solution of $5H_2SO_4$-H_2O_2-H_2O for 10 min at 60°C, subsequently rinsed with deionized water, finally immersed in HCl for 10 min at 30°C in order to remove the residual oxide layer, rinsed with deionized water, and dried with dry nitrogen. In the case of GaP, the substrates were etched with a stirring solution of HCl-$2HNO_3$-H_2O for 10 ~ 15 min at 55°C, then rinsed with deionized water, and dried with dry nitrogen.

After these chemical treatment processes, the samples were mounted on an Mo sample block using In for adhesion, immediately inserted into a loading chamber of an MBE system, and pumped down. The MBE system used in the present study was a RIBER-MBE 1000 which was equipped with a quadrupole mass spectrometer, a 10 keV RHEED, and an AES.

After being transferred into the growth chamber, which has a base pressure less than 10^{-10} Torr, the samples were treated thermally prior to growth for 15 min at each step of the temperature regions between 300° and 670°C. All of the epitaxial films were grown on both the GaAs and the GaP substrate. 6N-Zn, Se, and Ga metal were used as source materials. For growth, the Zn cell temperature and the Se cell temperature were normally kept at ~300° and ~210°C, respectively. Under this condition, the beam flux ratio of Zn to Se was about 1. For the growth of ZnSe on GaAs, the substrates were heated either to 320°C or to 360°C. For the growth of ZnSe on GaP, the substrates were heated to 360°C to maintain a smooth surface morphology. For doping, the Ga cell temperature was fixed at ~420°C to obtain the desired carrier concentration.

At each step of the various thermal treatments, RHEED and AES observations were made to evaluate the surface cleanliness of the substrate resulting from the removal of the surface contaminations. In-depth profile measurements of AES were used to determine the transition region between the growth layer and the substrate and also to detect the impurities embedded across the interface. The electrical and optical properties of the grown layers were studied by using the Van der Pauw method and by room temperature photoluminescence excited with a 3250Å He-Cd laser, respectively.

Results and Discussion

Figure 1 shows the Auger peak heights of various elements at the substrate surfaces as functions of the thermal treatment temperatures. The Auger peak heights obtained from GaAs and GaP are shown in Fig. 1(a) and (b), respectively. The peaks retained in the Auger spectra are a 273 eV KLL transition for C, a 503 eV KLL transition for O, a 1070 eV LMM transition for Ga, a 1229 eV LMM transition for As, and a 1865 eV LMM transition for P.

Carbon contaminants absorbed on both GaAs and GaP after chemical treatment can be explicitly decomposed by thermal treatment above 420°C, which is

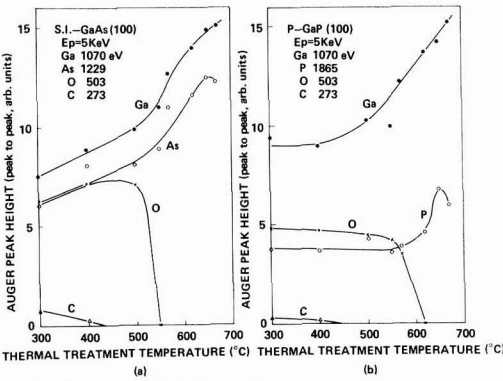

Fig. 1. Auger peak heights of various elements from different substrate surfaces of GaAs (a) and GaP (b) as a function of the thermal treatment temperatures.

slightly higher than the 350°C described by Chang *et al.* (9).

For GaAs, the oxygen peak height begins to decrease at the thermal treatment of 500°C and then disappears rapidly when a thermal treatment of 560°C is used. This corresponds to the removal behavior of an oxidation product consisting of Ga_2O_3. For GaP, the oxygen peak height decreases gradually as the thermal treatment temperature increases when thermal treatments above 500°C are used. However, this oxygen peak height will not disappear by thermal treatments unless the temperature is raised to 620°C. The above result indicates that there is quite a difference between GaAs and GaP with respect to the removal behavior of the residual oxide layers because the oxidation product on GaP is different from Ga_2O_3 on GaAs (10). With thermal treatments above 650°C, the As peak height for GaAs and the P peak height for GaP decrease as the thermal treatment temperature increases. This may be attributed to the desorption of volatile atoms from the surface due to the difficulty of maintaining a congruent evaporation.

For the growth of ZnSe on GaAs, the surface morphologies of the GaAs substrates and the subsequent epitaxial growth at the initial stage of the 1000Å thickness after different thermal treatments as observed from *in situ* RHEED patterns are shown in Fig. 2. The substrate temperature during growth was 320°C and a primary electron with a 10 keV was used along the [110] azimuth. At the thermal treatment of 550°C, the RHEED obtained from the substrate surface shows a ringed pattern due to the coverage of the oxide layer which remained after chemical treatment, as shown in Fig. 1(a). Thereafter, the RHEED obtained from the surface of the subsequent epitaxial growth at the initial stage of the 1000Å thickness also shows the ringed pattern arising from the polycrystal ZnSe growth. After thermal treatment above 560°C, the diffraction pattern obtained from the substrate surfaces changed to a spotty one. This indicates that the bare surfaces of the substrates exposed after the removal of the residual oxide layer are rough because of the congruent evaporation of Ga and As atoms from the surface. However, the surface morphologies of the subsequent ZnSe epitaxial growth with the 1000Å thickness achieve a smooth surface observed from a streak diffraction pattern, as shown by the RHEED studies.

For the growth of ZnSe on GaP, the surface morphologies of the GaP substrate, the subsequent epitaxial growth at the initial stage of the 1000Å thickness, and the total growth with a 3 μm thickness were observed from *in situ* RHEED patterns, as shown in Fig. 3. The important difference between the morphologies of GaAs and GaP after thermal treatment is a

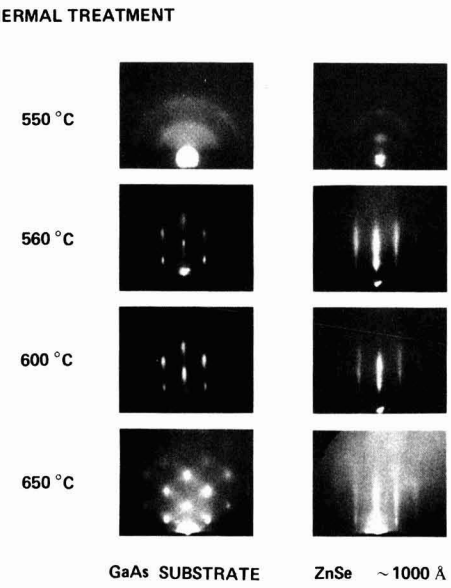

Fig. 2. RHEED patterns of the GaAs substrate prior to growth and the surface at the initial stage of the 1000Å ZnSe growth after different thermal treatments.

diffraction pattern resulting from the thermal treatment when the substrate surface is still covered with the residual oxide layers, as shown in Fig. 1. For GaP, the substrate surface exhibits a spotty pattern even at the thermal treatment temperature of 570°C. This indicates that the oxidation product on the surface of GaP is single crystalline, which is in agreement with previous work (10). The surface of the ZnSe epitaxial growth at the initial stage of the 1000Å thickness also exhibits a spotty diffraction pattern. However, the surface after the total 3 μm thickness growth changes to a streak pattern. The roughness of the growth surface at the initial stage of the 1000Å thickness may be attributed to the presence of the residual oxygen contaminations across the interface. The surface morphology after the total 3 μm thickness growth, however, could never be dominated by the detrimental oxygen contaminations. After thermal treatments above 620°C, which is the temperature required to completely remove oxide layers, as shown in Fig. 1(b), surface morphologies of the ZnSe epitaxial growth even at the initial stage of the 1000Å thickness exhibit a smooth surface observed from a streak diffraction pattern.

Figure 4 shows in-depth profiles of the Auger peak heights of various elements in the interface region between the ZnSe growth layer and the substrate at each step of the different thermal treatments for the ZnSe-GaP system and at the step of the thermal treatment of 600°C for the ZnSe-GaAs system. The substrate temperature during growth and the ZnSe growth thickness were 360°C and ~1000Å, respectively. For the ZnSe-GaP system, oxygen is embedded across the interface at the thermal treatment temperature of 570°C, as shown in Fig. 4(a). This result confirms that it is possible for oxide contaminations to dominate the surface morphology of the ZnSe growth at the initial stage. After thermal treatments above 620°C, no oxygen contaminants can be embedded across the interface, as shown in Fig. 4(b) and (c). Therefore, oxygen contaminants can arise not from the ambient during growth but from the chemical treatment. The depth of the transition region after the thermal treatment of 620°C for the ZnSe-GaP system is about 300Å, slightly wider compared to that of ~150Å after the

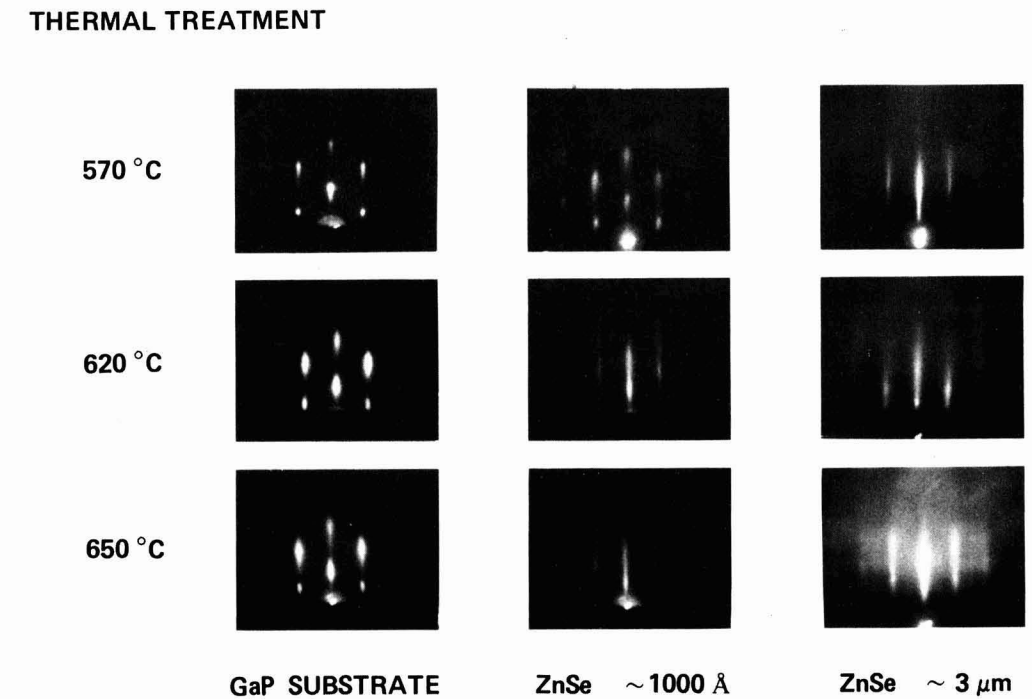

Fig. 3. RHEED patterns of the GaP substrate prior to growth and the surfaces at the initial stage of the 1000Å ZnSe growth and the sequential stage of the 3 μm growth after different thermal treatments.

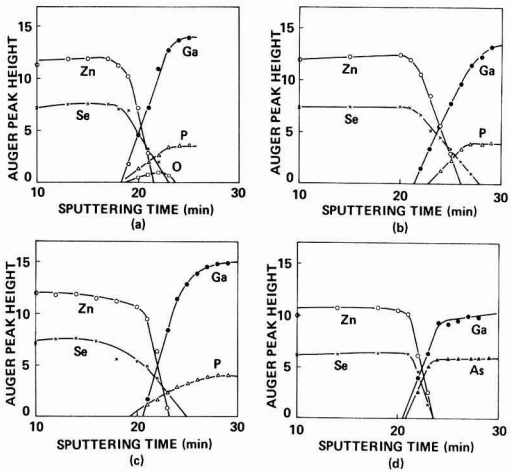

Fig. 4. In-depth profile of the Auger peak heights of various elements in the transition region between the substrate and the ZnSe grown layer after different thermal treatments of 570°C (a), 620°C (b), and 650°C (c) for the ZnSe-GaP system, and 600°C (d) for the ZnSe-GaAs system.

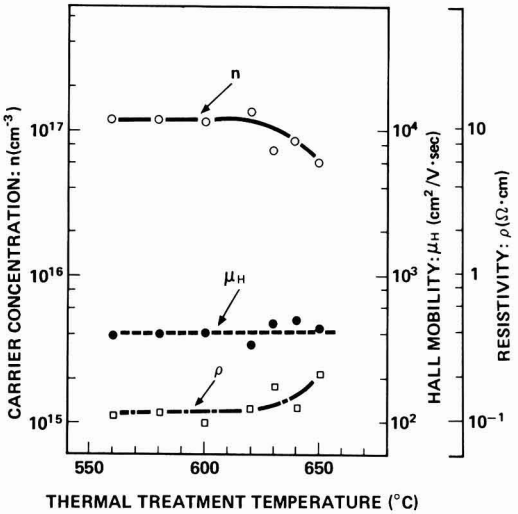

Fig. 5. The electrical properties of Ga-doped ZnSe layers grown on GaAs as a function of the thermal treatment temperatures, carrier concentration (○), Hall mobility (●), and resistivity (□).

thermal treatment of 600°C for the ZnSe-GaAs system, as shown in Fig. 4(d). The difference in the depth of the transition region between the ZnSe-GaAs and ZnSe-GaP systems may be attributed to the different lattice misfit. The Auger peak height of P for the ZnSe-GaP system at the thermal treatment temperature of 650°C gradually increases toward the substrate through the interface. This is attributed to the decrease in the concentration of P atoms at the surface due to the desorption during thermal treatment.

A Van der Pauw method and a photoluminescence measurement were employed to investigate the relation between the surface cleanliness of the substrate and the electrical and optical properties of Ga-doped ZnSe growth layers. The substrate temperature during growth was 320°C for the growth of ZnSe on GaAs and 360°C for the growth of ZnSe on GaP. The Ga cell temperature was fixed at 420°C for doping. Each sample used in the present study has a ~3 μm thick ZnSe grown layer.

Figures 5 and 6 show the dependence of electrical properties of the grown layer of Ga-doped ZnSe on GaAs and GaP on the thermal treatment temperatures, respectively. For the growth of ZnSe on GaAs, the carrier concentrations and resistivities remain unaltered until the thermal treatment temperature is raised to 630°C. For thermal treatment above 630°C, however, a decrease in the carrier concentration and an increase in the resistivity begin to appear. The mobilities do not change, though, for thermal treatment between 560° and 650°C. For the growth of ZnSe on GaP, the carrier concentration increases and the resistivity decreases as the thermal treatment temperature increases when the temperatures are raised from 550° to 630°C. This indicates that when higher thermal treatment temperatures are used, more improved electrical properties are obtained in the grown layers. This is possible because the reduction in the concentration of oxygen contaminants embedded across the interface can suppress the formation of the defect complexes associated with oxygen. On the contrary, the decrease in the carrier concentrations and the increase in the resistivities begin to appear at the thermal treatment temperature of 630°C, whereas the mobilities gradually increase even when the thermal treatment is raised to 650°C. For the growth of ZnSe on both GaAs and GaP, thermal treatments higher than 630°C result in a degradation of electrical properties. This may be attributed to the following. Since it is clear from the AES and RHEED observations that the surface roughness of the substrate results from the desorption of volatile host atoms (for example As and P) at the surface by thermal treatments higher than 650°C, a certain amount of volatile atoms can possibly be dissociated from the substrate surface even after being treated at 630°C and result in roughness of the substrate surface. As the result, we speculate that the degradation of electrical properties of the ZnSe layer may be due to the generation of unavoidable defect complexes into the epitaxial layer grown on the rough surface of the substrate.

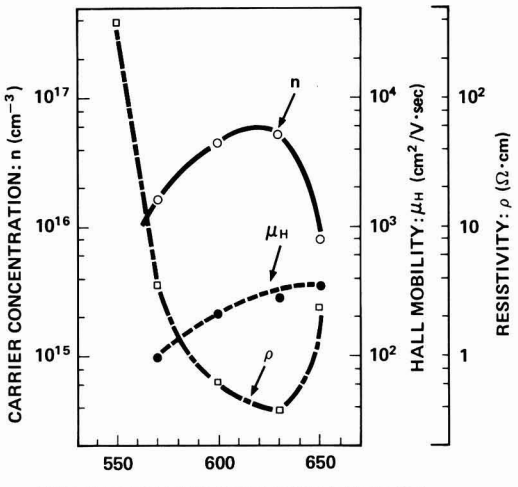

Fig. 6. The electrical properties of Ga-doped ZnSe layers grown on GaP as a function of the thermal treatment temperatures, carrier concentration (○), Hall mobility (●), and resistivity (□).

A room temperature photoluminescence spectrum of Ga-doped ZnSe grown by an MBE has a dominant

blue emission band with a peak of ~461 nm, which may be attributed to the recombination between donor electrons and free holes, and a longer wavelength broad yellow emission band with a peak of ~590 nm, which may be due to the defect complex centers associated with incorporated Ga atoms (6). Figures 7 and 8 show the relation of photoluminescence properties in the grown layer of Ga-doped ZnSe on GaAs and GaP to the thermal treatment temperatures, respectively. For the growth of ZnSe on GaAs, blue emission intensities remain unaltered until the thermal treatment of 630°C is used, whereas yellow emission intensities gradually increase as the thermal treatment temperature increases. For thermal treatment above 630°C, the reduction of both blue and yellow emission intensities begins to appear, as shown in Fig. 7. For the growth of ZnSe on GaP, the blue emission intensities monotonously increase, and the yellow emission intensities dramatically decrease as the thermal treatment temperature increases when the temperature is raised from 550° to 630°C. For thermal treatment above 630°C, however, a significant increase in yellow emission intensities begins to appear, whereas blue emission intensities slightly decrease.

From these electrical and optical data, we suggest that the degradation of characteristics in the ZnSe grown layers are probably based on the formation of defect complexes associated not only with oxygen contamination embedded across the interface during growth but also with the surface roughness arising from the desorption of volatile host atoms from the substrate surface by thermal treatments.

Summary

We have demonstrated that the surface morphologies and the electrical and optical properties of MBE grown ZnSe layers on both GaAs and GaP depend mainly on the surface cleanliness provided by a thermal treatment in a vacuum prior to growth.

After the chemical treatment procedure, the surfaces of both GaAs and GaP have carbon contaminants and residual oxide layers. Carbon contaminants left on the surface can easily be decomposed, but there is quite a difference in the removal behavior of oxidation products between GaAs and GaP. For GaAs, the thermal temperature required to explicitly remove oxidation products is around 570°C. For GaP, the removal of oxidation products begins to appear at ~550°C, and continues up to ~620°C. For GaAs, the surface shows a ringed diffraction pattern when oxidation products still remain. However, for GaP, the surface shows a spotty diffraction pattern caused by single crystalline oxidation products even though the surface is covered with the oxidation products. The important difference in the removal behavior of oxidation products between GaAs and GaP is attributed to the different oxidation products. For the growth of ZnSe on GaAs, after thermal treatment temperatures above 570°C, which is the temperature required to completely remove oxide layers, all of the surface morphologies of the growth at the initial stage of the 1000Å thickness exhibit a streak diffraction pattern. However, all of the substrate surfaces prior to growth show a spotty pattern. For the growth of ZnSe on GaP, the surface morphology of the growth at the initial stage of 1000Å thickness exhibits a spotty diffraction pattern, as does the substrate surface prior to growth, because oxidation products still remain across the interface. The surface morphology of growth at the total 3 μm thickness, however, changes to a streak diffraction pattern. After thermal treatment temperatures higher than 620°C, which is the temperature required to completely remove oxide layers, each surface morphology for growth at the initial stage of the 1000Å thickness exhibits a streak diffraction pattern.

We also investigated the relation of electrical and optical properties of the growth of ZnSe on GaAs and ZnSe on GaP to the surface cleanliness of the substrate after different thermal treatments. The electrical and optical properties of the growth of both ZnSe on GaAs and ZnSe on GaP depend mainly on the surface contaminations and morphologies of the substrate prior to growth.

In conclusion, we recommend that the most desirable thermal treatment temperature for the substrate prior to growth is in the temperature region between 560° and 630°C for the growth of ZnSe on GaAs, and between 620° and 630°C for the growth of ZnSe on GaP.

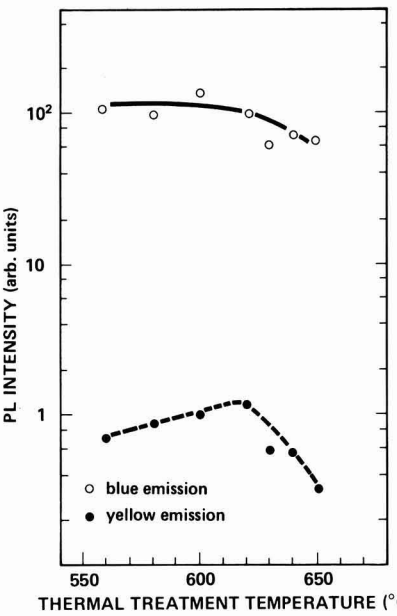

Fig. 7. The optical properties of Ga-doped ZnSe layers grown on GaAs as a function of the thermal treatment temperatures, blue emission (○) and yellow emission (●).

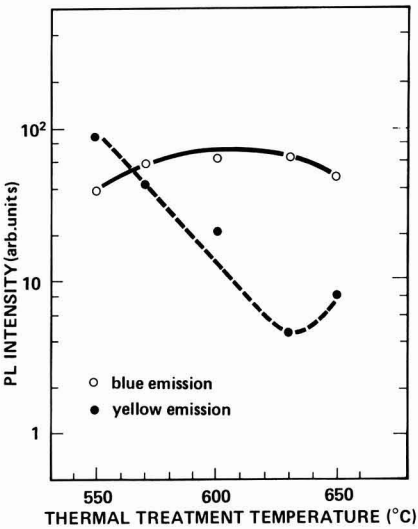

Fig. 8. The optical properties of Ga-doped ZnSe layers grown on GaP as a function of the thermal treatment temperatures, blue emission (○) and yellow emission (●).

Acknowledgments

The authors would like to thank Dr. M. Yamano and Dr. E. Komatsu of their Research Center for their guidance.

Manuscript submitted Feb. 7, 1983; revised manuscript received May 23, 1983.

Sanyo Electric Company, Limited assisted in meeting the publication costs of this article.

REFERENCES

1. C. C. Change, P. H. Citrin, and B. Schwartz, *J. Vac. Sci. Technol.*, **14**, 943 (1977).
2. A. Munoz-Yaque, J. Piqueras, and N. Fabre, *This Journal*, **128**, 149 (1981).
3. A. Trueba, E. Munoz, and J. Piqueras, *Solid State Commun.*, **15**, 199 (1974).
4. G. Laurence, F. Simondet, and P. Saget, *Appl. Phys.*, **19**, 63 (1979).
5. W. H. Koschel, R. S. Smith, and P. Hiesinger, *This Journal*, **128**, 1336 (1981).
6. T. Niina, T. Minato, and K. Yoneda, *Jpn. J. Appl. Phys.*, **21**, L387 (1982).
7. F. Kitagawa, T. Mishima, and K. Takahashi, *This Journal*, **126**, 341 (1979).
8. T. Niina, K. Yoneda, T. Toda, T. Minato, and K. Komeda, Collected papers of MBE-CST-2, 207 (1982) Tokyo.
9. C. A. Chang, *J. Vac. Sci. Technol.*, **21**, 663 (1982).
10. G. Lucovsky, *ibid.*, **20**, 761 (1982).

Hydrogen Gettering Effect of Mo_2N/Mo MOS Process

M. J. Kim* and D. M. Brown*

General Electric Company, Corporate Research and Development, Schenectady, New York 12301

ABSTRACT

Hydrogen plays a key role in maintaining the integrity of molybdenum film during high temperature processing. Hydrogen not only prevents Mo oxidation but also reduces Mo oxide, through an oxide gettering reaction at a high temperature, to produce pure molybdenum. γ-phase molybdenum nitride formed by direct reaction with ammonia can be converted to pure molybdenum after the nitride's beneficial properties have been utilized for MOS circuit fabrication. The recovery process is affected by hydrogen and the presence of an overlay layer. A recovery process for producing high conductivity Mo from Mo_2N and sputtered Mo film contaminated with oxygen was developed. This process always produces a consistent film regardless of the prior conditions to which the Mo film was subjected.

Molybdenum is receiving attention as a possible alternative to polysilicon, particularly as a VLSI interconnection, because of its high conductivity. The major problem associated with molybdenum film is its susceptibility to oxygen and moisture during the conventional semiconductor fabrication process. We have previously shown that a molybdenum nitride coating formed by direct reaction of molybdenum with ammonia improves film properties (1). This coating increased the resistance against oxidation, process chemicals, and implantation dopant penetration (2). The purpose of this study is to report the effect of hydrogen during the high temperature processing of molybdenum films. Hydrogen helps maintain the Mo film quality during the nitriding process and keeps the Mo film from oxidizing during subsequent annealing processes. It was found that Mo film resistivity which is high due to oxygen contamination is decreased by annealing in hydrogen through the reduction of the Mo oxide.

Experimental Procedure

Molybdenum films were deposited on thermally oxidized silicon wafers by using either a load-locked d-c magnetron or an S-gun sputtering system. The Mo deposition rate was 1500 Å/min with a d-c magnetron (MRC) and 720 Å/min with an S-gun (Varion). Films were sputtered at a 3 μTorr argon pressure, with the initial vacuum level about 10^{-7} Torr. The film thickness was varied from 1000 to 5000Å. (The film properties are dependent on the deposition conditions as discussed later.) Passivating Mo_2N films were made in the temperature range of 500°-750°C by direct reaction with 10% ammonia for 10 min in accordance with the method reported in Ref. (1). A submicron interconnection line could be patterned with reactive ion etch using CCl_4 and O_2. At a pressure of 250 μTorr, the etch rate of pure molybdenum was about 1000 Å/min and that of Mo_2N was 1400 Å/min.

Mo_2N was converted to pure Mo by a 1000°C annealing cycle in 10% hydrogen mixed with nitrogen. When it was necessary to retain Mo_2N, PSG or CVD SiO_2 was deposited prior to the high temperature annealing. Measurement of the sheet resistance was the most effective way to monitor the process. The thickness change of the Mo film was monitored by Sloan Dektak. All the temperature annealing processes were performed in a mixture of H_2 and N_2 gases with less than 10% of H_2. The hydrogen gettering effect was monitored by x-ray, SIMS, SEM, optical microscopy, and electrical measurements.

Experimental Results and Discussion

The qualification of Mo film for VLSI application has already been demonstrated (1, 2). Some of the features are listed in Table I. Primarily, Mo is stable in contact with SiO_2 at high temperature, with a high heat of formation [19 kcal/mol (3)] required for Mo to reduce SiO_2 to form molybdenum oxide, MoO_2. When the gettering technique is used, a highly conductive film, of better than 7.2×10^{-6} Ω-cm, can be produced. A submicron pattern can be achieved with either the RIE method or a wet etch. The patterned conductor can be passivated with Mo_2N. The film adhesion tested in accordance with ASTM D-3359-78 has been demonstrated to be excellent, with good thermal matching with silicon and SiO_2.

The Mo film properties, however, change with the deposition conditions as listed in Table II. The important properties for VLSI application, such as elec-

Table I. Qualification of Mo film for VLSI

1. Stable with SiO_2 (ΔH = 19 kcal/mol)
2. High conductivity (7.2×10^{-6} Ω-cm)
3. Easy to etch (RIE, wet)
4. Nitride passivation (Mo_2N)
5. Good adhesion (ASTM D-3359-78)
6. High melting point (2620°C)

* Electrochemical Society Active Member.

Key words: Mo films, VLSI, gettering, interconnection, conductivity.

Table II. Mo film property dependency

1. Deposition method
2. Equipment type
3. Growth rate
4. Initial vacuum
5. Residual pressure
6. Substrate temperature
7. Rotation rate
8. Deposition angle

trical and etching characteristics, are particularly sensitive to deposition conditions. Deposition methods, CVD, sputtering, and evaporation produce different structures and electrical properties. Although the films for this study were all sputtered, a film made in one type of equipment was different from that made in another. Even within a given system, the film properties vary with changes in growth rate, initial vacuum, residual pressure, substrate temperature,rotation rate, and deposition angle. Some of these parameters drastically change resistivity, while others affect etching characteristics such as etch rate and anisotropic etch. Since it is not easy to exactly control all of these parameters, films made at different times are not generally the same. A VLSI chip, on the other hand, requires consistent film properties. The following analysis shows that the hydrogen gettering process produces such consistent film characteristics, independent of deposition conditions and the past history of the film.

Mo_2N film is thermodynamically stable up to 900°C, above which temperature it dissociates into pure Mo and N_2 (4). Thus, Mo_2N can be converted to the higher conductivity Mo after the required properties of Mo_2N have been used. However, it is also possible to retain the Mo_2N film during the subsequent high temperature processing with an overlay layer such as SiO_2 or PSG deposited prior to the high temperature processing. The results with PSG and CVD SiO_2 were similar.

Figure 1 shows the change of sheet resistance of nitrided Mo films, ρ_s, with annealing time at 1000°C, with and without the PSG overlay film. The initial ρ_s is higher for samples nitrided at higher temperature, because a thicker nitride coating is formed. From our previous experiment (1), the six different temperatures would result in samples with different Mo_2N thicknesses; that is, they represent samples of 3000Å pure Mo, 220Å Mo_2N/Mo, 450Å Mo_2N/Mo, 870Å Mo_2N/Mo, 2000Å Mo_2N/Mo, and pure Mo_2N. The full curves represent the ρ_s changes of samples with the PSG overlay, and the dotted curves represent those with no PSG overlay. When the Mo_2N is exposed, the ρ_s is reduced rapidly to the lowest values, indicating the restoration to pure Mo; this is confirmed independently by x-ray diffraction analysis, which shows no trace of an Mo_2N diffraction line after annealing. It is interesting to note that the ρ_s of the nitrided samples reaches the minimum sooner than the ρ_s of the pure Mo sample. Table III shows the lattice parameter and the (110) Mo line broadening after the annealing of pure and nitrided Mo films. While no systematic change in lattice parameter was observed, there were significant line sharpenings of x-ray diffraction for the 1000°C annealed nitrided samples. The ρ_s of those samples that are covered with 5000Å PSG does not change significantly after annealing, indicating that most of the Mo_2N is still retained. In this case, the PSG presumably blocks the nitrogen escape required for the restoration.

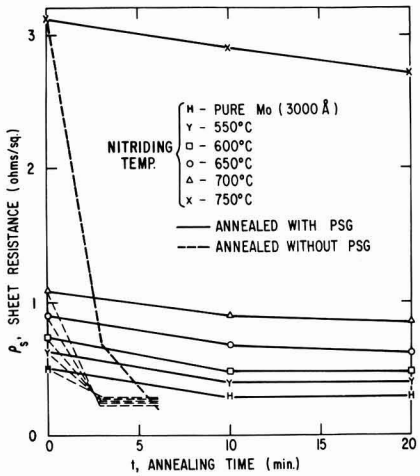

Fig. 1. Effect of annealing upon the resistance of nitrided Mo films. The annealing was performed at 1000°C in 10% H_2 + N_2, the full lines represent ρ_s changes during annealing with PSG overcoat and the dotted lines results without PSG.

Figures 2, 3, and 4 show, respectively. SEM photomicrographs of pure Mo, 650°C nitrided Mo, and 700°C nitrided Mo film with their subsequently annealed films. The pure, sputtered Mo (Fig. 2a) showed a uniform cross section, without crystal structures. When the 3000Å film was annealed for 30 min in 10% H_2 + N_2 at 1000°C, a columnar structure was developed, extending the grain boundary from the SiO_2 interface to the Mo surface, as shown in Fig. 2b. When the sample was annealed with the PSG overlay, a similar columnar structure was formed (Fig. 2c). For Fig. 3a the starting film was made by nitriding the 3000Å pure Mo film at 650°C in 10% ammonia for 10 min. This process resulted in about an 820Å Mo_2N film over the Mo but did not produce a columnar grain structure. Nor did the film shown in Fig. 4a, with 1900Å Mo_2N nitrided at 700°C, have any structural cross section. However, the annealed films with and without PSG overlays showed distinguished, large columnar grains. The only difference between these samples and the annealed pure Mo is that the grain size of the nitrided samples is not large enough to extend through 3000Å thickness for the samples shown in Fig. 3c and 4c, which are covered with PSG.

The structure of the nitrided Mo film did not show any columnar form (Fig. 3a and 4a). According to the structural analysis (1) the nitrogen atoms will not make a completely ordered structure but will randomly occupy the largest interstices. The nitriding converts the Mo β-phase to the Mo_2N γ-phase with fcc structure. According to SEM photomicrographs, the phase transformation apparently does not induce recrystallization, but, rather, maintains the partially amorphous state of the sputtered Mo film.

Table III. Lattice parameter and grain size changes observed by x-ray in Mo with different heat-treatments

Sample No.	T9-1	T9-2	T9-3	T9-4
Treatment history	No treatment (as sputtered)	1000°C anneal in (H_2 + N_2)	650°C nitriding, 1000°C anneal in (H_2 + N_2)	750°C nitriding, 1000°C anneal in (H_2 + N_2)
Lattice parameter a (angstrom)	3.144(3)	3.155(4)	3.139(2)	3.141(1)
2θ, Broadening 1/2 of (110) peak	0.442	0.369	0.255	0.270

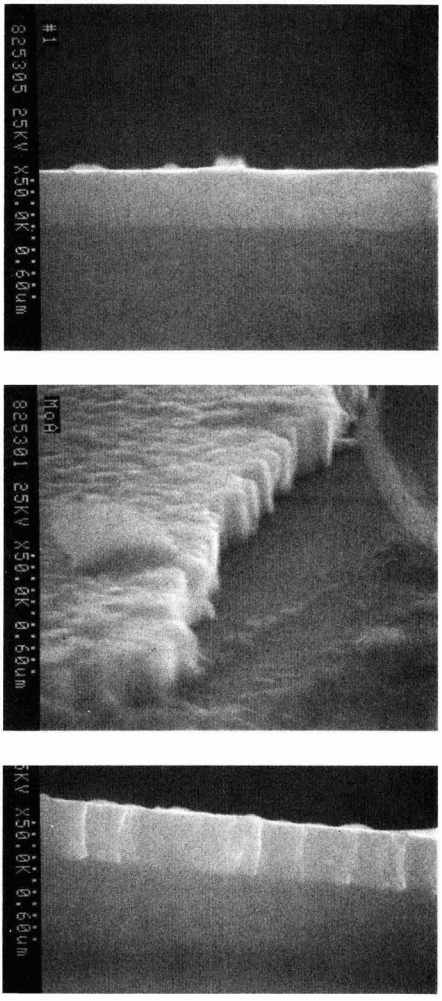

Fig. 2. SEM photomicrographs of pure Mo films of 3000Å; (a, top) as sputtered with a substrate temperature of 250°C; (b, center) annealed for 30 min in 10% H_2 + N_2 at 1000°C; (c, bottom) annealed same as (b) with PSG cover.

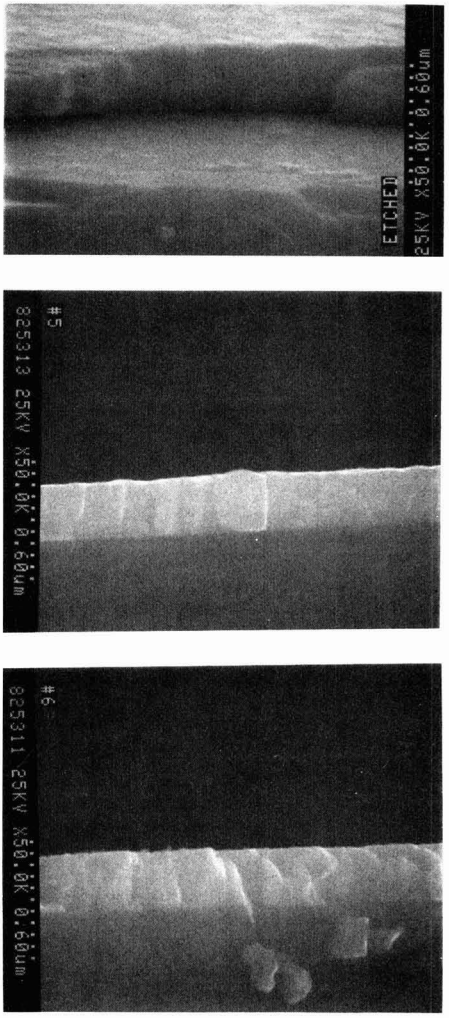

Fig. 3. SEM photomicrographs of 650°C Mo_2N/Mo film and its annealed films; (a, top) Mo_2N/Mo film made by nitriding at 650°C for 10 min to 820Å Mo_2N; (b, center) annealed for 30 min in 10% H_2 + N_2 at 1000°C; (c, bottom) annealed same as (b) with PSG cover.

Taking into account the dominance of (110) x-ray intensity in the annealed sample, the columnar direction is [110] perpendicular to the surface. As will be shown later, hydrogen annealing reduces Mo oxide near the grain boundary, and the columnar structure appears to have a tendency to increase the film tension during the annealing. A curvature measurement of the Mo film showed that the annealing increased the tension from the lower stress of the sputtered film. An original stress of 7.12×10^9 dyne/cm^2 for the sputtered film on a (100) silicon wafer at 3 μTorr Ar pressure was increased to 1.9×10^{10} dyne/cm^2 by annealing for 30 min at 1000°C. Another contributing factor to the resistivity reduction for the nitrided samples may be their larger grain size, which was observed with the line sharpening.

Figure 5 shows the ρ_s of the re-nitrided films. The pure Mo recovered from the nitride was again nitrided at the corresponding temperature for 10 min in 10% NH_3 + N_2. The nitriding reaction rate was very small in the temperature range of 500°-700°C but increased rapidly around 750°C. A resistivity peak, similar to the nitridation of sputtered Mo (1), as shown by the dotted curve, occurred at 820°C. The resistivity peak is caused by the transformation to the MoN δ-phase from the Mo_2N γ-phase. The position of the peak was shifted for the re-nitridation by a 30°C rise in temperature. The changes may also be caused by the grain size growth of Mo film during the annealing process; the growth of single crystals retards the nitrogen diffusion through the Mo, as observed in the significant reduction of the nitriding rate below 750°C. By way of contrast, corresponding heating in N_2 increased the ρ by about 30% without producing any trace of nitride.

Figure 6 shows the resistivities of S-gun-sputtered and d-c magnetron-sputtered Mo films as a function of film thickness, in their as-sputtered condition and after H_2 annealing. The substrate temperature for both cases was 250°C. The initial resistivity of the S-gun-sputtered film was more than three times that of the d-c magnetron-sputtered films and it increased rapidly below 3000Å. When the films were annealed at 1000°C in 10% H_2 + N_2, both resistivity values

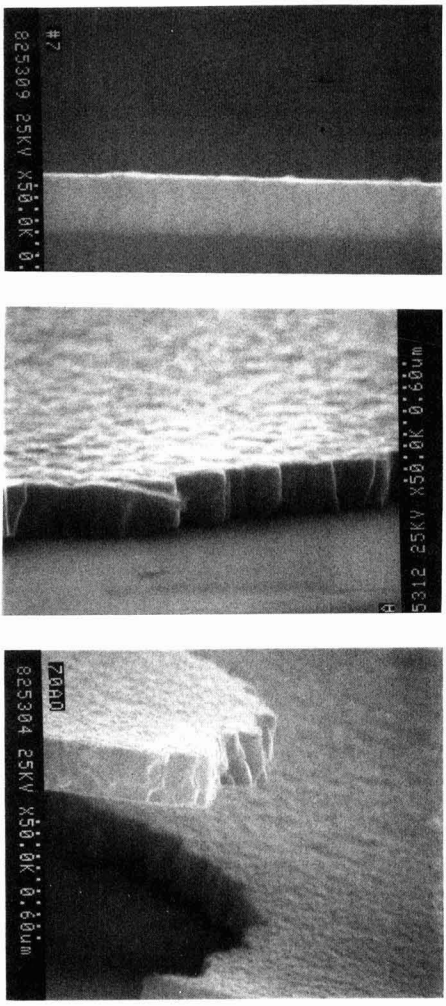

Fig. 4. SEM photomicrographs of 700°C Mo_2N/Mo film and its annealed films; (a, top) Mo_2N/Mo film made by nitriding at 700°C for 10 min to make 1900Å; (b, center) annealed for 30 min in 10% $H_2 + N_2$ at 1000°C; (c, bottom) annealed same as (b) with PSG cover.

converged to the same value, represented by curve C. The annealed resistivity, 7.1 $\mu\Omega$-cm was relatively independent of film thickness above 2000Å, a result that agrees well with an evaporated Mo film (5). The resistivity increase below 2000Å may be caused by columnar-like monolayer grain boundary scattering, as shown in SEM photomicrographs. The film quality recovery process was analyzed from the different origins. This behavior may be understood in terms of oxygen incorporation in the as-deposited films. In a low vacuum (5×10^{-7} Torr) the major constituent is observed to be water vapor (6), which can oxidize the Mo film grain boundary, increasing its resistivity.

The S-gun-sputtered Mo contains a larger amount of oxygen than does the magnetron-sputtered film because of its slow deposition rate. The high resistivity is correlated with the larger oxygen content for S-gun-sputtered Mo. Further, S-gun-sputtered films etch (RIE) 40% faster than do d-c magnetron films, probably due to accelerated formation of the volatile molybdenum oxychlorides as etch products (7). Hydrogen annealing removes the oxygen through the formation of volatile H_2O, and both types of film exhibit the same resistivity. Direct evidence is provided by SIMS analysis.

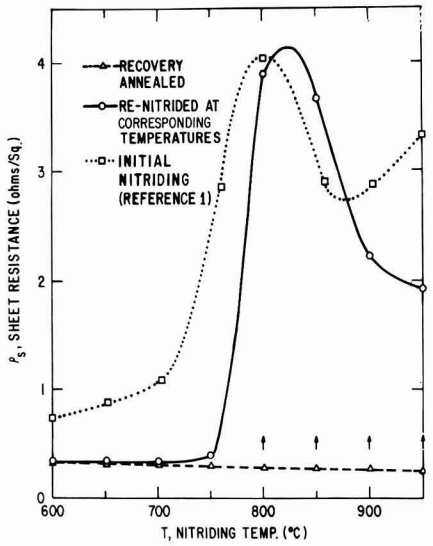

Fig. 5. Sheet resistance change as a function of re-nitriding temperature after the recovery annealing of the nitrided films at the corresponding temperature; ρ_S is compared with that of the initial nitride made from sputtered Mo.

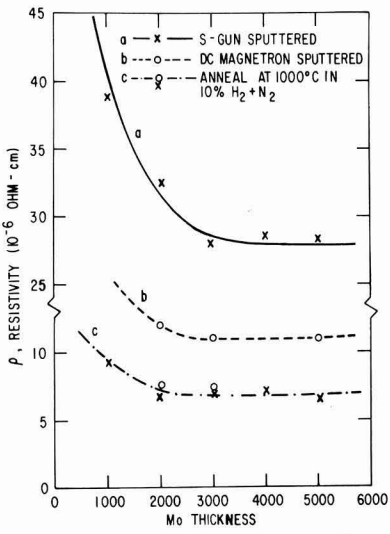

Fig. 6. Comparison of the resistivity of three different molybdenum films as a function of thickness. S-gun-sputtered Mo film (curve a) initially shows much higher resistivity than d-c magnetron-sputtered film (curve b) Mo, but both curves converge to a lower resistivity (curve c) after the annealing in H_2.

Figure 7 shows a SIMS profile analysis of the oxygen content for 4000Å S-gun-sputtered Mo samples like those in Fig. 4. In order to increase the sensitivity to oxygen, negative cesium ions were used. Curves a, b, and c represent ion intensity before annealing for oxygen (M. 16), silicon (M. 30), and molybdenum (M. 98), respectively. Curve a' represents the oxygen ion intensity after annealing in 10% $H_2 + N_2$ for

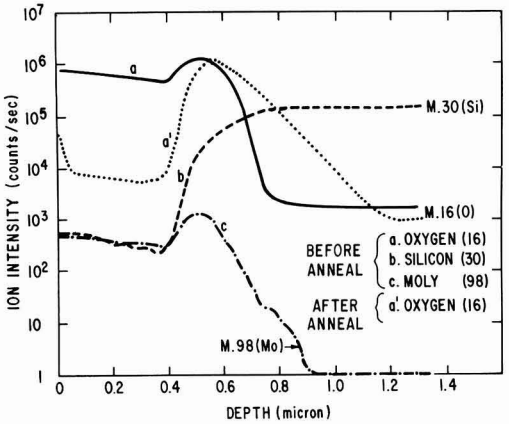

Fig. 7. SIMS depth profile of oxygen for the S-gun molybdenum film as sputtered and after the annealing. The oxygen intensity after the annealing (curve a') is two orders of magnitude lower than that before the annealing (curve a).

30 min at 1000°C. The oxygen content as measured by the intensity is reduced by two orders of magnitude by the annealing, a finding which proves that the large postannealing resistivity reduction shown in Fig. 6 is caused by the hydrogen gettering effect of the oxygen in the Mo film.

Figure 8 shows the effect of the gettering on the property of the films with different histories. The initial 3000Å film was sputtered with a d-c magnetron, and one wafer was divided into four specimens. Two of the four were nitrided at 650°C to coat with 870Å Mo_2N. A nitrided specimen and a sputtered specimen were annealed in 10% H_2 + N_2 for 30 min at 1000°C. The oxygen profiles in the four different Mo films are presented in Fig. 8. The Mo^- (M.90) and Si^- (M.30) for sputtered films are also shown as reference. Near the surface, the oxygen intensity of the sputtered specimen was about seven times higher than that of the nitrided specimen. The hydrogen by-product in the nitridation appears to partially getter the oxygen, and the nitride keeps oxygen from penetrating the Mo film afterward. The large oxygen step shift of curve b near the Mo/SiO_2 boundary is caused by the thickness expansion during the nitriding (1). When both types of film are annealed,

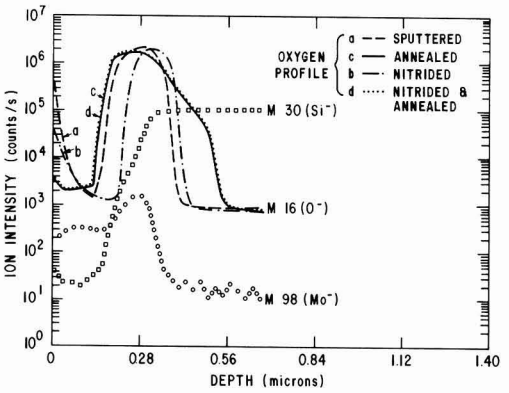

Fig. 8. Oxygen profile in d-c magnetron molybdenum films with different histories. Curve a represents a sputtered film, curve b the nitrided, curve c the annealed, and curve d the annealed after nitridation. The annealed curves have identical oxygen profiles.

their oxygen profiles, curves c and d, are exactly the same.

Figure 9 represents the Mo film process flow required to have a unique film quality. The Mo film can either be made by a high temperature process in a large grain form or sputtered at a low temperature to produce a partially amorphous state. The H_2 + N_2 annealing at the high temperature getters impurities, oxygen in particular, and makes a <110> columnar structure, resulting in a consistent film quality as an end product.

Molybdenum films increased in resistivity upon annealing in nitrogen due, we believe, to the presence of residual O_2 or H_2O in the gas. Any trace of oxygen will, upon heating, convert Mo near the grain boundary to MoO_2. The oxidized grain boundaries increase the reflection coefficient of electrons (4) at the grain boundary, causing a resistivity increase.

In the presence of hydrogen, MoO_2 can be reduced to pure molybdenum by the following reaction

$$\tfrac{1}{2}\,Mo_2O(s) + H_2(g) = \tfrac{1}{2}\,Mo(s) + H_2O(g) \quad [1]$$

$$K = P_{H_2O}/P_{H_2}$$

where K, P_{H_2O}, and P_{H_2} are the equilibrium constant, partial pressure of H_2O, and partial pressure of H_2, respectively. Thus, when the hydrogen partial pressure is high, Mo reduction can take place at relatively low temperatures. The most accurate measurement of K useful in our range of interest was done by Gocken (8). He reports the value

$$\log K = -1298/T + 0.798 \quad [2]$$

where T is the absolute temperature. At our annealing temperature of 1000°C, K is 0.575. Since we are using much higher H_2 partial pressure than Gocken's we expect rapid MoO_2 reduction at 1000°C. Even if we assume that all the resistivity reduction of the MRC film is contributed by the grain growth, the resistivity reduction of the S-gun film is more than 10 times higher than the contributions from grain growth. Thus, the amount of sheet resistance reduction during 10% H_2 annealing (Fig. 6) is much more than the expected contribution from grain size growth shown in Fig. 2 and 3, indicating that MoO_2 reduction is the dominant factor in the improvement of conductivity, particularly for poor films.

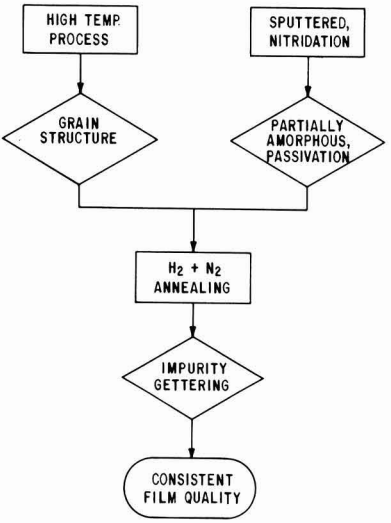

Fig. 9. Molybdenum film process flow

Conclusion

Hydrogen not only prevents oxidation of Mo but also reduces Mo oxide during high temperature annealing. Hydrogen partial pressure sufficiently in excess of the equilibrium required for reduction is easily obtained by a dilute mixture with any inert gas. For Mo nitriding in ammonia, the monatomic hydrogen dissociated from ammonia plays a key role in maintaining the integrity of the Mo underneath. Hydrogen also plays a key role in conversion to high conductivity Mo from Mo_2N by the high temperature recovery process. The high temperature gettering produces a consistent film integrity, independent of the past history of the Mo film.

Acknowledgments

The authors wish to thank M. Garfinkel, M. Ghezzo, and T. J. Soltys for their constructive advice. The authors also appreciate the processing assistance of P. A. Piacente, D. M. Skelly, and R. H. Wilson.

Manuscript submitted Jan. 25, 1983; revised manuscript received May 25, 1983.

General Electric Company assisted in meeting the publication costs of this article.

REFERENCES

1. M. J. Kim, D. M. Brown, and W. Katz, *This Journal*, **130**, 1196 (1983).
2. M. J. Kim and D. M. Brown, Extended Abstract IEDM, 560 (1982); *IEEE Trans. Electron Devices*, **ed-30**, 598 (1983).
3. G. V. Samsonov, "Handbook of High-Temperature Materials," No. 2, Plenum Press, New York (1964).
4. A. Sieverts and G. Z. Zapf, *Z. Anorg. Allg. Chem.*, **229**, 161 (1936) (.
5. K. Uda, Y. Matsushita, and S. Takasu, *J. Appl. Phys.*, **51**, 1039 (1980).
6. H. Oikawa, *J. Vac. Sci. Technol.*, **15**, 1117 (1978).
7. B. Gorowitz and R. Saia, To be published in *J. Am. Vac. Soc.*
8. N. A. Gocken, *Trans. AIME*, 1019 (1953).

The Retarded Diffusion of Arsenic in Silicon by Thermal Oxidation in Extrinsic Conditions

Y. Ishikawa, M. Tomisato, H. Honma, and S. Matsumoto

Department of Electrical Engineering, Keio University, Hiyoshi, Yokohama 223, Japan

T. Niimi

Department of Applied Physics, Tokai University, Hiratsuka 259, Japan

ABSTRACT

Arsenic diffusion in extrinsic conditions in silicon is investigated with different temperatures (950°-1100°C) and times under both oxidizing and inert atmospheres. Arsenic is prediffused into a silicon substrate from arsenic-silica film and is then subjected to a drive-in under oxidizing (dry O_2) and inert (dry N_2) atmospheres. The diffusion coefficient of arsenic is expressed by a third-order polynomial equation of arsenic concentration. This functional form is determined by fitting the arsenic concentration profile, which is calculated numerically from the diffusion equation with the functional form of diffusion coefficient assumed appropriately, to the concentration profile measured after drive-in. The diffusion coefficient is smaller under oxidizing atmosphere than under inert atmosphere at 1000°-1100°C. The degree of retarded diffusion decreases with the increase of diffusion time.

The diffusion of group III and group V elements in silicon under oxidizing atmosphere has been studied extensively. It is well known that the diffusion of boron, phosphorus, and arsenic is enhanced under oxidizing atmosphere in intrinsic conditions (1-7), and the model for this experimental result was proposed by Hu (8). The term of the intrinsic conditions means that the concentration of diffused impurity in silicon is lower than the intrinsic carrier concentration at the process temperature.

On the other hand, there are only a few works on the diffusion of boron and phosphorus under oxidizing atmosphere in extrinsic conditions, which were reported by Masetti *et al.* (9, 10) and Taniguchi *et al.* (11). Here the extrinsic conditions mean that the concentration of diffused impurity in silicon is higher than the intrinsic carrier concentration at the process temperature. There are no works on the diffusion of arsenic under oxidizing atmosphere in extrinsic conditions at present. In these cases, the diffusion coefficient depends on the concentration of impurity. This fact makes the analysis of the experimental results difficult. Both Masetti *et al.* (9, 10) and Taniguchi *et al.* (11) neglected the concentration dependence of the diffusion coefficient in their analysis. Practically, the situation that an impurity is diffused in extrinsic conditions is not uncommon for the fabrication of a device, *e.g.*, formation of drain and source wells of MOS transistor. Especially, arsenic diffusion in extrinsic conditions is important.

Key words: oxidation, diffusion, retardation, semiconductor.

In this paper, the diffusion of arsenic under oxidizing atmosphere is examined with different temperatures and times in extrinsic conditions in detail. The diffusion coefficient is expressed by a third-order polynomial equation of arsenic concentration. This functional form is determined by the numerical simulation.

Experimental

The substrates used were Czochralski-grown, p-type, dislocation-free, (100) oriented silicon wafers of resistivity 2.7-3.3 Ω-cm. Arsenic-silica film was attached on to the substrates, using a spinner. These substrates were baked at 200°C for 20 min in dry N_2. After baking, the thickness of the film was about 1500Å. Then arsenic contained in this film was prediffused into the substrates at 1100°C for 12 min. After the removal of the film, drive-in was carried out. For drive-in in dry N_2, the silicon surfaces were covered with a nondoped silicon dioxide film to avoid out-diffusion of arsenic.

Arsenic concentrations in the substrates were determined both after the prediffusion and the drive-in by the repetition of the sheet resistance measurements and anodic oxidation in phosphoric acid (H_3PO_4) solution. The average thickness of a thin layer removed by

a single run was about 100Å. Measured resistivities were converted into the concentrations of arsenic by the use of Irvin's curve (12).

In order to determine the relationship between the oxide growth rate and the oxidation time, the wafers in which arsenic was prediffused were oxidized thermally at 950°-1100°C for different times at respective temperatures in dry O_2. Silicon dioxide thickness was measured by the interference microscope.

Analysis

Under oxidizing atmosphere, the diffusion equation in silicon takes the form (13)

$$(\partial c/\partial t) = \partial/\partial x\{D(c)\ (\partial c/\partial x) + bc(dX_o/dt)\} \quad [1]$$

where t is the diffusion time, x is the depth from the silicon-silicon dioxide interface into silicon, $c(x,t)$ is the arsenic concentration in silicon, $D(c)$ is the diffusion coefficient of arsenic, which depends on arsenic concentration because arsenic concentration is higher than the intrinsic carrier concentration, $X_o(t)$ is the thickness of silicon dioxide that is growing on silicon surface, and b is the ratio of the thickness of silicon consumed by thermal oxidation to that of silicon dioxide grown on it [assumed to be 0.44 (13)].

The initial condition to solve Eq. [1] is

$$c(x,0) = c_{in} \quad [2]$$

Here, c_{in} denotes the concentration profiles measured after prediffusion. The boundary conditions are as follows

$$c(\infty,t) = 0 \quad [3]$$

$$D(c)\ (\partial c/\partial x) + c(0,t)\ (b - m)\ (dX_o/dt) = 0 \quad [4]$$

where m is the segregation coefficient of arsenic at silicon-silicon dioxide interface. The relationship

$$X_o = K\sqrt{t} \quad [5]$$

was confirmed and the proportional constant, K, was determined by thermally oxidizing the wafers in which arsenic was prediffused and by measuring the thickness of silicon dioxide. The values of K used in this work are shown in Table I.

Equation [1] was transformed into the finite-difference equation following Crank-Nicolson's implicit method. The relationship between D and c was expressed by Eq. [6]

$$D(c) = Ac^3 + Bc^2 + Cc + D \quad [6]$$

The finite-difference equation made from Eq. [1] was numerically solved by a computer simulation method with the function of $D(c)$ (Eq. [6]) assumed appropriately. The concentration profile $c(x,t)$, thus obtained, was compared with the experimental results. The function of $D(c)$ was determined so as to fit best the calculated concentration profile to the experimental concentration profile. In this simulation, a segregation coefficient m was adopted to be 0.01 irrespective of the diffusion temperature and the arsenic concentration at silicon surface. This value is the same as we used in our previous paper (16) which studied the oxidation-enhanced diffusion of arsenic and phosphorus in intrinsic conditions.

Under inert atmosphere, Fick's diffusion equation, which has a form of Eq. [1] without the second term of the right-hand side, was numerically solved like the case of oxidizing atmosphere under the blocking boundary conditions.

Table I. Values of K

Oxidation temperature (°C)	Values of K (cm/sec$^{1/2}$)
950	7.60×10^{-8}
1000	1.00×10^{-7}
1050	1.27×10^{-7}
1100	2.00×10^{-7}

Results and Discussion

Typical concentration profiles of arsenic under oxidizing and inert atmosphere are shown in Fig. 1 and 2, respectively. After the prediffusion, all samples in this work have the surface concentration of 5-7 $\times$ 10^{19} cm^{-3}. This value is much higher than the intrinsic carrier concentration at 950°-1100°C, satisfying the extrinsic conditions.

Figure 3 shows the concentration dependence of the arsenic diffusion coefficients. The diffusion coefficients of arsenic under inert atmosphere obtained by Fair and Tsai (14) and those obtained by Murota *et al.* (15) are shown together with our results. Also the intrinsic diffusion coefficients of arsenic obtained by the authors

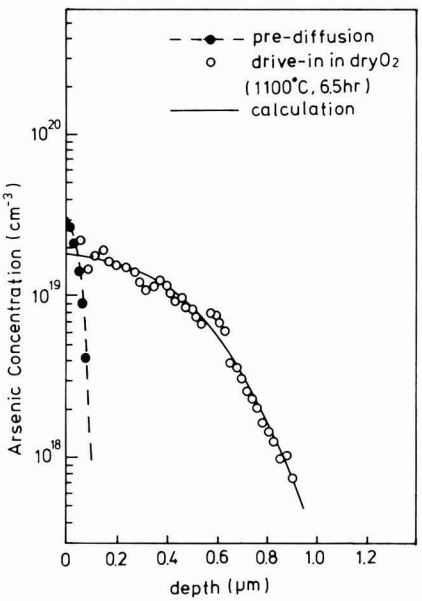

Fig. 1. Profiles of arsenic concentration (dry O_2)

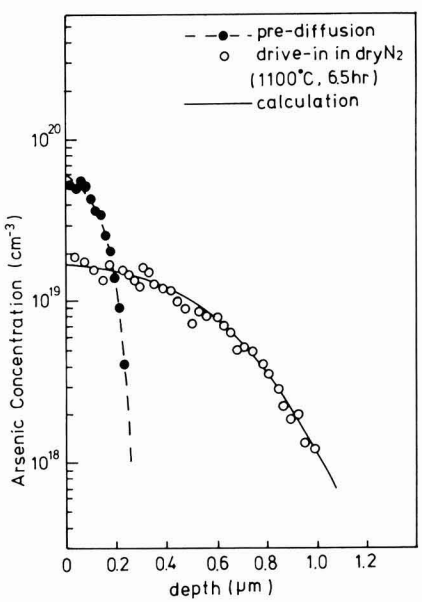

Fig. 2. Profiles of arsenic concentration (dry N_2)

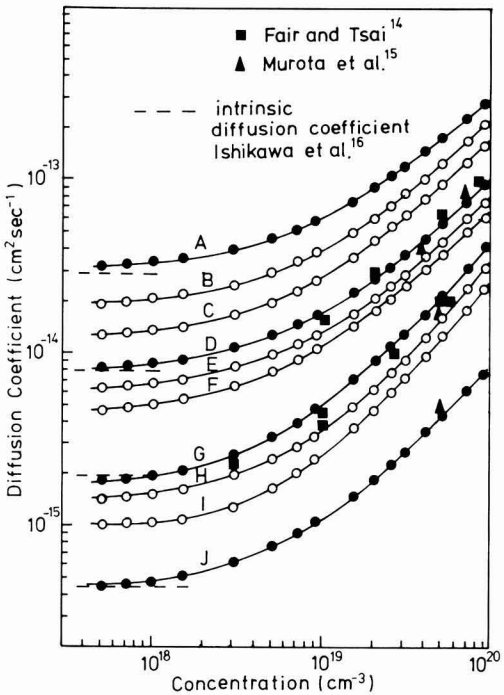

Fig. 3. Arsenic concentration dependence of diffusion coefficients. A: 1100°C 1 hr dry N_2 and 1100°C 6.5 hr dry N_2. B: 1100°C 6.5 hr dry O_2. C: 1100°C 1 hr dry O_2. D: 1050°C 6 hr dry N_2 and 1050°C 29.5 hr dry N_2. E: 1050°C 29.5 hr dry O_2. F: 1050°C 6 hr dry O_2. G: 1000°C 5.5 hr dry N_2 and 1000°C 30 hr dry N_2. H: 1000°C 30 hr dry O_2. I: 1000°C 5.5 hr dry O_2. J: 950°C 30 hr dry N_2, 950°C 54 hr dry N_2, 950°C 30 hr dry O_2, and 950°C 54 hr dry O_2.

are shown (16). A good agreement of our results under inert atmosphere with those of others supports the validity of the present procedure for the determination of the diffusion coefficient of arsenic. It is found, from Fig. 3, that the diffusion coefficients of arsenic under oxidizing atmosphere are smaller than the values under inert atmosphere all over the arsenic concentration range investigated in this work at 1000°-1100°C, that is, the retarded diffusion occurs. The degree of the retarded diffusion decreases with the increase of diffusion time. The retarded diffusion is not found at 950°C. We have already reported on oxidation-enhanced diffusion of arsenic in intrinsic conditions in Ref. (16). Our results in this work are in contrast with our previous results obtained in intrinsic conditions.

It is well known that the concentration dependence of the diffusion coefficient of arsenic under inert atmosphere in extrinsic conditions is explained by the generation of excess vacancies on the basis of the predominant contribution of the vacancy for arsenic diffusion (14, 18). Thus, we infer the present result as follows qualitatively. The concentration of vacancies is decreased by the recombination of vacancies and excess self-interstitials which are generated by thermal oxidation of silicon. Consequently, vacancy concentration becomes lower than the value under inert atmosphere, and the retarded diffusion occurs. Moreover, the diffusion coefficients under oxidizing atmosphere are smaller than the intrinsic diffusion coefficients at a relatively low concentration region at 1000°-1100°C (Fig. 3). This fact suggests that the vacancy concentration can become lower than the value under thermal equilibrium conditions at the deep region in arsenic concentration profiles.

The cause of the diffusion time dependence of the degree of the retarded diffusion may be considered briefly. The oxidation rate of silicon decreases with the increase of oxidation time. Thus, the degree of the excess in self-interstitial concentration decreases and the vacancy concentration is not decreased so much by the recombination. Therefore, the degree of the retarded diffusion decreases with the increase of diffusion time.

Conclusions

The arsenic diffusion coefficient in extrinsic conditions, which is a function of arsenic concentration, is determined under both oxidizing and inert atmospheres. It is found that the arsenic diffusion coefficient is smaller under oxidizing atmosphere than under inert atmosphere at 1000°-1100°C. The degree of this retarded diffusion decreases with the increase of diffusion time. We infer that excess silicon self-interstitials that are generated by thermal oxidation of silicon recombine with vacancies, and the concentration of vacancies becomes lower than the value under inert atmosphere, so the retarded diffusion occurs.

Manuscript submitted Feb. 3, 1983; revised manuscript received June 1, 1983.

Keio University assisted in meeting the publication costs of this article.

REFERENCES

1. G. N. Wills, *Solid-State Electron.*, **12,** 133 (1969).
2. W. G. Allen, *ibid.*, **16,** 709 (1973).
3. D. Antoniadis, A. G. Gonzales, and R. W. Dutton, *This Journal*, **125,** 813 (1978).
4. D. Antoniadis, A. M. Lin, and R. W. Dutton, *Appl. Phys. Lett.*, **33,** 1030 (1978).
5. R. Francis and P. S. Dobson, *J. Appl. Phys.*, **50,** 280 (1979).
6. A. M. Lin, D. Antoniadis, and R. W. Dutton, *This Journal*, **128,** 1131 (1981).
7. C. Hill, in "Semiconductor Silicon 1981," H. R. Huff, Y. Takeishi, and R. J. Kriegler, Editors, p. 988, The Electrochemical Society Softbound Proceedings Series, Pennington, NJ (1981).
8. S. M. Hu, *J. Appl. Phys.*, **45,** 1567 (1974).
9. G. Masetti, S. Solmi, and G. Soncini, *Philos. Mag.*, **33,** 613 (1976).
10. G. Masetti, S. Solmi, and G. Soncini, *Solid-State Electron.*, **19,** 545 (1976).
11. K. Taniguchi, K. Kurosawa, and M. Kashiwagi, *This Journal*, **127,** 2243 (1980).
12. J. C. Irvin, *Bell Syst. Tech. J.*, **41,** 387 (1962).
13. M. M. Atalla and E. Tannenbaum, *ibid.*, **39,** 933 (1960).
14. R. B. Fair and J. C. C. Tsai, *This Journal*, **122,** 1689 (1975).
15. M. Murota, E. Arai, K. Kobayashi, and K. Kudo, *J. Appl. Phys.*, **50,** 804 (1979).
16. Y. Ishikawa, Y. Sakina, H. Tanaka, S. Matsumoto, and T. Niimi, *This Journal*, **129,** 644 (1982).
17. R. B. Fair and G. R. Weber, *J. Appl. Phys.*, **44,** 273 (1973).
18. S. M. Hu and S. Schmidt, *ibid.*, **39,** 4272 (1968).

Photoelectrochemical Studies of Nearly Intrinsic Semiconductors Made Possible by Using Photoconductivity

H. Gerischer,* M. Lübke, and B. Bressel

Fritz-Haber-Institut der Max-Planck-Gesellschaft, D-1000 Berlin 33, Germany

ABSTRACT

Photocurrent generation for nearly intrinsic semiconductor electrodes has an extremely small quantum yield because the space charge layer is insufficient to promote the efficient separation of electron hole pairs when suitable biases are applied. However, if the bulk material can be made photoconductive, a space charge layer having a higher electric field strength will be created. It is demonstrated that thin platelets of GaS and CdS, although insulating in the dark, can be used as photoelectrodes if they are illuminated with light having energy less than the bandgap in addition to light having energy above the bandgap. With this arrangement, high quantum yields similar to those obtained for well-doped semiconductors are obtained. The charge distribution in a semiconductor platelet under various modes of illumination is discussed.

Photoelectrochemical studies are usually performed with adequately conducting n- or p-type materials where the doping level is high enough to keep the resistance low between the electrode/electrolyte and the ohmic contact at the rear. It is only with these materials that the bias applied creates a large enough electric field in the space charge layer underneath the semiconductor/electrolyte interface so that an efficient separation of the electron hole pairs generated by light absorption can occur (1-4). This condition, however, excludes many materials from photoelectrochemical studies because either they do not have a high enough doping level due to their formation conditions or they cannot be produced in such a state. The authors demonstrate here that many of these materials can be studied photoelectrochemically if their internal resistance can be far enough reduced by means of photoconductivity. For this purpose, one needs two light sources, one of which is only weakly absorbed and can penetrate the whole bulk of the material thus making it photoconductive. If the light from the other source is absorbed close to the interface, mainly within the diffusion length of the electronic charge carriers, photocurrents with high quantum yield can be obtained. This option was discovered during studies of GaS crystals when samples were available which were mainly of very low conductivity or were even insulating in character. Thin plates of insulating CdS crystals were used as models because the properties of this material are much better known. Some typical results are reported in order to demonstrate the principal features of this approach. A more detailed publication of these studies will follow.

Experimental

Thin slices of GaS crystals were obtained by cleaving thicker crystals received from F. Lévy, Lausanne. They were contacted with In-Hg and mounted on brass in Teflon cylinders which could be inserted into normal electrolysis cells. The edges of the crystal plates were protected with silicon rubber. The thickness of the crystal plates was in the order of 0.2-0.5 mm. Thin single-crystal plates of CdS, grown by sublimation of cadmium sulfide in a gas stream, were obtained from R. Broser of this institute. These were contacted with In and mounted in the same way described above. As electrolytes, 1M KCl for GaS and 0.5M Na_2SO_3 for CdS were used. Illumination was performed with chopped monochromatic light at different wavelengths. Continuous or pulsed light from the second lamp, which passed an interference filter or a cut-off filter cutting off all light above a fixed energy, could be superimposed. Photocurrents were measured by the lock-in technique. Voltages were measured against a saturated calomel electrode.

* Electrochemical Society Active Member.

Key words: photoconductivity, photocurrent relaxation, photoelectrochemistry, semiconductors, GaS, CdS.

Results

Figure 1 shows the absorption spectra of GaS (5) and CdS (6). The bandgaps are 2.7 eV for GaS (indirect) and 2.4 eV for CdS (direct). It turned out that the photocurrents generated by the monochromatic light source alone with a quantum energy larger than the bandgap were very small and increased linearly with increasing bias. However, after adding light from a second light source with a quantum energy cutoff below the bandgap energy, a much larger photocurrent was obtained compared to the monochromatic light source alone. The photocurrent caused by the second lamp alone was very small.

With sufficient intensity of the secondary light source (I'), the photocurrent caused by the primary light source (I) approached saturation and was thus similar

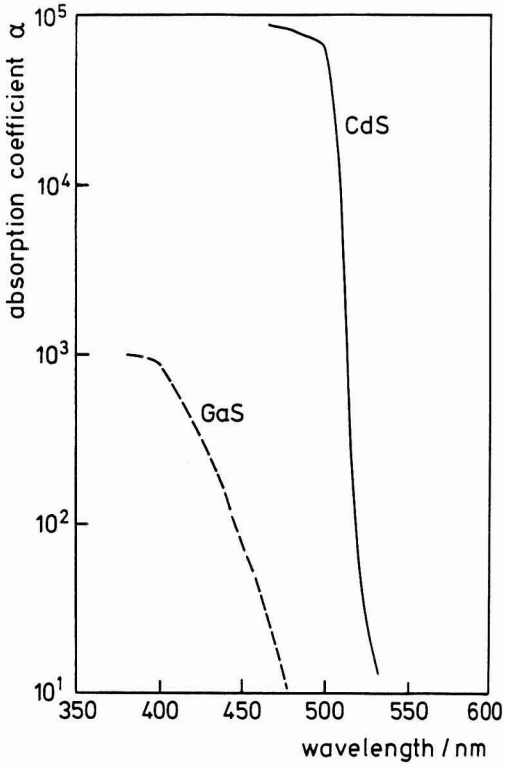

Fig. 1. Absorption coefficients of GaS (5) and CdS (6)

in behavior to that exhibited by a normally doped specimen. Figure 2 shows photocurrent voltage curves for a GaS slice with insulating character, illuminated with light of $\lambda = 360$ nm alone or with the admixture of light that had passed a cut-off filter of 495 nm. N- and p-type photoconductivity has been observed in this material depending on the method of crystal preparation (7). The GaS specimen exhibited a p-type photoconductivity. Therefore, a negative bias was applied so that the photocurrent was cathodic, resulting in hydrogen evolution because of the reduction of water by photogenerated electrons.

Analogous experiments have been performed with CdS, which is normally an n-type material. The specimen in this experiment had a doping level below 10^{13} cm^{-3} and was therefore essentially insulating. The photocurrent voltage curves for a specimen under illumination with light of $\lambda = 430$ nm alone and with admixture of light with $\lambda = 518$ nm are shown in Fig. 3. Since the CdS crystals have a much higher absorption coefficient than the GaS crystals, a saturation photocurrent was reached with a modest bias when a sufficient intensity of light from the secondary source (I') was added. The saturation current under these conditions was proportional to the intensity of the primary light source (I) as Fig. 3 indicates.

The photocurrent quantum yield obtained with one light source alone is shown as a function of wavelength in Fig. 4. This figure also shows the yield spectrum during additional illumination by the second light source with subbandgap energy. One clearly sees the enormous differences in the above bandgap energy range caused by the additional illumination.

The efficiency of the second light source is dependent on its wavelength as is demonstrated in Fig. 5 for GaS. This figure shows the additional photocurrent induced by the chopped light source with a wavelength of 400 nm (above bandgap) during a continuous illumination by the second light source. The wavelength of the latter light is varied with a monochromator. One sees

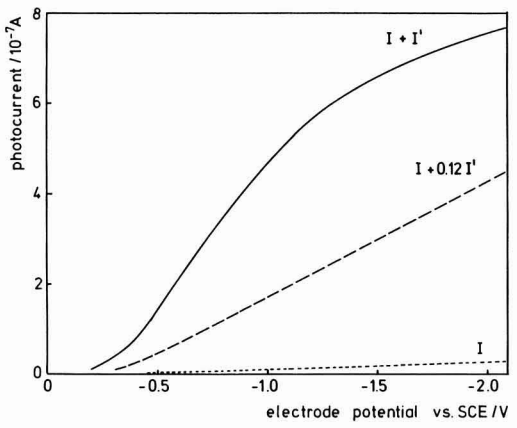

Fig. 2. Photocurrent voltage curves for a GaS crystal ($d = 0.5$ mm) in 1M KCl under illumination with 360 nm light (I) alone and with additional illumination by light with $\lambda > 495$ nm (I') at two different intensities.

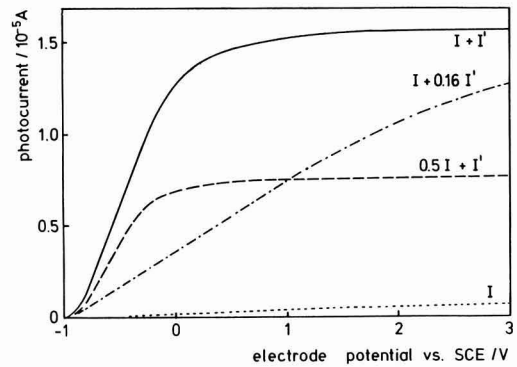

Fig. 3. Photocurrent voltage curves for a CdS crystal ($d = 0.2$ mm) in 0.5M Na_2SO_3 under illumination with 430 nm light (I) alone with additional illumination by light of $\lambda = 518$ nm (I').

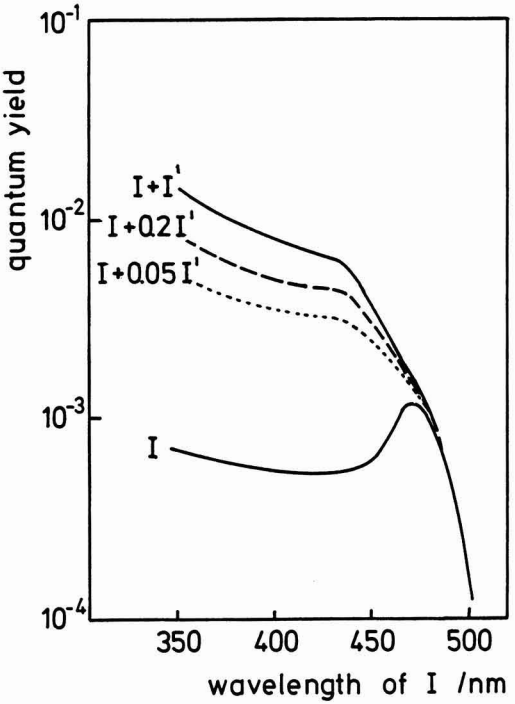

Fig. 4. Spectral dependence of the photocurrent quantum yield for chopped monochromatic light (I) alone and with additional continuous illumination by subbandgap light (I'). GaS at −1V bias vs. SCE in 1M KCl; I' ($\lambda > 495$ nm with cut-off filter).

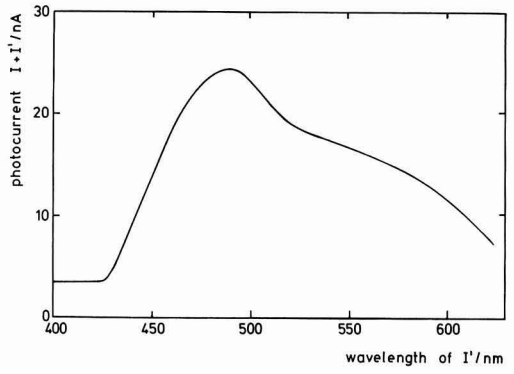

Fig. 5. Spectral dependence of the increase of the photocurrent due to chopped light at $\lambda = 400$ nm (I) by continuous illumination with a second light source (I'). GaS crystal of 0.48 mm thickness, electrolyte 1M KCl, bias −1.55V (vs. SCE).

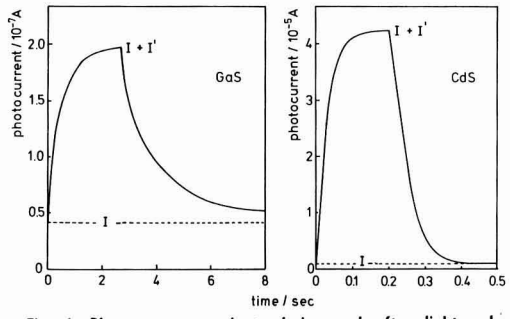

Fig. 6. Photocurrent transients during and after light pulse with subbandgap light I', added to above bandgap light I. GaS electrode as in Fig. 2 at −0.9V bias I at $\lambda = 390$ nm; I' with $\lambda > 495$ nm. CdS electrode as in Fig. 3 at +2.6V bias I at $\lambda = 440$ nm; I' with $\lambda = 518$ nm.

that there is an optimal wavelength for the effect of the second light source.

Finally, the photocurrent relaxation behavior, when a pulse of light having subbandgap energy is added, is shown in Fig. 6. The relaxation time for GaS is on the order of 1 sec and for CdS on the order of 10^{-2} sec. Such relaxation times, as shown in Fig. 6, are typical for photoconductivity (8-10). Photocurrent relaxation times for light pulses of the primary light source, maintaining constant illumination by the second light source, are much shorter.

Discussion

The very low quantum yield of the photocurrents generated by the primary light source alone is obviously caused by the high internal resistance of the semiconductor. The spectral dependence of the quantum yield with a single lamp is maximum at wavelengths where the light can penetrate the crystal to a considerable extent. This wavelength is dependent on the thickness of the crystal plate, as seen in additional experiments. The conclusion is that light absorption in the bulk reduces the internal resistance therein by photoconductivity. The increased conductivity of the bulk has the consequence that the voltage drop, caused by the applied bias, decreases in the bulk and is concentrated to a narrower region underneath the semiconductor/electrolyte contact where electron hole pairs can be separated more efficiently. Light which has wavelengths resulting in a small penetration depth compared to the thickness of the crystal cannot create considerable photocurrents because the electron hole pairs are generated in a region with a low electric field strength in the dark. Under illumination, the field in this region is to a large extent compensated or even overcompensated by an opposite field due to space charge generation. Only a very small fraction of carriers can escape recombination by diffusion or migration in the remaining electric field under these circumstances.

The situation is drastically changed if a second light source with the appropriate wavelength makes the bulk of the crystal photoconductive. The internal resistance of the crystal decreases, and the voltage applied concentrates at the interface between the crystal and the electrolyte. The existence of a maximum for the efficiency of the second light source, shown in Fig. 5 for GaS, demonstrates this photoconductivity effect. The optimum is to be expected for light which penetrates the whole crystal sufficiently well but is not too weakly absorbed. Light which is too strongly absorbed leaves the rear part of the crystal nonconductive, while light with a very small absorption coefficient induces a too low photoconductivity in the bulk.

With a higher electric field strength underneath the contact to the electrolyte, electron hole pair separation can become much more efficient for light with a high absorption coefficient. Mobile charge carriers with suitable sign, which are generated within this region of high field strength or reach it by diffusion during their lifetime, escape recombination and can at the semiconductor/electrolyte interface oxidize or reduce the redox components in solution.

Photoconductivity can have a rather long relaxation time if one of the photogenerated charge carriers is captured in deep traps which have a relatively small cross section for recombination. In the GaS samples, such traps were present for electrons but the holes remained mobile. The authors could therefore create large cathodic photocurrents. For CdS, the opposite situation existed in that holes were trapped in long-lived states (8-10) while the electrons remained mobile. If one assumes that the number of traps for electrons or holes is in the order of 10^{14}-10^{15} cm^{-3} (10), one can then easily imagine that a depletion layer similar to doped materials can be formed by such trapped charge carriers. Though a quantitative description has still to be developed, the authors can qualitatively explain their results with the above model.

The model is summarized in Fig. 7 for a thin insulating CdS specimen under anodic bias in part (a) for the run of the electric potential: (*i*) in the dark, (*ii*) under illumination by the primary light source alone (I), and (*iii*) with additional illumination by a second light source (I'). It is seen that the bias creates a kind of Schottky barrier in the photoconductive

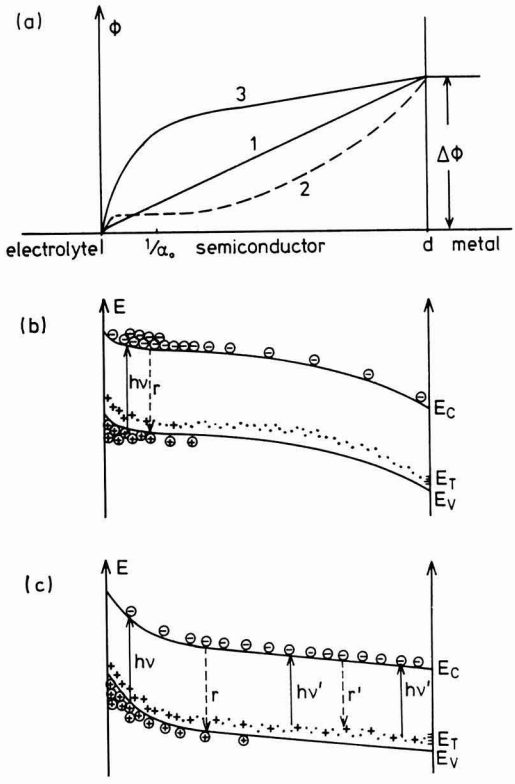

Fig. 7. (a) Run of the electric potential in a thin insulating CdS crystal with applied constant bias $\Delta\phi$. Case 1: in the dark; 2: with above bandgap illumination alone (I); 3: with additional subbandgap illumination (I + I'). (b and c): Schematic representation of the charge distribution in the energy bands and in traps for holes over the semiconductor slice in the steady state of illumination: (b) case 2; (c) case 3. r, r' = recombination.

crystal at the semiconductor/electrolyte interface and, if the illumination intensity from the second light source is intensive enough, the crystal can act like a doped material with a depletion layer at the contact to the electrolyte.

Parts b and c of Fig. 7 represent schematically the charge distribution, via an energy band diagram, under steady-state illumination for an insulating CdS crystal of thickness d at positive bias in accordance with the above model. Figure 7b shows the situation for above bandgap light alone, where electrons and holes remain concentrated at the illuminated surface and can easily recombine. Figure 7c illustrates the efficient charge separation made possible by the high electric field in the depletion layer because the trapped positive charge in the bulk (the energy position of the traps is indicated by dots) compensates the charge of the mobile electrons therein and keeps the bulk conductive.

That the quantum yield for GaS is considerably lower than for CdS can be explained by the absorption coefficient of GaS which is two orders of magnitude smaller than that of CdS at the wavelengths used in these experiments. This has the consequence that in GaS the penetration depth of the above bandgap light is much larger than the diffusion length of the holes, and it can only be expected that electron hole pairs, which are generated within a distance from the surface corresponding to the diffusion length, contribute to the photocurrents.

Acknowledgments

The authors express their gratitude to Dr. F. Lévy, Lausanne, and Dr. R. Broser for supplying the crystals of GaS and CdS, respectively. They also thank Dr. G. Scholz for his help in preparing the manuscript.

Manuscript submitted Dec. 6, 1982; revised manuscript received *ca.* April 1, 1983.

REFERENCES

1. H. Gerischer, in "Physical Chemistry," Vol. IX, H. Eyring, D. Henderson, and W. Jost, Editors, pp. 463-542, Academic Press, New York (1970).
2. A. J. Nozik, *Ann. Rev. Phys. Chem.*, **29**, 189 (1978).
3. R. H. Wilson, *J. Appl. Phys.*, **48**, 4292 (1977).
4. H. Reiss, *This Journal*, **125**, 937 (1978).
5. G. A. Akhundov, S. A. Musaev, A. E. Bakhyshev, N. M. Gasanly, and L. G. Musaeva, *Sov. Phys. Semicond.*, **9**, 94 (1975).
6. D. Dutton, *Phys. Rev.*, **112**, 785 (1958).
7. A. H. M. Kipperman and G. A. van der Leeden, *Solid-State Commun.*, **6**, 657 (1968).
8. I. Broser and R. Warminsky, *Ann. Physik*, **7**, 289 (1950).
9. J. Lambe, *Phys. Rev.*, **98**, 985 (1955).
10. R. H. Bube, *J. Phys. Chem. Solids*, **1**, 234 (1957).

Technical Notes

Efficient D-C Electroluminescence from ZnS:Mn and ZnS:TbF_3 Thin Films Prepared by RF Sputtering

H. Ohnishi, N. Sakuma, and K. Ieyasu

Department of Electronics Engineering, Faculty of Engineering, Ehime University, Matsuyama, Ehime 790, Japan

Y. Hamakawa

Department of Electrical Engineering, Faculty of Engineering Science, Osaka University, Toyonaka, Osaka 560, Japan

Intensive studies have been made on thin film electroluminescent (EL) devices because of their considerably higher potential in the commercial demands for a flat-type display unit. A doubly insulated ZnS:Mn a-c operated device, showing a good display performance in brightness, efficiency, and life, has approached the practical stage (1-3). The tremendous strides have been followed by the film preparation methods of molecular beam epitaxy (4), atomic layer epitaxy (5), and metal organic chemical vapor deposition (6). In contrast to a yellowish-orange emitter, more informative multicoloring devices have been fabricated by employing the rare earth fluorides as luminescent centers (7, 8). The doubly insulated ZnS:TbF_3 device, prepared usually by an electron beam evaporation, exhibits 0.1-0.2 lm/W of highest efficiency among rare earths (8, 9). Attention has been paid to the rf sputtering method because of high productivity, impurity controllability, etc. The authors have conducted a series of studies on the electroluminescence from ZnS films deposited by rf sputtering. It has been found that an efficiency beyond 0.15 lm/W is typically obtained from the system of Al-ZnS:TbF_3-$InSnO_x$ MS structure. This work presents the d-c excited characteristics of ZnS films activated with TbF_3 and Mn. The effects of impurity concentration and film thickness on the luminescence are also presented.

Key words: electroluminescence, ZnS thin films, rf sputtering.

The mixed powder of 5-nines ZnS and 3-nines TbF_3 or Mn metal was sintered at 400°-500°C for 3 hr in argon gas to exclude the absorbed gas. The mixture settled on a quartz saucer of 105 mm was used as a sputtering target. The phosphor films were deposited on an $InSnO_x$-coated glass substrate heated at 150°C under the sputtering condition of argon gas pressure = 1.45 Pa, rf power density = 1.27 W/cm^2, anode voltage = 1.5 kV. The target electrode and substrate-target space were 100 and 40 mm, respectively. The deposition rate was in a range of 150-250 Å/min. After the film preparation, heat-treatment was made at 450°-480°C in a vacuum to remove point or small defects neighboring the luminescent centers. The

Al-ZnS:TbF_3 (or Mn)-$InSnO_x$ structure was formed by depositing Al as a counterelectrode. The luminance was measured by a brightness meter, TOPCON BM-3.

The d-c electroluminescence is usually observed in a fabricated device with an Al electrode positively biased and often observed in a reversely biased case. The current-voltage and brightness-voltage relationships show nonlinear characteristics. Figure 1 shows the typical current-voltage and brightness-voltage characteristics of the both type devices. As can be seen, the voltage dependences are steeper in the ZnS:Mn device than the ZnS:TbF_3 device. The ZnS:Mn system has the threshold voltage from low to high conductance regions. The luminescent intensity increases with elevating applied voltage. The threshold field is about 1×10^6 V/cm, which is compatible with the strength reported conventionally. The ZnS:TbF_3 system, however, does not have a clear threshold and shows weaker voltage-dependence than ZnS:Mn. The reason for the steeper characteristics of the Mn device than the TbF_3 device is not understood as yet. The device sometimes suffers from damage called "burning out" beyond the voltage where the current abruptly increases. The obtainable brightness level is limited by permissible current through the device. A brightness level of 600 f-L has been obtained, but typically 200-300 f-L. Such limitation is due to the local thermal breakdown that gives rise to formation of a patch in the Al electrode. The efficiency depends on the electrical input power as shown in Fig. 2. The efficiency increases with increasing input power at low voltage because of its strong field dependence. The maximum efficiency is measured as 0.13 lm/W at 2.4×10^{-4} W/cm² for ZnS:Mn while it is 0.17 lm/W at 9×10^{-2} W/cm² for ZnS:TbF_3. As the input is further increased, the power dissipation raises the device temperature so that the efficiency decreases. One of the reasons for weak temperature quenching of the TbF_3 device can be explained on the basis that the rare earth centers have poorer

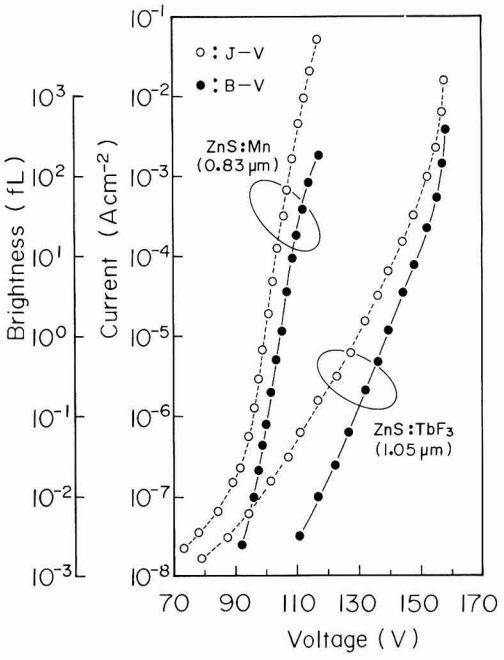

Fig. 1. Current-voltage and brightness-voltage characteristics of d-c EL devices consisting of ZnS:Mn 0.83 μm thick and ZnS:TbF_3 1.03 μm thick.

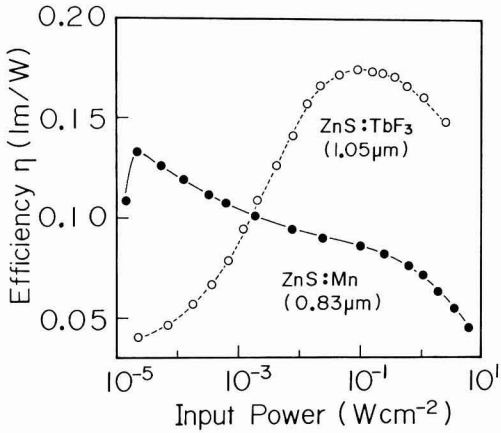

Fig. 2. Efficiency-input power relationships of ZnS:Mn and ZnS:TbF_3 d-c EL devices.

phonon impedance match with the ZnS host lattice than the Mn center.

Figure 3 shows the dependence of efficiency on the impurity concentration in sputtering target. The linear dependence at low densities is due to the increase in the number of the luminescent centers. The maximum efficiency, typically 0.15 lm/W and sometimes beyond 0.2 lm/W, is attained at 1.8 atomic percent (a/o) for ZnS:TbF_3 while it is 0.8 a/o for ZnS:Mn. An optimal density for ZnS:TbF_3 agrees with the value that Krupka *et al.* (10) have determined for the concentration in the films by x-ray fluorescence method. This agreement suggests that the rf sputtering method has a good controllability of impurity concentration. In the higher density region, the efficiency is decreased as a result of concentration quenching. This phenomenon contains two possible mechanisms: the increase of nonradiative transition, presumably due to pairing, and the decrease of electron mean free path. Figure 4 shows maximum efficiency as a function of the ZnS:TbF_3 layer thickness. Efficiency steeply increases up to 0.15 lm/W with the increase of the film thickness and saturates above 0.45 μm. Low efficiency in a thin region can be explained by the experimental results of the x-ray diffraction pattern, which has shown that the

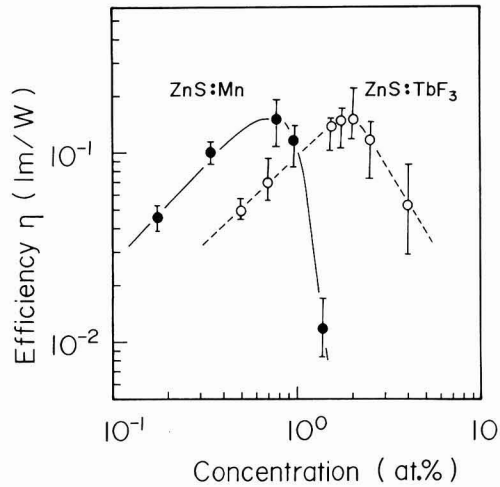

Fig. 3. Efficiency of ZnS:Mn and ZnS:TbF_3 as a function of impurity concentration.

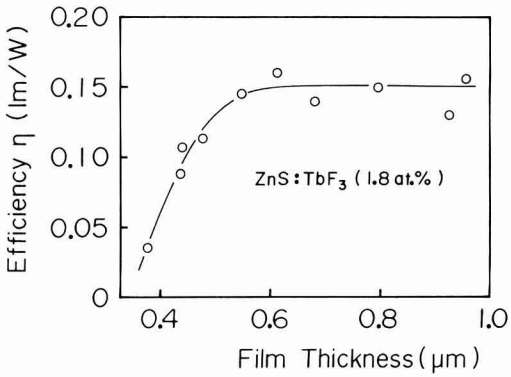

Fig. 4. Efficiency of ZnS:TbF_3 as a function of film thickness

crystallinity of the thin films is poorer than the thick films. The electric field is 1.5-1.8 $\times$ 10^6 V/cm at a high brightness level, which means the requirement of driving voltage is above 70V. Low voltage operation can be achieved if the crystallinity is improved in the thin region. The experimental approaches to reduce the threshold voltage and to optimize the film preparation condition are in progress.

Acknowledgments

The authors wish to express their gratitude to Drs. T. Nishino, M. Okuyama, and H. Takakura of Osaka University for their encouragement and valuable discussions throughout the course of this work. They also would like to thank H. Harada, H. Hamaguchi, H. Yoshino, and S. Takahara of Ehime University for their technical assistance during the investigation. This work is partially supported by Grant-in-Aid for Scientific Research from the Ministry of Education, Science, and Culture.

Manuscript submitted Feb. 14, 1983; revised manuscript received May 6, 1983.

REFERENCES

1. T. Inoguchi, M. Takeda, Y. Kakihara, Y. Nakata, and M. Yoshida, *SID Dig.*, 84 (1974).
2. T. Inoguchi and S. Mito, in "Electroluminescence," I. J. Pankove, Editor, Chap. 6, pp. 197-210, Springer-Verlag, Berlin (1977).
3. M. Takeda, Y. Kanatani, H. Kishishita, T. Inoguchi, and K. Okano, *SID Dig.*, 66 (1980).
4. T. Mishima, W. Quan-Kun, and K. Takahashi, *J. Appl. Phys.*, **52**, 5797 (1981).
5. T. Suntola, J. Anston, A. Pakkala, and S. Lindfors, *SID Dig.*, 108 (1980).
6. A. F. Cattell, B. Cockayne, K. Dexter, J. Kirton, and P. J. Wright, Conf. Record Inter. Display Res. Conf., p. 20 (1982).
7. E. W. Chase, R. T. Hepplewhite, D. C. Krupka, and D. Kahng, *J. Appl. Phys.*, **40**, 2512 (1969).
8. T. Suyama, N. Sawara, K. Okamoto, and Y. Hamakawa, *Jpn. J. Appl. Phys.*, **21**, Suppl. **21-1**, 383 (1982).
9. L. G. Hale, B. Garcia, R. D. Ketchpel, and T. C. Lim, *IEDM Dig.*, 719 (1980).
10. D. C. Krupka and D. M. Mahoney, *J. Appl. Phys.*, **43**, 2314 (1972).

Electrical Conduction Through Polysilicon Oxide: Interface Texture vs. Isolated Protuberances

P. A. Heimann,* P. S. D. Lin,* and T. T. Sheng

Bell Laboratories, Murray Hill, New Jersey 07974

The high electrical conductivity of oxides grown from polycrystalline silicon (poly-oxide), in comparison to the conductivity of oxides grown from single-crystal silicon, has been attributed by several workers (1-5) to asperities or protuberances at the polysilicon/poly-oxide interface. These protuberances cause a local enhancement of the electric field at the interface (3, 6) which leads to conduction through the poly-oxide by Fowler-Nordheim tunneling at a lower value of applied voltage than would be required for a smooth interface.

It has recently been found that polysilicon prepared with a smooth surface yields a marked improvement in poly-oxide dielectric properties (7), and this work was confirmed by the use of *in situ* phosphorus-doped polysilicon (8). Elevated oxidation temperature also appears to yield a smoother interface (5, 9).

The interface as seen in transmission electron micrographs (9) shows three types of textural features: a roughness due to the grain structure of the film, bumps about 0.1-0.3 μm wide due to growth anomalies during polysilicon deposition, and sharper protuberances formed during oxidation. The protuberances vary in height and surface density, with upper limits of about half the oxide thickness and about 1 $\times$ 10^7/cm^2, respectively.

The purpose of the present work was to determine whether the observed electrical currents are injected into the oxide mainly at the isolated sharp protuberances and large bumps or at the granular features and small bumps found all over the interface. Measurements were made of the current *vs.* field through samples of small areas which should contain few or no protuberances or large bumps, and of the current observed in a scanning electron microscope operated in the electron-beam-induced current (EBIC) mode.

Sample Preparation and Measurement

Low-pressure chemical vapor deposited (LPCVD) *in situ* phosphorus-doped polysilicon was deposited at 700°C onto substrates [1000Å oxide grown on 25 Ω-cm p-type (100) silicon wafers] and was oxidized at 1050°C in steam for 10 min, to yield a 1200Å thick oxide. The oxide thickness was determined from the capacitance of large-area devices, from a stylus step-height measurement after removing part of the oxide, and from TEM cross sections. All measurements agreed to within 10%. For EBIC studies, a thin ($\approx$1000Å) layer of evaporated aluminum was deposited using a shadow mask to yield 20 mil dots. For electrical measurements, 1200Å of LPCVD silicon nitride was deposited and contact windows of various areas from 7 μm^2 to 1.6 $\times$ 10^7 μm^2, were etched using CF_4/O_2 reactive ion etching. Aluminum electrodes were then deposited and patterned to yield the structure shown in Fig. 1.

Electrical conduction through the poly-oxide was measured using a home-built voltage ramp and a

* Electrochemical Society Active Member.

Key words: insulator, tunneling, capacitor, semiconductor.

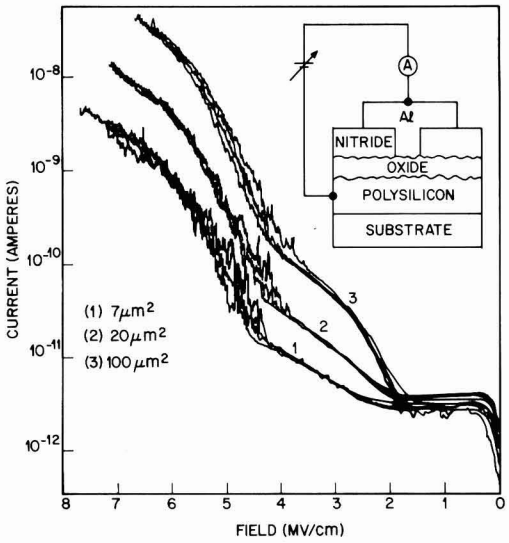

Fig. 1. Current vs. electric field for several poly-oxide samples. Note the similarity of the curves for devices of the same area.

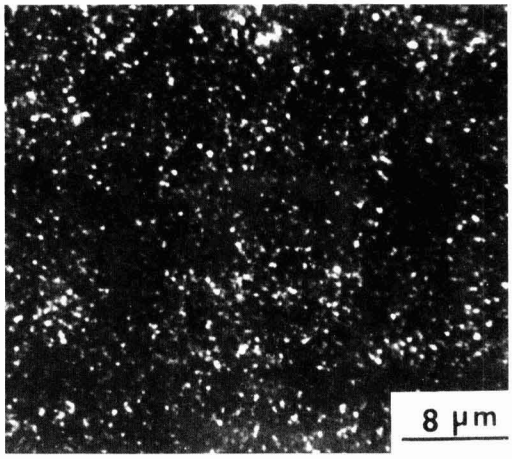

Fig. 2. EBIC image of capacitor (≈1000Å aluminum as top electrode, 1200Å of poly-oxide, +20V bias on electrode, 15 kV primary electron voltage). Bright features are interpreted as due to enhanced emission of electrons at protuberances.

Keithley Model 26120 logarithmic picoammeter. The details of this method have been described previously (5). If the electrical conduction arises from isolated protuberances or bumps, then the current-voltage curves for different small-area devices on a wafer should be markedly different.

The spatial variation of the electric current was also studied "directly" using a scanning electron microscope (Cambridge Stereoscan S4) in the high-field EBIC mode (10). In this technique, hot secondary electrons generated in the sample by the incident beam are injected into the poly-oxide. The injection is enhanced in regions of high local electric field, which gives rise to bright spots in the EBIC image.

Results and Discussion

The current-voltage curves for devices with areas of 7, 20, and 100 μm^2 (four devices each) are shown in Fig. 1. There is very little variation among different devices of the same area, which indicates that there must be many sites per square micron for enhanced-field injection of electrons into the poly-oxide. The same conclusion can be drawn from the EBIC image shown in Fig. 2, which shows that sites of locally enhanced current have a minimum spacing of about 0.3 μm. This is about the same spacing as that of the interface features in the TEM cross section (Fig. 3). This spacing is equivalent to about 5-25 active sites per square micron, or at least 35 active sites even in the smallest area tested for electrical conductivity.

These results show that the observed conduction through the poly-oxide arises from the enhanced electric fields at many closely spaced active sites at the polysilicon/poly-oxide interface. These sites are a property of the general texture of the interface, and one need not assume that there are large currents at isolated defect sites. These results do not pinpoint the exact nature of the active sites. They could be the high spots on the numerous bumps (see Fig. 3), since there is considerable electric field enhancement at the surface of even a moderately curved bump, as compared to the electric field at a flat interface (5). They could also be the points where the polysilicon grain boundaries meet the oxide, since the nonstoichiometry and strained bonds at these points could lower the silicon-oxide energy barrier.

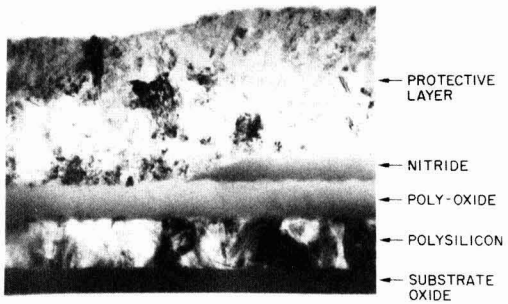

Fig. 3. TEM cross section of polysilicon/poly-oxide structure. The aluminum electrode has been replaced by a protective polysilicon layer. The substrate oxide is 1000Å thick.

Marcus *et al.* (9) have observed that the interface has nearly the same texture as that of the original polysilicon surface, which suggests that an initially smooth polysilicon surface is needed to achieve a poly-oxide with low leakage. Such oxides have recently been reported by Sternheim *et al.* (8).

Acknowledgments

We would like to thank R. A. Levy for depositing the *in situ* doped polysilicon, and R. B. Marcus and A. K. Sinha for their suggestions and encouragement.

Manuscript submitted April 5, 1983; revised manuscript received June 9, 1983. This was Paper 195 presented at the Detroit, Michigan, Meeting of the Society, Oct. 17-21, 1982.

Bell Laboratories assisted in meeting the publication costs of this article.

RERERENCES

1. D. J. DiMaria and D. R. Kerr, *Appl. Phys. Lett.*, **27**, 505 (1975).
2. R. M. Andersen and D. R. Kerr, *J. Appl. Phys.*, **48**, 4834 (1977).
3. H. S. Lee and S. P. Marin, *ibid.*, **51**, 3746 (1980).
4. H. R. Huff, R. D. Halvorson, T. L. Chiu, and D. Guterman, *This Journal*, **127**, 2482 (1980).
5. P. A. Heimann, S. P. Murarka, and T. T. Sheng,

J. Appl. Phys., **53**, 6240 (1982).
6. T. J. Lewis, *ibid.*, **26**, 1405 (1955).
7. R. B. Marcus, P. S. D. Lin, and T. T. Sheng, Private communication.
8. M. Sternheim, E. Kinsbron, J. Alspector, and P. A. Heimann, *This Journal*, **130**, 1735 (1983).
9. R. B. Marcus, T. T. Sheng, and P. S. D. Lin, *ibid.*, **129**, 1282 (1982).
10. P. S. D. Lin and H. J. Leamy, *Appl. Phys. Lett.*, **42**, 717 (1983).

JOURNAL OF THE ELECTROCHEMICAL SOCIETY

ACCELERATED

—BRIEF COMMUNICATIONS—

OCTOBER 1983

X-Ray Screen Performance Profile: Effect of Mechanical Energy during Phosphor

P. De Maayer* and W. Van Landeghem

Agfa-Gevaert NV, Research and Development Laboratories, Mortsel, Belgium

The effects of mechanical energy, supplied during eventual low-viscocity predispersion sandmilling, on the performance profile of x-ray intensifying screens, were studied for most phosphors in current use.

Experimental.-- Several 4 cm diameter PE-discs were rotated at 4000 rpm for varying times, in an 8 cm diameter PE-flask containing 55 w/o of 3 mm glass beads, 33 w/o of powder sample and 12 w/o of solvent-binder pre-mixture. From part of the predispersion screens were made using doctor-blade coating techniques, while the phosphor was recovered from the remainder by centrifugation and thorough appropriate solvent rinsing.

Resolution or square-wave-response $SWR(\nu) = \Delta E(\nu)/\Delta E_0$, with ΔE_0 the amplitude of intensity variation of the original signal and $\Delta E(\nu)$ that at fundamental frequency ν, was deduced from a microdensitometer scan of an imaged lead bar resolution test pattern (Funk type 36.882A), using the .027 x 1.081 mm light aperture of a Perkin Elmer PDS. The standard deviation of density fluctuations, total image noise σ_D, was also determined on a uniformly exposed film, using the .4 mm diameter aperture and measuring densities at 15,000 independant locations. For both procedures, the films were exposed to small focus, unfiltered 80 kVp tungsten radiation. The relative brightness S was evaluated by sensitometric exposure methods, described in a previous paper (1), and defined as

$$S = \log (E_s/E_{ref})$$

where E_s and E_{ref} are exposure intensities needed to cause a density 1.0 above fog on standard x-ray film for the experimental and reference Par Speed screens respectively. Agfa-Gevaert MR 4 (blind) film was used with UV-blue emitting phosphors, Kodak Ortho G film with green-emitting ones and both with 'white' emitting $Y_2O_2S:Tb^{3+}$.

Results.-- Although $CaWO_4$ and Tm^{3+} or Tb^{3+} activated LaOBr were included in our tests, table I only shows results for those screens appreciably changing their profile on milling. $Gd_2O_2S:Tb^{3+}$ and $Y_2O_2S:Tb^{3+}$.-- Both oxysulfides show a drastic depreciation in brightness S with a concomitant increase in resolving power, after only 5 minutes milling. SWR values are given at 2 lp/mm, a frequency of direct importance to medical diagnostics, but the trend persists both at higher and lower frequencies (.5 to 5 lp/mm) (2). σ_D-changes exceed the threshold of visual perceptibility. Table I also indicates a decrease in cross-over C.O. except for the $Y_2O_2S:Tb^{3+}$-ortho film combination, for which C.O. remains virtually constant. Cross-over defines the exposure intensity from light of an x-ray screen reaching the back emulsion of a double-sided film, relative to that received by the front emulsion. No changes in physical properties could be detected for either material. Both the average equivalent spherical diameter P_{50} and the interquartile distribution width $(P_{75}-P_{25})/P_{50}$ remain constant, as confirmed by SEM and specific surface area data.

Table I : Screen performance characteristics and cross-over data.

	S	ΔS	SWR (ν = 2 lp/mm)	ΔSWR	σ_D D = 1.5	Δ σ_D x 10^3	C.O.	ΔC.O. %
Gd_2O_2S: Tb								
before	.52		.18		10.9		50.36	
+ ortho		−.31		.15		−.7		3.01
after (5 min.)	.21		.33		10.2		47.35	
Y_2O_2S: Tb								
before	.47		.19		11.2		48.48	
+ ortho		−.14		.05		−6		.57
after (5 min.)	.33		.24		10.6		47.91	
Y_2O_2S: Tb								
before	.46		.22		—		45.94	
+ blind		−.18		.09		—		3.34
after (5 min.)	.28		.31		—		42.60	
BaFCl: Eu								
before	.48		.18		11.5		31.08	
+ blind		−.20		.14		−9		3.25
after (60 min.)	.28		.32		10.6		27.83	

coating weight Gd_2O_2S: Tb & BaFCl: Eu: 60 mg/cm² / Y_2O_2S: Tb: 45 mg/cm²

* Electrochemical Society Active Member.

Key words : x-ray, luminescence, coatings.

An overall decrease in spectral reflectance with the appearance of characteristic absorption bands with respective maxima at 437 and 468 nm were noted for the Y- and Gd-compounds (fig. 1).

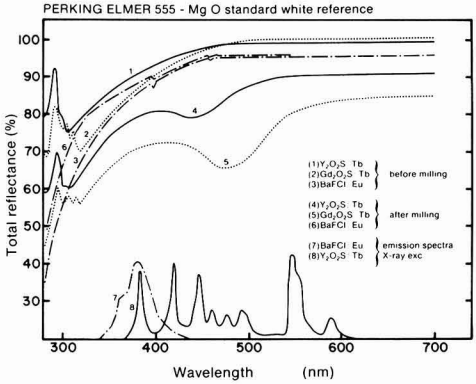

Fig.1. Total reflectance before and after milling for Y- and Gd-oxysulfides and BaFCl:Eu^{2+}.

Non-corrected emission spectra are also shown for BaFCl:Eu^{2+} and Y_2O_2S:Tb^{3+}. For the Gd-compound the position of the Tb^{3+} emission peaks is identical, but the UV-blue peaks are of considerably lower intensity than for Y_2O_2S.

BaFCl:Eu^{2+}.-- In contrast to the abrupt nature of the effects in case of the oxysulfides, equally large but gradual variations in S and SWR were found (fig. 2) as a function milling time. Again this trend was confirmed for a line pair frequency spectrum up to 5 lp/mm (2). P_{50} shows an equivalent monotonous decrease (fig.3), the steep initial drop in IDW indicating preferential fracturing of the larger grains along numerous cleavage planes of the tetragonal crystal structure. At the onset of milling a drastic increase in pyknometric density PD from 79 to 92 % was noted. The reflectance slightly increases in the UV-spectral range, while the C.O. and σ_D-changes are roughly equivalent to those of the oxysulfides (see table I).

Discussion and comments.-- The complexity of the optical phenomena involved in these multiphase systems do not allow as yet for a closely reasoned argumentation. Plausible but partial explanations may be given on the basis of the experimental evidence. Depreciation of oxysulfides, when heavily ball-milling or exerting large unilateral pressures, is caused by color center formation at stress induced atomically dispersed crystal defects, along with

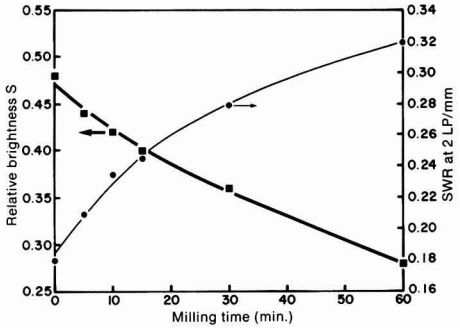

Fig.2. Brightness S and SWR (2 lp/mm) as a function of milling time for BaFCl:Eu^{2+}.

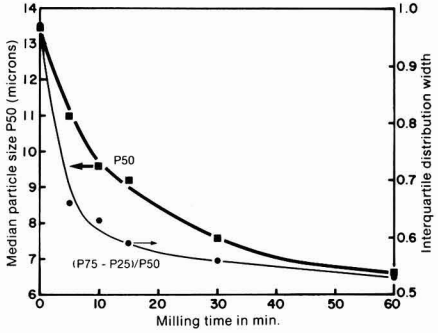

Fig.3. P_{50} and IDW as a function of milling time for BaFCl:Eu^{2+}.

particle size reduction (3,4). In our case the former effect and consequent phosphor coloring seems the only cause. The increase in sharpness is too drastic to be explained by phosphor color only, resolution being mainly scattering controlled and screens being virtually transparent to their own emission light. Stress induced changes in relative refractive index $m = n_p/n_o$ (n_p and n_o being the indices for phosphor and binder respectively) may therefore be of importance as shown by Clewell's simplified formula for the scattering coefficient $K = [(m^2-1)/(m^2+2)]/d$ at constant particle size d (5).

The variation in brightness S for BaFCl is clearly surface area controlled, as indicated by a linear relation with $1/P_{50}$ (fig.4). The scattering coefficient being inversely proportional to particle size, this plot reflects the fact that Lambert-Beer's law holds for scattering attenuation in this case. All screens were coated on highly reflective polyester base with a sharp absorption edge at 320 nm. The initial reflectance (fig. 1) is indicative of the rather transluscent character of BaFCl:Eu^{2+} screens (i.e. high transmis-

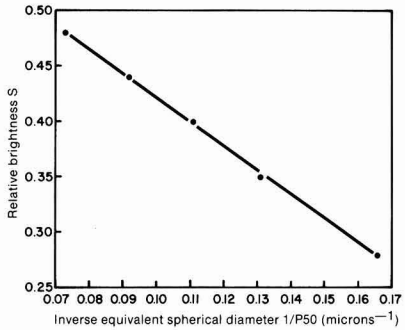

Fig. 4. S versus inverse particle size $1/P_{50}$.

sion,moderate scattering), n~1.64 being close to that of most current polymer systems used. The increase in UV reflectance on milling confirms our idea of increased internal scattering and explains part of the enhanced resolution. The large increase in packing density, with a substantial effect on physical thickness of the screens, explains for the large initial increase in SWR as a result of less geometrical unsharpness. Experiments on sieved fractions of equivalent size and distribution as samples milled for 30 minutes, showed much smaller effects (ΔS=-.07 ;ΔSWR(21p/mm) =.04). Some other milling induced factors have therfore to be of importance. These inconsistencies for both Tb-activated oxysulfides and BaFCl:Eu^{2+} need further investigation, but at least two factors related to milling may be pointed out:

a) redistribution and size reduction of the void phase at roughly constant packing density may cause substantial additional internal scattering; an example is given in fig.5 for $Y_2O_2S:Tb^{3+}$.
b) decrease in cross-over unsharpness in all cases where the absorption band is situated in the range of maximum film C.O. (>420 nm for blind and between 450 and 520 nm for ortho emulsions) and as a result of the increase in UV reflectance for BaFCl:Eu^{2+}.

Finally, the substantial decrease in image noise σ_D implies the resolution enhanced noise perceptibility to compensate only partially the lowered quantum noise resulting from milling induced system speed reduction.

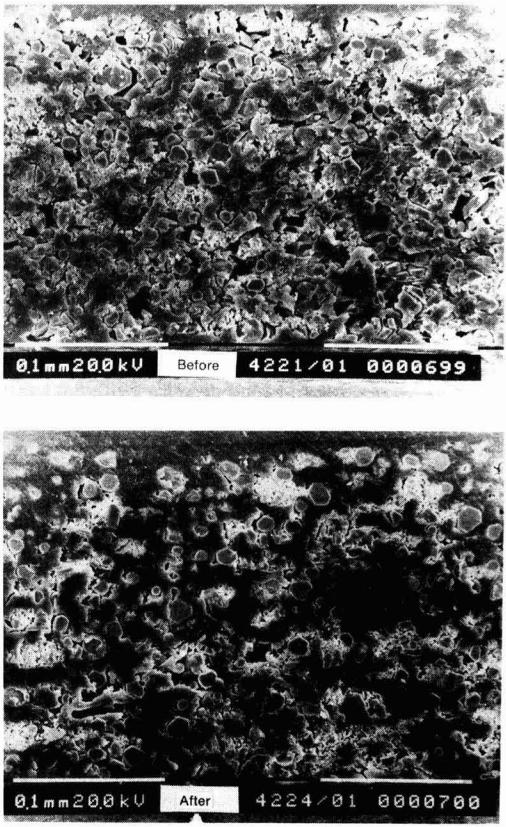

Fig. 5. SEM-cross-sectional view of $Y_2O_2S:Tb^{3+}$ screens before and after 5 minutes phosphor powder milling.

REFERENCES

1.P. De Maayer and R. Bollen, This Journal, 130, 437 (1983)
2.P. De Maayer et al,Abstract 601,905,The Electrochemical Soc. Extended Abstracts,San Francisco,California,May 8-13, 1983.
3.T. Nishimura et al,Mat.Res.Bull., 10, 747 (1975).
4.M. Tamatani et al, J. Lumin.,12/13, 935, (1976).
5.D. Clewell, J. Opt.Soc.Amer.,31,521 (1941).

Manuscript submitted June 29, 1983; revised manuscript received Aug. 28, 1983.

Agfa-Gevaert NV assisted in meeting the publication costs of this article.

This was paper 601 presented at the San Francisco, California, Meeting of the Society, May 8-13, 1983.

Characterization of Microdeformation and Crystal Defects in Silicon Wafer Surfaces

Koichi Kugimiya*

Matsushita Electronic Industry Company, Limited, Central Research Laboratory, Moriguchi, Osaka 570, Japan

Introduction: Recently increased attention has been payed to the characterization of silicon wafers and microdefects in silicon crystals in a very high degree due to the development of VLSI circuits and imaging devices with very high integration and fine performance. Intrinsic and extrinsic gettering techniques[1,2] have been intensively studied and their effectiveness has been proved in actual devices. These studies have concluded that the precise description of silicon wafers during the crystal growth is necessary for the improvements of the performance and the yield in the LSIs.

It has been also pointed out that some surface irregularities (SI's) are an indication of crystal defects beneath the wafer surfaces and that they are occasionally harmful to the device performance[3]. It is obvious that the surface defects like saw marks introduced in wafers during machining (slicing and polishing) processes are not annealed out by a heat treatment even at a high temperature, but act as a source of large crystal defects[1]. SI's are, at present, monitored in a dark-room by the naked-eye observation of the glaring surfaces or the reflected vague images of wafers[4]. This monitoring is obviously limited in sensitivity and reproducibity, and is not qualified for the VLSI specification.

To improve the image monitoring method, the author has derived a new principle combining "Makyo concept" and Schlieren apparatus, and developed a simple optical apparatus to observe directly the micro-topography of a mirror surface. As shown in Fig.1, white radiation of a W lamp is impinged on a mirror surface with a slight inclination from a normal. Reflected and scattered rays are projected on a monitor camera to form a defocussed image of a mirror surface. In this configuration, concavities and convexities are transformed to bright or dark areas on a defocussed wafer image. In term of curvature, R, which is directly related with the brightness, the apparatus is sensitive to pick up R of about 1 m and up to 100 m on a nearly perfect mirror surface. This paper describes the characteristic patterns observed in as-received and processed wafers.

Observation of surface irregularities (SI's): SI's were monitored by ZX-5100 (Matsushita Ind. Equip. Co., Ltd.) and recorded in VTR (Fig.2). It could pick up, for instance, very shallow concavities of 0.38 μm depth over about 10 mm span and 0.05 μm over about 1 mm span, corresponding to R of about 15 m and 2 m respectively. These depth profiles were measured by a surface profilometer.

Features of observed SI's on a monitor TV are shown in Figs.2 to 4. These patterns were classified to scratches, dimples, lapping (polishing) marks, saw marks and backside irregularities (Fig.2). Occasionally swirls, slips, dust crawlings, orange peels, insufficient front surface finishes and defects with a wale-like appearance were observed (Figs.3 and 4).

The SI's reflected venders wafer processing and inspection stabilities. Monitoring of wafer surfaces by the apparatus for some years has proved that the venders wafer processing characteristics were quite different from each other and even among factories of a vender. Thus their process instabilities or process changes could be readily noticiable. Number of dimples mostly reflected dust control stability. Polishing marks reflected the surface condition and quality of polishing cloths, and so on.

* Electrochemical Society Active Member
Key words: Makyo, Surface damage, Dimple, Saw mark

In-line monitoring of wafers in the IC fabrication process showed that most of these SI's persisted after annealing at high temperatures and even after the processing (Fig.4). The macroscopic surface contours and warps of wafers were also clearly observed. However SI's due to backside damages and backside scratches mostly disappeared after annealing. These facts indicated that most SI's were natural surface contours without accompanied by residual stress, therefore no crystal defect was assumed to be present beneath these SI's.

Crystal defects: Analyses of the slicing and polishing processes indicated that crystal defects might be present beneath saw marks, lapping marks and dimples. A fallowing experiment was carried out to see the presence of defects.

Slight scratches were made in a back surface of a wafer by a diamond point scriber at various loads. After breaking the wafer into 4 pieces, both sides of each piece were etched in Secco solution for 1 ∿ 10 min. Observed SI's of the wafer before and after etching are shown in Fig.5. Parallel bright lines before etching were clearly formed by the concavities made by slight stress caused by scratches in the back surface. A white spot in the figure was a dimple. After etching for 1 min, no bright line was observed but after etching for a longer time, brighter lines reappeared as shown in Fig.5b.

When scratches were made in the front surface of the wafer, dark lines were initially observed instead of bright lines and then bright lines appeared after etching as described above. These were due to (1) that etching quickly released the residual stress and thus the front surface deformation, because the etching rate was very high at scratched or damaged areas, and (2) that prolonged etching engraved the front surface along the defects which reached to the front surface from the backside scratches (or along the scratches in the front surface) and thus made concavities. This experiment showed that crystal defects and stresses were present beneath concavities if scratches were originally present in either front or back surfaces. Since crystal defects can penetrate deep into a crystal, 40 ∿ 100 μm by slicing or by scribing [5,6] and since lapping and polishing take some 10 μm off from the surface, crystal defects may be left in wafers and thus concavities may be accompanied with hidden defects.

Summary: A nondestructive optical imaging device based on a new principle to observe surface micro-topography has a very high sensitivity. It could monitor instabilities in the wafer machining process and also in the IC fabrication process.

Among the SI's, dimples and lapping (polishing) marks were most frequently observed. Most of the SI's were defect-free and thus harmless to the IC performance or to the yield. However some like saw marks, dimples and dust crawling may be accompanied with crystal defects and thus the yield may be reduced. Actually preliminary examination showed poor yield in wafers with heavy polishing marks.

This study showed that the total process management, including not only the precise specification of silicon crystals but also the wafer machining process adding to the IC fabrication process, is necessary for the improvement of the VLSI technology.

The author would like to express his thanks to Messrs. S. Tanigawa, T. Yonezawa and M. Katsuyama for designing the new apparatus and to Mr. A. Nishikawa for the cooperation in the evaluation of as-received wafers. Thanks are also due to Mr. M. Matsumoto of Matsushita Elec. Co. for the wafer and the yield evaluations in the IC production lines.

References:

1. K. Kugimiya, S. Akiyama, and S. Nakamura, Semiconductor Silicon 1981, 81-5, 294 (1981).
2. K. Inoue, K. Kotera, K. Kugimiya, and T. Yonezawa, Inst. Elect. Comm. Engr. Jpn. SSD 80-95, 13 (1981).
3. K. Kugimiya, and M. Matsumoto, Proc. 21th Symp. on Semicond. and IC Tech. (Tokyo) Electrochem. Soc. Jpn., 12 (1981).
4. S. Kato, H. Mizumaki, and R. Kawanaka, Inst. Elect. Comm. Engr. Jpn., SSD 77-81, 33 (1977).
5. H. Hirota, and K. Kugimiya, Natl. Tech. Rep., 22 (6), 753 (1976).

6. Y. Takano, H. Kozuka, N. Ogirima, and M. Maki, Semiconductor Silicon 1981, 81-5, 743 (1981).

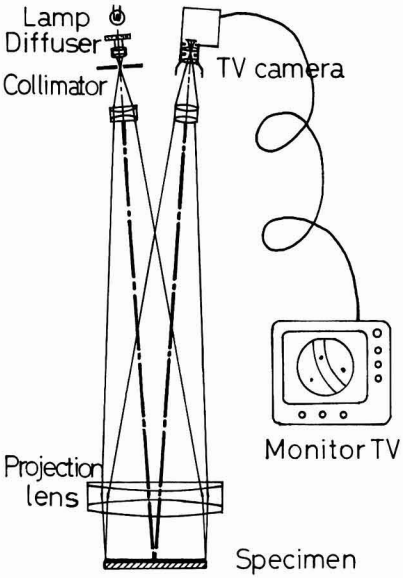

Fig.1. The simple concept of the nondestructive optical imaging apparatus.

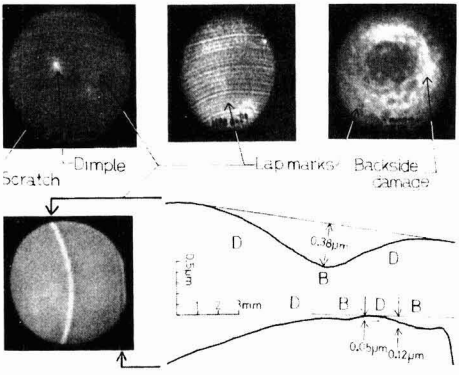

Fig.2. Representative types of microdeformation in the surface of 3" silicon wafers.

Manuscript submitted Nov. 15, 1982; revised manuscript received June 6, 1983.

Matsushita Electronic Industry Company, Limited assisted in meeting the publication costs of this article.

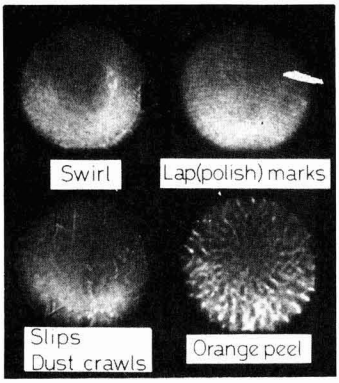

Fig.3. Examples of surface irregularities of as-received epitaxial silicon wafers.

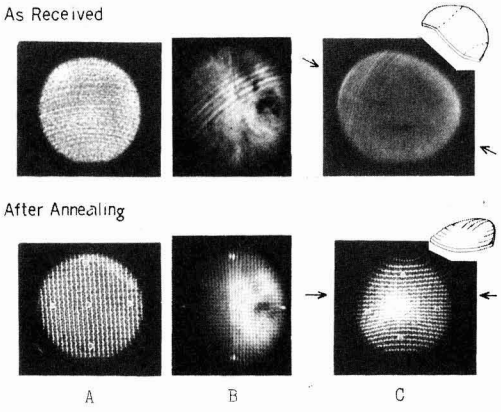

Fig.4. Warpage changes and surface irregularity preservation during the IC fabrication process.
Normal (A) and abnormal (B, C) 3" wafers.

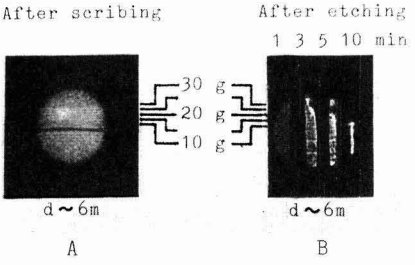

Fig.5. Microdeformation in the front surface caused by scribing the back surface of a 3" wafer.

The Incorporation of Ruthenium Oxide in Polypyrrole Films and the Subsequent Photooxidation of Water at n-GaP Photoelectrode

Rommel Noufi*

Solar Energy Research Institute, Golden, Colorado 80401

INTRODUCTION

The electrogenerated conducting polypyrrole (PP) polymer has been shown to remarkably enhance the stability of n-type photoelectrodes in photoelectrochemical cells[1-5]. In this communication, the electrogeneration of PP, the electrochemical incorporation of ruthenium oxide, and the subsequent photooxidation of H_2O at the n-GaP photoelectrode are reported. The reversible electrochemical activities of the PP polymer film, involve up-take of anions from the electrolyte upon oxidation to yield a conducting film and discharge anions upon reduction to yield an insulating film. This property allows the incorporation in the matrix of the film electroactive species or other species of interest as long as it is negatively charged. The incorporation of $Fe(CN)_6^{3-/4-}$ in PP films and its electrochemical activity as a surface attached species has been shown[1]. Here, the RuO_4^{2-} ion is incorporated electrochemically and then reduced in the matrix of the film to yield RuO_2.

EXPERIMENTAL

The procedure at a Pt electrode is explained in the following reaction scheme.

Scheme Of Incorporation of RuO_2 in Conducting Polypyrrole Film on Pt

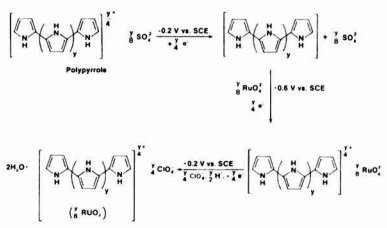

At n-GaP, the film was synthesized from an aqueous solution containing 0.1 M Na_2SO_4 and 1 M pyrrole at pH = 1. The electrode was potentiostated at 0 V versus SCE, and illuminated with 90 mW/cm^2 from a tungsten-halogen lamp. The resulting conducting film was then introduced into a solution containing only 0.1 M RuO_4^{2-} and pulsed several times between -1.1 and 0 V under illumination, terminating the pulsing at 0 V. The RuO_4^{2-} incorporated in the film is then reduced to RuO_2 by soaking for 1 hour in 0.1 M $HClO_4$ or by potentiostating the electrode in the dark at -1.15 V until the observed cathodic current decays to almost zero.

The n-GaP is single crystal S doped ($\sim 10^{17} cm^{-3}$) with <001> orientation. The crystal was etched for 5 seconds in a 1:1:3 mixture of $H_2O:H_2O_2$: and H_2SO_4. The electrodes were prepared as discussed in Ref. 1. The PP film thickness was about 0.1 μm. The counterelectrode was 20 cm^2 platinized Pt.

*Electrochemical Society Active Member.

RESULTS AND DISCUSSION

The incorporation scheme was first tested using a Pt electrode. The presence of RuO_4^{2-} was evident from the RuO_4^{2-} reduction wave (not shown) around +0.2 V superimposed over the film electroactivity. The films produced on Pt and n-GaP were confirmed to contain RuO_2, all through the thickness of film, by XPS, Auger, and ion microprobe. No Ru was detected above the limits of the previous techniques on the immediate surface after the removal of the PP-RuO_2 films. The quantitative results will be discussed in a following paper.

O_2 evolution from a 1 M $HClO_4$ solution on the PP-RuO_2 coated Pt-electrode occurs about 200 mV more negative compared to a bare and PP-coated Pt-electrode. However, the resulting current densities of the former were smaller. Continuous evolution of O_2 on the modified electrode resulted in the loss of the film after about two minutes.

Figure 1 shows a comparison between an n-GaP electrode modified with PP-RuO_2 film compared to one modified with PP film only. The photovoltage developed between the n-GaP and the Pt counterelectrode in 1 M $HClO_4$ is about 1.5 V. The onset of photocurrent in this solution under 100 mW cm^{-2} illumination starts about -1.2 V versus. NaSCE. This is true of the bare and the PP-modified electrodes. In the case of the bare and PP-modified electrodes, the onset shifts positive after the first scan and photocorrosion is evident. No O_2 evolution is observed in either electrodes. The PP-RuO_2 modified electrode exhibits stable photopotential for reversal scans during which O_2 evolution is clearly visible at the surface. The magnitude of the current is decreased after each scan with observable ballooning of the film in spots and the eventual bursting of the film under the pressure of O_2 trapped within the film. At this point, the current increases due to acceleration of photocorrosion. Figure 2 shows a magnification (100X) of a PP- and a PP-RuO_2-coated electrodes after 10 scans at 100 mV sec^{-1} and after the removal of the film. O_2 evolution sites (circular) are evident to the naked eye on the PP-RuO_2-coated electrode, and their appearance is the same as the pre-etched and intentionally protected sites. In between those sites, the surface is photodegraded due to the failure of intimate contact between the film and the n-GaP surface under trapped O_2 pressure. The uncatalyzed electrode (PP-coated), in comparison, shows a surface that is photodegraded compared to the pre-etched and protected surface. Electrodes catalyzed by the deposition of RuO_2 by the pyrolysis of $RuCl_3$ also exhibited immediate photodegradation of the surface.

The results, in this particular case, indicate that the presence of both the conducting film and RuO_2 is necessary for the photodissociation of H_2O. It seems that the mechanism of H_2O photooxidation is more complex than that of the semiconductor. The conducting polymer must act as a scavenger for photogenerated holes that are directed to the H_2O/O_2 redox couple sites catalyzed by the RuO_2, at a rate faster than the self-oxidation of the semiconductor.

In conclusion, a scheme was presented that incorporates RuO_2 in PP film deposited on Pt and n-GaP electrodes. Photodissociation of H_2O from 1 M $HClO_4$ was demonstrated to occur at the surface of n-GaP when modified with a film of RuO_2-catalyzed PP. The quantitative measurement of the quantum efficiency of the O_2 evolution reaction and improvement in the intimate contact between the film and the surface of the electrode are underway.

ACKNOWLEDGMENT

This work is supported by the Solar Energy Research Institute under U.S. Department of Energy contract EG-77-C-01-4042.

REFERENCES

(1) Noufi, R.; Tench, D.; Warren, L.F. J. Electrochem. Soc. 1981, 128, 2596-2599.

(2) Noufi, R.; Frank, A.J.; Nozik, A.J. J. Am. Chem. Soc. 1981, 103, 1849-1850.

(3) Cooper, G.; Noufi, R.; Frank, A.J.; Nozik, A.J. Nature (London) 1982, 295, 578-580.

(4) Fan, R.-R.F.; Wheeler, B.L.; Bard, A.J.; Noufi, R. J. Electrochem Soc. 1981, 128, 2042-2045

(5) Skotheim, T.; Lundström, I.: Prejza, J. J. Electrochem. Soc. 1981, 128, 1625-1626

Manuscript submitted April 25, 1983; revised manuscript received July 11, 1983.

Solar Energy Research Institute assisted in meeting the publication costs of this article.

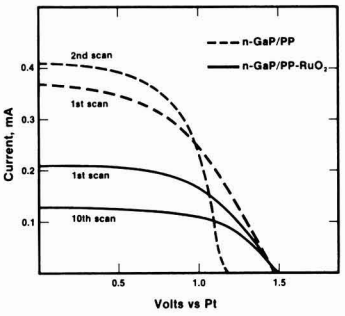

Fig. 1. Potentiostated current--voltage curves in 1 M $HClO_4$ for n-GaP/PP and n-GaP/PP-RuO_2. Scan rate = 100 mV sec^{-1}. Illumination is 100 mW/cm^{-2} from a tungsten-halogen lamp. Electrode area = 0.3 cm^2.

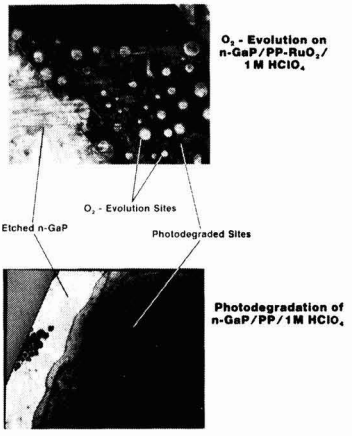

Fig. 2. Magnification (100X) of n-GaP/PP and n-GaP/pp-RuO_2 electrodes after 10 scans (100 mV sec^{-1}) and after removal of the films. Conditions are the same as in Fig. 1.

Transport of Hydrogen Through Pyrite

S. Mark Wilhelm*

Battelle Petroleum Technology Center, Houston, Texas 77073

Jose Vera,* and Norman Hackerman*

Department of Chemistry, Rice University, Houston, Texas 77001

The increased susceptibility of ferrous alloys to loss of ductility in aqueous solutions containing sulfide (sulfide stress cracking) is caused by an increase in the flux of atomic hydrogen into the metal. The increase in flux is presumably caused by an interfacial mechanism in which the sulfide participates.[1] The mechanistic details that account for the increase in hydrogen flux are not known conclusively. A prevalent "chemical" mechanism[2] is that adsorbed sulfur containing species inhibit hydrogen recombination (Tafel recombination) giving rise to an increased concentration of absorbed atomic hydrogen on the surface. Alternatively, a "solid state" mechanism[3] is that hydrogen can enter the metal via solid phase iron sulfide corrosion products on the metal surface.

As a part of investigation of the latter mechanism, measurements have been performed on the permeability of hydrogen through pyrite (FeS_2). The effort has been directed toward establishing the feasibility of hydrogen transport into a metal lattice via an iron sulfide film or precipitate on the metal surface or via iron sulfide inclusions present in the metal[4]. Pyrite is known to be a product of the corrosion of iron and iron base alloys in certain instances[5].

Of equal importance, however, is the general subject of hydrogen diffusion and solubility in crystalline sulfides and oxides. Few data exist concerning these systems. The following report offers data concerning the hydrogen/pyrite system.

The experimental technique used was essentially the same as that reported by Devanathan and Stachurski[6]. The electrochemical cell was separated into two compartments by a pyrite membrane. One side of the pyrite membrane was cathodically polarized at constant current density[7]. The other side was potentiostatically controlled such that the current for hydrogen oxidation (permeation current) could be measured.

Pyrite (FeS_2) was obtained as a naturally occurring (Ambasaquas, Spain) cubic single crystal. Microscopic examination did not reveal any visible inclusions. The particular crystal discussed (among several examined) had an edge dimension of approximately 2 cm. Specific conductivity was approximately 2 $\Omega^{-1}cm^{-1}$.

The crystal was mounted in epoxy and individual membranes were obtained by cutting parallel to the (1,0,0) crystal plane. Membrane faces were polished with alumina (0.05μ). The collection side was plated with palladium to increase collection efficiency and to prevent corrosion (background currents were less than $1\mu A/cm^2$ on the anodic side). Solutions were 0.1M NaOH in both anodic and cathodic compartments.

A typical normalized permeation curve obtained in a galvanostatic charging experiment is shown in Figure 1. A theoretical curve was calculated using the following equation[7]:

$$\frac{i_t}{i_\infty} = 1 - 4 \sum_{0}^{\infty} \frac{(-1)^n}{\pi(2n+1)} \exp\left(\frac{-(2n+1)^2 \pi^2 \tau}{4}\right)$$

where

$\tau = D_H t/L^2$

i_∞ = steady state permeation current

i_t = permeation current at time (t)

* Electrochemical Society Active, Student, Honorary members, respectively.

Key words: pyrite, diffusion, hydrogen

L = membrane thickness

D_H = diffusivity of hydrogen

The equation assumes boundary conditions for galvanostatic charging experiments i.e., the concentration of hydrogen at the exit side is zero, and the flux of hydrogen at the entry side is constant.

Diffusivities were obtained from a plot of $1 - \ln i_t/i_\infty$ vs t, by computer fitting the experimental data to the theoretical curve and by evaluating the time lag $(t_L)^*$.

$$t_L = L^2/2D$$

$$i_{t_L} / i_\infty = 0.629$$

Diffusivities obtained from the three methods were in general agreement.

The approximate coincidence of theoretical and experimental curves (Figure 1) suggests that hydrogen diffusion in pyrite is analogous to its diffusion in the single element metals normally analyzed by this technique. Furthermore the agreement of theoretical and experimental curves verifies the assumed galvanostatic boundary condition of a constant flux at the entry side.

The dependence of time lag on thickness (Figure 2) also indicates that hydrogen transport in pyrite is a purely diffusionary process. It should be mentioned that this conclusion is strengthened by the fact that the range of thickness (1 mm to 20 mm) over which D is independent of L is considerably greater than that which can be measured for materials of low permeability.

The mean diffusivity of the particular crystal sample examined is approximately $3.5 (\pm 1.0) \times 10^{-4}$ cm^2/sec. Measurements on different crystals exhibited a higher degree of variation (10^{-4} to 10^{-5} cm^2/sec). Subsurface solubilities[9] (C_0^H) were generally in the range 1×10^{-4} to 6×10^{-4} M/L.

Galvanastatic collection efficiencies of a 0.31 cm membrane are shown in Figure 3. The maximum hydrogen permeation flux of 18 $\mu A/cm^2$ was obtained at approximately 70 $\mu A/cm^2$ charging current density which corresponds to a 25% collection efficiency. Maximum efficiency (50 percent) was obtained at 25 $\mu A/cm^2$ charging current density. Permeation efficiency as a function of applied potential (cathodic side) is shown in Figure 4. Maximum efficiency (50 percent) occurred at approximately -0.8V.

The ambient temperature diffusivity of hydrogen in pyrite is greater in magnitude than most single element metallic materials (see Table 1). This fact coupled with a relatively large solubility makes pyrite highly permeable to hydrogen. The implications of this observation should impact several electrochemical applications in which pyrites are used as cathodes. In the present context, however, the rapid and efficient transport of hydrogen through iron disulfide supports the hypothesis of hydrogen entry into engineering materials via corrosion products or non-metallic inclusions. In some aqueous systems, the rate of hydrogen entry into a metal lattice determines the time to fracture of stressed materials.

Acknowledgement

The authors appreciate the financial support of the Robert A. Welch Foundation and Intevep (Venezuela).

REFERENCES

1. R. D. McCright, Stress Corrosion Cracking and Hydrogen Embrittlement of Iron Base Alloys, NACE, R. W. Staehle, et. al. editors, 306 (1977).

2. E. G. Daft, K. Bohnenkamp and H. J. Engell, Corrosion Science, 19, 591 (1979).

3. S. M. Wilhelm, J. Vera and N. Hackerman, to be published.

4. G. Wranglen, Corrosion Science, 9, 585 (1969).

5. D. W. Shoesmith, T. E. Rummery, M. G. Bailey and D. G. Owen, This Journal, 126, 911 (1979).

* Corrected for relaxation time[6].

6. M. A. V. Devanathan and Z. Stachurski, Proc. Roy Soc. A, 270, 90 (1962).

7. N. Boes and H. Zuchner, J of the Less Commom Metals, 49, 223 (1976)

8. J. Volkl and G. Alefeld, in Diffusion in Solids: Recent Developments, ed. by A.S. Nowick, J.J. Burton, Academic Press, New York, 231 (1975).

9. J. O'M. Bockris, Stress Corrosion Cracking and Hydrogen Embrittlement of Iron Base Alloys, NACE, R. W. Staehle, et. al. editors, 286 (1977).

TABLE 1

NOMINAL AMBIENT TEMPERATURE DIFFUSIVITIES (8)

Material	D_H^{298} (cm 2/s)
FeS_2	3.5×10^{-4}
Fe	10^{-5}
Ni	10^{-9}
Pd	10^{-7}
Nb	10^{-6}
Ta	10^{-6}

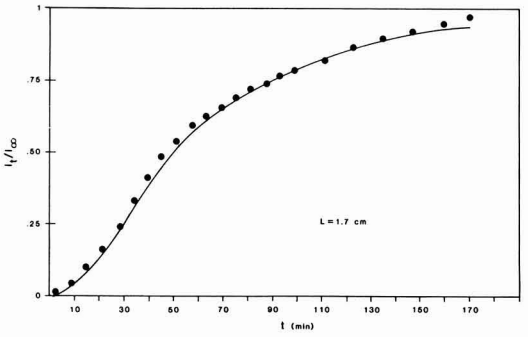

Figure 1 - PERMEATION TRANSIENT
EXPERIMENTAL POINTS
THEORETICAL CURVE

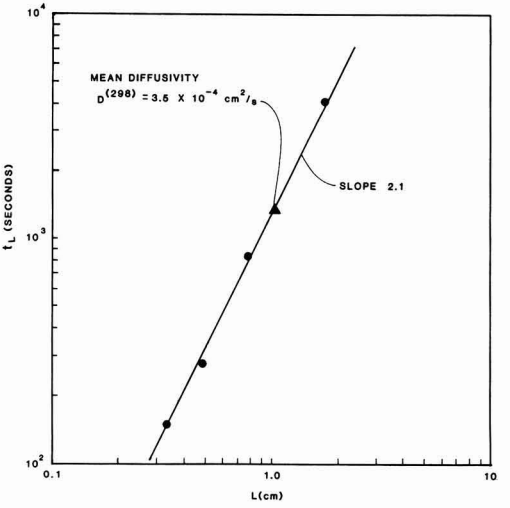

Figure 2 - TIME LAG VERSUS THICKNESS

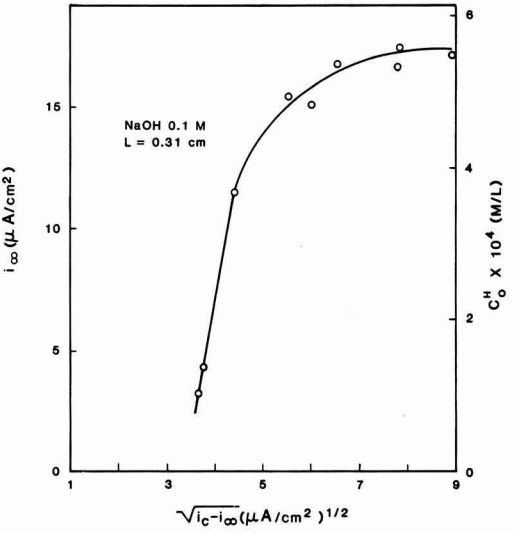

Figure 3 - PERMEATION EFFICIENCY IN GALVANOSTATIC CHARGING EXPERIMENTS

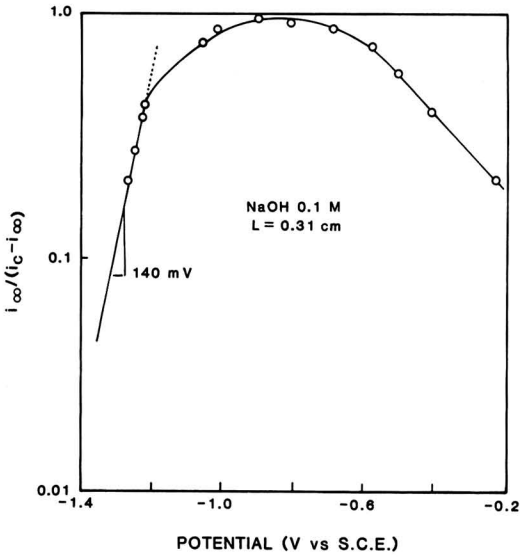

Figure 4 - PERMEATION EFFICIENCY IN POTENTIOSTATIC CHARGING EXPERIMENTS

Manuscript submitted April 14, 1983;
revised manuscript received ca. June 23, 1983.

JOURNAL OF THE ELECTROCHEMICAL SOCIETY

REVIEWS AND NEWS

OCTOBER 1983

DIVISION NEWS

Dielectric and Insulation Division

At the meeting of the Dielectric and Insulation Division's Executive Committee on May 12, 1983, in San Francisco, the following slate of officers and members-at-large was submitted by the Nominating Committee and unanimously elected to serve for the 1983-1984 term:

Officers:

Chairman—Werner Kern, RCA Laboratories

Vice-Chairman—John L. Mauer IV, IBM East Fishkill

Treasurer—Laura Rothman, IBM East Fishkill

Secretary—Norman Goldsmith, RCA Laboratories

Members-at-Large:

Symposium Committee Chairman—Robert B. Comizzoli, Bell Laboratories

Membership Committee Chairman—Henry G. Hughes, Motorola

Callinan Award Committee Chairman—Robert G. Poulsen, Northern Telecom

Immediate Past Chairman—James A. Amick, Exxon.

Past Chairmen—Rudy Frieser, IBM; Derwin I. Flowers, Motorola; Vikram J. Kapoor, University of Cincinnati.

SECTION NEWS

Cleveland Section

Case Center for Electrochemical Sciences will offer the second Workshop on Electrochemical Engineering on the Case Western Reserve University campus October 31-November 4, 1983. The workshop is being presented by Case Center for Electrochemical Sciences and the Chemical Engineering Department of Case Institute of Technology, Case Western Reserve University, in conjunction with The Electrochemical Society's Cleveland Section. Linking chemical engineering and electrochemistry, the workshop is designed for students from both disciplines. Topics to be covered include a brief review of the fundamentals of electrochemistry; current distribution and mass transport; analysis, design, and scale up; and industrial processes and applications. Special "Bring Your Own Problem" sessions will deal with relevant practical problems suggested by workshop participants. Principal instructor is Professor Uziel Landau of the Chemical Engineering Department.

For further information, please contact Diane Kortan, Case Center for Electrochemical Sciences, Case Western Reserve University, Cleveland, Ohio 44106.

Ontario—Quebec Section

Dr. André Bélanger, an electrochemist with the Institut de Recherche de l'Hydro-Québec (IREQ), Varennes, Quebec, is the 1983 recipient of the W. Lash Miller Award of the Ontario-Quebec Section of The Electrochemical Society. He was presented with the award at the spring meeting of the Section in Sherbrooke, Quebec, on April 29, 1983, where he delivered the award lecture entitled "Solid Electrolytes: Their Uses in Solid-State Pollution Sensors and in Rechargeable Lithium Batteries."

Dr. Bélanger completed his Ph.D. at the University of Quebec in 1978 in the field of electrochemistry. He has since made his chief contributions at IREQ in the area of room temperature polymer electrolyte lithium batteries as well as in the area of LiAl/LiCl-KCl/FeS high temperature battery systems. He has also made significant contributions to the study of the electrocatalysis of the hydrogen evolution reaction at metal electrodes. In addition, he has been involved in the development of electrochemical sensors for a variety of gases, based on solid electrolytes. One of these sensors is now being commercialized by Westinghouse for monitoring purposes of sulfur oxide emissions.

The W. Lash Miller Award, consisting of a certificate and a cash payment of $400.00 (Canadian), honors the memory of the late Dr. W. Lash Miller, a former President of the Society and a Head of the Department of Chemistry of the University of Toronto. It is presented every two years in recognition of outstanding technical contributions to the field of electrochemistry by a Canadian resident less than 36 years of age.

European Section

The European Section of The Electrochemical Society will organize the "First European Workshop on Electrodeposition" on April 11-14, 1984, in Paris. The general theme will be: "Significance of the Electrolyte Movement for the Deposition Process and the Layer Properties."

The purpose of the workshop is to bring together scientists and technicians from universities, research institutes, industrial laboratories, and also production lines actively interested in the subject under discussion. The workshop should stimulate the exchange of theoretical know-how and practical experience, provoke suggestions concerning new research themes, and facilitate the participants to update their knowledge in the field.

For more information and application forms, please contact one of the members of the organizing committee:

Dr. G. G. Perrault
Secretary of the European Section
LEI—CNRS
F-92190 Meudon, France

Dr. J. Vanhumbeeck
c/o Siemens NV
P.O. Box I
B-8020 Oostkamp, Belgium

Dr. Ch. Raub
Forschungsinstitut für Edelmetalle
Katharinenstrasse 17
D-7070 Schwäbisch Gmünd,
Germany

NEWS ITEM

31st Power Sources Symposium

Call for Papers

The 31st Power Sources Symposium will convene June 11-14, 1984, at The Deauville Hotel and Motor Inn, Atlantic City, New Jersey. The Symposium is sponsored by the US Army Electronics Technology and Devices Laboratory (ERADCOM), with other DOD agencies, COMSAT, NASA, and DOE.

Eleven unclassified technical sessions will be held, these being; fuel cell systems, rechargeable batteries (advanced rechargeable batteries, lithium rechargeable batteries, nickel rechargeable batteries, conventional rechargeable batteries), non-rechargeable batteries, lithium non-rechargeable batteries (lithium/SO_2 non-rechargeable batteries, lithium/oxychloride non-rechargeable batteries, lithium non-rechargeable batteries, lithium reserve batteries), and thermoelectric power sources.

For further information, contact Doris Yannetta, 201-544-2662, or John Murphy, 201-544-4735.

PEOPLE

Henry Leidheiser, Jr., winner of this year's NACE Willis Rodney Whitney Award, has been named to the ALCOA Foundation Professorship at Lehigh University, Bethlehem, Pennsylvania. Leidheiser is professor of chemistry and director of the Center for Surface and Coatings Research at Lehigh.

In addition to other pioneering research efforts, Leidheiser was among the first to pursue the application of impedance methods to predict the performance of painted metals and was an early leader in the use of Mossbauer spectroscopy in research directed toward a better understanding of corrosion. He has written more than 150 published articles and papers and is author or editor of five books. He has also been honored by The Electrochemical Society, the Oak Ridge Institute of Nuclear Studies, the Institute of Metal Finishing, the Electroplater's Society, and the Society of Automotive Engineers.

Dr. Howard R. Huff, has joined Monsanto Electronic Materials Company (MEMC) as market development director. MEMC is the world's leading manufacturer of single-crystal CZ silicon, the primary building block used in the manufacture of semiconductor devices and integrated circuits.

Dr. Huff is responsible for market development and marketing intelligence and for providing functional guidance to the applications engineering group on a worldwide basis. He reports to Haskell T. Waddle, MEMC's vice president of marketing.

Prior to joining MEMC, Dr. Huff was senior program coordinator at the Philips Research Laboratories Sunnyvale of Signetics Corporation. He has more than 20 years experience in materials development as related to device and integrated circuit performance for companies including Texas Instruments, Incorporated and Signetics Corporation and has an extensive background in silicon materials technology and integrated circuit process engineering.

Dr. Huff received his B.S. degree in engineering science from New York University, his M.S. degree in physics from Stevens Institute of Technology, and his Ph.D. degree in metallurgy from Massachusetts Institute of Technology.

He is the author of numerous scientific publications and a member of the Very Large Scale Integrated Circuit (VLSI) Executive Committee of the Electronics Division of The Electrochemical Society, and has participated both as a lecturer at the University of California, Berkeley, and as a member of the United States Navy's ad hoc study group on electronic materials.

NEW MEMBERS

It is a pleasure to announce the following new members of The Electrochemical Society as recommended by the Admissions Committee and approved by the Board of Directors in August 1983.

Continued on next page

Summer Fellowship Award Program of The Electrochemical Society

The Board of Directors of The Electrochemical Society has voted to allocate $6,000 for summer fellowships in 1984. The Award subcommittee shall have the discretion of deciding the number of recipients and the amount granted to each, within the limits of the appropriation.

The purpose of the award is to assist a student in continuing his/her graduate work during the summer months in a field of interest to The Electrochemical Society. According to the rules for the Society Summer Fellowship Program, if one award is given, it shall be called the Edward G. Weston Fellowship Award; if two awards are given, the second one shall be designated the Colin Garfield Fink Fellowship Award; if more than two are given, the third award shall be called the Joseph W. Richards Fellowship Award.

Candidate's qualifications: "The award shall be made without regard to sex, citizenship, race, or financial need. It shall be made to a graduate student pursuing work between the degree of B.S. and Ph.D., in a college or university in the United States or Canada, and who will continue their studies after the summer period. A previous holder of an award is eligible for reappointment."

Qualified graduate students are invited to apply for these fellowship awards. Applicants must complete an application form and supply the following information:

1. A brief statement of educational objectives.
2. A brief statement of the thesis research problem including objectives, work already accomplished, and work planned for the summer of 1984.
3. A transcript of undergraduate and graduate academic work.
4. Two letters of recommendation, one of which should be from the applicant's research adviser.
5. Successful recipients of fellowships shall agree not to hold other appointments or other fellowships during the summer of 1984.

Application forms are available from the Chairman of the Fellowship Awards Subcommittee, to whom completed applications and letters of recommendation should be sent: Dr. B. E. Conway, Department of Chemistry, University of Ottawa, Ottawa, Ontario, Canada K1N 9B4.

Deadline for receipt of completed applications will be January 1, 1984 and award winners will be announced on May 1, 1984.

Announcement of Energy Research Summer Fellowships

The Board of Directors of The Electrochemical Society has announced that there will be additional summer fellowships in 1984 supported by the Department of Energy. Each fellowship grant will be $2000. The Summer Fellowship Award subcommittee, with the approval of the Department of Energy, shall have the discretion of deciding the number of recipients and the amount granted to each, within the limits of the appropriation.

The purpose of the award is to assist a student in continuing his/her graduate work during the summer months in a field relating to energy research or technology of interest to The Electrochemical Society. Such field shall address energy-related aspects of electrochemical science and engineering as well as solid state science and engineering and shall involve the areas of batteries, fuel cells, photoelectrochemistry, photovoltaics, and electrochemical processes of materials aimed at reducing energy consumption.

Candidate's qualifications: "The award shall be made without regard to sex, citizenship, race, or financial need. It shall be made to a graduate student pursuing work between the degree of B.S. and Ph.D., in a college or university in the United States or Canada, and who will continue their studies after the summer period. A previous holder of an award is eligible for reappointment."

Qualified graduate students are invited to apply for these fellowship awards. Applicants must complete an application form and supply the following information:

1. A brief statement of educational objectives.
2. A brief statement of the thesis research problem including objectives, work already accomplished, and work planned for the summer of 1984.
3. A transcript of undergraduate and graduate academic work.
4. Two letters of recommendation, one of which should be from the applicant's research adviser.
5. Successful recipients of fellowships shall agree not to hold other appointments or other fellowships during the summer of 1984.

Application forms are available from the Chairman of the Fellowship Awards Subcommittee, to whom completed applications and letters of recommendation should be sent: Dr. B. E. Conway, Department of Chemistry, University of Ottawa, Ottawa, Ontario, Canada K1N 9B4.

The deadline for receipt of completed applications for these Summer Fellowships will be January 15, 1984 and award winners will be announced on May 1, 1984.

Active Members

Bifulco, H., Huntington Station, NY
Bolster, M-E., Clarence, NY
Day, A. E., Somerville, NJ
Dempsey, M. D., Revere, MA
Ebel, S. J., Buffalo, NY
Hogrefe, A. W., Palm Beach Gardens, FL
Kozak, S. L., Newton, MA
Lau, K. M., Amherst, MA
Levine, H. H., Dallas, TX
Maruyama, T., Yokohama, Japan
Mazzio, V. F., West Chester, PA
Morduchowitz, A., Beacon, NY
Ottaviani, G., Modena, Italy
Patel, J. R., Murray Hill, NJ
Pollak, F. H., Brooklyn, NY
Rengan, A., Melrose Park, IL
Rocklage, S. M., Mountain View, CA
Rogers, D. J., Ontario, Canada
Schmaderer, F., Turmergasse, Germany
Thonstad, J., Trondheim, Norway
Tsai, S-D., San Jose, CA
Vasilevskis, J., Mountain View, CA
Vichr, M., Sunnyvale, CA

Student Members

Armstrong, M. J., Lafayette, CA
Beam, E. A., III, Greensburg, PA
Chapple-Sokol, J. D., Cambridge, MA
Jeng, S-P., Stony Brook, NY
Lumsden, M. K., Baltimore, MD
Menon, M. M., University Heights, OH
Mlynko, W., San Rafael, CA
Norton, A., Princeton, NJ
Shoaee, S., Atlanta, GA

Reinstatement

Goodkin, J., Lawrenceville, NJ

POSITION WANTED

Please address replies to the box number shown, c/o The Electrochemical Society, Inc., 10 South Main Street, Pennington, N.J. 08534-2896.

Metallurgist/Electrochemist—Ph.D. with 5 years experience in process and product development, electroless plating, electroplating, bath formulation, selective separation of metals and waste treatment, corrosion, materials and surface characterization, and secondary batteries seeks any position. Available immediately and willing to relocate. Reply Box C-244.

MEETINGS CALENDAR

Telavi-84

"3rd International Conference on Electrodynamics and Quantum Phenomena at Interfaces"

October 1-5, 1984

Telavi, USSR

For further information, contact Professor R. R. Dogonadze, Institute of Inorganic Chemistry and Electrochemistry of the Academy of Sciences of the GSSR, Ulitza Dzhikiya 7, 380086 Tbilisi, USSR.

"3rd International Conference on III-V Semi-Insulating Materials"
April 24-25, 1984,
Warm Springs, Oregon

For further information, contact the Organizing Committee Chairman, Bill Ford, Harris Microwave Semiconductor, 1530 McCarthy Blvd., Milpitas, CA 95035, (408) 262-2222.

Notice to Members

Society Headquarters will mail dues bills for 1984 during October. These are special cards which must be returned in the envelope provided with the bill.

As your 1984 membership begins with January 1984, it is suggested that you forward your dues payment promptly.

Nominations Invited for Edward Goodrich Acheson Award and Prize

The Edward Goodrich Acheson Award and Prize was established in 1928 to recognize a person who, in the judgment of the directors of the Society, has made contributions to the advancement of any of the objects, purposes, or activities of The Electrochemical Society as to merit the award. Such contributions may consist of, but shall not be limited to, (a) a discovery pertaining to electrochemistry, electrometallurgy, or electrothermics, (b) an invention of a plan, process, or device, or research evidenced by a paper embodying information useful, valuable, or significant in the theory or practice of electrochemistry, electrometallurgy, or electrothermics, and/or (c) distinguished services rendered to the Society.

The Award consists of a gold medal, a bronze replica, and two thousand dollars ($2000). The following have received the Award:

1929—Edward G. Acheson
1931—Edwin F. Northrup
1933—Colin Garfield Fink
1935—Frank J. Tone
1937—Frederick M. Becket
1939—Francis C. Frary
1942—Charles F. Burgess
1944—William Blum
1946—H. Jermain Creighton
1948—Duncan A. MacInnes
1951—George W. Vinal
1953—J. W. Marden
1954—George W. Heise
1956—Robert M. Burns
1958—William J. Kroll
1960—Henry B. Linford
1962—C. L. Faust
1964—Earl A. Gulbransen
1966—Warren C. Vosburgh
1968—Francis L. LaQue
1970—Samuel Ruben
1972—Charles W. Tobias
1974—Cecil V. King
1976—N. Bruce Hannay
1978—David A. Vermilyea
1980—Ernest B. Yeager
1982—Harry C. Gatos

Nominations for the next Award to be presented at the Fall Meeting of the Society in 1984 in New Orleans, Louisiana, are invited. Nominees do not have to be members of the Society to be considered. Furthermore, there are no distinctions, restrictions, or reservations regarding age, sex, race, citizenship, or place of origin or residence.

Please send nominations before March 1, 1984 with supporting documents to Fritz G. Will, General Electric, R&D Center, P.O. Box 8, Schenectady, New York 12301.

ADVERTISERS' INDEX

REVIEWS & NEWS INDEX

Corrosion, Electrochemistry — Department of Chemical Engineering and Materials Science, University of Minnesota, has two openings; one for a tenured senior professor and one for a tenure track assistant professor. The successful candidates will teach undergraduate and graduate courses in electrochemistry, corrosion and chemical engineering, develop a strong interdisciplinary research program in corrosion, and cooperate in the conduct of the Corrosion Research Center with the Director. Applications with resumes and names of three professional references should be sent by November 15 to Professor L. D. Schmidt, 151 Amundson Hall, University of Minnesota, 421 Washington Avenue SE, Minneapolis, MN 55455. The University of Minnesota is an equal opportunity educator and employer and specifically invites and encourages applications from women and minorities.

Computer-Assisted Corrosion Measurements

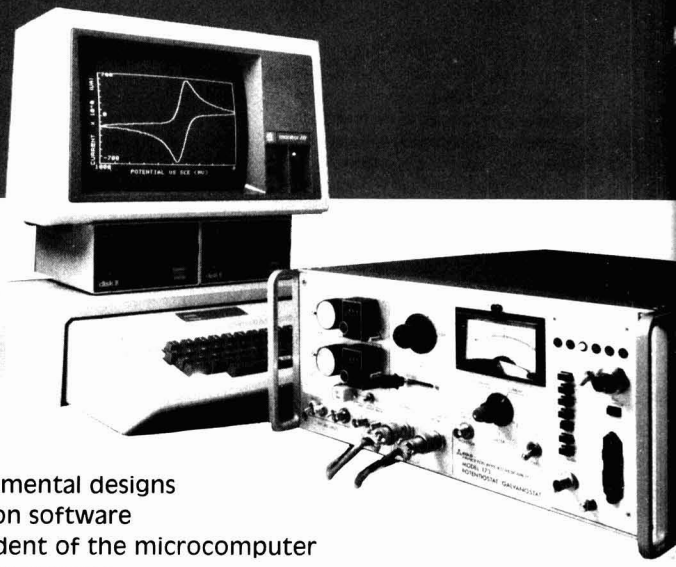

For ultimate flexibility... our new modular system based on the Model 276 Interface

- Available as an update for our Model 173 Potentiostat/Galvanostat
- Many alternatives for special experimental designs
- Detailed documentation of corrosion software
- Real time data acquisition independent of the microcomputer
- Expandable for ac impedance measurements
- IEEE-488 interface compatibility

For ultimate convenience... our Model 350-1 Microprocessor-Controlled Corrosion Measurement System

- Corrosion rates
- Pitting tendencies
- Sensitization
- Passivation and inhibition
- Galvanic couples
- Current-time behavior
- Corrosion behavior diagrams

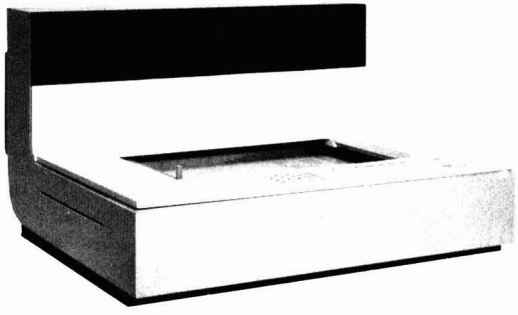

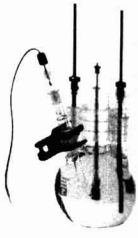

Our applications staff will be pleased to discuss your requirements. Write or call today.

EG&G PRINCETON APPLIED RESEARCH

P.O. BOX 2565 • PRINCETON, NJ 08540. U.S.A. • 609/452-2111 • TELEX: 843409

HIRE TECHNOLOGY

PUT ELECTROCHEMISTRY TO WORK!

BAS introduced the first commercial liquid chromatography/electrochemistry instrument in 1974. LCEC has become the fastest growing electrochemical technique. Thousands of our systems are in routine use for environmental, pharmaceutical, biomedical, industrial, and forensic applications. Nitro compounds, phenols, aromatic amines, thiols, and many heterocycles are ideal candidates for trace determination by LCEC. Detection limits of well below 1 picomole can now be achieved in a few minutes using apparatus of very modest cost.

The latest addition to our family is the BAS 100 ELECTROCHEMICAL ANALYZER. This interactive microprocessor based instrument is capable of performing over 25 electroanalytical techniques including cyclic voltammetry, chronocoulometry, differential pulse voltammetry, phase selective AC voltammetry, electrocapillary measurements, and virtually all forms of polarography. The BAS 100 is the first commercial instrument capable of square wave voltammetry, a powerful new technique for both analytical and fundamental studies. The first "smart" iR compensation approach is included, as are various statistical and background subtraction routines. Experimental parameters and data are available on a video screen and publishable figures are rapidly plotted.

The BAS 100 was designed by and for chemists. It's ready to go to work for you.

WE'LL CHANGE THE WAY YOU
THINK ABOUT ELECTROCHEMISTRY

BAS

2701 Kent Ave
West Lafayette
Indiana 47906
Telex: 276141
(317) 463-4527

APPLICATION FOR ADMISSION

TO

The Electrochemical Society, Inc.

Return completed application to:

Secretary
The Electrochemical Society, Inc.
10 South Main Street, Pennington, New Jersey 08534-2896
609-737-1902

For office use only

Date Rec'd. _____ $ _____

Notice of Ackn. _____

Checked: _____

Approved: _____

To the Board of Directors of The Electrochemical Society, Inc:

Please print complete name and address as it should appear on mailings.

Name: _____

Address: _____

_____

_____

_____

_____

Business Telephone: (include area code) _____

I hereby make application for admission to The Electrochemical Society, Inc., as a _____ member, and enclose the amount of $ _____ covering the first year's dues. (Please see reverse side for proper class of membership and dues applying thereto, noting the options with regard to the date of election and active life membership and the credit available for nonmember meeting registration.)

1. Date of Birth: _____ (month) _____ (day) _____ (year)

2. Please check LOCAL SECTION with which you wish to affiliate:

—— Boston (05)	—— European (27)	—— Natl. Capital Area (45)	—— Pacific Northwest (65)	—— San Francisco (85)
—— Chicago (10)	—— Indianapolis (30)	—— North Texas (55)	—— Philadelphia (70)	—— So. Calif.-Nevada (90)
—— Cleveland (15)	—— Japan (33)	—— Ontario-Quebec (60)	—— Pittsburgh (75)	—— Southern Wisconsin (92)
—— Columbus (20)	—— Metropolitan N.Y. (35)	—— Oregon (62)	—— Rocky Mountain (80)	—— Twin Cities (96)
—— Detroit (25)	—— Midland (Mich.) (40)			—— None (99)

3. Please indicate your DIVISIONAL and GROUP interests, noting your primary interest(s) with the number 1 and secondary interest(s) with the number 2.

—— Battery (AO)	—— Electronics (EO)	—— Industrial Electrolytic (IO)
—— Corrosion (BO)	☐ New Electronic Technologies (E1)	—— Luminescence and Display Materials (KO)
—— Dielectrics and Insulation (CO)	☐ Semiconductors (E3)	—— Organic and Biological Electrochemistry (FO)
—— Electrodeposition (DO)	—— Energy Technology (GO)	—— Physical Electrochemistry (JO)
	——High Temperature Materials (HO)	

4. Education:

Institution	Dates Attended	Major Subject	Degree Earned

5. Work Experience:

Name of Employer (current, followed by previous)	Dates	Position

6. The Society's Constitution provides that two Active Members of the Society (who can substantiate the above record) must recommend you for admission to membership. It will facilitate the handling of your application if you are able to have your references sign this application form; if this is not convenient, please list their names and addresses. On a student application, only a single faculty member recommendation with signature (including title and and institution) is required.

Name (please print)	Signature	Address
Name (please print)	Signature	Address

The undersigned certifies that the above statements are correct and agrees, if elected to the Society, to be governed by its Constitution and Bylaws and to promote the objects of the Society as stated in its Constitution.

Date _____ 19 —

_____
(Signature)

Rev. 5/83

EXTRACTS FROM THE CONSTITUTION AND BYLAWS

CONSTITUTION—Article II

Membership

Section 1. The individual membership shall consist of Active, Honorary and Emeritus Members. The Board of Directors may from time to time authorize other classifications of membership as defined in the Bylaws of the Society.

(Active Member—Annual Dues $50.00)

Active Member

Section 2. An Active Member shall be interested in electrochemistry or allied subjects and possess a Bachelor's degree, or its equivalent, in engineering or natural science. In lieu of a Bachelor's degree, or its equivalent, any combination of years of undergraduate study and years of relevant work experience in electrochemistry or allied subjects adding to at least seven years shall be required. Election to Active Membership shall require the recommendation of two Active Members in good standing.

BYLAWS—Article II

Non-Voting Membership
(Student Member—Annual Dues $10.00)

Student Member

Section 1. Student Member. A Student Member shall be a full-time undergraduate or graduate student registered for a degree in natural science or engineering. The applicant for Student Membership shall be recommended by a member of the faculty of the school. Upon graduation with a Bachelor's degree or equivalent in natural science or engineering, the Student Member may apply for Active Membership. The application shall be approved by two Active Members of the Society in good standing. If the Student Member enters graduate school as a full-time student, the person may choose to apply for Active Membership or remain a Student Member.

BYLAWS—Article XXI

Dues and Fees

Dues

Section 1. The annual dues for Active Members shall be fifty dollars. The annual dues for Student Members shall be ten dollars. Each member shall receive the JOURNAL OF THE ELECTROCHEMICAL SOCIETY.

Date of Election

Section 2. When individuals are elected to membership, they must elect to initiate their membership as of January 1 or July 1 of the year of election; or, if elected during the last quarter, January 1 of the year following election. In the case of a July 1 election for starting membership, dues will be prorated.

Active Life Membership

Section 3. Any Active Member who shall pay in one lump sum the amount equivalent to two-thirds of the remaining dues to age sixty-five at the time of payment, but not less than an amount of 5 years of full dues, shall be exempt from payment of any further dues and shall be considered an Active Member during the remainder of his or her life.

Nonmember Meeting Registration Credit

BOARD OF DIRECTORS ACTION OF OCTOBER 9, 1960

If application for new membership is received within four months of the payment of nonmember registration at a Society Meeting by the applicant, the difference between the nonmember and member registration fees shall be credited toward the first year's dues.

CONSTITUTION—Article III

Admission and Dismissal of Members

Section 1. Application for individual membership shall be in writing on a form adopted by the Board of Directors.

Section 2. The Admissions Committee shall be a rotating committee consisting of three members. One member shall be appointed each year by the President with the approval of the Board of Directors for a term of three years to replace the outgoing member. This Committee shall receive from the Secretary all properly executed and properly recommended applications for admission which he has received from persons desirous of becoming members of the Society. It shall be the duty of this Committee, after examining the credentials of applicants, to make appropriate recommendation to the Board as to approval or rejection of the applications. Unanimous approval of an applicant by this Committee shall be required before the candidate's name may be submitted to the Board of Directors for election. The election to membership shall be by a mail vote of the Board of Directors. The candidate shall be considered elected two weeks after the date the proposed membership list is mailed to the Board if no negative votes have been received by the Secretary. If a candidate receives one negative vote, his application shall then be considered and voted upon at the next meeting of the Board of Directors. Two negative votes cast at this meeting shall exclude a candidate. The Board of Directors may refuse to elect a candidate who, in its opinion, is not qualified for membership. The names of those elected shall be announced to the Society. Duly elected candidates shall have all the rights and privileges of membership as soon as their entrance fee, if any, and dues for the current year have been paid.

Section 3. A member desiring to resign shall send a written resignation to the Office of the Society.

Section 4. Upon the written request of ten or more Active Members that, for cause stated therein, a member be dismissed, the Board of Directors shall consider the matter and, if there appears to be sufficient reason, shall advise the accused of the charges against him. He shall then have the right to present a written defense, and to appear in person before a meeting of the Board of Directors, of which meeting he shall receive notice at least twenty days in advance. Not less than two months after such meeting the Board of Directors shall finally consider the case and, if in the opinion of the majority of the Board of Directors a satisfactory defense has not been made and the accused member has not in the meantime tendered his resignation he shall be dismissed from the Society.

Section 7. The entrance fee, if any, annual dues and any other payments to be made by the members of the Society shall be paid in accordance with regulations set forth in the Bylaws.

Section 8. Any member delinquent in dues after April 1 shall not receive the Society's publications and will not be allowed to vote in any Society election until such dues are paid. All members in arrears for one year after April 1 shall lose their membership status and can be reinstated only by action of the Board of Directors.

All members receive a subscription to the Journal of The Electrochemical Society.

THE ELECTROCHEMICAL SOCIETY, INC.

The Electrochemical Society is an international society concerned with a broad range of phenomena related to electrochemical science and technology and solid state science and technology.

OBJECTIVES

1. The advancement of the theory and practice of electrochemistry, electrometallurgy, electrothermics, electronics, and allied subjects.
2. The encouragement of research and the dissemination of knowledge in the fields of electrochemical science and technology and solid state science and technology.
3. The assurance of the availability of adequate training in the fields of electrochemistry and solid state science for chemists, engineers, metallurgists, physicists, solid state scientists, and others in related subjects.

BENEFITS OF MEMBERSHIP

1. The assurance of being kept aware of pertinent scientific and technical developments through the JOURNAL OF THE ELECTROCHEMICAL SOCIETY and other Society publications.
2. The opportunity to contribute to the advancement of science and technology through support of Society activities.
3. The stimulation of personal association and technical exchange with fellow scientists and engineers.

DIVISIONS

The activities of the Society are carried on by its nine Divisions and Groups as follows:

Battery
Corrosion
Dielectrics and Insulation
Electrodeposition
Electronics
New Electronic Technologies
Semiconductors
Energy Technology
High Temperature Materials
Industrial Electrolytic
Luminescence and Display Materials
Organic and Biological Electrochemistry
Physical Electrochemistry

SECTIONS

Local Sections of the Society have been organized in the following cities and regions:

Boston
Chicago
Cleveland
Columbus
Detroit
European
Indianapolis
Japan
Metropolitan New York
Midland (Michigan)
National Capital Area
North Texas
Ontario-Quebec
Oregon
Pacific Northwest
Philadelphia
Pittsburgh
Rocky Mountain
San Francisco
Southern California-Nevada
Southern Wisconsin
Twin Cities

THE ELECTROCHEMICAL SOCIETY BOOKS IN PRINT

Society Proceedings Series

The following softbound proceedings volumes are sponsored and published by The Electrochemical Society, Inc., 10 South Main Street, Pennington, N.J. 08534-2896. Orders filled at the list price given, subject to availability. Enclose payment with order.

Electron and Ion Beam Science and Technology, Fifth International Conference. R. Bakish, Editor. A 1972 symposium. 420 pages, **$5.50.**

Electrochemical Contributions to Environmental Protection. T. R. Beck, O. B. Cecil, C. G. Enke, J. McCallum, and S. T. Wlodek, Editors. A 1972 symposium. 173 pages, **$4.00.**

Electrochemical Bioscience and Bioengineering. H. T. Silverman, I. F. Miller, and A. J. Salkind, Editors. A 1973 symposium. 268 pages, **$8.00.**

Chlorine Bicentennial Symposium. T. C. Jeffery, P. A. Danna, and H. S. Holden, Editors. A 1974 symposium. 404 pages, **$11.00.**

Metal-Slag-Gas Reactions and Processes. Z. A. Foroulis and W. W. Smeltzer, Editors. A 1975 symposium. 1032 pages, **$20.00.**

Chemistry and Physics of Aqueous Gas Solutions. W. A. Adams, G. Greer, J. E. Desnoyers, G. Atkinson, G. S. Kell, K. B. Oldham, and J. Walkley, Editors. A 1975 symposium. 522 pages, **$11.00.**

Thermal and Photostimulated Currents in Insulators. D. M. Smyth, Editor. A 1975 symposium. 215 pages, **$7.00.**

Electron and Ion Beam Science and Technology, Seventh International Conference. R. Bakish, Editor. A 1976 symposium. 632 pages, **$18.00.**

International Symposium on Molten Salts. J. P. Pemsler, J. Braunstein, K. Nobe, D. R. Morris, and N. E. Richards, Editors. A 1976 symposium. 632 pages, **$16.00.**

Properties of High Temperature Alloys. Z. A. Foroulis and F. S. Pettit, Editors. A 1976 symposium. 851 pages, **$12.00.**

Semiconductor Silicon 1977. H. R. Huff and E. Sirtl, Editors. A 1977 symposium. 1100 pages, **$15.00.**

A History of The Electrochemical Society. The first 75 years. R. M. Burns with E. G. Enck. 160 pages, **$5.00.**

Semiconductor-Liquid Junction Solar Cells. A. Heller, Editor. A 1977 symposium. 340 pages, **$10.00.**

Load-Leveling. N. P. Yao and J. R. Selman, Editors. A 1977 symposium. 412 pages, **$13.00.**

High Temperature Metal Halide Chemistry. D. L. Hildenbrand and D. D. Cubicciotti, Editors. A 1977 symposium. 678 pages, **$17.00.**

Thin Film Phenomena—Interfaces and Interactions. J. E. E. Baglin and J. M. Poate, Editors. A 1977 symposium. 525 pages, **$14.00.**

Selected Topics in the History of Electrochemistry. George Dubpernell and J. H. Westbrook, Editors. A 1977 symposium. 523 pages, **$11.00.**

Battery Design and Optimization. S. Gross, Editor. A 1978 symposium. 486 pages, **$14.00.**

Chemical Vapor Deposition, Seventh International Conference. T. O. Sedgwick and H. Lydtin, Editors. A 1979 symposium. 658 pages, **$16.00.**

Laser and Electron Beam Processing of Electronic Materials. C. L. Anderson, G. K. Celler, and G. A. Rozgonyi, Editors. A 1979 symposium. 560 pages, **$13.00.**

Thin Film Interfaces and Interactions, J. E. E. Baglin and J. M. Poate, Editors. A 1979 symposium. 536 pages, **$16.00.**

Electrode Processes, S. Bruckenstein, J. D. E. McIntyre, B. Miller, and E. Yeager, Editors. A 1979 symposium. 500 pages, **$21.00.**

Power Sources for Biomedical Implantable Applications and Ambient Temperature Lithium Batteries. B. B. Owens and N. Margalit, Editors. A 1979 symposium. 652 pages. **$18.00.**

Electronic and Optical Properties of Polycrystalline or Impure Semiconductors and Novel Silicon Growth Methods. K. V. Ravi and B. O'Mara, Editors. A 1980 symposium. 280 pages, **$15.00.**

Electron and Ion Beam Science and Technology, Ninth International Conference, R. Bakish, Editor. A 1980 symposium. 672 pages, **$28.00.**

Lithium Nonaqueous Battery Electrochemistry. E. B. Yeager, B. Schumm, Jr., G. Blomgren, D. R. Blankenship, V. Leger, and J. Akridge, Editors. A 1980 workshop. 328 pages, **$18.00.**

Ion Exchange: Transport and Interfacial Properties. R. S. Yeo and R. P. Buck, Editors. A 1980 symposium. 396 pages, **$15.00.**

Materials and New Processing Technologies for Photovoltaics. J. A. Amick, E. Sirtl, P. Rai-Choudhury, and J. P. Dismukes, Editors. A 1980 symposium. 368 pages, **$14.00.**

Lithium Batteries. H. V. Venkatasetty, Editor. A 1980 symposium, 516 pages, **$26.00.**

Semiconductor Silicon 1981. H. R. Huff, R. J. Kriegler, and Y. Takeishi, Editors. A 1981 symposium. 1064 pages, **$25.00.**

Electrocrystallization. R. Weil and R. G. Barradas, Editors. A 1981 symposium. 352 pages, **$13.00.**

Chemical Vapor Deposition, Eighth International Conference. J. M. Blocher, Jr., G. E. Vuillard, and G. Wahl, Editors. A 1981 symposium. 836 pages, **$30.00.**

Corrosion and Corrosion Protection. R. P. Frankenthal and F. Mansfeld, Editors. A 1981 symposium. 304 pages, **$10.00.**

Third International Symposium on Molten Salts. G. Mamantov, M. Blander, and G. P. Smith, Editors. A 1981 symposium. 600 pages, **$23.00.**

Second International Symposium on Molten Salts. J. Braunstein and J. R. Selman, Editors. A 1978 symposium. 420 pages, **$16.00.**

High Temperature Materials Chemistry. D. D. Cubicciotti and D. L. Hildenbrand, Editors. A 1981 symposium. 498 pages, **$21.00.**

Electrocatalysis. W. E. O'Grady, P. N. Ross, Jr, and F. G. Will, Editors, A 1981 symposium. 428 pages, **$18.00.**

Photoelectrochemistry: Fundamental Processes and Measurement Techniques. W. L. Wallace, A. J. Nozik, S. K. Deb, and R. H. Wilson, Editors. A 1981 symposium. 736 pages, **$35.00.**

The Nickel Electrode. R. G. Gunther and S. Gross, Editors. A 1981 symposium. 324 pages, **$15.00.**

Semiconductor Technology. D. A. Doane, D. B. Fraser, and D. W. Hess, Editors. A 1982 symposium. 264 pages, **$18.00.**

Plasma Processing. J. Dieleman, R. G. Frieser, and G. S. Mathad, Editors. A 1981 symposium. 528 pages, **$25.00.**

VLSI Science and Technology. C. J. Dell'Oca and W. M. Bullis, Editors. A 1982 symposium. 392 pages, **$20.00.**

Materials and New Processing Technologies for Photovoltaics. J. P. Dismukes, E. Sirtl, P. Choudhury, and L. P. Hunt, Editors. A 1982 symposium. 544 pages, **$25.00.**

Inorganic Resist Systems. D. A. Doane and A. Heller, Editors. A 1982 symposium. 302 pages, **$15.00.**

Transport Processes in Electrochemical Systems. R. S. Yeo, T. Katan, and D-T. Chin, Editors. A 1982 symposium. 288 pages, **$18.00.**

Corrosion in Batteries and Fuel Cells and Corrosion in Solar Energy Systems. C. J. Johnson and S. L. Pohlman, Editors. A 1981 symposium. 554 pages, **$22.00.**

Electron and Ion Beam Science and Technology, Tenth International Conference, R. Bakish, Editor. A 1982 symposium. 474 pages, **$30.00.**

Membranes and Ionic and Electronic Conducting Polymers. E. B. Yeager, B. Schumm, Jr., K. Mauritz, K. Abbey, D. Blankenship, and J. Akridge, Editors. A 1982 symposium. 380 pages, **$22.00.**

Aggregation Phenomena of Point Defects in Silicon. E. Sirtl and J. Goorissen, Editors. A 1982 symposium. 216 pages, **$15.00.**

Corrosion in Fossil Fuel Systems. I. G. Wright, Editor. A 1982 symposium. 522 pages, **$20.00.**

Electrochemical Process and Plant Design. R. C. Alkire, T. R. Beck, and R. D. Varjian, Editors. A 1982 symposium. 288 pages, **$20.00.**

High Temperature Materials Chemistry II. Z. A. Munir and D. Cubicciotti, Editors. A 1983 symposium. 480 pages, **$25.00.**

Silicon Nitride Thin Insulating Films. V. J. Kapoor and H. J. Stein, Editors. A 1983 symposium. 522 pages, **$25.00.**

Defects in Silicon. W. M. Bullis and L. C. Kimerling, Editors. A 1983 symposium. 660 pages, **$30.00.**

Plasma Processing. G. S. Mathad, G. C. Schwartz, and G. Smolinsky, Editors. A 1983 symposium. 660 pages, **$35.00.**

Materials and New Processing Technologies for Photovoltaics. J. A. Amick, V. K. Kapur, and J. Dietl, Editors. A 1983 symposium. 512 pages, **$25.00.**

Electroplating Engineering and Waste Recycle—New Developments and Trends. D. D. Snyder, U. Landau, and R. Sard, Editors. A 1982 symposium. 428 pages, **$22.00.**

10/83

OUT-OF-PRINT SOCIETY VOLUMES

The following volumes sponsored or published by The Electrochemical Society, Inc. are now out-of-print. Xerographic copies* or reprints† of these volumes are available.

* **Vapor Plating.** C. F. Powell, I. E. Campbell, and B. W. Gonser, Editors. A 1955 symposium. 158 pages.
* **The Structure of Electrolytic Solutions.** W. J. Hamer, Editor. A 1957 symposium. 441 pages.
* **Technology of Columbium (Niobium).** B. W. Gonser and E. M. Sherwood, Editors. A 1958 symposium. 120 pages.
* **Surface Chemistry of Metals and Semiconductors.** H. C. Gatos, J. W. Faust, Jr., and W. J. La Fleur, Editors. A 1959 symposium. 526 pages.
* **Electrode Processes,** First Conference. E. Yeager, Editor. A 1959 symposium. 374 pages.
* **Mechanical Properties of Intermetallic Compounds.** J. H. Westbrook, Editor. A 1959 symposium. 435 pages.
* **Zirconium and Its Alloys.** J. P. Pemsler, E. C. W. Perryman, and W. W. Smeltzer, Editors. A 1965 symposium. 205 pages.
† **Measurement Techniques for Thin Films.** B. Schwartz and N. Schwartz, Editors. 1965 and 1966 symposia. 347 pages.
† **Electrode Processes,** Second Conference. E. Yeager, H. Hoffman, and E. Eisenmann, Editors. A 1966 symposium. 190 pages.
* **Electrolytic Rectification and Conduction Mechanisms in Anodic Oxide Films.** P. F. Schmidt and D. M. Smyth, Editors. A 1967 symposium. 230 pages.
* **Electrets and Related Electrostatic Charge Storage Phenomena.** L. M. Baxt and M. M. Perlman, Editors. A 1967 symposium. 150 pages.
* **Dielectrophoretic and Electrophoretic Deposition.** E. F. Pickard and H. A. Pohl, Editors. A 1967 symposium. 138 pages.
* **Electron and Ion Beam Science and Technology,** Third International Conference. R. Bakish, Editor. A 1968 symposium. 725 pages.
* **Optical Properties of Dielectric Films.** N. Axelrod, Editor. A 1968 symposium. 325 pages.
* **Thin Film Dielectrics.** F. Vratny, Editor. A 1968 symposium. 680 pages.
* **Ohmic Contacts to Semiconductors.** B. Schwartz, Editor. A 1968 symposium. 356 pages.
* **Semiconductor Silicon.** R. R. Haberecht and E. L. Kern, Editors. A 1969 symposium. 750 pages.
* **Chemical Vapor Deposition,** Second International Conference. J. M. Blocher, Jr. and J. C. Withers, Editors. A 1970 symposium. 872 pages.
* **Marine Electrochemistry.** J. B. Berkowitz, M. Banus, M. J. Pryor, R. Horne, P. L. Howard, G. C. Whitnack, and H. V. Weiss, Editors. A 1972 symposium. 416 pages.
* **Semiconductor Silicon 1973.** H. R. Huff and R. R. Burgess, Editors. A 1973 symposium. 936 pages.
* **High Temperature Oxidation of Metals.** By P. Kofstad. The Corrosion Monograph Series. 340 pages.
* **Chemical Vapor Deposition,** Fourth International Conference. G. F. Wakefield and J. M. Blocher, Jr., Editors. A 1973 symposium. 595 pages.
* **Electrets, Charge Storage and Transport in Dielectrics.** M. M. Perlman, Editor. A 1973 symposium. 675 pages.
* **Fine Particles.** W. E. Kuhn and J. Ehretsmann, Editors. A 1974 symposium. 352 pages.
* **Corrosion Problems in Energy Conversion and Generation.** C. S. Tedmon, Editor. A 1974 symposium. 484 pages.
* **Electrocatalysis.** M. W. Breiter, Editor. A 1974 symposium. 378 pages.
* **Electron and Ion Beam Science and Technology,** Sixth International Conference. R. Bakish, Editor. A 1974 symposium. 594 pages.
* **Energy Storage.** H. P. Silverman and J. B. Berkowitz, Editors. A 1975 symposium. 258 pages.
* **Chemical Vapor Deposition,** Fifth International Conference. J. M. Blocher, Jr., H. E. Hintermann, and L. H. Hall, Editors. A 1975 symposium. 848 pages.
* **Etching.** H. G. Hughes and M. J. Rand, Editors. A 1976 symposium. 203 pages.
* **Electrode Materials and Processes for Energy Conversion and Storage.** J. D. E. McIntyre, S. Srinivasan, and F. G. Will, Editors. A 1977 symposium. 340 pages.
* **Electron and Ion Beam Science and Technology,** Eighth International Conference. R. Bakish, Editor. A 1978 symposium. 297 pages.
* **International Symposium on Solar Energy.** J. B. Berkowitz and I. A. Lesk, Editors. A 1976 symposium. 372 pages.
* **High-Temperature Metallic Corrosion of Sulfur and Its Compounds.** Z. A. Foroulis, Editor. A 1969 symposium. 276 pages.
* **Properties of Electrodeposits—Their Measurement and Significance.** R. Sard, H. Leidheiser, Jr., and F. Ogburn, Editors. A 1974 symposium. 430 pages.
* **Chemical Vapor Deposition,** Sixth International Conference. L. F. Donaghey, P. Rai-Choudhury, and R. N. Tauber, Editors. A 1977 symposium. 596 pages.
* **The Electrocatalysis of Fuel Cell Reactions.** W. E. O'Grady, S. Srinivasan, and R. F. Dudley, Editors. A 1978 workshop. 228 pages.
* **Electron and Ion Beam Science and Technology,** Fourth International Conference. R. Bakish, Editor. A 1970 symposium. 680 pages.
* **Plasma Processing.** R. G. Frieser and C. J. Mogab, Editors. A 1980 symposium. 360 pages.
* **Oxide-Electrolyte Interfaces.** R. S. Alwitt, Editor. A 1972 symposium. 312 pages.
* **Industrial Water Electrolysis.** S. Srinivasan, F. J. Salzano, and A. R. Landgrebe, Editors. A 1978 Symposium. 297 pages.
* **Semiconductor Characterization Techniques.** P. A. Barnes and G. A. Rozgonyi, Editors. A 1978 Symposium. 532 pages.
* **Fundamentals of Electrochemical Machining.** A 1970 Symposium. 365 pages.

* Order from University Microfilms, Inc., 300 North Zeeb Street, Ann Arbor, Mich. 48106. Specify an Electrochemical Society volume.

† Order from Johnson Reprint Co., 355 Chestnut St., Norwood, N.J. 07648. Specify an Electrochemical Society volume.

10/83

The Electrochemical Society, Inc.
10 South Main Street, Pennington, New Jersey 08534-2896 • Telephone: 609-737-1902

Instructions to Authors

The **JOURNAL OF THE ELECTROCHEMICAL SOCIETY** is the official monthly journal of the Society. It contains three sections: Electrochemical Science and Technology, Solid-State Science and Technology, and Reviews and News. Technical Papers, Technical Notes, and Accelerated Brief Communications are published in the first two sections and Review Papers in the third. All manuscripts submitted are considered for publication, with the understanding that they have not been submitted, accepted for publication, or published elsewhere. A wide range of subject matter is acceptable. Manuscripts can be handled promptly and efficiently if these instructions are followed.

TYPES OF PAPERS

Technical Papers describe fundamental or applied studies in depth. They contain new data and/or new interpretations of existing data. Abstracts summarizing the results are required.

Technical Notes report briefly on limited research or development that is not being pursued further. No abstracts are required.

Accelerated Brief Communications present, in camera-ready format and limited to two (2) pages including figures, tables, and references, scientific or technological information warranting rapid dissemination. No abstracts are required. Instructions and typing forms are available from the Editorial Office.

Review Papers furnish critical analyses of topical subjects. Abstracts are required.

SUBMISSION

Submit three complete, clear copies of each manuscript and the originals of all figures and illustrations to:

Editorial Office
The Electrochemical Society, Inc.
10 South Main Street
Pennington, New Jersey 08534-2896

A letter accompanying the manuscript should give (a) the name and mailing address of the author to whom correspondence should be sent, (b) reference to any presentation of the work at a meeting of The Electrochemical Society, (c) the Division or Group of the Society or the Divisional or Group Editor (both are listed in the front of each issue of the Journal) whose interests are most closely related to the work being discussed, (d) the section of the Journal in which the work should appear, and (e) the names and addresses of people able to act as reviewers.

EDITORIAL PRACTICES

Following receipt by the Editorial Office, each manuscript is sent to a Divisional or Group Editor with knowledge of the subject matter. This editor arranges for review of the manuscript and communicates with the author(s) regarding revisions. Final acceptance or rejection of a manuscript is determined by the Editor.

Accelerated Brief Communications are handled as rapidly as possible, ordinarily with a response to the author(s) from the Divisional Editor, the Group Editor, or the Editor within three weeks of their arrival at Pennington. Response to the authors of other manuscripts usually takes place within six weeks. Following acceptance, authors are notified of the Journal issue in which publication is scheduled; about one month before publication, page proofs and an order blank for reprints are provided. Proofs must be promptly corrected and returned. Extensive alterations by the author may delay publication; their cost will be billed to the author(s).

PUBLICATION CHARGE

To help meet publication costs, a payment of $65.00 per printed page is requested for the publication of technical material. If at least one author is a Society member or an employee of a Patron or Sustaining member, a 10% reduction is allowed. Acceptance of manuscripts for publication is, however, based on merit and is in no way dependent on such payment, which may be waived in individual cases upon request.

PRESENTATION

Organization and clarity are essential elements of successful written communication. Identify the subject matter in the title, using words useful in indexing. State the purpose of the work early in the text. Avoid introductory and explanatory material that is overly familiar to those in the field. Present the work and the arguments in an order that leads naturally to clearly specified conclusions. Provide enough information for the work to be reproduced and the logic behind it to be understood. Identify and justify any assumptions that are made; avoid tacit assumptions. Omit details that are generally known or that can be covered by reference to other publications. Give the magnitude and define the significance of experimental errors. Use headings and subheadings as appropriate. Avoid proprietary and trade names, but capitalize them where their use is necessary. Define unusual technical terms and abbreviations. Where symbols are used extensively, list them with their definitions at the end of the paper. Avoid repetition in the text and duplication of material in figures and tables. Be brief but clear.

Edit and proofread the manuscript carefully; these are not the responsibilities of the editors or reviewers.

KEY-DESCRIPTORS

To aid in indexing, authors must supply standard key-descriptors, preferably four of them, from a list with instructions published annually in the December issue of the Journal and available from the Editorial Office. These key-descriptors must appear at the bottom of the first page of the manuscript.

MANUSCRIPT PREPARATION

Accelerated Brief Communications must be typewritten or printed on standard forms obtained, with detailed instructions for their use, from the Pennington Editorial Office.

All other manuscripts must be typewritten or printed, double-spaced throughout, on one side only of white 21.6 x 27.0 cm paper, with 2.5-3.8 cm margins. Do not use single spacing anywhere, in title, abstract, text, references, tables, or figure captions.

For general matters of style and format, see papers in recent issues of the **Journal** and consult a style manual such as that of the American Chemical Society or that of the American Institute of Physics. These also provide lists of common abbreviations and units. The following specific items should be noted:

(a) Systeme Internationale (SI) units are to be used; a description may be found in NBS Special Publication 330 or ASTM Metric Practice Guide E-380-72.

(b) The signs of cell and electrode potentials are to follow the IUPAC conventions of 1953.

(c) **Mathematical equations** should be written on a single line, if possible, using parentheses, brackets, the solidus, negative exponents, etc.

(d) **References** are to be listed separately at the end of the paper in the order they are cited in the text, being sure that each listed reference is cited. Authors' initials must be given, and Chemical Abstracts abbreviations must be used. Citations of other than the generally available literature should be avoided if possible.

(e) **Tables** are to be presented on individual sheets, with both captions and body double-spaced.

(f) **Figure captions** and numbers are to be included on a separate sheet and must not appear in the body of any figure or illustration.

(g) **Drawings** and **graphs** will ordinarily be reduced to column width (8.3 cm) and after such reduction should have lettering at least 0.15 cm high. Lettering must be of letter-guide quality. Originals in India ink on tracing cloth or paper are preferred, but India ink on coordinate paper with blue ruling is acceptable. When several curves are shown, each may be lettered and identified in the caption. The Editorial Office will not make corrections or additions to figures.

(h) **Photographs** should be used sparingly. The originals supplied must be glossy prints and should be protected against bending. Micrographs must have a labeled unit length within the body of the picture; reduction for printing makes magnifications meaningless.

Revised July 1, 1983

Printed in the United States of America

Call for Papers
165th Meeting
Cincinnati, Ohio, May 6-11, 1984

New procedure and deadlines have been established.

Selected symposium topics and planned General Sessions are described in the following pages:

Procedure for Submitting Papers

1. Submit one original 75-Word Abstract on the attached form or a facsimile together with one original Extended Abstract to The Electrochemical Society, Inc., 10 South Main St., Pennington, NJ 08534-2896. The deadline for receipt of **both** the 75-Word and Extended Abstracts at The Electrochemical Society Headquarters Office is **December 1, 1983.**

2. Send a copy of **both** the 75-Word and Extended Abstracts to the appropriate organizing symposium or General Session chairman listed.

No paper will be considered unless both the 75-Word and Extended Abstracts are received at Society Headquarters by December 1, 1983.

Instructions for Preparation of Extended Abstract

1. New Deadline—Extended Abstracts must be submitted with the 75-Word Abstract by **December 1, 1983.**

2. All scheduled papers will be published in the EXTENDED ABSTRACTS volume for this meeting. The volume is published photo-offset directly from typewritten copy submitted by the author. The volume will be 7" × 10"; therefore, it is essential that the typing be clear and all lettering should be the size of ordinary type or at least 1/16 inch high so that it will be legible after reduction. The EXTENDED ABSTRACTS volume is in a double-column format. Camera-ready typing mats may be obtained from The Electrochemical Society, Inc., 10 South Main St., Pennington, NJ 08534-2896, or you may use any white bond paper 11" × 17". The diagram below gives the dimensions of the Extended Abstract form.

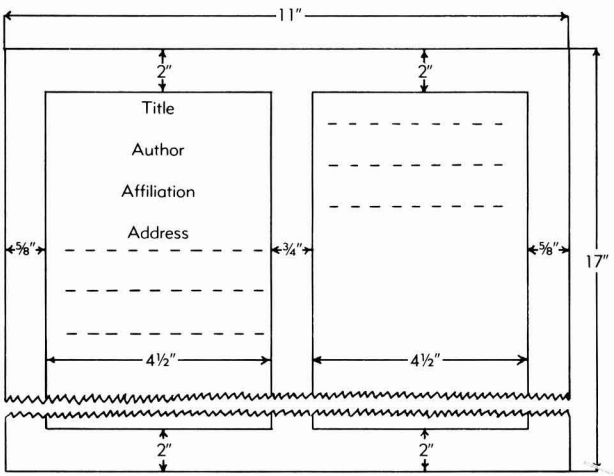

A. Use black typewriter ribbon only; type single-spaced.

B. Opaque lacquer may be used for corrections.

C. Type title, author(s), affiliation(s), and address(es) at top of first column (see diagram).

D. Tables and figures must be securely mounted within the margins with rubber cement.

E. Place references and figures after text.

3. The text of the abstract, including references, must not exceed one page (two columns) in length. An additional two columns are permitted for figures, if necessary. Papers exceeding this limit will be returned or rejected.

Mailing Instructions

Mail the original Extended Abstract together with the original 75-Word Abstract to The Electrochemical Society, Inc., 10 South Main St., Pennington, NJ 08534-2896 and a copy to the organizing chairman **for receipt before December 1, 1983.**

Notification of Paper Acceptance

Programming for this meeting will occur in early January. Organizing chairmen will notify those authors whose papers have not been accepted. In early March, a complete packet of program materials, including an Advance Program, will be sent to the presenting authors. Coauthors will receive a meeting packet without an Advance Program.

Manuscript Publication in the JOURNAL OF THE ELECTROCHEMICAL SOCIETY

Upon presentation, all meeting papers become the property of The Electrochemical Society, Inc. However, presentation incurs no obligation to publish. If publication in the JOURNAL OF THE ELECTROCHEMICAL SOCIETY is desired, papers should be submitted as promptly as possible in full manuscript form in order to be considered. "Instructions to Authors" for JOURNAL publication are available from the Society Headquarters office. If publication elsewhere is desired after presentation, written permission from Society Headquarters is required.

Cincinnati, Ohio, Meeting Symposia Plans—Spring 1984 May 6-11, 1984

New Deadline—Extended Abstracts must be submitted with the 75-Word Abstract by December 1, 1983.

CORROSION

General Session

Papers on all aspects of low and high temperature corrosion and associated phenomena will be considered. Experimental techniques for the study of corrosion processes and corrosion products are also of interest.

Suggestions and inquiries should be sent to the Session Chairman: F. Mansfeld, Rockwell International Science Center, 1049 Camino Dos Rios, Thousand Oaks, CA 91360.

CORROSION/HIGH TEMPERATURE MATERIALS/ENERGY TECHNOLOGY

Fundamental Aspects of High Temperature Corrosion

This symposium will deal with the mechanistic (atomistic) aspects of high temperature corrosion. Papers are solicited in the following areas: 1. mechanisms of scale growth, 2. details of alloy reactions with oxidizing gases, 3. fundamental aspects of mixed oxidant reactions, 4. chemistry and electrochemistry of hot corrosion, 5. mechanisms of corrosion/erosion interactions, 6. fundamental aspects of the creep/scaling interaction, and 7. theoretical considerations in high temperature corrosion, etc.

Papers simply reporting kinetics, morphologies, and product characterization are discouraged from submission here.

Suggestions and inquiries should be sent to the Symposium Chairman: R. A. Rapp, Dept. of Metallurgical Engineering, The Ohio State University, 116 West 19th Ave., Columbus, OH 43210.

DIELECTRICS AND INSULATION/ ELECTRODEPOSITION/ELECTRONICS

Electrophoretic Deposition

This symposium will cover the theory of electrophoresis to deposition of organic polymers, paints, and pigments for decorative, protective, and electronic functional purposes. This will include ceramic particulate deposition for metal glazing, glass application to electronic devices, and codeposition of particulates for wear and abrasion resistance, lubrication, and other applications requiring hardness, resistance to mechanical wear, electrical insulation, and other highly specialized properties.

Suggestions and inquiries should be sent to the Symposium Chairman: R. Scriven, PPG Industries, P.O. Box 9, Allison Park, PA 15101, or K. Hang, RCA Laboratories, David Sarnoff Research Center, Princeton, NJ 08450.

DIELECTRICS AND INSULATION/ELECTRONICS

Thin Films of Tunneling Dimensions

The purpose of this symposium is to promote a dialogue between scientists interested in the field of tunneling device physics with those working in the area of thin film surface and interface physics. Topics will include the following: 1. tunneling device processing, 2. thin oxide growth processes on metals and semiconductors, 3. interface characterization, 4. barrier defects and uniformity, 5. tunnel device physics, 6. solar cells, 7. superconducting tunneling devices, and 8. novel tunnel devices.

Suggestions and inquiries should be directed to the Symposium Co-Chairmen: S. I. Raider, IBM Corp., T. J. Watson Research Center, P.O. Box 218, Yorktown Heights, NY 10598; E. H. Nicollian, Bell Laboratories, Murray Hill, NJ 07974; or R. B. Comizzoli, Bell Laboratories, Murray Hill, NJ 07974.

ELECTRONICS/DIELECTRICS AND INSULATION

Second International Symposium on VLSI Science and Technology: Materials for High Speed/High Density Applications

This symposium will focus on materials for high speed/high density applications. The symposium will be specifically on materials, elemental and compound, for high speed/high density applications and will cover all aspects of materials development: 1. synthesis, 2. bulk crystal growth, 3. epitaxy, 4. dopant and impurity control, 5. formation and properties of dielectric and insulation materials, 6. metallization and contacts, 7. defects and control, and 8. materials characterization, etc.

Detailed instructions concerning participation in this symposium appear in the special Call for Papers appearing in the March, May, and June 1983 issues of the **Journal of the Electrochemical Society.** The publication of a proceedings volume, which will be available at the symposium, is being planned.

Authors must submit five copies of a 500 word, or longer, summary specifically stating the contribution that the paper makes to the field. These summaries will be used solely to select papers for presentation at the symposium. In-depth review papers which give wide coverage of a field are also sought, and those eminent in the fields of materials related device and VLSI technologies are invited to submit summaries. The summaries should be submitted by September 10, 1983, to either of the Co-Chairmen: K. Bean, Texas Instruments Inc., P.O. Box 25936, MS 147, Dallas, TX 75265 or G. Rozgonyi, Microelectronics Center of North Carolina, P.O. Box 12889, Research Triangle Park, NC 27709. Authors submitting abstracts will be notified if their papers have been accepted for presentation and will be given specific instructions for subsequent manuscript preparation for the proceedings.

Joint General Session

Papers that deal with all aspects of materials of interest for electronic devices, including their preparation, characterization, interactions, and device applications, and whose subject matter is not covered by the special symposia are invited to be submitted to this session. Also invited are papers on the basic chemistry and physics of materials, processing, and computer modeling of the formation and of the characterization of materials and devices. Of particular interest are new materials and processes.

Suggestions and inquiries should be sent to the Session Co-Chairmen: P. L. Castro, Hewlett-Packard Laboratories, 3500 Deer Creek Rd., Palo Alto, CA 94304; P. Rai-Choudhury, Westinghouse Research and Development Center, Beulah Rd., Pittsburgh, PA 15235; or G. C. Schwartz, IBM Corp., Dept. 206, Bldg. 300-48A, Hopewell Junction, NY 12533.

Joint Recent News Papers Session

Recent News Papers and Extended Recent News Papers consisting of topics covered by the symposia and sessions being sponsored or cosponsored by the Electronics and Dielectrics and Insulation Divisions are invited for presentation.

A special Call for Recent News Papers will appear in the January, February, and March 1984 issues of the JOURNAL.

Suggestions and inquiries should be sent to the Session Chairman: W. A. Pliskin, IBM Corp., Dept. 04A, Internal Zip 48A, Hopewell Junction, NY 12533.

ENERGY TECHNOLOGY

General Session

Papers are solicited in areas of energy conversion and storage not covered by current symposia. Of particular interest are new developments in photoelectrochemistry and novel methods for energy storage and transmission. Suggestions and inquiries should be sent to the session Co-Chairmen: A. J. Appleby, EPRI, P.O. Box 10412, Palo Alto, CA 94303 or V. K. Kapur, Arco Solar, 20554 Plummer St., Chatsworth, CA 91311.

HIGH TEMPERATURE MATERIALS/DIELECTRICS AND INSULATION/ELECTRONICS

Ninth International Conference on Chemical Vapor Deposition

This conference will provide a forum for those interested in CVD to exchange recent results. The scope of this conference is broad and will include papers on the following topics: 1. fundamentals—kinetics and gas flow dynamics; 2. measurement and control—*in situ* measurements and computer controls; 3. methods—low pressure, plasma, laser CVD, organometallic sources, and new reactor designs; 4. silicon epitaxy for VLSI—joint session with VLSI symposium; 5. structures—films and crystals, amorphous, polycrystalline, single crystal, and semiconductors on insulators; 6. applications—electronics, optics, hard coatings, nuclear materials, refractory materials, corrosion resist materials, and decorative coatings.

A proceedings volume will be published, and deadlines are described in detail in the special Call for Papers which appeared in the June and July 1983 issue of the JOURNAL.

Suggestions and inquiries should be sent to the conference Co-Chairmen: C. J. H. van den Brekel, Philips Research Laboratories, 5600 JA Eindhoven, The Netherlands; J. M. Blocher, Jr., 915 Silvoor Lane, Oxford, OH 45056; G. W. Cullen, RCA Laboratories, Princeton, NJ 08540; P. Rai-Choudhury, Westinghouse R and D Center, Beulah Rd., Pittsburgh, PA 15235; or McD. Robinson, Bell Laboratories, Murray Hill, NJ 07974.

INDUSTRIAL ELECTROLYTIC

Advances in the Chlor-Alkali and Chlorate Industry

This symposium will be concerned with recent advances in chlor-alkali and chlorate processing and equipment technology including theoretical and experimental aspects. Papers dealing with economic trends as affected by market location, technology selection, raw material costs, and shipping techniques will be included. Technology review papers will also be welcome.

Papers are solicited on the following general topics: 1. economic impact of plant size, market location, power costs, load leveling, cogeneration, and modular techniques; 2. brine treatment and processing, salt handling and dissolving techniques, and brine evaporation; 3. monopolar-biopolar cell design, current density, gas evolution, operating pressure, and thermal balance; 4. anodes, cathodes, and membranes and diaphragms; 5. cell room and plant layout, equipment innovations, computer modeling, and materials of construction; 6. analytical methods, computer and instrument control, and safety and environmental control.

Suggestions and inquiries should be sent to the Chlor-Alkali Chairman: M. M. Silver, The H. K. Ferguson Co., One Erieview Plaza, Cleveland, OH 44114 or the Chlorate Chairman: E. M. Spore, Kerr-McGee Chemical Corp., Kerr-McGee Center, Oklahoma City, OK 73125.

General Session

Original papers concerning any aspect of industrial electrolysis not included in other scheduled symposia are invited for this session. Of particular interest are new processes, developments, techniques, and application in industrial electrochemistry.

Suggestions and inquiries should be sent to the Session Chairman: R. S. Karpiuk, 4608 Bristol Ct., Midland, MI 48640.

INDUSTRIAL ELECTROLYTIC DIVISION/ENERGY TECHNOLOGY GROUP

Electrochemistry in Mineral and Metal Processing

An international symposium concerned with electrochemical aspects of concentrating and extracting metals from sulfide ores is being planned. Both fundamental and applied work will be covered. Several areas are to be considered: 1. mineral flotation—surface properties of sulfide minerals and thermodynamic aspects of mineral collector interaction; 2. hydrometallurgy—the focus here will be on dissolution reactions of sulfide minerals; and 3. electrowinning and electrorefining. Emphasis on these subjects will be on improving process efficiency and conserving energy. Papers on the removal and deposition of metals from dilute aqueous solutions for pollution abatement are also welcome.

The publication of a symposium volume is being considered. Suggestions and inquiries should be submitted to the symposium Co-Chairmen: S. Srinivasan, Los Alamos National Laboratory, MS D429, Los Alamos, NM 87545; R. Woods, Commonwealth Scientific and Industrial Research Organization, P.O. Box 124, Port Melbourne, Victoria 3207, Australia; or P. Richardson, U.S. Dept. of Interior, Bureau of Mines, 4900 LaSalle Rd., Avondale, MD.

LUMINESCENCE AND DISPLAY MATERIALS

Luminescence in Biological and Biomedical Applications

This symposium will cover several topics concerned with luminescence in biological applications and the research and development of luminescent materials for use in these same applications. Contributed papers are invited for presentation in sessions to be organized around the following topics: 1. phosphor development and fluorescent lighting in agriculture and plant growth; 2. phosphor development and uses as tracers, *e.g.*, agricultural insecticides and other entomological studies; 3. phosphor development and fluorescent lighting in animal husbandry; 4. phosphor development and fluorescent lighting in suntanning and cosmetics; 5. phosphor development and uses as biological probes; 6. phosphor development and intensification screen development in medical x-ray radiography; 7. phosphor development and fluorescent lighting in medical phototherapeutics, *e.g.*, psoriasis and neonatal hyperbilirubinemia; 8. phosphor development and fluorescent lighting in medical-surgical lighting; and 9. phosphor development and uses in denture technology.

Invited keynote speakers are being planned for some sessions for the purpose of providing overviews of specific topic areas.

Suggestions and inquiries should be sent to the Symposium Chairmen: C. F. Chenot, GTE Products Corp., Hawes St., Towanda, PA 18848 or M. Tecotzky, USR Optonix Inc., P.O. Box 409, Hackettstown, NJ 07840.

Phosphor Screening

This symposium will emphasize properties of phosphors which relate to the performance or fabrication of phosphor containing products such as fluorescent lamps, CRT's, flat panels, and high resolution display tubes.

Examples of subjects for papers might typically include the following: 1. optical properties of phosphors as they pertain to performance, 2. surface properties of phosphors and their relationship to deposition techniques, and 3. novel approaches to deposition such as dry screening.

Also invited are papers on the basic chemistry and physics of materials processing.

Suggestions and inquiries should be sent to the Symposium Co-Chairmen: M. R. Royce, RCA Corp., New Holland Ave., Lancaster, PA 17604 or P. Toch, Raytheon Corp., 465 Centre St., Quincy, MA 02169.

General Session

Papers concerning any aspect of luminescence are invited. Groups of papers will be organized, wherever possible, into the following topics: synthesis or characterization of luminescent materials; luminescent properties of lamp, cathode-ray tube, and x-ray phosphors; organic and organometallic phosphors; lasers; electroluminescence, thermoluminescence, or chemiluminescence; ultraviolet phosphors and lamps; special properties or uses of luminescent materials and luminescence theory.

Phosphor screening and luminescence of biological materials or biological uses of luminescence papers should be submitted to the appropriate special subject symposium. Twenty-five minutes will be allotted for each paper, including discussion. Review or survey papers requiring a longer time will also be considered.

Suggestions and inquiries should be sent to the Symposium Chairmen: G. R. Gillooly, General Electric Co., 1099 Ivanhoe Rd., Cleveland, OH 44110 or W. B. White, 210 Materials Research Laboratory, The Pennsylvania State University, University Park, PA 16802.

Recent News Papers Session

Recent News Papers and Extended Recent News Papers consisting of topics covered by the symposia and sessions being sponsored or cosponsored by the Luminescence and Display Materials Group are invited for presentation.

A special call for Recent News Papers will appear in the January, February, and March 1984 issues of the JOURNAL.

Suggestions and inquiries should be sent to the Session Chairman: T. E. Peters, GTE Laboratories, 40 Sylvan Rd., Waltham, MA 02154.

NEW TECHNOLOGY/ ELECTRODEPOSITION/INDUSTRIAL ELECTROLYTIC

Advance in Pollution Monitoring, Pollution Control, and Metal Abatement in Waste Streams

This symposium will study the changing face of pollution measurement and removal. It will be a forum for discussing new concepts and for considering manufacturing systems which integrate pollution management.

Appropriate topics include the following: 1. electrochemical, membrane, and electromembrane treatment and recovery; 2. new waste treatment/recycle concepts for industrial processes; 3. electrochemical pollution monitoring; 4. new pollutant sensors; and 5. systems which integrate pollution control, monitoring, and recycling with manufacturing.

Both original research papers and reviews of related areas are welcomed.

Suggestions and inquiries should be sent to the Symposium Chairmen: D. D. Snyder, General Motors Corp., Research Laboratories, Electrochemistry Dept., RCEL, Warren, MI 48090 or R. Wilmoth, U.S. Environmental Protection Agency, Cincinnati, OH 45268.

ORGANIC AND BIOLOGICAL ELECTROCHEMISTRY

Biomass Electrochemistry

This symposium will cover electro-organic syntheses of chemicals including fine chemicals from biomass and biomass-derived starting materials. Such starting materials include natural polymers such as cellulose, hemicelluloses, starch, and lignins, as well as chemicals derived from the polymers, such as monomers and derived materials. Electrosyntheses utilizing biomass-derived chemicals such as those contained in essential oils derived from plant materials (*e.g.*, from wood extractives or plant extractives in general) are also an integral part of this symposium. Though major emphasis of the symposium is directed towards synthetic processes. relevant mechanistic papers will also be accepted. Both invited and contributed papers are planned.

Suggestions and inquiries should be sent to the Symposium Co-Chairmen: H. L. Chum, Solar Energy Research Institute, 1617 Cole Blvd., Golden, CO 80401 or J. H. P. Utley, Dept. of Chemistry, Queen Mary College, University of London, Mile End Rd., London E1 4NS, England.

Electro-Organic Synthesis

The main focus of this symposium will be on laboratory scale (up to one lb per day) electrochemical conversions of organic compounds. Pilot-scale studies will be considered. Papers are solicited describing syntheses using direct or indirect electrochemical methods. Topics of special interest include the following: electrochemistry of small molecules, solvated electron reductions, organometallic electrosyntheses, electrosyntheses based on biomass-derived chemicals, electrochemistry of coal, use of new electrode materials, process variable effects, mechanistic aspects, and electroinitiated polymerizations.

Suggestions and inquiries should be sent to the Symposium Co-Chairmen: N. L. Weinberg, Electrosynthesis Co., Inc., P.O. Box 16, East Amherst, NY 14051 or S. J. Pietsch, Amoco Chemicals Corp., P.O. Box 400, Naperville, IL 60566.

Redox Mechanisms and Interfacial Properties of Molecules of Biological Importance. II

This symposium will present papers dealing with the applications of electrochemical and allied techniques to elucidate the redox chemistry and/or interfacial properties of naturally occurring biomolecules and related model systems. Furthermore, papers will be presented, and are solicited, concerned with newly developed techniques which might be employed to help obtain mechanistic information concerning the redox and interfacial behaviors of biomolecules. Finally, it is hoped to obtain papers dealing with the application and development of electrochemical techniques for the analysis of biomolecules. Both invited and contributed papers are planned.

Publication of a proceedings volume for the symposium is being considered. Suggestions and inquiries should be sent to G. Dryhurst, Dept. of Chemistry, University of Okalahoma, Norman, OK 73019.

General Session

Suggestions and inquiries should be sent to the Session Chairman: J. H. Wagenknecht, Monsanto Co., 800 North Lindbergh Blvd., St. Louis, MO 63166.

PHYSICAL ELECTROCHEMISTRY

Ultramicroelectrodes

This symposium will cover all aspects of electrochemical behavior at ultramicroelectrodes, including kinetics, mass transport, fabrication, and experimental applications. Work with single electrodes or with arrays of electrodes is of interest.

Suggestions and inquiries should be sent to the Symposium Co-Chairmen: R. Mark Wightman, Dept. of Chemistry, Indiana University, Bloomington, IN 47405 or L. R. Faulkner, Dept. of Chemistry, University of Texas, Austin, TX 78712.

General Session

Papers concerning any aspect of physical electrochemistry not included in the topic areas of the symposia are welcome.

Suggestions and inquiries should be sent to the Session Chairman: L. R. Faulkner, Dept. of Chemistry, University of Texas, Austin, TX 78712.

PHYSICAL ELECTROCHEMISTRY/ BATTERY/INDUSTRIAL ELECTROLYTIC

Separators and Membranes

This symposium will focus on a wide spectrum of topics on separators and membranes. Of particular interest are the fundamental studies of these materials and their applications to battery systems and industrial electrolytic, separation, and recovery processes. Papers are solicited on the following topics: 1. synthesis and fabrication of separators and membranes; 2. structure and properties of separators and membranes; 3. transport phenomena in ion selective membranes; 4. performance of separators in batteries and fuel cells; 5. theories and practices in industrial membrane processes such as chlor-alkali membrane cells, electrodialysis, Donnan dialysis, and others; and 6. modeling and optimization studies.

Publication of a proceedings volume is being planned. Suggestions and inquiries should be sent to one of the Symposium Co-Chairmen: D. N. Bennion, Dept. of Chemical Engineering, 350 CB, Brigham Young University, Provo, UT 84602; P. K. Ng, General Motors Corp., Research Laboratories, Electrochemistry Dept., Warren, MI 48090-9055; or R. S. Yeo, Pinnacle Research Institute, 10432 North Tantau Ave., Cupertino, CA 95014.

PHYSICAL ELECTROCHEMISTRY/ CORROSION/BATTERY/ENERGY TECHNOLOGY/HIGH TEMPERATURE MATERIALS

In Situ Nonelectrochemical Techniques for the Study of Electrode Reactions

Papers are solicited which are concerned with nonelectrical methods of studying surface processes. These techniques include, but are not limited to, ellipsometry, vibrational spectroscopy (IR, FTIR, Raman, SERS, etc.), and various related spectroscopy techniques. Sessions will be organized around the following topics: 1. electrolyte studies, including complex formation, kinetics, and equilibria in aqueous, nonaqueous, and molten salt solvents; 2. the detection and characterization of transient species, especially by means of pulsed laser, to observe time-resolved Raman scattering; 3. studies of the composition and structure of surface films on metals by infrared (FTIR) and Raman as related to corrosion problems and electrocatalysis; and 4. advanced techniques are applied to electrochemical problems such as surface-enhanced laser Raman scattering, coherent anti-Stokes Raman scattering (CARS), resonance Raman scattering, and computer-controlled data acquisition and manipulation.

The publication of a proceedings volume is being considered. Parties interested in submitting complete manuscripts should indicate this interest on the abstract presentation form. The deadline for receipt of complete manuscripts is March 1, 1984.

Suggestions and inquiries should be sent to the Symposium Co-Chairmen: P. N. Ross, Materials and Molecular Research, Lawrence Berkeley Laboratory, Berkeley, CA 94720; R. H. Heidersbach, School of Chemical Engineering, Oklahoma State University, Stillwater, OK 74078; or W. A. Adams, Dept. of National Defense, Defense Research, Energy Conv. Div., Ottawa, Ont., Canada K1A 0Z4.

New Deadline—Extended Abstracts must be submitted with the 75-Word Abstract by December 1, 1983.

75-Word Abstract Form

(New Deadline—Extended Abstracts must be submitted with the 75-Word Abstract by December 1, 1983)

CINCINNATI, OHIO, MEETING—MAY 6-11, 1984

Submit to: The Electrochemical Society, Inc.
10 South Main Street, Pennington, NJ 08534-2896

Abstract No. .....
(to be assigned by the Society)

Schedule for .....
(Title of Symposium)

Sponsored by .....
(Division/Group)

Title of paper .....

.....

Authors (Underline name of author presenting paper.) .....

.....

Business affiliation and address .....

.....

.....
(State or Country) (ZIP Code) (Telephone No.)

(Type abstract in this area—double-spaced.)

Do you require any audiovisual equipment?
☐ **35 mm (2 x 2 in.) slide projector**
☐ **Vu-Graph**
☐ **other (specify)**
Is a full length paper on this work to be submitted for Society Journal publication?
☐ **Yes** ☐ **No**

Papers presented before a Society technical meeting become the property of the Society and may not be published elsewhere without written permission of the Society. Papers presented at Society technical meetings must be authored by a member or sponsored by an active member.

.....
Insert name of Society member author or sponsor

This form should accompany your Extended Abstract.

THE ELECTROCHEMICAL SOCIETY PATRON MEMBERS

Bell Laboratories
Murray Hill, NJ

Dow Chemical Co.
Inorganic Chemicals Dept.
Midland, MI

ELTECH Systems Corp.
Chardon, OH

Exxon Research and Engineering Co.
Corporate Research
Advanced Energy Systems Laboratory,
Materials and Catalysis Sciences Laboratory
Linden, NJ
Technology Department
Chemical Engineering Technology Div.
Materials Technology Div.
Florham Park, NJ

General Electric Co.
Battery Business Dept., Gainesville, FL
Chemical Laboratory, Knolls Atomic Power Laboratory,
Schenectady, NY
Lamp Div., Cleveland, OH
Materials & Process Laboratory, Large Steam
Turbine-Generator Dept., Schenectady, NY
Research and Development Center,
Inorganic Materials Laboratory
Schenectady, NY

General Electric Co. (continued)
Signal Processing & Communication Laboratory,
Schenectady, NY
Semiconductor Products Dept.,
Syracuse, NY

International Business Machines Corp.
New York, NY

INCO Research and Development Center
Suffern, NY

Olin Corp.
Chemicals Div.
Charleston Technology Center
Charleston, TN

Philips Research Laboratories
Eindhoven, The Netherlands

Tadiran, Israel Electronics Industries, Ltd.
Tel Aviv, Israel

Westinghouse Electric Corp.
Electronic Tube Div., Elmira, NY
Lamp Div., Bloomfield, NJ
Semiconductor Div., Youngwood, PA
Research Laboratories, Pittsburgh, PA

THE ELECTROCHEMICAL SOCIETY SUSTAINING MEMBERS

The Aerospace Corp.
Los Angeles, CA

Airco Industrial Gases
Murray Hill, NJ

Allen Clark Research Centre
Plessey Research (Caswell) Ltd.
Towcester, Northants, England

Allied Corporation
C&D Batteries,
Plymouth Meeting, PA
Prestolite Div., Toledo, OH
Syracuse Research Laboratories,
Solvay, NY

Aluminum Co. of America
New Kensington, PA

AMAX Inc.
Greenwich, CT

AMP Inc.
Harrisburg, PA

Analog Devices, Inc.
Norwood, MA

Applied Materials, Inc.
Santa Clara, CA

ASARCO, Inc.
South Plainfield, NJ

Battelle Memorial Institute
Columbus, OH

Battery Technology Co.
A Division of Duracell International
Tarrytown, NY (2 memberships)

Bell-Northern Research
Ottawa, Ont., Canada

Boeing Co.
Seattle, WA

The Borg-Warner Corp.
Roy C. Ingersoll Research Center
Des Plaines, IL

BP Research Centre
Middlesex, England

Brown, Boveri & Co., Ltd.
Research Center
Baden, Switzerland

C-I-L Inc.
Industrial Chemicals Div.
Montreal, Que., Canada

Comdial Semiconductor, Inc.
Sunnyvale, CA

Cominco Ltd.
Trail, B.C., Canada

Corning Glass Works
Corning, NY

Crawford & Russell Inc.
Stamford, CT

CSIRO Division of Mineral Chemistry
Port Melbourne, Victoria, Australia

Diamond Shamrock Corp.
Painesville, OH

Duro-Test Corp.
North Bergen, NJ

Eagle-Picher Industries, Inc.
Electronics Div.
Joplin, MO

Eastman Kodak Co.
Rochester, NY

EG&G Princeton Applied Research Corp.
Princeton, NJ

Electric Power Research Institute
Palo Alto, CA

Electrochemical Technology Corp.
Seattle, WA

Energy Development Associates
A Gulf and Western Co.
Madison Heights, MI

Ever Ready Co. (Holdings) Ltd.
Whetstone, London, England

Exmet Corp.
Bridgeport, CT

SUSTAINING MEMBERS (CONTINUED)

Fairchild Camera & Instrument Corp.
Research & Development Laboratory
Palo Alto, CA

FMC Corp.
Inorganic Chemicals Div.
Buffalo, NY

Ford Motor Co.
Dearborn, MI

The Gates Corporation
Denver, CO

General Motors Corp.
Delco-Remy Div., Anderson, IN
Research Laboratories Div.
Warren, MI

Gould Inc.
Gould Research Center
Rolling Meadows, IL

Grelcon, Inc.
Niagara Falls, NY

GTE Laboratories
Waltham, MA

GTE Sylvania Inc.
Chemical & Metallurgical Div.
Towanda, PA

The Harshaw Chemical Co.
Cleveland, OH

Heliotronic GmbH
Burghausen, Germany

Hewlett Packard Co.
Loveland, CO

Hewlett Packard Laboratories
Palo Alto, CA

Hill Cross Co., Inc.
West New York, NJ

Hitachi, Ltd.
Central Research Laboratory
Tokyo, Japan

Hoechst-Uhde Corp.
Englewood Cliffs, NJ

Honeywell, Inc.
Power Sources Center
Horsham, PA

Hughes Research Laboratories
Div. of Hughes Aircraft Co.
Malibu, CA

IMI Marston Limited
Wolverhampton, England

Imperial Clevite, Inc.
Technology Center
Cleveland, OH

INCO ElectroEnergy Corp.
Engineering & Development Center
Ray-O-Vac Corp.
Madison, WI

International Lead Zinc Research Organization, Inc.
New York, NY

International Minerals and Chemical Corp.
Electrochemical Div.
Orrington, ME

Johnson Controls, Inc.
Milwaukee, WI

Kaiser Aluminum & Chemical Corp.
Pleasanton, CA

KBI
a division of Cabot Corp.
Boyertown, PA

Arthur D. Little, Inc.
Cambridge, MA

Lockheed Missiles & Space Co., Inc.
Research Laboratory
Palo Alto, CA

Marathon Battery Co.
Waco, TX

Mead Advanced Systems Research and Development Laboratories
Dayton, OH

Medtronic Energy Technology
Minneapolis, MN

Mepco/Electra, Inc.
Columbia, SC

Microwave Associates, Inc.
Burlington, MA

Molycorp, Inc.
New York, NY

Monsanto Co.
St. Louis, MO

Motorola Inc.
Phoenix, AZ

M&T Chemicals Inc.
Detroit, MI

NIFE Jungner AB
Oskarshamn, Sweden

Noranda Research Centre
Pointe Claire, Que., Canada

Occidental Chemical Corporation
Research & Development
(2 memberships)
Grand Island, NY
Udylite/Sel-Rex
Warren, MI

Occidental Research Corp.
La Verne, CA

Olin Corp.
Metals Research Laboratories
New Haven, CT

Owens-Illinois Inc.
Toledo, OH

Perkin-Elmer Corp.
Norwalk, CT

Phelps Dodge Refining Corp.
Maspeth, NY

Philips Laboratories, Inc.
Briarcliff Manor, NY

PPG Industries, Inc.
Chemical Div.
Pittsburgh, PA

Prototech Co.
Newton Highlands, MA

Public Service Electric and Gas Co.
PSE&G Research Corp.
Newark, NJ

RCA Corp.
Color Picture Tube Div.
Lancaster, PA

Reynolds Metals Co.
Reduction Research Div.
Sheffield, AL

Rockwell International
El Segundo, CA

SAFT America, Inc.
Power Sources Division,
Valdosta, GA
Advanced Battery Systems Division,
Cockeysville, MD

Sandia National Laboratories
Albuquerque, NM

Sanyo Electric Co., Ltd.
Shioya Research Center
Kobe, Japan

J. C. Schumacher Co.
Oceanside, CA

Shipley Company, Inc.
Newton, MA

Siemens Aktiengesellschaft
Munich, Germany

Signetics Corp.
Sunnyvale, CA

Siltec Corp.
Menlo Park, CA

Sperry Research Center
Sudbury, MA

Sprague Electric Co.
North Adams, MA

Standard Telecommunication Laboratories Ltd.
Essex, England

Stauffer Chemical Co.
Dobbs Ferry, NY

St. Joe Minerals Corp.
Monaca, PA

Tektronix, Inc.
Beaverton, OR

Teletype Corp.
Skokie, IL

Texas Instruments Inc.
Attleboro, MA
Dallas, TX

Tokyo Shibaura Electric Co., Ltd.
Toshiba Research and
Development Center
Kawasaki, Japan

Toyota Central Research and Development Labs, Inc.
Nagoya, Japan

Union Carbide Corp.
Battery Products Div.,
Corporate Research Dept.
New York, NY

United States Steel Corp.
Research Laboratory
Monroeville, PA

Varian Associates
Palo Alto, CA

Wacker Chemitronic
Burghausen, Germany

Western Electric
Princeton, NJ

Xerox Corp.
Webster Research Center
Rochester, NY

Yardney Electric Corp.
Pawcatuck, CT

Yuasa Battery Co., Ltd.
Osaka, Japan